Transactions of the ASME

Technical Editor
G. K. SEROVY
Associate Technical Editors
Advanced Energy Systems
M. J. MORAN
Environmental Control
H. E. HESKETH
Fuels and Combustion Technologies
D. W. PACER
Gas Turbine
T. H. OKIISHI
Internal Combustion Engine
J. A. CATON
Nuclear Engineering
S. M. CHO
Power
R. W. PORTER

BOARD ON COMMUNICATIONS
Chairman and Vice-President
R. NICKELL

Members-at-Large
W. BEGELL
T. F. CONRY
M. FRANKE
R. L. KASTOR
M. KUTZ
R. MATES
T. C. MIN
E. M. PATTON
R. D. ROCKE
F. W. SCHMIDT
W. O. WINER
A. J. WENNERSTROM
B. ZIELS

President, C. O. VELZY
Executive Director,
D. L. BELDEN
Treasurer, ROBERT A. BENNETT

PUBLISHING STAFF
Mng. Dir., Publ.,
CHARLES W. BEARDSLEY
Managing Editor,
CORNELIA MONAHAN
Sr. Production Editor,
VALERIE WINTERS
Editorial Prod. Asst.,
MARISOL ANDINO

Transactions of the ASME, Journal of Turbomachinery (ISSN 0889-504X) is published quarterly (Jan., Apr., July, Oct.) for $100 per year by The American Society of Mechanical Engineers, 345 East 47th Street, New York, NY 10017. Second-class postage paid at New York, NY and additional mailing offices. POSTMASTER: Send address change to Transactions of the ASME, Journal of Turbomachinery, c/o The AMERICAN SOCIETY OF MECHANICAL ENGINEERS, 22 Law Drive, Box 2300, Fairfield, NJ 07007-2300.

CHANGES OF ADDRESS must be received at Society headquarters seven weeks before they are to be effective. Please send old label and new address.

PRICES: To members, $29.00, annually; to nonmembers, $100.00. Add $15.00 for postage to countries outside the United States and Canada.

INDEXED by Applied Mechanics Reviews and Engineering Information, Inc.

Journal of Turbomachinery

Published Quarterly by The American Society of Mechanical Engineers

VOLUME 111 • NUMBER 3 • JULY 1989

TECHNICAL PAPERS

ANNOUNCEMENTS

S. M. Miner
Senior Engineer,
Westinghouse Electronic Systems Group,
Baltimore, MD 21203

R. J. Beaudoin
Research Assistant.

R. D. Flack
Professor.

Department of Mechanical and
Aerospace Engineering,
University of Virginia,
Charlottesville, VA 22901

Laser Velocimeter Measurements in a Centrifugal Flow Pump

A laser velocimeter was used to measure velocities within the impeller and volute of a centrifugal pump. Measurements were made at four circumferential and eight radial positions. Flow rates ranged from 40 to 105 percent of design flow. Blade-to-blade profiles for the four circumferential positions indicate the flow is circumferentially asymmetric around the pump even at the design flow. Blade-to-blade profiles show normal blade loading for 90 percent of the impeller, with reverse and zero loading occurring in the outer 10 percent of the impeller for design flow. Reversed blade loading over greater portions of the impeller is seen at off-design flow. At 40 percent of design flow, recirculating flow within the impeller was found. Axial traverses across the impeller show the radial velocity profile skewed toward the hub surface at the inlet and away from the hub surface at the exit. The stagnation point on the tongue moved from the outside to the inside as the flow rate was increased from 40 to 105 percent of design. Values for slip range from 0.96 to 0.71 from the inlet to the exit.

Introduction

Understanding and predicting the hydraulic and dynamic characteristics of centrifugal pumps requires detailed knowledge of the flow field. Even at design flow the interaction between the impeller and volute is significant, taking the form of asymmetries in the flow field. This paper presents measurements of the flow field in the impeller and volute of a laboratory centrifugal pump. These data detail the asymmetries in the flow, and the flow in the immediate vicinity of the tongue.

Early work on the flow in pump impellers was done by Fischer and Thoma (1932). They used die injection as a means of visualizing the flow in an impeller. The impeller discharged into a symmetric collector. For flows above 40 percent of design the flow pattern remained symmetric. Below 40 percent of design flow recirculating flow among the blade passages was seen.

Beveridge and Morelli (1950), Acosta (1954), and Acosta and Bowerman (1957) performed studies on a series of two-dimensional impellers operating in a symmetric collector. These studies measured the pressure distribution along the blades. For flows at and near design no separation was seen. Results indicated that about half of the impeller losses occurred at the inlet. These losses could be reduced if a more uniform inlet flow could be provided. These researchers also noted the recirculating phenomena seen by Fischer and Thoma.

Howard and Kittmer (1975) used hot-wire anemometry and hydrogen bubble flow visualization to investigate a shrouded impeller and an unshrouded impeller. Both impellers discharged into axisymmetric collectors. The impellers had backward swept blades and neither impeller showed signs of separation.

With the advent of laser velocimetry, a nonintrusive means of measuring velocity fields became available. Eckardt (1976, 1979) used the Laser-2-Focus method to take data in radially bladed and backward swept bladed centrifugal compressors. In both cases the impellers discharged into diffusers that did not distort the impeller flow. Results showed that the velocity profile in the backward swept impeller was not as prone to separation and was more uniform at the exit.

Adler and Levy (1979) and Howard et al. (1980) used a laser-Doppler velocimeter to measure the flow in shrouded, backswept impellers. In both studies the discharge was designed not to distort the flow within the impeller. The backswept impellers showed no evidence of separation. In addition, as the fluid approached the exit, the high-velocity flow shifted from the suction side to the pressure side of the blade.

Binder and Knapp (1936) took pressure and velocity data in the volutes of two centrifugal pumps. Their results showed that the radial velocities and the static pressures around the volute were nonuniform. These nonuniformities were present even at design flow.

Iverson et al. (1960) measured both the pressure distribution in the volute and the radial force on the impeller of a centrifugal pump. This study showed a nonuniform static pressure distribution and a force imbalance at design flow.

The effect of the volute on pump performance was studied by Bowerman and Acosta (1957) and Hira and Vasandani (1975). These studies showed that volute geometry has a direct effect on performance. This effect comes primarily from a nonuniform distribution of pressure and radial velocity around the impeller.

Thomas et al. (1986) used laser velocimetry (LV) to measure the velocities within the logarithmic spiral volute of a laboratory centrifugal pump. A swirl generator was used to

Contributed by the International Gas Turbine Institute and presented at the 33rd International Gas Turbine and Aeroengine Congress and Exhibition, Amsterdam, The Netherlands, June 5-9, 1988. Manuscript received by the International Gas Turbine Institute January 7, 1988. Paper No. 88-GT-95.

replace the impeller. Flows of 121 and 160 percent of design were simulated. In both cases the circumferential distribution of radial flow was nonuniform.

The studies listed above have taken data in impellers with axisymmetric flows at the exit or have taken data only in the volute. Other researchers have collected data for impellers operating in volutes.

Mizuki et al. (1971) and Murakami et al. (1980) measured pressures and velocities within single-blade passages of centrifugal impellers operating in volutes. However, no measure of the circumferential variation in flow was presented.

Hamkins and Flack (1987) used a two-directional laser velocimeter to measure the velocities in an unshrouded impeller and a shrouded impeller. Both impellers were 12.7 mm thick and were operated in a logarithmic spiral volute. Data were also taken at one radius just outside the impeller exit. Results showed that the flow was asymmetric, even at design flow. The asymmetries worsened as the flow rate differed from the design flow.

Brownell et al. (1985) used streak photography to measure streamlines in the tongue region of a centrifugal process pump. This pump was approximately the same geometric size, capacity, and specific speed as the idealized pump as used by Thomas et al. (1986) and Hamkins and Flack (1987). Comparison of the data (Thomas et al., 1986; Hamkins and Flack, 1987; Brownell et al., 1985) indicates that the laboratory pump operates with the same characteristics in the tongue region at design and off-design conditions.

Kannemans (1980) used a laser-Doppler velocimeter to measure the velocity field in a radial impeller operating in a volute. Data were collected in the impeller and just outside the impeller, for one circumferential position. Circumferential variations were not considered.

As summarized by the work listed here, much of the previous work in this field has focused on the impeller or the volute separately. Those studies that have used impellers operating in the volute have concentrated on the impeller. The previous work has clearly demonstrated that the asymmetries found in impeller flows are due to the interaction between the impeller and volute. When an impeller has been operated without a volute or with a symmetric discharge region, asymmetries in the impeller flow have not been measured. However, in the case of an impeller–volute combination, circumferential variation in the impeller flow field is frequently detected. Whether the flow has been above, below, or at design, these asymmetries have been measured. Therefore, in order to understand the flow in centrifugal pumps better both the impeller and volute are considered together.

The present work seeks to bridge the two components by providing measurements in both the impeller and volute for the same operating conditions. The data herein lend insight to the complex flow within the impeller and its interaction with the volute. The data can also be used for verification of ongoing computational predictions of internal flows.

The particular objectives of the present work are to make detailed velocity measurements with a two-directional LV in both the volute and impeller of a centrifugal pump. Design and off-design conditions are studied. Blade-to-blade velocity profiles were to be measured for both radial and tangential velocities. These were to be obtained at different circumferential positions around the pump. Axial traverses were also to be made. The pump is similar to that used by Hamkins and Flack (1987), except the passage thickness was increased to increase the specific speed of the pump.

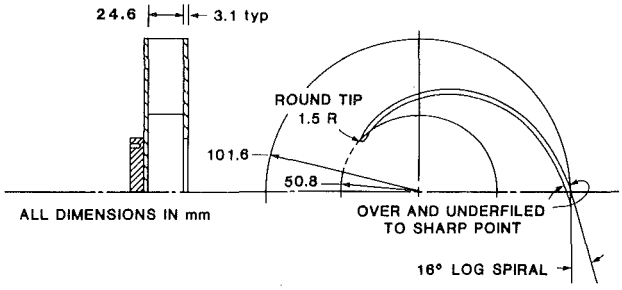

Fig. 1 Impeller geometry

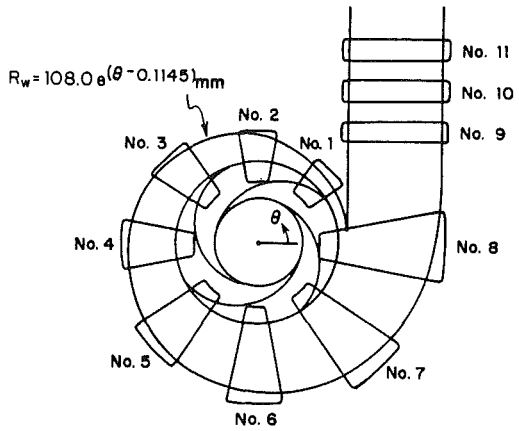

Fig. 2 Volute and window locations

Experimental Apparatus

Pump. The pump used for this study is documented by Hamkins and Flack (1987) and Lanes (1982). However, the flow width (b) has been increased from 12.7 mm to 24.6 mm. The specific speed of the pump studied by Hamkins and Flack was 1114 US Units. With the increased passage thickness the specific speed is now 1583. The design flow coefficient is 0.063, which is the same as that of Hamkins and Flack (1987). The impeller and volute geometry are shown in Figs. 1 and 2. The impeller has a four-bladed geometry with 16 deg logarithmic spiral blades. The volute is also a logarithmic spiral with an 83 deg angle. The location of windows for the laser velocimeter measurements is shown in Fig. 2. The pump is constructed of Plexiglas. The casing walls are 50.8 mm thick. However, in the windows the thickness is reduced to 9.5 mm, to facilitate the use of the laser velocimeter.

The flow loop is shown in Fig. 3. This is closed-loop system fed from a 2000 liter reservoir tank. The flow straighteners in the 76.2-mm-dia pipe upstream of the pump inlet provide a swirl free inlet flow to the pump. Static pressure taps are

Nomenclature

b = passage width
$\tilde{C}_\theta$ = mass-averaged absolute tangential velocity
C_r = absolute radial velocity
h_o = slip factor
n = number of blades
Q = flow rate through pump
r = radius
r_2 = outer impeller radius
R_w = volute radius
t = blade thickness
U_2 = impeller peripheral speed
W_θ = relative (to impeller) tangential velocity
z = axial position from centerline
β = blade angle
ϵ = vane blockage factor
θ = circumferential position

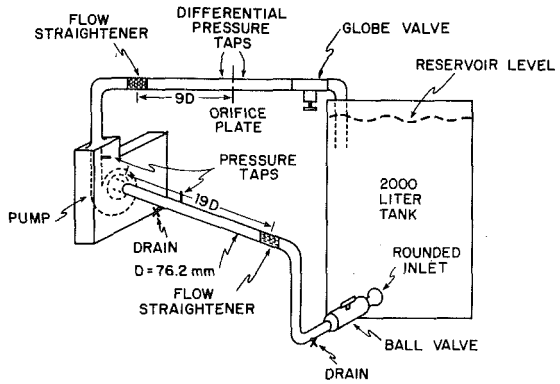

Fig. 3 Flow loop

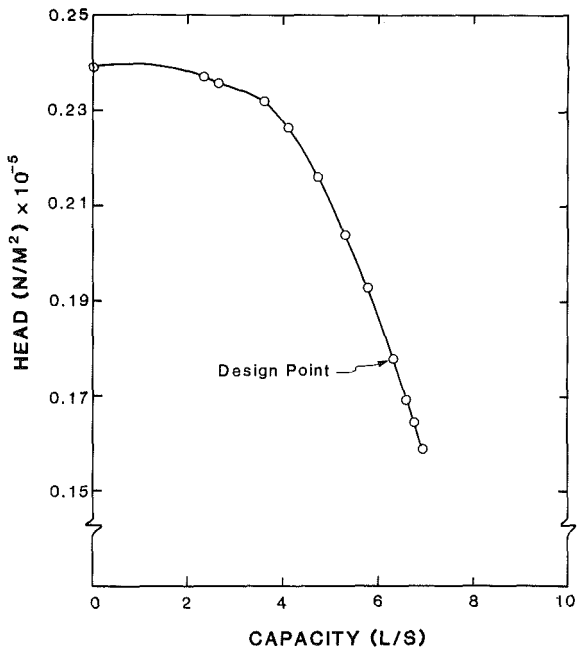

Fig. 4 Pump head-capacity curve

located 5 pipe diameters upstream of the impeller inlet and just beyond window 11 in the discharge. The second flow straightener, 9 pipe diameters upstream of the orifice flow meter, conditions the flow through the orifice plate. The globe valve is used to adjust the flow. Running speed for the pump is 620 rpm. The head-capacity curve is shown in Fig. 4. The design point for the present pump design is 6.3 L/s at 0.178×10^5 N/m^2. This design point is based on an estimate of the impeller–volute matching point. The matching point is the condition that causes the average angular momentum of the flow at the impeller exit to equal the average angular momentum in the throat of the volute. The volute throat is the section of the volute through which the entire pump capacity passes.

LV. The laser and optics for this system are shown in Fig. 5. The system is three-beam frequency shifted, and operated in the forward scatter mode. The Bragg cell performs the dual functions of beam separation and frequency shifting. A single primary beam enters the cell and the primary beam and an orthogonal grid of secondary beams emerge. However, only three of the beams are used, the primary beam and two secondary beams. The secondary beams are shifted by different frequencies. These three beams form a 90 deg angle. Therefore, when the beams are focused and crossed at the

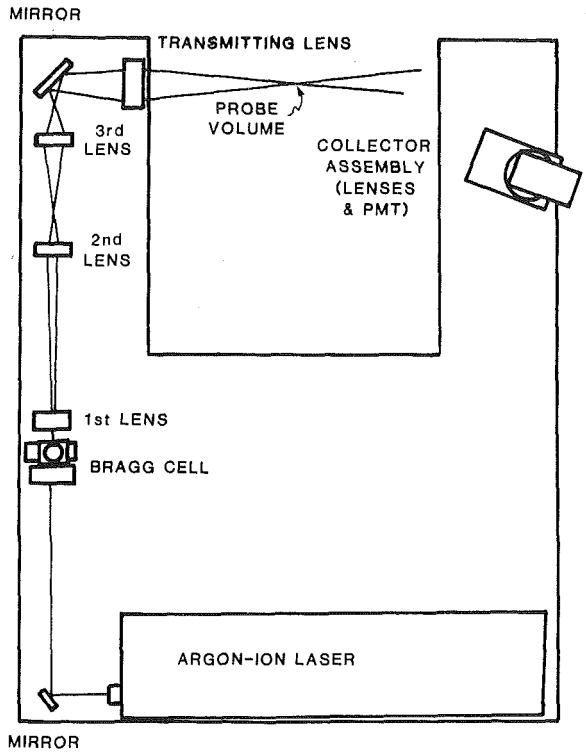

Fig. 5 LV system

probe volume, two sets of perpendicular interference fringes are created. These two sets of fringes allow the simultaneous measurement of two orthogonal components of velocity. The entire optical system was mounted on a three-directional traversing mechanism with digital position readouts. The probe volume was easily and accurately moved in the x, y, and z directions with this mechanism.

The frequency of light scattered from the probe volume determines the velocity. Light was scattered by naturally occurring particles in the water. The water was filtered, using a taste and odor filter. This provided particles of 5 μm and smaller. Two burst-type signal processors with adjustable threshold and five/eight count comparison with adjustable tolerances were used. Signals from both sets of beams are checked for coincidence. If the signals occur at the same time then they are considered valid. Once a valid signal is generated, the impeller angular position is recorded with a shaft encoder. The encoder divides each revolution into 256 parts. The two velocity signals and the shaft position are then recorded onto floppy disks by a dedicated microcomputer.

Procedure. A typical test had 5000 data points, roughly 20 for each of the 256 "shaft angle bins." This gave velocity and angular position data for the four blade passages. These four passages were then averaged together to give passage-averaged results. It is the passage-averaged results that are presented in this paper. This passage averaging is possible because of the fourfold symmetry of the impeller.

The uncertainty in probe volume position was 0.5 mm radially and 1 mm axially. The uncertainty in the angular position was 0.30 deg. The uncertainty in the angular orientation of the probe volume fringes with respect to the reference axes was 0.85 deg. This was the dominant factor in flow direction uncertainty. The typical uncertainty in the radial velocity component was 0.06 m/s and the typical uncertainty in the tangential velocity component was 0.06 m/s. These velocity uncertainties do not include the effect of positional uncertainty in the presence of velocity gradients. The position of the probe

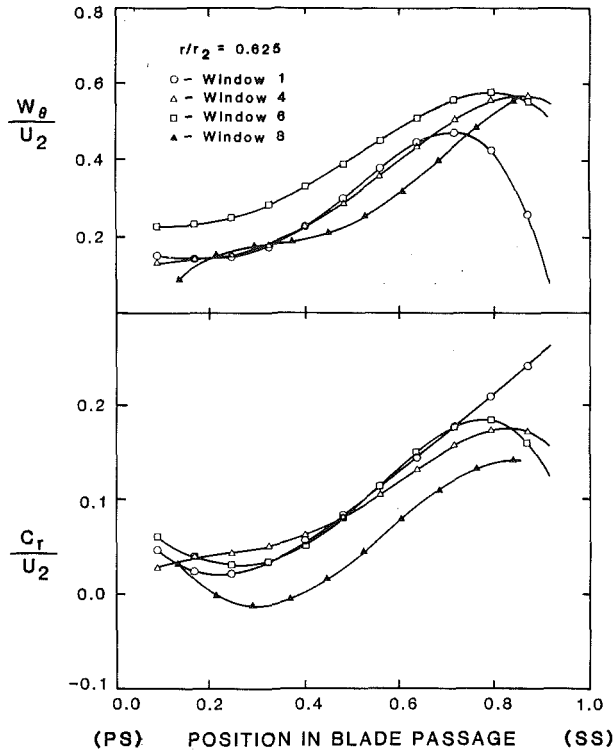

Fig. 6 Impeller velocity profiles; $r/r_2 = 0.625$

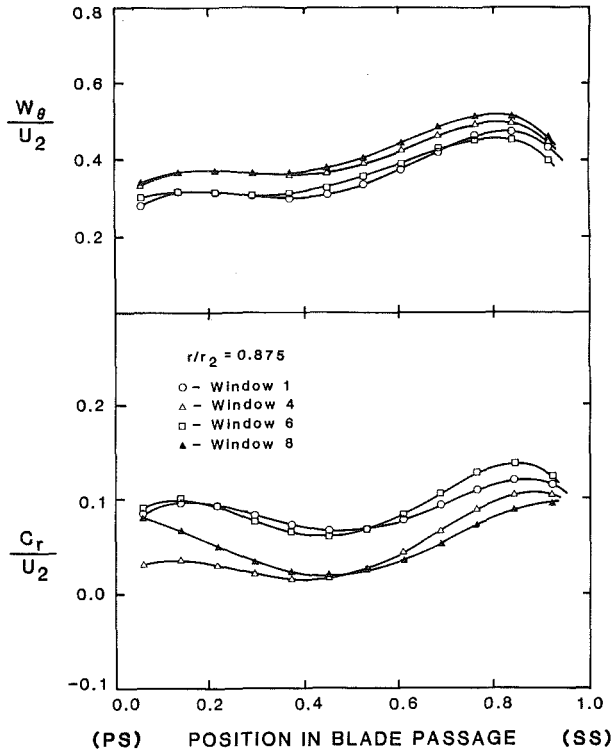

Fig. 7 Impeller velocity profiles; $r/r_2 = 0.875$

volume is uncertain, particularly in the axial direction. Since spatial velocity gradients are present, a misplaced probe volume will measure the incorrect velocity. This spatial uncertainty results in a total uncertainty of 0.10 m/s for the radial velocity and 0.10 m/s for the tangential velocity.

Results

Experimental data for this study were taken in windows 1, 4, 6, and 8. For each window, data were taken at five radial positions within the impeller. Volute data in window 1 were taken at only one radial position; data at four radial volute positions were measured in the other three windows. These data were taken at the axial centerline of the pump at the design flow of 6.3 L/s. In addition, data for five flow rates were taken in window 6 at the axial centerline. Axial traverses were performed for the impeller in window 6 and for the volute in window 4. Finally, data for nine points around the tongue were taken at five flow rates. Representative results are presented here and are nondimensionalized by the impeller tip velocity. Results are presented in the form of fourth-order polynomial least-squares curve fits to the average velocity data profiles. Complete presentation and discussion of the results are presented by Miner (1988).

Figures 6 through 9 are comparisons of the blade-to-blade nondimensional velocity profiles in the impeller around the pump at a constant radius. These are plots of axial centerline data at design flow. At a radius ratio of 0.625, the nondimensional radial velocity profiles are skewed toward the blade suction surface. The profiles measured in windows 1, 4, and 6 are similar in shape and magnitude, while the nondimensional profile in window 8 falls approximately 0.046 below the others in the central portion of the passage span. Even with the nondimensional experimental uncertainty of ± 0.015 considered, the window 8 profile falls below the other three. Tangential velocity profiles show little turning is done from 60 deg to the suction surface. The window 6 profile shows the lowest level of turning across the passage of the four circumferential positions tested.

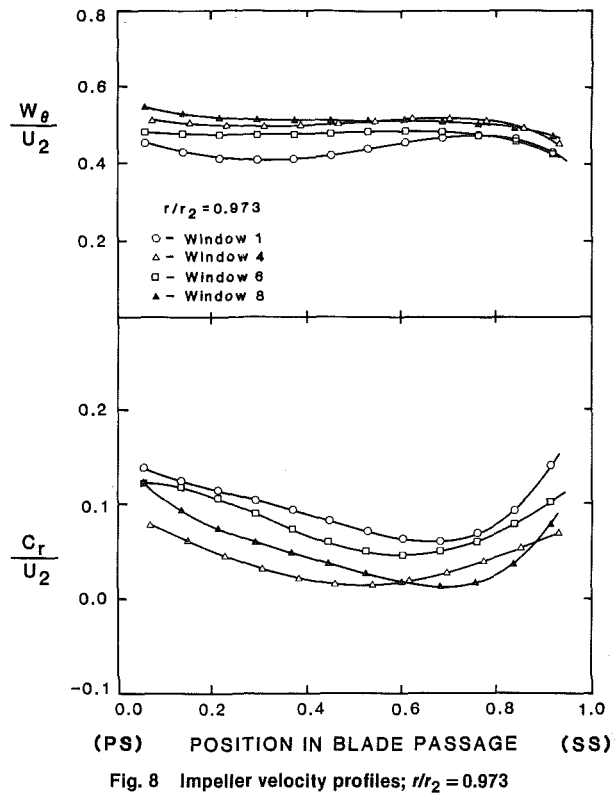

Fig. 8 Impeller velocity profiles; $r/r_2 = 0.973$

At $r/r_2 = 0.875$ two distinct levels of profiles were measured. The window 1 and 6 radial and tangential profiles are alike as are the profiles of windows 4 and 8. The window 1 and 6 profiles contain substantially higher radial and turning velocities than the profiles of windows 4 and 8, and are on the order of 0.061 for the nondimensional tangential velocity and 0.046 for the nondimensional radial velocity.

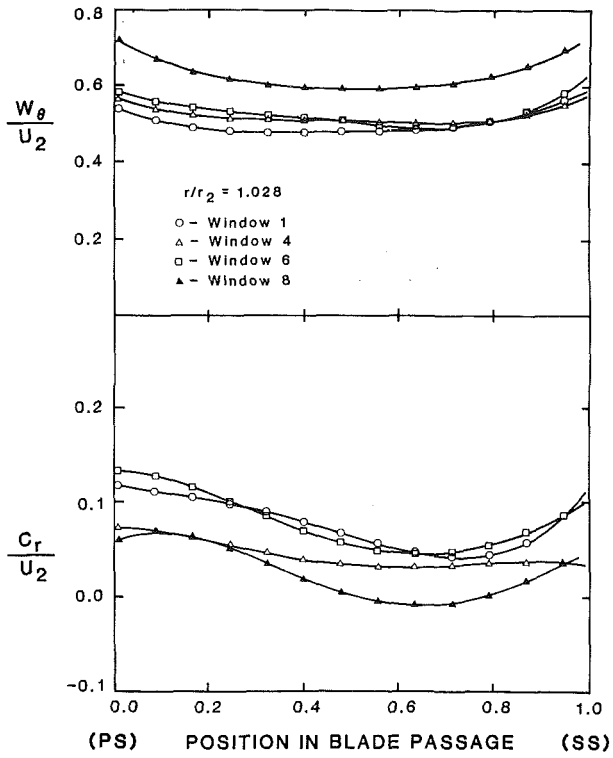

Fig. 9 Volute velocity profiles; $r/r_2 = 1.028$

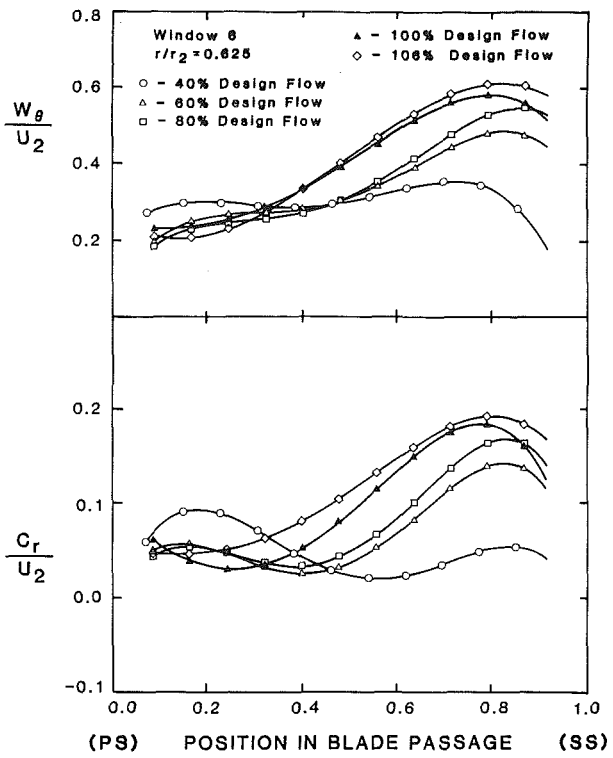

Fig. 11 Impeller flow rate studies; $r/r_2 = 0.625$

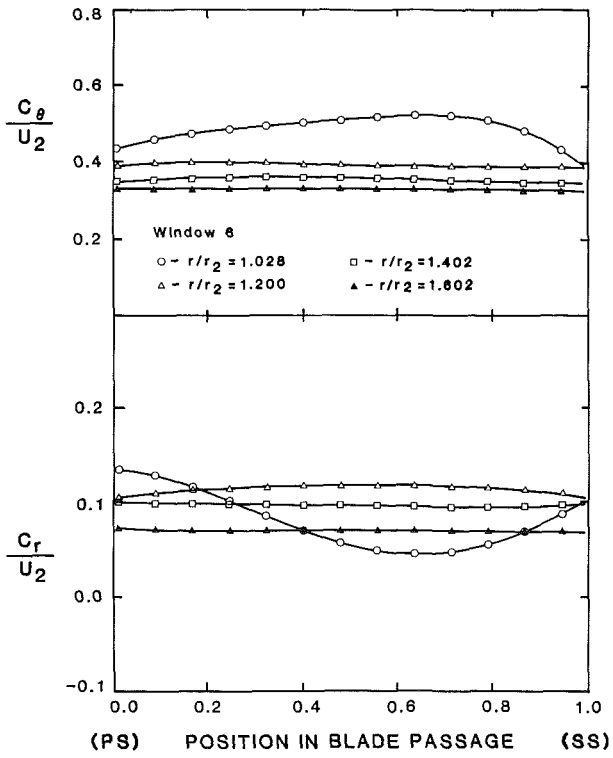

Fig. 10 Volute velocity profiles, window 6

At radius ratios of 0.973 and 1.028, just inside and outside of the impeller exit, the turning velocities are seen to decrease around the circumference of the impeller from window 1 to window 8. The differences are not uniform across the passage as the profiles tend to intersect one another in the region from 60 deg to the suction surface. The radial velocity profiles do not vary in a systematic way as do the tangential profiles.

These variations in the profiles imply that the momentum flux around the impeller is not symmetric. This asymmetry will produce a nonzero radial force on the impeller. Therefore, even at design flow there will be a radial unbalance force acting on the impeller. Figure 8 shows the asymmetry around the impeller at the radius immediately inside the impeller exit.

Another aspect of the pump performance that can be seen in Figs. 6 through 8 is the variation in the blade loading as a function of radius. Blade loading is the difference in the pressure acting on the pressure and suction surfaces of a blade. This pressure difference is directly related to the difference in the magnitude squared of the relative velocity, from the pressure surface to the suction surface of the blade. A positive loading has the relative velocity increasing from the pressure surface to the suction surface. When the blade loading is positive the blades are transmitting energy to the fluid by doing work on the fluid. This is the case in Figs. 6 and 7. However, Fig. 8 shows the relative velocity decreasing from the pressure surface to the suction surface, implying that the last 5 percent of the blade is unloaded and does not transmit energy to the fluid. Overall, trends in the impeller are similar to those found by Hamkins and Flack (1987).

Typical data for the volute are shown in Fig. 10. The data are for window 6 and for locations $(r-r_2)/(R_w-r_2) = 0.03$, 0.25, 0.50, and 0.75. An interesting result evident from the data is the absence of blade pass effects for values of $(r-r_2)/(R_w-r_2) = 0.25$ and higher in the volute. Also in this region, the absolute tangential velocity shows good agreement (± 5 percent) with a free vortex flow, where $V_\theta r = \text{const}$. The jet-wake phenomenon from the impeller is rapidly dissipated within the volute. This trend was present for all three windows, where four radial locations were studied in the volute.

Figures 11 and 12 show the results of varying flow rate on the blade-to-blade velocity profiles (window 6). The trends for all the flow rates, except the lowest, are similar. At the lowest flow, the possibility of fluid recirculation within the blade passage exists. This recirculation would have outward radial flow along the pressure surface and inward radial flow along

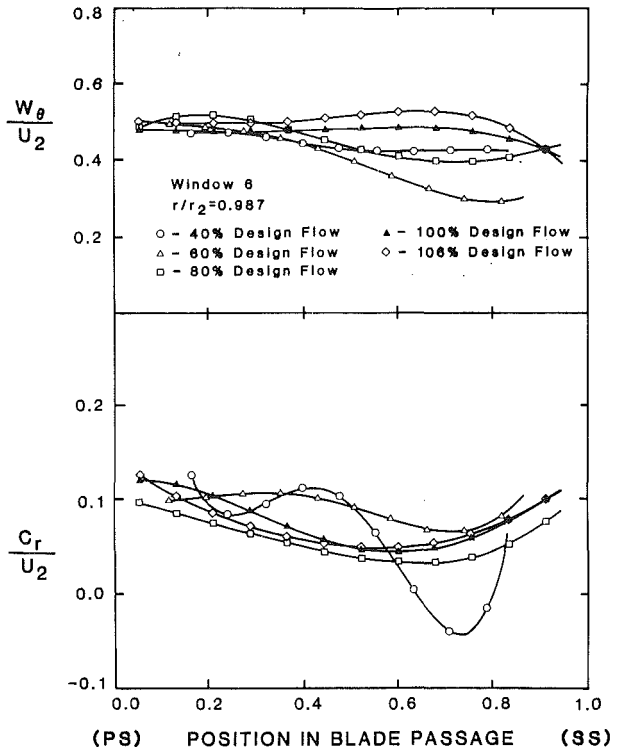

Fig. 12 Impeller flow rate studies; $r/r_2 = 0.987$

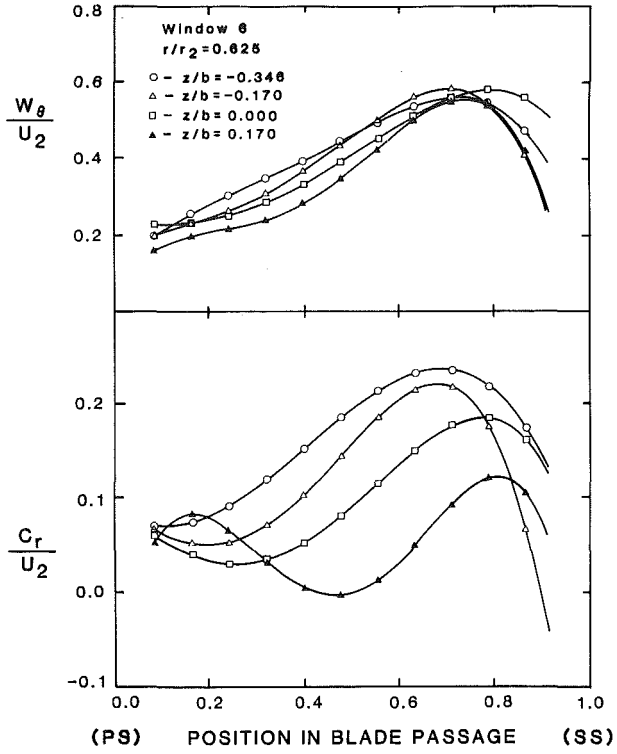

Fig. 13 Impeller axial traverse; $r/r_2 = 0.625$

the suction surface. Figure 12 shows a region of negative radial flow near the suction surface for the flow rate 40 percent of design. At the inner measurement radius ($r/r_2 = 0.625$) the flow along the suction surface is suppressed relative to the other flow rates. This could be the result of a recirculating flow within the blade passage. Figures 11 and 12 also show that blade loading is strongly a function of flow rate. With lower flow rates more reversal is present in blade loading at the impeller exit. This implies that the reversal in blade loading begins at smaller radii for lower flow rates.

The axial traverse data (window 6) for the impeller is shown in Figs. 13 through 15 at design flow. At $r/r_2 = 0.625$ the radial profile is heavily skewed toward the back face of the impeller with the peak occurring at 1/6 of the passage depth from the hub surface. This is caused by the 90 deg turn the fluid must make going from the inlet pipe into the impeller. The tangential velocity profile is much flatter. As the radius increases, the profiles flatten out and become more symmetric. At the exit the profile has a peak 2/3 of the passage depth from the hub surface. The maximum variation between the nondimensional radial velocity profiles is 0.203 at $r/r_2 = 0.625$, 0.129 at $r/r_2 = 0.800$, and 0.061 at $r/r_2 = 0.973$. Trends similar to those for the outer impeller radius were found in the volute axial traverses.

From velocity measurements near the tongue the change in the location of the tongue stagnation point was studied for five flow rates. The flow rates ranged from 40 percent of design to 112 percent of design flow. The stagnation point locations are shown in Fig. 16. As the flow increases from 40 percent of design to 112 percent of design, the direction of the flow changes from stagnating on the discharge side of the tongue to stagnating on the impeller side. The direction of the flow in the vicinity of the tongue depended on the position of the impeller blade tip relative to the tongue. The variation in direction was found to be ±6 deg due to the blade pass. The bands in Fig. 16 represent this variation.

The final parameter considered is the slip factor. This is calculated from

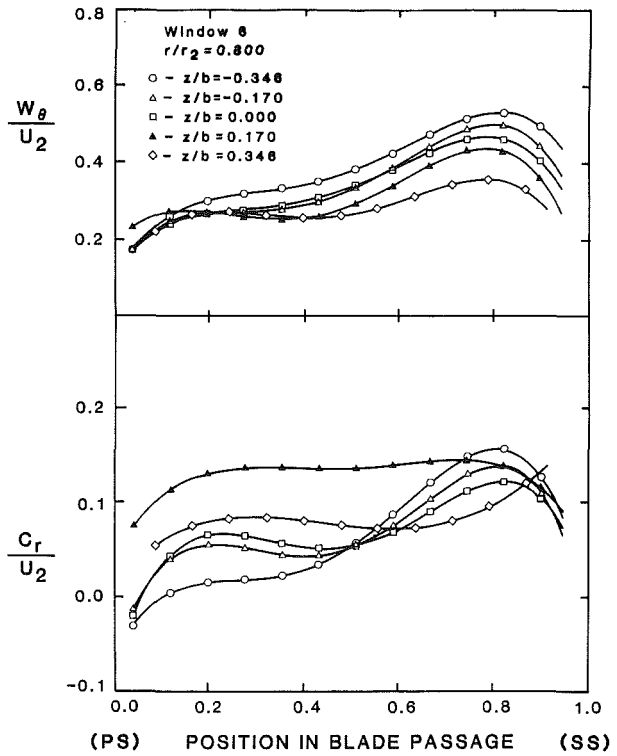

Fig. 14 Impeller axial traverse; $r/r_2 = 0.800$

$$h_o = \epsilon\left[\frac{Q}{2\pi rbU}\right]\cot\beta + \frac{\tilde{C}_\theta}{U}$$

where ϵ is the vane blockage factor and equal to

$$\epsilon = \left[1 - \frac{nt}{2\pi r \sin\beta}\right]$$

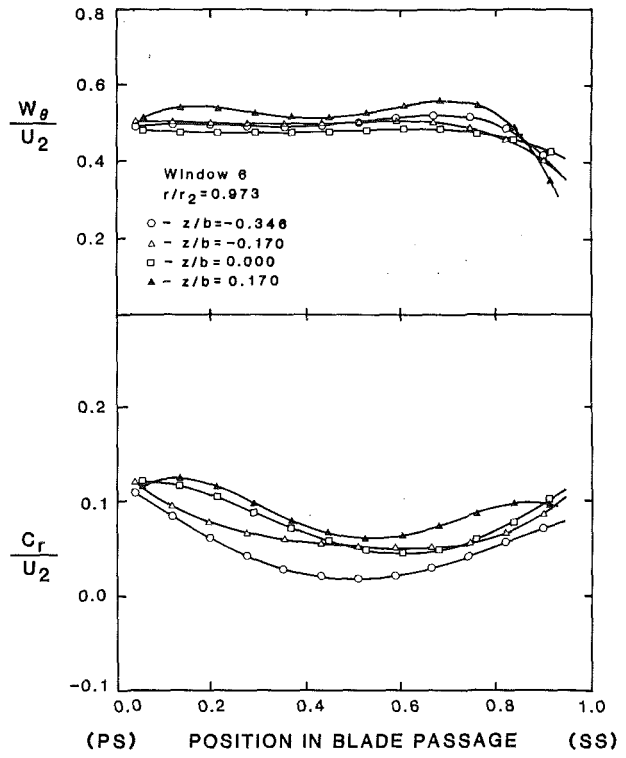

Fig. 15 Impeller axial traverse; $r/r_2 = 0.973$

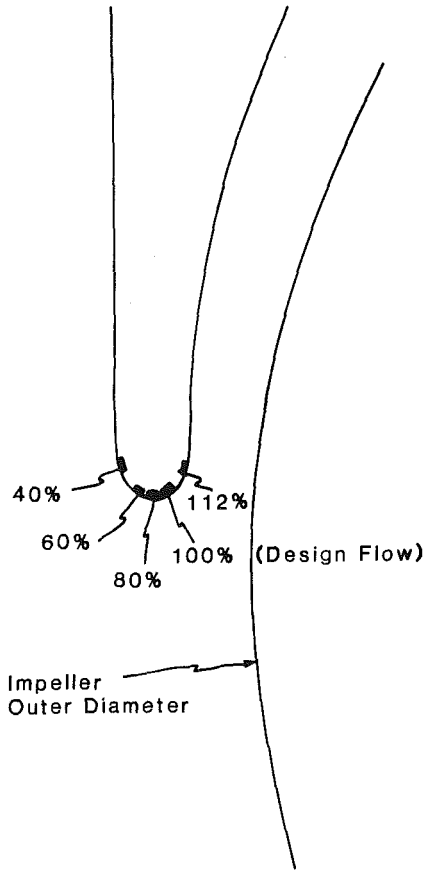

Fig. 16 Tongue stagnation point location

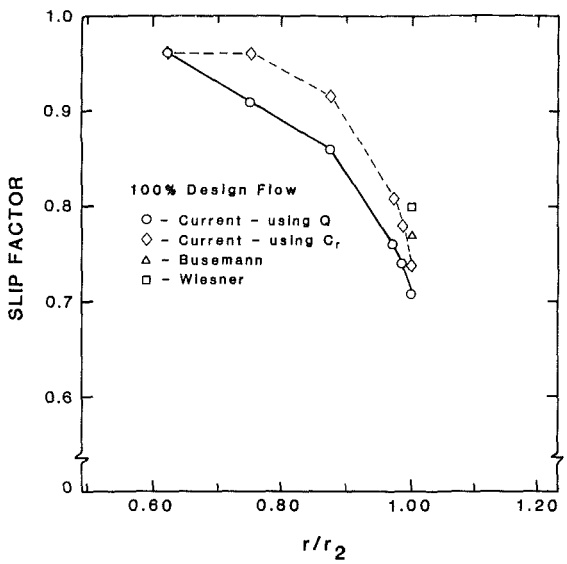

Fig. 17 Slip factor for different radii at design flow

U and r are evaluated at the radius of a particular set of data. $\tilde{C}_\theta$ is based on axial centerline data. By calculating the slip at various radii within the impeller, the development of the slip factor through the impeller can be seen. The results of this calculation are shown in Fig. 17. This was calculated for the design flow. The value for slip at the impeller exit is based on velocity data measured just beyond the impeller exit, at $r = 104.4$ mm. The $\tilde{C}_\theta$ term is corrected to the impeller exit radius by

$$\tilde{C}_{\theta_{2_c}} = \frac{r\,\tilde{C}_\theta}{r_2}$$

where $\tilde{C}_{\theta_{2_c}}$ = tangential velocity at the impeller exit; $r = 104.4$ mm; $\tilde{C}_\theta$ is mass-averaged tangential velocity at 104.4 mm; r_2 is the impeller exit radius 101.6 mm.

Slip factors based on Busemann's work and Wiesner's work (1967) are also shown in Fig. 17 for comparison.

The slip factor can be calculated by a second method. Namely, Q is based on the orifice meter and does not include leakage flow. Thus, one can also calculate h_o based on local velocities. If the axial profiles measured in window 6 are assumed to be representative for the entire impeller, then values for C_r and $\tilde{C}_\theta$, averaged over the impeller thickness, can be calculated. Using the averaged value of C_r in place of $Q/2\pi rb$ and the axially averaged value of $\tilde{C}_\theta$ yields the slip factor as a function of radius. These are also shown on Fig. 17. As can be seen, the slip based on C_r is somewhat higher than those found based on Q. This could be due either to leakage or the assumption that the axial profiles in window 6 were representative of those at other windows. At the impeller exit values of slip based on the current experimental data (using either C_r or Q) are within 5 to 10 percent of the values based on Busemann's or Wiesner's work. One should note that the value of slip does not reach a value of unity. This is due to the velocity gradients within the blade passage.

Conclusions

The velocities in a laboratory clear pump were measured with a laser velocimeter. Data were taken in the impeller and volute and represent a complete set of data for impeller/volute interactions. The data provide significant insight into flow complexities, as well as being useful for computational prediction evaluation. Specific conclusions are as follows:

1 Even at design flow the flow within the impeller is not axisymmetric. This asymmetry is due to the interaction between the impeller and volute. These variations have not been found for impellers operating with symmetric discharge regions.

2 The absolute tangential velocity exiting the impeller was

found to decrease from a maximum near the inside of the volute tongue to a minimum near the discharge plane.

3 For design flow the blade loading increased as the radius increased, except for the last 5 percent of the blade. This region showed zero or slightly reversed blade loading. For flow rates below design the blade loading was not as great and showed zero or reversed loading occurring at smaller radii.

4 Evidence of a recirculating flow within the blade passages was found, for a flow 40 percent of design. The recirculation had a backflow along the suction surface and outflow along the pressure surface.

5 The value of slip ranged from 0.96 to 0.71 within the impeller, with the lower value occurring at the exit. At no point in the impeller did the slip reach unity.

6 The flow within the volute exhibited the characteristics of a free vortex. In addition, the influence of blade passing was rapidly damped out within the volute.

Acknowledgments

This work was sponsored by the ROMAC Industrial Research Program at the University of Virginia.

References

Acosta, A. J., 1954, "An Experimental and Theoretical Investigation of Two-Dimensional Centrifugal Pump Impellers," *Trans. ASME*, Vol. 76, pp. 749–763.

Acosta, A. J., and Bowerman, R. D., 1957, "An Experimental Study of Centrifugal Pump Impellers," *Trans. ASME*, Vol. 79, pp. 1821–1839.

Adler, D., and Levy, Y., 1979, "A Laser-Doppler Investigation of the Flow Inside a Backswept, Closed, Centrifugal Impeller," *Journal of Mechanical Engineering Science*, Vol. 21, pp. 1–6.

Beveridge, J. H., and Morelli, D. A., 1950, "Evaluation of a Two Dimensional Centrifugal Pump Impeller," ASME Paper No. 50-A-147.

Binder, R. C., and Knapp, R. T., 1936, "Experimental Determination of the Flow Characteristics in the Volutes of Centrifugal Pumps," *Trans. ASME*, Vol. 58, pp. 649–661.

Bowerman, R. D., and Acosta, A. J., 1957, "Effect of the Volute on Performance of a Centrifugal-Pump Impeller," *Trans. ASME*, Vol. 79, pp. 1057–1069.

Brownell, R. B., Flack, R. D., and Kostrzewsky, G. J., 1985, "Flow Visualization in the Tongue Region of a Centrifugal Pump," *The Journal of Thermal Engineering*, Vol. 4, pp. 35–45.

Eckardt, D., 1976, "Detailed Flow Investigations Within a High Speed Centrifugal Compressor Impeller," ASME *Journal of Fluids Engineering*, Vol. 98, pp. 390–402.

Eckardt, D., 1979, "Flow Field Analysis of Radial and Backswept Centrifugal Compressor Impellers, Part 1: Flow Measurements Using a Laser Velocimeter," *Performance Prediction of Centrifugal Pumps and Compressors*, ASME I00127, pp. 77–86.

Fischer, K., and Thoma, D., 1932, "Investigation of the Flow Conditions in a Centrifugal Pump," *Trans. ASME*, Vol. 54, Paper No. HYD-54-8.

Hamkins, C. P., and Flack, R. D., 1987, "Laser Velocimeter Measurements in Shrouded and Unshrouded Radial Flow Pump Impellers," ASME JOURNAL OF TURBOMACHINERY, Vol. 109, pp. 70–78.

Hira, D. S., and Vasandani, V. P., 1975, "Influence of Volute Tongue Length and Angle on the Pump Performance," *Journal of the Institute of Engineers India*, Part M. E., No. 56, pp. 55–59.

Howard, J. H. G., and Kittmer, C. W., 1975, "Measured Passage Velocities in a Radial Impeller With Shrouded and Unshrouded Configurations," ASME *Journal of Engineering for Power*, Vol. 97, pp. 207–213.

Howard, J. H. G., Mukker, O. S., and Naoem, T., 1980, "Laser Doppler Measurements in a Radial Pump Impeller," *Measurement Methods in Rotating Components of Turbomachinery*, ASME I00130, pp. 133–138.

Iversen, H. W., Rolling, R. E., and Carlson, J. J., 1960, "Volute Pressure Distribution, Radial Force on the Impeller, and Volute Mixing Losses of a Radial Flow Centrifugal Pump," ASME *Journal of Engineering for Power*, Vol. 82, pp. 136–144.

Kannemans, H., 1980, "Radial Pump Impeller Measurements Using a Laser Doppler Velocimeter," ASME Paper No. 80-GT-94.

Lanes, R. F., 1982, "The Design, Construction and Testing of a Plexiglas Centrifugal Pump for Use with Laser Velocimetry," MS Thesis, University of Virginia, Department of Mechanical and Aerospace Engineering, Charlottesville, VA.

Miner, S. M., 1988, "Potential Flow Analysis of a Centrifugal Pump: Comparison of Finite Element Calculation and Laser Velocimeter Measurement," Ph.D. Dissertation, University of Virginia, Department of Mechanical and Aerospace Engineering, Charlottesville, VA.

Mizuki, S., Sakai, T., and Watanabe, I., 1971, "A Study of the Flow Pattern Within the Centrifugal and Mixed-Flow Impellers," ASME Paper No. 71-GT-41.

Murakami, M., Kikuyama, K., and Asakura, E., 1980, "Velocity and Pressure Distributions in the Impeller Passages of Centrifugal Pumps," ASME *Journal of Fluids Engineering*, Vol. 102, pp. 420–426.

Thomas, R. N., Kostrzewsky, G. J., and Flack, R. D., 1986, "Velocity Measurements in a Pump Volute With a Non-rotating Impeller," *Int. J. Heat and Fluid Flow*, Vol. 7, pp. 11–20.

Wiesner, F. J., 1967, "A Review of Slip Factors for Centrifugal Impellers," ASME *Journal of Engineering for Power*, Vol. 89, pp. 558–572.

Rotor-Stator Interaction in a Diffuser Pump

N. Arndt
Graduate Student.

A. J. Acosta
Professor.

C. E. Brennen
Professor.

T. K. Caughey
Professor.

California Institute of Technology,
Pasadena, CA 91125

The interaction between impeller blades and diffuser vanes in a diffuser pump was investigated. Steady and unsteady pressure measurements were taken on the diffuser vanes, and the shroud wall of a vaned and a vaneless diffuser. Steady, unsteady, and ensemble-averaged unsteady data, as well as frequency spectra, are presented. The measurements were made for different flow coefficients, shaft speeds, and radial gaps between impeller blade trailing and diffuser vane leading edge (1.5 and 4.5 percent based on impeller discharge radius). The resulting lift on the vane, both steady and unsteady, was computed from the pressure measurements at midvane height. The magnitude of the fluctuating lift was found to be greater than the steady lift. The pressure fluctuations were larger on the suction side than on the pressure side attaining their maximum value, of the same order of magnitude as the total pressure rise across the pump, near the leading edge. Pressure fluctuations were also measured across the span of the vane, and those near the shroud were significantly smaller than those near the hub. The pressure fluctuations on the shroud wall itself were larger for the vaned diffuser than a vaneless diffuser. Lift, vane pressure, and shroud wall pressure fluctuations decreased strongly with increasing radial gap.

Introduction

Blade and vane design in centrifugal pumps is currently based on the assumption that the flow in both impeller and diffuser is steady. This however implies that the radial gap between impeller discharge and diffuser inlet is large so that no flow unsteadiness of any kind due to blade row interaction will occur. If, however, the rows are closely spaced, there may be a strong interaction that influences both the aerodynamic and structural performance of blades and vanes. In some cases, this has led to vane failure. There are few practical analytical or numerical methods or experimental results available to provide knowledge about the magnitude of this unsteadiness.

The impeller-diffuser interaction may be divided into two different mechanisms: potential flow interaction and wake interaction. In general, wake interaction extends farther downstream, but if impeller and diffuser are closely spaced, both mechanisms will occur simultaneously. Most of the experimental work on blade row interaction with the aim of measuring unsteady blade pressures has been done in axial turbomachines. Among others, Dring et al. (1982) investigated blade row interaction in an axial turbine, and found both potential flow and wake interaction for closely spaced blade rows (15 percent based on chord). Gallus et al. (1979, 1980) reported measurements on axial compressors. The blade rows were spaced relatively far apart (60 percent based on chord), such that the potential interaction between rotor and stator was weak. In radial turbomachinery, impeller blade pressure measurements were reported by Iino and Kasai (1985) and flow field investigations in centrifugal impellers have been made among others by Krain (1981), and Inoue and Cumpsty (1984).

Herein, results on the interaction between a centrifugal impeller, namely, one half of the double suction pump of the HPOTP (High Pressure Oxygen Turbopump) of the SSME (Space Shuttle Main Engine), and a vaned diffuser will be reported. Data will be presented on steady and unsteady vane pressure measurements along midvane height as well as at different axial positions across the vane. Superimposing the steady and ensemble-averaged unsteady vane pressure, the ensemble-averaged vane pressure was obtained (it was assumed that the steady pressure value, measured with mercury manometers, was identical to the time mean pressure value about which the piezoelectric pressure transducers, used for the unsteady measurements, measured the unsteady pressure). Steady and unsteady computations of the force on the vane were made from the pressure measurements. The lift on the vane was defined as the force component normal to the chord joining the vane leading and trailing edge. Surface pressure measurements were also made at the front shroud of the vaned and a vaneless diffuser.

During the tests, the impeller could only be positioned on locations on an orbit concentric to the diffuser center (orbit radius = 1.27 mm), so that the radial gap between impeller blade trailing edge and the leading edge of any particular instrumented diffuser vane could be varied between 1.5 and 4.5 percent, based on impeller discharge radius. The experiments were performed for radial gaps between impeller blade trailing edge and diffuser vane leading edge of 1.5 and 4.5 percent. The flow past a diffuser vane is steady in the mean; for this reason we believe the pressure fluctuations observed there are due primarily to the local interaction between the impeller blades and the diffuser vane, and not to the proximity of

Contributed by the International Gas Turbine Institute and presented at the 33rd International Gas Turbine and Aeroengine Congress and Exhibition, Amsterdam, The Netherlands, June 5–9, 1988. Manuscript received by the International Gas Turbine Institute September 10, 1987. Paper No. 88-GT-55.

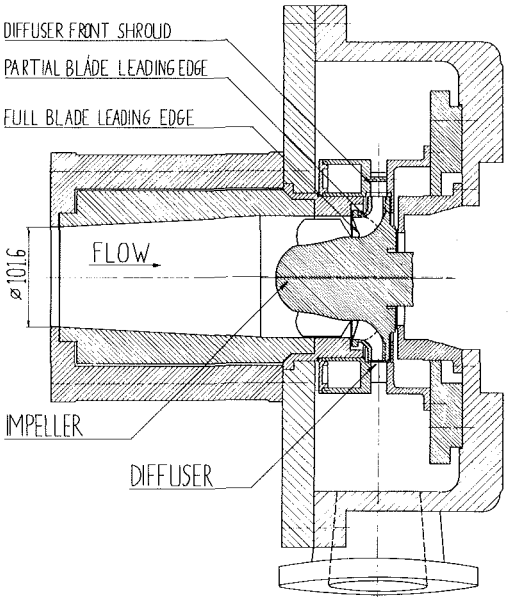

Fig. 1 Simplified view of the test section

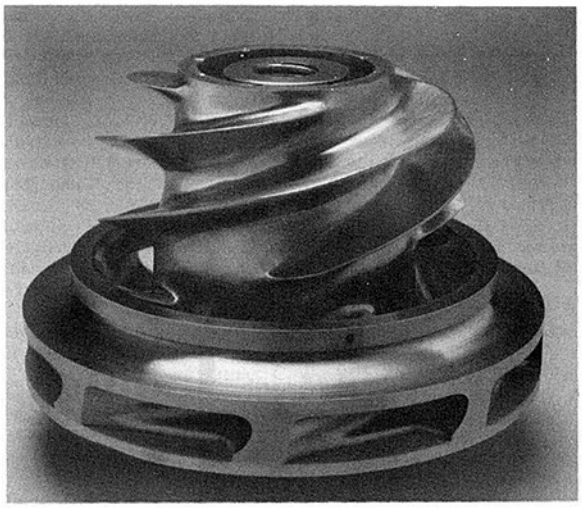

Fig. 2 Test impeller

neighboring diffuser vanes with a slightly different radial gap. Some preliminary results of this work have been previously reported by Arndt et al. (1987).

Test Facility and Instrumentation

The experiments were conducted in a recirculating water test loop. A simplified view of the test section is shown in Fig. 1. One side of the double suction pump impeller of the HPOTP of the SSME was used for the tests (Fig. 2). The impeller has eight blades in total with four partial blades, and an inducer with four inducer blades. In order to fit into the test facility, the impeller discharge diameter had to be reduced from 172.7 mm to 167.64 mm. The blade angle of both full and partial blades at impeller discharge is about 36 deg.

The vaned diffuser, referred to as Diffuser S, is a straight wall constant width diffuser with nine vanes. No volute, however, is provided. Thus, the flow is discharged from the diffuser into a large housing. The shape of a vane, with the pressure taps at midvane height, is shown in Fig. 3(*a*). It is identical to the one used in an early version of the diffuser of the HPOTP

Nomenclature

A_2 = impeller discharge area
c = vane chord
c_f = front shroud pressure coefficient = $p_f/(1/2)\rho u_2^2$
c_i = magnitude of ith Fourier coefficient, normalized by $(1/2)\rho u_2^2$
c_L = lift coefficient = $L/(1/2)\rho u_2^2 c$
$\bar{c}_p$ = steady vane pressure coefficient = $(\bar{p}_v - \bar{p}_{up})/(1/2)\rho u_2^2$
$\tilde{c}_p$ = unsteady vane pressure coefficient = $\tilde{p}_v/(1/2)\rho u_2^2$
$\tilde{c}_{p,av}$ = ensemble-averaged unsteady vane pressure coefficient = $\tilde{p}_{v,av}/(1/2)\rho u_2^2$
$c_{p,av}$ = ensemble-averaged vane pressure coefficient = $\bar{c}_p + \tilde{c}_{p,av}$
$\mathbf{F}$ = force vector on diffuser vane
f = frequency
f_b = impeller blade passage frequency = z_b (rpm/60)
L = lift (= component of the force vector on the vane normal to the chord joining the vane leading and the vane trailing edge)
$\mathbf{n}$ = outward normal vector on diffuser vane
p = pressure
p_t = total pressure
Q = flow rate
R = radius
R_2 = impeller discharge radius = 83.82 mm
R_3 = diffuser inlet radius
rpm = revolutions per minute
s = nondimensional arclength on vane suction side
u_2 = impeller tip speed = $2\pi R_2$ (rpm/60)
x, y = diffuser vane coordinates
z_b = number of impeller blades = 8
z_{fb}, z_{pb} = number of full impeller blades (z_{fb} = 4), number of partial impeller blades (z_{pb} = 4)
ξ = parametric diffuser vane coordinate
ρ = density
ϕ = flow coefficient = $Q/u_2 A_2$
ψ = total head coefficient = $(p_{down} - p_{up})/\rho u_2^2$

Subscripts

av = ensemble-averaged
b = impeller blade
$down$ = downstream
f = front shroud
fb, pb = full impeller blade, partial impeller blade
max = maximum
up = upstream
v = diffuser vane

Superscripts

$\bar{}$ = steady
$\tilde{}$ = unsteady

Abbreviations

FB = full impeller blade
FP = pressure side of full impeller blade
FS = suction side of full impeller blade
HPOTP = High Pressure Oxygen Turbopump
LE = diffuser vane leading edge
PCB = PCB Piezoelectronics, INC. Depew, NY 14043
PB = partial impeller blade
PP = pressure side of partial impeller blade
PS = suction side of partial impeller blade
PS = diffuser vane pressure side
SS = diffuser vane suction side
SSME = Space Shuttle Main Engine
TE = diffuser vane trailing edge

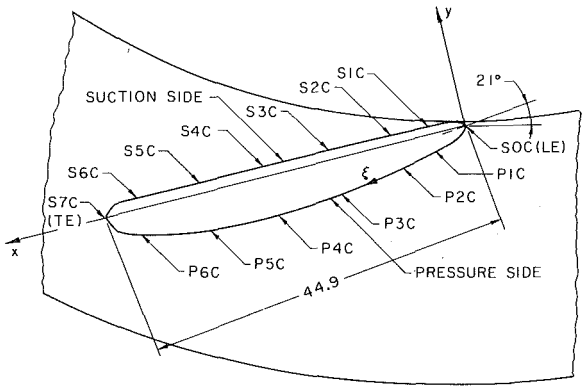

Fig. 3(*a*) Diffuser vane showing the location of the pressure taps at midvane height

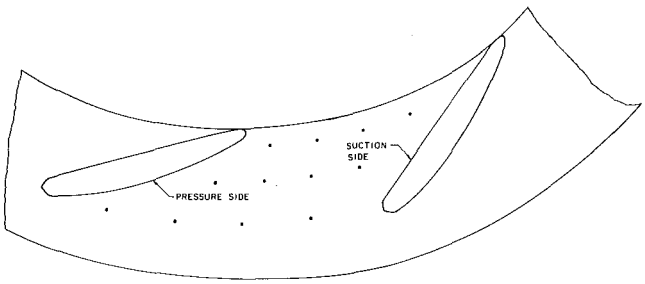

Fig. 3(*b*) Front shroud of Diffuser S showing the location of the diffuser front shroud pressure measurements

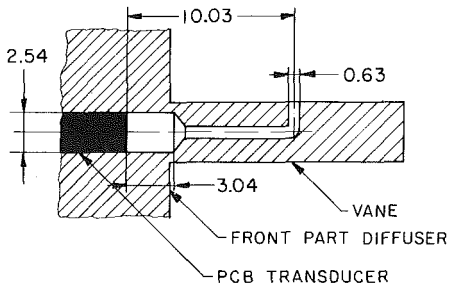

Fig. 4 Geometry of the vane pressure tap

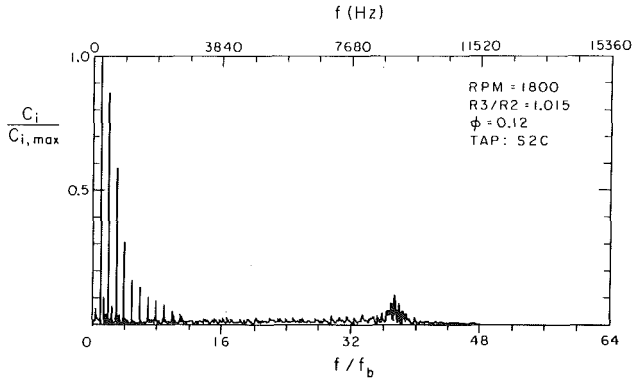

Fig. 5 Spectrum of unsteady vane pressure measurements at pressure tap S2C (ϕ = 0.12, R_3/R_2 = 1.015)

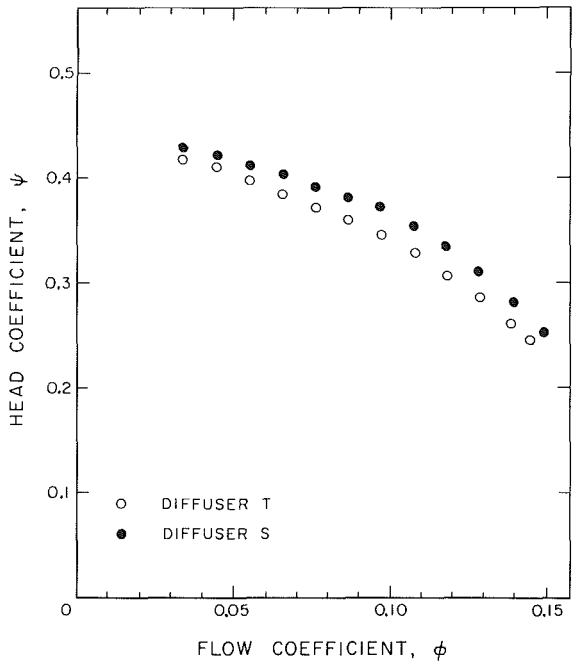

Fig. 6 Performance curves for Diffuser S and Diffuser T

of the SSME; however, the number of vanes was reduced from seventeen in the diffuser of the SSME to nine in the experiment. Vane and front shroud pressure measurements were made on this diffuser. A second diffuser, referred to as Diffuser T, of identical geometry as Diffuser S but vaneless, was used for front shroud pressure measurements.

Diffuser vane pressure measurements were made at twenty different locations on the vanes, fourteen of those located at midvane height of pressure and suction side (Fig. 3*a*), the remaining six being distributed axially between front shroud and hub (or back shroud) at two different locations downstream of the leading edge on the suction side of the vane. The size of the pressure transducer did not permit arbitrarily close spacing of the pressure taps on a single vane, so that a total of seven vanes was used for the twenty pressure taps. Front shroud pressure measurements were made for Diffuser S and Diffuser T at three different distances from the diffuser inlet. For Diffuser S, at any of those three distances four measurements were taken at different circumferential positions between suction and pressure side of two adjacent vanes (Fig. 3*b*).

Steady vane pressure measurements were obtained by using conventional mercury manometers. As reference pressure, the wall pressure at the intake about 260 mm upstream of the inducer blade leading edge of the impeller was used. The experimental error on those measurements was estimated to be ±0.5 percent. For impeller back flow observations, tufts were placed at different locations upstream of the inducer blade leading edge. For the flow coefficients, on which steady vane pressure measurements are presented (ϕ = 0.12 and 0.09) and for which steady vane pressure measurements are used in the vane lift computations (ϕ = 0.15, 0.12, and 0.09), the region of impeller back flow did at most extend to about 60 mm upstream of the inducer blade leading edge. Hence, the reference pressure was taken sufficiently far upstream of the impeller.

Piezoelectric pressure transducers from PCB Inc. were used for the unsteady measurements. The eigenfrequency (resonant frequency) of the transducer in air was given to be 300 kHz, therefore sufficiently high for the experiment. The linearity of the calibration, as provided by the manufacturer, was within 2 percent. The eigenfrequency of the pressure tap, the geometry of which is shown in Fig. 4, was estimated to be approximately 8000 Hz. Blade passage frequencies corresponding to shaft speeds from 1200 to 2400 rpm, which were used during testing, ranged from 160 to 320 Hz. The spectrum of unsteady pressure measurements (Fig. 5) taken at suction side tap 2 (S2C) at 1800 rpm and ϕ = 0.12 shows that the estimate of the eigenfrequency was reasonable. It can be seen that the blade passage frequency and its higher harmonics are "far" removed from the eigenfrequency of the tap, so that amplification and phase shift of

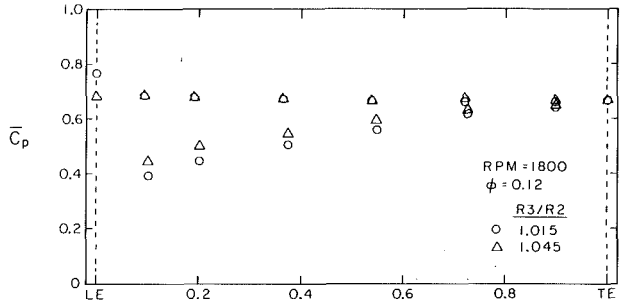

Fig. 7 Steady vane pressure measurements at midvane height (ϕ = 0.12)

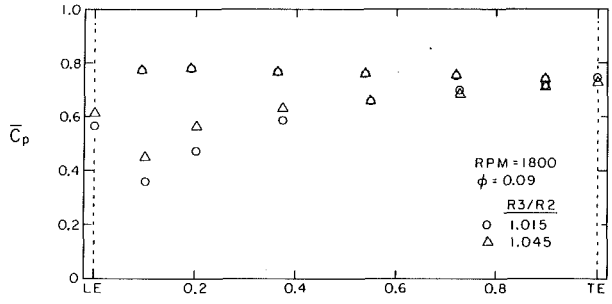

Fig. 8 Steady vane pressure measurements at midvane height (ϕ = 0.09)

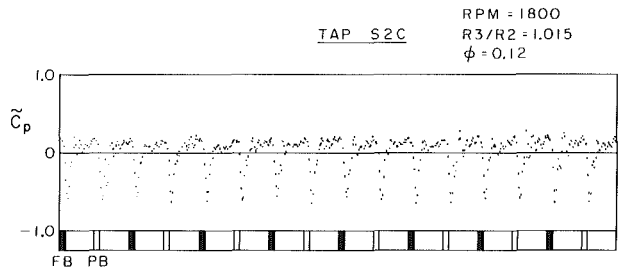

Fig. 9 Unsteady vane pressure measurements at pressure tap S2C

the signal were negligible. All front shroud pressure measurements were made with the transducers flush mounted.

The data were sampled and discretized in a 16 channel "data taker" made at Caltech. An encoder was used on the main shaft to trigger the data taker and to provide a clock for the data taker. The maximum sampling frequency of the data taker, using one channel for data taking only, is 32 kHz. 1024 data per main shaft cycle were taken for shaft speeds up to 1800 rpm, 512 for higher shaft speeds. This corresponds to 128 or 64 data per impeller blade passage, respectively. Since the signal contained some noise, the unsteady data were ensemble averaged over two impeller blade passages, a full and a partial blade passage. For shaft speeds up to 1800 rpm, 2048 full and partial impeller blade passages were used for ensemble averaging, for higher shaft speeds 4096. The experimental error was found to be less than ±5 percent for the magnitude and less than ±2 deg (360 deg corresponding to one impeller blade passage) for the phase of the ensemble-averaged unsteady pressure measurements.

Overall Performance

Performance curves for Diffuser S and Diffuser T are shown in Fig. 6. For the vaned diffuser, the maximum flow coefficient is about 2.5 percent and the total head coefficient is up to 9 percent larger than for the vaneless diffuser. The design flow coefficient for the impeller was not known. Hence, efficiency measurements were made at a number of shaft speeds to determine the best efficiency flow coefficient for the impeller and Diffuser S. From these results, the best efficiency point was found to be at approximately $\phi = 0.12$, nearly independent of shaft speed.

Discussion of Results

Data were taken for four flow coefficients, maximum flow coefficient ($\phi = 0.15$), best efficiency flow coefficient ($\phi = 0.12$), and two lower flow coefficients ($\phi = 0.09$ and $\phi = 0.06$), at three shaft speeds, 1200, 1800, and 2400 rpm, and for two radial gaps, 1.5 and 4.5 percent based on impeller discharge radius, between impeller discharge and the particular instrumented vane. At one tap on both the vane suction and the vane pressure side (S2C and P1C, respectively), measurements were taken for a total of eleven flow coefficients, ranging from $\phi = 0.05$ to $\phi = 0.15$.

Steady Vane Pressure Measurements. Normalized by the dynamic pressure based on impeller tip speed, the steady vane pressure measurements will be presented as a steady vane pressure coefficient

$$\bar{c}_p = \frac{(\bar{p}_v - \bar{p}_{up})}{(1/2)\rho u_2^2}.$$

Figures 7 and 8 show the steady vane pressure distribution at midvane height. The measurements were taken at 1800 rpm, for two flow coefficients, $\phi = 0.12$ and $\phi = 0.09$, and two different radial gaps, $R_3/R_2 = 1.015$ and 1.045. The vane loading is larger for $\phi = 0.09$ than for $\phi = 0.12$. For both flow coefficients, however, the vane pressure increases on the suction side, and remains unchanged on the pressure side with increasing radial gap. Hence, the steady lift on the vane decreases with increasing radial gap. Furthermore, the diffusion on the suction side is clearly noticeable.

Unsteady Vane Pressure Measurements. The unsteady vane pressure measurements are presented as an unsteady vane pressure coefficient, normalized by the dynamic pressure based on impeller tip speed

$$\tilde{c}_p = \frac{\tilde{p}_v}{(1/2)\rho u_2^2}.$$

In Fig. 9 a sample of unsteady vane pressure measurements taken at pressure tap S2C for 1800 rpm and $\phi = 0.12$ is shown. It is evident that the pressure fluctuations are periodic with impeller blade passage and of the same order of magnitude as the total pressure rise across the pump. The lowest pressure occurs after the impeller blade suction side has passed the diffuser vane leading edge. Again, the noise in the measurement is due to the resonant frequency of the pressure tap.

Spectra of Unsteady Vane Pressure Measurements. In Figs. 10–14 spectra of unsteady vane pressure measurements made at 1800 rpm are presented. The magnitude of the Fourier coefficients relative to the magnitude of the largest Fourier coefficient ($c_i/c_{i,max}$) for a particular test is shown versus frequency (upper horizontal scale) and frequency normalized by impeller blade passage frequency (f/f_b) (lower horizontal axis). The magnitude of the largest Fourier coefficient for the particular test is given in the caption of each figure. The spectra were obtained using 4096 data points, corresponding to four shaft revolutions or 32 impeller blade passages (the relative magnitudes of the first 512 frequencies are shown).

The spectrum presented in Fig. 10 corresponds to the unsteady data presented in Fig. 9, taken at the best efficiency flow coefficient, $\phi = 0.12$, rpm = 1800, and $R_3/R_2 = 1.015$. The dominant frequencies are the impeller blade passage frequency and its higher harmonics, which decay very slowly. At $f/f_b = 1/2, 3/2, 5/2$, etc., the relative magnitudes of the

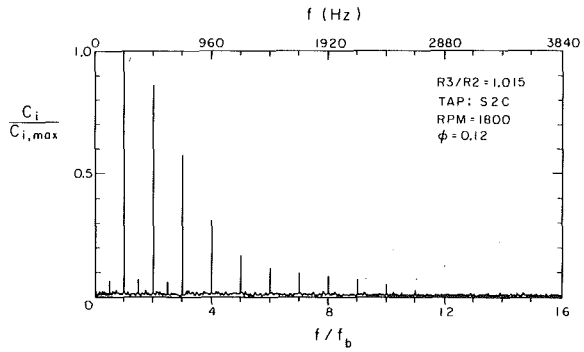

Fig. 10 Spectrum of unsteady vane pressure measurements at pressure tap S2C (ϕ = 0.12, R_3/R_2 = 1.015, $c_{i,max}$ = 0.194)

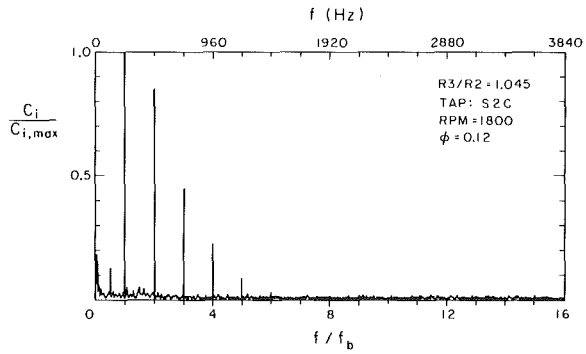

Fig. 11 Spectrum of unsteady vane pressure measurements at pressure tap S2C (ϕ = 0.12, R_3/R_2 = 1.045, $c_{i,max}$ = 0.096)

Fourier coefficients corresponding to full impeller blade passage frequency, f_{fb}, and its higher harmonics can be seen (since the impeller has a total of eight blades, four full and four partial blades, the full impeller blade passage frequency, f_{fb}, is equal to the partial impeller blade passage frequency, f_{pb}, and furthermore, $f_{fb} = (1/2)f_b$). The relative magnitudes of the Fourier coefficients at those frequencies indicate the difference on the vane pressure measurements between a full and a partial impeller blade passing the diffuser vane. For the measurements presented in Fig. 10, those differences are small. In Fig. 11, the spectrum of unsteady measurements at the same pressure tap and for the same flow coefficient but with the radial gap increased from 1.5 to 4.5 percent is presented. The relative magnitudes of the higher blade passage harmonics are smaller for the increased radial gap. The magnitude of the largest Fourier coefficient, at impeller blade passage frequency, is reduced by about 50 percent with the radial gap increased from 1.5 to 4.5 percent. Figure 12 shows the spectrum of unsteady measurements taken near the vane trailing edge on the suction side (tap S6C) for ϕ = 0.12 and a radial gap of 1.5 percent. The blade passage frequency is dominant; however, its magnitude has decreased to about a third of the magnitude of the impeller blade passage frequency at tap S2C, and its higher harmonics decay much faster than at tap S2C (Fig. 10). However, even on the rear part of the vane the fluctuations are still periodic with impeller blade passage frequency.

At some pressure taps, the relative magnitude of the full impeller blade passage frequency depends strongly on flow coefficient. This is shown for pressure tap P1C in Figs. 13 and 14. Decreasing the flow coefficient from ϕ = 0.12 to ϕ = 0.08 results in a significant increase in the relative magnitude of the full blade passage frequency, from less than 0.1 to about 0.55. Thus, for ϕ = 0.08 at pressure tap P1C, there is a significant difference in the pressure fluctuations caused by a full or a partial impeller blade passing by the diffuser vane.

Magnitudes of Vane Pressure Fluctuations. In Figs. 15–17 data on the magnitude of the ensemble-averaged unsteady vane

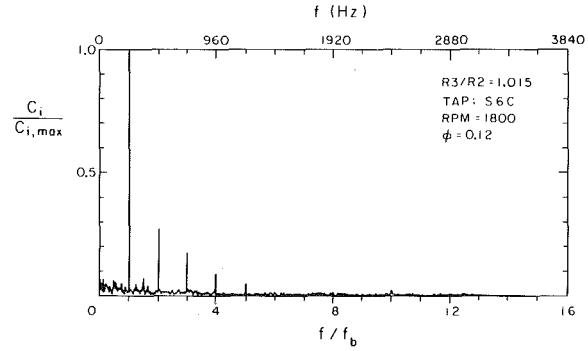

Fig. 12 Spectrum of unsteady vane pressure measurements at pressure tap S6C (ϕ = 0.12, R_3/R_2 = 1.015, $c_{i,max}$ = 0.070)

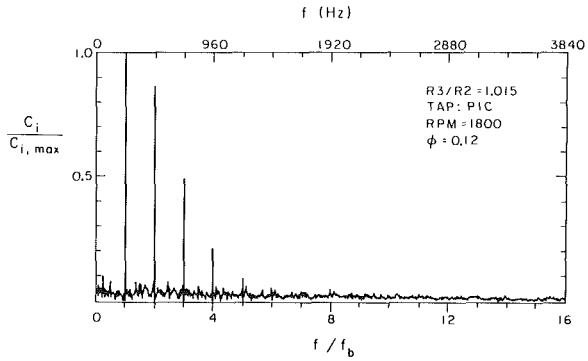

Fig. 13 Spectrum of unsteady vane pressure measurements at pressure tap P1C (ϕ = 0.12, R_3/R_2 = 1.015, $c_{i,max}$ = 0.060)

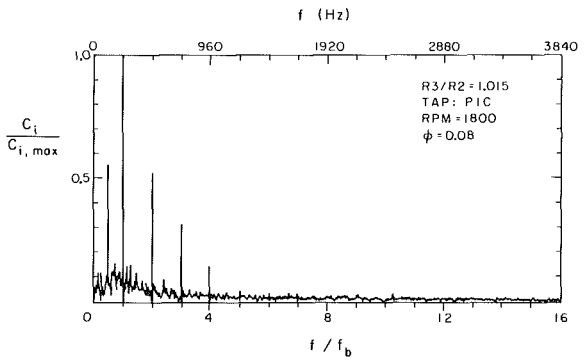

Fig. 14 Spectrum of unsteady vane pressure measurements at pressure tap P1C (ϕ = 0.08, R_3/R_2 = 1.015, $c_{i,max}$ = 0.071)

pressure fluctuations at midvane height are presented. The fluctuations are defined as the difference between the maximum and minimum pressure value in the averaging period, which corresponds to one full and one partial impeller blade passage. It can be seen that the largest fluctuations independent of experimental parameters such as flow coefficient, shaft speed, or radial gap occur on the front half of the suction side of the vane. Those fluctuations are of the same order of magnitude as the total pressure gain across the pump. Furthermore, the fluctuations on the pressure side are significantly smaller than those on the suction side. It is interesting to notice that although the fluctuations decrease on both pressure and suction side along the vane, they attain a relative maximum on the rear half of the vane. This observation is similar to that made by Dring et al. (1982) in turbine rotor–stator interaction. Dring also reported larger blade pressure fluctuations on the turbine rotor suction side than on the pressure side. In the compressor stage investigated by Gallus (1979), the largest fluctuations on the compressor stator were reported to occur at a tap on the pressure side. However, taking into account all the measurements reported on both pressure and suction side, it appears

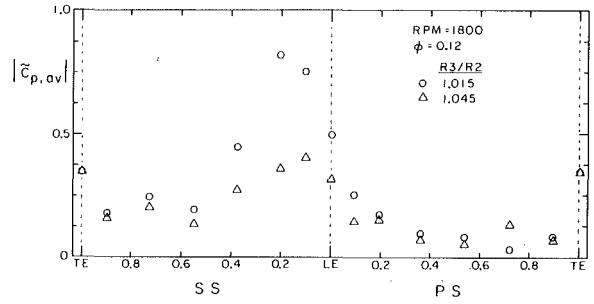

Fig. 15 Magnitude of ensemble-averaged pressure fluctuations at mid-vane height (ϕ = 0.12, R_3/R_2 = 1.015 and 1.045)

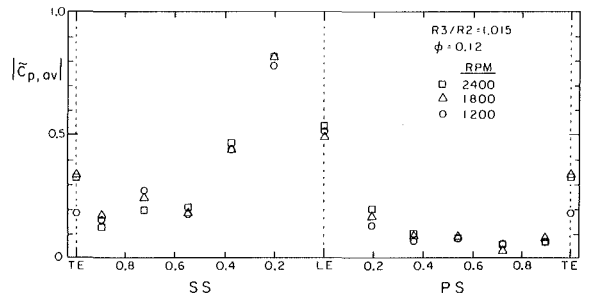

Fig. 16 Magnitude of ensemble-averaged pressure fluctuations at mid-vane height (ϕ = 0.12, rpm = 1200, 1800, and 2400)

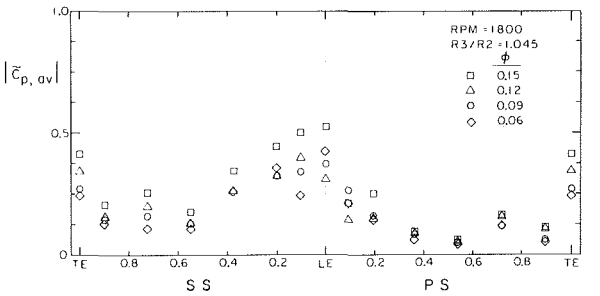

Fig. 17 Magnitude of ensemble-averaged pressure fluctuations at mid-vane height (R_3/R_2 = 1.045, ϕ = 0.15, 0.12, 0.09, and 0.06)

that the mean magnitude of the fluctuations is larger at the suction side taps than at the pressure side taps.

Figure 15 shows the dependence of the fluctuations on the radial gap for ϕ = 0.12. Increasing the radial gap resulted in a significant decrease, of about 50 percent, of the large fluctuations on the front half of the vane suction side and at the pressure tap on the pressure side closest to the leading edge. At most other measurement locations the fluctuations decreased slightly or remained constant. Only at one pressure tap, P5C, on the rear half of the pressure side, did they increase with increasing radial gap. Figure 16 compares the magnitude of the fluctuations at different shaft speeds, where data are presented for ϕ = 0.12 and a radial gap of 1.5 percent. With the exception of the pressure tap at the vane trailing edge, there is hardly any speed dependence of the normalized pressure fluctuations at any of the pressure taps. In Fig. 17 the magnitude of the fluctuations for four different flow coefficients, ϕ = 0.15, 0.12, 0.09, and 0.06, at 1800 rpm and a radial gap of 4.5 percent is shown. At all pressure taps on the suction side, the fluctuations are largest for maximum flow, ϕ = 0.15. At two suction side taps (S1C and S5C) the fluctuations decrease significantly with decreasing flow coefficient, whereas at all other suction side taps they are not significantly different for ϕ = 0.12 ϕ = 0.09, and ϕ = 0.06. On the vane pressure side, where the fluctuations are significantly smaller than on the suction side, the differences in magnitude of the fluctuations for the four flow coefficients investigated are small

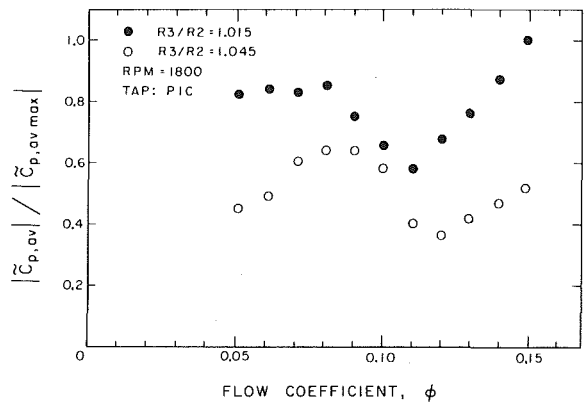

Fig. 18 Magnitude of ensemble-averaged pressure fluctuations at pressure tap P1C (R_3/R_2 = 1.015 and 1.045, ϕ = 0.05–0.15). Best efficiency flow coefficient: ϕ = 0.12.

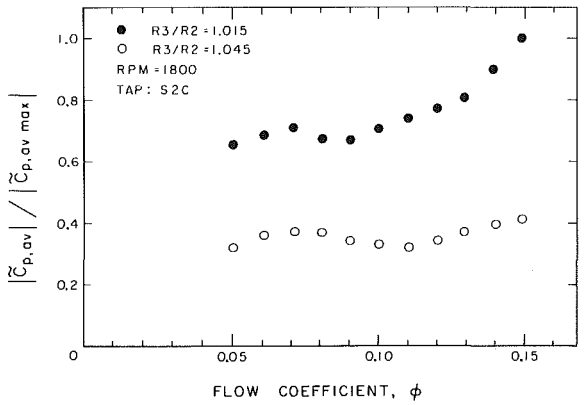

Fig. 19 Magnitude of ensemble-averaged pressure fluctuations at pressure tap S2C (R_3/R_2 = 1.015 and 1.045, ϕ = 0.05–0.15). Best efficiency flow coefficient: ϕ = 0.12.

at most pressure taps, except at P1C, where the fluctuations are largest for ϕ = 0.09 and for P2C, where they are largest for ϕ = 0.15.

To investigate in more detail the dependence of the magnitude of the fluctuations on the flow coefficient, measurements were made for radial gaps of 1.5 and 4.5 percent for a total of eleven flow coefficients, ranging from ϕ = 0.05 to ϕ = 0.15, on two pressure taps, P1C and S2C. The magnitude of the fluctuations as functions of flow coefficient and radial gap, relative to the magnitude of the fluctuations for maximum flow (ϕ = 0.15) at a radial gap of 1.5 percent, is presented for tap P1C in Fig. 18 and for tap S2C in Fig. 19. For both taps, the fluctuations are largest for maximum flow at a radial gap of 1.5 percent; however, they show different behavior for decreasing flow coefficient. For P1C at a radial gap of 1.5 percent, they attain a minimum for ϕ = 0.11, dropping about 40 percent below the maximum fluctuations for ϕ = 0.15. Increasing the radial gap to 4.5 percent results in a shift of the minimum fluctuations from ϕ = 0.11 to ϕ = 0.12. Furthermore, the largest fluctuations no longer occur for maximum flow, but for ϕ = 0.09. For tap S2C, the fluctuations are largest, for both radial gaps, for maximum flow, ϕ = 0.15, and decrease with decreasing flow coefficient. They attain relative minima and maxima for ϕ = 0.09 and ϕ = 0.07 (for a radial gap of 1.5 percent), and for ϕ = 0.11 and ϕ = 0.07 (for a radial gap of 4.5 percent).

Furthermore, the relative decrease of the pressure fluctuations with increasing radial gap is significantly different for the two taps. For tap P1C, the fluctuations decrease most strongly, by about 50 percent, for maximum flow, ϕ = 0.15, and for the smallest flow coefficient investigated, ϕ = 0.05, when increasing the radial gap from 1.5 to 4.5 percent. How-

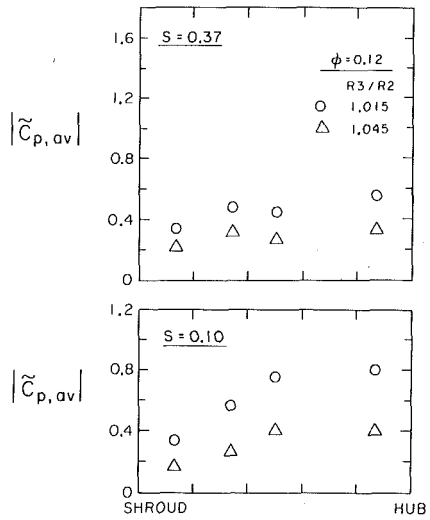

Fig. 20 Magnitude of ensemble-averaged pressure fluctuations across the span of the vane (ϕ = 0.12, R_3/R_2 = 1.015 and 1.045)

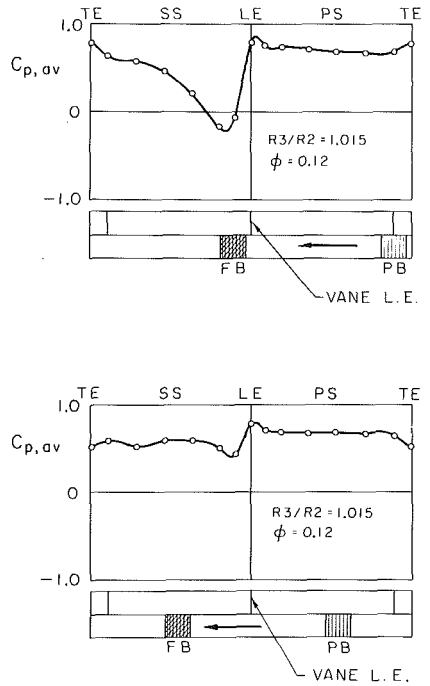

Fig. 21 Ensemble-averaged pressure distribution at midvane height (ϕ = 0.12, R_3/R_2 = 1.015)

ever, for medium flow coefficients such as ϕ = 0.10 the fluctuations decrease only by about 10 percent. For pressure tap S1C, the pressure fluctuations decrease with increasing radial gap most strongly, by about 60 percent, for maximum flow, ϕ = 0.15. When the flow coefficient is lowered, the decrease of the fluctuations with increasing radial gap is reduced slightly, up to about 50 percent for ϕ = 0.05.

Pressure measurements were also made on the suction side at four axial positions across the vane at two distances downstream of the leading edge (s = 0.10 and 0.37; the two pressure taps at midvane height corresponding to s = 0.10 and s = 0.37 are S1C and S3C, respectively). In Fig. 20 the magnitudes of the ensemble-averaged fluctuations are presented. At s = 0.10, the fluctuations near the hub were found to be more than twice as large than those near the shroud. At s = 0.37, the fluctuations near the hub were still found to be larger than those near the shroud, but the differences, especially for a radial gap of 4.5 percent, were smaller than at s = 0.10.

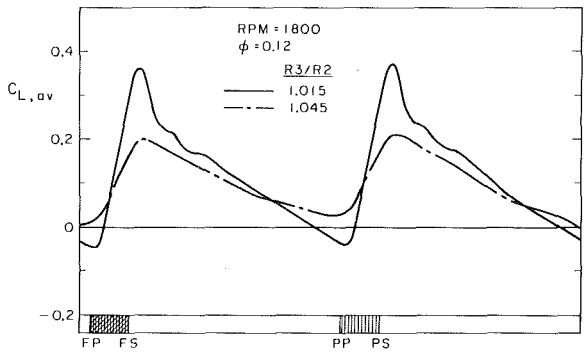

Fig. 22 Ensemble-averaged lift on diffuser vane at midvane height (ϕ = 0.12, R_3/R_2 = 1.015 and 1.045)

Steady and Unsteady Lift Computations. From the vane pressure measurements described earlier, the force on the vane at midvane height was computed. Since those measurements were obtained on different vanes they had to be phase shifted to one reference vane for the force computations. The steady force was computed from the steady pressure distribution around the vane. Superimposing the steady and ensemble-averaged unsteady pressure measurements, the ensemble-averaged vane pressure distribution was obtained (it was assumed that the steady pressure value obtained by the mercury manometer measurements was identical to the time mean value about which the piezoelectric transducer measured the unsteady pressure). From the ensemble-averaged pressure distribution, the ensemble-averaged force was computed. The steady and the ensemble-averaged pressure distributions on the vane were obtained by fitting a third-order periodic spline through the measured pressure values. A periodic spline fit was chosen to get continuity for the pressure and the first two pressure derivatives at the leading and trailing edge. Normalized, the steady and ensemble-averaged force were computed from the equations

$$\bar{\mathbf{F}} = -\oint \frac{(\bar{p}_v - \bar{p}_{up})(\xi)}{(1/2)\rho u_2^2 c}\,\mathbf{n}d\xi, \text{ and}$$

$$\mathbf{F}_{av} = -\oint \frac{(\bar{p}_v + \tilde{p}_{v,av} - \bar{p}_{up})(\xi)}{(1/2)\rho u_2^2 c}\,\mathbf{n}d\xi.$$

The lift on the vane was defined as the component of the force on the vane normal to the chord joining the vane leading and trailing edge. The lift on the vane was defined as positive if the force component normal to the vane chord is in the positive y direction (Fig. 3a).

In Fig. 21 the ensemble-averaged vane pressure distribution at midvane height is shown for two different locations of the impeller blades relative to the instrumented vane for best efficiency flow coefficient, ϕ = 0.12, at 1800 rpm, and a radial gap of 1.5 percent. (The full circles indicate actual measurement points, the curve connecting those points the pressure distribution as obtained by the interpolation scheme.) As the impeller blade passes the diffuser vane, the vane pressure on the vane suction side drops below upstream pressure, resulting in a large pressure difference between vane suction and pressure side. When the impeller blade is approximately halfway between two diffuser vanes the vane pressure distribution is similar to the steady pressure distribution presented in Fig. 7, except for the pressure fluctuations at the trailing edge.

In Fig. 22 the lift on a diffuser vane is presented for ϕ = 0.12, rpm = 1800, and radial gaps of 1.5 and 4.5 percent. The position of the impeller blades (shown is a full and a partial blade) is referenced to the diffuser vane leading edge of the instrumented vane. Maximum lift is attained immediately after the impeller blade suction side has passed the vane leading

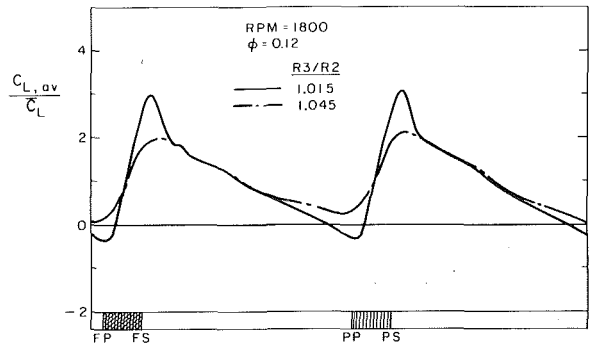

Fig. 23 Ratio of ensemble-averaged lift to steady lift at midvane height (ϕ = 0.12, R_3/R_2 = 1.015 and 1.045)

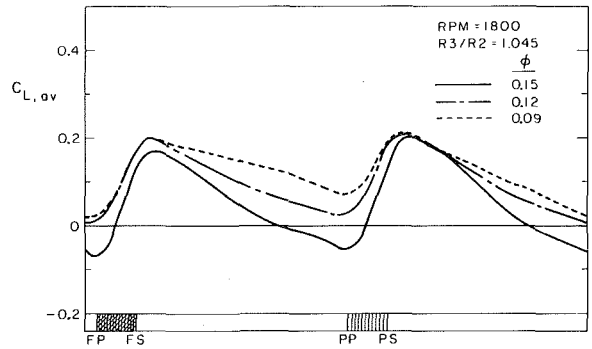

Fig. 24 Ensemble-averaged lift on diffuser vane at midvane height (ϕ = 0.15, 0.12, and 0.09, R_3/R_2 = 1.045)

edge. As seen in Fig. 21, for a radial gap of 1.5 percent the vane pressure on the suction side in the vicinity of the leading edge drops below upstream pressure at this instant of time. As the impeller blade moves on, the lift decreases, until the blade pressure side passes the vane leading edge. At this instant, the lift on the vane for the radial gap of 1.5 percent is slightly negative. Then, as the impeller blade trailing edge passes by, the lift increases sharply from its minimum to its maximum value. The increase of the radial gap from 1.5 to 4.5 percent results in a significant decrease in the fluctuating lift, as expected from a similar decrease of the magnitude of the vane pressure fluctuations.

The ratio of ensemble-averaged lift to steady lift is presented in Fig. 23. It was found that the magnitude of the ensemble-averaged lift was up to three times larger than the steady lift. Furthermore, the ratio of ensemble-averaged lift to steady lift decreased with increasing radial gap, which was not obvious *a priori* since an increase in radial gap resulted in a decrease in both the steady lift (Fig. 7), and the magnitude of the pressure fluctuations (Fig. 15).

In Fig. 24 the ensemble-averaged lift on the vane is presented for ϕ = 0.15, 0.12, and 0.09 for a radial gap of 4.5 percent. The fluctuations are largest for ϕ = 0.15, and decrease for ϕ = 0.12 and ϕ = 0.09. Differences in the magnitude of the lift fluctuations depending upon a partial or a full impeller blade passing the diffuser vane were observed. For best efficiency point and just below (ϕ = 0.12 and ϕ = 0.09), the lift fluctuations were larger for a full impeller blade passing the vane than for a partial impeller blade (by 5 and 22 percent, respectively). For maximum flow (ϕ = 0.15), however, the lift fluctuations were about 8 percent larger for a partial impeller blade passing the vane than for a full impeller blade. The large difference in lift fluctuation between a full and a partial impeller blade passing the diffuser vane for the low flow coefficient, ϕ = 0.09, coincides with the results of the spectra presented earlier. The spectra showed that with decreasing flow coefficient, from ϕ = 0.12 to ϕ = 0.08, the relative magnitude of the full blade passage frequency may increase significantly. The observation that the fluctuating lift decreases with decreasing flow coefficient is different from that reported by Gallus et al. (1979, 1980) where the fluctuating lift on the stator vanes was smallest for maximum flow, and increased with decreasing flow coefficient.

Front Shroud Pressure Measurements. Unsteady pressure measurements were made on the front shroud of the vaned diffuser (Diffuser S), and a second diffuser of identical geometry but vaneless (Diffuser T). For Diffuser T, the measurements were made at three distances to the diffuser inlet; for Diffuser S at any of those three distances to the diffuser inlet four measurements were made between the pressure and the suction side of two adjacent diffuser vanes (Fig. 3*b*). In Fig. 25 data on the magnitude of the ensemble-averaged front

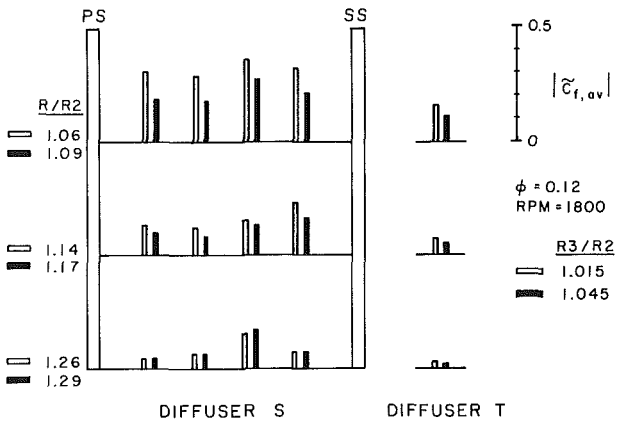

Fig. 25 Magnitude of ensemble-averaged front shroud pressure fluctuations on Diffuser S and Diffuser T (ϕ = 0.12, R_3/R_2 = 1.015 and 1.045)

shroud pressure fluctuations are presented for ϕ = 0.12 and radial gaps of 1.5 and 4.5 percent between impeller discharge and the diffuser inlet. The ratio R/R_2 in Fig. 25 describes the ratio of the radius of the particular front shroud pressure measurement location to the impeller discharge radius for the different radial gaps between impeller discharge and diffuser inlet (for Diffuser S the radial gaps between impeller discharge and diffuser vane leading edge and between impeller discharge and diffuser inlet are identical). It can be noticed that the fluctuations on the front shroud of the vaned diffuser are about twice as large as those on the vaneless diffuser. This is a clear indication that for the range of radial gaps investigated in this experiment both the potential interaction between impeller blades and diffuser vanes and the convection of the wakes shed by the impeller blades contribute to the unsteadiness of the flow. Furthermore, for the vaned diffuser, the magnitude of the front shroud pressure fluctuations depends on the circumferential position between suction and pressure side of two adjacent vanes. The fluctuations seem to be smaller and to decay faster in the vicinity of the pressure side than the vicinity of the suction side.

Conclusion

Steady and unsteady vane and front shroud pressure measurements were made for one half of the double suction pump impeller of the HPOTP (High Pressure Oxygen Turbopump) of the SSME (Space Shuttle Main Engine) and a vaned and a vaneless diffuser to investigate rotor–stator interaction in diffuser pumps. Spectra of the unsteady vane pressure measurements showed that the pressure fluctuations were periodic with impeller blade passage frequency. The vane pressure fluctuations were found to be larger on the suction side than on the pressure side attaining their maximum value, of about the same

order of magnitude as the total pressure rise across the pump, in the vicinity of the leading edge. For a radial gap of 1.5 percent (based on impeller discharge radius) between impeller discharge and diffuser vane leading edge, the pressure on the vane suction side was observed to drop locally below upstream pressure immediately after the impeller blade trailing edge has passed the vane leading edge. The large pressure fluctuations on the front half of the vane suction side decreased by about 50 percent when the radial gap was increased from 1.5 to 4.5 percent. The lift on the vane, steady and unsteady, was computed from the vane pressure measurements. The magnitude of the fluctuating lift was found to be larger than the steady lift, thus subjecting the vane to a large periodic load. Fluctuating lift as well as ratio of lift to steady lift decreased strongly when the radial gap was increased from 1.5 to 4.5 percent. Unsteady pressure measurements at different locations across the span of the vane showed that the pressure fluctuations near the hub were considerably larger than those near the shroud. The unsteady front shroud pressure fluctuations on the vaned diffuser were found to be considerably larger than those on a vaneless diffuser, indicating that the close spacing of impeller and diffuser strongly increased the unsteadiness of the flow.

Acknowledgments

The authors are indebted to the NASA George Marshall Space Flight Center for continued sponsorship of this research under contract No. NAS8-33108.

References

Arndt, N., Acosta, A. J., Brennen, C. E., and Caughey, T. K., 1987, "Unsteady Diffuser Vane Pressure and Impeller Wake Measurements in a Centrifugal Pump," *Conference Proceedings 8. Conference on Fluid Machinery*, Budapest, Sept., Vol. 1, pp. 49–56.

Dring, R. P., Joslyn, H. D., Hardin, L. W., and Wagner, J. H., 1982, "Turbine Rotor–Stator Interaction," ASME *Journal of Engineering for Power*, Vol. 104, pp. 729–742.

Gallus, H. E., 1979, "High Speed Blade-Wake Interactions," *von Kármán Institute for Fluid Mechanics Lecture Series 1979-3*, Vol. 2.

Gallus, H. E., Lambertz, J., and Wallmann, T., 1980, "Blade-Row Interaction in an Axial Flow Subsonic Compressor Stage," ASME *Journal of Engineering for Power*, Vol. 102, pp. 169–177.

Iino, T., and Kasai, K., 1985, "An Analysis of Unsteady Flow Induced by Interaction Between a Centrifugal Impeller and a Vaned Diffuser" (in Japanese), *Trans. JSME*, Vol. 51, No. 471, pp. 154–159.

Inoue, M., and Cumpsty, N. A., 1984, "Experimental Study of Centrifugal Impeller Discharge Flow in Vaneless and Vaned Diffusers," ASME *Journal of Engineering for Gas Turbines and Power*, Vol. 106, pp. 455–467.

Krain, H., 1981, "A Study on Centrifugal Impeller and Diffuser Flow," ASME *Journal of Engineering for Power*, Vol. 103, pp. 688–697.

Effects of Shock Waves on Aerodynamic Instability of Annular Cascade Oscillation in a Transonic Flow

H. Kobayashi
National Aerospace Laboratory,
Chofu, Tokyo, Japan

The effects of shock waves on the aerodynamic instability of annular cascade oscillation were examined for rows of both turbine and compressor blades, using a controlled-oscillating annular cascade test facility and a method for accurately measuring time-variant pressures on blade surfaces. The nature of the effects and blade surface extent affected by shock waves were clarified over a wide range of Mach number, reduced frequency, and interblade phase angle. Significant unsteady aerodynamic forces were found generated by shock wave movement, which markedly affected the occurrence of compressor cascade flutter as well as turbine cascade flutter. For the turbine cascade, the interblade phase angle significantly controlled the effect of force, while for the compressor cascade the reduced frequency controlled it. The chordwise extent of blade surface affected by shock movement was estimated to be approximately 6 percent chord length.

1 Introduction

Flutter caused in turbomachinery continues to be an important problem in engine design, and along with progress in predicting vibration modes of blades and disks, has promoted development of unsteady aerodynamic force analysis. The unsteady aerodynamic forces generated in a compressible flow are considered to be substantially different from those in an incompressible flow. Particularly, in a transonic flow, the movement of shock waves due to blade oscillation appears to generate significant unsteady aerodynamic forces and moments on blades.

Namba and Toshimitsu [1] have theoretically analyzed the effects of shock wave movement, applying an improved double-linear theory to a two-dimensional supersonic cascade case. His paper describes the significant effects of displacement of shock reflection points on aerodynamic instability of blade motion. Goldstein et al. [2] have shown the possibility of supersonic cascade flutter occurrence in bending mode under the effects of in-passage normal shock wave movement.

Meanwhile, Fleeter et al. [3], for example, found no effects attributable to shock wave movement in supersonic cascade experiments. Davies and Bryanston-Cross [4], using holography, have presented the shock system of a compressor annular cascade vibrating in torsional mode, and have clarified details of shock movement during a blade vibration cycle. Their resulting holography and numerical analysis data have presented the possibility of considerable time-variant pressure generation existing on the blade surface due to shock movement. However, in their experiment, time-variant pressure attributable to shock movement was not measured. Therefore, the nature of aerodynamic forces generated when a shock wave moves over the blade surface in a supersonic flow was unknown.

For both compressor and turbine blade rows, effects of shock waves on aerodynamic instability of cascade oscillation were examined over a wide range of Mach number, reduced frequency, and interblade phase angle, using a Freon gas annular cascade test facility [5]. In the facility, an annular cascade consisting of 16 complete blades was tested, while the blades were externally oscillated in torsional mode by a novel high-speed mechanical drive system. Both interblade phase angle and torsional amplitude were held constant up to a frequency of 350 Hz. For accurate measurement of time-variant pressure produced by shock movement, 13 miniature pressure transducers were aligned at intervals of 3 percent blade chord length in the chordwise direction, on the blade surface affected by shock waves.

It was clarified that the shock wave movement generated significant unsteady aerodynamic forces and moments, and contributed markedly to flutter occurrence of the compressor cascade as well as of the turbine. The effects of force on cascade flutter were significantly influenced by both interblade phase angle and reduced frequency. For the compressor cascade, shock movement promoted blade vibration and this effect was controlled mainly by the reduced frequency. For the turbine cascade, the shock movement effect was significantly controlled by the interblade phase angle. For interblade phase angle $\sigma = +67.5$ deg, shock movement promoted blade vibration, but when $\sigma = -67.5$ deg it damped blade vibration.

Contributed by the International Gas Turbine Institute and presented at the 33rd International Gas Turbine and Aeroengine Congress and Exhibition, Amsterdam, The Netherlands, June 5-9, 1988. Manuscript received by the International Gas Turbine Institute January 4, 1988. Paper No. 88-GT-187.

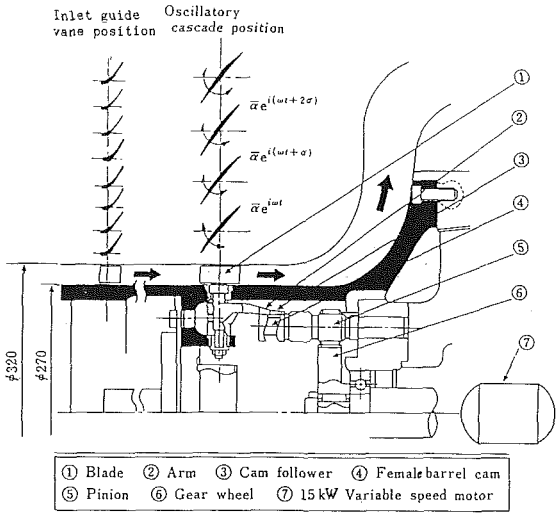

Fig. 1 Test section of annular cascade test facility and high-speed mechanical drive system

2 Test Facility

An annular cascade test facility using Freon gas was selected as a versatile rig for both steady and unsteady flow studies of turbine and compressor blade rows. An annular, rather than linear cascade, was chosen to reproduce better the acoustic properties of an actual machine. With the experimental equipment and measuring techniques developed, the natures of both unstalled transonic turbine cascade flutter and low back-pressure supersonic compressor cascade flutter were clarified [5–8].

Figure 1 shows a section of the test facility where an inlet guide vane (IGV), test compressor blade row, and a high-speed mechanical drive system are set. The drive system consists of cam follower assemblies, female barrel cams, pinions, a gear, and a 15-kW motor. The system can control and oscillate all 16 test blades at a common frequency up to 500 Hz, while maintaining both interblade phase angle and torsional amplitude constant. A blade oscillation frequency is changed by altering motor revolutions. Torsional amplitude control is achieved by the cam groove design. Any desired interblade phase angle of $2n\pi/16$ can be set by simply adjusting a spline combining the cam with the pinion, where n is an integer.

Averages and standard deviations of torsional amplitude and interblade phase angle of all 16 blades were 1.067 deg, 0.081 deg, and 67.6 deg, 6.36 deg, respectively, with nominal interblade phase angle 67.5 deg and oscillating frequency 150 Hz. These values were held almost constant up to 300 Hz in this experiment. These results proved that the drive system could provide reasonably uniform distribution of amplitude and interblade phase angle of the test blade row, and therefore the system was considered capable for carrying out flutter experiments.

Table 1 Steady and unsteady cascade data

Overall Dimensions	Working Fluid	
Tip Diameter 320mm	Freon 11 CCl_3F	
Hub Diameter 270mm		
Hub/Tip ratio 0.844		
Annular height 25mm		
Inlet Guide Vanes (IGV)	IGV is not used for transonic turbine cascade.	
Number of blades 32		
Spacing at mean diameter 29mm		
True chord 45mm		
Stagger angle 45°40"		
Air outlet angle 60°50'		
	Test cascade No.1 (Compressor Cascade)	Test cascade No.2 (Turbine Cascade)
Number of blades	16	16
Spacing at mean diameter	58mm	58mm
chord	72mm	72mm
Space/cord ratio	0.873(Tip), 0.804(Mid), 0.736(Hub)	
Stagger angle	58°	45°40"
Thickness	4%	12.4%
Blade inlet angle	61°	0°
Blade outlet angle	55°	60°50'
Type	Double-circular arc (Camber angle 6°)	
Reynolds number	$2.05*10^6$-$3.3*10^6$	$1.91*10^6$-$5.4*10^6$
Unstable Data		
Frequency (in experiment)	0-300Hz	0-300Hz
Reduced frequency, based on half chord	0.037-0.445	0.028-0.392
Torsional axis	mid chord	19.5% chord
Interblade-phase angle	+135.0°, +90.0°, +67.5°, 0.0°, -67.5°, -157.5°	+67.5°, 0.0°, -67.5°, -90.0°

Axial flow is steadily accelerated to inlet guide vanes installed at a distance of five vane chords upstream of the test cascade. They act as supersonic nozzles, accelerating and turning the flow onto the compressor blades. The IGV wakes pass between these blades. For the turbine cascade, IGV was not used. Details of steady and unsteady conditions of the cascades are listed in Table 1.

3 Measurement and Data Reduction

Steady flows upstream and downstream of the test cascade and on the blade surfaces were measured with a large number of static pressure tapping. They were fitted on the inner and outer walls of the test section and on the blade surfaces. Periodicity of the flow upstream and downstream of the test cascade was evaluated by circumferential distribution of static pressure on the wall. Two traversing five-hole cobra probes were installed upstream and downstream of the cascade for measuring radial distributions of inlet and outlet flows.

Measurement of time-dependent data includes airfoil oscillatory displacement and time-variant pressure chordwise

Nomenclature

A = amplitude of unsteady pressure
C = chord length
Cmt = unsteady aerodynamic moment coefficient, positive for blade in nose-up position
ΔE = unsteady aerodynamic energy acting on a blade surface element, per cycle of blade oscillation
f, ω = airfoil oscillating frequency
i = incidence angle
K = reduced frequency $= c\omega/2U$
M = Mach number
ΔPt = time-variant pressure having the same frequency as blade vibration
ΔPs = static pressure rise on blade surface due to shock wave
U = inlet flow velocity for a compressor cascade or outlet velocity for a turbine cascade
α = torsional amplitude, radian (positive nose up)
σ = interblade phase angle, deg (positive for forward-traveling wave)
ϕ = phase lead of unsteady pressure toward blade torsional motion

Superscripts and subscripts

1 = cascade inlet
2 = cascade outlet
+ = suction side
− = pressure side

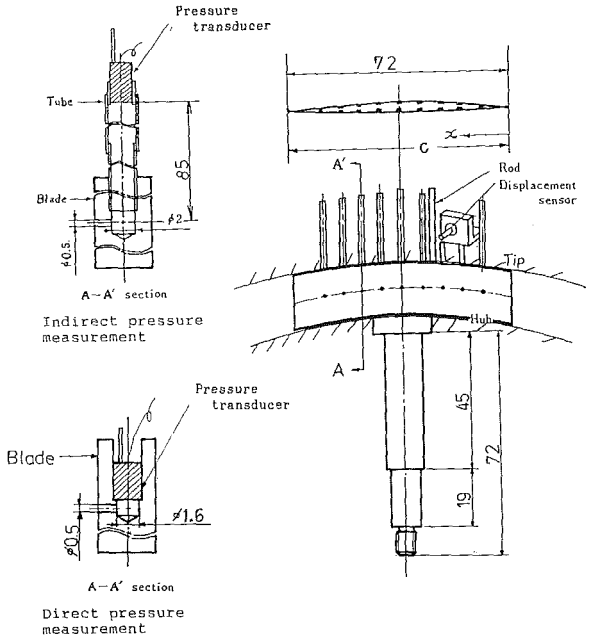

Fig. 2 Instrumented compressor airfoil

distribution on oscillating airfoil surface. Motion of an instrumented airfoil was measured with an eddy-current-type displacement sensor directed toward a small rod fixed on the airfoil tip section. Time-variant pressure was measured using two methods, as shown in Fig. 2. One was by indirect pressure measurement using probe tubes embedded in an airfoil for measuring both static and time-variant pressures on the airfoil surface. Each of the probe tubes was connected through a short vinyl tube to a miniature pressure transducer. The other was by direct pressure measurement with pressure transducers embedded in an airfoil.

The unsteady aerodynamic torsional moment was determined by measurement of chordwise distribution of unsteady pressure acting on both suction and pressure surfaces of the oscillating blades. For this, more than 20 probe tube systems were provided on the blade surfaces. For accurate measurement of time-variant pressure generated by shock movement due to blade oscillation, specially instrumented blades were devised as shown in Figs. 3(*a*) and 3(*b*). For each airfoil, 13 pressure measuring points were aligned at intervals of 3 percent chord length, in the chordwise direction, on the region of blade surface affected by the shock movement. For measurement, both indirect and direct methods were used.

The measured time-variant pressure signal was analyzed into a mean value of transfer function data as related to blade oscillatory displacement signal. Then, with the data, the following values were calculated by equations (1) to (5): unsteady aerodynamic torsional moment, chordwise distributions of unsteady pressure amplitude and phase lead, and partial aerodynamic energy produced by the unsteady pressure.

For indirect pressure measurement, in advance, the frequency response characteristics of probe tube-pressure transducer systems have to be recorded, to enable correction of measured time-variant pressure (amplitude and phase). Factors affecting the frequency response of the system are frequency of unsteady pressure, size of probe tube and vinyl tube, and the physical state of the Freon gas (temperature, static pressure, etc.), and velocity of flow grazing on the blade surface at the probe tube opening. The response functions (A_s, ϕ_s) of the probe tube systems were determined, using specially designed equipment at NAL to measure frequency response characteristics of the probe tube system [5, 6].

Next, the measured time-dependent pressure, namely

①	34.0	⑥	57.5	⑪	74.2
②	43.9	⑦	60.8	⑫	77.5
③	47.2	⑧	64.2	⑬	80.8
④	50.7	⑨	67.5		
⑤	54.2	⑩	70.8		

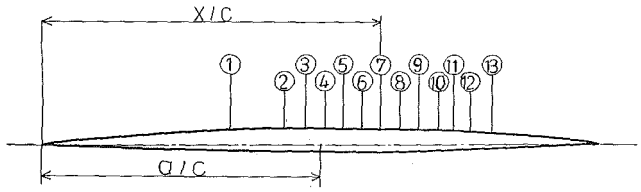

Pressure measuring point on blade suction surface (X/C %)

Fig. 3(a) Compressor airfoil

①	13.1	⑤	28.8	⑨	45.0	⑬	58.0
②	16.9	⑥	36.0	⑩	48.3	⑭	61.2
③	21.1	⑦	38.3	⑪	51.5	⑮	66.0
④	24.9	⑧	41.7	⑫	54.7	⑯	69.1

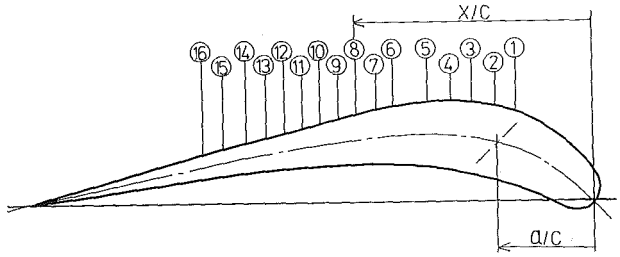

Pressure measuring point on blade suction surface (X/C %)

Fig. 3(b) Turbine airfoil

Fig. 3 Instrumented airfoil for measuring effects of shock movement

amplitude A_0 and phase lead ϕ_0, have to be corrected with three frequency responses consisting of the probe tube system (A_s, ϕ_s), and of the electronic data acquisition system, including d-c amplifier (A_d, ϕ_d) and data recorder (A_r, ϕ_r). Finally, the unsteady aerodynamic amplitude A_p and phase lead ϕ_p can be obtained using equations (1) and (2) as follows:

$$A_p = A_0/(A_s * A_r * A_d) \tag{1}$$

$$\phi_p = \phi_0 + \phi_s + \phi_r + \phi_d \tag{2}$$

(*i*) *Unsteady aerodynamic torsional moment coefficient Cmt.*

$$Cmt = \frac{1}{\frac{1}{2}\rho U^2 C^2 \alpha} \int_0^1 \{\Delta P_{ai}^{-} * (a^* - x_i^{*-}) - \Delta P_{ai}^{+} * (a^* - x_i^{*+})\} dx^* \tag{3}$$

(*ii*) *Partial aerodynamic energy ΔE acting on an oscillating blade element.*

$$\Delta E = \Delta P_{ai} * (a^* - x_i^*) \cdot \sin \phi_i / (\frac{1}{2}\rho U^2 C \alpha) \tag{4}$$

(*iii*) *Unsteady aerodynamic amplitude.*

$$A \equiv \Delta P_{ai}/(\frac{1}{2}\rho U^2 \alpha) \tag{5}$$

In this report, it is taken that cascade torsional flutter occurs when the phase lead of unsteady aerodynamic torsional moment ranges between 0 and 180 deg. The positive value of partial aerodynamic energy indicates that the unsteady aerodynamic force acting on a small portion of the blade surface stimulates blade oscillation.

4 Results for Transonic Turbine Cascade

4.1 Experimental Procedure. In an annular turbine cascade, shock waves are generated at the trailing edges of blades and reflect on suction surfaces of the adjacent blades, as shown in Fig. 4. Therefore, the effects of moving the shock reflection point because of blade oscillation on aerodynamic instability of the cascade were examined. Tests were carried out for four outlet Mach numbers, namely 1.214, 1.277, 1.359, and 1.397. For each Mach number, combinations of reduced frequency (vibration frequency) and interblade phase angle were selected, then the time-variant pressures were measured. The reduced frequency was in a range from 0.028 to 0.392, and the four interblade phase angles were +67.5, 0.0, −67.5, and −90.0 deg.

4.2 Steady Flow Properties of Turbine Cascade. Flows upstream and downstream of the cascade showed good periodicity in the cascadewise direction. Upstream of the cascade, inlet flow angle and velocity were uniform in both the radial and circumferential directions [6]. Figure 4 shows the chordwise distribution of local velocity on the blade suction surface for four outlet Mach numbers. The sonic point is near a point at 25 percent chord length and the flow downstream of the point is supersonic. Near a point at 45 percent chord length, a notable change of velocity occurs because of the reflection of shock wave emitted from the trailing edge of adjacent blade. The shock data were measured by a Schlieren visualization device and are presented in Fig. 4.

4.3 Effects of Shock Wave Movement on Aerodynamic In-

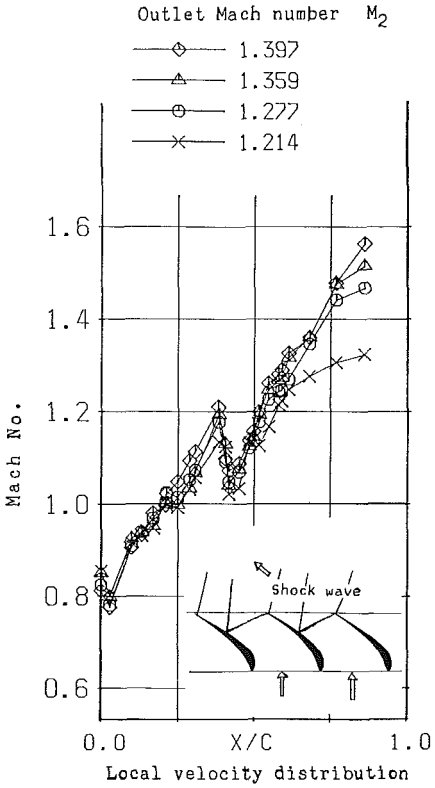

Fig. 4 Local velocity on blade suction surface of turbine

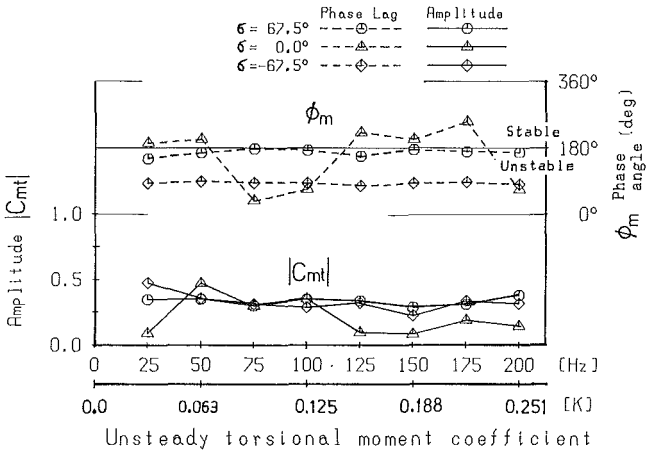

Fig. 5 Variation of unsteady aerodynamic moment against reduced frequency in a turbine (M_2 = 1.277)

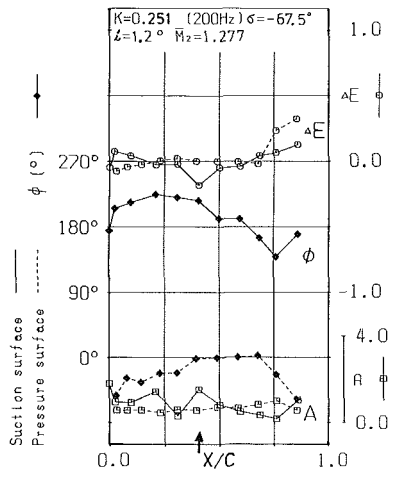

Fig. 6(*a*) Interblade phase angle of −67.5 deg

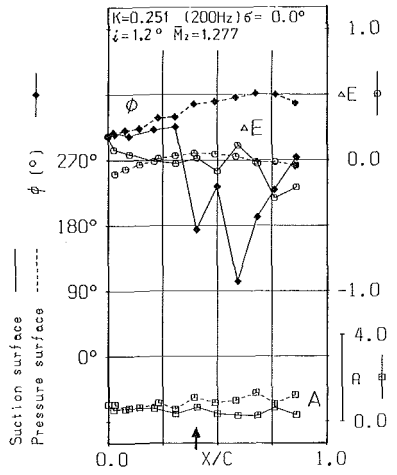

Fig. 6(*b*) Interblade phase angle of 0.0 deg

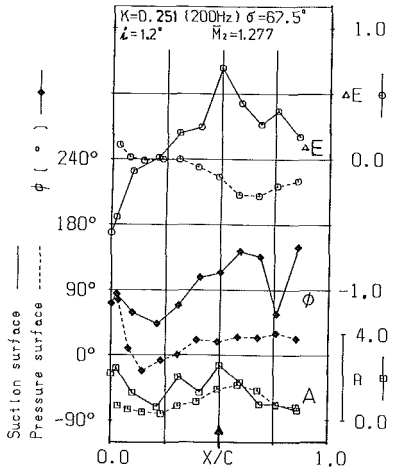

Fig. 6(c) Interblade phase angle of +67.5 deg

Fig. 6 Chordwise distributions of unsteady aerodynamic pressure on blade suction and pressure surfaces of turbines

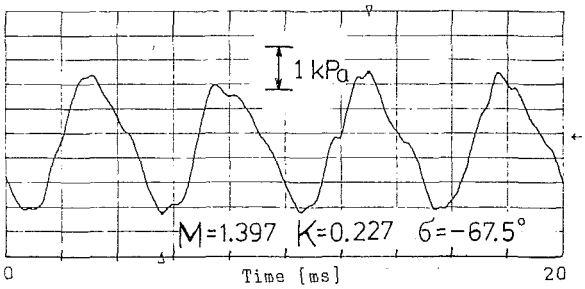

Fig. 7(*a*) Signal

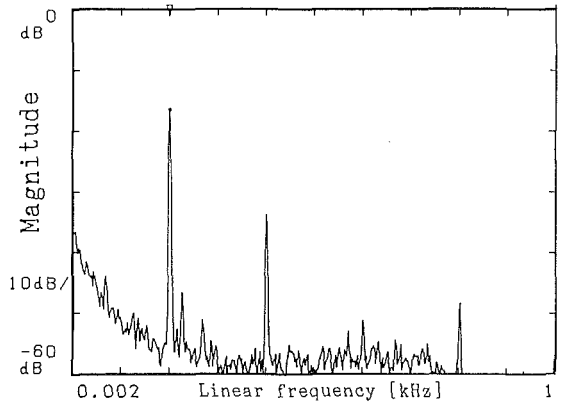

Fig. 7(*b*) Power spectrum

Fig. 7 Time-variant pressure generated by shock movement in a turbine

stability. Figure 5 shows variation of unsteady aerodynamic torsional moment against reduced frequency, for three different interblade phase angles. These data were determined by indirect pressure measurement, using 22 probe tube-pressure transducer systems aligned on both suction and pressure surface of the blade. Cascade flutter can occur when the phase angle of aerodynamic moment ϕ_m ranges between 0 and 180 deg. It has been reported by many researchers that in subsonic flow, unstalled turbine cascade flutter occurs at an interblade phase angle σ of -67.5 deg, but that it rarely occurs at $\sigma = +67.5$ deg. However, in my experiment it was clarified that in a transonic flow, cascade flutter occurs not only at interblade phase angles of $\sigma = -67.5$ deg, but also at $\sigma = +67.5$ deg.

As an example, Figs. 6(*a*) to 6(*c*) show chordwise distributions of unsteady pressure amplitude A, phase lead ϕ toward blade motion, and partial aerodynamic energy ΔE on both suction and pressure sides of the blade, for three different interblade phase angles. In the figures, the positive value of partial aerodynamic energy ΔE or the phase lead ϕ of unsteady aerodynamic pressure ranging from 0 to 180 deg indicates that the unsteady aerodynamic force acting on a small portion of the blade surface stimulates blade oscillation. The sign ↑ on the abscissa axis indicates a point of time-variant pressure generation attributable to shock movement. At an interblade phase angle of -67.5 deg, pressure amplitude A due to shock wave is greater by about three times than at adjacent points. The phase lead is 216 deg and the corresponding value of ΔE is negative. However, at an interblade phase angle of $+67.5$ deg, the phase lead is 117 deg and the corresponding value of ΔE is positive. These data indicate that unsteady aerodynamic force attributable to shock movement damps blade oscillation at interblade phase angle of -67.5 deg, but at $\sigma = +67.5$ deg it stimulates blade motion.

At an interblade phase angle of $+67.5$ deg, unsteady aerodynamic forces acting on the blade pressure surface downstream of the torsional axis dampen blade motion. Meanwhile, forces acting on the blade suction surface downstream of the torsional axis stimulate blade vibration where the force caused by shock wave movement plays an important role in causing stimulation. Cascade flutter occurs at this interblade phase angle because aerodynamic stimulation acting on the suction surface is greater than aerodynamic damping on the pressure surface.

At $\sigma = -67.5$ deg, the unsteady aerodynamic forces generated by shock wave movement dampen blade motion. However, the forces acting on other regions of the blade surface stimulate blade vibration, and therefore cascade flutter also occurs at this interblade phase angle.

4.4 Signal and Power Spectrum of Time-Variant Pressure Attributable to Shock Movement. Signals of time-variant pressure generated by shock movement were measured with miniature pressure transducers embedded in the blades, as shown in Fig. 3(*b*). As an example, a signal and power spectrum are shown in Figs. 7(*a*) and 7(*b*). At comparatively low reduced frequencies, signal shape was very similar to an harmonic wave of blade motion. In accordance with increase in reduced frequency, the shape changed into a distorted harmonic wave as shown in Fig. 7(*a*). However, Fig. 7(*b*) shows that the spectral component having the same frequency as blade motion is dominant. The signal shape was little affected by outlet flow Mach number or interblade phase angle.

4.5 Variation of Shock Movement Effects for Unsteady Parameters. Chordwise distributions of both unsteady pressure amplitude and phase lead on blade suction surfaces around the shock reflection point are shown in Figs. 8(*a*) and 8(*b*). The pressure amplitude attributable to shock movement is prominent in distribution. From a series of measured data, the chordwise extent affected by shock movement is estimated to be approximately 6 percent chord length.

In Figs. 9(*a*), 9(*b*), and 9(*c*), variations of shock movement effect against outlet Mach number and reduced frequency are clarified for three interblade phase angles. Pressure ratio $\Delta Pt/\Delta Ps$ indicates a ratio of unsteady pressure amplitude ΔPt to static pressure rise ΔPs on the blade surface due to the shock wave. For the turbine cascade, the effects of forces generated by the shock wave movement were markedly controlled by interblade phase angle rather than by both reduced frequency and outlet Mach number. With interblade phase angle $\sigma = +67.5$ deg, the shock movement stimulated blade motion, but when $\sigma = -67.5$ deg, it dampened blade motion. These phenomena are very different from those for the compressor cascade described in Section 5.

When $\sigma = +67.5$ deg, pressure ratio amplitude ranges from 20 to 40 percent and is affected a little by outlet Mach number or reduced frequency. The phase lead decreases a little along with increase in reduced frequency, but the value ranges from 80 to 130 deg. Therefore, at this interblade phase angle, the unsteady forces generated by shock movement stimulate blade motion.

With $\sigma = -67.5$ deg the pressure ratio amplitude is approximately 25 percent and changes little against both reduced frequency and outlet Mach number. The phase lead is held almost constant at 240 deg. At this interblade phase angle, the unsteady forces generated by shock movement dampened blade vibration. In addition, the experimental results for interblade phase angle of -90 deg are the same as those for $\sigma = -67.5$ deg.

When $\sigma = 0.0$ deg, the pressure ratio amplitude is less than those for the other interblade phase angles by about 10 percent. The amplitude increases a little along with increase in reduced frequency. The phase lead changes between 10 and -60 deg, and therefore, the effect attributable to shock movement is unstable. This phenomenon depends markedly on reduced frequency, not on outlet Mach number.

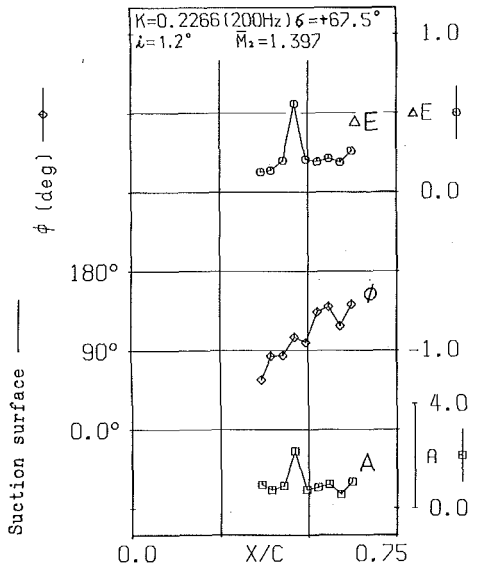

Fig. 8(*a*) Interblade phase angle of +67.5 deg

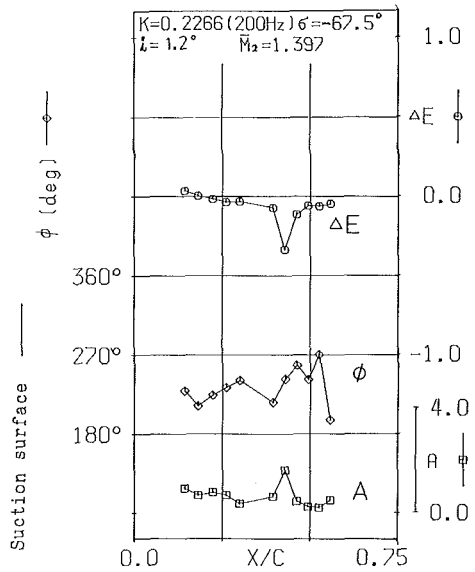

Fig. 8(*b*) Interblade phase angle of −67.5 deg

Fig. 8 Unsteady aerodynamic pressure distribution around the point of shock movement in a turbine

From these results, it is considered that for the turbine cascade, shock wave motion and its effect are controlled mainly by relative motion between the affected blade and the adjacent blade emitting a shock wave from its trailing edge rather than by shock-boundary layer interaction.

5 Results for Compressor Cascade

5.1 Experimental Procedure. For the compressor annular cascade, the effects of normal shock generating on the blade suction surface on the aerodynamic instability of cascade oscillation were investigated. In experiments, combinations of reduced frequency and interblade phase angle were selected for four inlet Mach numbers, namely 1.143, 1.130, 1.118, and 1.073. The range of reduced frequency was from 0.037 to 0.445, and six interblade phase angles selected were +135.0, +90.0, +67.5, 0.0, −67.5, and −157.5 deg. This paper mainly describes results obtained for interblade phase angles of +90.0 and −67.5 deg.

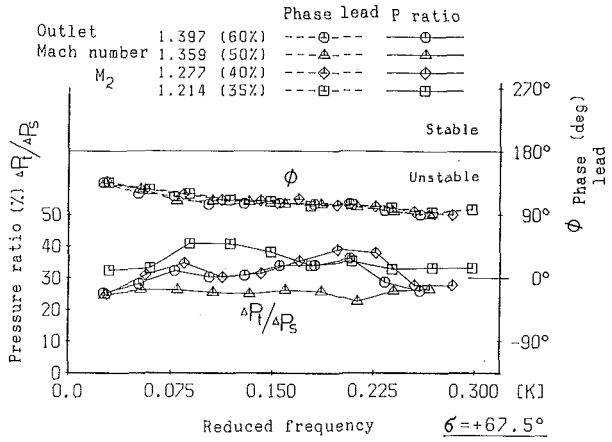

Fig. 9(*a*) Interblade phase angle of +67.5 deg

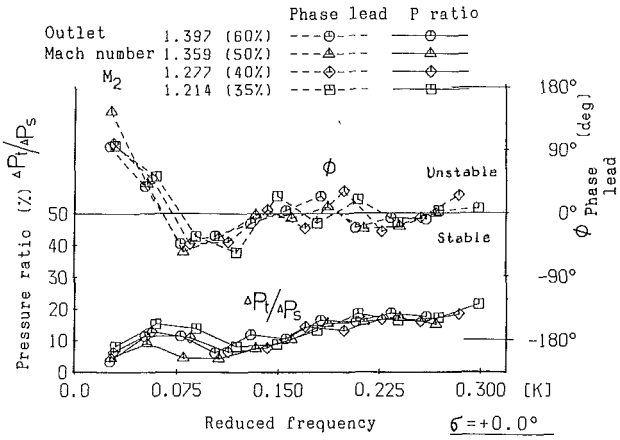

Fig. 9(*b*) Interblade phase angle of +0.0 deg

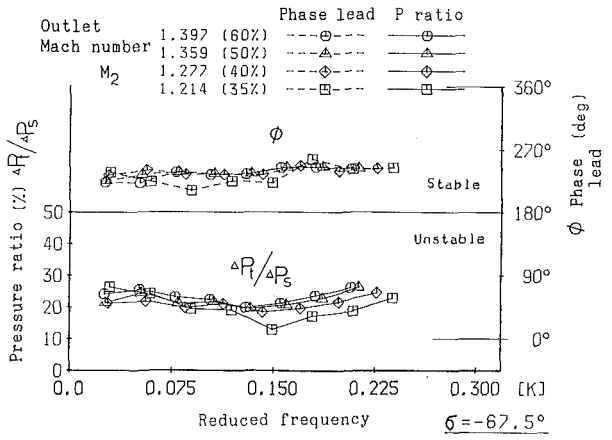

Fig. 9(*c*) Interblade phase angle of −67.5 deg

Fig. 9 Variation of unsteady pressure amplitude and phase angle attributable to shock movement against reduced frequency, in a turbine

5.2 Steady Flow Properties of Compressor Cascade. Steady flow properties of the DCA compressor cascade showed that radial distributions of inlet flow velocity and flow angle were almost uniform, especially around the midspan where the time-variant pressures were measured. Flow upstream of the cascade also showed good periodicity in the circumferential direction [7]. Figure 10 shows the chordwise distribution of local velocity on the blade suction surface for four inlet flow Mach numbers. The marked change of velocity attributable to

normal shock appears at 65 percent chord length. Normal shock data were measured with the Schlieren visualization device and are presented in Fig. 10.

5.3 Effects of Shock Movement on Aerodynamic Instability. To study low-back-pressure cascade flutter in the torsional mode [7], the time-variant pressures on both suction and pressure sides of the blade surface were determined by indirect pressure measurement using 18 probe tube–pressure transducer systems. It was determined that the following three phenomena caused low-back-pressure supersonic compressor flutter in accordance with decrease in reduced frequency: (1) change of aerodynamic force effects from positive damping into negative damping acting on the blade suction surface upstream of the torsional axis; (2) increase in negative aerodynamic damping on blade pressure surface upstream of the torsional axis; (3) generation of negative aerodynamic damping on the blade suction surface downstream of the axis. The shock movement plays an important role in negative aerodynamic damping generation on the blade suction surface downstream of the axis [8].

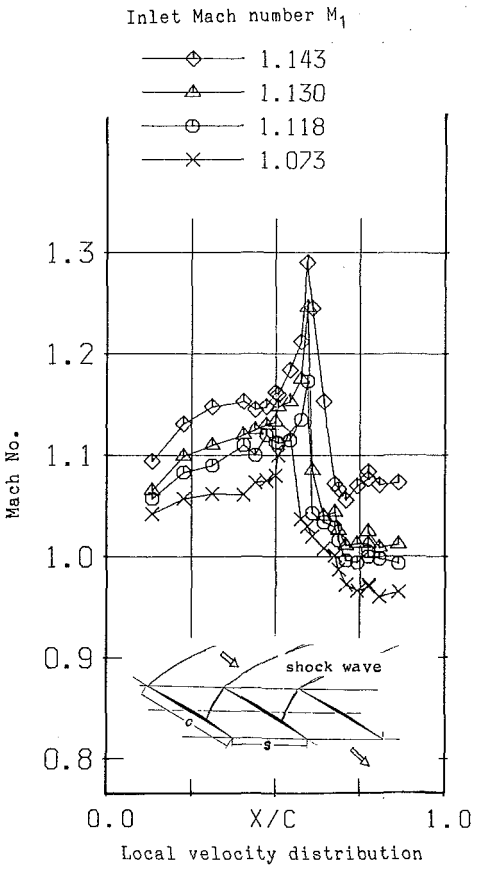

Fig. 10 Local velocity on blade suction surface of compressor

As an example of the results, Figs. 11(*a*) and 11(*b*) show unsteady pressure chordwise distributions on the blade suction surface for three different reduced frequencies and two different interblade phase angles. The sign ↑ on the abscissa axis indicates the measuring point of time-variant pressure attributable to shock movement. These figures show that unsteady pressures due to shock wave movement produce partial aerodynamic energy ΔE with positive values, and therefore, they stimulate blade vibration.

5.4 Signal and Power Spectrum of Time-Variant Pressure Attributable to Shock Movement. Signals of time-variant pressure attributable to shock movement were measured, using miniature pressure transducers embedded in the blade, as shown in Fig. 3(*a*), and examples of pressure signal and spectrum are shown in Fig. 12. The signal shape is similar to a square wave and this shape differs considerably from those of the turbine cascade.

5.5 Variation of Shock Movement Effects for Unsteady Parameters. Unsteady pressure amplitude and phase lead on the blade suction surface around the shock point were determined using indirect and direct pressure measurements, and one set of results is shown in Fig. 13. Unsteady pressure amplitude increases significantly at the shock movement point. The amplitude of the compressor cascade is greater than that of the turbine cascade as shown in Fig. 8. Partial aerodynamic energy ΔE due to shock movement is a positive value at the reduced frequency of $K=0.070$. However, at $K=0.350$, it changes to a negative value. These results reveal

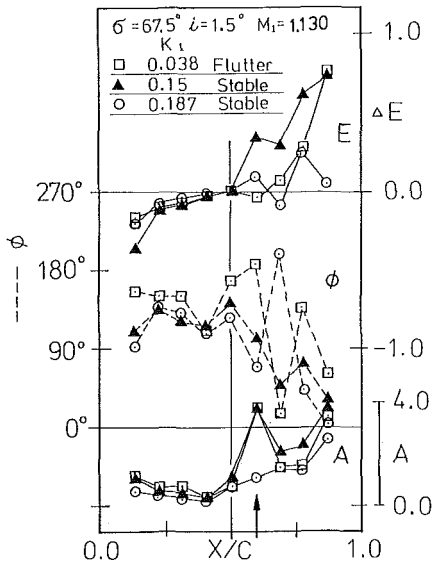

Fig. 11(*a*) Interblade phase angle of +67.5 deg

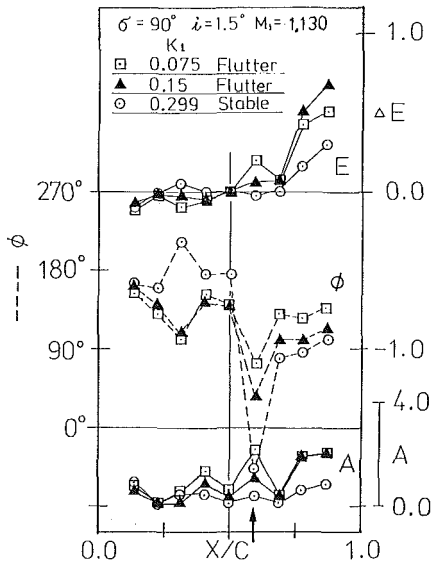

Fig. 11(*b*) Interblade phase angle of +90 deg

Fig. 11 Chordwise distribution of unsteady pressure on blade suction surface, in a compressor

that the effect of shock movement changes in accordance with increase in reduced frequency.

From a series of the measured data, the chordwise extent affected by shock movement is estimated to be approximately 6 percent chord length. This extent is the same as that for the turbine cascade.

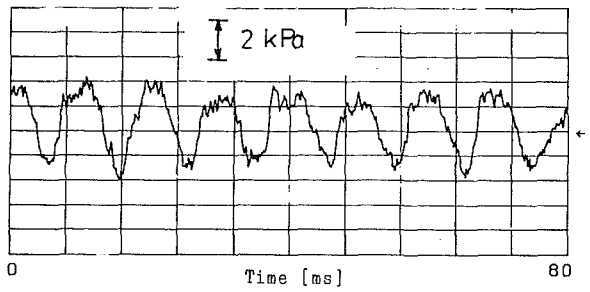

Fig. 12(*a*) Signal

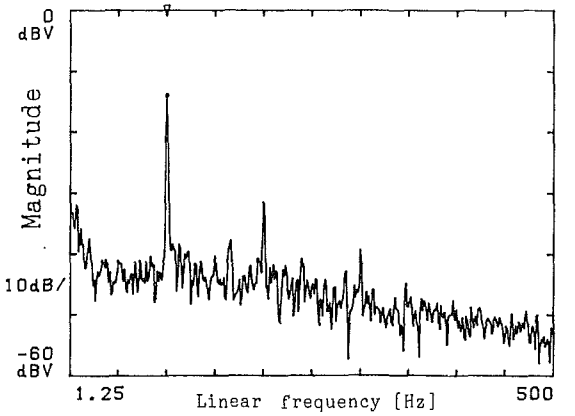

Fig. 12(*b*) Power spectrum

Fig. 12 Time-variant pressure generated by shock movement in a compressor

In Figs. 14(*a*) and 14(*b*) variations of shock movement effects against inlet Mach number, reduced frequency, and interblade phase angle are shown. For the compressor cascade, the effect does not appear to be adversely affected by interblade phase angle. This phenomenon is very different from that for the turbine cascade.

When interblade phase angle $\sigma = +90$ deg, pressure ratio amplitude falls from 80 to 30 percent along with increase in reduced frequency, but the value remains almost constant beyond $K = 0.15$. The amplitude is more than twice as great as for the turbine cascade and is strongly affected by inlet flow Mach number at lower reduced frequencies. While the phase lead decreases significantly in accordance with increase in reduced frequency, near $K = 0.25$ it changes from positive to negative value. Therefore, when $\sigma = +90$ deg, the effect of unsteady forces generated by shock movement markedly changes from that of blade motion stimulator to that of damper, along with increase in reduced frequency.

When $\sigma = -67.5$ deg, the range of pressure ratio amplitude is from 80 to 40 percent. The value is not so different from when $\sigma = +90.0$ deg. The phase lead ranges from 130 to 180 deg, and the value is hardly affected by reduced frequency or inlet Mach number. At this interblade phase angle, the unsteady forces generated by shock movement stimulate blade motion, but no cascade flutter occurs [7].

6 Conclusions

The effects of shock waves on aerodynamic instability of cascade oscillation were studied experimentally for both turbine and compressor cascades, using a controlled-oscillating annular cascade test facility and a method for accurately measuring time-variant pressures on the blade surfaces.

For the turbine cascade, the effects of moving the shock wave reflection point due to blade oscillation were examined, while for the compressor cascade, effects of normal shock movement were investigated. The nature of aerodynamic forces generated by shock movement was clarified over a wide range of reduced frequencies, interblade phase angles, and inlet or outlet flow Mach numbers.

The following conclusions are drawn:

For turbine cascade:

1 Significant unsteady aerodynamic forces were generated

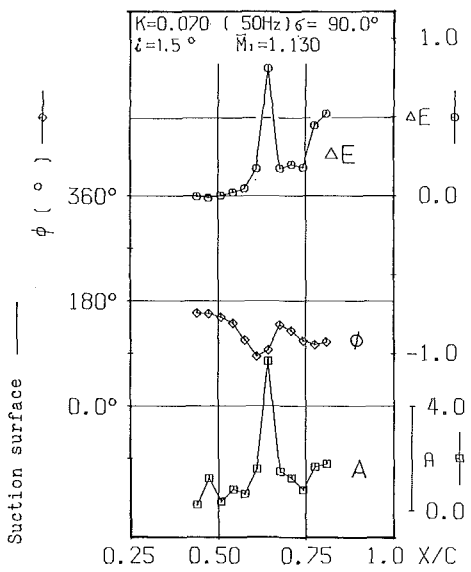

Fig. 13(*a*) Reduced frequency of 0.07

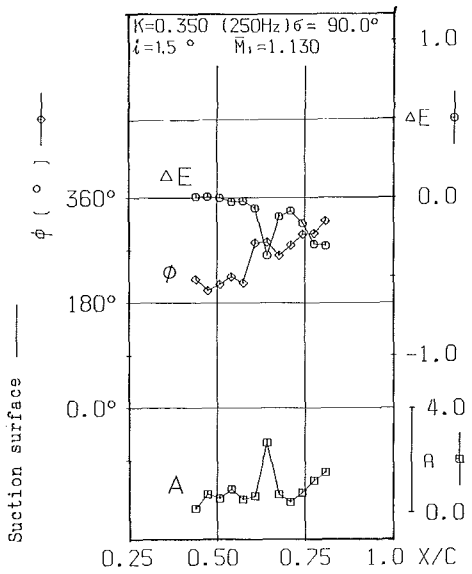

Fig. 13(*b*) Reduced frequency of 0.350

Fig. 13 Unsteady pressure distribution around the point of shock movement, in a compressor

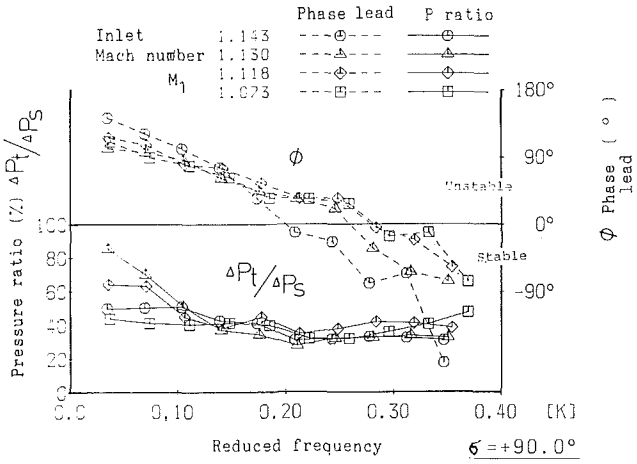

Fig. 14(a) Interblade phase angle of +90.0 deg

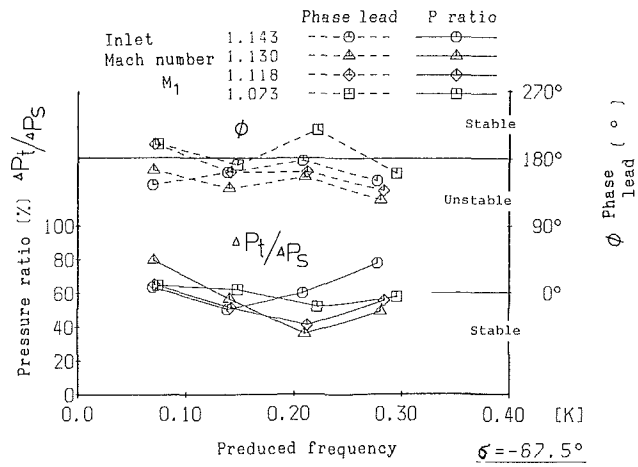

Fig. 14(b) Interblade phase angle of −67.5 deg

Fig. 14 Variation of unsteady pressure amplitude and phase angle attributable to shock movement against reduced frequency, in a compressor

due to shock movement and they markedly affected the occurrence of cascade flutter. The effects of forces were significantly controlled by choice of interblade phase angle. At an interblade phase angle σ of $+67.5$ deg, the force stimulated blade vibration, but when $\sigma = -67.5$ deg, it dampened blade vibration. In a transonic flow and at $\sigma = +67.5$ deg, cascade flutter occurs due to the forces, although at this interblade phase angle and in a subsonic flow flutter scarcely occurs. Shock wave motion and its effect are considered to be controlled mainly by relative motion between the affected blade and the adjacent blade emitting shock wave from its trailing edge rather than by shock-boundary layer interaction.

2 Pressure ratio amplitude $\Delta Pt/\Delta Ps$ ranged from 0.2 to 0.4 and its value was only little affected by reduced frequency or Mach number. Pressure ΔPt is unsteady pressure generated by the shock movement, while pressure ΔPa is static pressure rise due to the same shock wave on the blade surface. The chordwise extent of blade surface affected by shock movement was estimated to be approximately 6 percent chord length.

3 The signal shape of time-dependent pressure generated by shock movement was similar to a sine wave of blade motion. It was little affected by reduced frequency or interblade phase angle.

For compressor cascade:

4 Marked unsteady forces were generated due to shock movement and they significantly affected the occurrence of compressor cascade flutter as in the case of the turbine cascade. However, for the compressor cascade, the reduced frequency controlled effects of force rather than interblade phase angle. This phenomenon is quite different from that for the turbine cascade. At $\sigma = +90$ deg, the effect of force changes near the point of a reduced frequency $K = 0.25$, from that of blade vibration stimulator into that of damper. When $\sigma = -67.5$ deg, the force always stimulated blade vibration.

5 Pressure ratio amplitude $\Delta Ps/\Delta Pt$ fell from 0.8 to 0.4, in accordance with increase in reduced frequency. The value was twice that for the turbine cascade. The chordwise extent of blade surface affected by shock movement was approximately 6 percent chord length, the same as that for the turbine cascade.

6 The signal shape of time-variant pressure generated by shock movement was similar to a square wave.

Acknowledgments

The author is grateful to his many colleagues both in and outside NAL for giving valuable advice, and to the many students for offering assistance during this experiment. The present study has been undertaken as part of an advanced gas turbine project of the Industrial and Technology Agency, Ministry of International Trade and Industry, Japan.

References

1 Namba, M., and Toshimitsu, K., "Double Linearization Theory Applied to Unsteady Aerodynamic Analysis of 2-Dimensional Supersonic Cascade Vibrating With Finite Mean Loading," *Proceedings of JSME 65th Meeting*, Paper No. 87-0085A, 1987.

2 Goldstein, M. E., Braun, W., and Adamczyk, J. J., "Unsteady Flow in a Supersonic Cascade With Strong In-Passage Shocks," *J. Fluid Mech.*, Vol. 83, No. 3, 1977, p. 569.

3 Fleeter, S., Novick, A. S., Riffel, R. E., and Caruthers, J. E., "An Experimental Determination of Unsteady Aerodynamics in a Controlled Oscillating Cascade," ASME Paper No. 76-GT-17, 1976.

4 Davies, M. R. D., and Bryanston-Cross, P. J., "Holographic Measurements and Theoretical Predictions of Unsteady Flow in a Transonic Annular Cascade," ASME Paper No. 84-GT-174, 1984.

5 Kobayashi, H., "Unsteady Aerodynamic Characteristics of Annular Cascade Oscillating in Transonic Flow, 1st. Report, Measurement of Aerodynamic Damping With Freon Gas Controlled-Oscillated Annular Cascade Test Facility," *Bulletin of JSME*, Vol. 29, No. 256, 1986, p. 3303.

6 Kobayashi, H., "Unsteady Aerodynamic Force Acting on Controlled-Oscillating Transonic Annular Cascade," *Symposium Proceeding of Unsteady Aerodynamics of Turbomachines and Propellers*, Cambridge, 1984, p. 343.

7 Kobayashi, H., "Unsteady Aerodynamic Characteristics of Annular Cascade Oscillating in Transonic Flow, 3rd Report, Low-Back-Pressure Supersonic Compressor Blade Flutter," *Transactions of JSME*, Vol. 54, No. 480, 1986, p. 2920.

8 Kobayashi, H., "Annular Cascade Study of Low Back-Pressure Supersonic Fan Blade Flutter," ASME Paper No. 89-GT-297, 1989.

Experimental Research on Two-Dimensional Transonic Cascades of an 850-mm Steam Turbine Blade

Min Dafu

Ai Xiaoyi

Aerodynamic Laboratory,
Beijing Heavy Electric Machinery Works,
Beijing, People's Republic of China

Aerodynamic experiments on three cascades of an 850-mm steam turbine blade have been performed. Several Schlieren photographs that give clear shock structures and dynamic performances at different Mach numbers have been obtained by a Schlieren-videcorder system. On the basis of the experimental data, we analyzed the generation and development of the shock patterns in the transonic turbine casade channel and their influence on the aerodynamic performance was analyzed. Through discussions and analysis, it is shown that these cascades characterize high loading capacity with satisfactory efficiency.

Introduction

A new type of steam turbine blade with a height of 850 mm was designed at the Beijing Heavy Electrical Machinery Works. For studying its aerodynamic performance, three two-dimensional cascades located at the tip, middle, and root section of the blade, respectively, were made and tested in a transonic two-dimensional cascade wind tunnel in the Aerodynamic Laboratory of BHEMW. The tested Mach number range is from 0.6 to 1.7. Using a pressure transducer system and Schlieren-videcorder system, we obtained the main aerodynamic performance data of the cascades and a series of photographs in the channel of the cascades. Based upon the test results obtained, the shock wave structure model we proposed and its influences on the aerodynamic performance are discussed in detail.

Experiment

Experimental Facility. The main technical parameters of the cascade tunnel were given in a previous paper from this lab (ARG, 1976), and are listed in Table 1.

The total pressure P_{01} in the upstream plane is measured by a probe installed at the stabilizer in front of the testing section. The data of the inlet static pressure can be taken from 15 measurement holes located at $0.5b$ from the front edge of the cascade. The location of the exit static pressure P_{2i} holes is 8 mm away from the exit edge of cascade at a side turnable disk. The exit total pressure P_{02i} and velocity may be measured by a traveling wedge-type supersonic probe set up at a special coordinating system. For recording the velocity distribution on the blade section, tappings of holes are distributed on the midspan of 2 blades in the cascade (see Fig. 1). All pressure signals were recorded by an automatic recording system simultaneously.

Table 1

Type: temporary blow down
Air supply: four air tanks with 15 MPa and 4 m^3 each
Maximum mass flow rate: 14 kg/s
Maximum continued testing period: 75–150 s
Testing section: 400×100 mm
Exit Mach number: 0.7–1.7
Reynolds number: $(2–7) \times 10^6$
Inlet flow angle: 15–165 deg

A Schlieren recorder is used to take pictures of the static and dynamic processes of generation and development of the families of shock waves in the channel of cascades. Camera lens diameter is 200 mm.

Measurement error can be held within 0.3 percent in the loss coefficient and 15 min in exit flow angle.

Testing Cascades. Three shapes of the testing cascade profile are shown in Fig. 2. We can see that the cascade of the root section is a typical impulse cascade in which the channel convergence approaches zero, and the profile of the tip section is like a plane, with a very small blade turning angle. However the types of cascade are quite different. Typical geometric and aerodynamic data of these cascades are listed in Table 2.

Results and Analysis

Throughflow Performance and Wave Structure of Cascades. A series of typical Schlieren photographs in different cascades and Mach numbers (ARG, 1978a, 1978b, 1978c) is shown in Fig. 3. From these pictures we can see that in spite of big differences of the cascade type and testing Mach numbers, there are some common characteristics in the throughflow performance, as stated in the following:

Contributed by the International Gas Turbine Institute and presented at the 33rd International Gas Turbine and Aeroengine Congress and Exhibition, Amsterdam, The Netherlands, June 5–9, 1988. Manuscript received by the International Gas Turbine Institute December 1987. Paper No. 88-GT-53.

Table 2

Parameter	Symbol	Root	Middle	Tip
Relative blade height	Li/L	0.025	0.50	0.975
Pitch-to-chord ratio	t/b	0.3901	0.6864	0.9466
Stagger angle	β_y	82°58′	51°30′	23°24′
Design inlet Mach number	M_1	0.755	0.36	0.675
Design exit Mach number	M_{2t}	1.088	1.23	1.53
Inlet angle	β_1	52°	111.2°	157°
Geometry exit angle	β_{2g}	37.35°	30°	19.25°
Scale of testing cascade		1:4	1:2.5	1:2
Number of blades tested		17	7	9

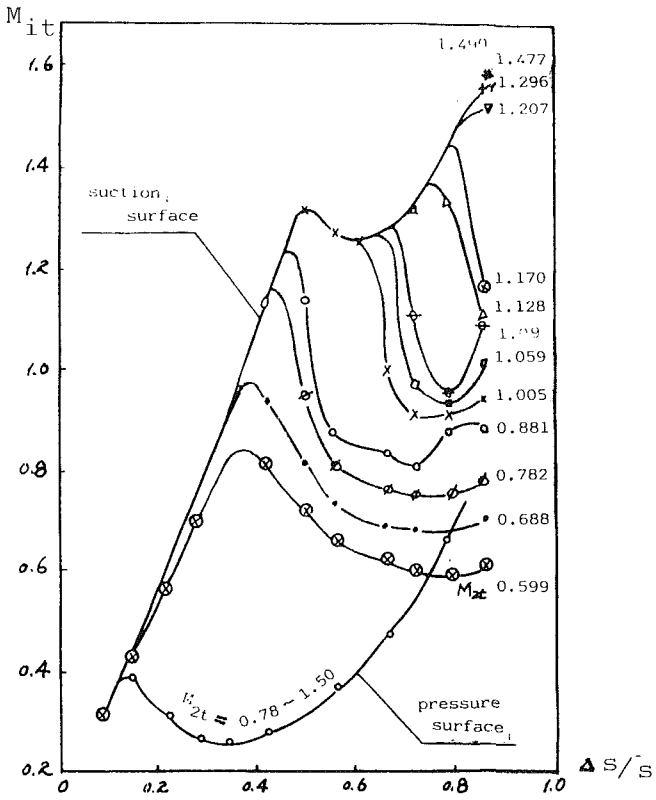

Fig. 1 The velocity distribution on the profile of the middle section

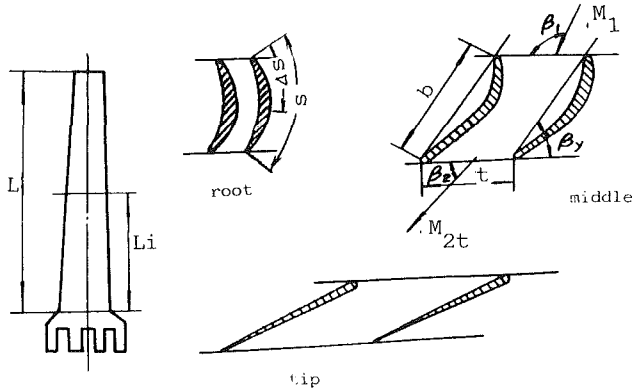

Fig. 2 Shapes of the testing cascade profile

When the exit Mach number M_{2t} reaches far less than 1, the throughflow field in the channel belongs to subsonic flow entirely. There is no supersonic bubble or shock wave in the channel. If M_{2t} is increased to a higher level, local supersonic bubbles are created near the maximum curvature on the suction surface of the blade. We define this Mach number as critical Mach number M_{cr}. The bubble has a bending sonic line as a front and ends at a shock wave as its bottom. The size and position of the bubble are dependent on the geometric factor of the cascades. It can be determined that the M_{cr} is about 0.75 for root profile and 0.69 for middle section profile of the blade.

The area of the supersonic bubble becomes broader as M_{2t} increases. Due to the rapid turning and accelerating of the flow at the trailing edge of the blade, the tail shock wave appears at a certain M_{2t}. It is shown in all pictures in Fig. 3. There are two branches of shock wave in the flow field. The first is called the outlet tail shock. It extends from the trailing edge to downstream. The second can be called the inner or channel shock wave. When the channel shock wave and the wave bottom of the supersonic bubble link up, then the sonic line runs through the channel. The choking condition is reached. The corresponding exit Mach number M_{2t} can be called the choking Mach number M_{ch}. At this working condition the mass flow rate and the inlet Mach number M_1 will not increase when M_{2t} is increased further, so $M_1 = M_{1,max}$ is called the maximum inlet Mach number. According to one-dimensional theory, M_{ch} has to equal 1 and the sonic line must coincide with the geometric throat of the cascades. But in our experiment, choking occurs when M_{2t} is about 0.9. Furthermore, the sonic line moves from the geometric throat. The more the curvature of the suction surface of the blade and the

Nomenclature

b = blade chord
K = ratio of specific heat
L = blade height
M_1 = inlet Mach number
$M_{1,max}$ = maximum inlet Mach number
M_{it} = surface Mach number derived from local static pressure and inlet total pressure
M_{2t} = mean downstream Mach number
M_{ch} = Mach number at choking condition
M_{cr} = critical Mach number
M_{Li} = limited loading Mach number
P = static pressure
P_0 = total pressure
$\Delta s/s$ = nondimensional surface length
t = pitch of the cascade
β = flow angle
ξ = loss coefficient

Subscripts

1 = upstream plane of the cascade
2 = exit plane of the cascade
i = local point along the blade surface

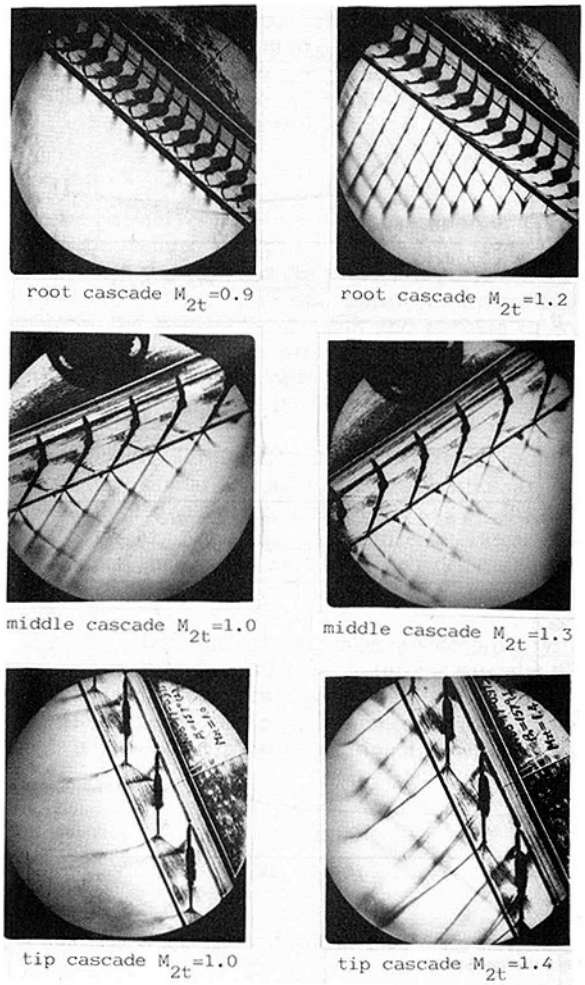

Fig. 3 Schlieren photographs in different cascade and Mach numbers

pitch-chord ratio of the cascade increase, the more deviation of the sonic line from the throat of the cascades appears.

After $M_{2t} > M_{ch}$ there is a series of expansional waves beginning at the trailing edge and shooting to the suction surface of the neighboring blade. It promotes the acceleration and deflection of the flow in the exit region of the cascades. These waves are ended by the channel shock. As M_{2t} is increased, the shock becomes oblique and deviates from the normal shock. When the shock reaches the trailing edge of the neighboring blade, the expansion has reached a limit. After that condition the expanding wave will occur outside of the channel. As we know, it will not perform work in the cascade. This condition can be defined as the limited loading condition of the cascade. The corresponding M_{2t} will be M_{Li}. Since there are rather different geometric parameters among these cascades, the value of M_{Li} will be quite different, as shown by both Schlieren photographs and the distribution curve of M_i along the profile of the blade.

According to the Schlieren photographs and their analysis, we can propose the model of the shock wave structure in the channel of the cascades. Figure 4 shows the sketch of the model (Min, 1981). There is a series of waves in the areas such as: sonic line SL, primary expansion wave E1, reflective expansion wave E2, primary shock K, primary channel shock K_1, reflective channel shock K_2, outer tail shock K_3, and the wake beginning at the trailing edge of the blade. The type of the waves and their position, especially the position of the primary channel shock, play a significant role affecting the aerodynamic performance of the cascades.

Cascade Loss Coefficient and Exit Flow Angle β_2. The most important aerodynamic performance factors of a

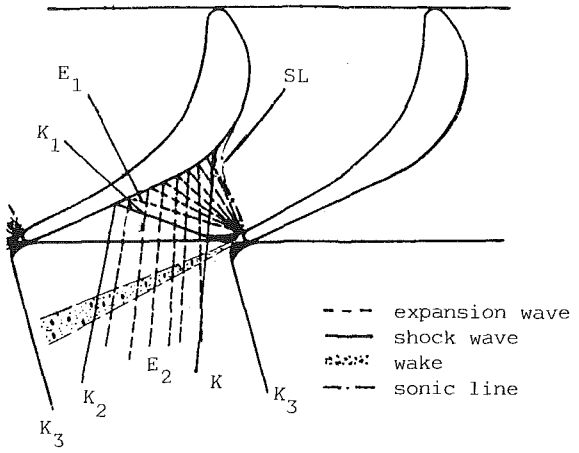

Fig. 4 Model of the shock wave structure in the channel of the cascades

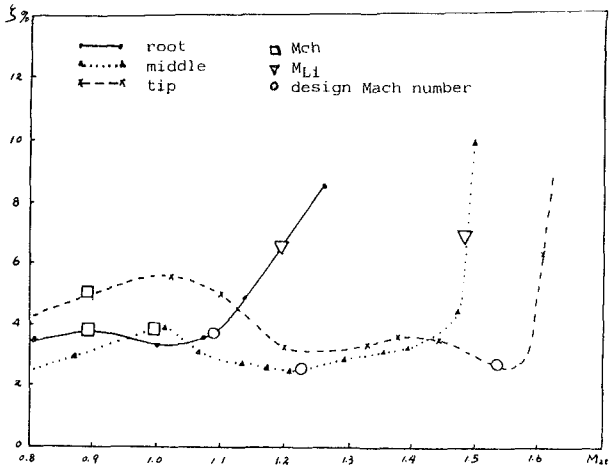

Fig. 5 The changes of loss coefficient according to M_{2t} of three cascades at design inlet flow angles

cascade at design attack angle are the loss coefficient ξ and exit flow angle β_2.

In this paper, we define the cascade loss coefficient ξ as the mean value of the local loss coefficient ξ_i along the pitch of a cascade; if it is represented by pressure, we have (as in [6])

$$\xi = \frac{1}{t}\int_0^t \frac{(P_{01}/P_{02i})^{\frac{K-1}{K}} - 1}{(P_{01}/P_{2i})^{\frac{K-1}{K}} - 1}\, dt$$

Based on the measurement data and the above formula, the changes of ξ according to M_{2t} of three cascades are shown in Fig. 5. Comparing it with Fig. 3, we can obtain the following general conclusion:

While $M_{2t} < M_{ch}$, the general estimation method of ξ (Qiang and Chen, 1982) is proved to be valid, even if the geometric parameters of the cascades characterize a transonic case. When M_{2t} approaches M_{ch}, the loss coefficients in three cascades all have a weak peak value. This can be explained by the fact that the supersonic bubble and the bottom shock may introduce an extra loss, and the cascade is near the choking working condition. The channel shock possesses the nature of a normal shock, so that the loss is rather high.

After exceeding M_{ch}, the exit velocity approaches supersonic. The strength of the channel shock is increased along with the increase of M_{2t}. The position of the shock moves downstream, and the degree of deviation from normal shock is larger. Since the loss of oblique shock is much less than that

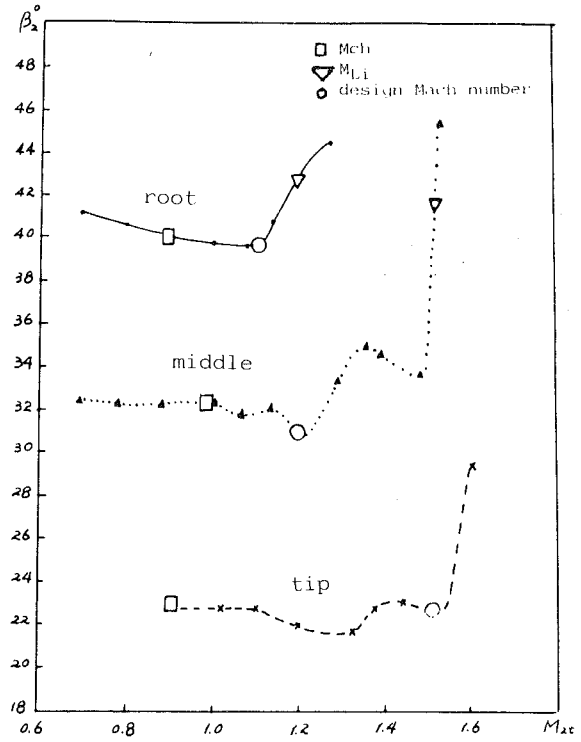

Fig. 6 Changes of exit flow angles β_2 according to M_{2t} of three cascades at design inlet flow angles

in a normal one, and the boundary layer on the suction surface of the blade is thin, therefore the oblique shock wave cannot force a serious detachment of the boundary layer, and the aerodynamic loss can be kept at a level as in the subsonic condition. This is the main reason why transonic turbine cascades are rapidly developed and utilized.

If M_{2t} increases even more, the value of loss coefficient becomes greater due to increasing shock strength. When M_{2t} reaches a value when the channel shock shoots to the subsonic region of the wake behind the neighboring blade, then the boundary layer of the trailing edge of suction surface will be thickened and detached from the wall. This is the reason explaining the rapid increase of loss coefficient near M_{Li}, described by Ai (1980).

As mentioned above, we can confirm that although the values of M_{cr}, M_{ch}, and M_{Limit} are rather different in these three cascades, the similarity in shape of curves is very good. It can be seen from Fig. 5 that the design points of these cascades are all selected in the lower region.

As to the exit flow angle β_2, the curves show the relation of β_2 versus M_{2t} of the three cascades in Fig. 6 with respect to the design inlet flow angles. The curves indicate the similarity of the changing tendency. Due to the Prandtl–Mayer expansion effect, the exit flow angle gradually increases at a low rate when M_{2t} increases. But when M_{2t} approaches M_{Li} the turning angle of the cascade falls down rapidly (Fig. 6).

Cascade Aerodynamic Performance Under Off-Design Attack Angle. From the research at ARG (1978a, 1978b, 1978c), we find that the change of ξ is less than 1 percent while the flow angle varies in the range of: for root β_1 = 40–70 deg, at middle 90–120 deg, and at the tip section 140–159 deg, respectively (see Fig. 7). But when β_1 goes over this range, the loss coefficient will be increased rapidly. This phenomenon appears especially in the tip section at β_1 = 160 deg. However the performance of the blade sections under off-design attack angles are basically satisfactory.

Estimation of Aerodynamic Performance Cascades. The

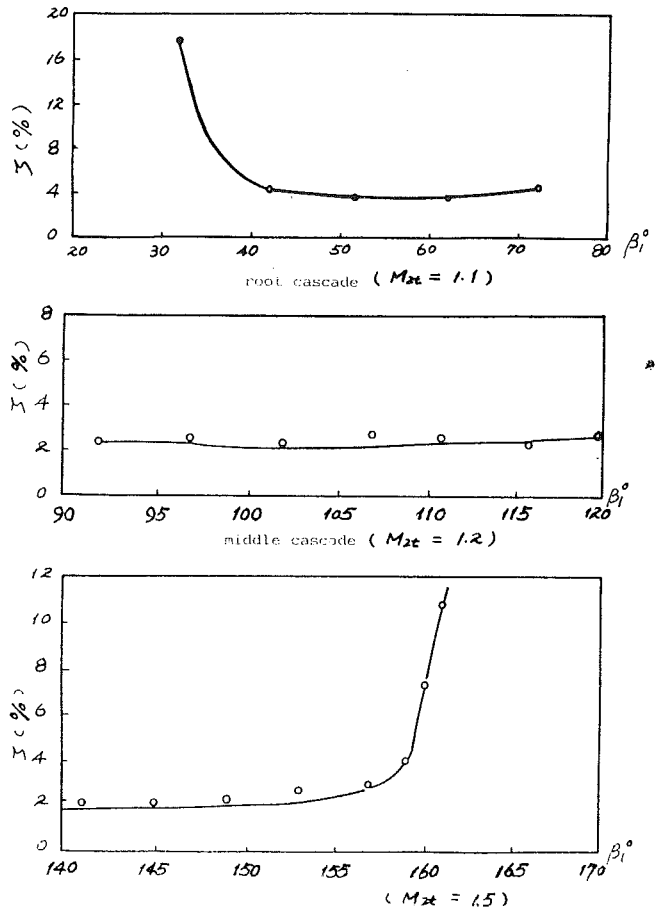

Fig. 7 Changes of loss coefficient according to inlet flow angle of three cascades

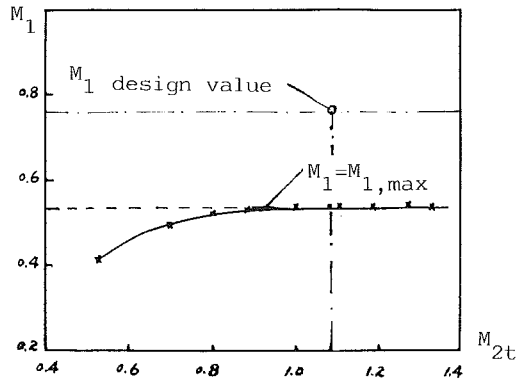

Fig. 8 Relationship of inlet Mach number M_1 versus M_{2t} for the root cascade

loss coefficients at the design point of the three cascades are less than 3.6 percent, when the exit flow angles equal the design value. The general aerodynamic performance is satisfactory. The method of aerodynamic design employed is shown to be adequate.

The aerodynamic performance under off-design condition of the middle section cascade is good. It can work satisfactorily extended over M_{2t} = 1.0 to 1.4 and β_1 = 90–120 deg; ξ are less than 4 percent and the changes of β_2 are limited to 3 deg.

From Fig. 8 we can find that under design β_1 and M_{2t}, the maximum inlet Mach number $M_{1,max}$ is less than the design value for the root section. This will lead the streamline upward and worsen the working condition of the section.

The aerodynamic performance will be worse for the tip cascades, if $\beta_{1t} \geq 160$ deg and $M_{2t} \geq 1.55$ (see Fig. 7) (ARG, 1978c). Unfortunately the design point is quite close to this limit. The future attention of blade designers might be directed at how to attenuate such an effect.

Conclusion

The experimental results of the previous section support the following conclusions:

1 Transonic turbine cascades provide a greater working capacity than subsonic. If we can control the change of the curvature of the profile, the strength and position of wave series, and the interference between shock and boundary layer, the loss coefficient can be kept at a reasonable level. It is shown that the design of the 850 mm turbine blade is successful.

2 The transonic turbine cascades with different geometric parameters have similar performance characteristics, and they are all well adopted to a broad range of M_{2t} and β_1. But as the values of M_{cr}, M_{ch}, and M_{Limit} for different cascades are rather different, such values can be precisely determined only by experiment. It is important to select the design points carefully.

3 It is very efficient to use the Schlieren-videcorder system in the experimental study of transonic turbine cascades. The photographs taken from such a system can be used for basic analysis of the aerodynamic performance of the cascades. Although it is only for a two-dimensional flow, we believe such a cascade experiment is a very simple and reliable method to evaluate the aerodynamic performance and design method of turbine cascades.

Acknowledgments

The authors are obliged to thank Dr. Wan Dingguo, Chief Engineer, for his instructions, valuable comments, and suggestions.

References

Aerodynamic Research Group, 1976, "F-01 Transonic Cascade Tunnel – Experiment and Estimation," Report No. 7, Aerodynamic Lab. BHEMP.

Aerodynamic Research Group, 1978a, "Experimental Data and Analysis on a Transonic Cascade of the Middle Section Blading With 850 mm Height," Report No. 11, Aerodynamic Lab. BHEMP.

Aerodynamic Research Group, 1978b, "Experimental Data and Analysis on a Transonic Cascade of the Root Section Blading With 850 mm Height," Report No. 13, Aerodynamic Lab. BHEMP.

Aerodynamic Research Group, 1978c, "Experimental Data and Analysis on a Transonic Cascade of the Tip Section Blading With 850 mm Height," Report No. 16, Aerodynamic Lab. BHEMP.

Ai Xiaoyi, 1980, "Experiment of Two-Dimensional Transonic Turbine Cascade," *Journal of Engineering Thermophysics*, Vol. 1, No. 1, pp. 55–63.

Min Dafu, 1981, "The Shock Wave Structure and the Analysis of the Flow Through Transonic Turbine Cascade," *Journal of Engineering Thermophysics*, Vol. 2, No. 1, pp. 28–34.

Qiang Kuofang and Chen Naixing, 1982, "New Correlations of the Two-Dimensional Turbine Cascade Aerodynamic Performance," ASME *Journal of Engineering for Power*, Vol. 104, pp. 458–466.

Smith, A., and Gibson, H. R., 1964, "The Measurement of Turbine Blade Losses in Cascade," *Parsons*.

S. A. Skillings

P. T. Walters

R. Jackson

Central Electricity Research Laboratories, Leatherhead, Surrey, United Kingdom

A Theoretical Analysis of Flow Through the Nucleating Stage in a Low Pressure Steam Turbine

In order to improve steam efficiency and reliability, the phenomena associated with the formation and growth of water droplets must be understood. This paper describes a theoretical investigation into flow behavior in the nucleating stage, where the predictions of a one-dimensional theory are compared with measured turbine data. Results indicate that droplet sizes predicted by homogeneous condensation theory cannot be reconciled with measurements unless fluctuating shock waves arise. Heterogeneous effects and flow turbulence are also discussed along with their implications for the condensation process.

1 Introduction

Steam turbines are the principal method by which thermal energy is converted into electrical energy, and economic considerations have always ensured that they command considerable attention from research engineers striving to improve machine efficiency and reliability. Of particular interest is the analysis of flow phenomena within a machine required to optimize blade profiles, and current design methods include advanced techniques of computational fluid dynamics along with experiments performed in two-dimensional cascades or model turbines.

However, one potentially important feature of the flow, the formation of droplets and the ensuing interphase heat transfer, has, to a large extent, been disregarded. In conventional and AGR plants these droplets will only exist in the latter stages of the LP turbine, while in PWR plants steam enters the high-pressure cylinder approximately saturated, and will therefore remain in the two-phase regime for most of the subsequent expansion. It has long been appreciated that stages operating with wet steam function at a lower efficiency than they would under dry, superheated conditions (Baumann, 1921), although until recently detailed evidence regarding the magnitude of this effect was absent. Measurements of the thermodynamic state of the steam have now been obtained from within many LP turbines using optical and aerodynamic probes developed at the Central Electricity Research Laboratories (CERL) of the CEGB (Walters, 1985). These results have indicated that an unusually high loss is often associated with the onset or early stages of condensation. This is demonstrated in Fig. 1 (Walters, 1985; Walters, et al., 1984, 1986) which shows the condition lines for several of the turbines where this effect has been observed. In particular, Fig. 1 (*a*) indicates that this loss depends significantly upon inlet superheat and consequently upon the position where droplets first appear (see Walters, 1985).

The complex loss mechanisms associated with steam wetness have been discussed in depth (e.g., Gyarmathy, 1962; Moore, 1976; Deich, 1984), but generally remain poorly understood to the extent that no firm explanations for the behavior illustrated in Fig. 1 have been forthcoming. Theoretical predictions of droplet nucleation have been largely restricted to one dimension (e.g., Gyarmathy and Meyer, 1965; Moore et al., 1973; Bakhtar et al., 1975; Young, 1982), although recently some two-dimensional codes have appeared (Bakhtar and Mohammadi Tochai, 1980; Simanovskii, 1982; Moheban and Young, 1984; Snoeck, 1987). However, these multidimensional solvers are in an early stage of development, and, since one-dimensional predictions have often been rigorously validated, it is tempting to apply this simplified approach directly to predict measured turbine droplet sizes. Successful prediction of measured outlet conditions from a stage using the measured inlet conditions would indicate that the flow was being adequately modeled, and provide clues as to the source of the high loss.

This paper describes an analysis of flow in the nucleating stage of a turbine where geometric information has been combined with data from traverse measurements, thus enabling comparisons to be made for droplet size between one-dimensional theory and the results of optical measurements. This analysis represents a crude approximation to the three-dimensional conditions prevailing in a real machine, but is believed to provide the most realistic model possible within the confines of a one-dimensional theory.

2 One-Dimensional Nucleating Steam Flows

A flow solver to predict phenomena associated with the release of latent heat into a steam flow following spontaneous condensation must involve many complex facets (theories for homogeneous nucleation and droplet growth, ability to solve transonic flow regimes, etc.), and the reader is referred to more detailed accounts (e.g., Gyarmathy, 1976). Of particular interest is the fact that this heat release to an initially supersonic flow can result in a number of flow regimes

Contributed by the Power Division for publication in the JOURNAL OF TURBOMACHINERY. Manuscript received by the Power Division March 1988.

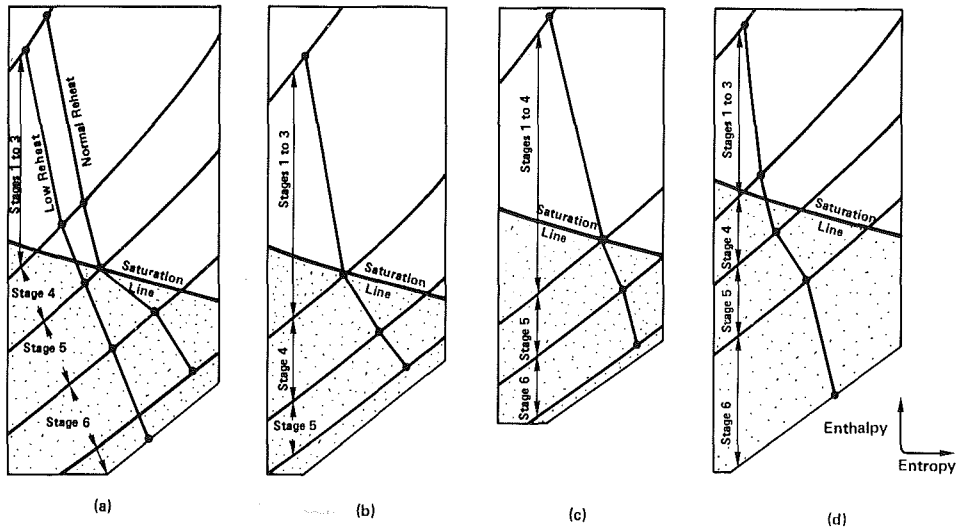

Fig. 1 Typical measured LP turbine condition lines (not drawn to scale)

(Barschdorff, 1970). In the subcritical regime the flow remains steady, continuous, and supersonic, while in the supercritical regime a shock wave will be established in the flow that may either be steady or periodically unsteady. Skillings and Jackson (1987) describe two computer programs written to predict one-dimensional nucleating steam flows. The first integrates the steady ordinary differential flow equations using a Runge–Kutta technique and an extrapolation procedure to progress from the elliptical subsonic domain to the hyperbolic supersonic domain. The second method, which is more general but time consuming, involves solution of the hyperbolic unsteady flow equations using MacCormack's finite difference scheme, with droplets considered using a Lagrangian approach. Of these, the Runge–Kutta program is only suited to prediction of subcritical flows, while the time-marching technique has been able to predict all the regimes that arise in one-dimensional flows (Skillings et al., 1987). These programs may be directly applied to analyze turbine flow, provided an equivalent one-dimensional geometry can be generated that adequately represents the three-dimensional turbine flow, and a minor modification is included to account for motion in a rotating frame (see Skillings, 1987).

Efforts to apply a one-dimensional theory to the turbine situation have fallen into two principal categories: those in which an effective one-dimensional duct is created by considering the blade geometries (e.g., Bakhtar et al., 1976; Bakhtar and Heaton, 1981) and those in which a pressure history is obtained for the turbine using the predictions of an axisymmetric through-flow program (e.g., Dibelius et al., 1987; Klietz et al., 1986). In the first case, the problem can be treated identically to a nozzle calculation, while in the second situation the area becomes a variable and the pressure distribution is fed into the flow equations as a source term. The pressure variation demanded for this latter approach is likely to have been produced by a simple interpolation and will be continuous, thus precluding the appearance of shock waves and unsteadiness. The calculated losses are therefore limited to those arising purely from thermodynamic irreversibilities, and, since such losses are never greater than a few percent, they will certainly not provide explanations for the effects illustrated in Fig. 1. The technique that involves a prescribed area variation is far more likely to provide clues as to the physical mechanisms causing these high losses, and was therefore chosen for the analysis described in this paper. However, there is a danger that arbitrary implementation of such a geometry may lead to extremely inaccurate predictions of parameters such as pressure and mass flow rate. An element of flexibility in the area variation must therefore be retained to ensure that physically reasonable solutions are produced.

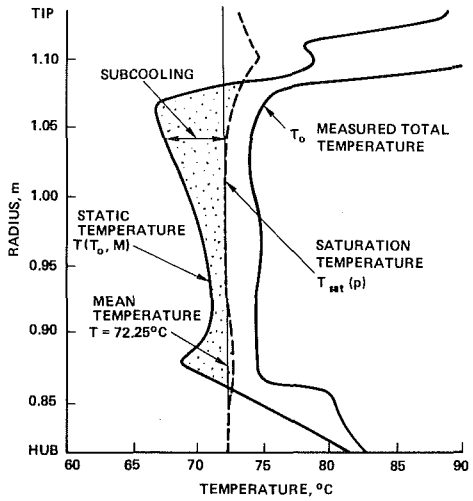

Fig. 2 Temperature profiles at inlet to Stage 5

3 Analysis Technique

A machine was selected for investigation from which consistent and well-documented data have been obtained (Walters et al., 1984). The condition line for this turbine is given in Fig. 1(*c*) and it can be seen to display an increased loss over the nucleating stage (albeit less pronounced than that observed in many other machines). Optical measurements revealed that the flow was dry at inlet to the fifth stage; however, recovery of the static temperatures (from measured totals using the corresponding Mach number distribution and assuming a dry expansion) revealed the flow to be subcooled over most of the blade (Fig. 2). Three streamtubes were chosen for investigation and were positioned at approximately one quarter, half, and three quarters blade height. The measured conditions at the outlet are given in Table 1(*a*). Flow streamlines within a stage were obtained using the CEGB's axisymmetric through-flow computer program "SLEQ," and consequently inlet radii were found that correspond to the outlet radii of interest, in addition to values for radii at intermediate positions throughout the stage. Given these inlet radii, the aerodynamic

Table 1(a) Measured streamtube outlet conditions

	Radius (m)	Static Pressure (bars)	Droplet Diameter (μm)	Velocity (m/s)	Yaw Angle (°)
Streamtube A	0.958	0.1458	0.295	124.6	-1.7
Streamtube B	1.111	0.1437	0.264	137.0	5.4
Streamtube C	1.251	0.1417	0.319	160.8	11.7

Table 1(b) Measured streamtube inlet conditions

	Radius (m)	Total Pressure (bars)	Total Temperature (K)	Velocity (m/s)	Yaw Angle (°)
Streamtube A	0.884	0.3698	347.6	140.8	2.7
Streamtube B	0.974	0.3638	347.8	136.7	15.5
Streamtube C	1.049	0.3824	347.3	166.8	32.5

and thermodynamic conditions at inflow for the three streamtubes could be acquired from traverse data (Table 1 (b)).

In addition to the traverse data given in Table 1, geometric information regarding blade passages was also required, and this was obtained from engineering drawings. Initially, only the two-dimensional blade section was considered. The generation of an equivalent one-dimensional streamtube was simplified by calculating only inlet, outlet, and throat areas, the complete geometry being produced by fitting two general cubic expressions such that the duct was parallel at inlet and outlet and continuous in first derivatives at the throat. These three areas were obtained from the blade geometry, measured inlet flow angle, and an outlet angle, coupled to an arbitrary value for streamtube height, with an effective streamtube length being extracted from the drawings. Figure 3 illustrates this process for the stator passage of Streamtube A.

For simplicity it was assumed that the flow choked in either the stator or the rotor passage, but not in both. With flow choking in the stator passage the analysis could proceed as follows. No information exists concerning the outlet flow angle from the stator blades and consequently the outlet area for the stator streamtube was unknown; this parameter was treated as a variable with calculations performed for a number of alternatives. However, the choking mass flow is defined uniquely by the ratio of inlet to throat areas and it was found that the inlet velocity resulting from this geometry differed from the measured values. This was attributed to a "flare" in the streamtubes and the area ratios were adjusted accordingly to give approximately the measured inlet velocities (Fig. 4).

A number of solutions could now be produced corresponding to different values of outlet flow angle, thus providing the inlet conditions for the rotor passage, with the correct relative inlet velocity being calculated in the rotating frame. The equivalent one-dimensional streamtube could then be generated in the same way as for the stator. Since it was assumed that the flow was subsonic throughout the rotor passage, it was sometimes necessary to introduce a small angle of streamtube flare to ensure that subsonic conditions prevailed. Again no direct information exists as to the value of the outlet flow angle in the rotating frame, and solutions were therefore produced for a number of alternatives. Calculations in the rotor passage involved modifications to the flow equations to allow for acceleration effects associated with a rotating frame.

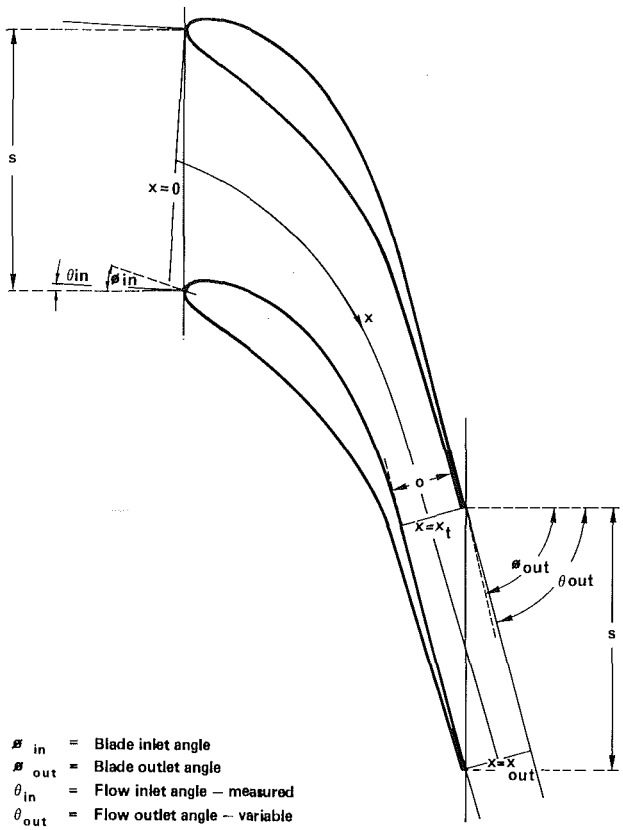

ϕ_{in} = Blade inlet angle
ϕ_{out} = Blade outlet angle
θ_{in} = Flow inlet angle – measured
θ_{out} = Flow outlet angle – variable
x_t = 0.221 m
x_{out} = 0.341 m
A_{in} = Streamtube inlet area = $h_{in} s (\cos\theta_{in})$
A_t = Streamtube throat area = $h_t o$
A_{out} = Streamtube outlet area = $h_{out} s (\cos\theta_{out})$
Where s = Blade pitch
o = Blade opening
h = Streamtube height (see Fig. 4)

Fig. 3 Generation of equivalent one-dimensional geometry for stator passage of Streamtube A

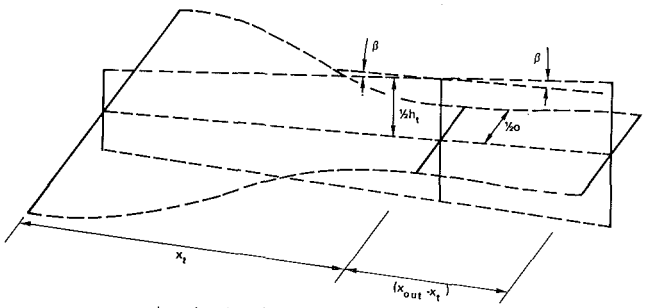

$h_{in} = h_t - 2x_t \tan\beta \cos\theta_{in}$

$h_{out} = h_t + 2(x_{out} - x_t)\tan\beta\cos\theta_{out}$

Where 'flare' angle β is chosen to give the correct choking mass flow and blade inclination angles θ_{in} and θ_{out} are included to account for the flow turning with respect to the axial direction

Fig. 4 Calculation of streamtube height

Having created a series of possible outlet conditions corresponding to different outlet flow angles from the stator and rotor, comparisons could be made with the traverse measurements. The correct values for the outlet flow angles were taken to be those that resulted in the best agreement with measurements of pressure and velocity vector (the calculation results having been transformed out of the rotating frame).

Table 2 Predicted outlet conditions from stator in Streamtube A

Outlet Angle (°)	Static Pressure (bars)	Static Temperature (K)	Velocity (m/s)	Droplet Size (μm)	Oscillation Frequency (Hz)
72.00	0.1051	318.33	607.73	0.1318	2319
74.16	0.1379	323.51	538.89	0.1814	870
75.40	0.1683	325.98	482.89	0.1909	794
75.50	0.1721	326.24	476.09	0.1951	784
75.55	0.1742	326.42	472.40	0.1980	776
75.60	0.1763	326.47	468.61	0.2021	767
75.65	0.1785	326.62	465.25	0.2040	753
75.70	0.1808	326.70	460.70	0.2090	737
75.75	0.1832	326.79	456.57	0.2113	735

The level of agreement between measured and calculated droplet sizes could then be assessed.

If it was assumed that the flow choked in the rotor, the techniques applied to calculations in the stator and rotor were simply reversed. Consequently, in the stator the streamtube flare was adjusted where necessary to ensure the flow remained subsonic, while in the rotor it was varied to give the correct choking mass flow. Since the time-marching program was used for the rotor calculation, it was necessary to ensure that the corrections demanded for a rotating frame were expressed in conservation form.

The time-marching program was only employed to perform the transonic computations. Flows in the subsonic passages were calculated using the Runge–Kutta program; apart from the obvious advantage in computation time, this approach was considered reasonable since flows can be expected to be continuous and steady in an elliptic computational regime.

4 Streamtube A

At one quarter blade height it was predicted by SLEQ that the flow would choke in the stator passage, and Streamtube A was analyzed by assuming this to be the case. With a streamtube height of 1 cm at the throat, the angle of flare required to produce the correct inlet velocity was found to be 0.68 deg.

A number of different outlet flow angles were investigated and the results are summarized in Table 2. All of these calculations predicted the heat release to be supercritical and of these, only at an outlet angle of 72 deg was the flow virtually steady, exhibiting small, high-frequency fluctuations around the shock wave. In unsteady flows that display significant movement of the shock position, the nucleation zone is being periodically quenched, and this consequently results in a larger mean droplet size and also a lower mean wetness fraction (see Skillings and Jackson, 1987). The outlet angle of 74.16 deg was considered, since this was the value predicted by SLEQ. Values given in Table 2 represent the arithmetic mean of the unsteady outlet conditions, which could then be used as inlet data for the rotor passage. Typical variations in outlet pressure, droplet size, and wetness fraction are shown in Fig. 5. For the larger outlet angles, significant spatial oscillations

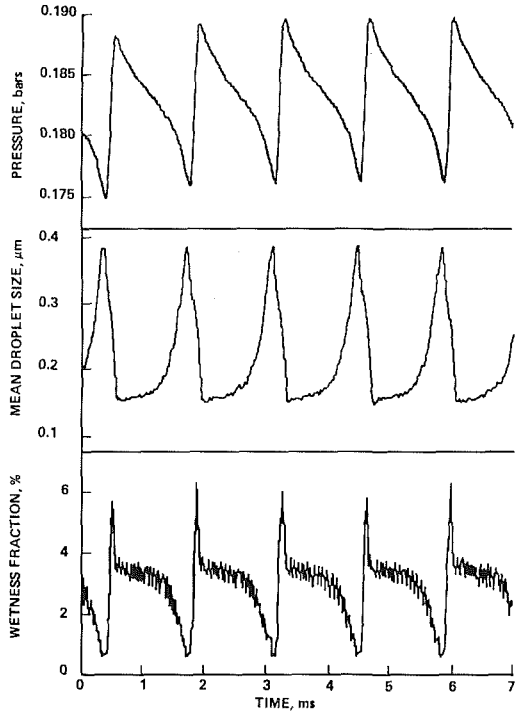

Fig. 5 Variation in outlet pressure, droplet size, and wetness fraction from stator in optimized Streamtube A

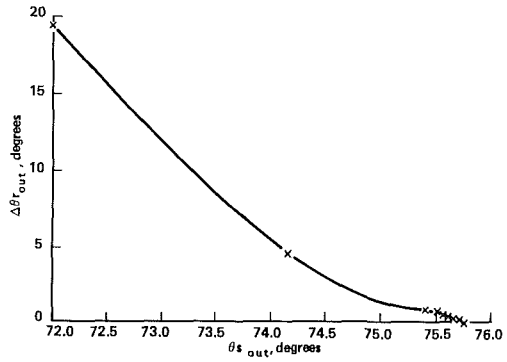

Where θs_{out} is the stator outflow angle and $\Delta\theta r_{out}$ is the difference between the rotor outflow angle which provides best agreement with measured pressure and that which provides best agreement with measured velocity vector

Fig. 6 Selection of optimum outflow angles for Streamtube A

in the predicted flow field were generated near the outflow boundary, which is suspected to be a consequence of the boundary conditions producing errors when the outflow is continually changing between subsonic and supersonic. In order to prevent these inaccuracies from being transferred to the rotor inlet, the streamtube was artificially lengthened, thus producing the true outlet conditions away from the outflow boundary.

The rotor analysis was then performed with the aim of finding which combination of outlet flow angles produced the best agreement with measured pressure and velocity vector (both magnitude and direction being considered). The results are plotted in Fig. 6. The correct flow outlet angles were taken to be those that produced optimum predictions of both pressure and velocity, and this was found to occur at an outlet flow angle from the stator of 75.75 deg and of −65.4 deg from the rotor. Outlet conditions for this optimized streamtube are compared with measured values in Table 3; this comparison shows that the prediction for droplet size was slightly low.

Table 3 Comparison between measurement and prediction for Streamtube A outlet conditions

	Static Pressure (bars)	Flow Velocity (m/s)	Flow Angle (°)	Droplet Diameter (μm)
Measurement	0.1458	124.6	-1.7	0.295
Prediction	0.1457	135.2	-0.6	0.242

Table 4 Comparison between measurement and prediction for Streamtube A outlet conditions with aerodynamic loss included in the calculation

	Static Pressure (bars)	Flow Velocity (m/s)	Flow Angle (°)	Droplet Diameter (μm)
Measurement	0.1458	124.6	-1.7	0.295
Prediction	0.1458	137.2	-1.0	0.286

Bakhtar et al. (1976) note that droplet size can change significantly if consideration is given to aerodynamic loss, which they modeled in their turbine analysis by using friction factors. In order to investigate the influence of this frictional reheat, friction factors were introduced into the program in terms of a loss coefficient and the calculation for Streamtube A repeated with a 10 percent loss included over each blade row. The general effect of introducing a loss was to increase the droplet size. The predicted conditions at the rotor outlet are compared with measured values in Table 4.

Considering the gross simplification of the model, the results produced are very interesting. In particular, it should be noted that the level of agreement attained, with or without loss included in the calculation, could only be approached if the flow out of the stator passage was unsteady; steady flow in the stator resulted in conditions that were totally unreconcilable with traverse data.

5 Streamtubes B and C

The analysis was repeated for the streamtubes at approximately one half and three quarters blade height (no frictional loss being included). For Streamtube B, physically reasonable results were only obtained when the flow was assumed to have choked in the stator passage. It was again predicted that condensation-induced instabilities would arise in this transonic flow passage, and the subsequent agreement with traverse data at outlet from the rotor passage is given in Table 5.

For Streamtube C, best agreement with traverse data was attained with the flow choking in the rotor passage. Thus, in this case, the flow was steady in the subsonic stator passage, while in the transonic rotor passage it was predicted to be unsteady. The comparison with measured results at outlet from the rotor is given in Table 6.

The significant result to emerge from these analyses has been the inability of measured turbine droplet sizes to be predicted in terms of steady flow regimes arising from homogeneous nucleation theory, since this appears to produce droplet sizes that are too small. Comparisons have been made between the predictions of one-dimensional theory and droplet sizes measured at the outflow from a cascade of turbine blades (Skillings, 1987), and in this case, homogeneous nucleation theory predicted a droplet size that was too large. We can therefore conclude that steady homogeneous nucleation within a blade passage is unlikely to be the sole mechanism by which water droplets are produced in turbines.

Table 5 Comparison between measurement and prediction for Streamtube B outlet conditions

	Static Pressure (bars)	Flow Velocity (m/s)	Flow Angle (°)	Droplet Diameter (μm)
Measurement	0.1437	137.0	5.4	0.264
Prediction	0.1436	130.1	16.5	0.301

Table 6 Comparison between measurement and prediction for Streamtube C outlet conditions

	Static Pressure (bars)	Flow Velocity (m/s)	Flow Angle (°)	Droplet Diameter (μm)
Measurement	0.1417	160.8	11.7	0.319
Prediction	0.1424	166.5	11.8	0.177

Table 7 Results at stator outlet for optimized Streamtube A with heterogeneous nucleation included in the calculation

Impurity Radius (nm)	Number Concentration (/kg)	Flow Regime
1.0	2.4×10^{15}	Stable - no nucleation
2.0	3.0×10^{14}	Stable - subcritical
3.0	8.8×10^{13}	Small oscillations
4.0	3.7×10^{13}	Strong oscillations
5.0	1.9×10^{13}	Strong oscillations

Impurity Radius (nm)	Static Pressure (bars)	Static Temperature (K)	Velocity (m/s)	Droplet Size (μm)	Oscillation Frequency (Hz)
1.0	0.1693	326.11	481.68	0.2954	----
2.0	0.1627	311.32	489.07	0.5237	----
3.0	0.1875	328.50	448.34	0.2548	431
4.0	0.1845	325.61	453.09	0.2772	441
5.0	0.1841	326.09	454.27	0.2418	532

Much closer agreement with traverse data was produced when condensation-induced shock fluctuations were predicted to arise in the flow passage. It was shown by Skillings (1987) that trailing edge shock fluctuations will arise in transonic flows over a range of mean outlet Mach numbers that are approximately sonic or subsonic, and this fluctuating shock will interact strongly with the nucleation zone producing much larger droplets ($\simeq \times 2$). Outlet Mach numbers have been

predicted in this analysis that would potentially give rise to this phenomenon, and it therefore appears that this unsteady regime may well be important in the nucleating stage.

6 Heterogeneous Nucleation

The calculations discussed above consider the liquid phase to have appeared spontaneously from the vapor phase via random kinetic processes within the gas. Atmospheric physicists concerned with the formation of clouds and aerosols rarely encounter this homogeneous nucleation, and are principally concerned with heteromolecular nucleation onto ions or other molecules and heterogeneous nucleation onto airborne particles. It has regularly been suggested that these mechanisms are also important within turbines (e.g., Dibelius and Mertens, 1982; Martsinovskii, 1983), and experiments have recently been performed in the USA (Steltz et al., 1983) that reveal the presence of a liquid phase containing concentrated impurities in the region of the saturation line. This indicates a near-equilibrium progression into the two-phase regime, and is held responsible for promoting corrosion induced blade failures. It is probable that within turbines, droplets arise as a result of combined homogeneous and heterogeneous processes, and it is particularly significant to notice that a mean droplet diameter of 2.48 μm and a wetness fraction of 0.3 percent are quoted by Steltz et al. (1983) at one of the positions where concentrated impurities were detected. Such large droplets are virtually inert as regards interphase transfer, and would certainly not prevent the critical supersaturation required to initiate spontaneous condensation from being attained in a subsequent blade passage. Within a turbine the mechanisms by which the liquid phase appears is likely to be complicated, with flow heterogeneity also potentially important (i.e., nonuniform attainment of critical supersaturation in regions such as blade vortices, flow turbulence, boundary layers, etc). However, Dibelius et al. (1987) have recently highlighted the significant influence particulate impurities can potentially exert over the ultimate droplet size,[1] and it is therefore interesting to consider these effects in the current analysis.

It is possible to investigate the influence of heterogeneous nucleation provided values for mean particle size and number concentration are available. These condensation centers are considered inactive until the critical radius (at which droplet growth becomes an energetically favorable process) is lower than the particle radius. It is assumed at this juncture that condensation can proceed onto these impurities in the same way as if they were tiny water droplets. It is possible that this assumption is slightly erroneous at the very initial stages of condensation due to the different water-water and water-impurity affinities, and the fact that condensation coefficients may be significantly different for a droplet containing concentrated impurities.

No measurements have been obtained regarding the size and concentration of impurity particles for dry steam within a turbine, although Dibelius et al. (1987) have investigated heterogeneous nucleation in slow expansions and suggest that a droplet number concentration of 3.5×10^{14} kg^{-1} is produced regardless of the initial impurity mass fraction. It is known that silica is typically the major impurity found in power plant live steam and has been detected in concentrations of up to 20 ppb. Assuming this impurity mass fraction, an approximate relationship between particle size and number concentration can be obtained (ρ is density, y is mass fraction, n is number density, m is particle mass, and subscript s refers to silica).

[1] It should be noted that the impurity concentration of 3 ppm used by Dibelius et al. (1987) is considerably greater than that commonly encountered in power plant steam.

Table 8 Comparison between stator outlet conditions produced using a steady and a fluctuating inflow for optimized Streamtube A

Inlet Condition	Static Pressure (bars)	Static Temperature (K)	Velocity (m/s)	Droplet Size (μm)
Steady	0.1832	326.79	456.57	0.2113
Unsteady	0.1848	326.75	452.89	0.2255

Taking

$$\rho_s \simeq 2000 \text{ kgm}^{-3} \text{ and } y_s \simeq 2\times10^{-8}$$

Since

$$n_s m_s = y_s \text{ and } m_s = \frac{4}{3}\pi r_s^3 \rho_s$$

We have

$$n_s r_s^3 \simeq 2.4\times10^{-12}$$

Calculations were performed using the optimized Streamtube A in order to reveal the influence that this level of impurity can exert upon the nucleation and growth phenomena. The results at outlet from the stator, for a range of impurity particle sizes, are given in Table 7. It was found that a mean particle radius of ≤ 5 nm was required in order to alter the flow characteristics significantly. However, unsteady conditions prevailed with a radius ≥ 3 nm, the effect of introducing heterogeneous nucleation being to increase droplet size and reduce the oscillation frequency.

The Dibelius number concentration of 3.5×10^{14} kg^{-1} implies a particle radius $\simeq$ 2 nm and this is indeed sufficient virtually to eliminate spontaneous nucleation. Creation of such particles can only be envisaged in terms of a separate impurity nucleation process and a computational analysis of this combined effect can be expected to be complex (particularly if the different water-water, water-impurity, and impurity-impurity affinities are considered). However, the significant influence that particles of this size can exert is evident and there exists an obvious requirement for further study in this area. The importance of these particulate impurities can be seen to diminish rapidly as their size increases, and, in the particular context of this study, calculations have indicated that a radius <3 nm is required to suppress the existence of condensation-induced unsteadiness.

7 Flow Turbulence

An additional phenomenon that could potentially govern the onset of nucleation is that resulting from the levels of turbulence existing within a machine. Wood (1973) has reported temperature fluctuations $\simeq$ 20 K and it is easy to imagine that a small pocket of fluid containing 20 K additional subcooling could prematurely initiate nucleation of droplets, which then proceed to inhibit nonequilibrium conditions from developing in the remainder of the flow.

Due to the unsteady formulation of the time-marching program it is possible to model turbulence effects by considering simple temporal variations in inlet conditions. The influence of a fluctuating inflow condition on the droplet size predicted in Streamtube A was investigated. A significant source of flow turbulence incident upon the stator blade row is that produced by the periodic passing of blade wakes from the upstream rotor, and inflow fluctuations were included at the blade passing frequency to represent this effect. The turbulent change was considered only in terms of a temperature fluctuation and

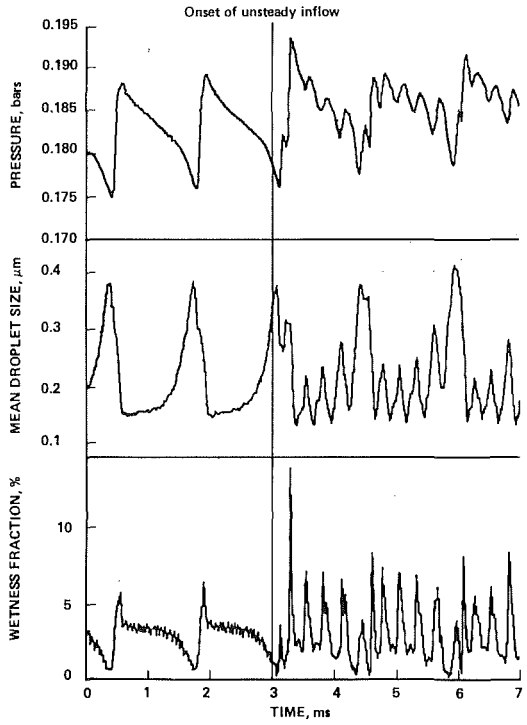

Fig. 7 Change in stator outlet conditions produced by introducing an unsteady flow

the inlet pressure was held constant. Wood measured rms temperature fluctuations downstream of the rotor hub to be $T'_0/T_0 = 0.029$. For $T_0 = 347.58$ K, $T'_0 \simeq 10$ K and this value was incorporated. A periodic temperature wave was considered, comprising positive and negative rectangular pulses to simulate pockets of superheated and subcooled steam.

Figure 7 illustrates the effect at the stator outlet upon droplet size, wetness fraction, and pressure when a perturbation of this nature was introduced. The fundamental oscillation frequency was maintained with the higher frequency component superimposed. The mean values of the outlet conditions produced with the fluctuating inflow conditions are compared with those produced by a steady inflow in Table 8, and they show that these mean values have not been greatly affected.

This result demonstrated that a typical level of fluctuation in the inflow conditions did not destroy the unsteady nature of the solution or significantly alter the mean outlet conditions. Additionally, and perhaps more importantly, the time-marching program has proved robust toward the introduction of unsteady inlet conditions, and this technique will consequently provide a useful facility should further studies of this nature be attempted.

8 Conclusions

A one-dimensional analysis of flow through the nucleating stage of a turbine has been described, and represents the first reported occasion where such predictions have been linked closely with turbine traverse data enabling comparisons to be made with measured droplet sizes. The actual flow within a turbine is three dimensional, and the appearance of the liquid phase is almost certainly strongly influenced by particulate and gas-dynamic heterogeneity. Consequently, this one-dimensional approach is an extremely crude approximation and any conclusions should only be drawn tentatively. However, a number of extremely important results have arisen, and, if viewed in the context of condensation phenomena observed under more representative conditions (e.g., Skillings, 1987), it is reasonable to speculate upon their implications for operating turbines.

1 The conditions at the inlet to the nucleating stage were such that a supercritical heat release was produced in all transonic passages investigated. This implies that an additional aerodynamic shock wave may arise in the trailing edge shock system, which will add a small shock loss, and possibly give rise to adverse separation effects.

2 Droplet sizes measured in turbines cannot be predicted accurately in terms of steady homogeneous condensation, since this results in droplets that are too small.

3 Unsteady flows that arise in the region of the nucleation zone are known to significantly increase the droplet size. The results presented have indicated that these effects are potentially important in the turbine situation.

4 The influence of particulate impurities in the condensation process remains a point of much contention, since heterogeneous nucleation can give rise to larger droplets. However, calculations presented in this paper have suggested that, given the levels of impurity commonly encountered in power plant steam, a particle size of order a few nanometers would be required to alter the homogeneous process significantly. Mechanisms may nevertheless exist that are capable of producing such centers, and it is evident that further work is required in this area.

5 A temporal variation in inlet temperature was considered to simulate blade wake passing effects. Within the considerable limitations of the model it appeared to exert a surprisingly small influence.

Acknowledgments

The work was carried out at the Central Electricity Research Laboratories of the Technology Planning and Research Division and the paper is published with permission of the Central Electricity Generating Board. The investigation described forms part of the PhD project of SAS and he gratefully acknowledges the help and advice of his supervisors, Dr. M. J. Moore and Dr. F. Bakhtar. The authors would also like to thank Messers R. W. Langford and K. R. Keeley for supplying flow distributions measured in turbines.

References

Bakhtar, F., and Heaton, A. V., 1981, "A Theoretical Comparative Study of Wetness Problems in a Model and Full Scale Turbine," *Aerothermodynamics of Steam Turbines*, ASME, New York.

Bakhtar, F., and Mohammadi Tochai, M. T., 1980, "An Investigation of Two-Dimensional Flows of Nucleating and Wet Steam by the Time-Marching Method," *Int. J. Heat and Fluid Flow*, Vol. 2, No. 1, pp. 5–19.

Bakhtar, F., Ryley, D. J., Tubman, K. A., and Young, J. B., 1975, "Nucleation Studies in Flowing High Pressure Steam," *Proc. IMechE*, Vol. 189, pp. 427–436.

Bakhtar, F., Young, J. B., and Ghoniem, Z., 1976, "A Study of Nucleating and Wet Steam Flows in Turbines," *Heat and Fluid Flow*, Vol. 6, No. 2, pp. 119–133.

Barschdorff, D., 1970, "Droplet Formation, Influence of Shock Waves and Instationary Flow Patterns by Condensation Phenomena at Supersonic Speeds," Brd. Int. Conf. of Rain Erosion and Associated Phenomena, Farnborough, United Kingdom.

Baumann, K., 1921, "Some Recent Developments in Large Steam Turbine Practice," *J. Instn. Elec. Engrs.*, Vol. 59, p. 565.

Deich, M. E., 1984, "Wet-Steam Turbines: Some Problems in Economy and Reliability," *Power Eng.*, New York, Vol. 22, No. 1, pp. 53–69.

Dibelius, G., and Mertens, K., 1982, "Wet Steam in Turbines," *Proc. 14th Symp. Int. Centre for Heat and Mass Transfer*, Dubrovnik, Yugoslavia.

Dibelius, G. H., Mertens, K., Pitt, R. U., and Strauf, E., 1987, "Investigation of Wet Steam Flow in Turbines," Int. Conf. on Turbomachinery, IMechE Paper No. C271/87, Cambridge, United Kingdom.

Gyarmathy, G., 1962, "Basis for a Theory for Wet Steam Turbines," Bull. 6, Inst. for Thermal Turbomachines, Federal Technical University, Zurich, Switzerland.

Gyarmathy, G., 1976, in: *Two-Phase Steam Flow in Turbines and Separators*, M. J. Moore and C. H. Sieverding, eds., Hemisphere Pub. Corp., Washington, DC, Chap. 3.

Gyarmathy, G., and Meyer, H., 1965, *Spontaneous Condensation Phenomena*, V.D.I. Forschungsheft 508 (C.E. Trans. 4160).

Klietz, A., Laali, A. R., and Marty, C., 1986, EdeF, Private Communication.

Martsinkovski, S., 1983, "An Experimental Determination of the Site of Occurrence of Condensation in a Steam Turbine," *Teploenergetika*, No. 1, pp. 69–72 (in Russian).

Moheban, M., and Young, J. B., 1984, "A Time-Marching Method for the Calculation of Blade-to-Blade Non-equilibrium Wet-Steam Flows in Turbine Cascades," IMechE Conference Publications, Computational Methods for Turbomachinery, Paper C76/84, Birmingham, United Kingdom.

Moore, M. J., 1976, *Two-Phase Steam Flow in Turbines and Separators*, M. J. Moore and C. H. Sieverding, eds., Hemisphere Pub. Corp., Washington, DC, Chap. 2.

Moore, M. J., Walters, P. T., Crane, R. I., and Davidson, B. J., 1973, "Predicting the Fog Drop Size in Wet-Steam Turbines," IMechE Conf., Wet Steam 4, Paper No. C37/73, Warwick, United Kingdom.

Simanovskii, G. P., 1982, "A Numerical Investigation Into Nonhomogeneous Mixed Flows With Nonequilibrium Phase Transformations in Nozzles and Cascades of Turbine Blades," Dissertation for the Degree of Candidate of Technical Sciences (in Russian), MEI, Moscow, Soviet Union.

Skillings, S. A., 1987, "An Analysis of the Condensation Phenomena Occurring in Wet Steam Turbines," PhD Thesis, CNAA, CERL, United Kingdom.

Skillings, S. A., and Jackson, R., 1987, "A Robust Time-Marching Solver for One-Dimensional Nucleating Steam Flows," *Int. J. of Heat and Fluid Flow*, Vol. 8, No. 2, pp. 139–144.

Skillings, S. A., Walters, P. T., and Moore, M. J., 1987, "A Study of Supercritical Heat Addition as a Potential Loss Mechanism in Condensing Steam Turbines," Int. Conf. on Turbomachinery, IMechE Paper No. C259/87, Cambridge, United Kingdom.

Snoeck, J., 1987, *Aerothermodynamics of LP Turbines and Condensers*, M. J. Moore and C. H. Sieverding, eds., Hemisphere Pub. Corp., Washington, DC, Chap. 4.

Steltz, W. G., Lee, P. K., and Lindsay, W. T. Jr., 1983, "The Verification of Concentrated Impurities in Low-Pressure Steam Turbines," ASME *Journal of Engineering for Power*, Vol. 105, pp. 192–198.

Walters, P. T., 1985, "Wetness and Efficiency Measurements in LP Turbines With an Optical Probe as an Aid to Improving Performance," ASME Paper No. 85-JPGC-GT-9.

Walters, P. T., Langford, R. W., and Keeley, K. R., 1986, CERL Internal Communication.

Walters, P. T., Langford, R. W., Keeley, K. R., and Jackson, R., 1984, CERL Internal Communication.

Wood, N. B., 1973, "Flow Unsteadiness and Turbulence Measurements in the Low-Pressure Cylinder of a 500 MW Steam Turbine," IMechE, Wet Steam 4, C54/73 Conference.

Young, J. B., 1982, "The Spontaneous Condensation of Steam in Supersonic Nozzles," *PCH*, Vol. 3, No. 1, pp. 57–82.

Tip Leakage in a Centrifugal Impeller

T. Z. Farge

M. W. Johnson

T. M. A. Maksoud

Department of Mechanical Engineering,
The University of Liverpool,
Liverpool, L69 3BX,
United Kingdom

The effects of tip leakage have been studied using a 1-m-dia shrouded impeller where a leakage gap is left between the inside of the shroud and the impeller blades. A comparison is made with results for the same impeller where the leakage gap is closed. The static pressure distribution is found to be almost unaltered by the tip leakage, but significant changes in the secondary velocities alter the size and position of the passage wake. Low-momentum fluid from the suction-side boundary layer of the measurement passage and tip leakage fluid from the neighboring passage contribute to the formation of a wake in the suction-side shroud corner region. The inertia of the tip leakage flow then moves this wake to a position close to the center of the shroud at the impeller outlet.

Introduction

The effect of tip leakage on the performance of centrifugal compressors has been studied for many years. Hamrick (1954) observed that the efficiency of a radial inlet centrifugal impeller was, in general, improved by reduction in tip clearance gap. This result has since been confirmed by many authors (e.g., Mashimo, 1979; Ishida and Senoo, 1981). Detailed flow measurements in a low-speed impeller for five different tip clearances ranging from zero to about 12 percent of blade height were made by Fowler (1966). His results showed clearly how the wake was moved from the suction-side shroud corner with zero tip leakage to a position about midway along the shroud wall for his maximum tip leakage. Senoo et al. (1968) were able to visualize the three-dimensional nature of the tip leakage flow by using colored dye in water flowing through a centrifugal impeller. They concluded that most of the crossflow in the shroud boundary layer passes through the tip leakage gap and that this leads to some relaxation of the blade-to-blade pressure gradient.

Objective

The objective of this work was to determine the effect of the tip leakage flow on the complex three-dimensional flow pattern that occurs within the impeller. Accordingly, the authors measured distributions of all three velocity components and static and total pressures throughout the impeller for two flows, one with tip leakage and a second reference flow with no tip leakage.

Test Rig

The test rig (Fig. 1) has been described previously by Johnson and Moore (1983) and in detail by Johnson (1979). Only a brief description is given here together with modifications specific to the current work. The 1-m-dia shrouded impeller rotates at 500 rpm. A traverse gear enables a five-hole pressure probe to be traversed within the rotating impeller between the hub and shroud at various blade-to-blade locations on each of five cross-sectional measurement planes (see Fig. 2). The probe is connected to four differential pressure transducers whose amplified signals pass through sliprings to an analog-to-digital converter and microcomputer. The microcomputer then determines the three velocity components, together with static and total pressures, from the probe calibration curves. In the current work, two flows were measured: the first with an "oversize" shroud where a tip leakage gap of 2.5 mm (equivalent to 1.4 percent of the inlet blade height) was left between the inside of the shroud and the impeller blades, and the second as a reference flow where the gap was closed. The tip leakage flow between this rotating shroud and impeller is therefore different from the true flow between a stationary casing and a rotating impeller, as there is no relative motion between the surfaces forming the gap. Nevertheless, the important features of tip leakage and its influence on the flow in the impeller passage can be studied.

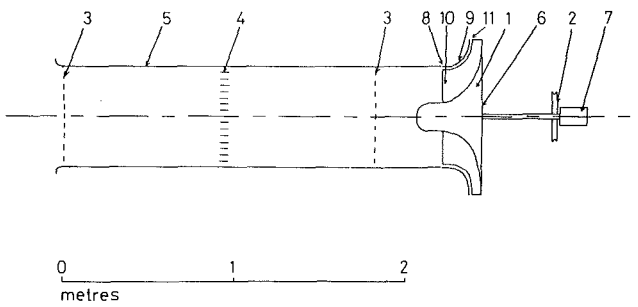

Fig. 1 Schematic of test rig: (1) impeller; (2) pulley driven by motor; (3) screens; (4) honeycomb; (5) inlet duct; (6) pressure transducers and amplifiers; (7) sliprings; (8) seal; (9) shroud attached to impeller; (10) boundary layer trips; (11) tip leakage gap

Contributed by the International Gas Turbine Institute and presented at the 33rd International Gas Turbine and Aeroengine Congress and Exhibition, Amsterdam, The Netherlands, June 5–9, 1988. Manuscript received by the International Gas Turbine Institute January 6, 1988. Paper No. 88-GT-210.

Table 1 Limiting rotary stagnation pressure

	Tip leakage	No tip leakage
P^*_{max} (N/m^2 gage)	−209	−237
P^*_{min} (N/m^2 gage)	−557	−633
Passage flow rate (kg/s)	0.133	0.128

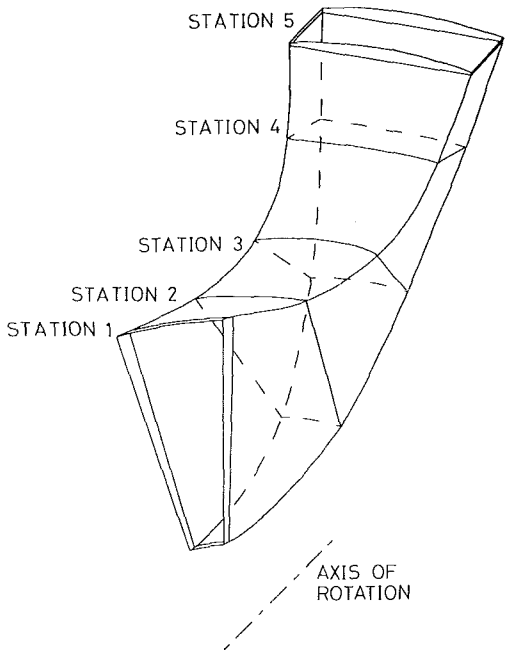

Fig. 2 Impeller passage with measurement planes

Presentation of Results

Rotary Stagnation Pressures. The maximum and minimum values of rotary stagnation pressure (p^*_{max} and p^*_{min}) are determined by examination of the measured flow data. At the impeller inlet, where the flow is more or less uniform, the p^* value obtained will be the maximum value observed in the flow. p^*_{min} will occur in regions of negligible velocity and low static pressure. The lowest values observed were close to the wall in the shroud suction-side corner of the inducer. The values used are given in Table 1.

Dimensionless pressures are defined from the limiting values as

$$P^* = \frac{p^* - p^*_{min}}{p^*_{max} - p^*_{min}} \quad (1)$$

and

$$P_r = \frac{p_r - p^*_{min}}{p^*_{max} - p^*_{min}} \quad (2)$$

where the reduced static pressure $p_r = p - 1/2\ \rho\ \omega^2 r^2$.

Both these dimensionless quantities will have values between 0 and 1. In particular, it should be noted that P^* will be unity throughout the inviscid potential flow region of the flow. The experimental accuracy is estimated to be ± 0.03 for both P^* and P_r.

Relative Velocities. Velocities are presented as contours representing the velocity component perpendicular to the measurement plane and arrows representing the remaining component in the measurement plane. The measurement planes are not perpendicular to the passage walls and

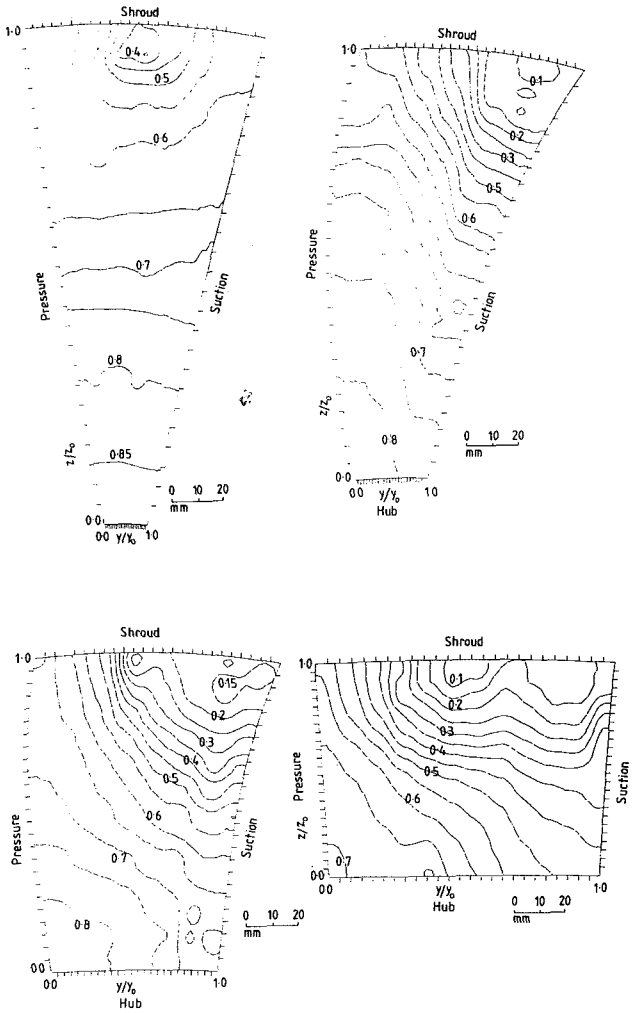

Fig. 3 Reduced static pressures with tip leakage

therefore, even when no secondary velocities are present, arrows result where the passage walls converge or diverge, particularly in the inducer. The estimated experimental accuracies are ±5 deg for flow direction.

Discussion

The impeller flow without tip leakage is at a slightly lower flow rate than that described previously by Johnson and Moore (1983). In the current paper this flow is used merely as a reference for the tip leakage case and is therefore not described in detail.

Reduced Static Pressures. The static pressure distributions are shown in Fig. 3 for the flow with tip leakage. These results are largely the same as for the flow without tip leakage, although the pressure gradient in the blade-to-blade direction

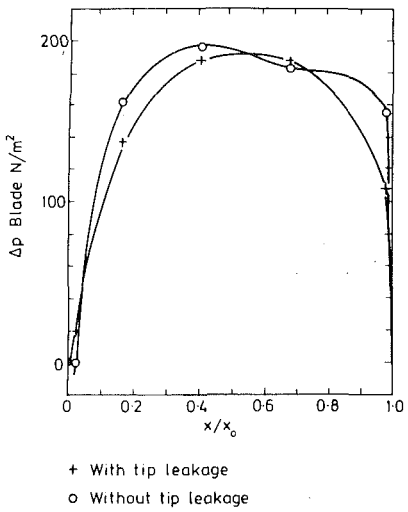

Fig. 4 Pressure differences across the blade at the shroud (derived from passage pressure probe measurements)

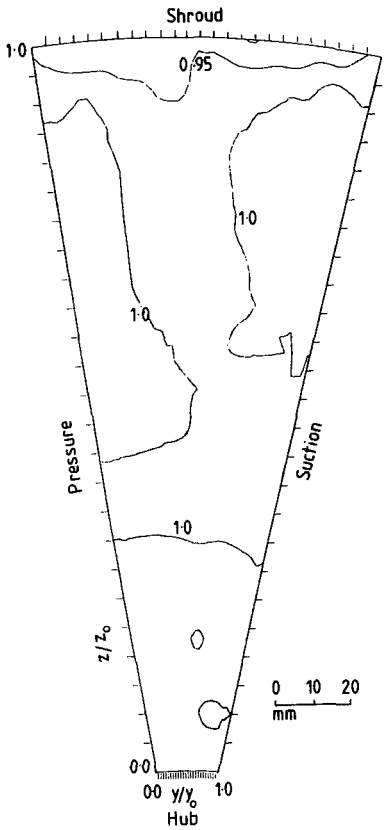

Fig. 5 Station 1—dimensionless rotary stagnation pressure P^* with tip leakage

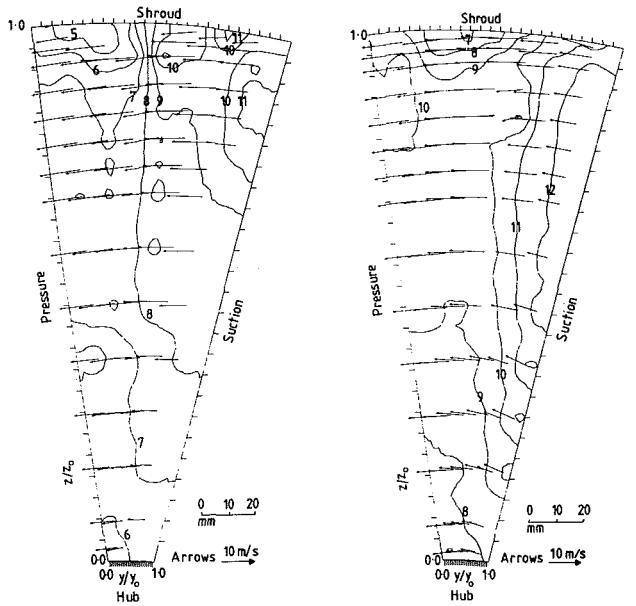

Fig. 6 Station 1—relative velocities/contours in m/s, (*a*) with, and (*b*) without tip leakage

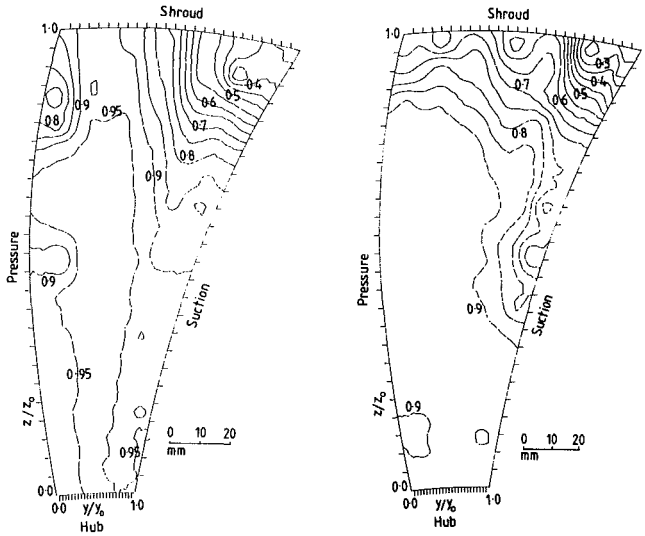

Fig. 7 Station 2—dimensionless rotary stagnation pressure P^*, (*a*) with, and (*b*) without tip leakage

close to the shroud is relieved slightly by the tip leakage flow (see Fig. 4). The pressure gradients are attributable to:

1 The passage curvature, which induces centrifugal pressure gradients in the blade-to-blade direction in the inducer and in the hub-to-shroud direction in the axial-to-radial bend, and

2 the Coriolis forces induced by the passage rotation, which lead to the pressure gradient in the final radial part of the impeller passage.

Three-Dimensional Flow

Station 1. Figure 5 shows that, in terms of the total pressure, the inlet flow is uniform, with the exception of the shroud boundary layer that has developed in the inlet duct upstream of the impeller. No significant differences exist due to the presence of tip leakage except in the velocity distributions in Fig. 6, where differences exist in the shroud region. This is attributable to the slightly higher flow rate in the tip leakage case, which leads to a different blade loading at the inlet (see Fig. 4).

Station 2. Figure 8 shows how a significant tip leakage flow has now been established, which substantially alters the secondary flow pattern near the shroud. In the no tip leakage case, the secondary flow convects the low p^* fluid from the shroud boundary layer into the suction-side shroud corner region (see Fig. 7*b*). With tip leakage, the presence of the blades only slightly diminishes the strong crossflow exhibited near the shroud at the inlet (Fig. 6). This crossflow therefore convects the low p^* fluid (Fig. 7*a*) from the shroud boundary layer toward the pressure-side corner where some of the fluid

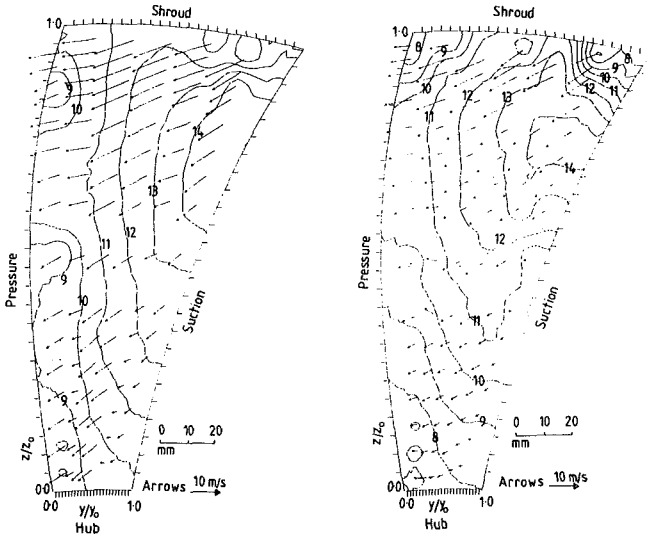

Fig. 8 Station 2—relative velocities/contours in m/s, (*a*) with, and (*b*) without tip leakage

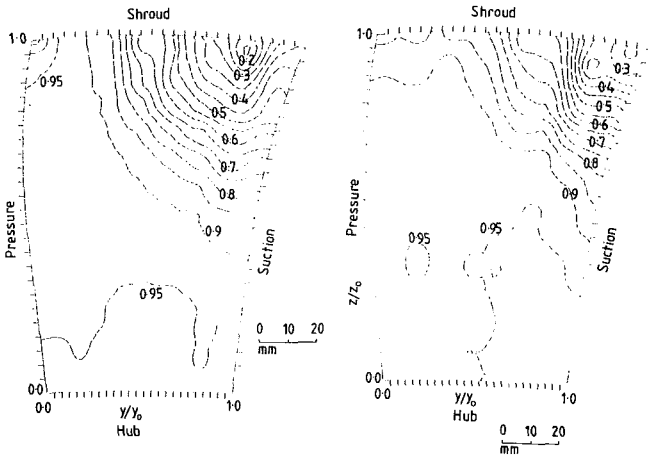

Fig. 9 Station 3—dimensionless rotary stagnation pressure P^*, (*a*) with, and (*b*) without tip leakage

passes through the tip leakage gap and hence contributes to the low-energy region in the suction-side shroud corner of the neighboring passage. The secondary flow that convects low p^* fluid from the suction surface boundary layer to the shroud corner region is little affected by the tip leakage.

Station 3. The total pressure distributions (Fig. 9) show that the wakes in both flows are located in the suction-side shroud corner. The tip leakage flow has however led to larger losses. Most of the low-energy fluid in the pressure-side corner at Station 2 has passed through the tip leakage gap to the suction-side corner of the neighboring passage, as shown by the cross velocities in Fig. 10(*a*). This figure also shows how strong secondary flows have developed in the center of the shroud that are tending to move the wake closer to the suction-side corner. A complex flow pattern is therefore developed in the wake region where the secondary flows from the shroud and suction surfaces meet the tip leakage flow.

Station 4. The pressure difference across the blade is particularly strong between Stations 3 and 4 (Fig. 4) and this will therefore strengthen the tip leakage flow. Figure 11 shows how this strengthened flow moves the wake a considerable distance along the shroud towards the pressure surface. The cross velocity pattern (Fig. 12) is summarized in Fig. 13, where it can be seen that the centrifugally induced secondary flow com-

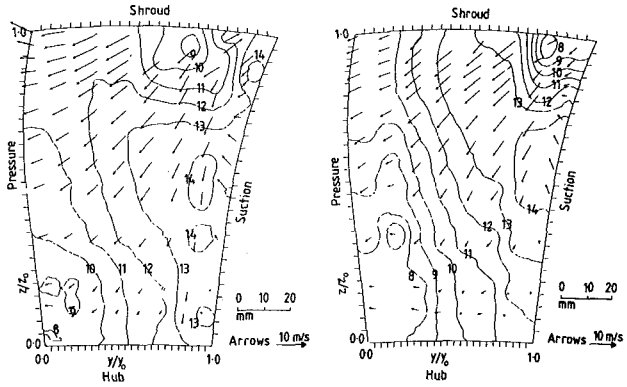

Fig. 10 Station 3—relative velocities/contours in m/s, (*a*) with, and (*b*) without tip leakage

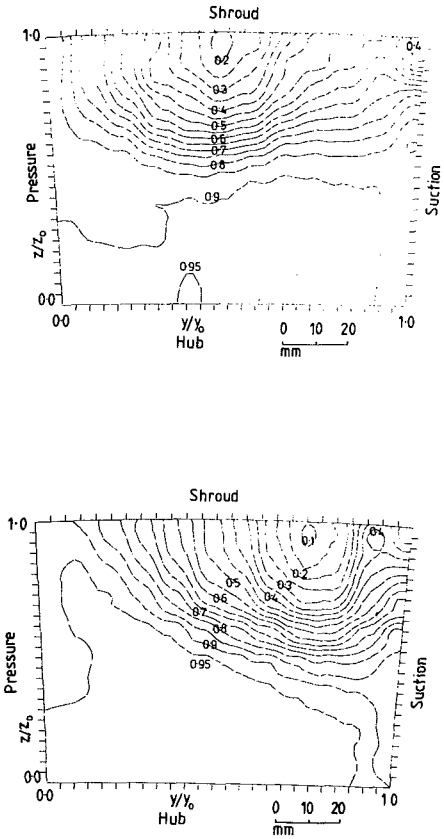

Fig. 11 Station 4—dimensionless rotary stagnation pressure P^*, (*a*) with, and (*b*) without tip leakage

bines with the tip leakage flow to carry low p^* fluid toward the wake. However, the stable location for this fluid is in the suction-side corner and the Coriolis-induced secondary flow therefore acts as a countercurrent carrying wake fluid back to this corner. This flow pattern is very similar to that depicted by Eckardt (1976) at his Station IV, although his tip leakage flow was comparatively weaker.

Station 5. At the impeller outlet, the wake is still much closer to the pressure surface when tip leakage is present than when it is not (Fig. 14). The wake has however moved back toward the suction surface as the tip leakage has weakened due to the unloading of the blades. There is also little curvature in the meridional plane to induce secondary flow along the suction surface (see Fig. 15) and the Coriolis force induced secondary flow along the shroud toward the suction side has strengthened.

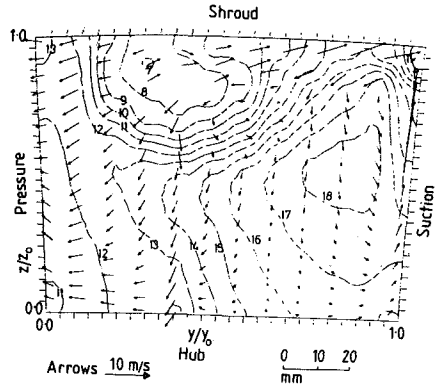

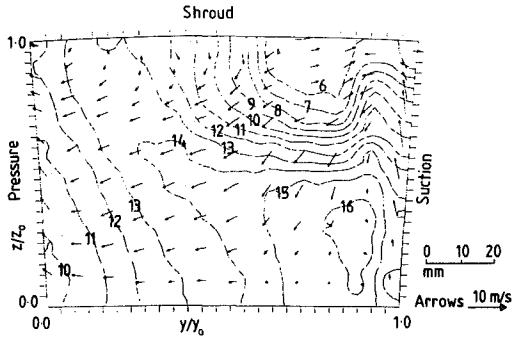

Fig. 12 Station 4—relative velocities/contours in m/s, (*a*) with, and (*b*) without tip leakage

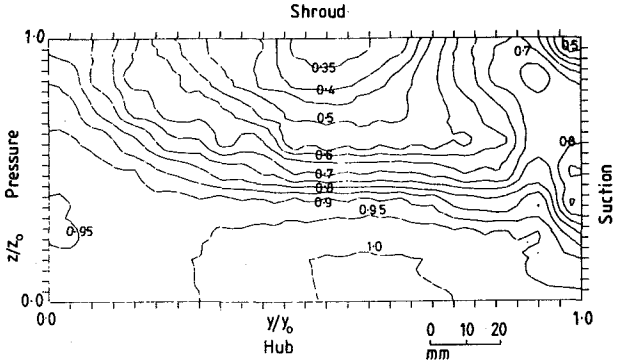

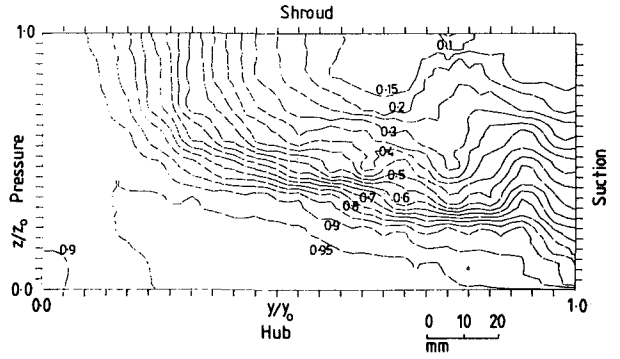

Fig. 14 Station 5—dimensionless rotary stagnation pressure P^*, (*a*) with, and (*b*) without tip leakage

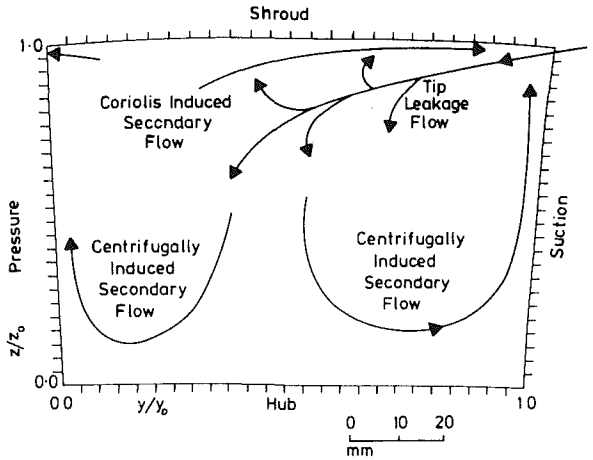

Fig. 13 Station 4—overall flow pattern

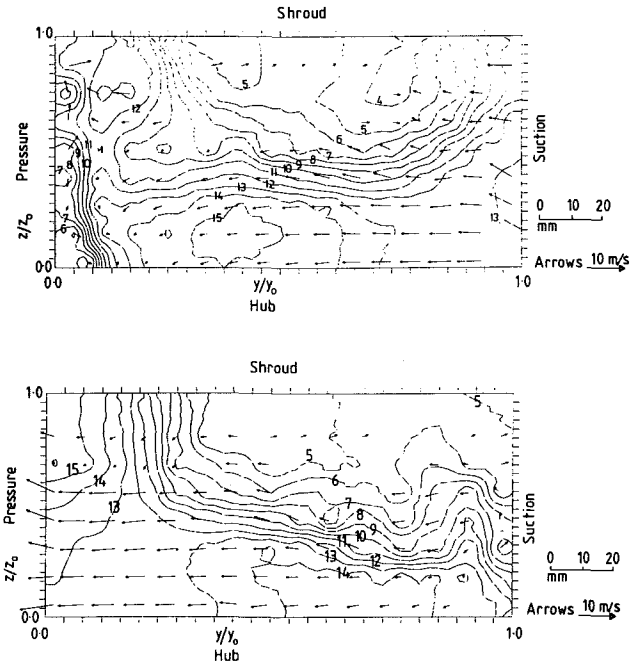

Fig. 15 Station 5—relative velocities/contours in m/s, (*a*) with, and (*b*) without tip leakage

Overall Flow Pattern. In the flow without tip leakage, Johnson and Moore (1983) concluded that the wake tended to seek the "stable location for low p^* fluid," which is also the region of lowest reduced static pressure. However, the inertia of the secondary velocities developed to transport this fluid may carry it beyond the stable location. The same conclusion is true of the flow with tip leakage, the significant difference being that the low p^* fluid can move from the pressure-surface shroud corner to the stable location in the suction-side corner by escaping through the tip leakage gap to the adjacent passage rather than taking the much longer route across the shroud to the suction-side corner of the measurement passage. The tip leakage flow also increases the inertia of the secondary flow up the suction surface to carry the wake beyond its stable location in the final radial part of the passage.

It is interesting to compare the current results for no relative motion between the shroud and impeller, with those of Inoue et al. (1986) for tip leakage in an axial compressor, with relative motion between the impeller and casing. Inoue (1986) also observed the combination of a secondary flow up the suction surface with the tip leakage flow, which resulted in a region of low-energy fluid on the shroud near the pressure surface.

Conclusions

1 The reduced static pressure distribution is little affected by tip leakage. However, the small decrease in the blade-to-blade pressure gradient close to the shroud can be attributed to tip leakage.

2 The low-momentum fluid convected into the wake is made up of fluid from the suction surface boundary layer of the measurement passage and the shroud and pressure surface boundary layers of the neighboring passage.

3 Tip leakage alters the secondary flow pattern within the impeller, particularly in the region close to the shroud.

4 Once the wake has formed, the tip leakage flow tends to move it from its stable location in the suction-side shroud corner along the shroud. At the impeller outlet therefore, the wake is closer to the pressure surface with tip leakage than without.

Acknowledgments

The authors gratefully acknowledge the financial support of the Science and Engineering Research Council. Thanks are also due to Dr. D. J. Lacey for the development of the microcomputer software and Dr. M. K. Aldoory for the preliminary experimental work.

References

Eckardt, D., 1976, "Detailed Flow Investigations Within a High-Speed Centrifugal Compressor Impeller," ASME *Journal of Fluids Engineering*, Vol. 98, pp. 390-402.

Fowler, H. S., 1966, "An Investigation of the Flow Processes in a Centrifugal Compressor Impeller," National Research Laboratories, Canada, Report No. ME-220.

Hamrick, J. T., et al., 1954, "Study of the Three Dimensional Internal Flow Distribution Based on Measurements in a 48-inch Radial Inlet Centrifugal Compressor," NACA TN 3101.

Inoue, M., et al., 1986, "Behavior of Tip Leakage Flow Behind an Axial Compressor Rotor," ASME *Journal of Engineering for Gas Turbines and Power*, Vol. 108, pp. 7-14.

Ishida, M., and Senoo, Y., 1981, "On the Pressure Losses Due to the Tip Clearance of Centrifugal Blowers," ASME *Journal of Engineering for Power*, Vol. 103, p. 271.

Johnson, M. W., 1979, "Secondary Flows in Centrifugal Compressor Impellers," Ph.D. Thesis, Cambridge, United Kingdom.

Johnson, M. W., and Moore, J., 1983, "Secondary Flow and Mixing Losses in a Centrifugal Impeller," ASME *Journal of Engineering for Power*, Vol. 105, pp. 24-32.

Mashimo, T., et al., 1979, "Effects of Fluid Leakage on Performance of a Centrifugal Compressor," ASME *Journal of Engineering for Power*, Vol. 101, pp. 337-342.

Senoo, Y., et al., 1968, "A Photographic Study of Three-Dimensional Flow in a Radial Compressor," ASME Paper No. 68-GT-2.

Structure of Tip Clearance Flow in an Isolated Axial Compressor Rotor

M. Inoue

M. Kuroumaru

Faculty of Engineering,
Kyushu University,
Fukuoka, Japan

Ensemble-averaged and phase-locked flow patterns in various tip clearances of two axial compressor rotors were obtained by a periodic multisampling technique with a hot wire in the clearance and with a high-response pressure sensor on the casing wall. A leakage flow region distinct from a throughflow region exists at every clearance. In the case of a small tip clearance, the leakage jet flow interacts violently with the throughflow near the leading edge, and a rolling-up leakage vortex decays downstream. As the clearance increases, a stronger leakage vortex comes into existence at a more downstream location, and a reverse flow due to the vortex grows noticeably. A scraping vortex is recognized at the pressure side near the trailing edge only for the small clearance. A horseshoe vortex appears in the upstream half of the through flow region for every tip clearance. The solidity does not affect the flow pattern substantially except for the interaction of the leakage vortex with the adjacent blade and wake.

Introduction

In an axial flow compressor rotor, a substantial proportion of the total loss arises from the blade tip region, where a complex flow phenomenon is attributed to a mutual interaction of the endwall boundary layer, a tip leakage flow, the blade passage secondary flow, and the blade-surface boundary layer. Much effort has been made to clarify this complex flow due to the need of higher efficiency, more reliable designs or precise prediction methods. The location of accumulated low-energy fluid and the rolling-up of the leakage flow have been clearly identified by detailed flow measurements behind the rotor with a five-hole probe and a hot-wire anemometer (Dring et al., 1982; Hunter and Cumpsty, 1982; Inoue and Kuroumaru, 1984; Wagner et al., 1985; Inoue et al., 1986, Lakshminarayana, 1986). Measurements in the tip clearance and inside the rotor by a rotating probe, a hot wire, and an LDV anemometer have suggested the violent interaction of leakage flow with blade passage flow and the onset of vortex roll up (Lakshminarayana et al., 1982a, 1982b; Pandya and Lakshminarayana, 1983; Smith and Cumpsty, 1984; Murthy and Lakshminarayana, 1986).

On the other hand, numerical studies have been performed for the three-dimensional viscous flow inside a rotor including the tip clearance flow (Hah, 1986; Dawes, 1987). The calculated results are useful in understanding the basic phenomenon that takes place in the tip region. In both the stationary cascade (Pouagare and Delaney, 1986) and the transonic-compressor rotor (Dawes, 1987), they show the existence of a separating line (or zone) between the leakage flow and the incoming main flow and the existence of a reverse flow associated with the leakage flow.

The general nature of the tip clearance flow can be grasped by these investigations. However, it has not been clarified yet how the structure varies with the tip clearance.

In the present study, a statistically accurate measurement has been made in the tip clearance flow by inserting a hot wire into the clearance to examine the variation of a phase-locked flow pattern with the tip clearnace. The structure of the clearance flow has been deduced in detail from this experimental result together with the phase-locked pressure distributions on the casing wall and the phase-locked flow patterns behind the rotor.

Experimental Equipment and Instrumentation

The tip-clearance flow measurements were made in the low-speed rotating cascade facility described in the previous paper (Inoue et al., 1986). Two 449-mm-dia rotors with hub/tip ratios of 0.6 were used for the experiments reported herein. The rotors (A and B), designed for free vortex rotation with an axial inlet condition, have the same blade profiles (NACA $65(3.2A_{10})$ 06) at the tip section but different solidities. The design specifications and geometry of both the rotors are summarized in Table 1. For each rotor, the tip clearance was varied from $\tau = 0.5$ mm to 5 mm by changing the diameter of the casing wall so as to keep the blade geometry constant at tip section during the experiment.

The overall stage performance for both the rotors satisfied the design point in the case of the minimum clearance ($\tau = 0.5$ mm). The flow measurements for various tip clearances were made at a constant speed of 1300 rpm and at the flow rate required to get the designed value of inlet axial velocity near the midspan. The displacement thickness of the inlet boundary layer δ^* was about 0.7 mm.

Contributed by the International Gas Turbine Institute and presented at the 33rd International Gas Turbine and Aeroengine Congress and Exhibition, Amsterdam, The Netherlands, June 5-9, 1988. Manuscript received by the International Gas Turbine Institute December 18, 1987. Paper No. 88-GT-251.

Table 1 Design specifications and geometry of the rotors

	root	mid-span	tip
Common			
Radius	135.0 mm	180.0 mm	224.5 mm
chord length	106.1 mm	117.8 mm	117.5 mm
maximum thickness /chord	10.00 %	8.00 %	6.00 %
trailing edge thickness /chord	1.41 %	1.27 %	1.28 %
Rotor A ($\phi=0.5$, $\psi=0.4$)			
camber *	1.30	0.62	0.32
solidity	1.50	1.25	1.00
stagger **	31.5 deg	47.2 deg	56.2 deg
inlet flow angle **	49.1 deg	57.0 deg	62.5 deg
exit flow angle **	22.2 deg	44.4 deg	55.8 deg
Rotor B ($\phi=0.455$, $\psi=0.513$)			
camber *	1.73	0.73	0.32
solidity	2.00	1.67	1.33
stagger **	25.3 deg	45.5 deg	56.2 deg
inlet flow angle **	51.8 deg	59.4 deg	64.7 deg
exit flow angle **	12.0 deg	42.0 deg	55.9 deg

* isolated airfoil lift coefficient of NACA 65 profile camber line at zero angle of attack in potential flow

** angle measured from the axial direction

ϕ = flow rate coefficient (area averaged axial velocity divided by blade tip speed)

ψ = pressure rise coefficient (dimensionless total pressure-rise referring to equivalent dynamic pressure of blade tip speed)

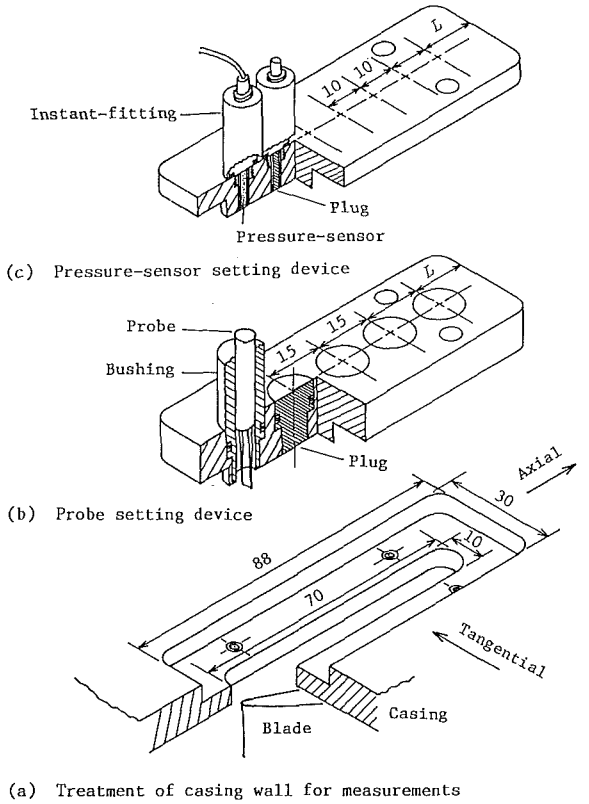

Fig. 1 Schematic views of a probe-setting device and a pressure-sensor setting device on the casing

A phase-locked flow pattern in the tip clearance was obtained by a constant temperature hot-wire anemometer and a periodic multisampling and averaging technqiue with a computerized data acquisition system (Kuroumaru et al., 1982). The sensor used was a slanted single hot wire of 5 μm dia and 1 mm effective length. The slant angle of 30 deg was employed to get three-dimensional velocity vectors for tip clearances of 2.0, 3.0, and 5.0 mm. In the cases of $\tau=0.5$ mm and 1.0 mm, however, only two-dimensional vectors were obtained by use of a normal wire (slant angle = 0 deg).

The hot wire was inserted by a probe-setting device on the casing wall as shown in Figs. 1(a) and 1(b). Although a cavity exists on the wall to move the hot-wire probe, the casing was hermetically sealed. Three probe-setting devices with $L=$ 14 mm, 19 mm, and 24 mm were used. The flow surveys were made at 5 mm intervals in the axial direction from 3 mm upstream of the leading edge to 57 mm downstream of it by changing the probe-setting device. The survey planes were 0.2 mm above the casing wall for $\tau=0.5$ mm, 0.2 and 0.5 mm for $\tau=1.0$ mm, 0.3 and 0.7 mm for $\tau=2.0$ mm, 0.3 and 1.7 mm for $\tau=3.0$ mm, and 0.3, 2.5, and 3.7 mm for $\tau=5.0$ mm. At each survey plane, 20 positions of the hot-wire sensor were set by rotating the probe axis. At each sensor position, the hot-wire signals were acquired and summed up during 512 revolutions of the rotor for 100 circumferential sampling points, which cover the progress of two complete blade passages. Therefore, a set of 20 ensemble averages of the hot-wire signal, which is the sum of the data divided by 512, is obtained corresponding to the 20 hot-wire orientations. Three components of the flow velocity were determined from the 20 ensemble averages by solving the calibration equation of the hot wire with the method of least-squares. As the velocity is determined from 10,240 ($=20\times512$) signals, they are accurate in the statistical sense.

Nomenclature

C_p = wall pressure coefficient = $(\overline{p_w}-p_{01})/(\rho u_t^2/2)$

C_p' = dimensionless pressure fluctuation = $\sqrt{(p_w-\overline{p_w})^2}/(\rho u_t^2/2)$

L = length in Figs. 1(b) and 1(c)

l_t = chord length of blade tip section

p_{01} = stagnation pressure at rotor inlet

p_w = wall pressure

r = radius of survey plane

r_t = radius of blade tip section

$T.L.$ = turbulence level normalized by u_t

u_t = peripheral speed of the rotor blade tip

z = axial distance from trailing edge to measuring plane

δ^* = displacement thickness of inlet boundary layer

ϵ = angle of turning

ζ_D = dimensionless kinetic energy defect of the relative flow

ζ_n, ζ_s = vorticity components normal and parallel to streamline

ρ = density

τ = tip clearance

ϕ = flow rate coefficient in Table 1 (area-averaged axial velocity divided by u_t)

ψ = total pressure-rise coefficient in Table 1 (pressure rise normalized by $\rho u_t^2/2$)

Subscripts and Superscripts

$\bar{}$ = ensemble average

1 = rotor inlet

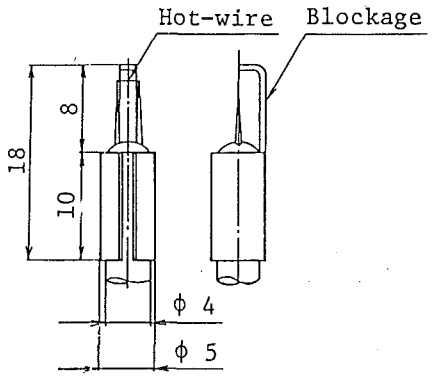

Fig. 2 Hot wire with an interference block

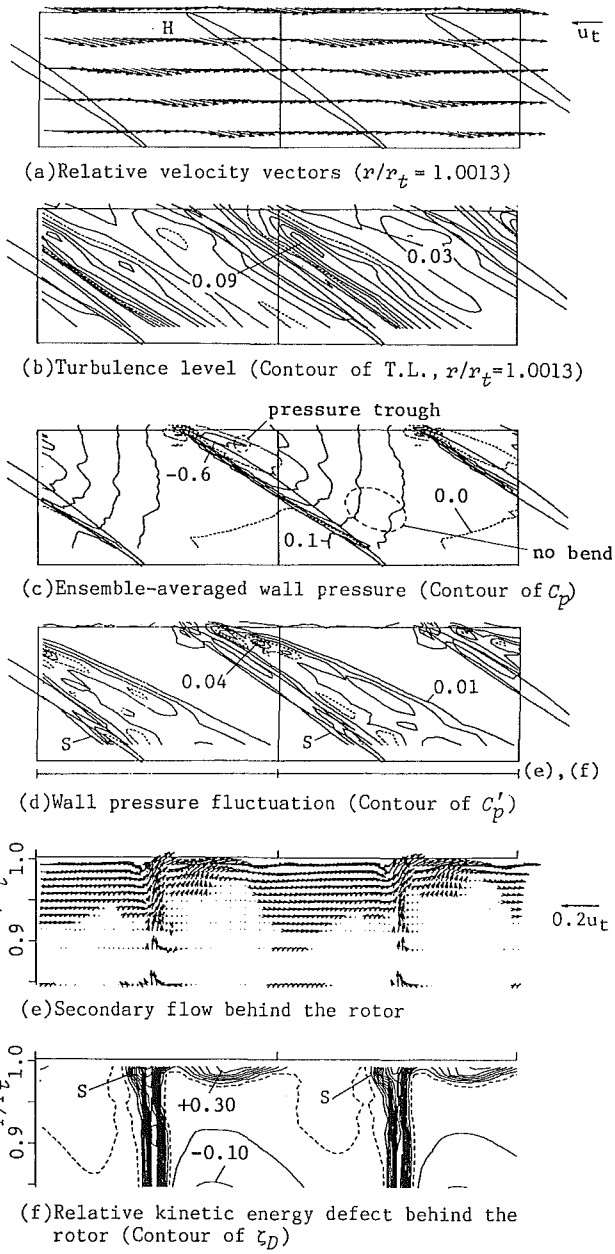

Fig. 3 Typical phase-locked flow pattern in small tip clearance (rotor A, τ = 0.5 mm)

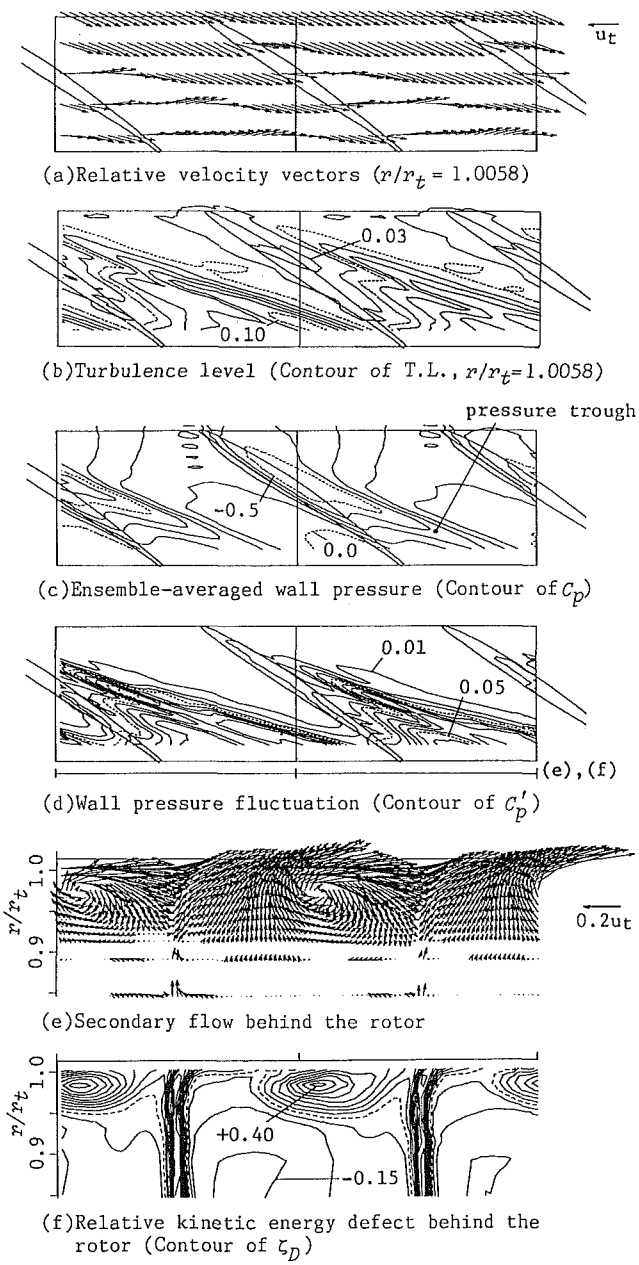

Fig. 4 Typical phase-locked flow pattern in large tip clearance (rotor A, τ = 3.0 mm)

Since a reverse flow appeared in some regions, it was impossible to determine the flow direction even by rotating the single hot wire by 360 deg about the probe axis. Therefore, a special hot wire with an interference block as shown in Fig. 2 was prepared. After the direction had been roughly determined by this hot wire, the regular measurement described above was made.

The phase-locked turbulence level of the clearance flow was obtained based on 20 variances of 512 hot-wire output data, which were gathered at the prescribed 20 orientations of the hot wire.

The periodic multisampling and averaging technique was also employed with a high-response pressure sensor to get the phase-locked pressure distribution and its fluctuation on the casing wall. The Kulite pressure sensor XCQ-080-1G was installed with the sensor setting device as shown in Fig. 1(*c*). Two sensor-setting devises with L = 14 mm and 19 mm were used to measure at the same measuring locations in the axial direction as those for the hot-wire survey.

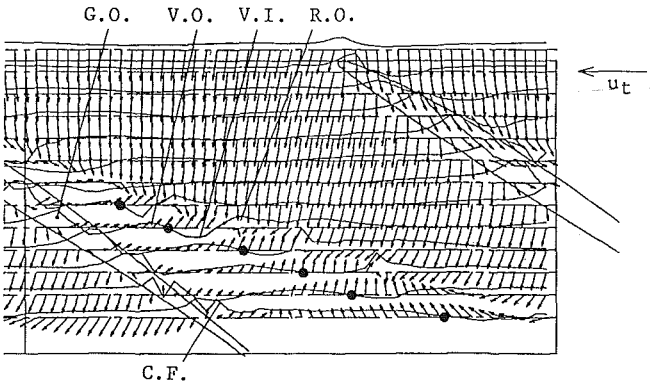

Fig. 5 Absolute flow vectors and radial velocity distributions in the tip clearance (rotor A, $\tau = 3.0$ mm, $r/r_t = 1.0058$ mm)

Experimental Results and Discussion

The structure of tip clearance flow is deduced from the phase-locked patterns of the ensemble-averaged relative and absolute velocity vectors and the phase-locked contour maps of the turbulence level, the ensemble-averaged wall pressure, and the pressure fluctuation.

The velocity vectors, the roots of which are put on the measuring point, are projected on the tip section plane and should be compared with the blade tip velocity vector u_t indicated on the right side of the figure (Figs. 3(*a*), 4(*a*), 5, 7, 11(*a*), and 11(*b*)). In Figs. 5 and 11(*b*), the radial velocity component is also shown by the curved lines along the survey lines. The measure of the radial component is indicated by the distance between the curved line and the survey line in the double scale of the projected vector, and the upside of the survey line corresponds to the outward flow. The turbulence level (*T.L*) is normalized based on the blade tip speed u_t (Figs. 3(*b*) and 4(*b*)).

In the pressure contour (isobar) maps (Figs. 3(*c*), 4(*c*), and 8), the dimensionless pressure C_p is defined as the pressure rise from the inlet stagnation pressure p_{01} divided by the dynamic pressure corresponding to the blade tip speed $\rho u_t^2/2$. The pressure fluctuation C_p' is also nondimensionalized by this dynamic pressure (Figs. 3(*d*) and 4(*d*)).

Adding to these phase-locked patterns, the secondary flow map (Figs. 3(*e*), 4(*e*), 12(*a*), and 13(*a–d*)) and the kinetic energy defect contour just behind the rotor (Figs. 3(*f*), 4(*f*), 12(*b*), and 13(*e*)) are also discussed to help the understanding of the phenomenon. The secondary flow vector was defined by a velocity component perpendicular to the design relative flow direction. The kinetic energy defect ζ_D was defined by the difference of relative kinetic energy between the measured and designed value divided by the designed one. The detail of the definition is explained by Inoue and Kuroumaru (1984).

Flow in the Small Tip Clearance. Figures 3(*a–f*) show the phase-locked flow pattern in the small clearance ($\tau = 0.5$) of rotor A together with information on the casing wall and behind the rotor. The flow field can be clearly divided into two regions: a leakage flow region on the suction side and an incoming throughflow region on the pressure side. The leakage flow region grows rapidly near the leading edge and increases gradually in the downstream. This is due to the strong jet flow in the contrarotating direction caused by the large pressure difference between the pressure and the suction surface near the leading edge. This jet flow meets the incoming flow and causes a violent interaction resulting in the high turbulence level near the leading edge (Fig. 3(*b*)).

The point of minimum wall pressure is located near the suction surface at the leading edge. The lowest pressure contour line is drawn into the leakage flow region, and a small trough of low pressure is observed near the suction surface (Fig. 3(*c*)). Anticipating the later discussion in the case of large tip clearance, this phenomenon suggests an onset of rolling-up of the leakage vortex. However, it is highly probable that the leakage vortex does not grow but decays in the downstream direction. This is inferred from the fact that the isobars downstream of the pressure trough are not so bent as seen in Fig. 4(*c*) and the bend attenuates in the downstream direction. Therefore, the rolling-up of the leakage vortex is not clearly seen behind the rotor (Fig. 3(*e*)) although its existence can be inferred from the relative kinetic energy-defect map (Fig. 3(*f*)).

In the aft half of flow passage, the width of the leakage flow region changes less and the turbulence level is low at the interference zone because of the weak leakage jet flow. The low-energy fluid in the casing wall boundary layer tends to accumulate on the pressure side to reduce the relative velocity. As a result, the small scraping vortex appears on the corner between the pressure side and the casing wall, denoted by *S* in Fig. 3(*f*). The scraping vortex may cause the appreciably high pressure fluctuation on the pressure side near the trailing edge (Fig. 3(*d*)).

A small axial velocity in the throughflow region marked by *H* in Fig. 3(*a*) will be discussed later.

Flow in the Large Tip Clearance. Typical flow behavior of the large tip clearances is shown in Figs. 4(*a*) to 4(*f*) in the same arrangement as Figs. 3(*a*) to 3(*f*). The leakage flow and the incoming throughflow regions can also be identified in this case. From the direction of the relative velocity vectors on the blade tip section, it is presumed that the leakage jet flow is weak near the leading edge but becomes stronger in the downstream direction and is the strongest near the midchord. Therefore, the leakage flow is rather narrow in the forward half of the blade passage and grows rapidly in the downstream half. At the exit of the rotor, it becomes broader than that of the smaller tip clearance. Corresponding to the strength of the jet flow, the turbulence level at the interference zone becomes high in the downstream half. In the leakage flow region, a reverse flow zone appears, the width of which becomes broader toward the rotor exit. The reverse flow, which was observed in the case of $\tau \geq 2.0$ mm, becomes more developed with τ.

The behavior of the leakage flow is made clearer on investigation of the radial velocity distributions. In Fig. 5, the radial velocity components are shown by the solid curved lines along the survey lines together with absolute velocity vectors. At the pressure side of blade, an outward flow (marked by G.O.) is induced to get over the blade. It may include a radial flow due to the centrifugal force in the boundary layer on the pressure surface. But the latter effect should be small as the outward flow cannot be observed on a large portion of the suction surface. The radial flow due to centrifugal force (marked by C.F.) becomes noticeable only near the trailing edge of the suction surface. The dot symbols in Fig. 5 are positions at which the radial component vanishes near the midst of the reverse flow zone. It is found that an outward flow (marked by V.O.) appears on the left side of the dot and an inward flow (marked by V.I.) on the right side of it. This is due to the rolling up of the leakage vortex as will be clearly seen in the following discussion. On the right side of the reverse flow zone where the turbulence level is high (Fig. 4(*b*)), an outward flow (marked by R.O.) is noticeable. This fact suggests that the throughflow runs on the leakage flow in the interference zone.

In Fig. 4(*c*), the minimum pressure exists near the midchord followed by noticeable bends of isobars in the downstream direction. The bends form a trough of low

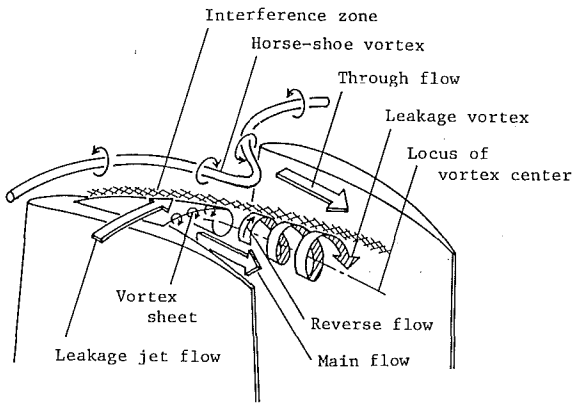

Fig. 6 Illustration of structure of the tip clearance flow

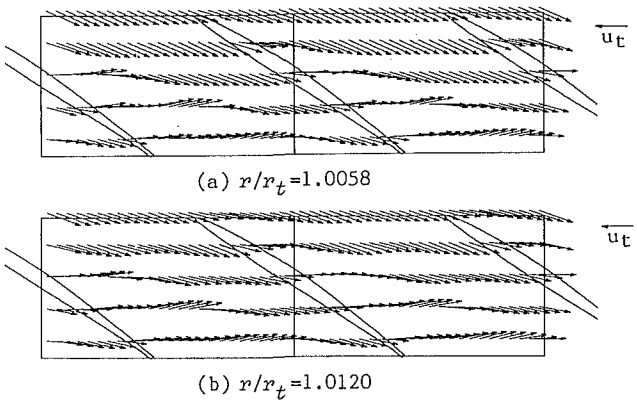

Fig. 7 Comparison of relative flow vectors on different survey planes (rotor A, $\tau = 3.0$ mm)

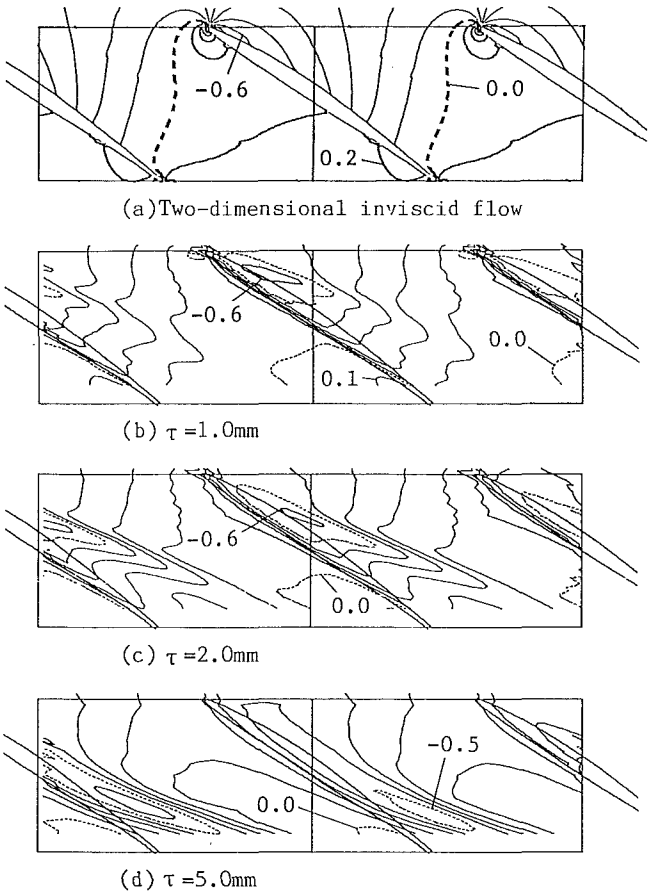

Fig. 8 Pressure contour on the casing wall for various tip clearances (rotor A)

pressure. The dot symbols in Fig. 5 are located nearly in the center of the pressure trough. In the right side of the dot symbols, the reverse flows occurs in spite of a favorable pressure gradient in the axial direction. Therefore, the reverse flow must be attributed to the vortex rollup as illustrated in Fig. 6. The trough of wall pressure is caused by interaction of the leakage vortex with the casing wall. That is, the leakage vortex axis is along the center of the pressure trough. This is supported by the following fact: When the centerline of the trough is extended toward the rear of the rotor, the extension passes through the position of the maximum kinetic energy defect behind the rotor which was correlated with the leakage vortex center in the previous paper (Inoue et al., 1986).

Regions of strong pressure fluctuations are exhibited at the both sides of the vortex axis where the pressure gradient is large. This is due to the fact that the leakage vortex fluctuates in the peripheral direction, as stated by Inoue and Kuroumaru (1984).

Evidence of a scraping vortex is not present in the blade passage and behind the rotor for the large tip clearance case.

Behavior of Leakage Vortex. In the present experiments, the leakage flow region can be distinguished from the through flow region in all the cases tested. These results back up qualitatively the recent numerical studies. The flow pattern in the tip clearance does not show a significant change depending on the radius of the survey plane as shown in Fig. 7. However, referring to a flow inside a different rotor measured by Smith and Cumpsty (1984), the flow direction on the suction side is probably aligned nearly with the main flow at the radius slightly smaller than blade tip radius. This requires a thin vortex sheet with high vorticity to exist between the leakage jet flow and the main flow, as illustrated in Fig. 6. The vorticity may be the highest at the location of the maximum pressure difference between the pressure and the suction surface. As a result, the vortex sheet possibly rolls up due to the induced velocity near the location of the maximum pressure difference. The onset of the rolling up appears to be near the location of the minimum surface pressure. This was also noted by Rains (1954) in his observation of the inception point of cavitation in an axial water pump.

The variation of the isobar on the casing wall with tip clearance is shown in Figs. 8(*a*) to 8(*d*). In the figures, the cases of $\tau = 0.5$ and 3.0 mm are omitted to avoid duplication in Figs. 3(*c*) and 4(*c*). For reference, Fig. 8(*a*) shows the calculated result of the two-dimensional inviscid flow for the condition of design inlet and exit flow angle at the tip section (calculated without Kutta's condition). There is no pressure trough following the minimum pressure in the case of the two-dimensional inviscid flow. The location of the minimum pressure moves downstream as the tip clearance is larger. In the case of $\tau = 5.0$ mm, the minimum-pressure location is detached from the blade surface where the formation of a large vortex is expected. The low-pressure trough following the minimum pressure, which corresponds to a locus of the leakage vortex center, is more inclined toward the peripheral direction with the tip clearance increasing.

The variations of the loci of the leakage vortex center with the tip clearance are shown in Fig. 9. They were determined from the center of the low pressure trough in the tip clearance and from the position of the minimum kinetic energy behind the rotor.

Effect of Casing Wall Boundary Layer. According to a recent numerical study for a stationary cascade, there is a passage vortex contrarotating against the leakage vortex (Pouagare and Delaney, 1986). However, such a secondary flow is not observed in the present experiment. This is due to a

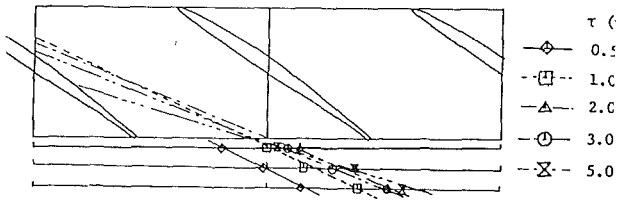

Fig. 9 Loci of vortex center for various tip clearances (rotor A)

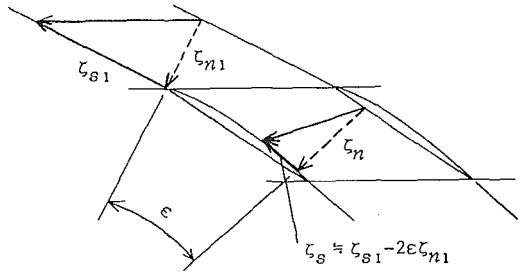

ζ_s, ζ_{s_1} : streamwise vorticity
ζ_n, ζ_{n_1} : vorticity normal to streamline
ε : angle of turning

Fig. 10 Illustration of passage vorticity in the rotor with axial inlet condition

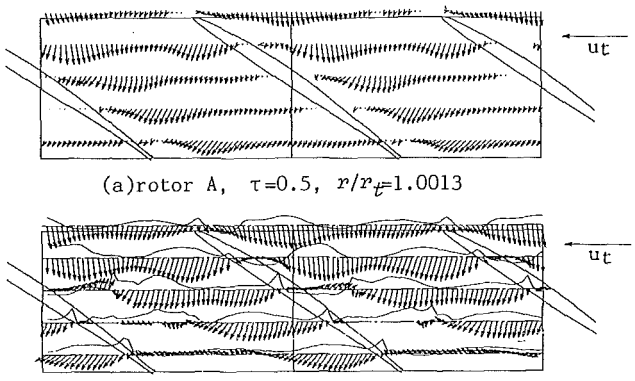

Fig. 11 Absolute flow vectors in the tip clearance

different inlet flow condition in the casing wall boundary layer. Horlock (1963) states that the direction of secondary rotation may be reversed due to the streamwise component of vorticity at inlet. In the rotor with an axial inlet condition, the casing wall boundary layer has a large component of vorticity in the relative streamwise direction. According to his analysis, the direction of the passage vortex in this rotor was the same as the rotation of leakage vortex as illustrated in Fig. 10. Therefore, the leakage vortex and the passage vortex become one vortex behind the rotor in this experiment.

In the actual flow, a horseshoe vortex, illustrated in Fig. 6, appears as a result of interaction of the casing wall boundary layer with the blade row. Evidence for the horseshoe vortex was given by the low-velocity region marked by H in Fig. 3(a). Such a low-velocity region, which can be seen more clearly from the absolute velocity vectors as shown in Figs. 11(a) and 11(b), exists in all the data measured. It becomes more noticeable for the smaller tip clearance. In Fig. 11(b), the radial inward flow is recognized in the low-velocity region and the outward flow on both sides of it. These flow directions coincide with the rotation of the horseshoe vortex. As the inward flow in the horseshoe vortex carries the low energy fluid from the wall region to the survey plane, the low-velocity region comes into existence.

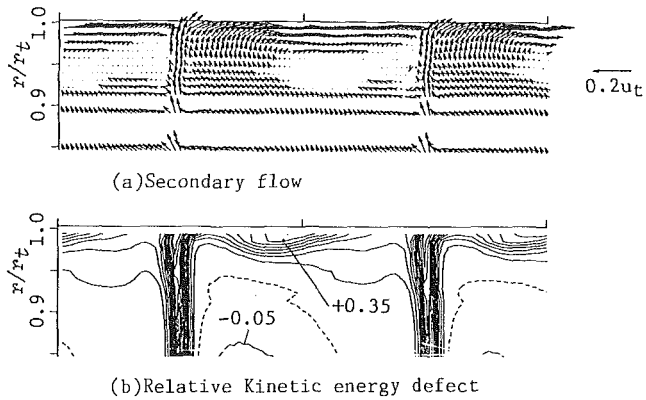

Fig. 12 Phase-locked flow pattern behind the rotor at thick inlet boundary layer (rotor A, $\tau = 0.5$ mm, $z/l_t = 0.068$, $\delta^* = 2.2$ mm)

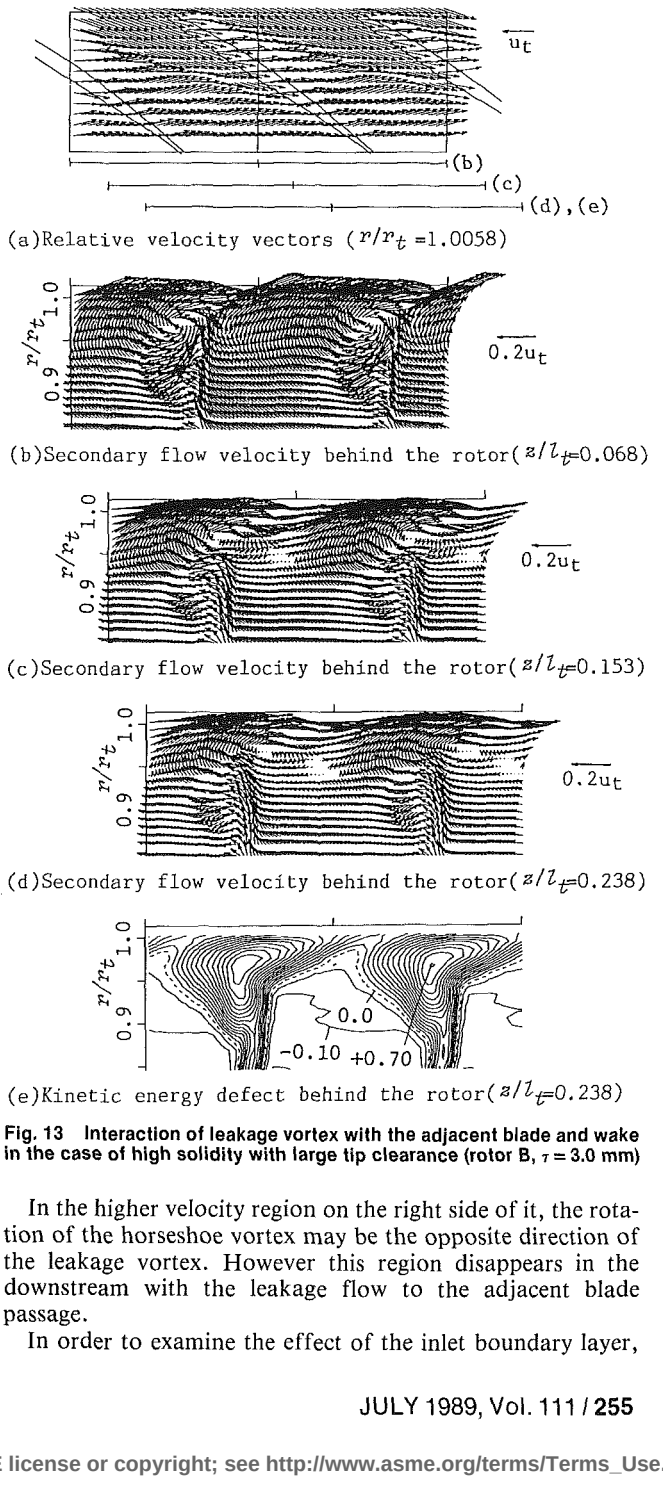

Fig. 13 Interaction of leakage vortex with the adjacent blade and wake in the case of high solidity with large tip clearance (rotor B, $\tau = 3.0$ mm)

In the higher velocity region on the right side of it, the rotation of the horseshoe vortex may be the opposite direction of the leakage vortex. However this region disappears in the downstream with the leakage flow to the adjacent blade passage.

In order to examine the effect of the inlet boundary layer,

additional experiments were done in the artificially thickened boundary layer. The displacement thicknesses of the casing wall boundary layer were $\delta^* = 2.2$ mm and 3.1 mm. Figures 12(a) and (b) show the phase-locked flow pattern behind the rotor with $\tau = 0.5$ mm at $\delta^* = 2.2$ mm. The secondary rotation, which indicates the underturning at the casing wall, becomes more pronounced than that of Fig. 3(e). Therefore, the region of the low kinetic energy defect moves away from the suction surface in comparison with that of Fig. 3(f). However, the structure of the tip clearance flow did not change essentially with the displacement thickness.

High Solidity Case. The tip clearance flows of rotor B have been measured for various tip clearances and compared with those of rotor A to examine the effect of solidity on the flow. The phase-locked flow pattern is substantially similar to that of rotor A, especially in the case of small tip clearance. In the case of large tip clearance, however, the leakage flow region reaches the pressure side of the adjacent blade, as shown in Fig. 13(a). At the rotor exit, the leakage vortex moves inward due to the presence of the adjacent blade surface and interacts with the blade wake. It seems to pass through the wake and is weakened by it as the flow proceeds downstream (Figs. 13(b) to 13(d)). Therefore, it is hard to distinguish the leakage vortex from the wake in the contour map of the relative kinetic energy defect shown in Fig. 13(e). The point of the maximum kinetic energy defect does not correspond to the center of the rollup.

Conclusions

Detailed measurements of the tip clearance flow have been made in two axial compressor rotors with various tip clearances. The structure of the clearance flow has been clarified by a phase-locked multi-sampling technique with a slanted hot wire in the clearance and a high-response pressure sensor on the casing wall. The results are summarized as follows.

1 There are two distinguishable flow regions in the clearance: the leakage flow region and the incoming throughflow region.

2 In the case of small clearance, the leakage jet flow is stronger near the leading edge and interacts violently with the through flow. The wall pressure contour shows evidence of the rolling-up of the leakage flow in the forward half of the flow passage, but the vortex decays toward the trailing edge. The scraping vortex appears near the trailing edge where the leakage flow rate is low.

3 As the tip clearance increases, the position of the maximum pressure difference between pressure and suction surface of blade moves downstream. Therefore, the leakage jet flow becomes stronger at a more downstream location.

4 In the case of large tip clearance, a reversed flow develops due to the rolling-up of leakage flow.

5 The onset of the rolling-up of the leakage flow is near the location of the minimum wall pressure. The leakage vortex axis is aligned with the trough of low pressure following the minimum pressure on the casing wall.

6 With the tip clearance increasing, the position of the rolling-up onset moves more downstream and the locus of the vortex center is more inclined toward the peripheral direction.

7 A horseshoe vortex appears in the forward half of the throughflow region. It becomes more pronounced in the smaller tip clearance.

8 In the case of high solidity with large tip clearance, the leakage flow region reaches the adjacent blade. The leakage vortex moves inward (toward the hub) inside the rotor and interacts with the adjacent wake behind the rotor.

Acknowledgments

The authors appreciate the assistance of Messrs. K. Wakahara and T. Iwamoto during the experimental work. They also gratefully acknowledge the financial support of a Kurata Research Grant.

References

Dawes, W. N., 1987, "A Numerical Analysis of the Three-Dimensional Viscous Flow in a Transonic Compressor Rotor and Comparison With Experiment," ASME JOURNAL OF TURBOMACHINERY, Vol. 109, No. 1, pp. 83–90.

Dring, R. P., Joslyn, H. D., and Hardin, L. W., 1982, "An Investigation of Axial Compressor Rotor Aerodynamics," ASME *Journal of Engineering for Power*, Vol. 104, No. 1, pp. 84–96.

Hah, C., 1986, "A Numerical Modeling of Endwall and Tip-Clearance Flow of an Isolated Compressor Rotor," ASME *Journal of Engineering for Gas Turbines and Power*, Vol. 108, No. 1, pp. 15–21.

Horlock, J. H., 1963, "Annulus Wall Boundary Layers in Axial Compressor Stages," ASME *Journal of Basic Engineering*, Vol. 85, No. 1, pp. 55–65.

Hunter, I. H., and Cumpsty, N. A., 1982, "Casing Wall Boundary Layer Development Through an Isolated Compressor Rotor," ASME *Journal of Engineering for Power*, Vol. 104, No. 4, pp. 805–818.

Inoue, M., and Kuroumaru, M., 1984, "Three-Dimensional Structure and Decay of Vortices Behind an Axial Flow Rotating Blade," ASME *Journal of Engineering for Gas Turbines and Power*, Vol. 106, No. 3, pp. 561–569.

Inoue, M., Kuroumaru, M., and Fukuhara, M., 1986, "Behavior of Tip Leakage Flow Behind an Axial Flow Compressor Rotor," ASME *Journal of Engineering for Gas Turbines and Power*, Vol. 108, No. 1, pp. 7–13.

Kuroumaru, M., Inoue, M., Higaki, T., Abd-Elkhalek, F. A., and Ikui, T., 1982, "Measurements of Three-Dimensional Flow Field Behind an Impeller by Means of Periodic Multi-sampling of a Slanted Hot Wire," *Bulletin of the JSME*, Vol. 25, No. 209, pp. 1674–1681.

Lakshminarayana, B., Pouagare, M., and Davino, R., 1982a, "Three-Dimensional Flow Field in the Tip Region of a Compressor Rotor Passage—Part I: Mean Velocity Profiles and Annulus Wall Boundary Layer," ASME *Journal of Engineering for Power*, Vol. 104, No. 4, pp. 760–771.

Lakshminarayana, B., Pouagare, M., and Davino, R., 1982b, "Three-Dimensional Flow Field in the Tip Region of a Compressor Rotor—Part II Turbulence Properties," ASME *Journal of Engineering for Power*, Vol. 104, No. 4, pp. 772–781.

Lakshminarayana, B., Sitaram, N., and Zhang, J., 1986, "End-Wall and Profile Losses in a Low-Speed Axial Flow Compressor Rotor," ASME *Journal of Engineering for Gas Turbines and Power*, Vol. 108, No. 1, pp. 22–31.

Murthy, K. N. S., and Lakshminarayana, B., 1986, "Laser Doppler Velocimeter Measurement in the Tip Region of a Compressor Rotor," *AIAA Journal*, Vol. 24, No. 5, pp. 807–814.

Pandya, A., and Lakshminarayana, B., 1983, "Investigation of the Tip Clearance Flow Inside and at the Exit of a Compressor Rotor Passage. Part I: Mean Velocity Field," ASME *Journal of Engineering for Power*, Vol. 105, No. 1, pp. 1–12.

Pouagare, M., and Delaney, R. A., 1986, "Study of Three-Dimensional Viscous Flows in an Axial Compressor Cascade Including Tip Leakage Effect Using a SIMPLE-Based Algorithm," ASME JOURNAL OF TURBOMACHINERY, Vol. 108, No. 3, pp. 51–58.

Rains, D. A., 1954, "Tip Clearance Flows in Axial Flow Compressors and Pumps," California Institute of Technology, Hydrodynamics and Mechanical Engineering Laboratories, Report No. 5.

Smith, G. D. J., and Cumpsty, N. A., 1984, "Flow Phenomena in Compressor Casing Treatment," ASME *Journal of Engineering for Gas Turbines and Power*, Vol. 106, No. 3, pp. 532–541.

Wagner, J. H., Dring, R. P., and Joslyn, H. D., 1985, "Inlet Boundary Layer Effects in an Axial Compressor Rotor: Part 1—Blade to Blade Effects," ASME *Journal of Engineering for Gas Turbines and Power*, Vol. 107, No. 2, pp. 374–386.

The Measurement and Formation of Tip Clearance Loss

J. P. Bindon
Associate Professor,
University of Natal,
Durban, South Africa
Visiting Scholar,
Whittle Laboratory,
Cambridge, United Kingdom
Mem. ASME

The detailed development of tip clearance loss from the leading to trailing edge of a linear turbine cascade was measured and the contributions made by mixing, internal gap shear flow, and endwall/ secondary flow were identified, separated, and quantified for the first time. Only 13 percent of the overall loss arises from endwall/secondary flow and of the remaining 87 percent, 48 percent is due to mixing and 39 percent is due to internal gap shear. All loss formation appears to be dominated by phenomena connected with the gap separation bubble. Flow established within the bubble by the pressure gradient separates as the gradient disappears and most of the internal loss is created by the entrainment of this separated fluid. When this high-loss leakage wake enters the mainstream, it separates due to the suction corner pressure gradient to create virtually all the measured mixing loss. It is suggested that the control of tip clearance loss by discharge coefficient reduction actually introduces loss. Performance improvements may result from streamlined tip geometries that optimize the tradeoff between entropy production and flow deflection.

1 Introduction

Tip clearance loss in unshrouded blading is generally associated with the quantity of fluid leaking through the gap between blade and casing. Clearance gap discharge coefficient is often used to describe the leakage quantity and as a yardstick of tip loss. Many correlations quantify this loss and many models exist that allow a loss calculation to be made based on the blade loading. There is however not a detailed understanding of the actual loss mechanisms at work or of the fundamental flow physics occurring between the leading and trailing edges of a blade row with clearance.

Loss measurements are normally made on a time-averaged basis in the outlet plane of a rotor. While this is sufficient for an accurate assessment of stage and loss model performance, no information is provided regarding the flow and loss phenomena on the endwall and within the clearance gap. A simple linear cascade with clearance may be made large enough to provide detailed measurements of the flow inside the clearance gap. Despite the fact that the experimental model does not match the real situation with respect to rotation, recent studies (Bindon, 1987a, 1987b, 1987c; Sjolander, 1987; Moore and Tilton, 1987) have revealed a wealth of new information regarding the microflows existing inside the gap and about the way losses develop between the leading and trailing edge. The effect of relative motion on these minute flow structures is the subject of a companion paper (Morphis and Bindon, 1988).

Apart from the data analyzed in this paper, no other measurements of tip clearance loss between cascade inlet and outlet both on the endwall and within the gap appear to have been made before. This paper therefore carefully examines the data of Bindon (1986a, 1986b) in terms of identifying and quantifying the loss processes in the whole endwall region with tip clearance. The data are not always ideal for the purpose. However the accuracy is sufficient to demonstrate clearly a number of new facts regarding tip clearance loss.

This study relates only to a simple flat blade tip geometry with sharp cornered (unradiused) edges and a particular profile. While it is accepted that many different blade tip shapes and blade profiles are used in practice, it is hoped that some of the principles will be sufficiently general to be of wide use.

2 Cascade and Operating Parameters

The instrumentation and flat tipped seven-blade 152-mm chord linear cascade with end clearance has already been fully described (Bindon, 1986a, 1986b, 1987a, 1987b, 1987c). The total pressure on the endwall and at the gap exit were measured using a 1-mm-dia single-hole cylindrical probe with a 0.25-mm hole. This was yawed for a maximum pressure reading as was the 0.18-mm-dia tip total pressure tube used inside the gap. Velocity data were deduced from total pressures and an interpolation of wall static pressures. The table below summarizes the cascade data:

Pitch/chord	0.7
Maximum thickness	15 percent
Camber angle	73 deg
Blade length	456 mm
Reynolds number (exit)	200,000 to 300,000

3 Review of Tip Clearance Microflow Detail and Loss Development

A narrow separation bubble has long been known to form on the pressure side of the flat clearance gap surface, while the

Contributed by the International Gas Turbine Institute and presented at the 33rd International Gas Turbine and Aeroengine Congress and Exhibition, Amsterdam, The Netherlands, June 5–9, 1988. Manuscript received by the International Gas Turbine Institute November 15, 1987. Paper No. 88-GT-203.

leakage flow passes above it, almost normal to the chord, and reattaches behind the bubble to continue on to leave the gap and to form the leakage vortex in the suction corner. Bindon (1986b, 1987b) showed that the pressure distribution on the blade gap surface has a deep depression at midchord, and the pressure coefficient is 2.7 times lower than at cascade outlet and 1.7 times lower than the minimum suction surface value. Bindon (1986b, 1987a), using microscopic velocity probes in the clearance gap, found that a strong chordwise flow develops inside the bubble. This flow was also seen in flow visualization (Bindon, 1986a, 1987c) and is due to the separation bubble over the leading half of the blade being subject to an accelerating pressure gradient.

Microtraverses at gap exit showed an increased loss leaving the gap after midchord, which was attributed to the highly sheared flow inside the separation bubble emerging from the gap (Bindon, 1986b, 1987a). On the blade passage endwall the total loss coefficient was shown to be significantly higher with tip clearance and rises dramatically above the value for zero clearance from midchord onward. The tip clearance vortex reduces the pressure in the suction corner significantly and there are actually major increases in blade loading above the two-dimensional value.

4 Loss Development on the Endwall

The net growth of total loss (secondary, endwall, and clearance) in the endwall region was presented for the cascade of Bindon (1987a). In order to provide a suitable basis for directly comparing the losses for various clearances, the results are recalculated and shown in Fig. 1 for zero clearance and for gap sizes of 1, 1.5, and 2.5 percent chord. As shown in the Appendix, the integrated loss coefficients throughout this paper are related to an undisturbed flow through an upstream area of 1 pitch by a 1/4 chord blade height. The 1/4 chord was chosen as being roughly the maximum depth of the vortex-affected zone at cascade exit. The loss coefficient may be converted to any blade height desired.

As already stated in the review, tip clearance causes a dramatic rise in loss from midchord onward. For all clearance values including zero, the loss development is identical up to midchord. This is an unexpected result since there is a significant amount of leakage taking place that is obviously not immediately appearing as a mixed-out loss. Also shown in the figure is the effect of clearance on the total exit loss. Between the minimum and maximum clearances, the loss is seen to be very nearly proportional to gap size, which is in keeping with the concept of loss being related to leakage mass flow. However between zero clearance and the smallest gap the curve is far from linear, indicating that the presence of clearance gives birth to fundamentally new phenomena. The shape of these curves will be discussed again later once the various loss components and new phenomena have been identified.

5 Measurement of Internal Clearance Gap Loss

The previous data analysis (Bindon, 1987a) shows that the leakage flow at gap exit shows a very high loss content at midchord and the question arises as to how much of the overall leakage loss actually takes place within the gap itself. If it should turn out that entropy generation inside the gap is

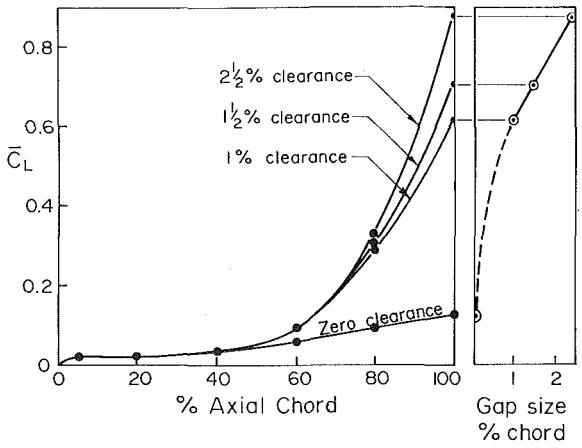

Fig. 1 The growth of total integrated loss coefficient from leading to trailing edge for various values of tip clearance gap size

significant, then leakage loss is not simply related to mass flow but also to the manner in which this flow occurs.

The measurement of internal gap loss formation is a somewhat formidable task even when the intention is specifically that of loss determination. The loss at inlet and outlet to the clearance gap is required preferably with detailed chordwise variations rather than merely an overall figure so that the variation of loss with chord can be assessed. Thus traverses between blade and endwall at gap inlet and outlet of velocity, pressure, and direction are required. Not only is the gap small (3.8 mm for 2.5 percent of chord) thus precluding a five-hole probe, but at inlet all gradients are singularly intense and the zone particularly inaccessible.

The data available from Bindon (1986a, 1986b) were not primarily intended for loss measurement since the study was a tentative exploration that actually revealed many of the phenomena that must now be quantified. Despite this, the data are adequate to provide a reasonably accurate assessment of the loss and to provide a guide as to how future measurements may be made. These detailed data are however only available for a gap size of 2.5 percent chord. Traverse data were mainly acquired with the 0.18-mm probe but at gap outlet the cylindrical probe was also used with the stem in contact with the suction surface. Both of these probes could only be yawed in the plane of the endwall.

For the inlet loss two methods are attempted, neither of which are particularly accurate. The first is to make the best assessment of gap loss traverse data assuming that the vorticity present at gap inlet will be concentrated above the high-loss fluid near the blade surface, which is associated with the separation bubble. Figure 2 shows the various data points available and an intuitive fit through them that ignores the high values obtained at midchord, which are thought to be affected by the emergence of the separation bubble flow. The figure shows how the loss is distributed and how it grows from leading to trailing edge to a total loss of 0.074 for the whole gap.

The second method establishes what proportion of the inlet boundary layer loss is drawn into the clearance gap. Using the quantitative streamline gas tracer technique described by Bindon (1986a), all upstream flow that enters the gap can be iden-

Nomenclature

$\bar{C}_L$ = mass-integrated loss coefficient

$\bar{C}'_L$ = one-dimensional loss coefficient

$\bar{C}'_D$ = one-dimensional integrated gap discharge coefficient

$\bar{C}_D$ = integrated discharge coefficient for whole gap

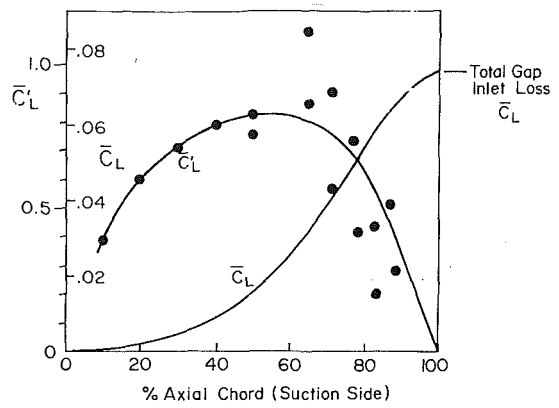

Fig. 2 Distribution of one-dimensional loss coefficient at gap inlet and the accumulated gap inlet loss from leading to trailing edges

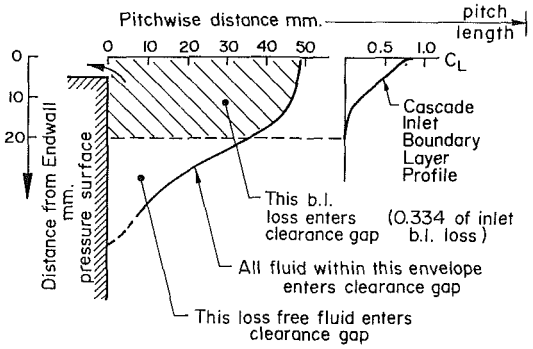

Fig. 3 Inlet boundary layer fluid that is drawn into clearance gap as determined from quantitative gas tracer flow visualization

tified. This upstream zone is demarcated in Fig. 3. A simple integration of the inlet boundary layer across this zone gives a loss of 0.043 or 45 percent of the cascade inlet loss. Since this excludes the contribution made by endwall shear and secondary flow between cascade inlet and gap inlet, a proportion of the zero clearance endwall and secondary loss of 0.118 is added based on the endwall area seen by this leakage fluid. The gas tracer results show that this is 0.334 of the total endwall area. When a loss of $0.334 \times 0.118 = 0.039$ is added to 0.043, the final total is 0.082, which is similar to the first result.

The gap exit loss content is the easier of the two quantities to measure since the gradients are more uniform between blade and endwall and because the zone is more accessible. The probes do not however provide accurate flow angle data. The quantitative gas tracer flow visualization results of Bindon (1986a) were used to find the leakage flow direction for purposes of integration where areas normal to the flow are needed.

Figure 4 shows the variation of one-dimensional integrated loss coefficient with suction surface axial chord. This quantity is equivalent to loss concentration or momentum thickness and therefore describes the distribution of gap efflux loss. Also shown are some of the loss traverses giving rise to the integrated loss values.

The net loss generated internally within the gap is obtained by subtracting the gap inlet from the gap outlet loss. The one-dimensional net loss distribution and the growth of net overall gap loss is given in Fig. 5. The most important result is that at cascade exit (100 percent chord) the total internal gap loss amounts to 0.34 or 39 percent of the total endwall loss. This is a very significant result because of its magnitude, because it is not known to have been measured or calculated before, and because it indicates that tip clearance loss is much more than fluid leaking through a gap without doing work. The result

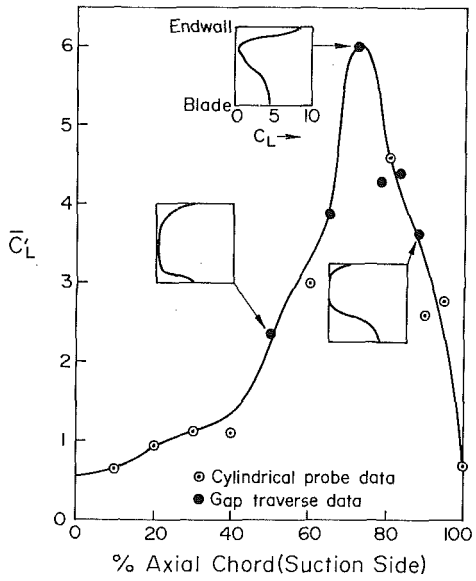

Fig. 4 Gap exit efflux loss distribution between leading and trailing edges and some of the gap loss profiles that give rise to the efflux loss

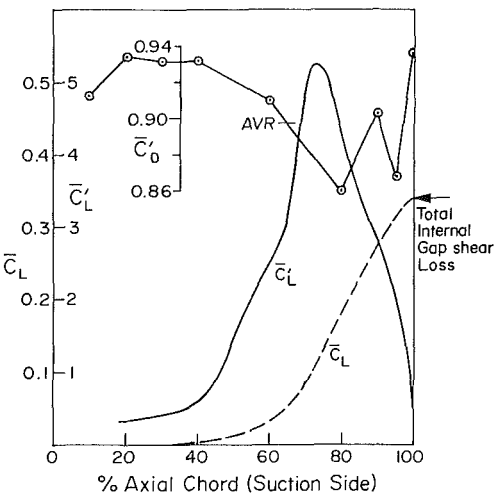

Fig. 5 Distribution of internal gap shear loss, accumulated internal gap loss, and gap discharge coefficient

also opens up very real possibilities for loss reduction once all the parameters have been established and the criteria for better tip geometries laid down.

As already stated in the review, of particular note is the rapid rise in internal gap loss from 40 percent chord to an intense loss concentration that is 10 times higher at 70 percent chord than over the forward half of the blade, where the leakage fluid was seen to flow over the separation bubble and reattach onto the blade gap surface. At the peak of the curve, the gap loss traverses of Fig. 4 show that the boundary layer has grown to fill the clearance gap while at other stations a clear loss-free leakage core flow can be seen. It therefore appears that the loss mechanisms at midchord are quite different from those over the leading part of the blade.

As shown in Fig. 8, it is postulated that the chordwise flow, established within the bubble by the accelerating nature of the pressure gradient over the forward part of the clearance gap, separates as the gradient falls away and becomes positive. This now truly separated flow accumulates. Since the pressure coefficient at the suction side gap exit is 1.7 times higher than in the bubble (Bindon, 1987b), the low-velocity fluid is entrained by the as yet loss-free gap inlet jet, which imparts sufficient

momentum to enable the fluid to reach the gap exit. A high-loss wake therefore forms and leaves the gap over the latter half of the blade. This wake flow forms a major part of the internal gap loss and the entrainment explains why the boundary layer is so deep at this point. It should be noted that the inlet leakage jet velocity is extremely high since it is induced at the point of minimum gap pressure coefficient, 2.7 times lower than at the cascade outlet (Bindon, 1987b). This high velocity also explains why the loss formation is so intense. A very useful model relating entropy generation to velocity differential has been formulated by Denton and Cumpsty (1987).

Also shown in Fig. 5 is the variation in gap discharge coefficient. As could be expected the minimum coincides with the emergence of the high-loss entrainment wake, which appears to be the only factor that reduces the mass-averaged value from around 0.88 over the forward half of the blade to mean for the whole gap of 0.84. Thus it would seem that most of the gap loss is generated for the saving of a mere 4 percent of gap leakage flow.

Despite the fact that the gap width is narrowing and the blade loading is falling toward the trailing edge, the loss concentration does not return to the same low level as the front of the blade. There appears to be more here than mere leakage flow reattaching. The traverses of Fig. 4 shows a relatively thick loss layer on the blade surface. One possibility is that over this narrower portion of the profile the leakage flow does not reattach and a separation bubble extends right across the width of the blade. It should also be noted that the pressure gradient is such as to drive any fluid inside a separation bubble forward toward the leading edge. This contraflow will be opposed viscously by the chordwise component of the free-stream leakage jet. The fluid will therefore tend to move very sluggishly and stagnate to mix with the jet flow above. A comprehensive study of the leakage flow in this region is needed because the flow pattern is unclear and the loss formation is quite significant.

The very distinct nature of the high-loss wake leaving the clearance gap at 70 percent chord in contrast to the even jet of relatively loss-free fluid over the forward part of the blade leads to the suggestion that these two radically different flows may look very different when visualized with smoke and could explain the double vortex reported by Sjolander (1987).

6 Quantifying the Mixing Loss of the Tip Leakage Vortex

Since the distribution of overall endwall loss and internal gap loss are determined, the remaining loss on the endwall comprises the mixing of the leakage jet (or vortex), the endwall shear, and the secondary flow. The endwall loss is due to the skin friction shear stress of the fluid flow across the endwall. The secondary loss is due to all other shear apart from that on the blade profiles. While it should be possible to measure the skin friction on the endwall carefully to find the endwall loss, it will be impossible to separate the shear due to leakage mixing and the other "normal" shear since the flows are all intermingled and very complex. Therefore both "normal" and leakage shear will always have to be lumped together, unless it is assumed that the "normal" component is that of the zero clearance case, which is relatively easily found. This is what is assumed in the present analysis and in addition the endwall shear loss is also assumed the same as that for zero clearance.

The internal gap loss development from Fig. 5 is inserted into Fig. 1 (2.5 percent clearance only) to give the breakdown of the three loss components shown in Fig. 6. The mixing loss is now separated from the remainder of the endwall losses for the first time. At cascade exit the mixing loss is 48 percent of the total, and is thus of similar magnitude to the internal gap shear loss. The rise is so steep at the trailing edge that it is

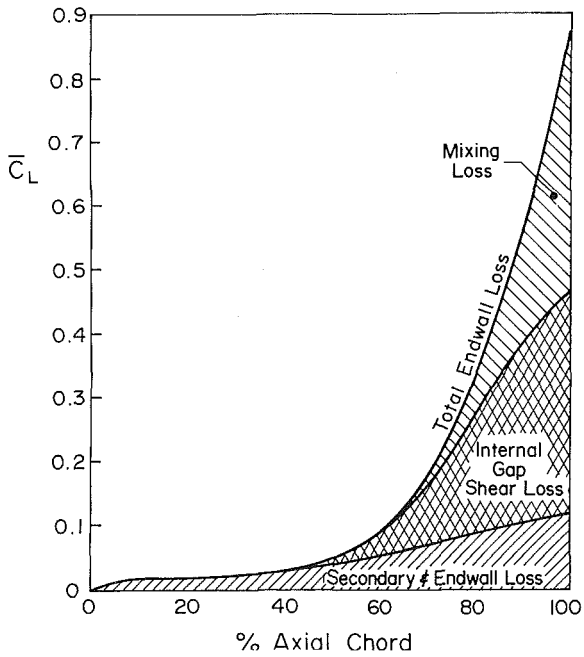

Fig. 6 Total endwall loss development showing contributions due to internal gap shear, leakage jet mixing, and secondary/endwall flows

suspected that the mixing process and loss formation are far from complete and will increase significantly before falling off to the levels normal for wake decay.

The initial sharp rise in total loss just after midchord is seen not to be due to mixing but to internal gap shear. The mixing loss only starts to rise significantly at 80 percent chord and the increase over this last 20 percent is eightfold. Thus despite massive amounts of fluid mixing into the mainstream up to this point, the contribution to mixing loss is almost negligible. It is suspected that a mechanism is at work other than shear due to the mismatch of direction and velocity. It should however be noted that the direction of the leakage flow is almost constant with chord, which means that the directional mismatch is lower over the forward half of the profile.

Kind (1987) has observed that since the tip clearance flow emerges into the suction corner of the blade passage where a diffusion is demanded of the flow, the leakage wake could stagnate and form the equivalent of a separation or zone or reverse flow. This type of flow could enhance the losses in the suction corner as seen in Fig. 6. The fact that the leakage flow has been shown in this paper to contain a large segment of high-loss fluid arising from the gap bubble adds weight to this hypothesis. This low-velocity body of fluid is far less likely to have enough energy for diffusion than the relatively loss-free layers of leakage flow emerging from the gap. When the internal gap loss distribution curve of Fig. 5 is compared with Fig. 6, the peak of the bubble wake is seen to enter the suction corner flow at 70 percent chord just as the very rapid rise in mixing loss starts and it seems likely that the two phenomena are related.

The endwall loss contours at various axial stations presented by Bindon (1987a) are re-examined for evidence of such a "separation" within the leakage vortex zone of the suction corner flow. As shown in Fig. 7, a minute core of high-loss fluid at 60 percent chord appears to grow as rapidly in size as the mixing loss does. The integrated loss of these zones is very close (within 11 percent at exit) to the estimated mixing loss. In the exit plane the center of this zone has a loss coefficient of 5 whereas the maximum loss possible is 6. Thus the flow is very near to true separation. These factors appear therefore to corroborate that the high-loss leakage flow core separates and that the mixing loss is concentrated in a very specific flow

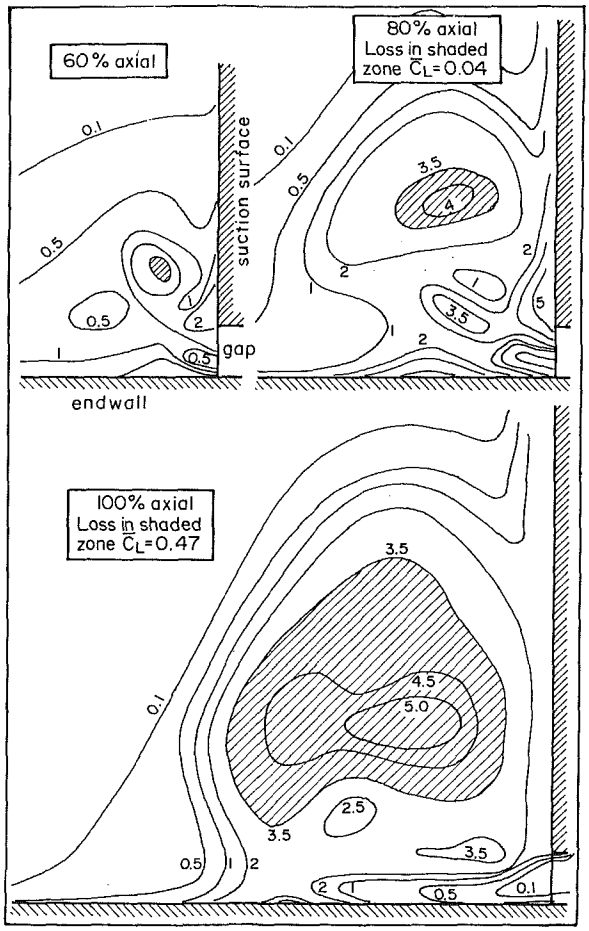

Fig. 7 Suction corner loss coefficient contours in tangential planes at 60, 80, and 100 percent axial chord with contours greater than 3.5 emphasized to show possible increase and separation of high-loss leakage jet core

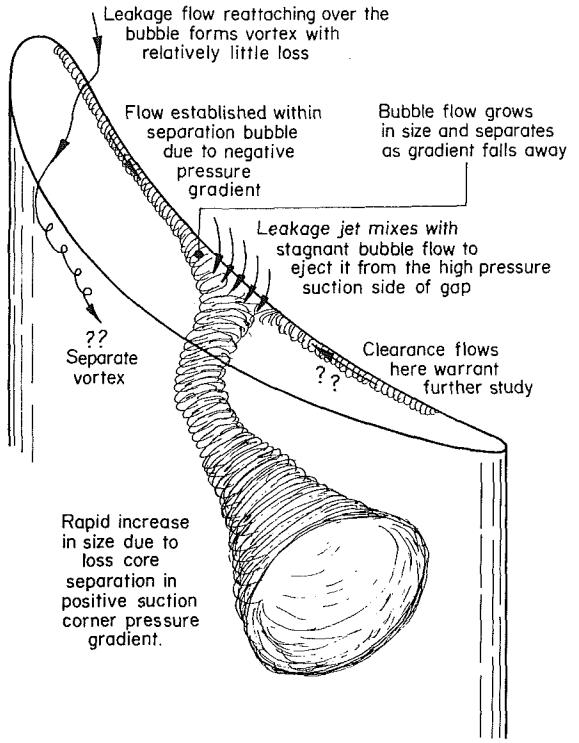

Fig. 8 Suggested history and effects of clearance gap separation bubble in terms of loss formation internal to the gap and in the suction corner mixing zone

envelope. These ideas are however not conclusively proven. A careful study is required in which the orgins of the suction corner mixing loss is established beyond doubt, since it may be possible that any leakage vortex, even that deposited over the forward region, could separate in the fashion observed.

As illustrated in Fig. 8, where a complete history of the clearance gap separation bubble is suggested, it appears that the bubble could be responsible not only for most of the internal gap shear loss but also for the massive core of loss occurring in the mixing region and a full understanding and control of the phenomena could lead to significant loss reductions. It is strongly felt that these losses are an inordinate penalty to pay for a discharge coefficient of only 0.84.

7 A Conceptual Model for Tip Clearance Loss Formation

It has been shown that there is not a single flow pattern that leaks through the clearance gap. A tentative model of the various types of flow occurring is therefore presented in Fig. 9 in the hope that it will be an aid to understanding the processes and perhaps in enabling simple computational models to be derived. The clearance flow, instead of being linearly spread along the chord is shown as leaking through channels 1, 2, and 3.

Channel 1 represents normal boundary layer and core flow without any separations but with a convergent divergent shape to ensure the correct pressure distribution, which occurs due to the blockage of the separation bubble. When this flow mixes with the mainstream it does so as core *a* and wake *b*

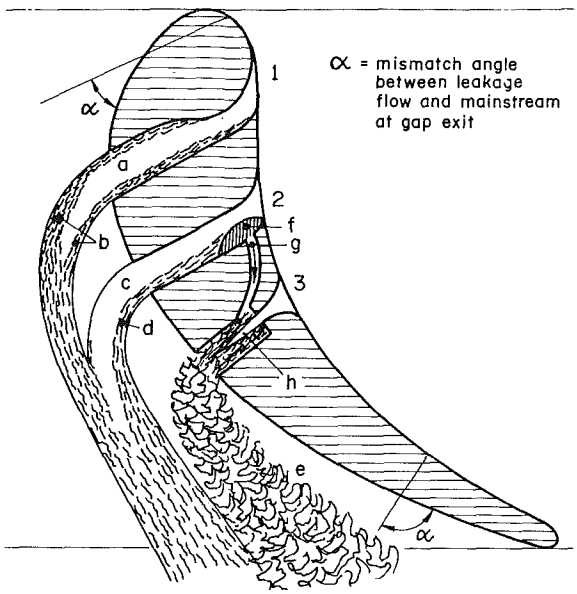

Fig. 9 Conceptual model showing various types of flow active in the tip clearance region

both have mismatch angles which depend on the chordwise position.

Channel 2 contains a separation bubble *f* with a reattachment of flow behind it to represent the flow over the forward part of the blade. The leakage jet is therefore a reattachment wake *d* and core flow *c*.

Channel 3 is shaped to be an ejector exhausting separation bubble fluid *g* to the suction corner flow as an entrainment wake *e*. The stagnant fluid *g* is given momentum to climb up the pressure gradient to gap exit by the mixing out of the jet flow *h*. Channel 3 can be regarded as being at a single point in the flow, probably just after the point of maximum blade

loading. Wake *e* is subject to the suction corner pressure rise and is shown to increase in size and form most of the mixing loss.

8 Conclusions and Future Work

Tip clearance loss varies linearly with gap size. The linearity does not however extend down to zero clearance, showing that there are fundamentally different loss mechanisms present.

The total tip clearance loss on the endwall was separated for the first time into three basic components. Internal gap loss made up 39 percent of the total, suction corner mixing loss formed 48 percent, and endwall/secondary loss the remaining 13 percent.

The measurement of internal gap loss is important because it demonstrates that tip clearance involves not only the quantity of leakage fluid but also the losses the fluid encounters in its passage through the gap. It is fair to say that the only concern of a blade row is to deflect the flow at minimum loss. These two factors are the only real criteria. Gap discharge coefficient is not a sound basis for judging gap geometry since the connection with loss and deflection is uncertain.

It was suggested that the major part of the gap loss arises when the slow-moving separation bubble flow is ejected from the low-pressure zone in the gap by the high-speed leakage jet induced at midchord. Some uncertainty exists as to the nature of the flow and loss formation within the gap over the trailing part of the profile.

Mixing loss was seen to emerge only over the last 20 percent of axial chord. This means that the leakage over the forward half of the blade contributes little. The mixing loss found appears to be related to the high-loss wake as the stagnant bubble is ejected from the gap. The fluid seems to have insufficient momentum to negotiate the suction corner diffusion and it separates to form an extremely large wake that contains all the mixing loss. The growth of mixing loss seems far from complete at the trailing edge and a study of mixing loss downstream is called for.

Since tip leakage loss both inside and outside the gap is primarily related to separation rather than to leakage flow quantity, future study should investigate loss reduction using specially streamlined blade tips that minimize entropy generation and maximize tip region flow deflection. One such tip is a simply radiused tip edge to avoid the formation of the separation bubble. This geometry is the subject of a companion paper (Morphis and Bindon, 1988). The whole subject of finding new tip clearance geometries reveals the need for computational techniques able to cope with the intricate gap spaces as well as the viscous effects of mixing.

The subject of tip clearance loss needs to be related to deflection and work transfer. A distinction should also be made between a single-stage machine (or a last-stage rotor) in which there is no possibility of recovering a loss of work through decreased tip deflection and a multistage turbine in which the outlet flow is passed to the next stator where a decreased tip deflection may be partially recovered.

The measurement techniques used to separate the components of leakage need to be improved, particularly with respect to finding a reliable probe to measure the gap inlet total pressure where there are such steep gradients of pressure and direction. An alternative may be to suck off the cascade inlet boundary layer and carefully to suck off the endwall layer just before the gap entry so to ensure zero loss. It is unlikely that the flow in the gap will be dependent on the vorticity at the gap inlet.

Acknowledgment

The continued encouragement and inspiration provided by the members of the Whittle Laboratory Cambridge, where the experimental work was done, is gratefully acknowledged.

References

Bindon, J. P., 1986a, "Visualisation of Axial Turbine Tip Clearance Using a Linear Cascade," Report No. CUED/A-Turbo TR122, Whittle Laboratory, Cambridge University, United Kingdom.

Bindon, J. P., 1986b, "Pressure and Flow Field Measurements of Axial Turbine Tip Clearance Flow in a Linear Cascade," Report No. CUED/A-Turbo TR123, Whittle Laboratory, Cambridge University, United Kingdom.

Bindon, J. P., 1987a, "The Measurement of Tip Clearance Flow Structure on the Endwall and Within the Clearance Gap of an Axial Turbine Cascade," *Proc. IMechE Int. Conference Turbomachinery-Efficiency Prediction and Improvement*, Cambridge, United Kingdom, Paper No. C273/87.

Bindon, J. P., 1987b, "Pressure Distributions in the Tip Clearance Region of an Unshrouded Axial Turbine as Affecting the Problem of Tip Burnout," ASME Paper No. 87-GT-230.

Bindon, J. P., 1987c, "Visualisation of Tip Clearance Flow in a Linear Turbine Cascade," 8th International Symposium on Air Breathing Engines, Cincinnati, OH.

Denton, J., and Cumpsty, N., 1987, "Loss Mechanisms in Turbomachines, *Proc. IMechE Int. Conf. Turbomachinery-Efficiency Prediction and Improvement*, Cambridge, United Kingdom, Paper No. C260/87.

Kind, R. D., 1987, Private Communication, Carleton Univeristy, Ottawa, Canada.

Moore, J., and Tilton, J. S., 1988, "Tip Leakage Flow in a Linear Turbine Cascade," ASME JOURNAL OF TURBOMACHINERY, Vol. 110, pp. 18–26.

Morphis, G., and Bindon, J. P., 1988, "The Effects of Relative Motion, Blade Edge Radius and Gap Size on the Blade Tip Pressure Distribution in an Annular Turbine Cascade With Tip Clearance," ASME Paper No. 88-GT-256.

Sjolander, S. A., and Amrud, K. K., "Effects of Tip Clearance on Blade Loading in a Planar Cascade of Turbine Blades," ASME JOURNAL OF TURBOMACHINERY, Vol. 109, pp. 237–244.

APPENDIX

Extended Nomenclature and Mass Integration of Loss and Discharge Coefficients

A_{ref} = reference area = 1 pitch × 1/4 chord
C_L = loss coefficient $= \Delta p_o / 1/2\ \rho\ V_1^2$
C_v = velocity coefficient $= V/V_1$
$\dot{m}$ = mass flow rate
p_o = total pressure
V = velocity
V_{is} = isentropic velocity at a point
x = distance normal to flow
z = distance normal to endwall
Z = distance of boundary layer integration or gap width normal to endwall
ρ = density
1 = upstream of cascade
2 = any point within cascade

Loss Coefficients

$$\bar{C}_L = \frac{\overline{\Delta p_o}}{\frac{1}{2}\rho V_1^2} = \frac{\sum^{\dot{m}} \Delta p_o\, d\dot{m}}{\frac{1}{2}\rho V_1^2\, \dot{m}_{ref}}$$

$$= \frac{\sum^{A} C_L \rho\, V\, dA}{\rho\, V_1 A_{ref}} = \frac{1}{A_{ref}} \sum^{A} C_L\, C_V\, dA$$

$$= \frac{1}{A_{ref}} \int_0^X \int_0^Z C_L\, C_V\, dz\, dx$$

$$= \frac{Z}{A_{ref}} \int_0^X \int_0^Z C_L\, C_V\, dz/Z\, dx$$

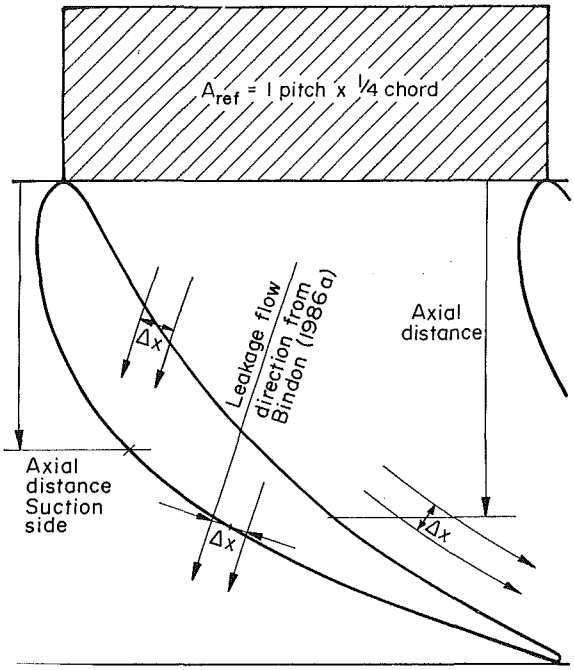

Fig. A1 Blade profile and distances used in plots and integrations

$$= \frac{Z}{A_{\text{ref}}} \int_0^X \bar{C}'_L \, dx$$

$$\bar{C}'_L = \int_0^Z C_L \, C_V \, dz/Z$$

Discharge Coefficients

$\bar{C}'_D = \dot{m}/\dot{m}_{is}$ through gap height Z of width Δx

$$= \int_0^Z \rho V \, \Delta x \, dz \Big/ \int_0^Z \rho \, V_{is} \Delta \, x \, dz$$

$$= \rho \Delta x \int_0^Z V \, dz / \rho \, V_{is} \Delta x \int_0^Z dz$$

$$= \int_0^1 V/V_{is} dz/Z$$

$\bar{C}_D = \dot{m}/\dot{m}_{is}$ for whole gap

$$= \int_0^X \int_0^Z \rho \, V \, dz \, dx \Big/ \int_0^X \int_0^Z \rho \, V_{is} dz \, dx$$

$$= \int_0^X \int_0^1 C_v dz/Z \, dx \Big/ \int_0^X \int_0^Z V_{is}/V_1 \, dz/Z \, dx$$

Endwall Flow/Loss Mechanisms in a Linear Turbine Cascade With Blade Tip Clearance

A. Yamamoto
National Aerospace Laboratory,
Chofu, Tokyo, Japan

This paper discusses the mechanisms of three-dimensional flows and of the associated losses occurring near the tip endwall region of a linear turbine cascade with tip clearance. The clearance gap sizes and the cascade incidences were chosen as the most important variables affecting the mechanisms. Flows close to the endwall and inside the clearance were surveyed in great detail using a micro five-hole pitot tube of 0.6 mm head size. The results gave very detailed information on the mechanisms, such as leakage flow vectors and pressure distributions throughout the clearance. Interaction of leakage flow with the endwall flow and their associated separation lines, effects of gap size and inlet flow angle on loss generation, and skewness of the three-dimensional endwall flows are also discussed.

Introduction

The leakage flow passing through the tip clearance between the blade tips and the tip endwall causes a major part of the total pressure losses in a turbine blade row with tip clearance. Many empirical and semitheoretical correlations between tip clearance gap size and cascade overall loss exist for design purposes. Some correlations were summarized (Yamamoto et al., 1976) in a form that says leakage loss is proportional to clearance gap size, but the proportional constants differ among various researchers. Studies of leakage loss made up to 1963 were reviewed by Lakshminarayana and Horlock (1963). Lakshminarayana (1970) devised a more sophisticated method for predicting the loss (i.e., the proportional variable) from his basic experimental research on the leakage vortex (Lakshminarayana and Horlock, 1965). The method was applied to the loss estimation of compressors, pumps, and turbines. Recently, rather than the bulk studies undertaken in the past, more detailed studies have been made to understand the physics of leakage flow and the loss generating mechanism, and to gain some new ideas for reducing leakage loss; Booth et al. (1982) presented a case study of the flow vectors through the clearance in a water table cascade. These vectors were analyzed from their flow visualization data and compared with the vectors calculated by a simple model based on Rains' theory (1954). It was noted that three dimensionality of the cascade flows near the leading and trailing edge caused large errors between the theory and the test data. Wadia and Booth (1982) and Wadia (1985) found that a great pressure drop occurred at the blade pressure side, from where the leakage flow enters the tip gap. Graham (1986) studied the leakage flow in a water cascade of linear blades with a moving belt that simulated the moving endwall. His flow visualization showed very irregular movements of the leakage flow tracer at various belt speeds. This indicates the scraping effects due to viscous force supplied by the belt. Sjolander and Amrud (1987) have discussed the effects of leakage flow on blade loading of a linear cascade. With their pressure measurements and flow visualization by oil smoke, they showed the existence of separation lines on the cascade endwall and of separation bubbles on the tip or the wall, caused by leakage flow. Bindon (1986) measured the leakage flow within the gap of a linear cascade with moderate turning. He used fine pressure taps on the tip surface and on the endwall, and a total pressure tube for flow measurements. He confirmed the great pressure drop at the pressure side edge of the tip and concluded that it occurred due to highly accelerated flows at the gap corner.

As seen in some flow visualizations of leakage vortex systems (e.g., Sjolander and Amrud, 1987; Yamamoto, 1988), details of the leakage flow mechanism depend strongly on the cascades used and the operating conditions. The mechanism, therefore, should be understood in relation to the other three-dimensional vortices generated in the cascade used. Since operating conditions such as incidence variation easily change the three-dimensional vortices, systematic studies on the mechanism are needed. Most of the studies so far, however, have been limited to the design inlet flow condition and only a few researchers have measured flows inside the tip clearance. To the author's knowledge, however, none of the studies so far, except for the theoretical work by Hah (1986) and Pouagare and Delaney (1986) on compressor cascades, have presented flow vectors "within" the gap. To understand the flow mechanism in the gap, direct flow measurements within the gap with three-dimensional sensors such as a five-hole pitot tube or a hot wire are urgently needed. Yamamoto (1988) has presented an example of such direct measurements of the leakage flow in a linear cascade and discussed the interaction of the leakage flow with the passage vortex. The example, however, was limited to the design incidence condition. In the

Contributed by the International Gas Turbine Institute and presented at the 33rd International Gas Turbine and Aeroengine Congress and Exhibition, Amsterdam, The Netherlands, June 5-9, 1988. Manuscript received by the International Gas Turbine Institute September 1987. Paper No. 88-GT-235.

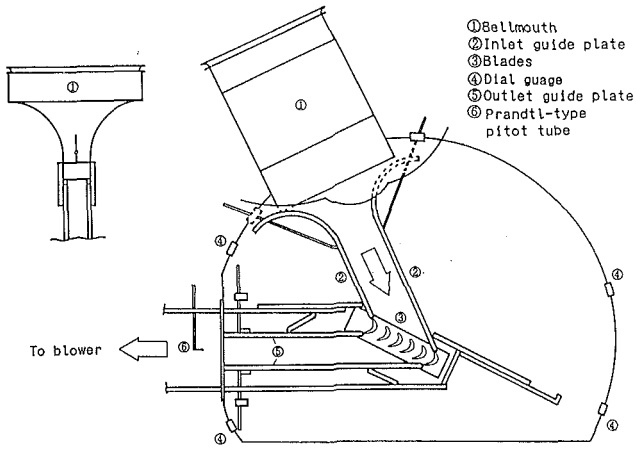

Fig. 1 General view of test cascade

present paper, full description of the measurements will be given for various incidences and for other gap sizes. This three-dimensional flow survey will quantify the leakage vectors, the associated loss, and other quantities under various incidences, not only near the endwall of the cascade with tip clearance but also within the clearance gap. The paper will give a new experimental insight into the flow physics of turbine cascade with tip clearance, although the endwall motion is not taken into account.

Test Facilities and Test Methods

Low-Speed Linear Cascade Wind Tunnel. Figure 1 shows a general view of the NAL linear cascade wind tunnel, which the author designed to investigate various three-dimensional flow phenomena occurring in turbine blade rows. The wind tunnel is of a suction type with the low inlet turbulence level normally less than about 0.5 percent. The inlet flow angle can be varied with two inlet guide plates. A more detailed description of the tunnel was given by Yamamoto (1987, 1988). For the present test with rotor blades, only the major specifications of the cascade are given here:

- Blade chord $C = 73.5$ mm
- Axial blade chord $Cax = 72.6$ mm
- Blade pitch $S = 61.42$ mm
- Aspect ratio $H/C = 1.37$
- Solidity $C/S = 1.20$
- Blade maximum thickness/blade chord = 0.257
- Blade LE radius = 8.17 mm; TE radius = 4.08 mm

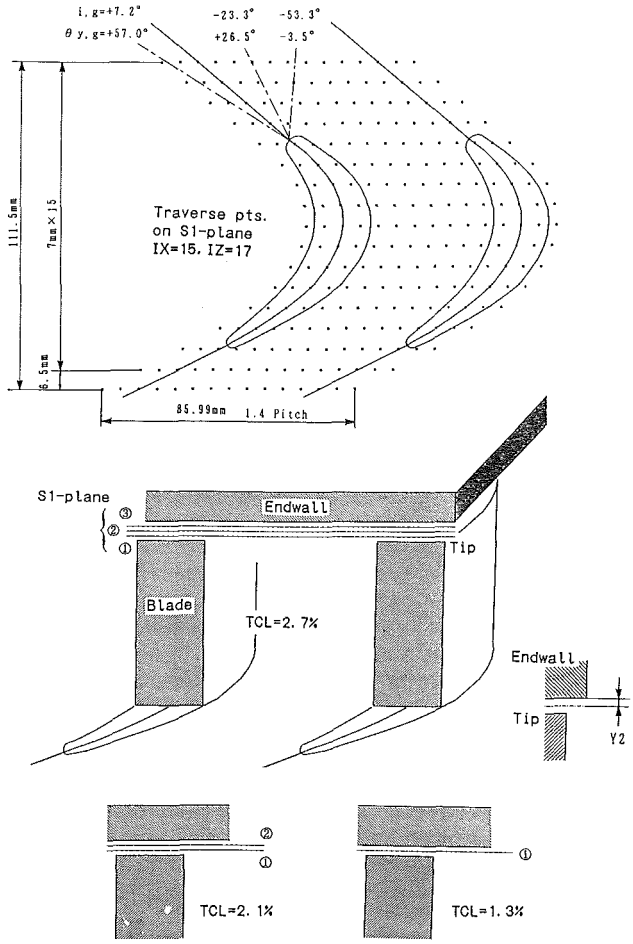

Fig. 2 Traverse points in blade tip gap

- Number of blades $N = 6$
- Cascade camber angles, inlet = 49.8 deg
  outlet = −63.5 deg
- Design cascade turning angle = 113.3 deg
- Design flow angles, inlet = 43.6 deg
  outlet = −63.5 deg
- Design turning angle of flow = 107.1 deg

The clearance gap was varied by changing the width between the two endwalls. For zero clearance, the gap of each blade was sealed by attaching felt material to the tip.

Nomenclature

Cax = blade axial chord
CPs = static pressure coefficient based on nominal outlet velocity, Vm', measured far downstream from the cascade = $(Ps - Patm)/(0.5 \times \rho \times Vm'^2)$
CPt = total pressure loss coefficient based on Vm' = $(Patm - Pt)/(0.5 \times \rho \times Vm'^2)$
H = cascade passage span
i = incidence
k = tip clearance gap
$Patm$ = atmospheric pressure
Ps = static pressure
Pt = total pressure
TCL = tip clearance = k/H, percent
Vm' = resultant velocity measured far downstream of cascade (setting velocity of 40 m/s)
Vs' = magnitude of secondary flow vector based on mass-averaged flow direction
W = velocity component projected onto the endwall
$Y2$ = spanwise distance from tip endwall
Z = axial distance from blade leading edge
Δ = interval of contour plot
θ_y = yaw angle measured from cascade axial direction
ρ = density
①, ②, ③ = number of blade-to-blade (S1-)plane

Subscripts

g = inlet guide plates

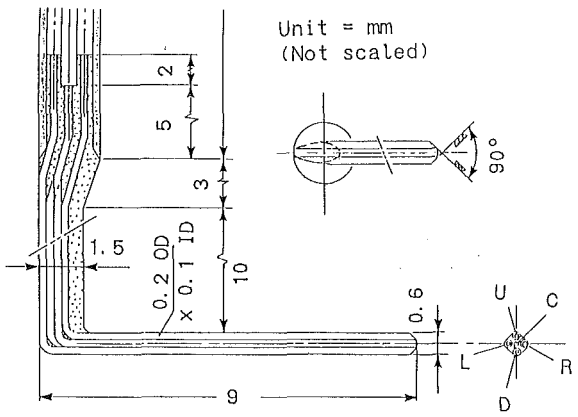

Fig. 3 Dimensions of micro five-hole pitot tube

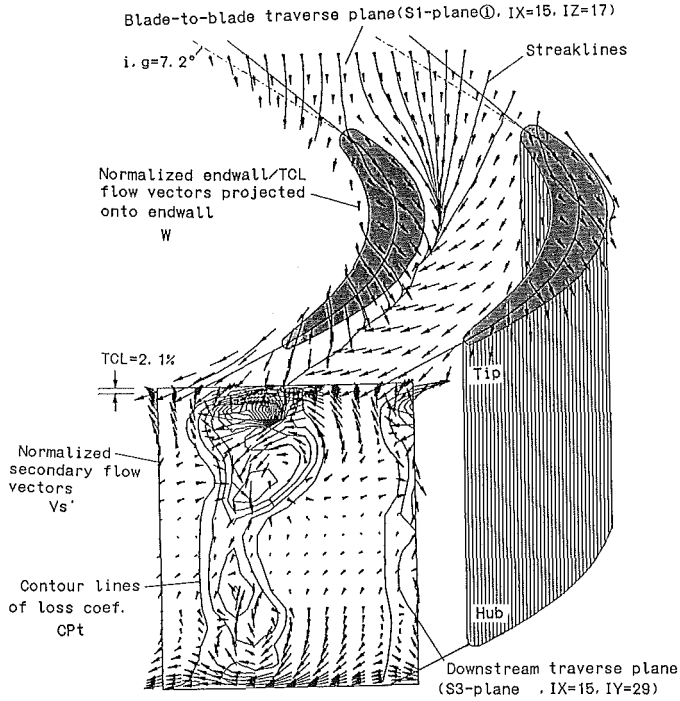

Fig. 4 Traverse planes and typical test result

Traverse Measurements. Figure 2 shows the traverse points on a blade-to-blade plane (called S1-plane) located in the gap between the blade tips and the endwall. Three S1-planes were located in the largest tip clearance and two S1-planes in the medium clearance. On the last pitchwise line downstream of the cascade ($Z/Cax = 1.19$), an additional spanwise and pitchwise traverse was conducted to determine the cascade downstream flow field. As described in the previous study (Yamamoto, 1987), the pitchwise (X) traverse was made by moving a tip-side endwall plate in that direction, while the axial (Z) traverse was done by rotating a disk contained in the pitchwise traverse plate. On the rotating disk, a radial (Y) traverse gear with a yaw (θ_y) revolution gear was installed. All of the traverses were done automatically by a four-axis pulse motor controller connected to a microcomputer.

Table 1 shows the distances of the traverse S1-planes measured from the endwall. The numbers in parentheses indicate test gap sizes measured and those in the first column show the nominal (averaged) values. For each gap, the traverse measurements were made at three inlet guide plate angles: 57.0, 26.5, and −3.5 deg. These correspond to incidences of 7.2, −23.3 and −53.3 deg, respectively.

Figure 3 shows the five-hole pitot tube with a head width of only 0.6 mm used in the present survey. To be able to access both endwalls as closely as possible, the probe was made **L**-shaped. Since the yaw direction of the flow near the tip endwall ranges very widely beyond the probe calibration range of −30 to 30 deg, all the traverse points on each S1-plane were surveyed three times with the probe fixed at 0, −60, and 60 deg from the cascade axis. This method enables the probe to sense the flow over a range of −90 to 90 deg. Owing to the **L**-shaped sensor head (the sensing front of the sensor is not on the probe axis), the front deviates when the probe rotates. Therefore, to locate the sensing front at the location desired, a somewhat complicated correction was necessary in the traverse program. After the three surveys, only the data set with the largest center-hole pressure was chosen from the three sets of data obtained at the same traverse point. The Reynolds number (Re, c) of the present test series based on the blade chord and the mass-averaged cascade downstream velocity at about Z/Cax of 1.19 was about 1.7×10^5.

Experimental Results and Discussion

A Sample Result Showing Analysis Method and an Overall View of Leakage Loss Mechanisms. Figure 4 illustrates a typical result of the present serial tests. Two kinds of vectors, W and Vs', streaklines (or particle path lines) on a blade-to-blade plane, and downstream total pressure loss contours, CPt, are illustrated. This result was obtained with the medium clearance of 2.1 percent. The test direction of the inlet guide plates is shown by the two alternate long and short dash lines, and is 7.2 deg in the present case. The solid lines throughout the blade profiles indicate the cascade camber lines, and the inlet and the outlet blade angles. The vector W was defined as the component of velocity projected to the blade-to-blade (S1-)plane or to the endwall, and normalized by a cascade downstream setting velocity of 40 m/s (measured by a Prandtl-type pitot tube as shown in Fig. 1). The vector W in Fig. 4 corresponds to that obtained on the S1-plane 1 closest to the blade tip (see Fig. 2 and Table 1 for the location). The lines associated with W show the streaklines originating from the upstream traverse points and from the points at both right and left traverse edges. These lines would indicate the movements of upstream endwall (boundary layer) fluids and of some leakage fluids. The figures at the downstream traverse plane (called the S3-plane) show secondary flows seen from the cascade downstream side, and the associated losses. The secondary flow, Vs' here, was defined as the component of velocity normal to the mass-averaged flow direction.

From this three-dimensional representation, the relation of the endwall flow and the leakage flow to the cascade loss generation process could be easily understood. Leakage flows through the clearance, for example, interact near the suction surface with the endwall flow and roll down away from the endwall along an interaction (separation) line, and form a leakage vortex with significant loss generation. The vortex interacts intensely with the tip-side passage vortex, which rotates contrary to the leakage vortex. The present sample result gives an introduction to the flow mechanisms, which will be discussed in more detail in the following sections. As the main variables affecting the mechanisms, clearance gap sizes, incidence angles of the inlet guide plates, and positions of the blade-to-blade planes within the gap will be chosen in the subsequent discussion.

Behavior of Leakage/Endwall Flows and Downstream Secondary Flows. Figure 5 shows the endwall/leakage flows under three incidences and three gap sizes. All of the S1-planes shown here correspond to the planes closest to the blade tip, i.e., S1-plane 1. They are located roughly at the same distance

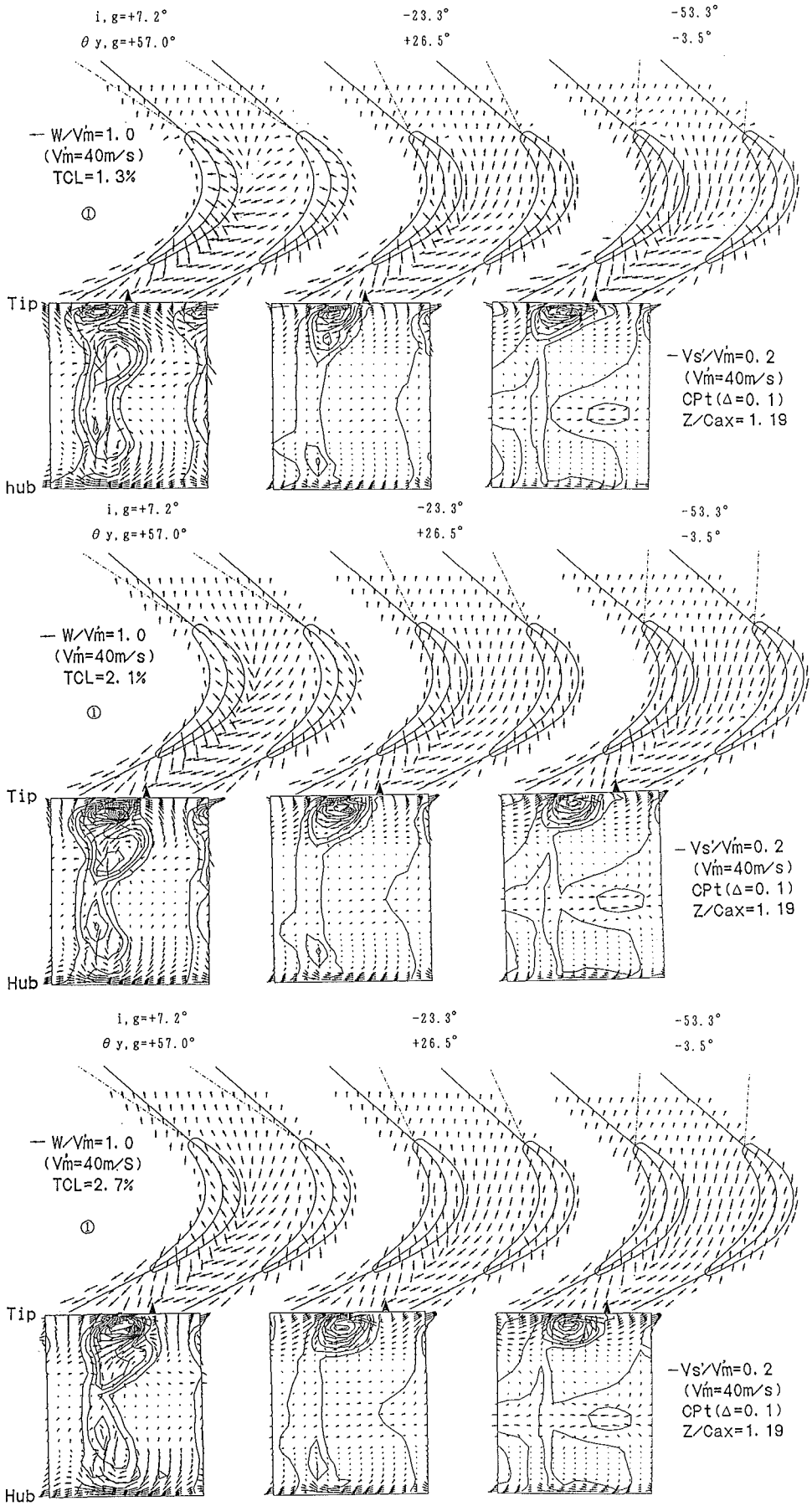

Fig. 5 Endwall/TCL flows at S1-plane ① and downstream secondary flows/losses for three TCL and three inlet guide angles

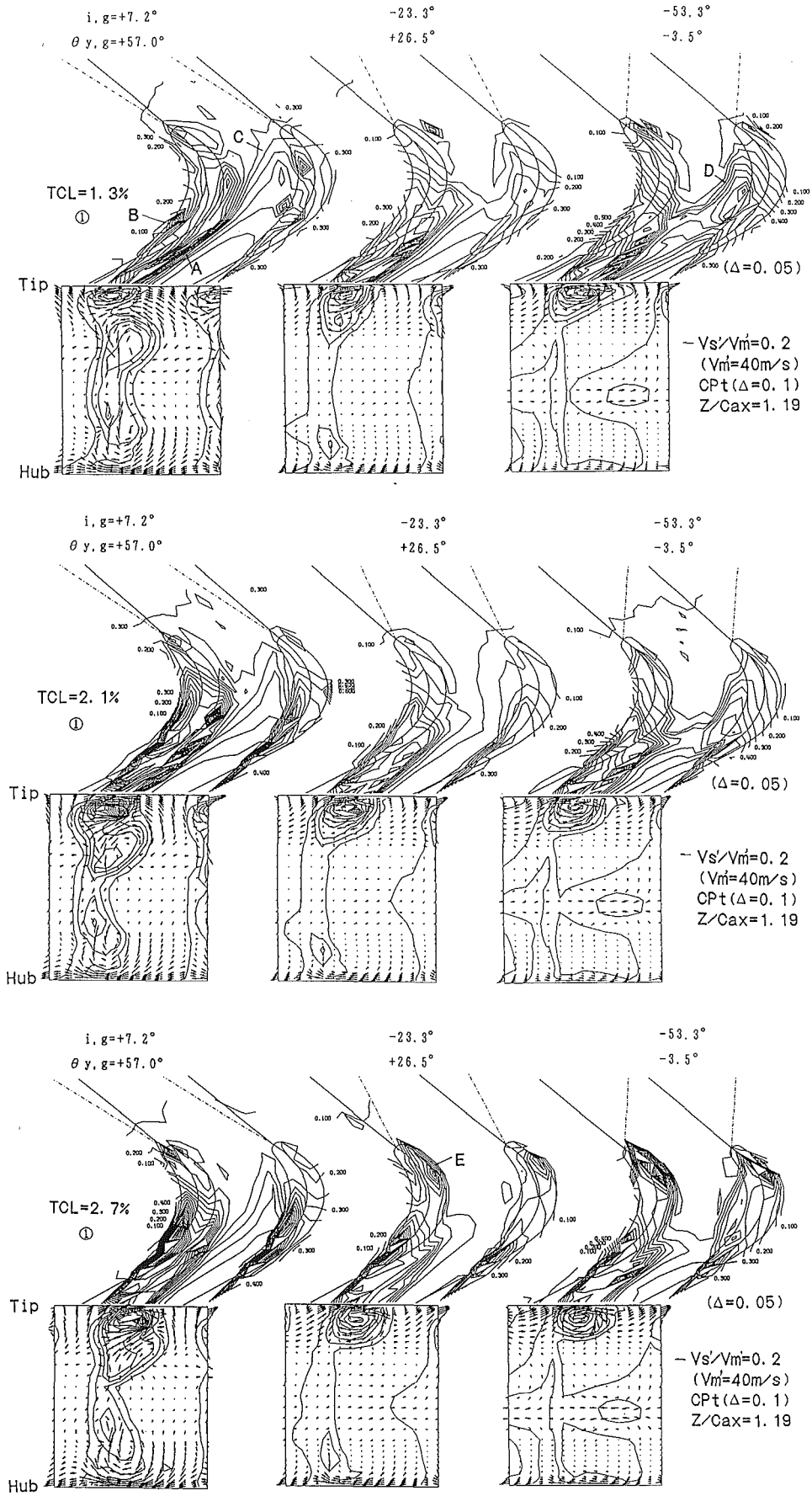

Fig. 6 Endwall/TCL losses at S1-plane ① and downstream losses with secondary flows for three TCL and three inlet guide angles

(about 0.6–0.7 mm) from the blade tip surface for all test clearances, but at different distances from the casing.

Let us first discuss the flows on the blade-to-blade (S1-)planes. As incidence decreases, some of the inlet flows tend to enter the gap from the suction side and exit from the same suction side, to interact with the endwall flow outside the tip. The same behavior can be seen in a flow visualization made by Joslyn (1983) on a rotating turbine blade tip at a negative incidence. In the rear part of the tip, however, the leakage flow always passes the blade tip from the pressure side to the suction side. Thus, the leakage flows over the front part of the tip are more sensitive to incidence variation than those over the rear part. At a positive incidence, the leakage flow passes the front part of the tip nearly normal to the blade camber line in the minimum clearance case. The flows, however, tend to follow the camber line in the larger clearance cases. This means that the inertia forces of the inlet boundary layer fluids become an important cause of the leakage flow with larger clearances, while the pressure gradient within the gap is more important with small clearance. With larger clearance, the increased amounts of leakage flow cause the interaction region to extend farther away from the suction surface, as shown by solid arrows.

Next let us look at the downstream flows, especially the secondary flows, since the losses will be discussed in the next section. As the incidence decreases, the strength of the passage vortices at both endwall sides rapidly decreases except in the regions very close to the endwalls, while the leakage vortex apparently remains. Interaction, therefore, still occurs between the flow (passage vortex) very close to the tip endwall and the leakage vortex. A new secondary flow from the pressure side toward the suction side appears about the midspan. When the gap size increases, the leakage vortex generally grows up in size in the present cascade and the vortex center approaches the wake center, as clearly seen in the positive incidence case. The leakage vortex is less sensitive to the incidence change than the passage vortices. The lower sensitivity of the leakage flow is due to the fact that (1) the leakage flow through the front part of the tip depends strongly on the inlet endwall flow (usually in the boundary layer), which is relatively less sensitive to incidence change than the flow away from the wall, and (2) most of the leakage flows that are significant to the vortex formation occur in the rear half of the cascade passage, where the incidence effects have already been reduced.

Loss Generation on Endwall and Within Tip Clearance. Figure 6 shows the total pressure loss close to the tip endwall. In the following discussion, a cross reference between Fig. 5 (vectors) previously discussed and Fig. 6 (losses) will help in understanding the loss generation mechanism.

The first high-loss region (indicated by A) can be found along the suction surface where the leakage flow interacts with the endwall flow (passage vortex) and separate from the endwall. The second high-loss region (B) can be seen on the blade pressure side endwall from which leakage flows enter the gap. The region extends downstream. The first and second high-loss regions can be found with all the incidences and gap sizes tested. As incidence decreases, the first high-loss region along the suction surface moves farther downstream and the loss level decreases. This means that formation of the leakage vortex starts farther downstream as incidence decreases.

The third high-loss region (C) starts at the pressure side of the leading edge and extends toward the suction surface of about midaxial chord of the adjacent blade. This region corresponds roughly to a migration path of low-energy fluids, along which path the inlet boundary layer is swept as seen later in Fig. 14. At the minimum incidence of -53.3 deg, the fourth high-loss region (D) occurs near the pressure side of the

Table 1 Location of S1-planes (①-③) in Fig. 2

Inlet guide angle	i, g=+7.2° θy, g=+57.0°		-23.3° +26.5°		-53.3° -3.5°	
TCL $\bar{k}$ (mm)	S1-Plane	Distance Y2(mm)	S1-Plane	Distance Y2(mm)	S1-Plane	Distance Y2(mm)
1.3% 1.29		(1.225)		(1.328)		(1.276)
	①	0.638	①	0.664	①	0.638
2.1% 2.14		(2.243)		(2.056)		(2.108)
	①	1.527	①	1.392	①	1.392
	②	0.695	②	0.716	②	0.716
2.7% 3.03		(3.044)		(3.060)		(2.992)
	①	2.328	①	2.328	①	2.328
	②	1.548	②	1.548	②	1.548
	③	0.716	③	0.716	③	0.716

Traverse meshes: IX=15, IZ=17, ( )=k measured

cascade passage, owing to the flow separation from the leading edge (Yamamoto and Nouse, 1988). Owing to the migration of low-energy fluids toward the suction side in the rear half of the cascade passage, the high-loss regions at the pressure side (D) and at the suction side (A) are connected to each other.

The fifth high-loss region (E) can be found around the suction side of the leading edges, with the largest gap and negative incidences. This high-loss region corresponds to another entrance region of the leakage flow into the tip gap, as does the second high-loss region (B).

Static Pressure Near/On Endwall and Within Tip Clearance. Figure 7 shows the static pressure distribution obtained on the S1-plane 1 closest to the blade tip. Most interesting is the variation of static pressures with incidence and gap size. Two local minimum pressure peaks were found: One is located along the rear part of the pressure surface when incidence is positive, and the other along the front part of the suction surface when incidence is negative. The former pressure peak was found also by Bindon (1986) at the cascade pressure side of a relatively low-turning blade. He explained the occurrence as due to the flow acceleration when the leakage fluids turn around the tip edge to enter the gap. Both pressure peaks found in the present results probably stem from the same cause, considering the vector plots in Fig. 5. These peaks are apparently affected by incidence and gap size: As incidence decreases, the former peak tends to disappear, while the latter tends to grow larger. Detailed characteristics of the flows at these peaks will be seen later in Fig. 10. The pressure distribution in the front part of the cascade passage is strongly affected by the incidence variation, but in the rear part it is not so. The pressure contours ahead of the blade leading edge show an area of nearly stagnated flows. As the incidence decreases, the stagnated region moves around the blade leading edge to the suction side.

Blade Loading at the Tip. As reported by Lakshminarayana and Horlock (1965), and more recently Sjolander and Amrud (1987), the clearance flow has been discussed related to the blade surface pressure (loading) distribution at the tip. In the present study, detailed static pressure measurements on the tip casing were made at a total of 1476 (41 pitchwise × 36 axial) points as shown in Fig. 8, for five tip clearances and four incidence cases. The traverse pitches were 2.05 mm and 4 mm in the cascade pitchwise and the axial direction, respectively. The endwall pressure distribution and its general tendency with gap size and incidence were similar to those measured on

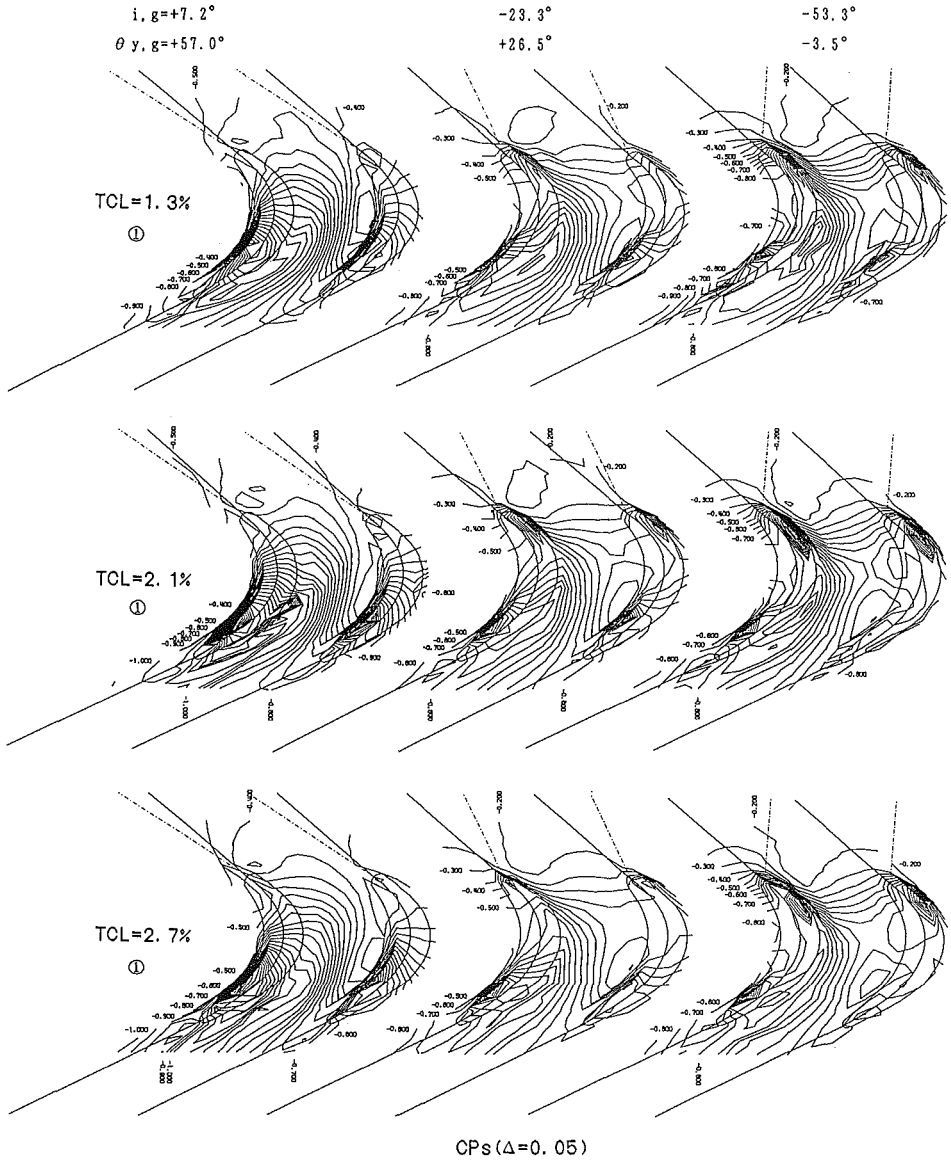

Fig. 7 Endwall/TCL static pressure for three TCL and three inlet guide angles at S1-plane ①

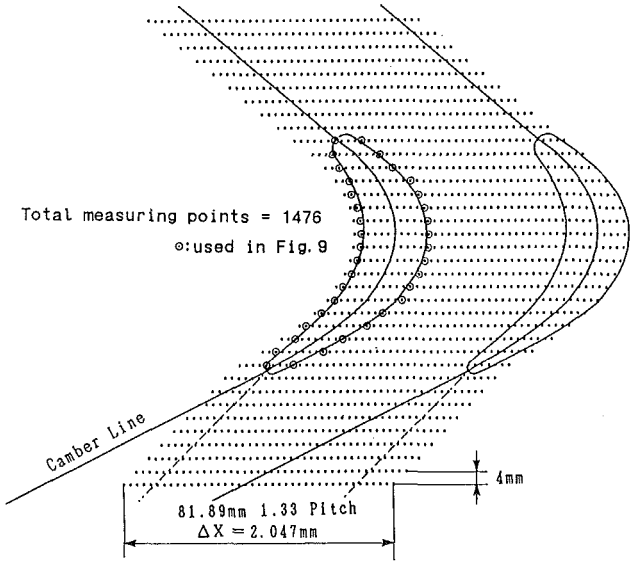

Fig. 8 Measuring points of tip-endwall static pressures

S1-planes. Figure 9 shows the endwall static pressure distributions around the blade surface as shown in Fig. 8, for zero and 2.1 percent clearances and for three incidences. The pressure difference between the blade pressure and the suction surfaces indicates roughly the blade loading at the tip. When leakage flows occur, the resultant pressure distributions around the blade are completely different from those without clearance and the blade loading at the tip region is much reduced. From the reduced loading distributions, it appears a little difficult to understand or predict the directions of leakage flows in the tip gap obtained (Fig. 5). It will turn reasonable, however, when we notice that since the leakage flows do not always pass the tip gap from the blade pressure side to the suction side but often pass from the front part of the tip to the suction side, their directions are not necessary to coincide with the loading or the static pressure difference between the blade surfaces at the same Z/Cax. When we look at the pressure distributions within the gap shown in Fig. 7, the directions of leakage flows can be more easily understood. Also the inertia forces of endwall flows would make the leakage flow vectors difficult to predict.

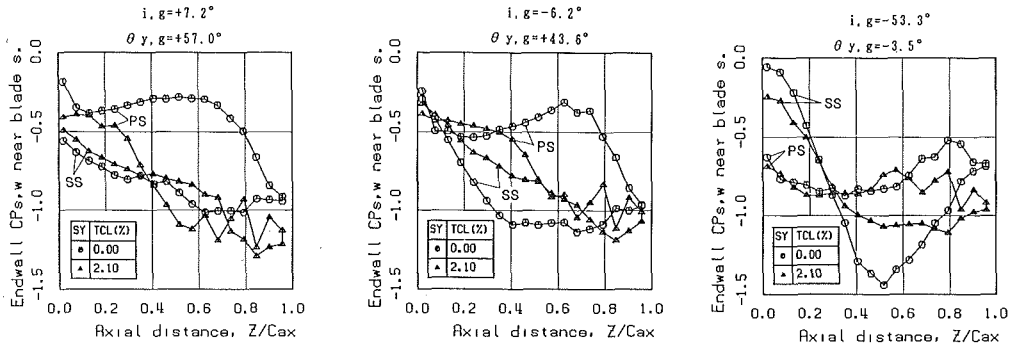

Fig. 9 Tip endwall static pressure around blade surface for zero and 2.1 percent TCL

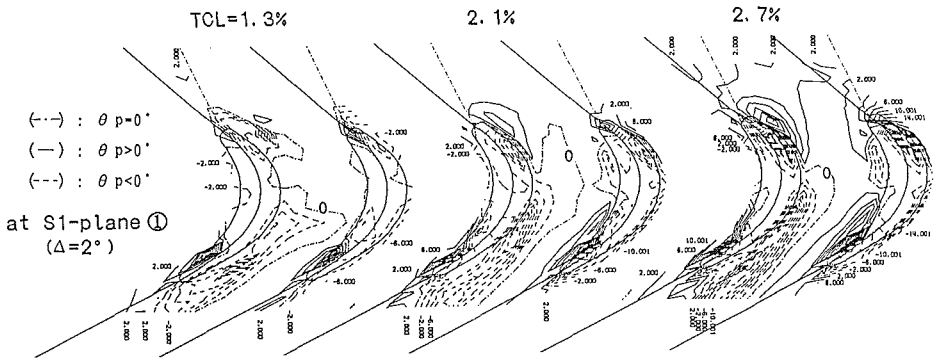

Fig. 10 Pitch angle distribution for three tip clearances at i, $g = -23.3$ deg

Pitch Angle Distribution Near Tip Endwall. Figure 10 shows pitch angle distributions of flows on the S1-plane 1 for the three gap sizes tested. A positive pitch angle (solid line) indicates the flow from the midspan side toward the endwall. The results with the medium negative incidence are presented here, since they include the two regions with low pressure peaks and can show the general three-dimensional features of the leakage flows near these peaks. At one of the entrance regions of the leakage flow along the rear part of the pressure surface, the pitch angle is always positive. This indicates that the fluids there move from the midspan side toward the tip endwall, for all the tip clearances tested. At the other entrance region along the front part of the suction surface, however, the angle is negative for a clearance of 1.3 percent, but positive for 2.1 and 2.7 percent clearances. This means that the flow entering the gap rolls down away from the wall when the clearance is small, and turns to roll up toward the wall for larger clearances. Negative pitch angles are also seen along the suction surface downstream from roughly the mid chord. The fluids in this region roll down toward the midspan side to form the leakage vortex and the tip-side passage vortex. This trend with gap size also holds true for the other incidences tested.

Skewness of Endwall/Leakage Flows. Figure 11 shows a comparison of the vectors on two S1-planes closest to the blade tip and closest to the endwall. The medium and maximum clearance cases are presented. At positive incidence, differences between the two vectors can be recognized in three regions: from the leading-edge of the right-side blade to the suction surface of the adjacent blade, in the interaction region between the endwall flow and the leakage flow, and within the blade tip. These regions indicate areas with highly skewed flows. As incidence decreases to negative values, the differences disappear in the first and the third regions but remain in the second interaction region.

Comparison of Streaklines on Two S1-planes. The vector plots shown in Fig. 11 did not give us a clear image of the flow paths. Using the vectors on each S1-plane, streaklines were analyzed. Note that the streaklines may not necessarily indicate the correct paths of real fluid particles, since the particles would not always stay on the same S1-plane owing to the three dimensionality of the fluids. On some S1-planes located very close to the endwall and at the midspan, however, the streaklines will roughly indicate the real particle paths, since spanwise flows on these planes are generally small. Figure 12 compares the streaklines on two S1-planes located within the gap. The right side one of the two streaklines originating from the same upstream point corresponds to the streakline at the blade side, while the left one corresponds to that at the endwall side. (The latter should be dotted lines, but the line appears solid owing to the density of the dots on the line.)

Let us compare the results for two gap sizes with the same positive incidence. Flow patterns in the two gap cases are very similar at the same incidence although a little difference can be seen between the two. Between two streaklines that originate from the same point, a large deviation can be seen, particularly at the cascade inlet region for the maximum test incidence, and at the rear part of the cascade passage for the minimum incidence. Divergence of two streaklines means a rotational (or skewed) motion of the flows. From this point of view, the leakage flow rotates even inside the gap. Amounts of the inlet endwall fluids passing through the tip gap and becoming the leakage flow depend on incidence. Most of the inlet endwall fluids and the leakage fluids migrate to a single line (separation line) along the blade suction surface. The fluids at the endwall side start to gather farther upstream than those at the blade side.

Comparison of Endwall/Leakage Flows at Two Incidences. Figure 13 compares the flow vectors and streaklines at the maximum and minimum incidence, obtained at the S1-plane closest to the endwall. Differences between the

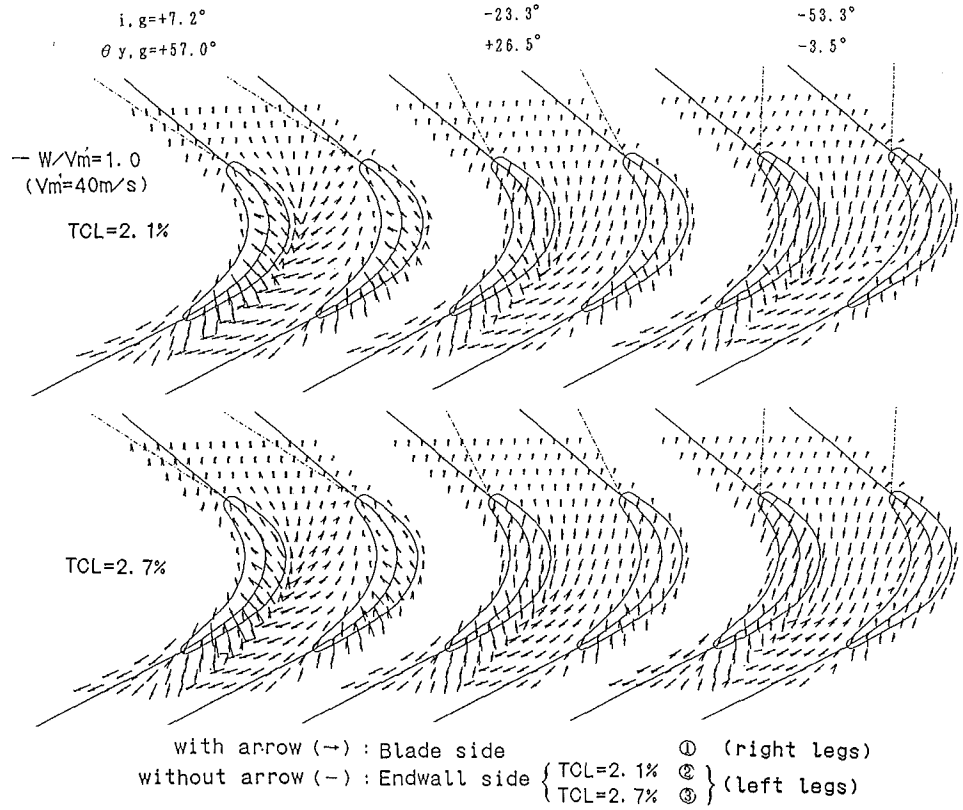

Fig. 11 Comparisom of endwall/TCL flow vectors at two different S1-planes

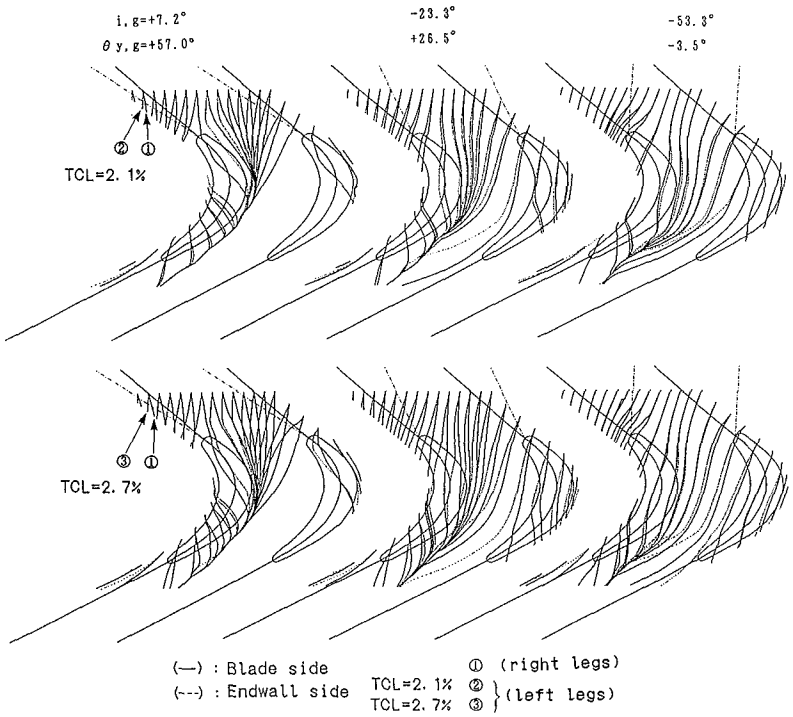

Fig. 12 Comparison of streaklines at two different S1-planes

two superimposed vectors show strong effects of incidence on the flows, not only in the cascade passage but within the gap. In the streakline results, the left streakline of the two originating from the same upstream point corresponds to a negative incidence. A large discrepancy between the two lines shows that the path of each fluid is strongly affected by the incidence variation. At any incidence, however, all the endwall/leakage fluids tend to gather to a single (separation) line along the suction surface, as was seen before in Fig. 12, but farther downstream with negative incidence than with positive incidence.

Quantitative Visualization of Three-Dimensional Flows. Figure 14 visualizes the endwall/leakage flows and

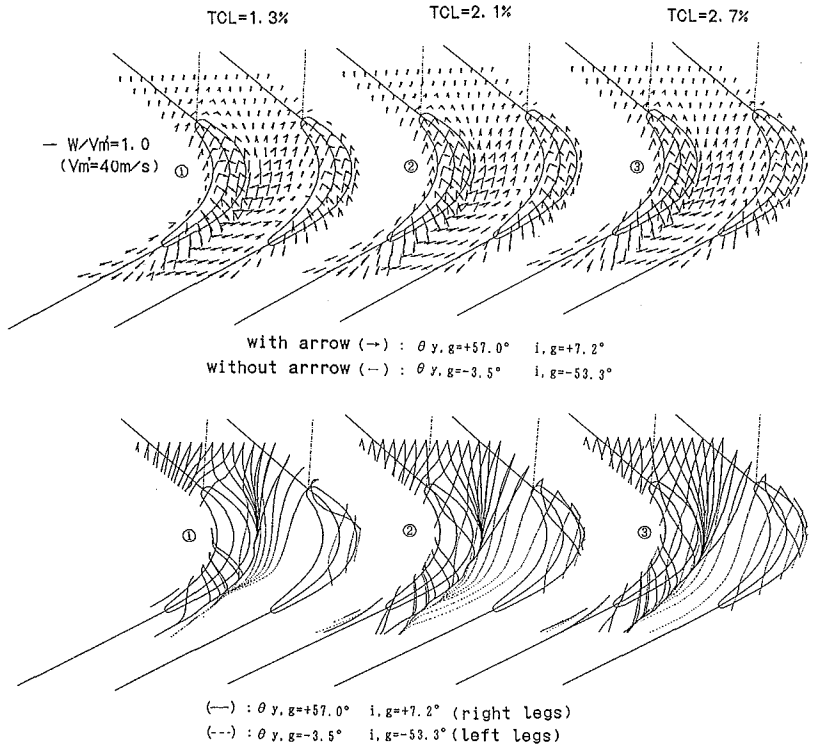

Fig. 13 Comparison of endwall/TCL flow vectors/streaklines at two different incidences

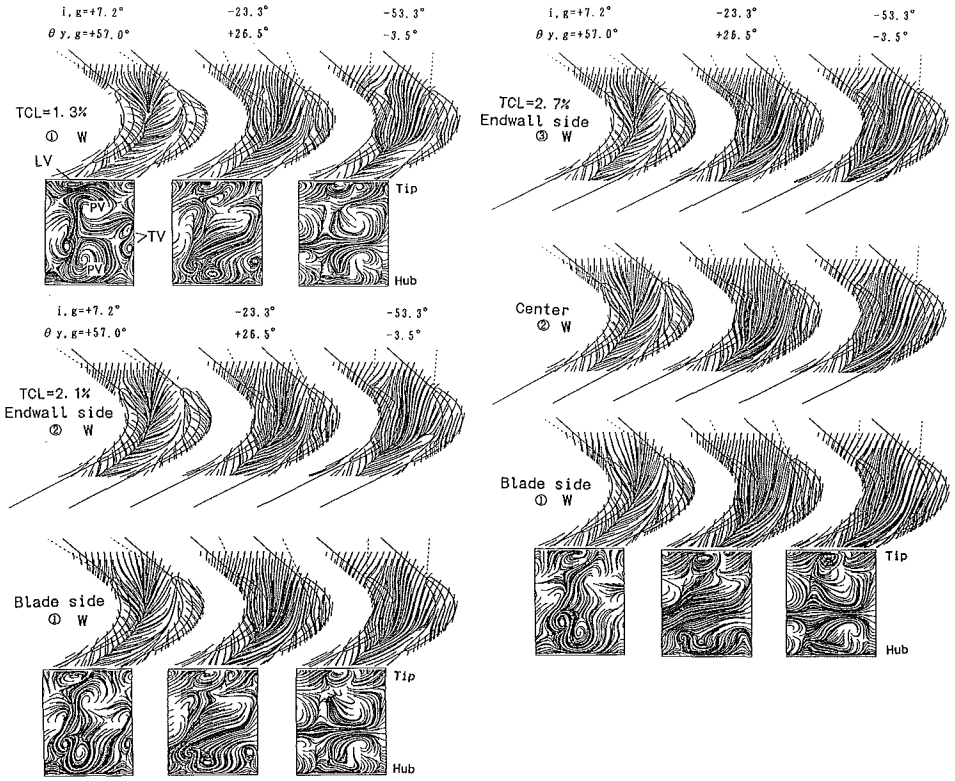

Fig. 14 Oil flow representation of endwall/TCL flows and downstream secondary flows for three TCL, three inlet guide angles, and three S1-planes

the secondary flows downstream of the cascade, based on the present measurements. The flows on S1-planes are represented as so-called surface oil flows, and those on a downstream S3-plane as oil-smoke flows, which are visualized by cutting with a light sheet. The present quantitative visualizations will reveal even small effects that are due to the various incidences, gap sizes, and different S1-planes and give detailed behavior of endwall flows in other regions that have not been illustrated yet.

Let us first look at the data obtained with the minimum

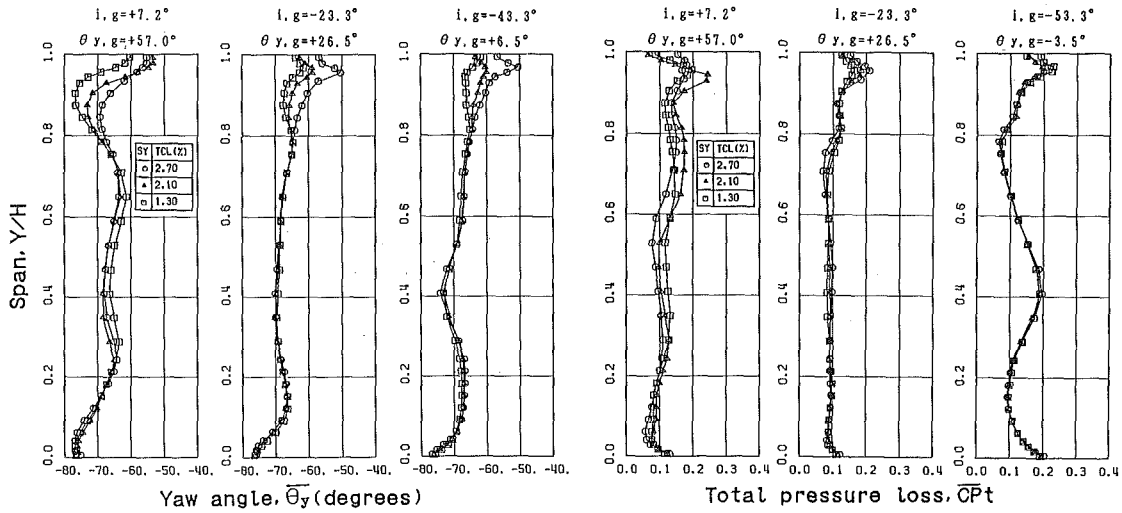

Fig. 15 Radial distributions of pitch-averaged yaw flow angle and total pressure loss downstream of cascade

clearance of 1.3 percent. A clear three-dimensional separation line, at which the leakage flow and the endwall (passage) flow converge and then separate from the endwall, can be seen along the suction surface. The line moves downstream and becomes short as incidence decreases. As seen from the figure at positive incidence, the inlet endwall fluids have already been swept completely toward the suction side at the cascade inlet; the leakage flow includes only the fluids from newly generated boundary layer. This is not true for other (negative) incidences: The leakage flow includes large amounts of the inlet endwall fluids entering the gap from the front part of the suction surface. Near the blade pressure surface, endwall flows diverge in two opposite directions to become the endwall flow (passage vortex) and the leakage flow. This divergence area also moves downstream as incidence decreases. At the minimum incidence, the divergence gets stronger and intense migration of the endwall fluids from the blade pressure side toward the suction side occurs. In the secondary flow field downstream, on the other hand, the leakage vortex, two passage vortices, and some trailing shed vortices can clearly be identified when the incidence is positive. As the incidence decreases, the passage vortices rapidly disappear, although the leakage vortex remains nearly the same.

Next, let us look at the results of the 2.1 percent clearance. The same incidence effects as described before for 1.3 percent clearance are found. The intense migration of endwall fluids from the pressure side can be seen also in the present case: The migration is relatively more intense on the endwall side S1-plane 2 than on blade side S1-plane 1. The downstream secondary flows show a larger leakage vortex, compared to that of a 1.3 percent gap.

Finally let us look at the maximum clearance case of 2.7 percent. The intense migration of endwall fluids in the rear half of the cascade passage that was seen with the other two clearances has already disappeared from all three S1-planes. The strength of the leakage vortex in the downstream flow field seems to increase, while the circulatory motion of the tip-side passage vortex has been fairly destroyed in this maximum clearance case even at the positive incidence.

Downstream Pitch-Averaged Flow Angle and Loss. Figure 15 shows radial distributions of pitchwise mass-averaged yaw angle and total pressure loss downstream of the cascade ($Z/Cax = 1.19$). At the maximum incidence, the leakage flow affects the yaw angle and the loss at nearly the whole span, while at other two incidences, the effect is limited to the blade tip region. Between these two negative incidences, the yaw angle and loss distributions in the tip region are not very sensitive to the incidence change. In the rest of the region, on the other hand, the distributions are always very sensitive to the incidence variation. This corresponds to the fact that passage vortex is more sensitive to the incidence than the leakage vortex, as seen previously.

Conclusions

The present study has provided new information on endwall/leakage flows and on the associated loss generation mechanisms. The major results are summarized here:

1 Leakage flow vectors within the clearance gap depend strongly on the incidence and the gap size, particularly within the front part of the gap where the inlet boundary layer fluids pass as a part of the leakage flow.

2 Most of the leakage flow that forms the vortex, however, occurs at the rear part of the tip. This results in the fact that leakage vortices are less sensitive to incidence variation than the passage vortex. The interaction region between the two vortices depends on incidence and gap size.

3 Five high-loss regions on the endwall were identified. They are affected by incidence and gap size.

4 Two entrance regions of leakage flows into the gap were found where the endwall static pressures drop significantly. In these regions the flows roll away from or toward the endwall, depending on incidence and gap size.

5 At small clearance gap, the leakage flow tends to follow the pressure gradient within the gap. As the gap size increases, the inertial force of the inlet endwall flow appears to become an important factor in determining the leakage flow vectors in the front part of the tip.

6 Quantitative flow visualization can clearly show detailed behavior of the endwall/leakage flows. A convergence (separation) line and a divergence region of endwall flows were identified. They are strongly affected by incidence and gap size.

Acknowledgments

The author wishes sincerely to thank Mr. K. Kaba, formerly a student of Nippon University and presently a staff member of Avionics Co., for his assistance in the experimental and analytical work made during his one year graduate study at the NAL, and Mr. H. Nouse, Director of the Aeroengine Division, for his support through the present study.

References

Bindon, J. P., 1986, "Pressure and Flow Field Measurements of Axial Turbine Tip Clearance Flow in a Linear Cascade," Cambridge University Engineering Department, Report No. CUED/A-Turbo TR 123.

Booth, T. C., Dodge, P. R., and Hepworth, H. K., 1982, "Rotor-Tip Leakage: Part 1—Basic Methodology," ASME *Journal of Engineering for Power*, Vol. 104, pp. 154–161.

Graham, J. A. H., 1986, "Investigation of a Tip Clearance Cascade in a Water Analogy Rig," ASME *Journal of Engineering for Gas Turbines and Power*, Vol. 108, pp. 38–46.

Hah, C., 1986, "A Numerical Modeling of Endwall and Tip-Clearance Flow of an Isolated Compressor Rotor," ASME *Journal of Engineering for Gas Turbines and Power*, Vol. 108, pp. 15–21.

Joslyn, H. D., 1983, "Negative Incidence Flow Over a Turbine Rotor Blade," ASME Paper No. 83-GT-23.

Lakshminarayana, B., and Horlock, J. H., 1963, "Review: Secondary Flows and Losses in Cascades and Axial-Flow Turbomachines," *Int. J. Mech. Sci.*, Vol. 5, pp. 287–307.

Lakshminarayana, B., and Horlock, J. H., 1965, "Leakage and Secondary Flows in Compressor Cascades," ARC R and M No. 3483.

Lakshminarayana, B., 1970, "Methods of Predicting the Tip Clearance Effects in Axial Flow Turbomachinery," ASME *Journal of Basic Engineering*, Vol. 92, pp. 467–480.

Pouagare, M., and Delaney, R. A., 1986, "Study of Three-Dimensional Viscous Flows in an Axial Compressor Cascade Including Tip Leakage Effects Using a SIMPLE-Based Algorithm," ASME JOURNAL OF TURBOMACHINERY, Vol. 108, pp. 51–58.

Rains, D. A., "Tip Clearance Flows in Axial Flow Compressor and Pumps," 1954, California Institute of Technology, Hydrodynamics and Mechanical Energy Lab., Report No. 5.

Sjolander, S. A., and Amrud, K. K., 1987, "Effects of Tip Clearance on Blade Loading in a Planar Cascade of Turbine Blades," ASME JOURNAL OF TURBOMACHINERY, Vol. 109, pp. 237–245.

Wadia, A. R., and Booth, T. C., 1982, "Rotor-Tip Leakage: Part 2—Design Optimization Through Viscous Analysis and Experiment," ASME *Journal of Engineering for Power*, Vol. 104, pp. 163–169.

Wadia, A. R., 1985, "Numerical Solution of Two and Three-Dimensional Rotor Tip Leakage Models," *AIAA Journal*, Vol. 23, No. 7, pp. 1061–1069.

Yamamoto, A., Takahara, K., Nouse, H., Mimura, F., Inoue, S., and Usui, H., 1976, "An Experimental and Analytical Study of Blade Tip-Clearance Effects on an Axial-Flow Turbine Performance," NAL TR-466; see also NASA TM75138 (1976) or NAL TR-466T (1982).

Yamamoto, A., 1987, "Production and Development of Secondary Flows and Losses in Two Types of Straight Turbine Cascades: Part 1—A Stator Case: Part 2—A Rotor Case," ASME JOURNAL OF TURBOMACHINERY, Vol. 109, pp. 186–200.

Yamamoto, A., 1988, "Interaction Mechanisms Between Tip-Leakage Flow and the Passage Vortex in a Linear Turbine Rotor Cascade," ASME JOURNAL OF TURBOMACHINERY, Vol. 110, pp. 329–338.

Yamamoto, A., and Nouse, H., 1988, "Effects of Incidence on Three-Dimensional Flows in a Linear Turbine Cascade," ASME JOURNAL OF TURBOMACHINERY, Vol. 110, pp. 486–496.

M. Yaras
Graduate Research Assistant.

Zhu Yingkang[1]
Visiting Scholar.

S. A. Sjolander
Associate Professor.
Assoc Mem. ASME

Department of Mechanical and Aeronautical Engineering,
Carleton University,
Ottawa, Ontario, Canada K1S 5B6

Flow Field in the Tip Gap of a Planar Cascade of Turbine Blades

Measurements are presented for the flow in the tip gap of a planar cascade of turbine blades. Three clearances of from 2.0 to 3.2 percent of the blade chord were considered. Detailed surveys of the velocity magnitude, flow direction, and total pressure within the gap were supplemented by blade surface and endwall static pressure measurements. The results help to clarify the relationship between the leakage mass flow rate distribution and the driving pressure differences. It was found that even for the present relatively large clearances, fluid near the endwall experiences a pressure difference that is comparable with the blade pressure difference. It is also shown that a simple model can predict with good accuracy the mass flow rate distribution and the magnitude and direction of the velocity vectors within the gap.

Introduction

It is widely recognized that tip leakage has a significant effect on the aerodynamic and thermal performance of gas turbines. For example, losses from the leakage flow can account for as much as one third of the losses through a turbine stage (Waterman, 1986). Also, high heat transfer rates, associated with local regions of high velocity in the gap flow, have been a source of "burnout" of turbine blades (Bindon, 1987a).

The modeling of any aspect of the leakage flow requires a prediction of the magnitude and distribution of the mass flow rate through the gap. The most common approach to this was introduced by Rains (1954) in connection with his model for the rollup of the tip leakage vortex. Rains assumed that the chordwise pressure gradients acting on the gap flow were small compared with those normal to the blade. The blade pressure difference thus acts to induce a component of velocity normal to the blade only, and Rains calculated its magnitude by applying Bernoulli's equation to the acceleration process. The same approach was subsequently used by, for example, Lakshminarayana (1970) in his modified lifting-line analysis for the leakage flow and by Ishida and Senoo (1981) and Senoo and Ishida (1986) in their prediction of the pressure losses due to tip clearance in centrifugal and axial-flow blowers. Booth et al. (1982) have suggested a variation on Rains' model, as will be described later. More elaborate methods for calculating the leakage flow have been introduced recently; for example, the two- and three-dimensional viscous analyses of Wadia and Booth (1982) and Wadia (1985). However, none of these models can be regarded as adequately verified because of a lack of detailed data from within the gap.

Until recently, the main source of data was the experiments of Booth et al. (1982) (also Wadia and Booth, 1982), who investigated the leakage flow in a water rig using single- and double-sided idealized gaps and a turbine cascade with clearance. The gap flow rates were obtained either from overall water flow rates or from high-speed films of dye streaks. For flat-tipped, unshrouded turbine blades the authors suggested a discharge coefficient for the gap flow of about 0.80 to 0.85. Graham (1986) also investigated the clearance flow in a turbine cascade using a water rig, although his included a moving belt to simulate rotation. Based mainly on flow visualization, he concluded that with sufficient belt speed the net leakage could be reduced to zero. He also measured the gap velocity distributions at about 25 percent of chord for three different clearances. Interestingly, as the gap increased the separation bubble on the blade tip filled an increasingly large fraction of the gap. Thus, if Graham had evaluated the discharge coefficient for the gap he would probably have found that it decreased with increasing clearance. More recently, Moore and Tilton (1988) presented measurements from within the tip gap at about 60 percent chord in a planar turbine cascade. They also compared the results with those obtained from a combined potential flow and mixing model. They predicted and measured a local discharge coefficient of about 0.85, in agreement with Booth and his co-workers. However, it is of course not clear that this is a suitable discharge coefficient for the whole of the gap flow. Finally, Bindon (1987a, 1987b, 1987c) has reported very extensive turbine cascade measurements aimed at clarifying the phenomenon of tip burnout. To this end he made very detailed pressure measurements on the blade tip and on the endwall. In addition, he obtained velocity distributions within the gap at ten chordwise stations, but because of uncertainty about the flow direction he could not determine accurate values of the mass flow rate. Thus, while progress has been made in understanding and documenting the gap flow field, the available data are still not detailed enough to test the gap flow models.

The present study is a continuation of the work reported by Sjolander and Amrud (1987). In the earlier study, a large, planar cascade of turbine blades was used to investigate the effects of leakage flow on the blade loading. This was done

[1]Permanent address: Department of Power Machinery Engineering, Xi'an Jiaotong University, Xi'an, Shaanxi Province, The People's Republic of China.

Contributed by the International Gas Turbine Institute and presented at the 33rd International Gas Turbine and Aeroengine Congress and Exhibition, Amsterdam, The Netherlands, June 5–9, 1988. Manuscript received by the International Gas Turbine Institute September 15, 1987. Paper No. 88-GT-29.

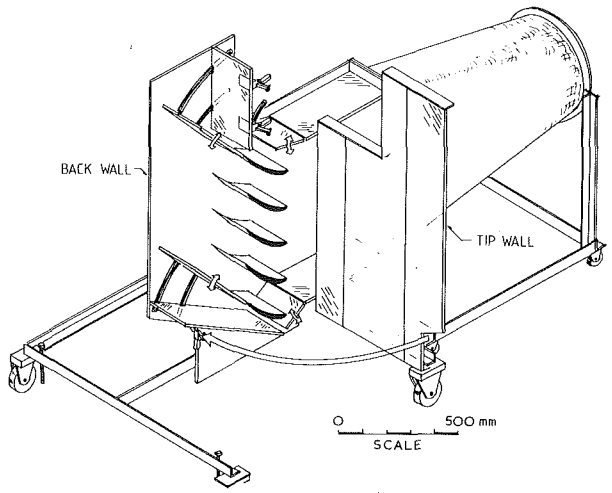

Fig. 1 Cascade test section

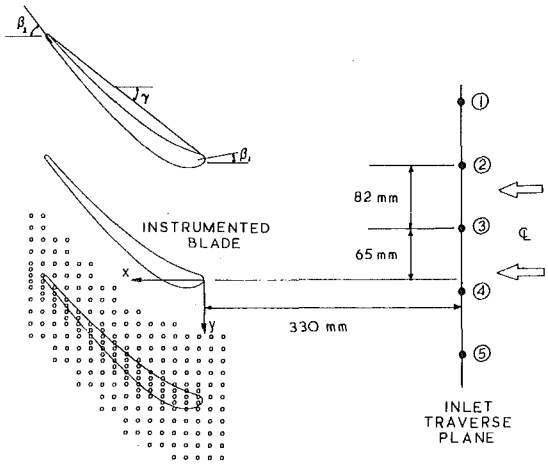

CHORD LENGTH, c	:	250 mm
BLADE THICKNESS, t_{MAX}	:	24.6 mm
BLADE SPAN, h	:	200 mm
BLADE SPACING, s	:	150 mm
ASPECT RATIO, h/c	:	0.8
SOLIDITY, c/s	:	1.667
STAGGER ANGLE, γ	:	38.3 deg.
BLADE INLET ANGLE, β_1	:	10.9 deg.
BLADE OUTLET ANGLE, β_2	:	48.3 deg.

Fig. 2 Summary of cascade geometry

through detailed pressure measurements on the blade surfaces. Flow visualization using smoke and surface oil flow was also used to gain insight into the physics of the flow. It was observed, apparently for the first time, that the leakage flow can form multiple tip leakage vortices as the clearance increases. These vortices in turn produced a very distorted pressure distribution on the suction surface of the blade. This distortion clearly affects the flow turning ability of the blade. It was also speculated that the distorted pressure field might modify the distribution and magnitude of the leakage flow, thus making it more difficult to predict. The present study (Yaras, 1987) was undertaken to clarify the behavior of the clearance flow, through detailed flow field measurements inside the gap.

The experiment is inevitably somewhat idealized: it was conducted at essentially incompressible conditions, with a low level of free-stream turbulence, in the absence of heat transfer, and without relative motion at the tip wall. Nevertheless, many of the insights gained can be applied to the real turbine flow, and the results can be used to evaluate gap flow prediction models.

Experimental Apparatus

Test Section and Test Cascade. The cascade test section has been described previously by Sjolander and Amrud (1987) and is shown schematically in Fig. 1. To vary the tip clearance, the tip wall is moved outward using shims inserted between the tip wall and the side walls. The tail-boards and side-flaps are used to establish periodic flow in the five-bladed cascade. The periodicity is adjusted approximately using static pressures measured at pairs of taps on the back wall at about 1/4 chord in each blade passage. Final adjustments are made on the basis of measurements of flow velocity and direction made at midspan across all blade passages at about 1/4 axial chord downstream of the trailing edge. Flow periodicity was checked and adjusted for each clearance.

The geometry of the test cascade is summarized in Fig. 2. The blade represents the tip section of a turbine of recent design. The same blades were used as in the earlier study although the stagger angle has been changed slightly. The angles quoted in Fig. 2 are estimated to be accurate to within ±0.2 deg. The middle blade in the cascade is instrumented

Nomenclature

A = area
c = blade chord length
C_D = discharge coefficient (equations (3) and (4))
C_P = $(P - P_{CL})/(1/2\ \rho V_{CL}^2)$ = static pressure coefficient
C_{Po} = $(P_o - P_{oCL})/(1/2\ \rho\ V_{CL}^2)$ = total pressure loss coefficient
h = blade span
H = δ^*/θ = boundary layer shape factor
$\dot{m}$ = mass flow rate
P = static pressure
P_o = total pressure
q = $1/2\ \rho V^2$ = dynamic pressure
Re = $\rho V_{CL} c/\mu$ = Reynolds number based on blade chord
s = blade spacing
t_{max} = blade maximum thickness
V = velocity
V_N = component of velocity normal to chord line
V_T = component of velocity parallel to chord line
x, y, z = coordinates in axial, tangential, and spanwise directions (Fig. 2; z measured from blade tip)
x' = coordinate in chordwise direction
β = blade metal angle (Fig. 2)
γ = blade stagger angle (Fig. 2)
δ = boundary layer thickness
δ^* = $\int_0^\delta (1 - V/V_e)dz$ = boundary layer displacement thickness
θ = $\int_0^\delta (V/V_e)(1 - V/V_e)dz$ = boundary layer momentum thickness
μ = viscosity
ρ = density
τ = tip gap
ϕ = flow angle, measured relative to the axial direction

Subscripts

CL = undisturbed centerline value
e = boundary-layer edge value
PS = pressure side of blade
SS = suction side of blade
1, 2 = cascade inlet, outlet

with 14 rows of static taps, from the blade tip to about midspan. Each row consists of 37 taps on the pressure surface and 36 on the suction surface. The row nearest the tip is at 2 percent of the blade span; this is slightly larger than in the blade-loading study since the blades have subsequently been fitted with 2.3-mm-thick removable tips. An array of static taps has also been added to the tip wall, as shown in Fig. 2. The taps lie on a rectangular 15 mm × 15 mm grid, with some additional taps near the blade tip. The grid covers one complete passage width.

Instrumentation. As in the earlier study, the flow entering the cascade was traversed at the plane indicated in Fig. 2 using a pitot tube of 0.81 mm outer diameter. The positioning accuracy of this probe is estimated at ±0.05 mm for measurements within 25 mm of the tip wall, which includes the extent of the tip wall boundary layer.

Measurements within the tip gap were made using a three-hole pressure probe that is 0.7 mm thick and 2.0 mm wide; the probe thickness corresponds to 9 to 14 percent of the gap heights considered. It is estimated that the probe was positioned to an accuracy of 0.25 mm in the spanwise direction. Because of the difficult access, the probe was used in the non-nulling mode. It was therefore calibrated over a range of misalignment angles of ±70 deg in yaw. When the flow is in the plane of the probe, it is estimated that the flow quantities inferred from the three probe pressure have the following uncertainties: flow angle, ±3 deg; dynamic and total pressures, ±5 percent of the local dynamic pressure. In some regions near the blade tip, the flow undoubtedly has a radial component of velocity, which represents pitch misalignment relative to the probe. Therefore, the effect on the probe pressures of pitch misalignment of up to 50 deg was measured. It was determined that in the extreme case of 50 degrees of pitch misalignment, there would be errors of $-0.6q$ and $-1.0q$ on the dynamic and total pressures, respectively, as inferred from the probe pressures, while the flow angle would still be accurate to within 10 deg. For less than 30 deg of pitch misalignment, the errors introduced are quite small. It would of course have been preferable to traverse the flow using a probe that could resolve the three-dimensional flow field. However, we wanted to minimize interference with the flow by using a probe that was as compact as possible. As will be discussed later, the uncertainties introduced by pitch misalignment do not have a serious impact on, for example, the mass flow rate obtained for the gap.

All pressures were measured using capacitive-type pressure transducers, some of which were connected to Scanivalves. The analogue pressure signals were converted to digital form using either a Hewlett-Packard 3054A Data Acquisition and Control System or a Taurus data acquisition board mounted in an IBM PC microcomputer. Sampling times for the pressure signals were established in the earlier study and verified during the present one. As before, it was found that sampling times of 20 s for static pressures and 30 to 40 s for probe pressures gave mean values that were typically within ±0.2 percent of the very long time averages.

Experimental Results

Relationship to Gap Flow Calculations. It is useful and convenient to discuss the measurements in the context of the simpler gap flow prediction methods mentioned in the Introduction. The assumptions made most frequently in these methods can be identified with reference to Fig. 3:

(*i*) All fluid entering the gap is assumed to be at the undisturbed free stream total pressure P_o.

(*ii*) The tangential velocity of the fluid before it is accelerated into the gap (e.g., at point A) is assumed to be given by the pressure side static pressure P_{PS} at that chordwise position. That is:

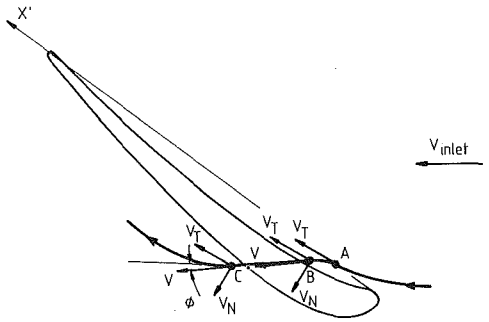

Fig. 3 Gap flow model for simple prediction methods

$$V_T = [2(P_o - P_{PS})/\rho]^{1/2} \tag{1}$$

(*iii*) It is generally assumed that the pressure gradient parallel to the blade mean line (or approximately, the chord line) is small. Thus V_T remains constant as the flow crosses the tip. The pressure difference driving the flow into the gap therefore acts to increase only the normal component of velocity, V_N, and assuming no losses then

$$V_N = [2(P_{PS} - P_{SS})/\rho]^{1/2} \tag{2}$$

The driving static pressure difference is generally taken to be the blade pressure difference at the chordwise position being considered. The distortion in the blade loading due to the tip leakage is not taken into account since this would not in general be known.

Having obtained the ideal normal velocity distribution, the resulting mass flow through the gap is obtained from

$$\dot{m} = C_D \int \rho \; V_N \, dA \tag{3}$$

where C_D is the discharge coefficient for the gap. The approach described to this point will be referred to as the Simple Method.

Booth et al. (1982) presented a variation on this method. The value of V_T is obtained as above, but the static pressure difference that determines V_N is taken along the trajectory of the streamline in question; that is, from the blade surface pressures at points such as B and C in Fig. 3. Furthermore, the magnitude of V_N is taken to be reduced by the discharge coefficient according to

$$V_N = C_D[2(P_{PS} - P_{SS})/\rho]^{1/2} \tag{4}$$

The mass flow rate is then given by

$$\dot{m} = \int \rho \; V_N \, dA \tag{5}$$

Since P_{SS} depends on V_N and vice versa, Booth's method is iterative.

The validity of the assumptions made in these methods will be examined in the light of the present measurements.

Operating Conditions. All measurements to be presented here were obtained at a Reynolds number of 4.3×10^5 ±2 percent, where the Reynolds number is based on the blade chord and the undisturbed upstream velocity. The corresponding inlet velocity was about 30 m/s and the maximum velocity seen in the tip gap was about twice this. Conditions were thus essentially incompressible everywhere.

Gap heights of 7.9, 7.1, and 5 mm were examined. The heights were measured using feeler gages and are estimated to be accurate to ±0.2 mm. The values correspond to 3.2 to 2 percent of the blade chord or 33 to 20 percent of the blade maximum thickness. Smaller clearances were included in the blade loading study but this was not feasible here because the probe height becomes too large a fraction of the gap height.

After the completion of the measurements at 7.9 mm clear-

Table 1 Gap geometries and inlet flow conditions

	Case		
	1	2	3
τ, mm	7.9	7.1	5
τ/t_{max}	0.33	0.29	0.20
u'/U, percent	0.4	1.4	1.4
δ^*/τ	0.19	1.09	1.15
θ/τ	0.14	0.72	0.84
H	1.34	1.52	1.38

ance, the original axial-flow wind-tunnel fan failed and was replaced by a centrifugal fan. This resulted in a rise in the free-stream turbulence from about 0.4 to 1.4 percent and the endwall boundary layers became somewhat thicker. The flow parameters obtained at inlet traverse station 3 (see Fig. 2) for each of the clearance cases considered are summarized in Table 1. As seen from the table, the inlet conditions for the two smaller clearances are essentially identical. The measurements obtained for them thus demonstrate the effects of clearance changes alone. The results for the largest clearance show the influence of changes in endwall boundary layer thickness and free-stream turbulence, as well as clearance, although it is of course not possible to separate the various effects here.

The results for the three clearances were in fact very similar. Therefore, detailed results will be given for the intermediate clearance (2.8 percent of chord) but only selected results for the other two.

Gap Flow and Driving Pressure Differences. To document the gap flow field, detailed traverses were made along the blade mean line using the three-hole probe. In addition, the flow development across the gap was examined at five chordwise stations. Finally, to clarify the pressure differences driving the flow into the gap, static pressure measurements were made on the blade surfaces and on the endwall.

The measurements on the mean line were made at 10 to 14 points from the blade tip to the endwall, at 37 stations from leading to trailing edge. The velocity vectors at selected planes, for 2.8 percent clearance, are shown in Fig. 4. It is clear that close to the tip the velocity vector varies rapidly in both magnitude and direction, particularly on the rearward portion of the blade. These variations are undoubtedly the result of the separation bubbles that form on the blade tip at the pressure surface edge. The presence of these bubbles had been identified by Sjolander and Amrud (1987) from surface flow visualization on the blade tip. On the rearward half of the blade and close to the tip, the behavior of the velocity vector is at first sight somewhat unexpected in that it is directed from the suction to the pressure surface. However, this is consistent with the bubble taking the form of small vortex whose axis lies along the mean line. The centerline of the vortex is at about 20 percent of the gap in this case, as evident from the reversal in the direction of the velocity vector at that height. It is reasonable that the separated fluid should roll up into a vortex where the separation occurs in the presence of a chordwise pressure gradient. The same phenomenon was clearly evident in Bindon's (1987b) smoke flow pictures.

The results obtained near the blade tip should of course be viewed as approximate since the spanwise components of velocity associated with the separation vortices result in pitch errors in the probe measurements. In addition, there will be errors due to the large chordwise velocity gradients present in places. However, it is also evident that the flow in the region of the separation vortices contributes relatively little to the mass flow through the gap. Thus the uncertainty in the probe measurements will introduce little error in the calculated total mass flow rate.

Toward the endwall the velocity varies far more slowly in the chordwise direction and is nearly constant in the spanwise direction. There is no evidence of the endwall boundary layer even at the outermost plane, which is less than 2 mm from the wall, except perhaps near the leading edge. The uniformity of the flow in the region where most of the leakage occurs is obviously encouraging from the point of view of devising leakage flow prediction methods.

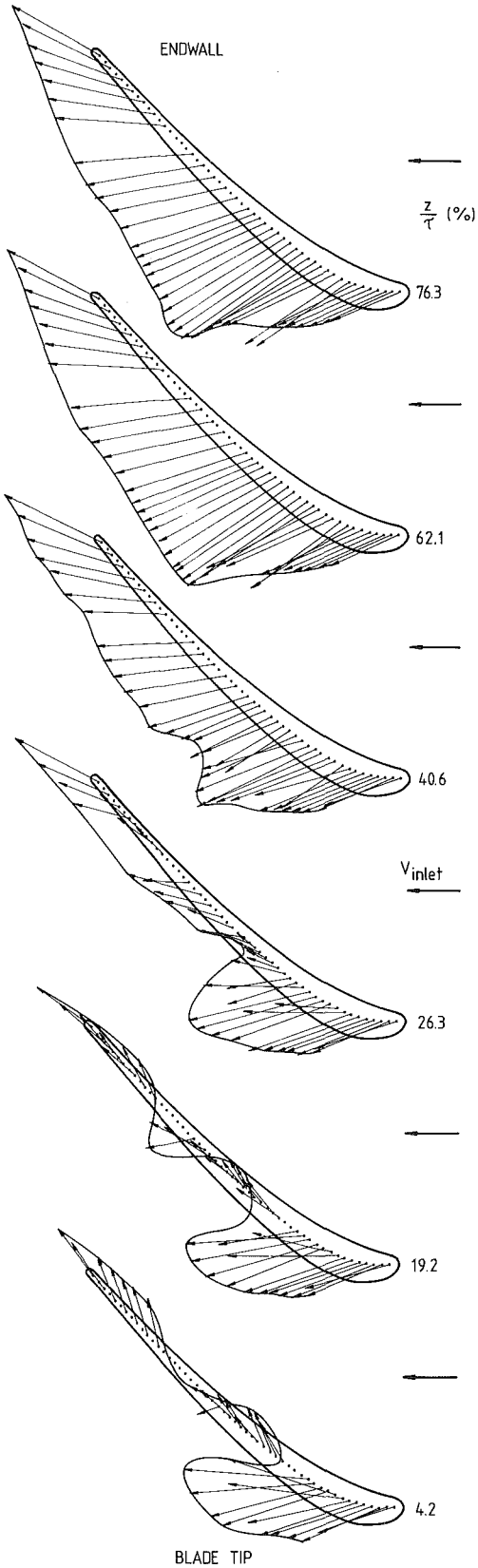

Fig. 4 Gap flow field at the blade mean line (τ/c = 0.028)

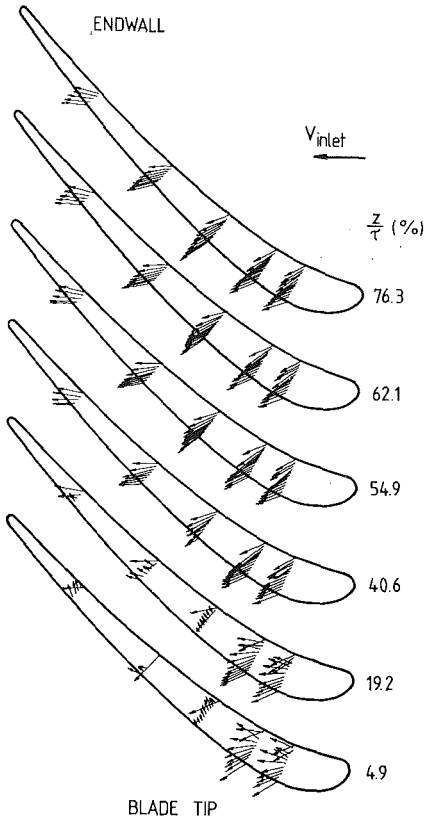

Fig. 5 Flow field development normal to the mean line (τ/c = 0.028)

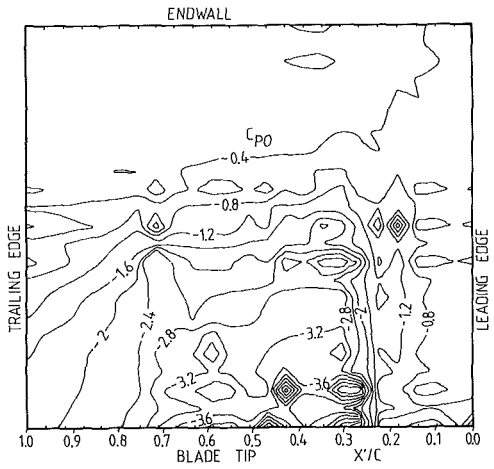

Fig. 6 Gap total pressure distribution (τ/c = 0.028)

From continuity, the average normal component of velocity (V_N in Fig. 3) must be constant within the gap since the area is essentially constant. There could of course be local regions of accelerating gap flow provided they are offset by other regions of decelerating flow. Figure 5 follows the flow development across the gap. It indicates that in the outer part of the gap, where most of the leakage occurs, the velocity vectors are in fact reasonably constant in magnitude and direction as the flow crosses the gap. This shows firstly that the assumption of a constant tangential component of velocity V_T is justified. Secondly, it indicates that the acceleration is largely completed, and the flow experiences its driving pressure difference, *before* it enters the gap.

Further insight into the gap flow is obtained from the total pressure distribution in the gap. This is presented in the form of a contour plot in Fig. 6. It is seen that away from the separation vortices, the total pressure is essentially equal to

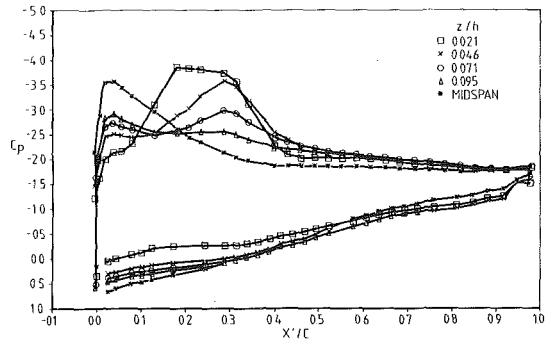

Fig. 7 Blade static pressure distributions (τ/c = 0.028)

the inlet free-stream value, as is assumed in the simple gap flow models. The exception to this is the upstream 10 percent of the gap where some loss is evident. Sjolander and Amrud concluded from smoke flow visualization that about a quarter of the incoming endwall boundary layer fluid passed through the tip gap and did so very close to the leading edge. This observation seems to be confirmed by the present measurements. From about 20 percent of chord, where the formation of the separation vortices was observed to begin, regions of high total pressure loss are apparent near the blade tip. Such losses are to be expected in connection with the separations and the corresponding local regions of very high shear. However, the magnitudes shown are probably not reliable because total pressures will be underestimated in regions of pitch misalignment. The total pressure plots were used mainly to determine approximately the extent of the separation bubbles or vortices. It is evident that for this case, the separated zone extends over nearly half the gap in the central part of the blade and is somewhat smaller towards the trailing edge. For the smaller clearance, it was found that the separated zone occupied a smaller spanwise extent, presumably due to the constraining effect of the endwall; the reduced blockage resulted in a higher discharge coefficient for the gap. It will be recalled that Graham's (1986) data suggested the same trend in discharge coefficient with clearance.

Turning to the static pressure field, Fig. 7 shows the blade surface pressures at several spanwise locations from close to the tip to midspan. As discussed by Sjolander and Amrud, the stronger suction peak near the blade tip is caused by the tip leakage vortex that begins to form in the blade passage at about 20 percent of chord. In fact, for this clearance Sjolander and Amrud's data suggest the presence of two tip leakage vortices, the second beginning to form at about 60 percent of chord. It will be noted from Fig. 4 that the tip separation vortices show discontinuities at the points where the tip leakage vortices begin. There is undoubtedly a connection, although the cause and effect relationship is not clear at this point. Sjolander and Amrud speculated that the considerable distortion of the blade loading near the tip would complicate the prediction of the gap mass flow, since this flow is generally assumed to be driven by the blade pressure difference. However, more recent data suggest that this concern was not justified. In the first place, Fig. 4 indicates that the fluid closest to the blade tip, which might be seeing a distorted pressure distribution, does not contribute greatly to the leakage mass flow. Furthermore, Bindon (1987a) showed from his very detailed measurements of the pressures at the blade tip that the pressure distortion is a highly localized effect. For example, by far the lowest pressure he observed was at the corner between the *pressure* surface and the tip. This was of course the result of the very high streamline curvature occurring there; this pressure would vary rapidly away from the corner and the low pressure would not be imposed on the gap flow in any significant way. Finally, there is the evidence of the present meas-

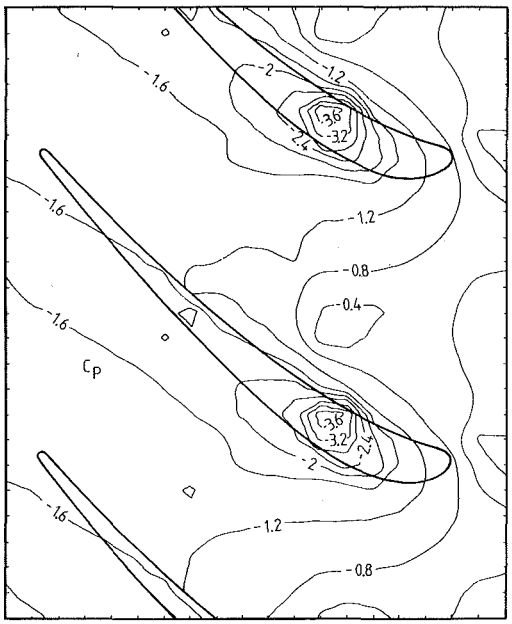

Fig. 8 Tip endwall static pressure distribution (τ/c = 0.028)

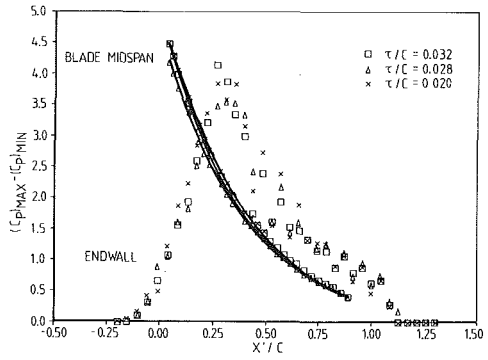

Fig. 9 Comparison between blade midspan pressure differences and driving pressure differences at endwall

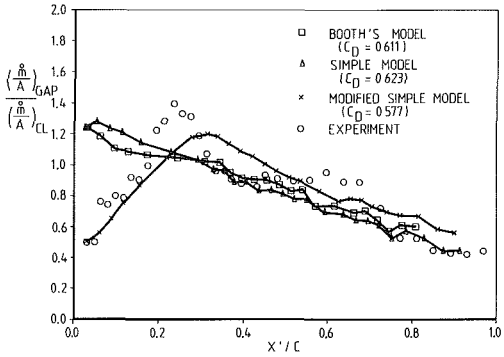

Fig. 10 Measured and predicted mass flow rate distributions in the tip gap (τ/c = 0.028)

urements that the flow experiences its accelerating pressure difference before it enters the gap. This clearly tends to decouple the acceleration process from the pressure distortion that occurs locally near the blade tip on the pressure and suction surfaces. The spanwise uniformity of the flow in the outer part of the gap, where most of the leakage is concentrated, suggests that all the leakage flow at a particular chordwise station experiences essentially the same driving pressure difference. This must be the pressure difference present at the endwall.

As the tip clearance approaches infinity, the pressure variations seen on the endwall will obviously tend to zero. However, for the clearances used in practice, the blade-to-blade pressure field appears to be projected onto the endwall with little attenuation. This is illustrated in Fig. 8, which shows the endwall pressure distribution in the form of a contour plot. It is seen that the pressure minimum on the endwall is comparable in magnitude with the undisturbed (midspan) suction peak on the blade (see Fig. 7). The maximum pressure on the endwall occurs at about quarter passage width. From there the fluid experiences an accelerating pressure field, either toward the suction side of the passage or toward the tip gap. Furthermore, for the fluid entering the gap the pressure drop is largely complete at the entrance to the gap. This is consistent with the acceleration being completed by the time the fluid enters the gap, as inferred from the gap flow measurements. With minor differences, Bindon (1987a) found a very similar pattern in his endwall measurements. In his case, the pressure maximum occurred closer to the blade but the pressure drop was again essentially complete at the entrance to the gap. He likewise found no attenuation of the pressure variations, up to a clearance of 5 percent of chord (33 percent of maximum thickness for his 15 percent thick blades). In fact, his pressure minimum on the endwall was even slightly lower than the suction peak on the blade.

To quantify the accelerating pressure differences, the pressure variations along diagonal rows of taps on the endwall (see Fig. 2) were examined. These rows of taps are nearly normal to the chord line and therefore essentially parallel to the induced normal component of velocity V_N. The chordwise variation of the maximum pressure differences seen along these lines is compared in Fig. 9 with the midspan pressure differences on the blade. The pressure differences are remarkably similar in magnitude and trend for all three clearances, except for a rearward shift of the endwall curves by about 20 percent of chord. Clearly, the undisturbed tip loading (represented here by the midspan measurements) is a very good approximation to the driving pressure field seen by the flow near the endwall. As noted earlier, this is a common assumption made in simple gap flow prediction methods.

Gap Mass Flow Rate and Discharge Coefficients. The very detailed gap flow measurements allow us to define the gap mass flow rate distribution to a degree not previously possible, as far as we know. Mass flow rates were calculated for each rectangular panel formed by the measurement points, assuming linear variations in the flow quantities between the points. It is difficult to assign uncertainties to the resulting flow rates. The three-hole probe measurements are subject to errors due to pitch and shear, but as noted earlier these errors are present primarily close to the blade tip, where the leakage is fairly low. In addition, there are the usual uncertainties introduced by the data acquisition process. Overall, we estimate that the total gap mass flow rates obtained are accurate to better than 10 percent and we regard this figure as conservative.

The distribution obtained for 2.8 percent clearance is given in Fig. 10. The plot shows the mass flow rate per unit area in the gap divided by the upstream mass flow rate per unit area; for incompressible flow, this is equivalent to V_N/V_{CL}. Also shown are the predictions obtained using Booth's method and two versions of the Simple Method. The basic Simple Method uses the blade midspan pressure differences. The second version uses the midspan differences shifted 20 percent rearward, as suggested by Fig. 9, together with a linear rise in pressure difference from the leading edge to the 20 percent chord point. The values of C_D indicated on Fig. 10 are those needed to match the measured total mass flow rate. It will be noted that Booth's method required a considerably lower value of C_D than the 0.8 suggested by Wadia and Booth (1982). It is evident that the Simple Method with shifted pressure distribution predicts the measured flow rate distribution quite closely. This is

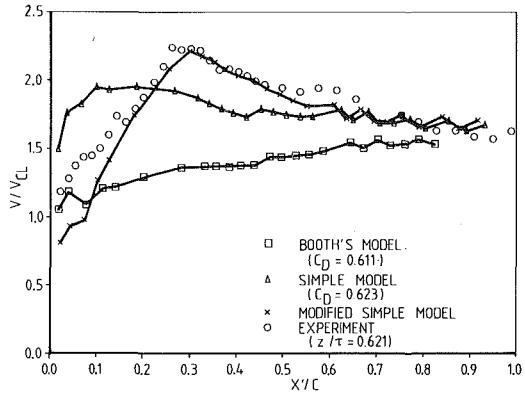

Fig. 11 Measured and predicted resultant velocity magnitudes in the tip gap (τ/c = 0.028)

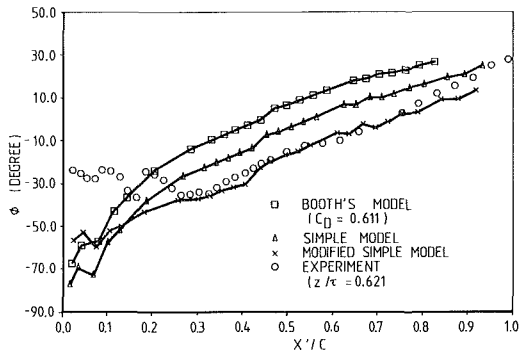

Fig. 12 Measured and predicted resultant velocity directions in the tip gap (τ/c = 0.028)

the case even near the leading edge where the leakage flow is partly endwall boundary layer fluid and where there is some chordwise pressure gradient within the gap (see Fig. 8) so that V_T is not constant, as assumed. The accuracy of the distribution could of course be improved by varying C_D along the blade to reflect the varying blockage associated with the separation bubbles. However, we do not at present have a basis for predicting the chordwise distribution of C_D for an arbitrary blade. Nevertheless, given a suitable overall value of C_D, the modified Simple Method results in a very satisfactory mass flow rate distribution. It should however be pointed out that while the shift in driving pressure distribution was independent of clearance for our blade, this may not be a general result. Bindon's (1987a) data for a turbine blade that was rearward loaded, unlike ours, appears to show a comparable shift in the endwall pressure pattern, but the shift was apparently reduced with increasing clearance.

In addition to predicting the mass flow rate distribution, it is highly desirable that a gap flow model should predict well the magnitude and direction of the resultant velocity vectors in the gap. This information can then be used to design features, such as minishrouds or endwall treatments, which reduce or alter the tip leakage flow. Figures 11 and 12 compare the magnitudes and directions of the measured velocities with the values predicted by the three models. The experimental values are those obtained at 62 percent of the gap height and as such are representative of the bulk of the leakage flow. The agreement is generally similar to that obtained for the mass flow rates, with the modified Simple Method again producing very satisfactory results. It should be noted that the results for the Simple Methods are independent of any discharge coefficient. On the other hand, by using C_D directly to obtain V_N, Booth's method leads to a resultant velocity that is not very representative of the gap flow.

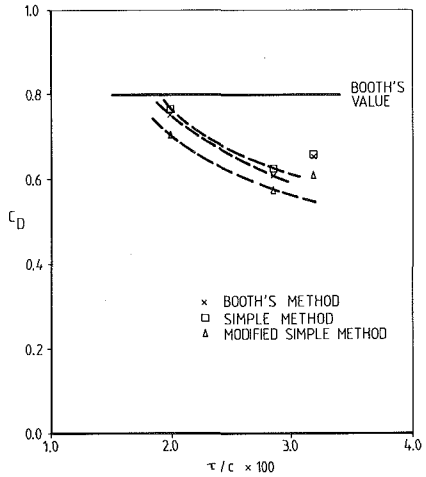

Fig. 13 Variation of discharge coefficient with clearance

Finally, Fig. 13 summarizes the discharge coefficients for all three clearance cases. It will be noted that C_D decreases with increasing clearance, even allowing for a 10 percent uncertainty in the measured mass flow rates. This trend is consistent with the observed behavior of the separation bubbles: From the total pressure plots it was clear that they filled a larger fraction of the gap as the clearance was increased. The discharge coefficient is somewhat higher for the largest clearance. As mentioned earlier, this case had a considerably thinner endwall boundary layer and a lower level of free-stream turbulence. The results therefore suggest that these factors have some influence on the gap flow, although we are unable to assess the relative importance of each. It is again noticeable that all the measured values of discharge coefficient were lower than the value of about 0.8 suggested by Booth.

Conclusions

Measurements in a planar cascade of turbine blades have clarified the physics of the tip gap flow. It has also been shown that while the flow is fairly complicated, it can nevertheless be predicted well using a relatively simple model.

It was concluded that the highly distorted pressure field near the blade tip, which was investigated in an earlier study, is a very localized effect that does not significantly influence the flow through the gap. On the blade tip, separation bubbles were noted starting from the pressure side corner. Particularly toward the rear of the blade, these separation bubbles took the form of vortices, apparently the result of the separated fluid being driven chordwise by a mild pressure gradient in that direction. From the measurements, it was clear that the region close to the tip contributed little to the total leakage through the gap. In a prediction scheme, the flow structures at the blade tip are thus conveniently accounted for by a reduction in the effective flow area, as expressed by a discharge coefficient.

Most of the leakage occurs toward the endwall. Here the pressure field was observed to match closely the blade-to-blade pressure distribution within the passage, rather than the distorted pressures near the blade tip. It was thus found that the leakage flow is accelerated into the gap by driving pressure differences which are essentially equal to the *undisturbed* blade pressure differences. This has been assumed in the simple gap flow models, but probably with the expectation that it is more of an approximation than it seems to be. The flow was found to have essentially completed its acceleration before it enters the gap. At a given chordwise station, the velocity distribution within the gap was quite uniform. Finally, the bulk of the leakage flow was found to be free-stream fluid that had entered

the gap with essentially no loss. Even at the two smaller clearances, for which the endwall boundary layers were relatively thick, it was clear that the endwall boundary layer fluid passed over the tip very close to the leading edge and had little impact on the gap flow as a whole.

As described above, it was found that the assumptions made in simple gap flow predition methods are valid to a surprising degree. It was also shown that the results obtained from these methods could be improved significantly through a simple modification; namely, by accounting for the observed rearward shift in the driving pressure differences. The resulting predictions of the gap mass flow rate distribution and the velocity vectors in the main part of the gap flow must be viewed as very satisfactory. It was found that the values required for the discharge coefficient were somewhat lower than those recommended by others.

Acknowledgments

Financial support for this study provided by the Natural Sciences and Engineering Research Council of Canada under Grant A1671 and by Pratt and Whitney Canada is gratefully acknowledged.

References

Bindon, J. P., 1987a, "Pressure Distributions in the Tip Clearance Region of an Unshrouded Axial Turbine as Affecting the Problem of Tip Burnout," ASME Paper No. 87-GT-230.

Bindon, J. P., 1987b, "Visualization of Axial Turbine Tip Clearance Flow Using a Linear Cascade," ISABE Conference, Cincinnati, OH, July.

Bindon, J. P., 1987c, "The Measurement of Tip Clearance Flow Structure on the Endwall and Within the Clearance Gap of an Axial Turbine Cascade," Proc. I.Mech.E., Conference 1987-6, *Turbomachinery—Efficiency Prediction and Improvement*, Sept., pp 43-52.

Booth, T. C., Dodge, P. R., and Hepworth, H. K., 1982, "Rotor-Tip Leakage: Part 1—Basic Methodology," ASME *Journal of Engineering for Power*, Vol. 104, pp. 154-161.

Graham, J. A. H., 1986, "Investigation of a Tip Clearance Cascade in a Water Analogy Rig," ASME *Journal of Engineering for Gas Turbines and Power*, Vol. 108, pp. 38-46.

Ishida, M., and Senoo, Y., 1981, "On the Pressure Losses Due to the Tip Clearance of Centrifugal Blowers," ASME *Journal of Engineering for Power*, Vol. 103, pp. 271-278.

Lakshminarayana, B., 1970, "Methods of Predicting theTip Clearance Effects in Axial Flow Turbomachinery," ASME *Journal of Basic Engineering*, Vol. 92, pp. 467-480.

Lakshminarayana, B., 1986, "Tip Clearance Effects in Turbomachines," von Karman Institute/Pennsylvania State University Lecture Course on Tip Clearance Effects in Axial Turbomachines, Apr.

Moore, J., and Tilton, J. S., 1988, "Tip Leakage Flow in a Linear Turbine Cascade," ASME JOURNAL OF TURBOMACHINERY, Vol. 110, pp. 18-26.

Rains, D. A., 1954, "Tip Clearance Flows in Axial Flow Compressors and Pumps," Rept. 5, Hydrodynamics and Mechanical Engineering Laboratories, California Institute of Technology.

Senoo, Y., and Ishida, M., 1986, "Pressure Loss Due to the Tip Clearance of Impeller Blades in Centrifugal and Axial Blowers," ASME *Journal of Engineering for Gas Turbines and Power*, Vol. 108, pp. 32-37.

Sjolander, S. A., and Amrud, K. K., 1987, "Effects of Tip Clearance on Blade Loading in a Planar Cascade of Turbine Blades," ASME JOURNAL OF TURBOMACHINERY, Vol. 109, No. 2, pp. 237-244.

Wadia, A. R., 1985, "Numerical Solution of Two- and Three-Dimensional Rotor Tip Leakage Models," *AIAA Journal*, Vol. 23, No. 7, pp. 1061-1069.

Wadia, A. R., and Booth, T. C., 1982, "Rotor-Tip Leakage: Part II—Design Optimization Through Viscous Analysis and Experiment," ASME *Journal of Engineering for Power*, Vol. 104, pp. 163-169.

Waterman, W. F., 1986, "Turbine Loss Correlations and Analysis," von Karman Institute/Pennsylvania State University Lecture Course on Tip Clearance Effects in Axial Turbomachines, Apr.

Yaras, M. I., 1987, "Flow in the Tip Gap of a Rectilinear Turbine Cascade," M.Eng. Thesis, Dept. of Mech. and Aero. Engineering, Carleton University, Ottawa, Canada.

The Influence of Turbine Clearance Gap Leakage on Passage Velocity and Heat Transfer Near Blade Tips: Part I—Sink Flow Effects on Blade Pressure Side

D. E. Metzger
Professor.
Fellow ASME

K. Rued[1]

Mechanical and Aerospace Engineering Department,
Arizona State University,
Tempe, AZ 85287

A study has been conducted to investigate influences of tip leakage flow on heat transfer and flow development along the pressure side of a gas turbine blade. An analysis of the sink character of the flow situation indicates that high velocities and accelerations are generated very near the gap, and an apparatus was specifically designed to model the phenomena and to permit resolution of the expected localized near-gap heat transfer enhancement. In the experiments, leakage flow was drawn from an adjustable streamwise corner slot in a straight square test channel. A thin stainless steel ohmic-heated test surface adjacent to the slot simulated the airfoil surface. Supporting nonintrusive mean and fluctuating flowfield measurements were conducted with a laser-Doppler anemometer to aid interpretation of the heat transfer results and to provide a basis for comparison with future numerical predictions. The flowfield measurements confirm that near the gap the flow is highly accelerated, and indicate apparent relaminarization of the initially turbulent boundary layer. The heat transfer measurements show that leakage generates large increases in local heating near the gap. The presence of this undesirable enhancement helps to explain observed in-service material distress and failures of blades that appear to initiate at the pressure side tip.

Introduction

In gas turbine engines, the unshrouded blades of axial turbine stages rotate in close proximity to the stationary outer wall, or seal, of the turbine housing. The pressure difference between pressure and suction sides of the blade induces a leakage flow through the gap between rotating blade tip and adjacent wall, as indicated in Fig. 1 for a typical set of three blades. The major detrimental effect usually associated with tip leakage flow is degradation in blade aerodynamic performance [1], but a second effect increasingly recognized as very important is the convection heat transfer that occurs between the blade tip and the flow through the leakage group.

There has long been evidence, in terms of observed in-service local distress and failure of blades, that intense thermal loading is at least sometimes present at blade tips. Only recently, however, has the magnitude and nature of the convection phenomena on the blade tip proper been investigated quantitatively [2, 3]. Thermal loads on the blade tip surfaces themselves can produce structural damage if the tip area and heating are not adequately accounted for in blade internal cooling designs [4].

However, knowledge of convection on only the blade tip proper may not be sufficient to account for all of the thermal loading associated with a tip leakage flow. In addition, the effects of the leakage on the flow and heat transfer along the blade pressure and suction sides *near* the tip need to be considered in order to assess the total impact of the gap leakage flow. Previous investigations [5–9] have shown that on the suction side near the tip leakage flow encounters the oncoming wall flow, and tends then to separate and roll into a vortex, increasing the total amount of secondary flow within the turbine blade passage. Consequently, an increase in local heat transfer rates near the suction side blade tip is expected. On the blade pressure side near the tip, the leakage flow has a sink character with the clearance gap acting like a line sink imposed on the

[1] Current address: Motoren-u. Turbinen-Union, Munich, Federal Republic of Germany.

Contributed by the International Gas Turbine Institute and presented at the 33rd International Gas Turbine and Aeroengine Congress and Exhibition, Amsterdam, The Netherlands, June 5–9, 1988. Manuscript received by the International Gas Turbine Institute January 1, 1988. Paper No. 88-GT-98.

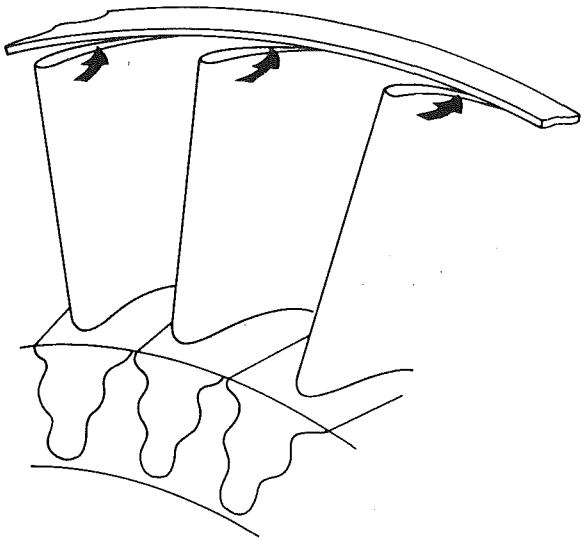

Fig. 1 Pressure side view of tip leakage as sink flow

mainstream flow. The sink strength distribution along the blade varies as dictated by the local pressure difference across the blade tip. The superposed sink flow imparts an additional acceleration to the near-tip flow [3, 5, 6], which leads to thinning and possible relaminarization of the near-tip boundary layer and therefore may result in significant modifications to the local heat transfer rates. These sink flow effects are of particular importance from midchord to the blade trailing edge where the typical secondary flows present in the blade passage as a whole tend to bring very hot portions of the mainstream flow toward the blade tip region.

Present knowledge about the influence of blade tip leakage flow on pressure and suction side flow is basically derived from investigations in isothermal flow without heat transfer [5–9]. Consequently, there is a total absence of experimental information on the effects of tip leakage flow on blade pressure and suction side *heat transfer*, with the sole exception of a few measured spanwise heat transfer variations (discussed further in [10]) that were initially discounted as a tip leakage effect.

The present study was designed and conducted to provide some understanding and assessment of the character, magnitude, and importance of the heat transfer effects of tip leakage on the blade aerodynamic surfaces near the tip. Experimental modeling of the different phenomena on both the pressure and suction sides of airfoils was performed in a water tunnel with flow directed through an adjustable streamwise corner slot in a straight square test channel. The experiments were performed for representative gap sizes and flow parameters and describe both heat transfer and flow development along the gap. The results presented in this paper are confined to the case of flow removal through the corner slot, or corner sink flow, which model the effects on blade pressure sides. A companion paper [10] presents results for the reverse case of slot blowing into the test channel, modeling the effects on blade suction sides.

Analytical Considerations

An analytical approximation of the flow field, based on the sink flow character of the leakage on blade pressure sides, gives insight to the impact of a corner gap flow on the mainstream and heat transfer development along the test plate, and, in fact, provided the initial motivation for the present experiments. As indicated in [3], major features of tip leakage on the pressure side of a blade are its sinklike effect on the flow near the gap, with resulting high flow accelerations, extreme thinning of the boundary layer as flow approaches the gap, and potential flow character of the gap entrance flow. The accelerations of the fluid toward the gap will generally be much larger than the streamwise accelerations associated with the blade passage flow without leakage present. An acceleration parameter k_{sink} for the spanwise component of the acceleration near the gap can be easily calculated [3] by assuming a line sink velocity distribution having a sink strength q equal to the gap leakage flow $v_G \cdot s$. Hence,

$$k_{\text{sink}} = (\nu/c^2)dc/dr = \pi/(2\text{Re}_s) \tag{1}$$

where $c(r)$ is the radial velocity component toward the gap, and r is the radial distance measured from the gap. From potential flow theory, the corresponding sink velocity distribution is

$$c(r) = -2q/\pi r \tag{2}$$

These sink flow acceleration intensities and velocities can be extremely high in terms of the leakage flow associated with blade clearance gaps. For a typical value of $\text{Re}_s \approx 2 \times 10^4$, $k_{\text{sink}} \approx 7 \times 10^5$. This value is very much larger than the 3×10^{-6} value often associated with boundary layer relaminarization.

In the present flow situation the sink is superposed on a mainstream flow with streamwise velocity u, and a better picture of overall flow character near the gap can be seen in terms of the resultant velocity

$$w = \sqrt{u^2 + c(r)^2} \tag{3}$$

and resultant total acceleration intensity

Nomenclature

c = radial sink flow velocity
c_p = specific heat
h = heat transfer coefficient
k_{sink} = sink flow acceleration intensity
L = characteristic length = 0.35 m
q = sink strength = $v_G \cdot S$
$\dot{q}$ = local heat flux
Q_{inlet} = mainstream flow rate at test section entrance
Q_{gap} = flow rate through gap
r = radial distance from gap
Re_L = mainstream Reynolds number = $u_B \cdot L/\nu$
Re_s = gap flow Reynolds number = $v_G \cdot S/\nu$
s = gap width
St = Stanton number = $\dot{q}/[\rho \cdot c_p \cdot u_B (T_w - T_\infty)]$
T_w = local temperature of test surface
T_∞ = free-stream temperature
u = velocity in streamwise (x) direction
u_B = bulk velocity at the test section entrance
u' = turbulence component in streamwise direction
v_G = mean value of gap flow velocity
v = velocity in y direction
W = test channel total span
x = streamwise direction
y = normal distance from the test surface
z = spanwise distance from channel sidewall
z' = spanwise distance from edge of the gap
ν = viscosity
ρ = density
ω_i = velocity bias correction factor

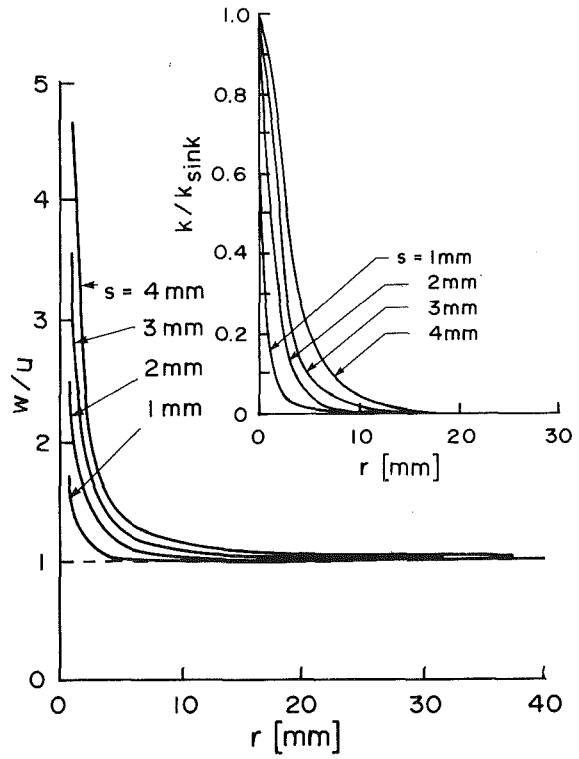

Fig. 2 Calculated near-gap velocity and acceleration

$$k = (\nu/w^2)dw/ds' \tag{4}$$

where s' denotes the streamline direction.

Combining equations (2) and (3) yields a solution for the nondimensional velocity distribution w/u.

$$\frac{w}{u} = \sqrt{1 + \left(\frac{2}{\pi}\frac{v_G}{u}\frac{s}{r}\right)^2} \tag{5}$$

Equation (5) gives an indication of the nondimensional parameters of primary importance for the gap flow effect, i.e., v/u and the geometric distance r/s, recognizing that the ratio v_G/u is directly related to the gap and mainstream Reynolds numbers Re_s and Re_L.

Figure 2 shows the velocity distribution near the gap for varying gap sizes $s = 1$–4 mm and a representative constant ratio of $v_G/u = 1.7$. The figure shows that the region where leakage is the dominant influence is very close to the gap, and that this region is expanded with larger gap sizes.

A similar analysis can be performed for the acceleration parameter k. Combining equations (4) and (5) yields the following:

$$k = k_{\mathrm{sink}} \Big/ \left(1 + \left(\frac{\pi}{2}\frac{u}{v_G}\frac{r}{s}\right)^2\right)^2 \tag{6}$$

The first term is the denominator of equation (6) represents the pure sink-flow acceleration as given by equation (1), and the second term indicates that at larger distances from the gap, acceleration intensity is reduced by the superposed mainstream flow.

The inset of Fig. 2 presents calculated distributions of k/k_{sink} near the gap corresponding to these same typical velocity distributions. There is a rapid decrease of the acceleration intensity away from the immediate vicinity of the gap, and the major leakage flow influence on k extends out on the pressure surface only to about 4 to 10 clearance gap widths. Nevertheless, k_{sink} is very high, as mentioned above, with a corresponding strong possibility for significant effects on local heat transfer rates, albeit very near the gap. Both the predicted high near-gap velocities and the narrowness of the region containing such velocities are also indicated in the pressure measurements of Bindon [6], where very large decreases in local static pressures were measured over a distance of a few gap widths down the blade pressure side from the clearance gap.

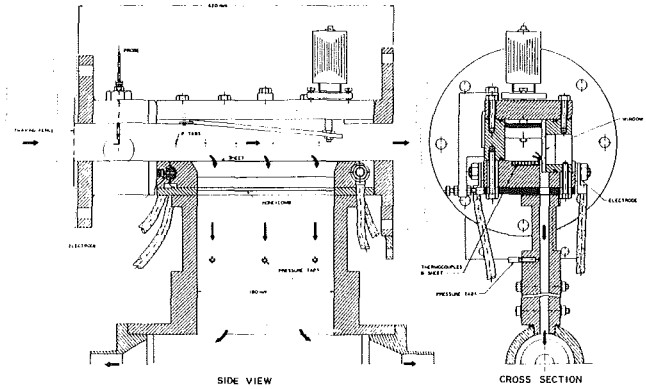

Fig. 3 Test section

The analysis thus indicates the possibility of strong leakage flow effects on near-tip heat transfer on the pressure side of turbine blades, which, together with the observation that blade tip failures are often indicated on the pressure side, was again the driving motivation for the present study. In addition, the analysis indicates that this effect, if present, is likely to be confined to a narrow region very close to the clearance gap. Thus the analysis also dictates demanding requirements for the experimental apparatus, and the test section size and instrumentation were chosen to meet these requirements, as described in the following section.

Apparatus and Procedures

The test section, specially designed and fabricated for these experiments, is shown schematically in Fig. 3. The test section was installed in a stainless steel recirculating water tunnel that has been fully described in a previous paper [10]. The dimensions of the test section were determined using the analysis given in the previous section. The cross section was chosen as wide as possible to provide minimum sink flow interference with the opposite channel wall boundary layers. The selected test section is square in cross section, 50×50 mm, and 420 mm long. The corner gap begins approximately 170 mm downstream of the test section entrance and extends 200 mm in the streamwise direction. In addition to the test section shown in Fig. 3, the apparatus includes a new square cross-sectioned settling chamber and inlet nozzle designed to match the chosen test section dimensions. The settling chamber is 223×223 mm square with five meshed wire grids and honeycomb insert (between the third and fourth grids), designed in accordance with the results of [12]. The contraction contour of the inlet nozzle was designed in accordance with the suggestions of [13] to foster a uniform velocity distribution at the nozzle exit with an attached laminar boundary layer.

Gap width is continuously adjustable from 0 to 5 mm. The flush channel floor near the gap in these experiments represents a turbine blade pressure side adjacent to the tip. Correspondingly, flow is removed from the test section through the gap into the attached vertical channel as indicated in Fig. 3. Immediately adjacent to the gap the test section channel wall is covered with a thin stainless steel sheet, ohmically heated with a regulated d-c power supply. A 200 mm length for the heated sheet was selected in order to model turbine airfoil Reynolds numbers up to $\approx 3 \times 10^5$, based on blade chord. The stainless test surface is 40 mm wide with 0.047 mm thickness to minimize heat conduction effects. It is

mounted on an insulating Plexiglas plate, which itself is embedded in another 40-mm-thick Plexiglas support frame (see cross-sectional view in Fig. 3). The conducting sheet was electrically heated through two copper electrodes as indicated also in Fig. 3. The upstream edge of the sheet is located 25 mm upstream of the leading edge of the gap, and is instrumented with thermocouples at four measurement planes located 20, 60, 110, and 170 mm downstream from the leading edge of the gap. As a result of the estimated velocity and acceleration parameter distributions shown in Fig. 2, a large number of thermocouples had to be placed very close to the gap in order to provide satisfactory resolution of the heat transfer rates. Miniature thermocouples were therefore placed at nominally 1, 2, 3.5, 5, 6.5, 8, 10, 12.5, 17.5, 23, 30, and 36 mm distances from the edge of the gap. The bare thermocouples (0.003-in. copper-constantan) were electrically insulated from the sheet by a 0.06-mm polyester tape.

A honeycomb section was utilized in the gap flow channel for straightening the gap flow, and approximately 130 mm beneath the heat transfer surface three pressure taps were mounted across the gap channel width to determine (together with the static pressure probes in the test section) the pressure drop across the gap. For all measurements presented in this paper, pressure in the gap channel was uniform at the gap measurement location.

The top wall of the test section was designed to be adjustable in order to compensate for the mainstream velocity reduction caused by the slot flow extraction during the sink flow experiments. Constant velocity in the test channel was obtained by adjusting the top wall for uniform static pressure distribution along the test section, as determined from the static pressure reading at the opposite channel sidewall.

The quantities measured during the heat transfer investigations included wall and free-stream temperatures, flow velocities, and electric power inputs. The local heat transfer coefficient was determined as

$$h = \dot{q}/(T_w - T_\infty) \tag{7}$$

in which $\dot{q}$ is the rate of heat passing from the wall into the fluid per unit area, T_w is the local test surface temperature, and T_∞ is the free-stream temperature. The heat transfer rate $\dot{q}$ is determined from an energy balance within a control volume taking into account the local temperature dependency of the sheet resistivity. The stainless sheet thickness (0.047 mm) was selected with the aid of preliminary testing with sample sheets of different thicknesses, with the objective of maximizing the strength and rigidity of the sheet while at the same time keeping temperature resolution problems due to lateral conduction acceptably low. The relatively high level heat transfer coefficients, obtained with the use of water as the test fluid, allowed used of the fairly thick sheet chosen while still holding lateral conduction errors far below those normally tolerated for air experiments.

A laser-Doppler anemometer (LDA) system was utilized to measure both mean and fluctuating velocities both upstream of the heated wall and at four streamwise planes within the heated length. Optical access to the flow is through large window areas included in the sidewall near the gap. The laser and optics are mounted on a movable platform, which provides accurate positioning of the optical probe volume in all three directions. The system was used in backscatter mode to provide data as close as possible to both the heat transfer surface and the sidewall.

Probe volume was nominally 1.9 mm long and 0.18 mm in diameter, and its position was determined by considering the differing refraction indices of water inside the test section and air outside. Signal processing was done with a counter connected to a minicomputer system. To provide high signal-to-noise ratio the flow was seeded with highly reflecting metallic coated particles (TSI 10087). The particle shape is spherical with mean diameter of 4 μm (geometric standard deviation 1.7) and the specific gravity is 2.6. Analysis indicates that the particles will follow the flow accurately for velocity fluctuation frequencies up to 40 kHz. This compares with expected fluctuation frequencies in the turbulent boundary layer of at most 10 kHz. The particles are thus expected to follow the flow accurately.

Table 1 Test conditions

Test #	s (mm)	Re_s	u_B (m/s)	v_G (m/s)	Q_{Inlet} (GPM)	Q_{GAP} (GPM)
$Re_L = 2.8x10^5$						
1.1	0	0	0.89	0	35.25	0
1.2	1.3	1300.	0.89	1.09	35.2	4.5
1.3	1.3	2833.	0.89	2.38	35.2	7.8
1.4	1.3	3873.	0.89	3.25	35.2	13.4
1.5	3.4	1271.	0.90	0.41	35.7	4.4
1.6	3.4	2804	0.88	0.84	35.0	4.7
1.7	3.4	3772.	0.87	1.21	34.5	13.05
1.8	5.0	1315.	0.89	0.29	35.30	4.55
1.9	5.0	2775.	0.88	0.70	34.90	9.60
1.10	5.0	3861.	0.89	0.84	35.20	13.30
$Re_L = 3.9x10^5$						
2.1		0	1.23	0	48.60	0
2.2	1.2	1312.	1.23	1.18	48.8	4.5
2.3	1.2	2857.	1.22	2.58	48.5	9.8
2.4	1.2	4548.	1.23	4.10	48.65	15.6
2.5	3.2	1315.	1.23	0.45	48.80	4.55
2.6	3.2	2847.	1.23	0.97	48.55	9.85
2.7	3.2	4437.	1.23	1.47	48.40	15.35
2.8	5.4	1268.	1.23	0.25	48.75	4.35
2.9	5.4	2813.	1.22	0.56	48.30	9.65
2.10	5.4	4475.	1.22	0.90	48.50	15.35

For increasing the data rate, and especially for identifying the flow component perpendicular to the mainstream near the gap, frequency shifting was applied by means of a Bragg cell. Data rates were between 1000 and 6000/s and signal-to-noise ratio was always better than 10–20, as estimated by monitoring the burst signals with an oscilloscope. The mean velocity was determined from computing

$$\Sigma\omega_i u_i / \Sigma\omega_i \tag{8}$$

where ω_i's are weighting factors that include velocity bias correction. The mean square of the turbulent fluctuation similarly was determined by calculating

$$\overline{u'^2} = \Sigma\omega_i [u_i - u]^2 / \Sigma\omega i \tag{9}$$

The second component of the mean velocity, perpendicular to the mainstream flow, was measured by an $\alpha = \pm 45$ deg rotation of the probe volume about its original plane in the mainstream direction or orientation. For bias correction the suggestion of McLaughlin and Tiederman [14] was applied, defined by

$$\omega_i = 1/\sqrt{u_i^2} \tag{10}$$

More detailed information about the experimental setup and measurement techniques is available in [15].

The experimental conditions imposed in the present study are summarized in Table 1. The channel floor and sidwall boundary layers were tripped at the inlet of the test section, utilizing a 0.9-mm-high tripping fence. The flow conditions of Table 1 are generally defined by the corresponding mainstream Reynolds number Re_L and the gap flow Reynolds numbers Re_s. Re_L is based on the bulk velocity u_B at the test section entrance and on the distance L between the boundary

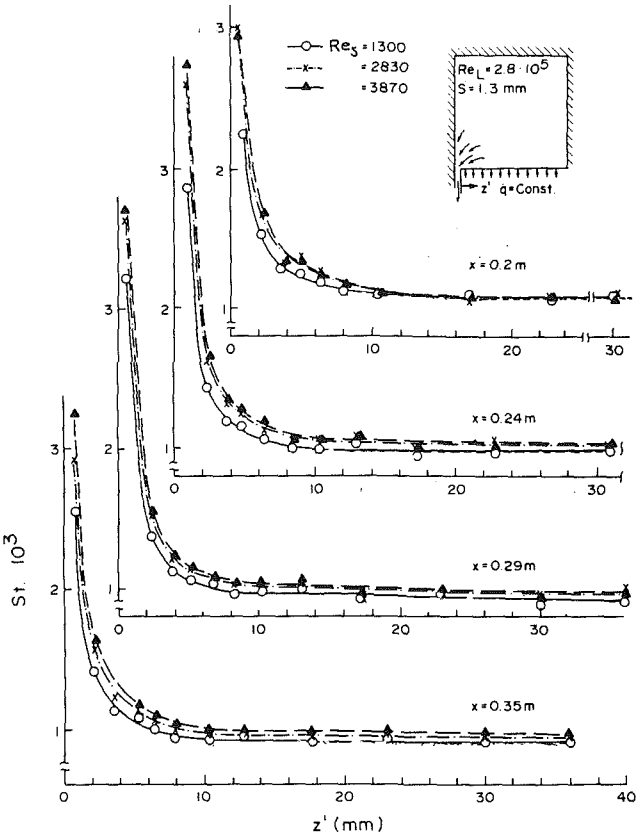

Fig. 4 Heat transfer with small gap and low mainstream Re

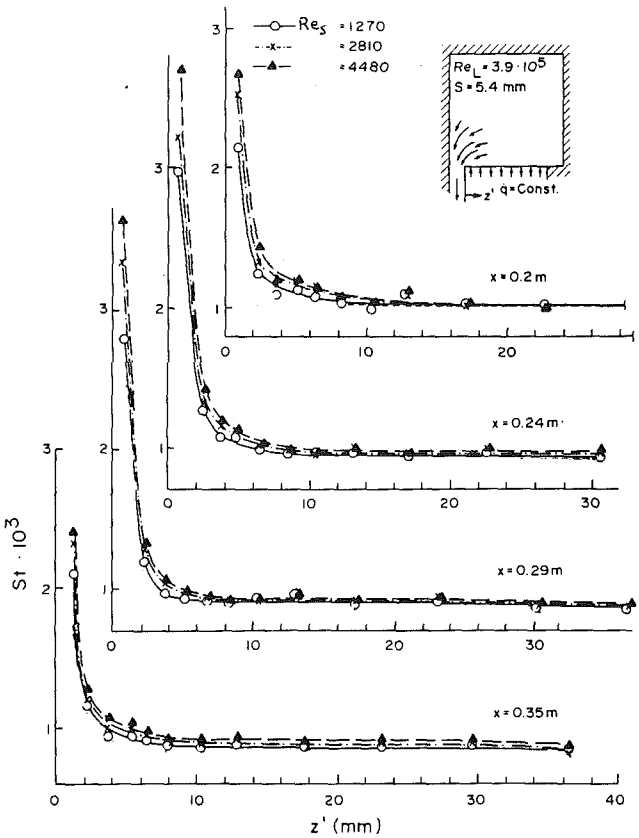

Fig. 5 Heat transfer with large gap and higher mainstream Re

layer trip ($x=0$) and the last heat transfer measurement plane located at $x=L=0.35$ m. The gap flow Reynolds number Re_s is similarly determined by the mean velocity v_G in the gap and the gap width s. Mean velocities are derived from calibrated turbine flow meters installed in the mainstream path and in the gap flow path.

Experiments were performed for two mainstream Reynolds numbers $Re_L = 2.8\times10^5$ and 3.8×10^5 and the gap sizes were varied over $s=0$, 1, 3, and 5 mm. The relative gap widths s/h, normalized by the channel width $h=50$ mm, are consequently $s/h=0$, 2, 6, and 10 percent. The Reynolds numbers Re_s for characterizing the gap flow intensity were varied at each gap size from $Re_s=0$ to $Re_s\simeq1300$, 2800, and 2900. The flow parameters and gap sizes were selected to be representative of actual gas turbine tip leakage flows. The heat transfer sheet was throughout all experiments only slightly heated to at most 5°C above free-stream temperature ($T_\infty\approx18$°C). For this temperature difference the corresponding local heat flux q was approximately 19.5×10^3 W/m^2.

Results and Discussion

Initial experiments were performed with closed gap, $s=0$, and have been reported in a previous paper [15]. In the absence of a gap, the local Staton number values and streamwise development along the center of the test surface are in good agreement with expected turbulent boundary layer values. Near the corner intersection between the heated test surface and the unheated sidewall, an increase in heat transfer rates is observed that appears to be associated with both the change in thermal boundary condition and observed flow nonsymmetry and nonisotropy near the corner.

Figures 4 and 5 show the present Stanton numbers obtained with open gap and flow removal simulating turbine blade pressure side flow into a tip clearance gap. Figure 4 shows results for the lower mainstream Reynolds number $Re_L=2.8\times10^5$ and small gap size ($s=1.3$ mm), as a function of distance from the edge of the gap. Stanton numbers are based on the inlet velocity u_B, and have an estimated uncertainty of ±6 percent, based on the methods of Kline and McClintock [16]. Measurements were made at four streamwise locations within the gap region with the first measurement plane ($x=0.2$ m) located only 20 mm downstream of the leading end of the gap. The last measurement plane ($x=0.35$ m) is 25 mm upstream of the trailing end of the 200-mm-long gap. During the experiments the sink flow was increased from $Re_s=1300$ to $Re_s\approx2800$ and $Re_s\approx3900$.

The heat transfer distributions in Fig. 4 show the typical impact of the gap sink flow on the adjacent test surface. Far distant from the gap the heat transfer is highly uniform spanwise as previously measured [15] for flow with the gap closed. Closer to the gap, however, a systematic increase in the local Stanton numbers is evident. Heat transfer enhancement near the gap increases with increased gap flow rate between $Re_s=1300$ and $Re_s=2830$, whereas for $Re_s=3870$ no significant further increase is observed. Heat transfer enhancements up to 200 percent are obtained closest to the gap, while further distant from the gap the enhancement reduces to the order of 10 to 50 percent, dependent on Reynolds number and the distance from the gap.

Figure 5 shows similar results at higher inlet Reynolds number Re_L and a larger gap size of 5.4 mm. The bulk velocity at the test section entrance has been increased from 0.89 m/s to 1.22 m/s, generating a mainstream Reynolds number $Re_L=3.9\times10^5$, which is 40 percent higher than in the previous sink flow experiments. It should be noted that the velocity increase is associated with a strong increase of the dynamic bead $\rho/2\cdot u_B^2$ of almost 90 percent. The mainstream streamwise momentum of the flow entering the gap is therefore higher with smaller deflection of the flow in the near neighborhood of the gap.

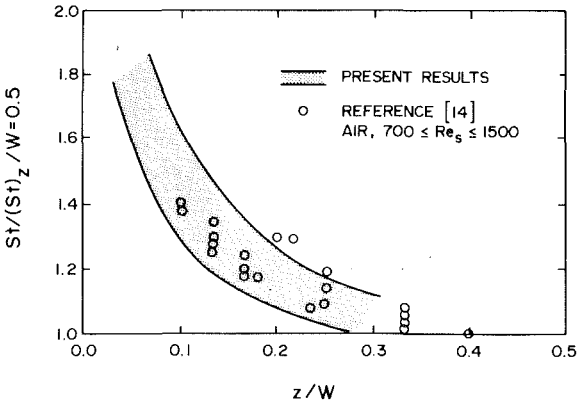

Fig. 6 Summary of near-gap heat transfer enhancement

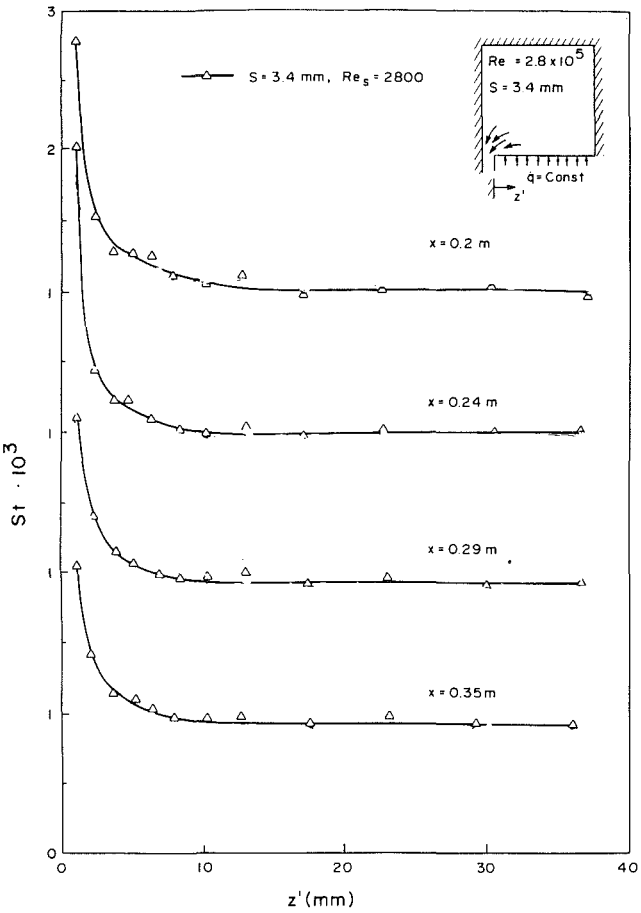

Fig. 7 Heat transfer with intermediate gap size and flow

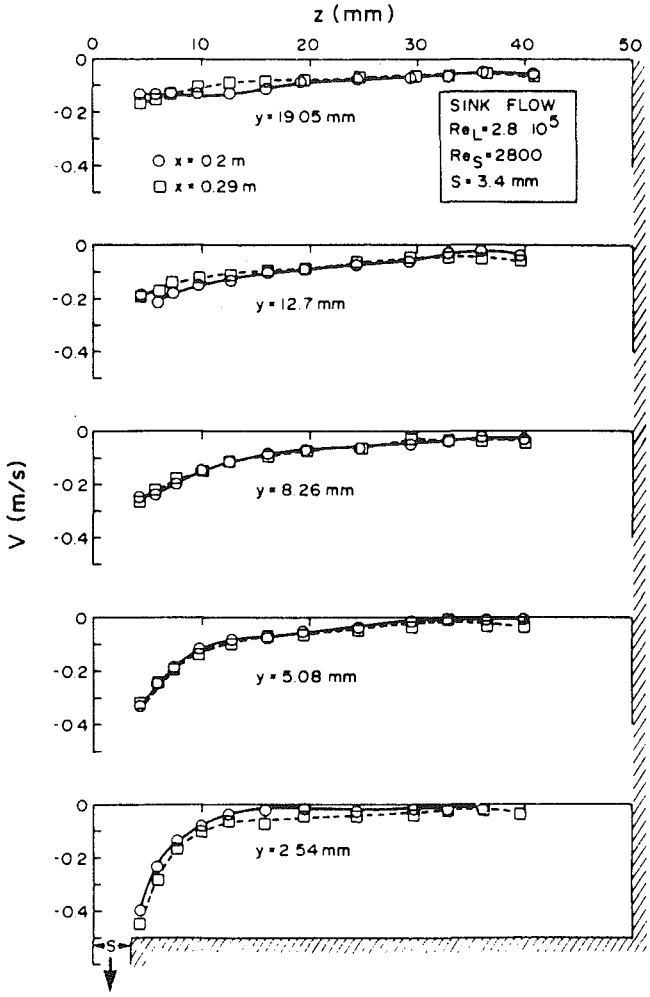

Fig. 8 Sink flow development along the gap

Comparison of the results of Fig. 5 with the corresponding values of Fig. 4 for the lower mainstream Reynolds number shows the influence of sink flow to be confined to a region closer to the gap, probably reflecting a more dominating impact of the larger momentum of the mainstream. Very close to the gap, however, the heat transfer increase is nevertheless again on the order of 100 to 200 percent.

In general, the increased gap size appears to have a relatively minor effect on the heat transfer enhancement. The shaded region of Fig. 6 summarizes the near-gap enhancement (relative to the midchannel heat transfer rates) for all of the present results, and compares them with similar results from a more recent limited study conducted in a separate apparatus with air, specifically to check the present results [17]. Although the resolution of local heat transfer in the air tests did not allow values to be determined as close to the gap, the agreement down to $z/W = 0.1$ is quite good, and confirms the significant heat transfer effect that the sink flow into a turbine tip clearance gap can have on the pressure side heat transfer rates near the tip. It is also worth noting that the thermal boundary condition in the air tests is close to a uniform temperature boundary condition on both channel walls adjacent to the corner slot; thus the heating of only one wall in the present tests does not appear to have an independent effect on the results.

To help better understand the nature of the observed heat transfer enhancement near the tip, detailed LDA measurements were conducted to define the flow development along the gap. Combined velocity and turbulence measurements were performed for an intermediate gap width of 3.4 mm with a fairly strong sink flow situation defined by a gap flow Reynolds number $\mathrm{Re}_s = 2800$ and mainstream Reynolds number $\mathrm{Re}_L = 2.8 \times 10^5$. Figure 7 displays the heat transfer distributions for this case. The results again reveal strong heat transfer enhancement close to the gap.

Figures 8–12 present the corresponding flow development along the gap. Velocity and turbulence structures were measured within the gap flow region at $x = 0.2$ and 0.29 m, corresponding to two of the four heat transfer measurement planes shown in Fig. 7.

To quantify the local sink strength distribution, Fig. 8 presents the normal (v) velocity component. The data describe spanwise velocity distributions at different heights

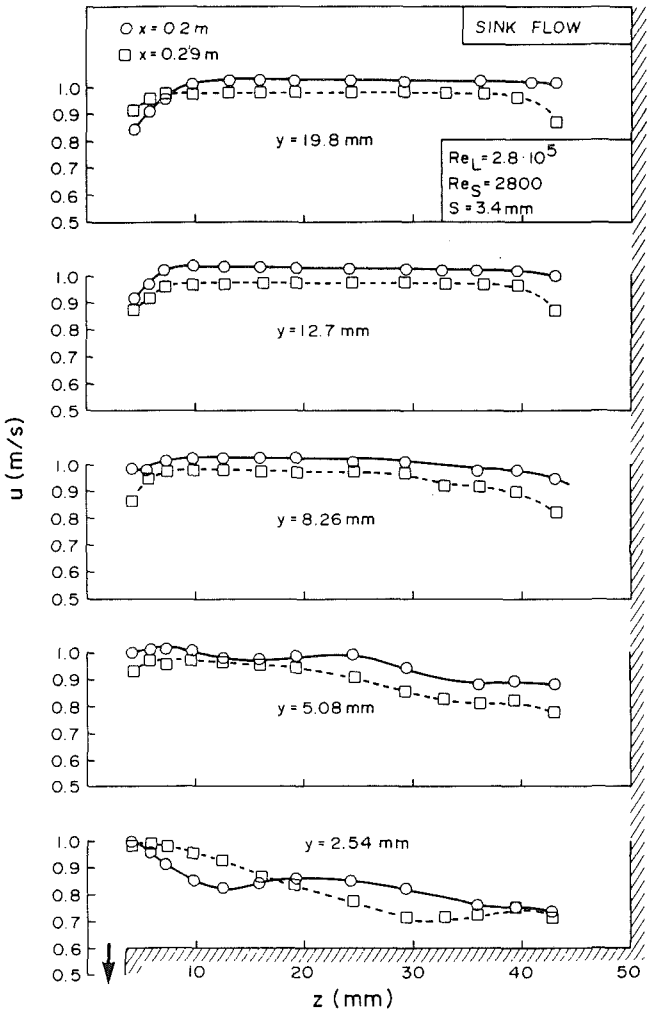

Fig. 9 Influence of sink flow on mainstream velocity

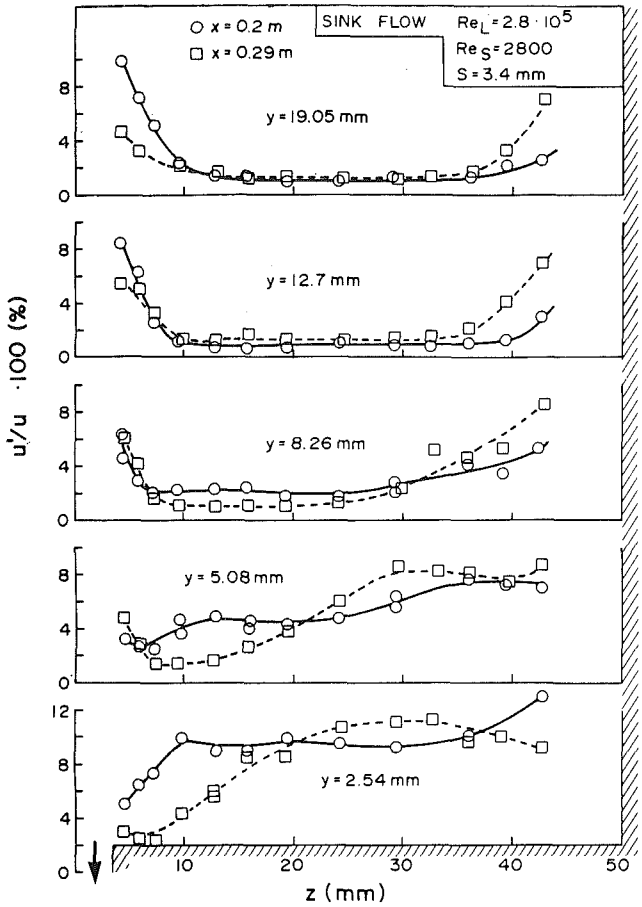

Fig. 10 Influence of sink flow on turbulence development

from the plate. The spanwise measurements start at $z = 4.5$ mm, which is approximately 1 mm from the edge of the gap. Closer to the sidewall the signal quality was too poor to provide reliable velocity results.

Figure 8 reveals only slight differences in the velocity distributions for the two downstream locations. Therefore, the sink flow development along the gap appears quite uniform. The data also confirm that the highest sink flow velocities appear nearest to the gap. Further distant from the plate a steady decrease of the velocities near the sidewall can be observed. This effect is accompanied by a further spanwise extension of the gap flow influence region as is indicated by increasingly negative v components for larger distances from the sidwall. At $y = 19$ mm the data show that the gap flow influence has effectively extended over the entire test section width, despite the fact that the heat transfer increase is confined to a region close to the gap.

Figure 9 shows the impact of the gap flow on mainstream velocity distribution. Again, the major influence is observed closest to the plate ($y = 2.5$ mm) and next to the gap. Extracting fluid through the gap leads to acceleration of the mainstream flow, which is expressed by higher velocity values near the gap than further inside the plate. Additionally, it can be seen that the velocity development near plate ($y = 2.5$ mm and $y = 5.08$ mm) is now different for the two downstream locations. The difference can be interpreted as a downstream varying gap flow influence yielding a larger influence region at the further downstream position. At increased distances from the plate the velocity profiles become more uniform. At distances (y) greater than 8 mm typical channel flow velocity distributions are present with no further discernible influence of the gap flow, in contrast to the v component shown in Fig. 8. It can be concluded that with respect to streamwise velocity, sink flow effects are mostly confined to an area close to the wall.

Figure 10 compares the local turbulence distributions u'/u as measured for the two streamwise positions under the influence of sink flow. Data were obtained at the same local positions (y, z) as shown before for the u and v velocity components. The turbulence distributions reflect a behavior that is very similar to the mainstream velocity distributions of Fig. 8. At larger distances from the plate typical turbulence distributions for pure channel flow can be observed that appear unaffected by the presence of gap flow. The increased turbulence intensities close to the sidewalls are associated with the sidewall boundary layers. In the vicinity of the gap ($y = 2.5$ and 5 mm) deformations of the turbulence distributions are evident, which are dictated by flow acceleration near the gap. These deformations vary even more between the two streamwise positions ($x = 0.2$ and $x = 0.29$ m) than shown in Fig. 9 for the velocity profiles. The effects are most pronounced at the further downstream location $x = 0.29$ m. For this case the acceleration of the flow close to the gap apparently leads to strong reduction of the local turbulence intensity; from approximately 12 percent far distant from the sidewall down to nearly 2 percent at the end of the gap. Similar behavior is also evident at $y = 5.08$, except that close to the sidewall the turbulence intensities increase again, which is plausibly a starting interaction with the sidewall boundary layer. The reduction of the turbulence intensity close to the gap shows relaminariza-

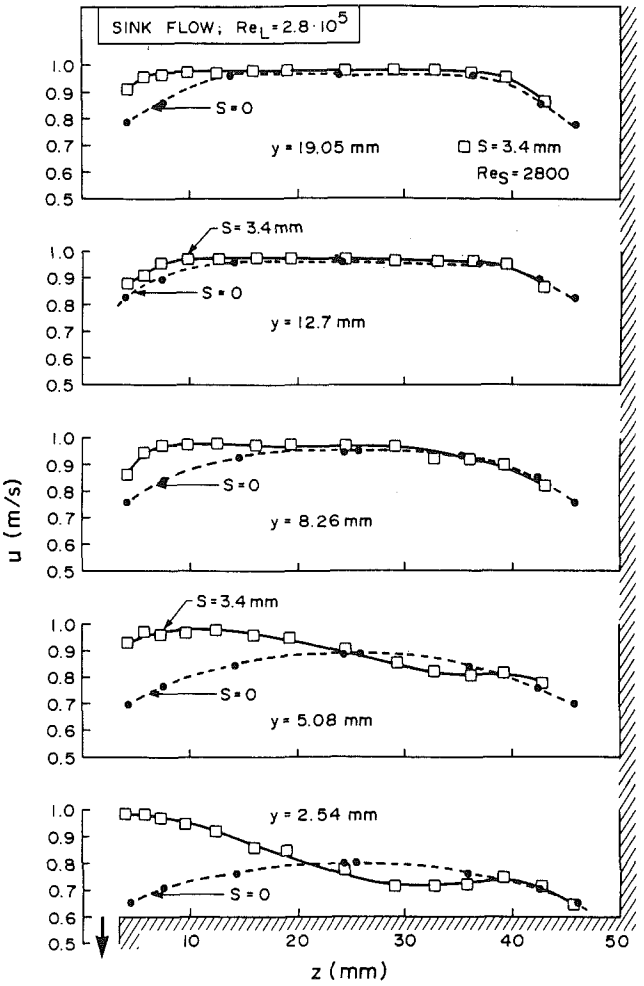

Fig. 11 Comparison of mainstream velocity distributions with and without gap flow

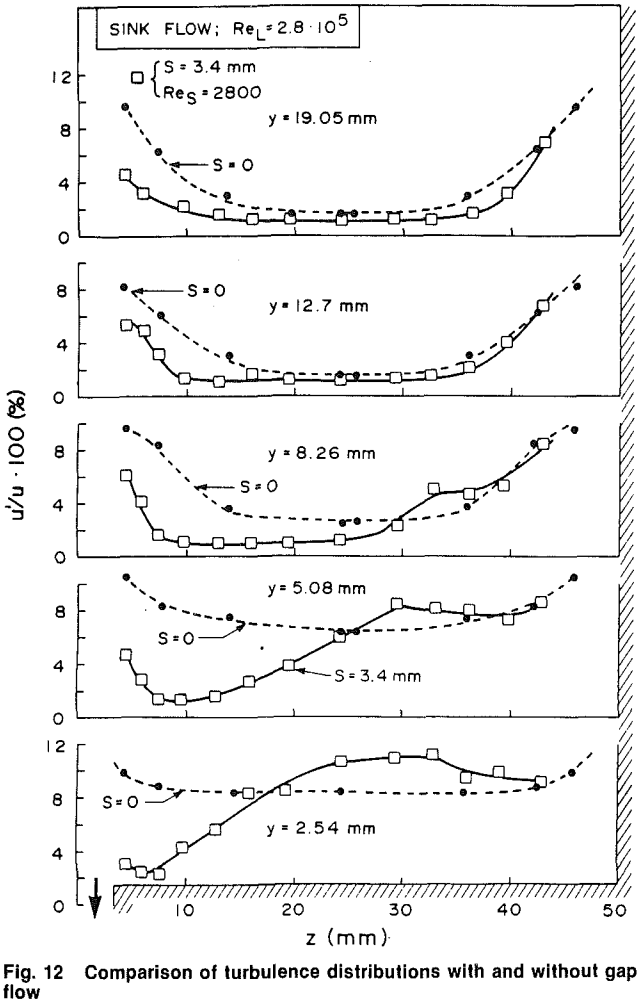

Fig. 12 Comparison of turbulence distributions with and without gap flow

tion of the formerly turbulent flow, as suggested by the large accelerations predicted by the analysis. The lower turbulence values indicate laminarization is more advanced at $x = 0.29$ m than it is further upstream at $x = 0.2$ m, close to the leading edge of the gap. This difference in the degree of relaminarization apparently contributes to the lower heat transfer increase nearest the gap at $x = 0.29$, as shown by the Stanton number distribution in Fig. 7.

The velocity and turbulence results of Figs. 9 and 10 are also usefully compared to those of pure channel flow with $s = 0$, as shown typically in Figs. 11 and 12 for $x = 0.29$ m. The $s = 0$ data obtained at spanwise locations $z = 4.5$ mm, $z = 7.6$ mm, 14.5 mm, and $z = 24$ mm were interpolated as indicated by the dashed lines and for completeness mirrored about the center plane of the channel.

Figure 11 displays a comparison of the mainstream velocity profiles at different heights from the channel floor, and again shows the gap flow influence extending into the mainstream. The differences between the $s = 0$ and sink flow data are largest closest to the test surface ($y = 2.54$ mm). Near the gap the velocities with sink flow are approximately 60 percent higher than those for flow without corner gap. Farther inside the test plate ($y = 2.54$ mm) the velocity in mainstream direction declines to values that are smaller than those for pure channel flow. It is plausible that this strong velocity reduction far inside ($z > 20$ mm) is associated with a deflection of the flow toward the gap. At larger heights from the test surface differences between the velocity distributions with and without gap flow gradually decrease. Some differences remain that reflect a continuing impact of sink flow acceleration, but are confined to the side nearest the gap.

A comparison of the turbulence intensity distributions with and without gap flow is shown in Fig. 12. At the closest distance from the gap ($y = 2.54$ mm, $z = 4.5$ mm) the apparent relaminarizing effect of the gap sink reduced the local turbulence intensity from approximately 10 percent to almost 2 percent. This large difference changes strongly with distance from the gap with the consequence that higher turbulence intensities than those for pure channel flow eventually prevail. The enhanced turbulence values are associated with the lowered mainstream velocities.

It can be concluded that the existence of the corner gap and the acceleration of the flow toward it produce a completely new flow situation compared to the case of a pure corner flow with $s = 0$. The secondary vortices associated with highly turbulent motions, as found in a solid corner flow, are replaced by a laminarizing flow with higher velocities but much lower turbulence intensities. Despite laminarization, the heat transfer measurements show that the net result of this combination of factors is a very strong near-gap heat transfer enhancement with sink flow present.

Summary and Conclusions

A study has been conducted to investigate the influence of tip leakage flow on heat transfer and flow development along

the pressure side of a gas turbine blade. Analysis of the sink-flow character of the flow situation shows that very high velocities and accelerations are generated very near the gap, and an experimental apparatus was specifically designed to allow resolution of the local near-gap heat transfer characteristics. The experiments were performed in a water tunnel, and the measured results show that leakage flow through the test section corner gap is associated with large but highly localized increases in local heat transfer rates near the gap (up to 200 percent). The observed region of increased heat transfer varied from 2 to 10 gap widths, and the magnitudes of the increases are in good agreement with a more limited confirmation study conducted with air.

Parameters of primary importance for the impact of flow extraction through the gap are sink strength expressed as gap flow Reynolds number, together with mainstream Reynolds number. Independent effects of gap size were observed only for the smaller mainstream Reynolds numbers. At higher mainstream Reynolds numbers the gap flow influence region was reduced. Supporting LDA measurements of the mean and fluctuating velocity fields with the gap sink flow show that near the gap the flow is highly accelerated, with apparent relaminarization of the initially turbulent boundary layer. The degree of relaminarization varies with streamwise distance along the gap, and this is reflected in the heat transfer results. Comparing heat transfer and flow measurements shows that the gap and sink flow influence on the flowfield in general is much larger than indicated by the heat trasnfer results alone.

In summary, the results indicate that sink flow effects near the tip of the pressure sides of gas turbine blades are associated with flow modifications that produce additional heating loads in the blade tip region. The present paper presents the first documentation and rationale for such a detrimental heat transfer enhancement. Its presence helps to account for observed distress and failures of in-service blades that appear to initiate at the pressure side tip. The companion to the present paper [10] shows that a different, but coexisting, heat transfer enhancement mechanism acts on the blade suction side very near the tip. The presence of both of these enhancements to heat transfer should be accounted for in blade cooling designs, and the present results provide, at least in an initial quantitative form, required understanding and data.

References

1 Metzger, D. E., and Mayle, R. E., "Heat Transfer—Gas Turbine Engines," *Mechanical Engineering*, Vol. 105, 1983, pp. 44–52.

2 Dunn, M. G., Rae, W. J., and Holt, J. L., "Measurement and Analysis of Heat Flux Data in a Turbine Stage: Parts 1 and 2," ASME *Journal of Engineering for Power*, Vol. 106, 1983, pp. 229–240.

3 Mayle, R. E., and Metzger, D. E., "Heat Transfer at the Tip of an Unshrouded Turbine Blade," *Proceedings 7th International Heat Transfer Conference*, Vol. 3, 1982, pp. 87–92.

4 Metzger, D. E., and Chyu, M. K., "Clearance Effects on Heat Transfer at the Tips of Plain and Grooved Turbine Airfoils," *Turbomachinery Performance Deterioration*, ASME FED-Vol. 37, 1986, pp. 107–114.

5 Bindon, J. P., "Visualization of Axial Turbine Tip Clearance Flow Using a Linear Cascade," Cambridge University Engineering Department, TR 122, 1986.

6 Bindon, J. P., "Pressure and Flowfield Measurements of Axial Turbine Tip Clearance Flow in a Linear Cascade," Cambridge University Engineering Department, TR 123, 1986.

7 Hansen, A. G., and Herzig, H. Z., "Secondary Flow Studies in Turbomachines," *Trans. ASME*, Vol. 77, 1955, pp. 249–266.

8 Allen, H. W., and Kofskey, M. G., "Visualizaton Study of Secondary Flows in Turbine Rotor Tip Regions,'" NACA TN 3519, 1955.

9 Graham, Y. A. H., "Investigation of Tip Clearance Cascade in a Water Analogy Rig," Trans. ASME, Vol. 108, 1986, pp. 38–46.

10 Rued, K., and Metzger, D. E., "The Influence of Turbine Clearance Gap Leakage on Flowpath Velocity and Heat Transfer Near Blade Tips, Part II: Source Flow Effects on Blade Suction Sides," ASME Paper No. 87-GT-XX.

11 Dellenback, P. A., Metzger, D. E., and Neitzel, G. P., "Heat Transfer to Turbulent Swirling Flow Through a Sudden Axisymmetric Expansion," ASME *Journal of Heat Transfer*, Vol. 109, 1987, pp. 613–620.

12 Baines, W. D., and Peterson, E. G., "An Investigation of Flow Through Screens," ASME Paper No. 50-A-23, 1950.

13 Chmielewski, G. E., "Boundary Layer Considerations in the Design of Aerodynamic Contractions," *Journal of Aircraft*, Vol. 11, 1977, pp. 435–438.

14 McLaughlin, D. K., and Tiederman, W. G., "Biasing Correction for Individual Realization of Laser Anemometer Measurements in Turbulent Flows," *Physics of Fluids*, Vol. 16, No. 12, Dec. 1973.

15 Rued, K., Murthy, J. Y., and Metzger, D. E., "Turbulent Convection Heat Transfer at the Corner Intersection of Heated and Unheated Walls in a Square Flow Channel," ASME HTD-Vol. 87, 1987, pp. 49–55.

16 Kline, S. J., and McClintock, F. A., "Describing Uncertainties in Single Sample Experiments," *Mechanical Engineering*, Vol. 75, 1953.

17 Metzger, D. E., Bunker, R. S., and Ruff, B. F., "Confirmation Testing With Air for Effects of Tip Clearance Leakage Flow on Turbine Blade Pressure Side Heat Transfer Near the Tip," Arizona State University ERC/TR 87351, 1987.

The Influence of Turbine Clearance Gap Leakage on Passage Velocity and Heat Transfer Near Blade Tips: Part II—Source Flow Effects on Blade Suction Sides

K. Rued[1]

D. E. Metzger
Professor.
Fellow ASME

Mechanical and Aerospace Engineering Department,
Arizona State University,
Tempe, AZ 85287

An experimental study has been designed and conducted to investigate turbine blade suction side heat transfer and flow near the tip clearance gap. Modeling of the phenomena was carried out in a water tunnel with injection through an adjustable streamwise corner slot in a square test channel. A thin stainless steel ohmic-heated test surface adjacent to the slot simulated the airfoil surface and permitted fine resolution of local heat transfer rates. Mean and fluctuating flowfield measurements were conducted with a laser-Doppler anemometer to aid interpretation of the heat transfer results and to provide a basis for comparison with future numerical predictions. The results indicate that flow leakage from the turbine tip clearance gap into the suction side hot gas path results in more extensive and complex heat transfer effects than those measured for the blade pressure side in the companion Part I study. The character of the heat transfer and flowfield deviations from closed gap conditions is strongly dependent on the particular combination of flow and geometry parameters present. The observed characteristics have been partitioned into categories of similar behavior, and the parameter combinations that define the boundaries between categories have been tentatively identified for the benefit of designers. The overall conclusions of this study and of the parallel study reported in Part I are that the effects of tip leakage flow on airfoil surface heat transfer near the blade tip can be very significant on both pressure and suction sides, and should be taken into account in blade cooling specification and design.

Introduction

The clearance gap between the tip of an axial turbine blade and the adjacent stationary peripheral wall provides a narrow passage, which allows an undesirable leakage flow over the tip from pressure to suction side of the blade, as indicated in Fig. 1, viewed from the blade suction side. A major detrimental effect of tip leakage is on the aerodynamic performance of the blade, but a second important effect is heat transfer to the blade tip associated with the clearance flow. These two effects have provided the primary motivation for recent research studies. Efforts aimed at minimizing aerodynamic performance losses by reducing the leakage flow have been reported [1, 2], as well as efforts to provide understanding of the nature of heat transfer to the blade tip [3, 4]. Experience has shown that the combination of temperature and heat transfer coefficients associated with the gap flow can impose strong thermal loads on the blade tip [5]. This thermal load can produce structural damage if the additional amount of heat is not adequately accounted for in the blade internal cooling design.

In addition to forced convection on the blade tip proper, the effects of the leakage flow on the flow and heat transfer along the blade pressure and suction sides near the tip need to be considered in order to assess the total impact of the gap leakage flow. Previous cascade investigations [6–10] have indicated that on the suction side near the tip the leakage flow encounters the oncoming wall flow, and tends to separate and roll into a vortex, unloading the blade tip and increasing the total amount of secondary flow within the turbine blade passage. Under these conditions, it is generally expected that the leakage flow will generate an increase in blade suction side

[1] Current address: Motoren-u. Turbinen-Union, Munich, Federal Republic of Germany.

Contributed by the International Gas Turbine Institute and presented at the 33rd International Gas Turbine and Aeroengine Congress and Exhibition, Amsterdam, The Netherlands, June 5–9, 1988. Manuscript received by the International Gas Turbine Institute January 1, 1988. Paper No. 88-GT-99.

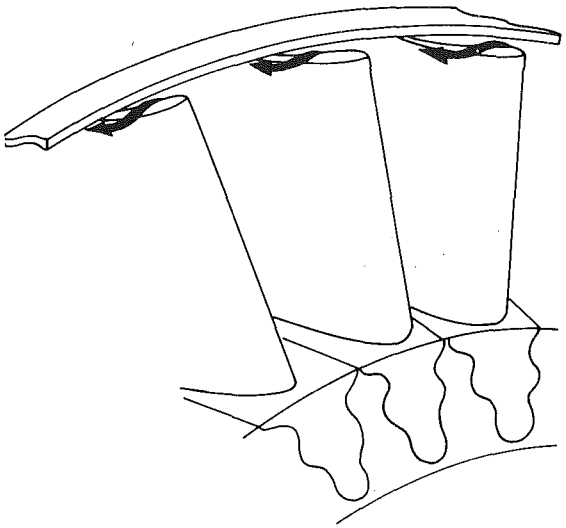

Fig. 1 Suction-side view of tip leakage as source flow

heat transfer near the tip, but there are apparently no studies that have been made previously to confirm or refute the expectation.

The present study was conducted to provide quantitative local heat transfer information about the effects of tip leakage on blade suction side heat transfer. The experimental modeling of the phenomena was carried in a water tunnel with flow directed through an adjustable streamwise corner slot in a straight square cross-sectioned test channel. Experiments were performed for representative gap sizes and flow parameters and they describe both heat transfer and flow development along the gap. The results presented in this paper are confined to the case of flow supplied to the test channel through the corner slot, or corner source flow. A companion paper [11] presents results for the reverse case of slot suction from the test channel, modeling the effects of tip leakage flow on blade pressure surfaces.

Apparatus and Procedures

The test apparatus used for simulating gap flow effects along the suction side of a gas turbine blade is the same as used in the companion study for simulating the pressure side effects. It has previously been described in detail [11, 12], so only a brief overview will be included here. A specially designed and fabricated test section is used in a stainless steel recirculating water tunnel. The test section is 420 mm long with a square 50 × 50 mm cross section. The corner gap begins approximately 170 mm downstream of the test section entrance and extends 200 mm in the streamwise direction. The flush channel floor near the gap in these experiments represents a turbine blade suction side adjacent to the tip. Correspondingly, flow is supplied to the test section through a corner gap from an attached vertical channel as indicated in Fig. 2 of [11].

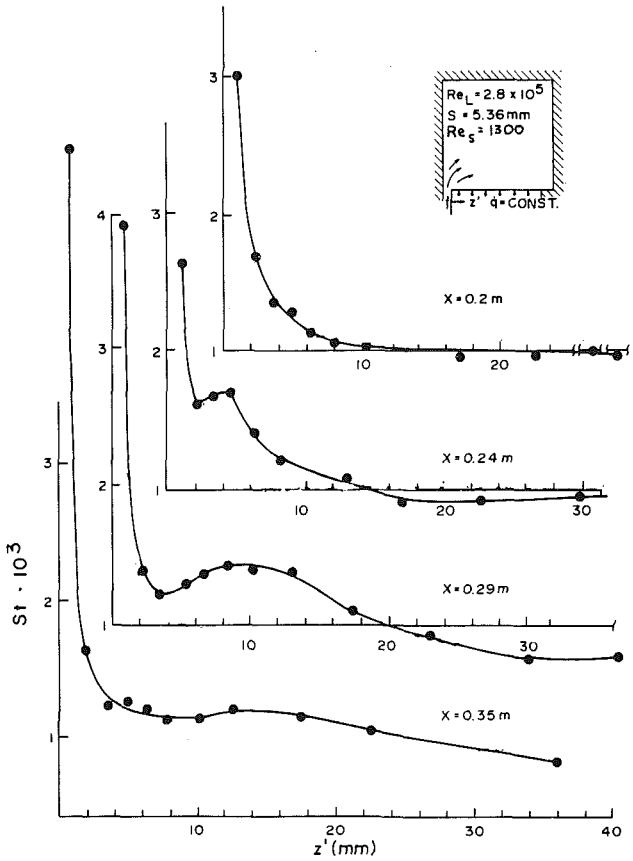

Fig. 2 Heat transfer with large gap and medium gap flow

Immediately adjacent to the gap the test section channel wall is covered with a heated stainless steel sheet, 0.047 mm thick and 40 mm wide in the spanwise direction. Miniature thermocouples are attached beneath the stainless sheet at nominally 1, 2, 3.5, 5, 6.5, 10, 11.5, 17.5, 23.0, 30.0, and 36 mm distances from the edge of the gap. To straighten the gap flow before entering the test channel, honeycomb mesh was installed in the gap flow channel. Approximately 130 mm beneath the test transfer surface three pressure taps were

Nomenclature

c_p = specific heat
h = heat transfer coefficient
L = characteristic length = 0.35 m
M = injection momentum parameter
$\dot{m}_{gap}$ = mass flux through the gap
$\dot{m}_{inlet}$ = mass flux at the inlet of the test section
n = number of measurements per sample
N_r = test identification number
$\dot{q}$ = local heat flux
Q_{inlet} = mainstream flux rate at test section entrance
Q_{gap} = flow rate through gap
Re_h = channel Reynolds number = $u_B \cdot W/\nu$
Re_L = mainstream Reynolds number = $u_B \cdot L/\nu$
Re_s = gap flow Reynolds number = $v_G \cdot s/\nu$
s = gap width
St = Stanton number = $q/[\rho \cdot u_B \cdot c_p (T_w - T_\infty)]$
T_w = test surface temperature
T = free-stream temperature
u = local mainstream velocity
u_B = bulk velocity at the test section entrance
u' = turbulence component in mainstream direction
v_G = mean value of gap flow velocity
v = velocity in normal (y) direction
W = test channel total span
x = mainstream direction
y = normal distance from the plate
z = spanwise distance from channel sidewall
z' = spanwise distance from edge of the gap
ν = viscosity
ρ = density

mounted across the gap channel width and indicated uniform gap supply pressure throughout all measurements of this study.

The quantities measured during the heat transfer investigations included wall and free-stream temperatures, flow velocities, and electric power inputs. The local heat transfer coefficient was determined as

$$h = \dot{q}/(T_w - T_\infty) \tag{1}$$

where $\dot{q}$ is the heat flux from the wall into the fluid, T_w is local test surface temperature, and T_∞ is the free-stream temperature. The heat transfer rate q is determined from an energy balance within a control volume taking into account the local temperature dependency of the sheet resistivity.

A laser-Doppler anemometer (LDA) system was utilized to measure both mean and fluctuating velocities both upstream of the heated wall and at four streamwise planes within the heated length. The laser and optics are mounted on a movable platform, which provides accurate positioning of the optical probe volume in all three directions. The system was used in backscatter mode to provide data as close as possible to both the heat transfer surface and the sidewall.

Probe volume was nominally 1.9 mm long and 0.18 mm in diameter, and its position was determined by considering the differing refraction indices of water inside the test section and air outside. Signal processing was done with a counter connected to a minicomputer system. To provide high signal-to-noise ratio the flow was seeded with highly reflecting metallic coated particles (TSI 10087). The particle shape is spherical with mean diameter of 4 μm (geometric standard deviation 1.7) and the specific gravity is 2.6. It could be shown that the particles follow the flow accurately for the highest fluctuation frequencies within the test section.

The mean velocity and the turbulent fluctuations were calculated as

$$u = \frac{1}{n} \Sigma u_i \tag{2}$$

$$\overline{u'^2} = \frac{1}{n} \Sigma (u_i - u)^2 \tag{3}$$

The second component of the mean velocity was measured by a ± 45 deg rotation of the probe volume about its original plane or orientation.

In order to reduce velocity bias effects, the one-dimensional bias convection suggested by McLaughlin and Tiedermann [13] was also applied. However, in analyzing the source flows associated with strong flow recirculation near the gap it appeared more appropriate to rely on the pure data without correction. The one-dimensional bias-corrected data revealed unrealistic turbulence and velocity values. Similar experiences in other recirculating flows have been noted by Stevenson et al. [14] and by Tiedermann [15], with recommendation that the bias correction be omitted, or a multidimensional correction procedure be applied. The latter option was not possible with the LDA system used here.

The experimental conditions for the present study are summarized in Table 1. The channel floor and sidewall boundary layer were tripped at the inlet of the test section, utilizing a 0.9-mm-high tripping fence. The flow conditions of Table 1 are generally defined by two different mainstream Reynolds numbers Re_L ($Re_L = 2.8 \times 10^5$ and 3.9×10^5) and by gap flow Reynolds number Re_s ranging from $Re_s = 0$ to $Re_s = 3900$. The gap size was varied from $s = 0$ to $s = 5$ mm reflecting relative gap widths s/W up to 11 percent. Re_L is based on the bulk velocity u_B at the test section entrance and on the distance L between the boundary layer trip ($x = 0$) and the last heat transfer measurement plane located at $x = L = 0.35$ m. The gap

Table 1 Test conditions

Test #	s (mm)	Re_s	u_B (m/s)	v_G (m/s)	Q_{Inlet} (GPM)	Q_{GAP} (GPM)
$Re_L = 2.8 \times 10^5$						
1.1	1.25	1160	0.89	1.01	35.2	3.9
1.2	1.25	1313	0.89	1.15	35.34	4.56
1.3	1.25	3000	0.88	2.67	34.9	10.4
1.4	1.25	3960	0.89	3.44	35.2	13.7
1.5	3.56	1154	0.89	0.36	35.3	4.0
1.6	3.56	1310	0.89	0.40	35.35	4.5
1.7	3.56	2850	0.89	0.88	35.2	9.9
1.8	3.56	3920	0.89	1.20	35.3	13.6
1.9	5.4	1170	0.89	0.24	35.45	4.05
1.10	5.4	1300	0.90	0.27	35.3	4.5
1.11	5.4	2870	0.89	0.59	35.2	9.95
1.12	5.4	3900	0.89	0.79	35.3	13.45
$Re_L = 3.9 \times 10^5$						
2.1	0.36	330	1.22	1.01	48.55	1.15
2.2	0.36	762	1.22	2.36	48.45	2.65
2.3	1.26	1130	1.22	0.99	48.35	3.95
2.4	3.56	1170	1.22	0.36	48.15	4.05
2.5	3.56	1300	1.20	0.40	47.45	4.55
2.6	5.4	1176	1.22	0.24	48.15	4.05

flow Reynolds number Re_s is similarly determined by the mean velocity v_G in the gap and the gap width s.

The mean velocities u_B and v_G are derived from two calibrated turbine flow meters installed in the mainstream path gap flow paths. The test surface was throughout all experiments only slightly heated, $\dot{q} = 19.5 \times 10^3$ W/m^2. The corresponding temperature difference between wall and free stream was at most 5 deg ($T_\infty \approx 18$°C).

Results and Discussion

In modeling the effects of leakage flow related to the suction side of a gas turbine blade, systematic comparisons of flows with different gap flow and mainstream parameters were performed. The gap flow has a source character with the clearance gap acting as a line source to the mainstream fluid. The source strength distribution along the gap was dictated by the local pressure difference across the gap. As a result, the amount of flow injected through the gap generally increased in the downstream direction. In addition, the cross section of the test channel was constant, and the injection produced an acceleration of the mainstream flow.

Initial tests were conducted with a large gap size ($s = 5.36$ mm) and a comparatively small gap flow Reynolds number, $Re_s = 1300$. For these tests the mainstream Reynolds number Re_L was maintained constant at 2.8×10^5. Figure 2 presents the measured heat transfer development along the gap. The results reveal substantial source flow effects.

Closest to the gap ($z \to 0$), a strong increase of the local heat transfer rates (200 percent and more) can be observed for all four measurement planes. Farther distant from the gap, however, the heat transfer variations reveal systematic differences at each plane. At $x = 0.2$ m, the data show a monotonic decrease of the Stanton number toward a uniform value far distant from the sidewall. For $x = 0.24$ m and farther downstream the drop of the heat transfer rates is interrupted by an additional heat transfer increase starting at 2–4 mm distance from the gap. The spanwise influence region of gap flow strongly enlarges in the downstream direction. At the largest distances for the sidewall the results reveal slightly but systematically lower Stanton numbers (10–15 percent) than obtained for channel flow in the absence of corner source

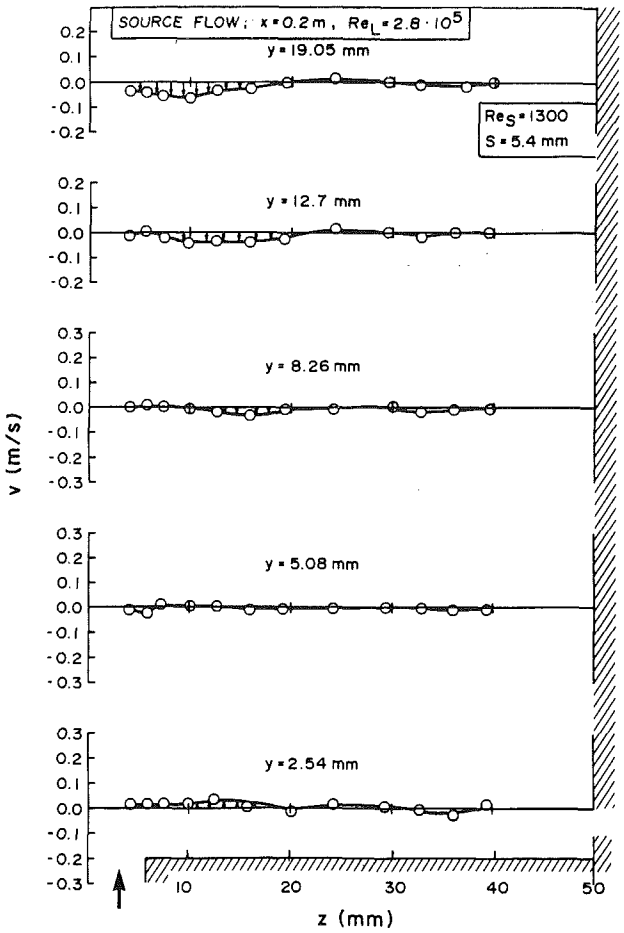

Fig. 3 Normal velocity component near the gap leading edge

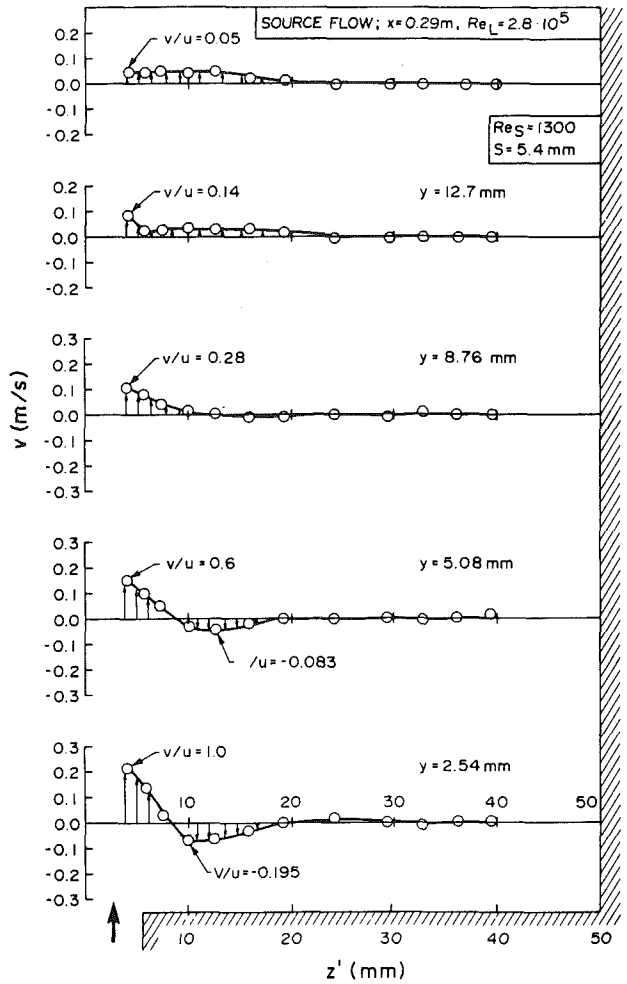

Fig. 4 Normal velocity component downstream from the gap leading edge

flow. Again, the uncertainty in the local Stanton numbers is estimated to be ±6 percent, based on the methods of Kline and McClintock [16].

To help better understand the nature of the observed heat transfer enhancement near the tip, detailed LDA measurements were conducted to define the flow development along the gap (Figs. 3–8). The data were obtained for the two basically different heat transfer distributions observed in plane 1 ($x = 0.1$ m) and plane 3 ($x = 0.29$ m). Figure 3 displays the transfer y-velocity components as measured near the leading edge of the gap ($x = 0.2$ m), and reveals two regions with normal velocities in opposite directions. Close to the test surface ($y = 2.54$ mm) a slight injection of fluid through the gap can be observed. The injection rate at this streamwise position near the leading edge of the gap is weak as a result of a nonuniform source flow distribution, which increases in the downstream direction. It should be emphasized that the injection gap flow appears stratified since the data show no evidence for vortex formation near the gap. Stratified flow injection is thus a dominant feature of the heat transfer distribution observed in plane 1 ($x = 0.2$ m, Fig. 2). Figure 3 shows also that the maximum velocity at $y = 2.54$ mm appears outward from the edge of the gap. This can be interpreted as deflection of the incoming flow into the spanwise (z) direction.

At $y = 5.08$ mm, no normal velocity can be detected, whereas at larger heights a new secondary motion has developed, which sweeps the incoming flow downward and farther away from the sidewall. The new secondary motion is thought to be due to the blockage effect produced by the jetlike source flow through the gap.

Figure 4 illustrates the normal velocity distributions at the farther downstream position ($x = 0.29$), where strong nonuniformities in the spanwise heat transfer development were observed. Figure 4 indicates that the heat transfer character in this region is produced by pronounced flow recirculation in the zone near the gap. The recirculation is demonstrated by the alternating normal velocity directions present at $y = 2.5$ mm and $y = 5.08$ mm above the plate. The apparent reattachment point of this recirculation zone is located approximately 12 to 15 mm from the edge of the gap, which is indicated by disappearing v components in the flow. At the same spanwise location the Stanton numbers describe, as is to be expected, a maximum in local heat transfer rates. At larger heights from the plate ($x \geq 8.7$ mm), the vorticity is replaced by a stratified deflection of the flow away from the gap. This process is now opposite from the flow deflection observed in plane 1 at the larger heights, which indicates a complexity in source flow effects even far distant from the gap. Figures 5 and 6 present the mainstream velocity distributions $u(x, y)$ at the same two downstream positions $x = 0.2$ m and $x = 0.29$ m. Both figures demonstrate the blockage effect due to flow injection in the corner with severely reduced mainstream velocities near the gap. With increasing height from the plate the impact of injection on the mainstream velocities gradually declines. The blockage is particularly evident in Fig. 6 for the farther downstream location ($x = 0.29$ m), where extended flow recirculation near the gap was observed. For comparison, the corresponding velocities measured for the same mainstream flow in the absence of corner injection are shown as dashed lines on the figure. The blockage effect has reduced the velocities nearest the gap from

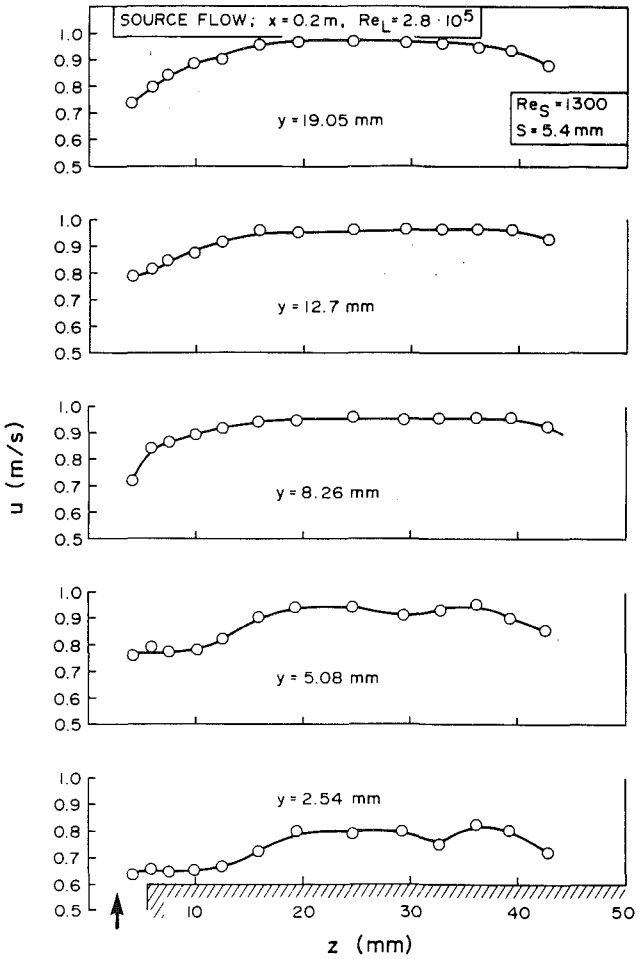

Fig. 5 Streamwise velocity component near the gap leading edge

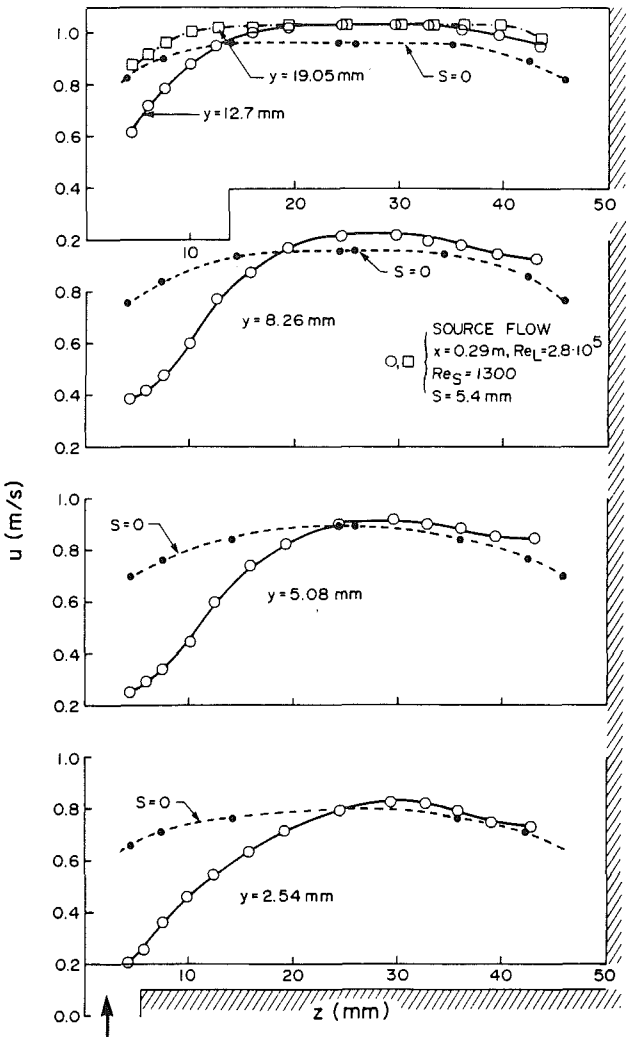

Fig. 6 Streamwise velocity component downstream from the gap leading edge

0.6 m/s to 0.2 m/s, or approximately 65 percent. Furthermore, it can be seen that the gap flow effect has strongly extended spanwise and covers almost half of the channel width.

Figures 7 and 8 present the velocity fluctuations as influenced by the injection through the clearance gap. Figure 7 shows the local turbulence distributions associated with the stratified and weak flow injection in plane 1 ($x = 0.2$ m). The overall higher turbulence level for $y < 8$ mm is associated with the channel floor boundary layer. Closest to the test surface ($y = 2.54$ mm), the turbulence distribution is very similar to those measured without injection [12]. Farther distant, however, a distinct main and source flow interaction is reflected in the distorted turbulence distributions. This effect is likely related to the previously shown deflection of the flow at larger heights for the plate.

The results of Fig. 8 were obtained for the $x = 0.29$ m downstream location. The data demonstrate that the vortices produced by flow injection lead to very intensive velocity fluctuations, much higher than those for stratified source flow injection. Nearest the gap, Fig. 8, turbulence intensities (based on the local velocity) up to 55 percent were measured, which indicates that this flow is probably not properly classified as steady. The turbulence, or more accurately, the "relative variation of the mean velocity," is reduced farther away from the gap as a result of the simultaneously increasing mainstream velocities. In analyzing the turbulence data in more detail, it can be seen that close to the gap the velocity fluctuation first increases from approximately 40 percent at $y = 2.5$ mm to 55 percent at $y = 5$ mm. Beyond $y = 5$ mm the tendency is reversed; the turbulence intensity then systematically decreases both near the gap and also farther inside the channel.

It is likely that the large velocity fluctuations near the wall strongly contribute to the enhancement of the heat transfer rates within the influence region of the gap. At the largest distance from the plate ($y = 19$ mm) the source flow effects are reduced, which is also confirmed by the close agreement with the corresponding data obtained with closed gap.

To summarize at this point, the information derived from the detailed flow measurements and corresponding heat transfer together provides considerable insight into the corner injection phenomena. The investigation was performed for only one particular combination of gap flow and mainstream parameters, but reveals a flow situation that has previously been observed in cascade experiments [9, 10] without heat transfer. In those studies, leakage flow also starts with stratified injection near the leading edge of the gap, and only farther downstream separates and forms into a vortex. This qualitative flow agreement lends confidence to the present modeling of the phenomena, and suggests that the typical suction side, near-tip heat transfer character on turbine blades may be as observed in the tests just described: upstream, a monotonic spanwise decrease of heat transfer enhancement and lower overall enhancement, and downstream, additional heat transfer enhancement starting farther away from the gap and higher overall enhancement. This picture is consistent with the often observed character of blade tip durability

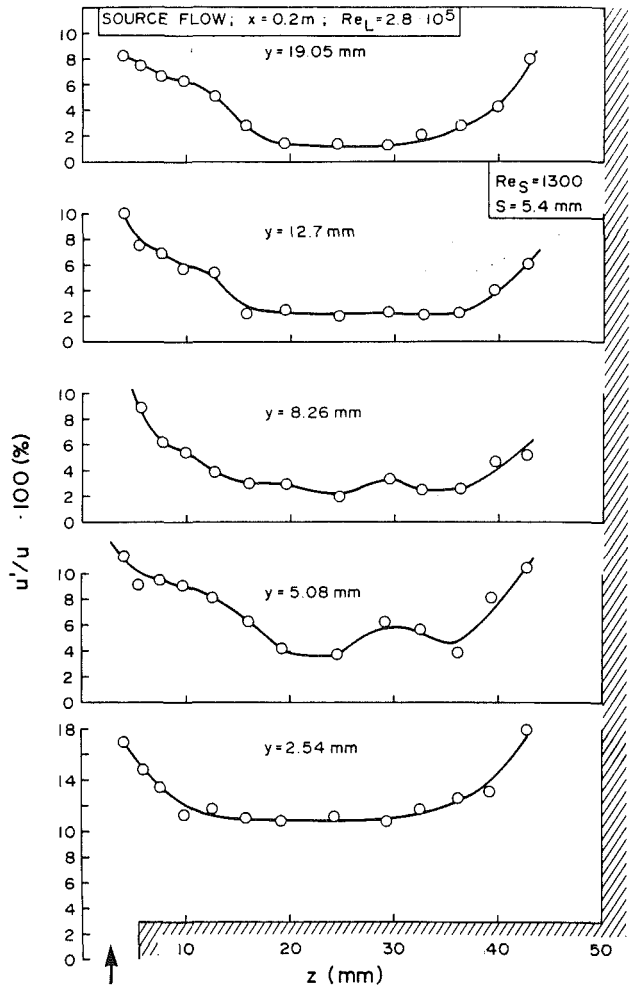

Fig. 7 Turbulence distributions near the gap leading edge

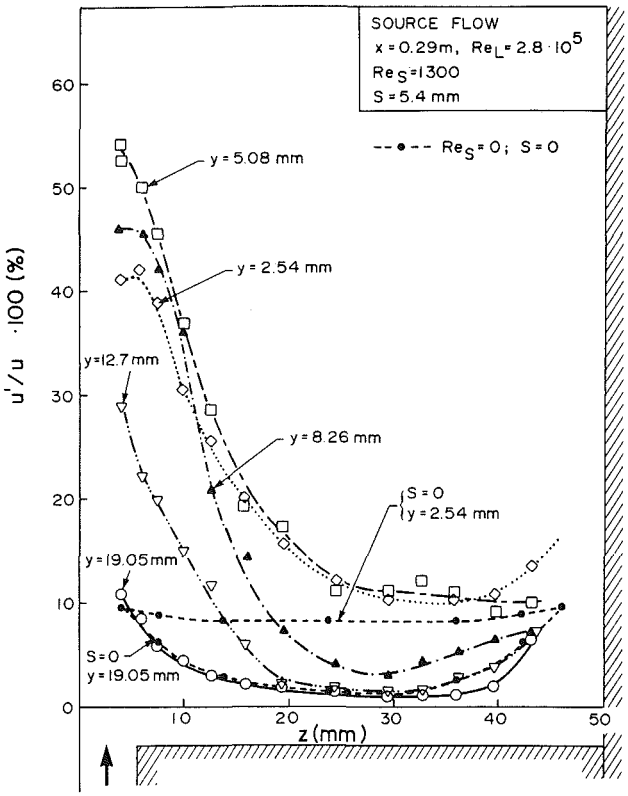

Fig. 8 Velocity fluctuations in regions of gap flow separation

problems; moreover, the latter spanwise decreasing-increasing behavior displays a striking similarity to some of the few actual turbine local heat transfer data available. In [17], local spanwise heat transfer rates were obtained at a fixed suction side streamwise location, with the highest values (about 40 percent above the midspan value) measured at 80 percent span. Closer to the tip, at 90 percent span, the enhancement was down to 20 percent, which is very consistent with the behavior shown in Fig. 2 at $x = 0.29$ m.

Heat transfer measurements were also made for combinations of gap flow and mainstream parameters different from the typical combination just discussed in detail. Figure 9 presents some results obtained with smaller injection intensity. Compared to the previous case the gap size and gap flow Reynolds number are reduced from $s = 5.4$ mm to $s = 0.36$ mm and from $\mathrm{Re}_s = 2800$ to $\mathrm{Re}_s = 330$. In terms of a momentum injection parameter M

$$M = \frac{\dot{m}_{\mathrm{gap}} \cdot V_G}{\dot{m}_{\mathrm{inlet}} \cdot u_B} \tag{4}$$

the injection intensity has been reduced from $M = 0.037$ to $M = 0.017$. As a result of this parameter variation the heat transfer development near the gap is for all streamwise positions similar to the distribution obtained previously for only the relatively weak stratified outflow out of the gap. Therefore it can be inferred that for these weak injection conditions, no vortex production is induced all along the gap. In consequence the remaining heat transfer effect is comparatively weak and confined to a zone much closer to the gap. The data presented

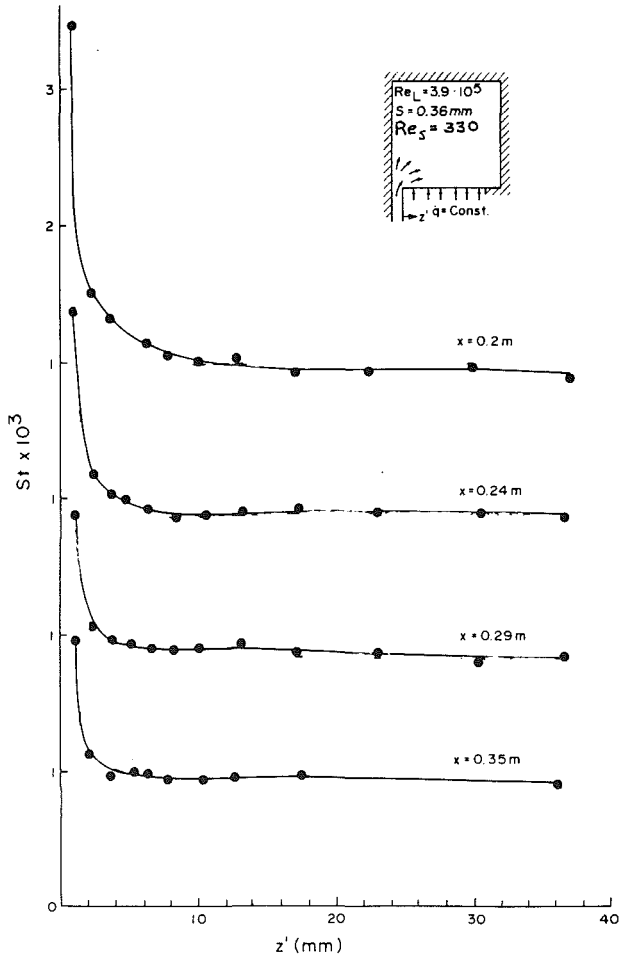

Fig. 9 Heat transfer with small gap and small gap flow

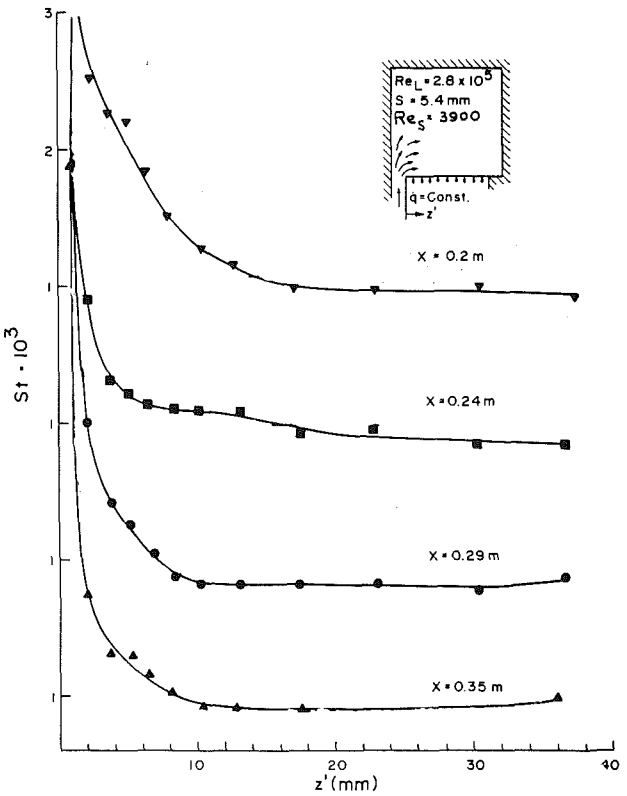

Fig. 10 Heat transfer with large gap and large gap flow

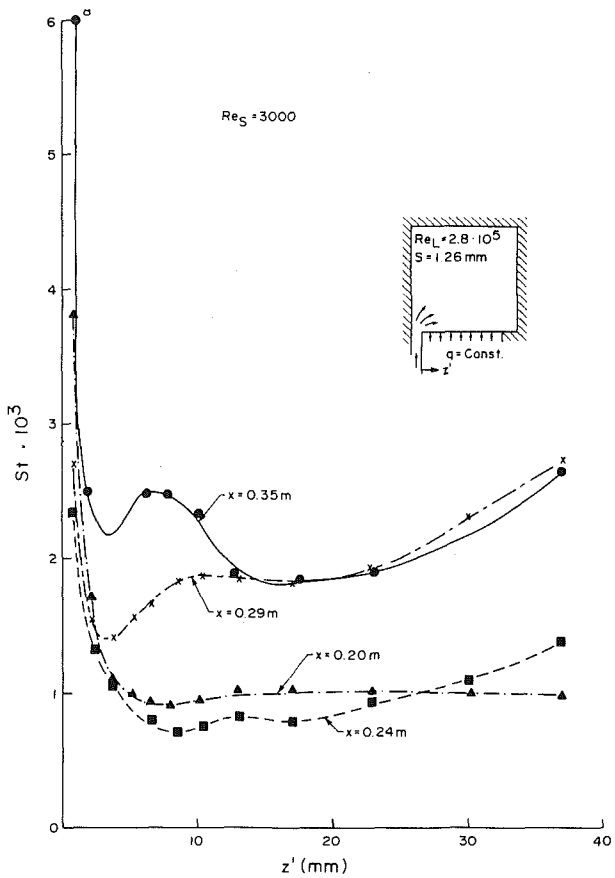

Fig. 11 Heat transfer with small gap and moderate gap flow

in Fig. 9 indicate that the detrimental tip leakage heat transfer effects on turbine blades can be significantly reduced by minimizing both gap size and gap flow intensity through accurate blade tip design.

Figure 10 presents another set of heat transfer results that appear in form similar to those of Fig. 9 with weak injection. The flow parameters of Fig. 10 are, however, totally different. The gap flow Reynolds number is increased to 3900 and the gap size is also increased from 0.36 mm to 5.4 mm. Correspondingly, the relative injection momentum is raised by a factor of 20 from $M=0.017$ to 0.34. Nevertheless, Fig. 10 shows monotonic spanwise heat transfer distributions, which appear to belong to the category of stratified gap flow injection without vortex formation.

In contrast to Fig. 9, however, the Fig. 10 results reveal very high heat transfer augmentation (up to 300 percent) near the gap. It should be noted also that the largest augmentation is at the most upstream measurement plane ($x=0.2$ m). Similar behavior was repeatedly observed throughout the experiments, as for instance also for the previously discussed case shown in Fig. 9. This latter effect might be the result of streamwise increases of the effective fluid temperature near the gap as a consequence of gap flow and mainstream interaction.

Another set of heat transfer experiments describing still another source flow and mainstream interaction situation is shown in Fig. 11. The experiments were performed with small gap size $s=1.2$ mm, which corresponds to approximately 2 percent of the channel width. The gap flow Reynolds number, 2800, is similar in magnitude to that of the previous case, Fig. 10. This combination produces high injection momentum, $M=0.9$. The results show a large impact of such strong injection. A prominent feature is an additional heat transfer increase starting out from the opposite sidewall of the test section ($z\rightarrow 50$ mm). This effect is continuously growing in the downstream direction and is highly developed in plane 3 ($x=0.29$ m) and plane 4 ($x=0.35$ m). At these planes there is

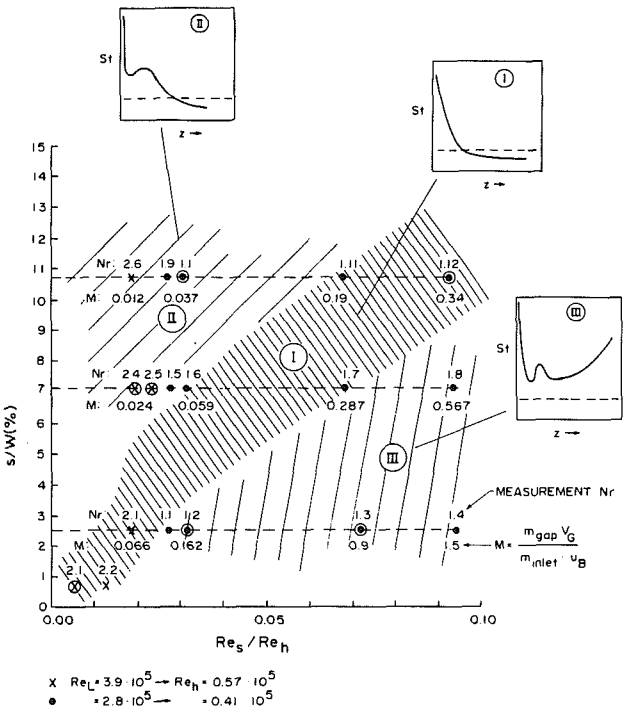

Fig. 12 Flow classification

an overall heat transfer enhancement of the order of 100 percent and more. It seems plausible that this very large gap flow effect is the result of a secondary vortex flow enveloping the whole test section area, with the source flow influence no longer confined to a zone near the gap.

In an attempt to consolidate all of the heat transfer results acquired in the present study, Fig. 12 classifies gap injection effects by categorizing the parameter combinations associated with the different variations in heat transfer and flow development observed. Each test point is identified by values of nondimensional gap size s/W, normalized gap flow Reynolds number Re_s/Re_h, and injection momentum parameter M.

Figure 12 includes *all* of the results of the present study acquired for various combinations of gap sizes, source flow intensities, and mainstream Reynolds numbers. The tests for which detailed results have been presented in this paper are identified in the figure by a surrounding circle. Further information about individual test conditions can be found in Table 1, which contains the test identification number, N_r, also shown for each point in Fig. 12.

To interpret Fig. 12, recall that three different categories of source flow effects have been observed in the present tests. Each heat transfer measurement set is assignable to one of these categories. Category I is defined as those experiments that demonstrated stratified flow injection over the total length of the gap. Category II is those experiments associated with downstream vortex formation near the gap, and category III contains the flow situations that apparently lead to a rotation of the total channel flow. Figure 12 shows that these source flow categories partition into characteristic regimes or combinations of gap size and Reynolds number. Category II, for instance, which is associated with vortex formation near the gap, is most likely to develop for combinations of larger gap sizes s/W and lower gap Reynolds numbers. As also indicated in Fig. 12, this category of flow is generally associated with smaller values of the momentum injection parameter M. Category III, in contrast, which represents the strongest overall injection impact, is to be expected with small gap sizes and large gap Reynolds numbers, combinations that yield high values of M.

Finally, the stratified flow injection of Category I is described by a regime of parameter combinations located between those of category II and category III. Flows of category I are the result of combinations of gap size and Reynolds number that lead to injection momentum of intermediate intensity.

Summary and Conclusions

Corner source flow experiments have been performed in a water tunnel to model the influence of tip leakage flow on heat transfer and flow development along the suction side of a gas turbine blade. The results indicate that a primary effect of the leakage flow is a strong increase of local heat transfer rates immediately adjacent to the gap. This increase is similar to the near-gap increases measured in the companion Part I of this study for sink flow on the pressure side of the blade except that the heat transfer enhancements for the suction side are even higher.

On the pressure side, however, the large near-gap heat transfer enhancement appears to be directly associated with the strong acceleration of leakage flow into the clearance gap, as predicted by the sink flow analysis [11]. The mechanism for the even higher near-gap enhancement on the suction side must be quite different from acceleration into a sink, but the explanation is not readily apparent from the present study. In [10], unexpected low pressures, similar to those measured on the pressure corner, were measured along the suction side corner with micro-sized pressure taps, and this could indicate the presence of a very small but intense vortex located at the gap edge.

The region of primary enhancement closest to the gap varied from 2 to 10 gap widths, but for some combinations of gap size and flow, a second increase in heat transfer farther out from the gap extends the spanwise extent of the source flow considerably. This latter behavior appears to occur with combinations of gap size and flow encountered in practice, and appears to agree with some limited available actual turbine data, previously thought to be anomalous. This behavior, and two other different types of heat transfer behavior observed in the present study, have been partitioned into three categories, and the boundaries between them have been tentatively identified for designers. In all cases the observed heat transfer effects appear to be very important from the standpoint of blade tip durability, and appear to at least partially account for the sometimes unexplained thermal distress and material failures experienced on blade tips in practice.

References

1 Booth, T. C., Dodge, P. R., and Hepworth, H. K., "Rotor-Tip Leakage: Part I—Basic Methodology," ASME *Journal of Engineering for Power*, Vol. 104, 1982, pp. 154–161.

2 Wadia, A. R., and Booth, T. C., "Rotor Tip Leakage: Part 2—Design Optimization Through Viscous Analysis and Experiment," ASME *Journal of Engineering for Power*, Vol. 140, 1982, pp. 162–169.

3 Mayle, R. E., and Metzger, D. E., "Heat Transfer at the Tip of an Unshrouded Turbine Blade," *Proceedings, 7th Int. Heat Transfer Conf.*, Vol. 3, 1982, pp. 87–92.

4 Metzger, D. E., Bunker, R. S., and Chyu, M. K., "Cavity Heat Transfer on a Transverse Grooved Wall in a Narrow Flow Channel," ASME *Journal of Heat Transfer*, Vol. 111, 1989, pp. 73–79.

5 Funn, M. G., Rae, W. J., and Holt, J. L., "Measurement and Analysis of Heat Flux Data in a Turbine Stage: Parts 1 and 2," ASME Papers No. 83-GT-121 and No. 83-GT-122, 1983.

6 Hansen, A. G., and Herzig, H. Z., "Secondary Flow Studies in Turbomachines," *Trans. ASME*, Vol. 77, 1955, pp. 249–266.

7 Allen, H. W., and Kofskey, M. G., "Visualization Study of Secondary Flows in Turbine Rotor Tip Regions," NACA TN 3519, 1955.

8 Graham, Y. A. H., "Investigation of Tip Clearance Cascade in a Water Analogy Rig," ASME *Journal of Engineering for Gas Turbines and Power*, Vol. 108, 1986, pp. 38–46.

9 Bindon, J. P., "Visualisation of Axial Turbine Tip Clearance Flow Using a Linear Cascade," Cambridge University Engineering Department, TR 122, 1986.

10 Bindon, J. P., "Pressure and Flowfield Measurements of Axial Turbine Tip Clearance Flow in a Linear Cascade," Cambridge University Engineering Department, TR 123, 1986.

11 Metzger, D. E., and Rued, K., "The Influence of Turbine Clearance Gap Leakage on Flowpath Velocity and Heat Transfer Near Blade Tips, Part I: Sink Flow Effects on Blade Pressure Sides," ASME Paper No. 87-GT-XX.

12 Rued, K., Murthy, J. Y., and Metzger, D. E., "Turbulent Convection Heat Transfer at the Corner Intersection of Heated and Unheated Walls in a Square Flow Channel," ASME HTD-Vol. 87, 1987, pp. 49–55.

13 McLaughlin, D. K., and Tiedermann, W. G., "Biasing Correction for Individual Realization of Laser Anemometer Measurements in Turbulent Flows," *Phys. Fluids*, Vol. 16, No. 12, 1973.

14 Stevenson, W. H., Thompson, H. D., and Gould, R. D., "Laser Velocimeter Measurements and Analysis in Turbulent Flows With Combustion, Part II," School of Mechanical Engineering, Purdue University, West Lafayette, IN, Report AFWAL-TR-82-2076, July 1983.

15 Tiedermann, W. G., "Interpretation of Laser Velocimeter Measurements in Turbulent Boundary Layers and in Regions of Separation," School of Mechanical Engineering, Purdue University, West Lafayette, IN, 1977.

16 Kline, S. J., and McClintock, F. A., "Describing Uncertainties in Single Sample Experiments," *Mechanical Engineering*, Vol. 75, 1953.

17 Dunn, M. G., "Heat Transfer Measurements for the Rotor of a Full Stage Turbine," ASME JOURNAL OF TURBOMACHINERY, Vol. 108, 1986, pp. 90–97.

J. Moore

J. G. Moore

G. S. Henry

U. Chaudhry

Mechanical Engineering Department,
Virginia Polytechnic Institute and State
University,
Blacksburg, VA 24061

Flow and Heat Transfer in Turbine Tip Gaps

The effects of Reynolds number on flow through a tip gap are investigated by performing laminar flow calculations for an idealized two-dimensional tip gap geometry. The results of the calculations aid in understanding and reconciliation of low Mach number turbine tip gap measurements, which range in tip gap Reynolds number from 100 to 10,000. For the higher Reynolds numbers, both the calculations and the measurements show a large separation off the sharp edge of the blade tip corner. For a high Reynolds number, fully turbulent flow calculations were also made. These also show a large separation and the results are compared with heat transfer measurements. At high Mach numbers, there are complex shock structures in the tip gap. These are modeled experimentally using a water table.

Introduction

Turbine blade life and performance deterioration are two factors in gas turbine design whose prediction requires a detailed understanding of the flow and heat transfer in turbine tip gaps. Recently, several experimental investigations of incompressible flow have been performed (Graham, 1985; Bindon, 1986a, 1986b, 1987a, 1987b, 1987c; Moore and Tilton, 1988) and an experimental study of heat transfer, from essentially incompressible flow, to a simulated turbine rotor blade tip has been published (Metzger and Bunker, 1985). But, as yet, it appears that only Wadia and Booth (1982) have attempted to calculate tip leakage flow in detail and there appear to be no published attempts to calculate heat transfer to turbine blade tips. There also appear to be no published studies of compressible flow in tip gaps, either experimental or computational.

It is clear that there is a need for improved prediction capability for heat transfer to the tips of unshrouded turbine rotor blades. The designer needs to know the metal temperature distributions at the blade tips in order to predict the thermal stresses, the oxidation rate, and the susceptibility to erosion and corrosion. With this information, he will be better prepared to assess the relative importance of tip deterioration in determining blade life and to assess the need for improved tip cooling or improved material properties.

In the present paper, two-dimensional flow calculations are used to reconcile the available experimental data on flow separation and reattachment, tip static pressures, and contraction coefficients. A calculation of the combined heat transfer in the flow and in the blade tip allows an estimate of the corresponding maximum blade metal temperature in an engine to be made. Results of a water table flow simulation are described that suggest the sort of shock configurations that can be expected with transonic and supersonic flow in tip gaps.

Contributed by the International Gas Turbine Institute and presented at the 33rd International Gas Turbine and Aeroengine Congress and Exhibition, Amsterdam, The Netherlands, June 5–9, 1988. Manuscript received by the International Gas Turbine Institute September 30, 1987. Paper No. 88-GT-188.

Velocity and Pressure at Low Mach Numbers

Potential Flow. Moore and Tilton (1988) found that potential flow for about the first $2h$ (h = tip gap height) of the tip gap followed by mixing explained their wall pressure measurements upstream of and in the tip gap of the VPI&SU cascade. In two dimensions, the potential flow into a tip gap may be viewed as one half of the flow field for potential flow into an orifice. Milne-Thomson (1968) presents in closed form the solution for potential flow into an orifice in terms of complex variables giving equations for the position, velocity, and the complex potential. The velocity field described by his equations is shown in Fig. 1. The velocity vectors cover only part of the tip gap region with the remainder being a region of no flow. Thus the potential flow does not stay attached; instead it separates off the tip gap corner. Note also that the magnitude of the velocity all along the free streamline including near the tip corner is the same.

The static pressure in the no-flow region is uniform and it is useful to evaluate it in terms of a static pressure coefficient based on the mean velocity in the tip gap, $U_m = \dot{m}/\rho h$.

$$C_{ps} = [p - (p_o - 0.5\rho U_m^2)]/(0.5\rho U_m^2) \quad (1)$$

For the potential flow, $U_m = U\pi/(\pi+2) = 0.61U$, where U is the terminal velocity, and the jet covers 61 percent of the tip gap height. The static pressure coefficient, C_{ps}, in the no-flow region is then -1.68.

Laminar Flow Calculations. Two-dimensional laminar incompressible flow calculations for an idealized tip gap geometry have been performed for three Reynolds numbers, 110, 1100, and 11,000. The Reynolds number is based on the mean velocity in the tip gap and the tip gap height. The calculations were performed using the Moore Elliptic Flow Program, which solves the steady form of the Navier–Stokes equations using a pressure correction method (Moore, 1985a). For accuracy, the convection terms are discretized using an upwind control volume approach (Moore, 1985b).

Geometry. The 31 by 21 by 2 grid used for the calculations

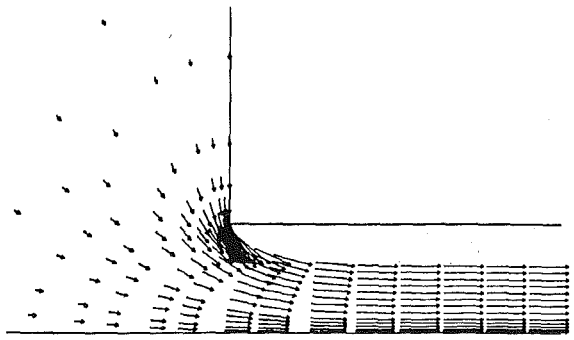

Fig. 1 Potential flow velocity vectors

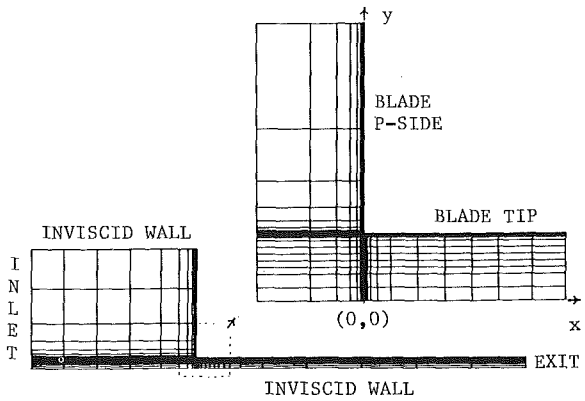

Fig. 2 Grid for laminar flow calculations

with Re = 11,000 is shown in Fig. 2. The computational inlet is 15 tip gap heights upstream of the tip gap inlet. The overall contraction (inlet height:tip gap height) is 11:1. According to Rouse (1946), this contraction is sufficiently high that, in the region of the tip gap, the potential flow for this configuration differs very little from flow entering an orifice from an infinite tank. For Re = 11,000, the calculations extended 30 tip gap heights downstream of the tip gap inlet. For Re = 110 and 1100, a tip gap length of 10 tip gap heights was sufficient to ensure no reverse flow at the tip gap exit.

An enlargement of the grid near the "pressure side/blade tip" corner is also shown in Fig. 2. The near-wall spacing was $0.025h$ next to the corner, and increases in relative spacing of no more than a factor of two were used to spread the grid points away from the corner.

Initialization and Boundary Conditions. An extremely simple initial guess for the whole flow field was used to start the calculations: in S. I. units, $u = 5$, $v = 0$, $\rho = 1$, $p - p_o = -12.5$. At the computational inlet, the total pressure corresponding to the initial guess was held fixed ($p_t = p_o$) as was the inlet flow angle ($v/u = 0$). The pressure was kept uniform across the inlet but was not imposed as fixed. At the exit, the pressure was also kept uniform, the level being determined by the inlet mass flow rate of the initial guess.

The top wall (at $y/h = 11$) and the bottom wall ($y = 0$, corresponding to the shroud in a blade row) were treated as symmetry planes, i.e., inviscid walls, so that it was not necessary to grid close to them. The walls adjacent to the corner, corresponding to the pressure surface and blade tip in a blade row, were viscous walls with $u = v = 0$ at the wall.

Calculated Velocities. The velocity vectors in Fig. 3(*a*), for Re = 110, show the velocity very quickly establishing a parabolic profile, corresponding to fully developed laminar flow. There is no significant separated or dead flow region as for the potential flow.

With viscous effects a factor of 10 smaller than for Re = 110, the velocity vectors for Re = 1100 (Fig. 3*b*) show the flow developing a large dead flow or separated region similar to the potential flow. The calculated separation region extends 7 tip gap heights downstream of the inlet. When viscous effects are lowered by another factor of 10, i.e., for Re = 11,000, the results are qualitatively unchanged except that a distinct jet and wake extends to the computation exit at 30 tip gap heights downstream of the tip gap inlet.

Bindon, Flow Visualization. Sketches of smoke flow visualization by Bindon (1986a) are given in Fig. 4. The smoke traces are copies from his Figs. 38, 39, and 41, for which smoke was injected through holes in the blade tip. Shown on the sketch are the estimated tip gap Reynolds numbers and the distances across the blade in terms of tip gap heights.

For the 1.5 percent tip gap, the Reynolds number is 200. Like the low Reynolds number laminar calculation, Re = 110, the smoke visualization at Re = 200 shows no separation.

At the larger tip gaps, 2.5 and 5 percent, with Reynolds numbers of 350 and 700, the flow does separate from the blade tip. The separation region is from the pressure side corner to about $2h$ across the blade tip. The smoke traces are approximately perpendicular to the bulk tip gap flow direction marked as x/h on the sketch. Thus, when viewed in the x-y plane, there is a separated zone, which is a dead flow region as in the laminar calculations for Re = 1100.

Graham, Measured Velocity Profiles. Graham (1985) measured tip gap exit velocity profiles, near the suction surface, in a water flow turbine cascade model. The model was scaled to give Reynolds numbers corresponding to high-pressure axial turbine blades for small gas turbines. Scaling his overall Reynolds number of 100,000 to tip gap height, his measurements were for tip gap Reynolds numbers in the range of 1500 to 3500. Graham's measured velocity profiles, for three different tip gap heights (from his Fig. 21), are redrawn in Fig. 5, placing them in their respective locations in terms of

Nomenclature

c_f = skin friction coefficient
C_c = contraction coefficient, equation (3)
C_{ps} = static pressure coefficient, equation (1)
h = tip gap height
H = water depth
H_o = upstream (inlet) water depth
k = thermal conductivity
Nu = Nusselt number
p = static pressure
p_B = back pressure
p_t = reference (inlet) total pressure
p_A = total pressure
r = corner radius
Re = Reynolds number = $\rho U_m h/\mu$
T = temperature
u, v = Cartesian velocity components
U_m = mean velocity in tip gap
W = channel width
x, y, z = Cartesian coordinates, Figs. 2, 4
γ = ratio of specific heat capacities = c_p/c_v
μ = viscosity
ρ = density

Subscript

∞ = fully developed two-dimensional flow

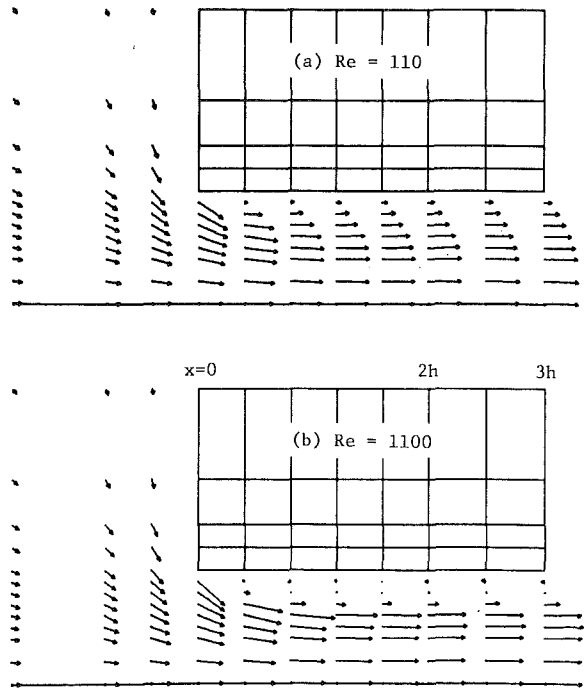

Fig. 3 Velocity vectors calculated for laminar flow

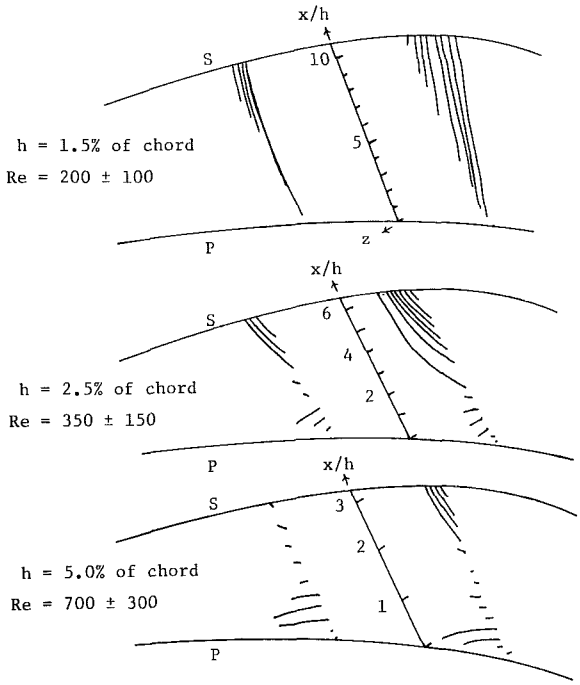

Fig. 4 Sketch of Bindon's flow visualization (1986a) for smoke injected through holes in the blade tip; *P, S* = blade pressure and suction surfaces; flow around blade is from right to left

x/h. These may be compared with the velocity profiles for the laminar calculations with Re = 1100 also shown on Fig. 5.

For Graham's measurements at $x/h = 2.5$ and 3.5 there is a distinct jet covering 60 to 70 percent of the height, as in the laminar calculation. However, the flow appears to have already reattached at $x/h = 2.5$, whereas for the laminar calculation the flow did not reattach until $x/h = 7$. Graham's measurements at $x/h = 5.2$ show a nearly parabolic profile similar to the calculation at $x/h = 10$. The length of the separated zone, $< 2.5h$, is consistent with Bindon's flow visualization even though Graham's measurements have higher Reynolds numbers. While the laminar calculations are

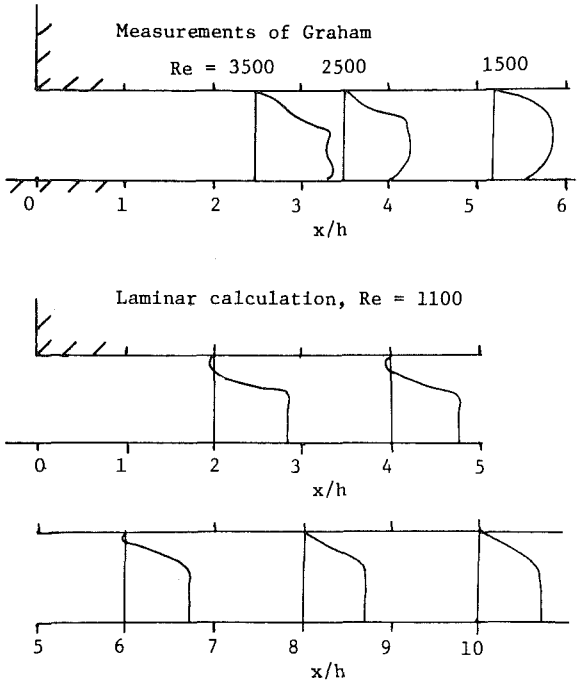

Fig. 5 Qualitative comparison of the (turbulent) velocity profiles measured by Graham (1985), for three different tip gap heights, with the velocity profiles from the laminar calculation with Re = 1100

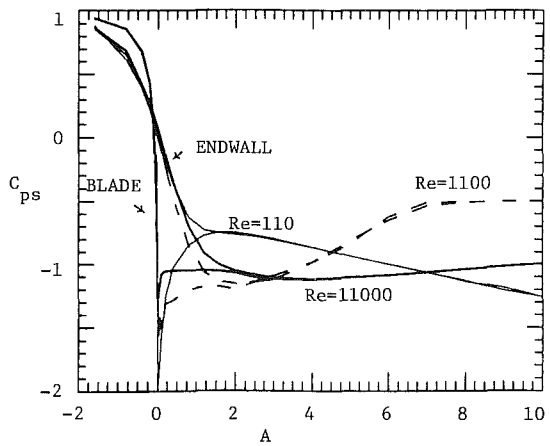

Fig. 6 Calculated static pressure coefficients on the endwall and the blade pressure and tip surfaces; $A = x/h$, except for blade when $A < 0$, then $A = 1 - y/h$

qualitatively similar to Graham's results, they show the importance of including turbulence in tip gap calculations in this Reynolds number range.

Calculated Wall Static Pressures. The wall static pressure coefficients for all three laminar calculations are shown in Fig. 6. For each tip Reynolds number, two curves are drawn. One is the static pressure along the endwall; the second curve is the static pressure coefficient along the "pressure surface" and then along the "blade tip."

The pressure distributions for the three cases show markedly different character. For Re = 110, the pressure falls continuously along the endwall. On the blade, after falling along the pressure surface to a low value at the corner, the pressure then rises along the blade tip for the first $2h$; then the pressure across the tip gap height is approximately uniform and the pressure falls linearly to the exit, due to friction on the walls.

For Re = 1100, the pressure along the endwall falls until $x/h = 2$, then rises, as the jet and wake mix. After the flow

Table 1 Effect of near-corner grid spacing on blade tip static pressure

Near-wall grid spacing	C_{ps} on blade tip at $x/h=2$
$0.1h$	−0.75
$0.05h$	−0.90
$0.25h$	−1.07
$0.0125h$	−1.36
$0.00625h$	−1.61
potential flow	−1.68

reattaches, at about $x/h=7$, the pressure remains approximately constant. Along the blade tip, the recovery of the pressure, after the very low pressure at the corner, occurs over a much shorter distance than for Re = 110, so that there is a region of uniform pressure between $x/h=1$ and 2.

For Re = 11,000, only the corner point has a low static pressure; otherwise the pressure along the blade tip is approximately constant wth C_{ps} varying between −1.0 and −1.1. The level is somewhat higher than for the potential flow, which has a uniform $C_{ps}=-1.68$ along the blade tip.

Two possible reasons for the difference between the calculated and potential flow tip static pressure coefficients were investigated. First, the mass-averaged total pressure loss for this case (Re = 11,000) was checked. It was found to be near zero, as it should be for this nearly inviscid flow. In particular, in terms of a total pressure loss coefficient

$$C_{pt}=(p_o-p_t)/(0.5\rho U_m^2), \qquad (2)$$

the mass-averaged total pressure loss varied from 0 to +0.08 to −0.1 back to −0.02. This provides a numerical error band of ±0.1, much smaller than the difference between the calculated and potential flow tip static pressure coefficients.

Effect of Near-Wall Grid Spacing on Calculated Results. Another possible cause of the tip pressure discrepancy is the effective rounding of the blade tip corner due to the coarseness of the grid at the corner. This was investigated by both adding and eliminating grid lines near the blade tip corner. Qualitatively the calculated results were grid independent; for all the grids tested, the flow separated off the corner, forming a jet and wake, as expected. However, the results showed the tip static pressure (and correspondingly the height of the jet or contraction coefficient) to be quite sensitive to the near-corner grid spacing, as seen in Table 1.

Thus, in order to obtain the tip static pressure coefficient within 0.1 of the sharp-corner potential flow value, the near-corner grid spacing must be less than one percent of the tip gap height.

Bindon Blade Tip Pressure Measurements. Bindon's wall static pressure measurements within and upstream of the tip gap at 60 percent of axial chord are shown in Fig. 7. These results are taken from Figs. 19 and 20 of Bindon (1986b). The data shown are for tip gap heights of 1.0, 1.5, and 2.5 percent of chord with tip gap Reynolds numbers in the range 2500 to 7000. (The data for the 5 percent tip gap are omitted because of the very short tip gap length for this case, only $2.2h$). In Fig. 7, the static pressures have been renormalized using the mean velocity in the tip gap instead of the cascade inlet velocity. This is consistent with the definition of C_{ps} used here, equation (1). The mean velocity was estimated to be $U_m=2.77$ times the cascade inlet velocity using the measured velocity profile approximately midway across the blade at 65 percent chord, given in Bindon's Fig. 35.

The pressure distributions in Fig. 7 are all qualitatively the same as those from the laminar calculation for Re = 1100, shown in Fig. 6. The pressure falls similarly along the pressure surface for all tip gap heights. It then has a very low value at the corner. Recovery from this very low pressure occurs over the first $0.2h$ of the blade tip. The pressure is then flat, corresponding to the initial dead flow region on the blade tip in the laminar calculations, before rising again as the wake mixes out. In the case of Bindon's flow the mixing process is transitional or turbulent and so the flow mixes out much more rapidly than in the laminar calculations. Once the mixing is complete, the pressure stays approximately constant until the tip gap exit, so that similar to the laminar calculations at Re = 1100, wall shear is not a significant contributor to total pressure losses.

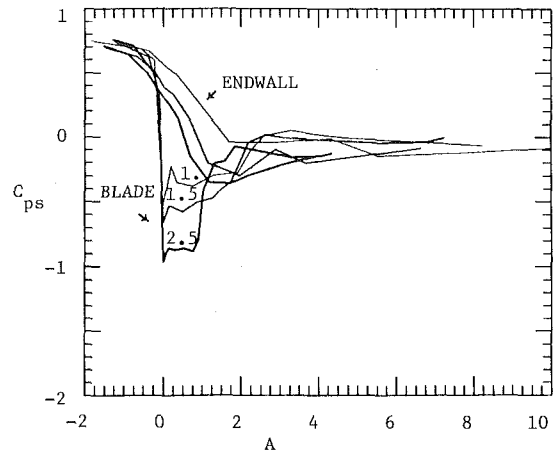

Fig. 7 Wall static pressure coefficients from Bindon's measurements (1986b) at 60 percent of axial chord, for tip gap heights of 1.0, 1.5, and 2.5 percent of chord; $A=x/h$, except for blade when $A<0$, then $A=1-y/h$

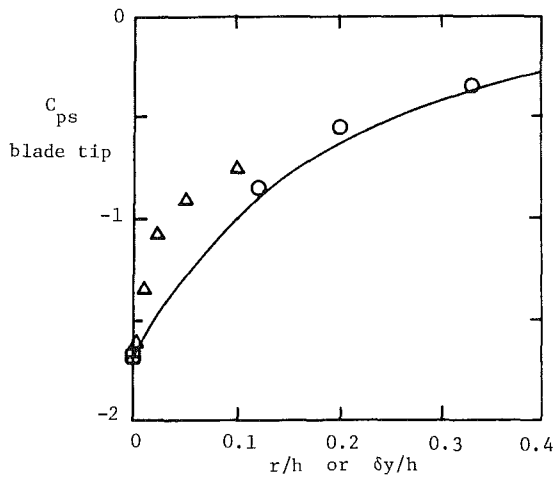

Fig. 8 Effect of rounded corner on blade tip static pressure; ○ = from Bindon's measurements, C_{ps} at $x/h=0.5$ versus corner radius/h; □ potential flow; △ = calculated for Re = 11,000, C_{ps} versus near-corner grid spacing/h; ——— McGreehan and Schotsch (1988), correlation for short orifices

Corner Radius Effect on Blade Tip Pressure. Bindon's measured pressures on the blade tip, before the large recovery due to mixing, vary with tip gap height. At $x/h=0.5$, $C_{ps}=-0.35$, −0.55, and −0.85 for tip gap heights of 1, 1.5, and 2.5 percent of chord, respectively. From the laminar calculations, we do not expect this to be a Reynolds number effect for the range Re = 2500 to 7000. Bindon gives a measured radius of curvature for the corner of the blade tip on the pressure surface of 0.3 percent of chord. The ratios of corner radius to tip gap height, r/h, are then 0.33, 0.2, and 0.12, respectively. Also, in the present laminar calculations for high Reynolds numbers, it was noted that the pressure on the blade tip was a strong function of the location of the near-wall grid point; see Table 1. We therefore compare in Fig. 8 Bindon's measure blade tip pressures, as a function of r/h, with the calculated tip static pressures, as a function of near-wall spac-

ing/h. The variations are remarkably consistent, indicating the importance of corner radiusing on tip gap flow development.

Corner Radius Effect on Contraction Coefficient. From Fig. 8, it is probable that a vena contracta is formed in Bindon's flow. However, the contraction coefficient is a function of r/h and is larger than that for the sharp-edged potential flow. The contraction coefficient may be calculated from the blade tip static pressure assuming the total pressure in the jet corresponds to potential flow. Thus,

$$C_c = U_m/U_{\text{jet}} = [1/(-C_{ps}+1)]^{1/2} \tag{3}$$

For Bindon's data at 60 percent chord, we then obtain contraction coefficients of 0.86, 0.80, and 0.74 for tip gap heights of 1, 1.5, and 2.5 percent, respectively. This value for 2.5 percent is consistent with the apparent size of the jet in Bindon's velocity measurements, shown in his Figs. 34 and 35.

Corner radius effects have also been discussed for orifice discharge coefficients by McGreehan and Schotsh (1988). Their correlation for thin orifice discharge coefficients is

$$C_{d:r} = 1 - f(1 - C_{d:\text{Re}}) \tag{4}$$

with

$$f = 0.008 + 0.992\exp[-5.5(r/d) - 3.5(r/d)^2] \tag{5}$$

where d is the orifice diameter, r is the corner radius, and $C_{d:\text{Re}}$ is the discharge coefficient of the sharp edge orifice. The hydraulic diameter of a tip gap $d = 2h$, and taking the thin orifice discharge coefficient $C_{d:r}$ as equivalent to the contraction coefficient C_c for tip gap flow, we can evaluate a blade tip static pressure coefficient as a function of r/h using equations (3), (4), and (5). Table 2 shows values of C_c and r/h evaluated in this way for a series of values of blade tip pressure in the separated flow zone. These range from $C_{ps} = 0.0$ to -1.679, i.e., from no contraction to sharp-edged potential flow. Interestingly, Fig. 8 shows this correlation of orifice data to be in excellent agreement with Bindon's tip gap measurements.

Tip Gap Exit Static Pressure. The potential flow plus mixing analysis of Moore and Tilton (1988) gives the tip gap exit static pressure in terms of the contraction coefficient. It is extended in Table 2 to include contraction coefficients other than 0.611 and mixing to a parabolic as well as to a uniform velocity profile. The parabolic profile represents reattached laminar flow while the uniform velocity profile corresponds approximately to mixed-out turbulent flow.

As noted in Fig. 7, the static pressure coefficients in the separated flow zone on Bindon's blade tip were in the range -0.35 to -0.85. Table 2 gives corresponding exit static pressure coefficients for turbulent flow of -0.03 to -0.13, in good agreement with the value of approximately -0.1 from Bindon's measurements. This is in contrast with the laminar calculation for Re = 1100, for which $C_{ps,\text{exit}} = -0.5$. These results are therefore consistent with Bindon's flows being turbulent with contraction coefficients between 0.74 to 0.86, followed by mixing to an approximately uniform velocity.

Heat Transfer to Blade Tips

Turbulent Flow Calculations. Two-dimensional turbulent flow calculations were made for two tip geometries to understand heat transfer to blade tips better. The first geometry was the same as one used for heat transfer measurements by Metzger and Bunker (1985). In particular the "pressure side/blade tip" corner had a 70 deg chamfer and the tip had no cavity. The second geometry had a 90 deg corner. For both geometries, the tip gap height was 0.508 cm, the tip gap length was 6.98 cm, and the distance from the blade tip to its "base" was taken as 5.08 cm. The tip gap Reynolds number for both

Table 2 Potential flow and mixing in tip gap

C_{ps} blade tip wake	C_c	r/h	C_{ps} exit parabolic profile laminar	C_{ps} exit uniform profile ~turbulent
0.000	1.000			0.000
−0.200	0.913	0.481		−0.009
−0.400	0.845	0.309		−0.034
−0.600	0.791	0.213		−0.070
−0.800	0.745	0.149		−0.117
−1.000	0.707	0.101	−0.572	−0.172
−1.200	0.674	0.064	−0.634	−0.234
−1.400	0.645	0.034	−0.702	−0.302
−1.600	0.620	0.009	−0.775	−0.375
−1.679	0.611	0.000	−0.805	−0.405

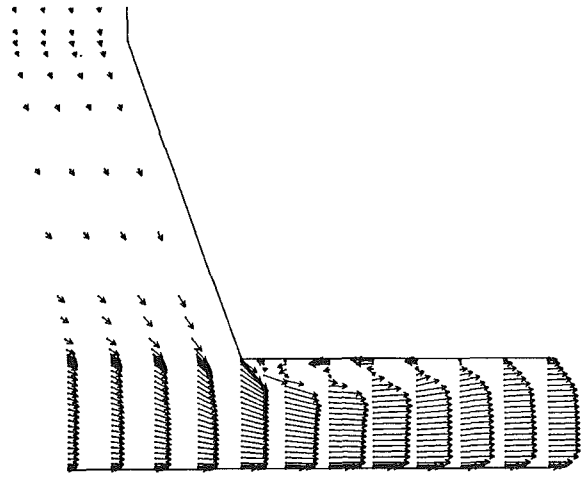

Fig. 9 Velocity vectors from turbulent flow calculation

calculations was 15,000, and the "shroud" was treated as a viscous wall with $u = v = 0$. From the experience gained in the laminar calculations, a finer grid was employed with 20 equally spaced grid points spanning the tip gap height plus mesh refinement near the wall (using factor of 2 spacings) to get the near wall point to less than 1 percent of the tip gap height. The turbulence model used for the calculations was the same Prandtl mixing length model previously employed by the authors for both turbine and compressor calculations (Moore, 1985a) with the mixing length equal to 0.41 "y" times a van Driest correction or 0.08 times the width of the shear or boundary layer. Outside of shear and boundary layers the mixing length was set to zero.

The velocity vectors for the 70 deg chamfer case are shown in Fig. 9. Unlike the laminar calculations, which had a dead flow separation zone, the separation for both of the turbulent calculations took the form of a robust recirculation. For the 70 deg chamfer, the separation bubble blocks up to 27 percent of the tip gap height and has a length of $2.2h$. For the 90 deg corner the peak blockage is 41 percent, consistent with the 39 percent expected for potential flow, and the flow reattaches at $2.9h$, consistent with the reattachment point of $3h$ deduced from the blade tip pressure measurements of Moore and Tilton. The effect of the chamfer on the flow is then simply to reduce the size of the separation bubble, similar to rounding the corner.

Heat Transfer Calculations. After the velocity field was determined assuming incompressible flow, an energy equation in the form

$$c_p \rho \mathbf{u} \cdot \nabla T - \nabla \cdot k \nabla T = 0 \tag{6}$$

was solved for T, the temperature distribution, throughout *the*

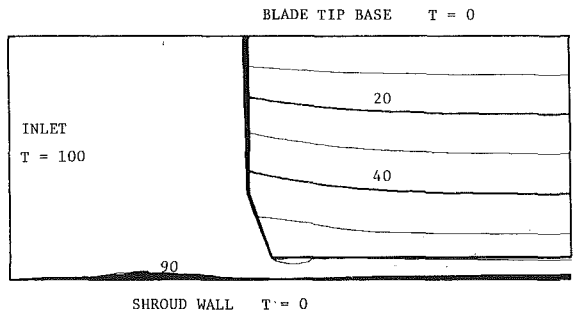

Fig. 10 Temperature contours from the solution of the energy equation (6) for flow field and blade; contour interval $\Delta T = 10$

flow and the blade. The thermal conductivity for the flow was calculated using a laminar Prandtl number of 0.7 and a turbulent Pr of 1.0.

$$k_{\text{gas}} = c_p\,(\mu_{\text{laminar}}/0.7 + \mu_{\text{turbulent}}) \tag{7}$$

The thermal conductivity of the blade was taken consistent with metal properties as 300 times the laminar thermal conductivity of the gas.

Since all the terms in equation (6) are linear in T, the levels of the temperature used for the calculation are arbitrary. For convenience, we will define the hot gas at inlet to be at $T = 100$. The cold boundary conditions were taken as $T = 0$ at the "shroud" ($y = 0$) and $T = 0$ at the base of the blade tip ($y = 11h$). These are shown in Fig. 10 together with the calculated results for the 70 deg chamfer. The suction side of the blade is not considered in the two-dimensional model and so an adiabatic boundary was taken on the blade surface at $x = x - \text{exit}$. In the calculation, heat transfer to the blade takes place through the pressure side and blade tip surfaces.

Comparison With Data of Metzger and Bunker. Figure 11 shows the heat transfer rate to the blade tip as a normalized Nusselt number. Here, $\text{Nu}/\text{Nu}_\infty$ is defined as the wall heat flux/$(T_{\text{maximum}} - T_{\text{wall}})$, evaluated locally, divided by the corresponding value for fully developed two-dimensional flow. Shown with Metzger and Bunker's measurements are two calculations: first the one described above and corresponding to the temperature contours in Fig. 9, and then a control calculation to see whether the heat transfer rate was sensitive to the boundary conditions. For the control calculation, the temperature in the blade was not solved for using equation equation (6) but was fixed at $T = 0$. The calculated results are quite insensitive to the blade boundary condition and in good agreement with the measurements.

Shown also on Fig. 11 is the normalized skin friction coefficient. $c_f/c_{f\infty}$ is simply the local wall shear stres divided by the wall shear stress for fully developed two-dimensional flow. The skin friction is negative in the separation bubble, and then increases to only about 70 percent of the fully developed flow value by 8 tip gap heights downstream of the corner. This is due to the very slow mixing out of the asymmetric velocity profile caused by the tip corner separation. The thermal boundary layer on the other hand shows Nusselt numbers within 10 percent of fully developed flow values by this location.

The maximum value of Nusselt number occurred upstream of reattachment. Metzger and Bunker measured a peak augmentation of the heat transfer coefficient by a factor of 1.6 with a corner chamfer of 70 deg; the present turbulent calculations gave 1.85 for the 70 deg chamfer and 2.05 for the right-angle corner. These results are consistent with the data of Vogel and Eaton (1985) for reattaching flow downstream of a backward-facing step. They found that "reattachment causes a local augmentation of the heat transfer coefficient by a factor of about two, the maximum heat transfer coefficient occurs slightly upstream of reattachment, . . . (and) the heat transfer coefficient recovers fairly rapidly to flat-plate behavior donwstream of reattachment." All these observations can be made about the results in Fig. 11.

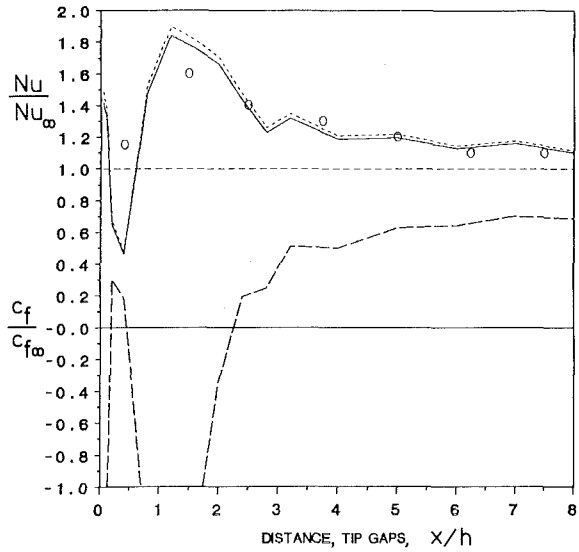

Fig. 11 Blade tip heat transfer for the 70 deg chamfer geometry: o = $\text{Nu}/\text{Nu}_\infty$ measured by Metzger and Bunker (1985); ——— $\text{Nu}/\text{Nu}_\infty$ calculated with $T = 0$ in blade; — — — $\text{Nu}/\text{Nu}_\infty$ calculated with $T = 0$ at blade tip base; —— —— —— calculated skin friction coefficient, $c_f/c_{f\infty}$

Near the corner on the blade tip at $x/h = 0.4$, the calculation gave a heat transfer coefficient of about half the fully developed value and well below the measured value. The most likely reason for this discrepancy is an underprediction of the turbulence by the mixing length model in this low velocity region. Whether or not the measurement technique could have resolved the large gradients in heat transfer coefficient that were predicted should also be considered.

The calculated blade tip temperatures for both the 70 deg chamfer and the 90 deg corner are shown in Fig. 12. Due to the high conductivity in the blade they are much smoother than might at first be expected from the results in Fig. 11. The 90 deg corner shows a higher corner temperature than the 70 deg chamfer with the corner temperature 64 percent of the difference between the gas and tip-base temperatures for the 90 deg corner and 59 percent for the 70 deg corner.

Implications for Turbine Blade Life. Turbine rotor blade metal temperatures at the tip on the pressure side can be estimated from these results. Suppose the temperature at the base of the blade tip is 1200 K (1700°F or 927°C) and the relative total temperature of the gas entering the tip gap is 1650°K (2510°F or 1377°C). The corner temperature will then be approximately 1488 K (2218°F or 1215°C) for a 90 deg corner. This is approaching the range of melting temperatures of modern gas turbine rotor blade alloys (ASM, 1973) and is a temperature level at which significant oxidation and material weight loss can rapidly occur (Wasielewski and Rapp, 1972). Thus this enhanced heat transfer to unshrouded turbine blade tips can be a major factor in determining blade life in high-temperature jet engines.

Shock Structure in High Mach Number Tip Gap Flows

In practice, turbine rotor blades in gas turbines operate with transonic flow. Flow in the tip clearance gaps then exhibits regions of supersonic flow at least over part of the blade chord. Moore and Tilton (1988) found no published literature on tip leakage flow and heat transfer in this compressible flow regime.

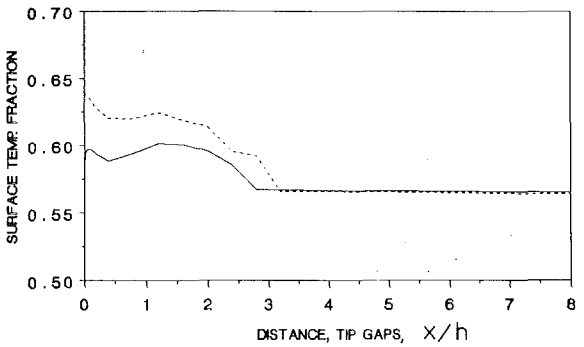

Fig. 12 Calculated blade tip temperature as a fraction of $T_{inlet} - T_{blade\ tip\ base}$; geometry: ——— 70 deg chamfer; — — — 90 deg corner

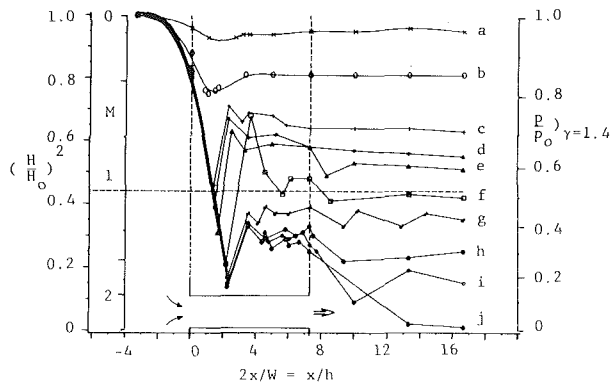

Fig. 13 Water flow analogy pressure ratios measured on the channel centerline for back pressures, $(H_B/H_o)^2$, from 0.01 to 0.96; M = isentropic Mach number

Water Table Flow Simulation. The hydraulic analogy between free surface liquid flow and two-dimensional compressible flow (Johnson, 1964) is used here in a preliminary study to determine Mach number distributions and shock patterns in a simulated turbine tip clearance gap. The flow passed through a narrow channel, of length to width ratio 3.65, on a water table, as shown in Fig. 13. With this configuration the flow modeled a tip gap of length to height $x/h = 7.3$ and its mirror image. The shroud wall of a turbine is then modeled as a plane of symmetry or inviscid wall. The upstream water depth H_o was about 2 cm and the Reynolds number based on "sonic" velocity and the tip gap height h ($= W/2 = 1.52$ cm) was about 6000. The water table flow was steady with no cavitation at the corner.

Shroud Wall Pressure Measurements. Water surface heights, H were measured along the channel centerline (the turbine "shroud wall"). According to the hydraulic analogy, the equivalent static pressure ratio for a gas with $\gamma = c_p/c_v = 2$ is $(H/H_o)^2$. The equivalent isentropic Mach number is given by $[2(H_o - H)/H]^{1/2}$. Figure 13 shows the distributions of these quantities for a range of downstream water depths, H_B. For convenience, a third scale has been added to Fig. 13 showing the equivalent static pressure ratio for a gas with $\gamma = 1.4$. This pressure scale is used in the following discussion; it makes use of the assumption that the Mach numbers in a gas flow are the same as those in a water table simulation.

With high back pressure, $(p_B/p_o)_{\gamma=1.4} = 0.97$, curve (a) of Fig. 13 shows a pressure distribution similar to those measured by Moore and Tilton and by Bindon on the endwalls of turbine tip gaps. There is a minimum pressure at about 2 tip gap heights from the inlet and a pressure rise due to flow mixing by $x/h = 3$. As the back pressure is reduced, curve (b), $p_B/p_o = 0.85$, the minimum pressure decreases and its location moves upstream. When the maximum Mach number,

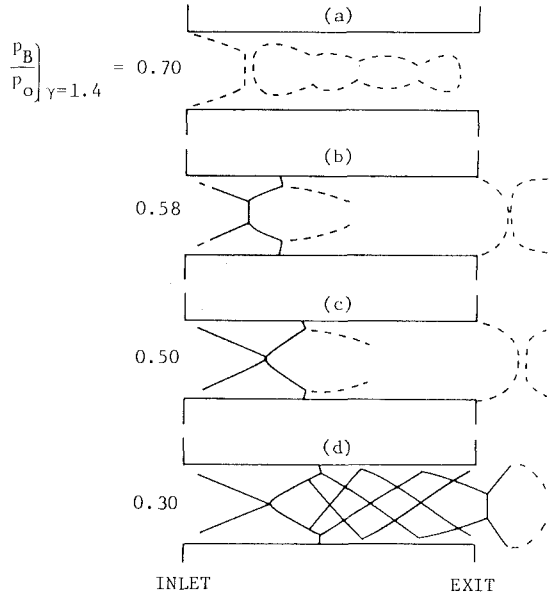

Fig. 14 Top view sketches of wave patterns in the channel

associated with the minimum pressure, becomes larger than one, curve (c) to curve (d), $p_B/p_o \sim 0.67$, the pressure rise due to mixing has been enhanced by a steeper pressure rise due to a normal shock at the channel centerline (shroud wall). Further reductions in back pressure, curves $(d\text{-}h)$, $p_B/p_o = 0.62\text{–}0.30$, cause increases in the maximum Mach number up to a peak value of about 1.8. Even lower back pressures, curves (i) and (j), $p_B/p_o < 0.30$, did not appear to change the pressure distribution in the channel significantly and the maximum Mach number remained about 1.8.

The pressure rise across the shock on the centerline changes dramatically between curves (f) and (g) indicating a change in shock structure. (The measurements of curve (f) were repeatable.)

Surface Visualization of Shock Structure. Top-view sketches of the surface flow visualizations are shown in Fig. 14. "Subsonic" flow was difficult to interpret but as the back pressure was reduced the waves became steeper and more sharply defined. Figure 14 shows as solid lines those oblique and normal shock waves that were most clearly visible; dotted lines are used for apparent flow boundaries and regions of less well defined compression and expansion.

Figure 14(a) is a sketch of the limiting case of all subsonic flow on the centerline; this corresponds to the results in curve (c) of Fig. 13, $p_B/p_o = 0.70$, and the maximum measured centerline Mach number was 0.97, just upstream of an incipient normal shock. There is also evidence of incipient oblique shocks emanating from the inlet corner regions, and these may be associated with local pressure minima and over expansion near the corners, as seen in Fig. 6. At a back pressure $p_B/p_o = 0.58$ (Fig. 14b), clearer definition was observed with oblique shocks and near-normal shocks due to Mach reflections; on the centerline, the Mach reflection was at $x/h = 1.7$ and on the walls they were at $x/h = 2.4$. On the centerline, the maximum measured Mach number was about 1.3 and downstream of the shock the flow remained subsonic.

The flow pattern in Fig. 14(c), at $p_B/p_o = 0.50$, curve (f), is similar to that for the higher back pressure in Fig. 14(b). This is the limiting case of Mach reflection on the centerline, with a maximum Mach number of about 1.5 at $x/h = 2.2$, shocking down to Mach number of about 0.7, but rapidly reaccelerating to near Mach one. It also appears to be the limiting case of all subsonic flow downstream of the Mach

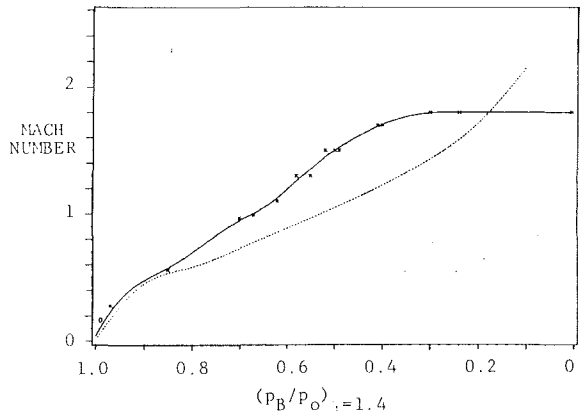

Fig. 15 Maximum Mach numbers (x) measured on the centerline (shroud wall) of the water flow channel (tip gap) compared with the Mach numbers (• • •) for isentropic flow to the back (suction surface) pressure

reflections (at $x/h = 2.2$ and 3.1) and their connecting oblique shocks.

Figure 14(*d*) for $p_B/p_o = 0.30$, curve (*h*), shows shock patterns typical of those for $p_B/p_o < 0.40$. It is also a limiting case in that little changes were observed within the channel at lower back pressures. Now the oblique shocks from the inlet corners undergo regular reflection at the centerline at $x/h = 2.2$; there is a relatively small pressure rise on the centerline and the flow remains supersonic, decreasing from a Mach number of 1.8 to 1.2. The Mach reflections at the walls remain (now at $x/h = 3.5$), and a complex pattern of weak oblique waves fills the channel downstream.

Suction Surface and Tip Gap Mach Numbers. The maximum Mach numbers measured on the centerline (shroud wall) are plotted in Fig. 15 as a function of back pressure, p_B/p_o, for a gas with $\gamma = 1.4$. Also shown is the isentropic Mach number corresponding to the back pressure. The measured values are consistently higher until the peak value of 1.8 is reached. This figure gives a useful way of relating isentropic suction surface Mach numbers in turbines to maximum Mach number in tip gaps. For example, as observed in Fig. 13, even with a suction surface Mach number of 0.78, sonic flow can occur in the tip gap. Note that here tip gap Mach numbers are estimated using the pressure ratio p_B/p_o and not the static pressure ratio across the blade, $p_{\text{suction}}/p_{\text{pressure}}$. The latter influences the direction of the flow through the tip gap and thus the mass flow rate through the gap.

The Difficulty of Turbine Shroud Measurements. The minimum static pressure on the channel centerline (turbine shroud wall) is seen in Fig. 13 to occur within about two tip gap heights of the inlet. There is then a rapid pressure rise within the next two tip gap heights. Indeed most of the significant shock structure revealed in this water flow visualization study occurred in the first four tip gap heights. In practice, turbine tip gaps are typically in the range 0 to 0.6 mm; thus the large pressure variations due to the flow development occur within about 2.4 mm. It may be difficult to resolve such variations with measurements on the stationary shroud wall of test turbines. Similarly it may be difficult to measure rapid changes in local heat transfer.

Conclusions

Scope of Present Work. The present work considers tip leakage flow over ungrooved, highly loaded blade tip sections, with the flow essentially perpendicular to the camberline. The two-dimensional flow models address the large effects of Reynolds number and Mach number on the flow development. Effects of low blade loading, Coriolis acceleration, and endwall movement relative to the rotor blade tip are not discussed.

Velocity and Pressure at Low Mach Numbers. The pressure and velocity measurements considered here, together with the flow calculations, suggest the following understanding of incompressible flow in tip gaps with lengths greather than $5h$.

Low Reynolds Number Flow, Re ~ 100 or Below. The flow does not separate off the tip gap corner. It quickly becomes fully developed laminar flow in the tip gap. Wall shear losses significantly affect the static pressure.

Medium Reynolds Number Flow, Re ~ 1000. The flow separates off the tip gap corner forming a vena contracta. The contraction coefficient depends on the radius of curvature of the tip gap corner. Small amounts of turbulence are produced when the laminar viscosity is insufficient so that the flow reattaches at about $x = 2h$. However, the turbulent viscosities are probably of the same order as the laminar viscosity so that the exit profile may more closely resemble a parabola than uniform velocity.

High Reynolds Number Flow, Re ~ 10000 or Above. Similar to the medium Reynolds number, the flow separates off the tip gap corner forming a vena contracta with a contraction coefficient depending on the radius of curvature of the tip gap corner. Turbulent mixing occurs so that the flow reattaches between $x = 2h$ and $3h$.

Heat Transfer to Blade Tips. Turbulent flow calculations gave good agreement with the distribution and level of enhanced heat transfer to the model blade tip of Metzger and Bunker. The peak heat transfer coefficient was calculated to be about 1.85 times the fully developed value downstream; its location upstream of reattachment and its magnitude are consistent with other data on reattachment heat transfer.

Solutions of the energy equation in the flow field and in the blade tip combined allow calculations of maximum metal temperatures in gas turbine rotor blades to be made. Metal temperatures at the pressure side corners of uncooled blade tips can approach melting temperatures of modern rotor blade alloys and are reaching a level where significant oxidation and material weight loss occurs. Calculations of the type performed here can contribute to blade design for increased blade life and reduced performance deterioration.

Shock Structure From Water Flow Simulation. As a preliminary study, high Mach number tip gap flow has been modeled on a water table with the shroud wall as a plane of symmetry in a channel flow. The results suggest the following picture of compressible flow in tip gaps.

With back pressure ratios, p_B/p_o, below about 0.67, i.e., suction surface Mach numbers in excess of 0.78, supersonic flow occurs in tip gaps. Overexpansion of flow around the pressure surface corner leads to an oblique shock wave, which extends from the inlet corner region to the shroud wall at about two heights into the tip gap and then reflects back to the turbine blade tip. From suction surface Mach numbers of 0.78 to 1.05, a Mach reflection occurs at the shroud wall and the peak Mach number in the tip gap, near the shroud wall, rises from 1.0 to 1.5. Above a suction surface Mach number of 1.05, regular reflection occurs at the shroud wall and the peak Mach number increases to a maximum value of about 1.8 for suction surface Mach numbers above 1.4. The second reflection, at the blade tip, is a Mach reflection occurring between about 2.4 and 3.5 heights into the tip gap.

In practice, turbine tip gaps are typically in the range 0 to 0.6 mm; thus, these shock configurations and any associated heat transfer variations will occur within 2 to 3 mm. Experimental resolution of such rapid variations may be difficult in turbines.

Acknowledgments

The authors wish to thank Rolls-Royce plc, Aero Division, for their support of this project under a cooperative agreement with Virginia Polytechnic Institute and State University.

References

ASM Handbook Committee, 1973, *Metals Handbook*, 8th ed., Vol. 8, *Metallography Structures and Phase Diagrams*, American Society of Metals.

Bindon, J. P., 1986a, "Visualization of Axial Turbine Tip Clearance Flow Using a Linear Cascade," CUED/A-Turbo/TR 122.

Bindon, J. P., 1986b, "Pressure and Flow Field Measurements of Axial Turbine Tip Clearance Flow in a Linear Cascade," CUED/A-Turbo/TR 123.

Bindon, J. P., 1987a, "Pressure Distributions in the Tip Clearance Region of an Unshrouded Axial Turbine as Affecting the Problem of Tip Burnout," ASME Paper No. 87-GT-230.

Bindon, J. P., 1987b, "Visualization of Axial Turbine Tip Clearance Flow Using a Linear Cascade," *Eighth Int. Symposium on Air Breathing Engines*, Cincinnati, OH, AIAA, pp. 436–444.

Bindon, J. P., 1987c, "Measurement of Tip-Clearance Flow Structure on the End-Wall and Within the Clearance Gap of an Axial Turbine Cascade," Int. Conf. on "Turbomachinery—Efficiency Prediction and Improvement," Cambridge, England, IMechE 1987-6, pp. 43–52.

Graham, J. A. H., 1985, "Investigation of a Tip Clearance Cascade in a Water Analogy Rig," ASME Paper No. 85-IGT-65.

Johnson, R. H., 1964, "The Hydraulic Analogy and Its Use with Time Varying Flows," General Electric Research Lab, Report No. 64-RL-(3755C).

McGreehan, W. F., and Schotsch, M. J., 1988, "Flow Characteristics of Long Orifices With Rotation and Corner Radiusing," ASME JOURNAL OF TURBOMACHINERY, Vol. 110, pp. 213–217.

Metzger, D. E., and Bunker, R. S., 1985, "Cavity Heat Transfer on a Transverse Grooved Wall in a Narrow Flow Channel," ASME Paper No. 85-GT-57.

Milne-Thomson, L. M., 1968, *Theoretical Hydrodynamics*, 5th ed., The Macmillian Press Ltd., London, pp. 332–333.

Moore, J., and Tilton, J. S., 1988, "Tip Leakage Flow in a Linear Turbine Cascade," ASME JOURNAL OF TURBOMACHINERY, Vol. 110, pp. 18–26.

Moore, J. G., 1985a, "An Elliptic Calculation Procedure for 3-D Viscous Flow," AGARD Lecture Series No. 140 on "3-D Computational Techniques Applied to Internal Flows in Propulsion Systems."

Moore, J. G., 1985b, "Calculation of 3-D Flow Without Numerical Mixing," AGARD Lecture Series No. 140 on "3-D Computational Techniques Applied to Internal Flows in Propulsion Systems."

Rouse, H., 1946, *Elementary Mechanics of Fluids*, Dover, New York, pp. 56–57.

Vogel, J. C., and Eaton, J. K., 1985, "Combined Heat Transfer and Fluid Dynamic Measurements Downstream of a Backward-Facing Step," ASME *Journal of Heat Transfer*, Vol. 107, pp. 922–929.

Wadia, A. R., and Booth, T. C., 1982, "Rotor-Tip Leakage: Part II—Design Optimization Through Viscous Analysis and Experiment," ASME *Journal of Engineering for Power*, Vol. 104, pp. 162–168.

Wasielewski, G. E., and Rapp, R. A., 1972, "High Temperature Oxidation," in: *The Superalloys*, C. T. Sims and W. C. Hagel, eds., Wiley, New York.

Influence of Secondary Flow on Turbine Erosion

A. Hamed
Department of Aerospace Engineering and Engineering Mechanics, University of Cincinnati, Cincinnati, OH 45221

This work presents the results of an investigation conducted to study the effect of secondary flow on blade erosion by coal ash particles in axial flow gas turbines. The particle dynamics and their blade impacts are determined from a three-dimensional trajectory analysis within the turbine blade passages. The blade material erosion behavior and the particle rebound characteristics are simulated using empirical equations derived from experimental measurements. The results demonstrate that the secondary flow has a significant influence on the blade erosion intensity and pattern for the typical ash particle size distribution considered in this investigation.

Introduction

Three-dimensional effects must be carefully considered in modern highly loaded axial turbine designs with large flow turning angles and low aspect ratios. Under these conditions, secondary flow not only plays a significant role in the turbine performance through secondary flow losses, but can also significantly influence the dynamics of the small ash particles and the resulting blade erosion, which in turn causes additional losses. The gas flow affects the particle trajectories through the aerodynamic forces. The secondary flow influence is reflected in the spanwise and pitchwise flow velocities. The smaller ash particles with their lower inertia are more susceptible to these influences.

Turbomachinery blade erosion (Hamed and Fowler, 1983; Tabakoff and Hamed, 1977, 1988; Tabakoff, 1987) and blade material erosion characteristics (Tabakoff et al., 1980; Tabakoff, 1988) have been the subject of many analytical and experimental investigations. It has been shown that the particle characteristics significantly affect the blade impact patterns (Hamed, 1984; Tabakoff and Hamed, 1984, 1986) and consequently the resulting blade erosion. In multistage axial flow turbines, the large sand particles were found to return after they impact the blade row leading edge, and re-enter the preceding blade row to impact its blade trailing edge suction side (Hamed, 1988). The small ash particle trajectories, on the other hand, tend to follow the gas flow field more closely (Hamed, 1988). The same particles, however, would be more affected by the secondary flow, which can influence the blade erosion pattern near the hub and tip.

The present study was conducted to investigate the effect of secondary flow on stator and rotor blade erosion by ash particles in axial flow turbines. This is accomplished by computing the blade erosion by ash particles when a secondary flow model is included in the particle trajectory analysis. Langston (1980) presented crossflow correlations in the endwall boundary layer based on detailed measurements of subsonic flows in a large-scale turbine cascade. The secondary flow based on this correlation is superimposed (Adkins and Smith, 1982) on the quasi-three-dimensional irrotational flow field solution in the blade passage on a number of blade-to-blade stream surfaces (Katsanis, 1965). Results are presented to compare the blade erosion patterns by ash particles with and without secondary flows.

Analytical Approach

Under conditions prevailing in turbomachines, the particle concentrations are such that intraparticle interactions are negligible and the aerodynamic forces on a single particle are sufficient to account for the effect of the flow field on the particle dynamics. The low concentrations also allow the effects of the particles on the flow field to be neglected. The drag force is considered as the main aerodynamic force on the suspended particles as they travel through the various blade passages.

The particle trajectory calculations consist of numerical integration of the equations governing the particle motion in a typical blade passage flow field, up to the point of blade, hub, or tip impact (Hamed and Tabakoff, 1988). The magnitude and direction of the particle rebound velocity after impact are dependent on the particle impacting conditions and on the impacted surface material. Experimental studies have been conducted at the University of Cincinnati Propulsion Laboratory to determine experimentally the particle restitution characteristics for coal ash particles using the LDV system (Tabakoff and Malak, 1987; Tabakoff et al., 1987). The measurements are conducted in the erosion tunnel through a glass window, which was especially designed for this purpose. For a given blade material, the experimentally measured incoming and rebounding velocities are analyzed to determine the mean value and the standard deviation for each data set at a given impact velocity and impingement angle. Correlations are obtained for the restitution ratio (the ratio of the rebounding to incoming particle velocities) and the direction coefficient (the ratio of the particle rebounding to incoming angle measured from the surface of the sample). These ratios were found to depend on the impingement angle for each turbine blade material, and these empirical correlations are used in the particle trajectory correlations. The blade surface coordinates at a number of sections between the hub and tip are

Contributed by the International Gas Turbine Institute and presented at the 33rd International Gas Turbine and Aeroengine Congress and Exhibition, Amsterdam, The Netherlands, June 5-9, 1988. Manuscript received by the International Gas Turbine Institute December 1987. Paper No. 88-GT-264.

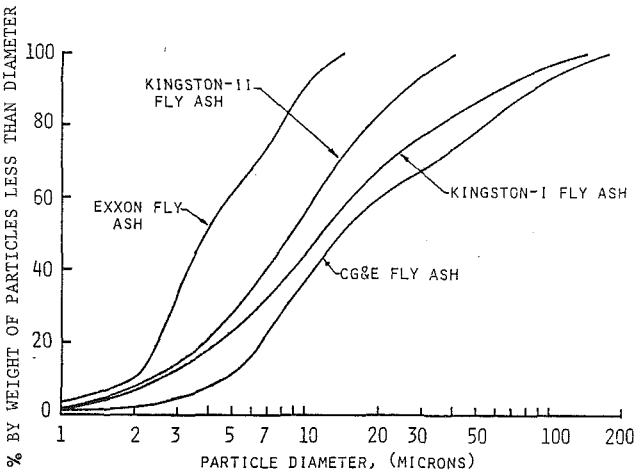

Fig. 1 Fly ash particle size distributions

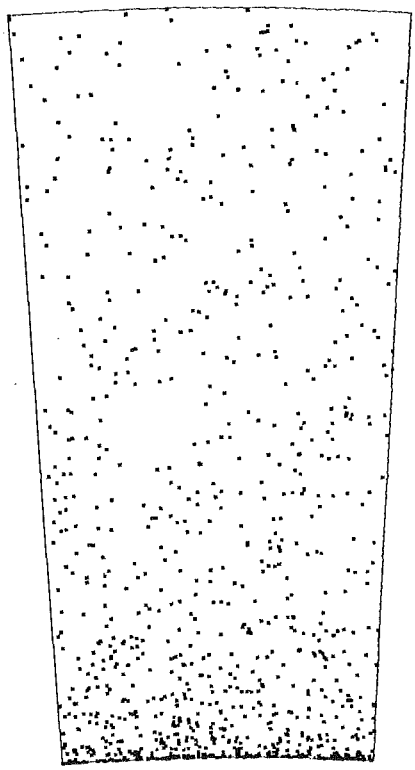

Fig. 2 Particle distribution at the stator inlet

used to describe the turbine blade in the particle trajectory calculations (Hamed and Tabakoff, 1988). These data are used in computing the particle impact location and in determining the direction of the blade surface at impact, and hence the impingement angle relative to the blade surface. The details of the particle trajectory analysis and blade erosion predictions were presented by Hamed et al. (1986), Tabakoff and Hamed (1986), and Hamed and Tabakoff (1988).

The flow in the blade passage is represented by an irrotational quasi-three-dimensional flow field, which is synthesized from a number of solutions (Katsanis, 1965) on blade-to-blade axisymmetric stream surfaces, which are determined from a hub-to-tip two-dimensional mean stream surface solution (Katsanis and McNally, 1977). The secondary flow model, representing the distribution of the three gas velocity components at the plane of the blade trailing edge, increments the

Table 1 Ash particle size distribution

Diameter, μm	Percent
1–2	24
2–3	12
3–4	22.7
4–5	2.7
5–6	6.7
6–7	—
7–8	2.7
8–9	5.3
9–10	1.3
10–15	17.3
15–20	4.0
20–25	1.3

irrotational gas flow field. The secondary flow variation inside the blade passage is assumed to increase linearly in the axial direction from zero at the leading edge to the maximum at the trailing edge.

Flow Field and Particle Characteristics

The computational model was applied for the Bureau of Mines turbine, which was especially designed for coal burning (Smith et al., 1967). In this design, an annulus after the first stage stator provides space for the particles to be centrifuged toward the outer side wall. This concentrates the particles toward the rotor blade tip, where the erosion is less critical than on the highly stressed roots, and permits the removal of the ash through extraction slots in the outer sidewalls. The results are presented for the erosion of the blade surfaces in the first stator and first rotor. The ash particles are usually not uniform, as demonstrated in Fig. 1, which presents the size distribution for different types of ash particles. The size distribution of West Virginia fly ash, as listed in Table 1, was used in the analysis.

Results and Discussion

The ash particle trajectories were determined through the first stage of the Bureau of Mines turbine (Smith et al., 1967), for the ash particle size distribution of Table 1. The particle distribution at the stator inlet is presented in Fig. 2, which shows that the particle concentration is high near the inner diameter. The concentration of the ash at the inner diameter was caused by a 90 deg turn made by the ash-laden gas before entering the turbine (Smith et al., 1967). The trajectories for a large number of particles provide the particle impact condition at the blade surface (Hamed and Tabakoff, 1988). These data, including the frequency of impacts, the impact velocity, and impingement angle relative to each blade surface, are used with the empirical equation for the blade material erosion by ash particles to determine the blade surface erosion (Hamed and Tabakoff, 1988).

The computed blade surface erosion results are presented in Figs. 3–10. Two sets of results are presented for each blade surface, one representing the resulting blade erosion in an irrotational flow field that does not include secondary flow effects, and the second for the blade erosion when the secondary flow is modeled in the three-dimensional flow field. Figures 3 and 4 present the predicted stator blade pressure surface erosion without and with secondary flow model. Both figures show generally the highest blade pressure surface erosion near the trailing edge. The general trend of higher erosion near the hub is due to particle distribution at the stator inlet, which is shown in Fig. 2. Comparing Figs. 3 and 4, one observes that when the secondary flow effect is not considered in the analysis, the maximum erosion of the first stator blade pressure surface is predicted at the corner of the hub and the trailing edge. The velocities of the small ash particles are

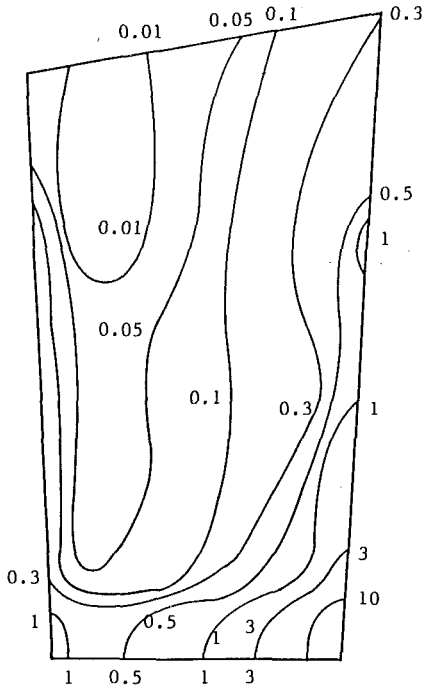

Fig. 3 Stator pressure surface erosion (mg/g/m^2), no secondary flow

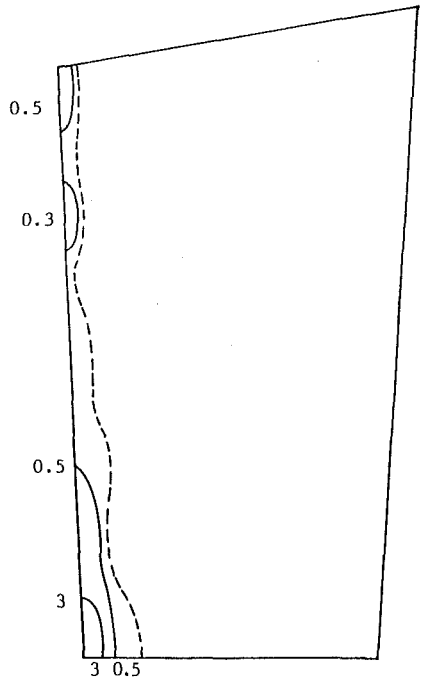

Fig. 5 Stator suction surface erosion (mg/g/m^2), no secondary flow

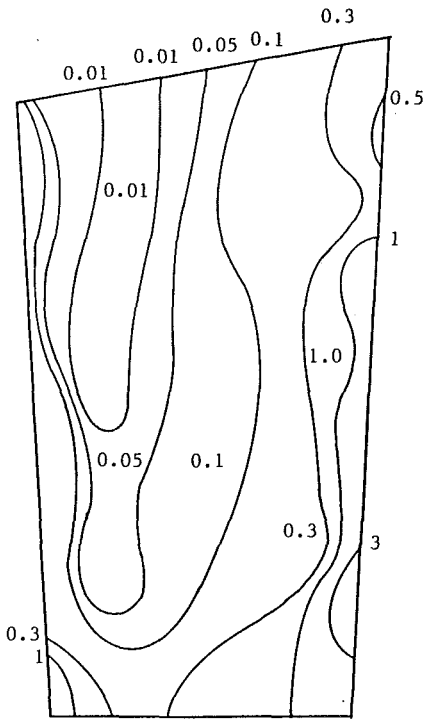

Fig. 4 Stator pressure surface erosion (mg/g/m^2)

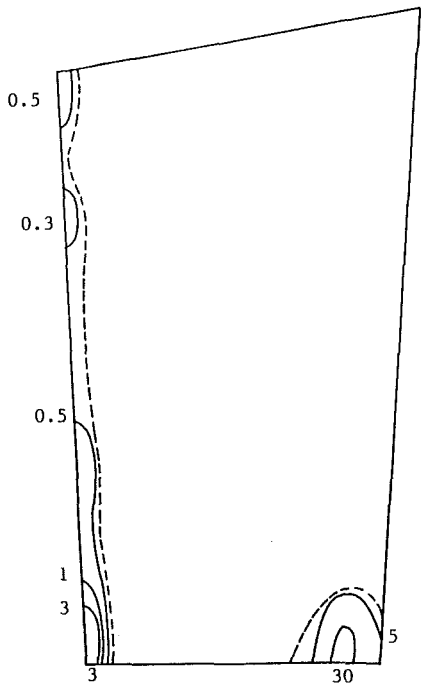

Fig. 6 Stator suction surface erosion (mg/g/m^2)

highest near the blade trailing edge and their impacts therefore cause the severest erosion damage. The secondary flow tends to reduce the erosion in this critical region as the ash particles are swept away from the blade pressure surface in the pitchwise direction. The predicted blade erosion with the secondary flow model (Fig. 4) shows the maximum at the trailing edge, but a little more removed from the endwall in the spanwise direction. The magnitude of the maximum local erosion is also reduced when the secondary flow is taken into consideration. The stator blade suction side erosion is presented for the two cases in Figs. 5 and 6. Figure 5 shows that most of the suction surface is not subject to erosion except near the leading edge. Figure 6 shows extensive blade erosion in a very small region in the corner at the hub near the trailing edge.

The predicted rotor blade surface erosion results are presented in Figs. 7–10. Figures 7 and 8 show that except near the leading and trailing edges, the inner half of the rotor blade pressure surface suffers little erosion. The rotor blade pressure surface erosion generally increases toward the tip since the particles are centrifuged radially in the annulus between the

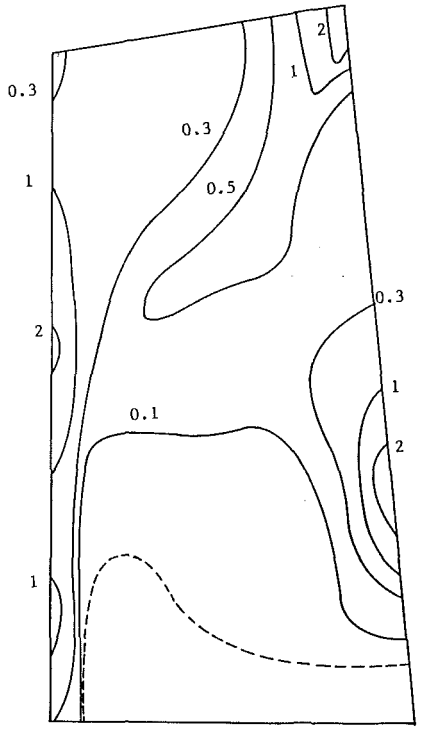

Fig. 7 Rotor pressure surface erosion (mg/g/m^2), no secondary flow

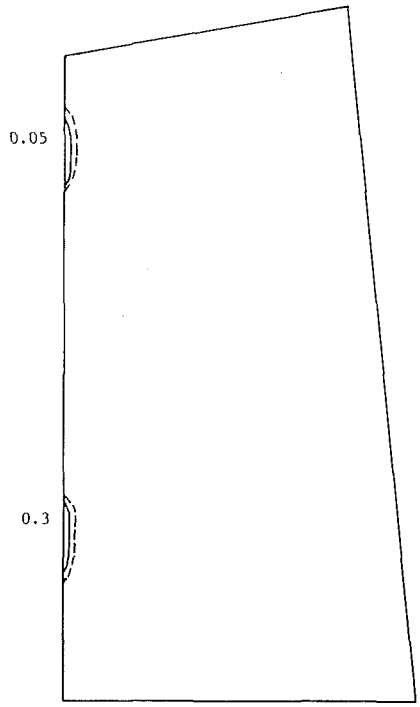

Fig. 9 Rotor suction surface erosion (mg/g/m^2), no secondary flow

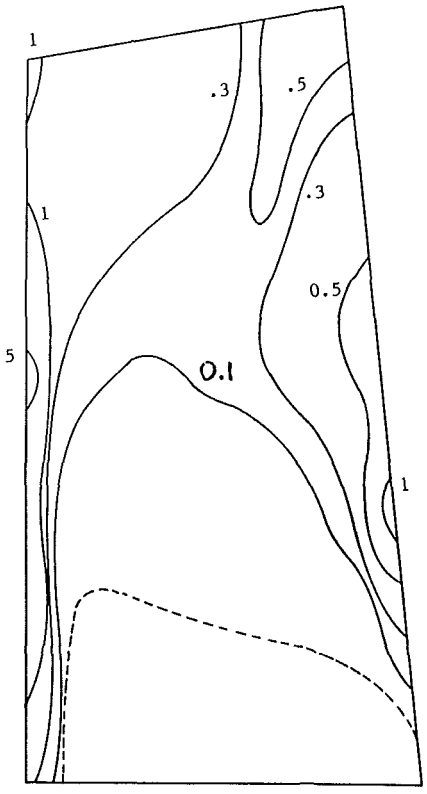

Fig. 8 Rotor pressure surface erosion (mg/g/m^2)

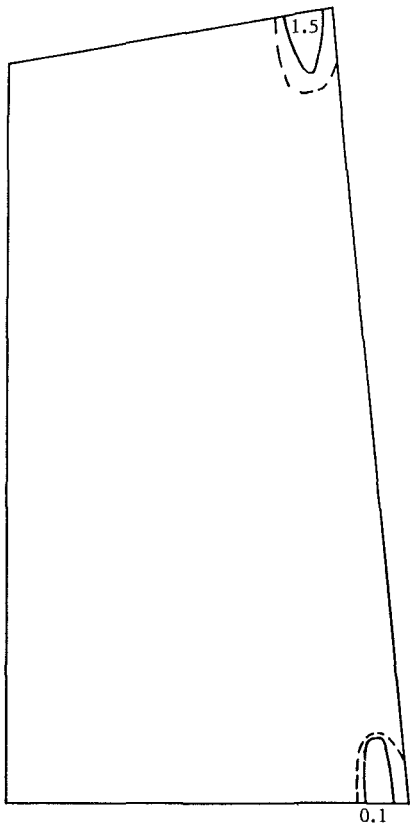

Fig. 10 Rotor suction surface erosion (mg/g/m^2)

stator and rotor. Figures 7 and 8 demonstrate that the secondary flow reduces the rotor blade pressure surface erosion near the trailing edge at the tip. Figures 9 and 10 show that the rotor suction surface is practically not subjected to any erosion except for small regions at the endwalls near the trailing edge, where the secondary flow sweeps the ash particles relative to the blade passage toward the suction surface. Comparing Figs. 9 and 10 with 5 and 6, one can see that the rotor suffers much less erosion compared to the stator, in these very small localized suction surface areas. Table 2 presents a summary of the stator and rotor blade pressure surface erosion for

Table 2 Effect of secondary flow blade pressure surface erosion, mg/g

Secondary flow	Stator	Rotor
Yes	0.00149	0.00136
No	0.00213	0.00182

the two cases. The magnitude of the overall suction surface erosion by ash particles is much smaller than the pressure surface, but is concentrated in the trailing edge endwall corners.

Conclusions

The secondary flow influences the erosion of the stator and rotor blade surfaces at the trailing edge–endwall corners. When the blade passage secondary flow is not modeled in the ash particle trajectory analysis, the blade pressure surface is overpredicted at these corners. The erosion of the blade suction surfaces near the same corners cannot be predicted without the secondary flow model. The effect of erosion on the blade aerodynamic performance requires careful consideration of the change in the trailing edge geometry and blade surface conditions.

Acknowledgments

This research work was sponsored by the U.S. Department of Energy Advanced Research and Technology Development Fossil Energy Material Program, Oak Ridge National Laboratory, Contract No. 19X89628C.

References

Adkins, G. G., Jr., and Smith, L. H., Jr., 1982, "Spanwise Mixing in Axial-Flow Turbomachines," ASME *Journal of Engineering for Power*, Vol. 104, pp. 97–110.

Hamed, A., 1984, "Solid Particle Dynamic Behavior Through Twisted Blade Rows," ASME *Journal of Fluids Engineering*, Vol. 106, No. 3, pp. 251–256.

Hamed, A., 1988, "Effect of Particle Characteristics on Trajectories and Blade Impact Patterns," ASME *Journal of Fluids Engineering*, Vol. 110, No. 1, pp. 33–37.

Hamed, A., and Fowler, S., 1983, "Erosion Pattern of Twisted Blades by Particle Laden Flows," ASME *Journal of Engineering for Power*, Vol. 105, pp. 839–843.

Hamed, A., and Tabakoff, W., 1988, "Particulated Flows and Blade Erosion," von Karman Lecture Series, May.

Hamed, A., Tabakoff, W., and Mansour, M., 1986, "Turbine Erosion Exposed to Particulate Flow," ASME Paper No. 86-GT-258.

Katsanis, T., 1965, "Fortran Program for Calculating Transonic Velocities on a Blade-to-Blade Stream Surface of a Turbomachine," NASA TND 2809.

Katsanis, T., and McNally, W. D., 1977, "Revised Fortran Program for Calculating Velocities and Streamlines on the Hub-Shroud Mid Channel Stream Surface of an Axial, Radial, or Mixed Flow Turbomachine or Annular Duct, Vols. 1 and 2," NASA TND 8430 and NASA TND 8431.

Langston, L. S., 1980, "Crossflows in a Turbine Cascade Passage," ASME *Journal of Engineering for Power*, Vol. 102, pp. 866–873.

Smith, J., Cargill, R. W., Strimbeck, D. C., Nabors, W. M., and McGee, J. P., 1967, "Bureau of Mines Coal-Fired Gas Turbine Research Project—Test of New Turbine Blade Design," RI 6920, U.S. Department of Interior, Bureau of Mines.

Tabakoff, W., 1987, "Compressor Erosion and Performance Deterioration," ASME *Journal of Fluids Engineering*, Vol. 109, pp. 297–306.

Tabakoff, W., 1988, "Turbomachinery Alloys Affected by Solid Particles," ASME Paper No. 88-GT-295.

Tabakoff, W., and Hamed, A., 1977, "Aerodynamic Effects on Erosion in Turbomachinery," ASME–JSME Joint Gas Turbine Congress, Tokyo, Japan, Paper No. 70.

Tabakoff, W., and Hamed, A., 1984, "Installed Engine Performance in Dust Laden Atmosphere," AIAA Paper No. 84-2488.

Tabakoff, W., and Hamed, A., 1986, "The Dynamics of Suspended Solid Particles in a Two Stage Gas Turbine," ASME JOURNAL OF TURBOMACHINERY, Vol. 108, pp. 298–302.

Tabakoff, W., and Hamed, A., 1988, "Temperature Effect on Particle Dynamics and Erosion in Radial Inflow Turbines," ASME JOURNAL OF TURBOMACHINERY, Vol. 110, No. 2, pp. 258–264.

Tabakoff, W., Hamed, A., and Ramachandran, J., 1980, "Study of Metals Erosion in High Temperature Coal Gas Streams," ASME *Journal of Engineering for Power*, Vol. 102, pp. 148–152.

Tabakoff, W., and Malak, M. F., 1987, "Laser Measurements of Fly Ash Rebound Parameters for Use in Trajectory Calculations," ASME JOURNAL OF TURBOMACHINERY, Vol. 109, pp. 535–541.

Tabakoff, W., Malak, M. F., and Hamed, A., 1987, "Laser Measurements of Solid Particles Rebound Parameters Impacting on 2024 Aluminum and 6A1-4V Titanium Alloys," *AIAA Journal*, Vol. 25, No. 5, pp. 721–726.

Measurement and Modeling of the Gas Turbine Blade Transition Process as Disturbed by Wakes

J. E. LaGraff
Syracuse University,
Dept. of Mechanical
and Aerospace Engineering,
Syracuse, NY 13244

D. A. Ashworth
Rolls-Royce plc,
Blade Cooling Research Section,
Derby, United Kingdom

D. L. Schultz[1]
Oxford University,
Dept. of Engineering Science,
Oxford, United Kingdom

Heat transfer measurements have been made on a transonic turbine blade undergoing natural transition and with a simulation of the effect of NGV wake interactions. The use of wide bandwidth heat transfer instrumentation permits the tracking of individual unsteady events that were identified as being due to either the impinging wakes or to the turbulent spots occurring within the transition process. Trajectories of these events as seen by the blade surface instrumentation have been measured. Numerical models have been developed for the effects of both types of turbulent activity. The convection of the wake through the passage is predicted, allowing for estimations of the expected times for which the boundary layer is disturbed by the wake fluid. The new model for the random generation and subsequent growth and convection of the turbulent spots produces a time-resolved prediction of the intermittent heat transfer signals by use of a time-marching procedure. By superimposing the two numerical models it is possible to simulate the measured instantaneous heat transfer characteristics.

Introduction

The ability to model the onset and progression of the boundary layer transition process successfully is fundamental to the accurate prediction of the skin friction and heat transfer distribution on surfaces such as gas turbine blades. At Reynolds numbers typical of gas turbine operation, the extent of the transition process can be a significant fraction of the surface length. Thus, failure to model the transition region accurately can lead to serious errors in local heat transfer distribution and total heating load, for example. It is often the case that the development of an accurate model is preceded by the existence of detailed experimental data from a realistic simulation. An inherently complex phenomenon such as transition has eluded routine modeling for many years. The further complication introduced by the unsteady NGV/rotor wake interactions in the gas turbine environment has made the understanding of the turbine blade transition process that much more difficult.

Recent developments in experimental facilities and instrumentation have resulted in significant progress in our understanding of the wake interaction problem through its effects on the time-resolved and mean heat transfer rates to gas turbine blades (e.g., Doorly and Oldfield, 1985b; Pfeil et al., 1983; Dunn, 1985; Ashworth et al., 1985). More recently, Ashworth et al. (1987) have reported experimental results where the end stage of the transition process (three-dimensional turbulent spot inception and growth) on a gas turbine blade under realistically simulated engine conditions has been followed with considerable detail using wide bandwidth surface heat transfer instrumentation. The onset and length of this turbulent spot region is of considerable importance to engine heat transfer code designers because this is where rapid changes in the heat transfer rate to the blade surface take place. The existence of turbulent spot data with this level of detail provided an opportunity to test various models of this region against observations. The experiments reported also included simulated wake-passing events and thus allowed comparison with combined wake/turbulent spot models to be made. The paper presents a detailed picture of both naturally transitioning turbine blade boundary layers and transitional boundary layers disturbed by wake events. A numerical model is then described that first predicts the wake interaction with the blade passage and then predicts transitional behavior by a random generation of turbulent spots and the subsequent growth, convection, and merging of the spots eventually to form a fully turbulent boundary layer. The transition model allows the generation rate, growth rate, and convection rate to be independently varied to compare low-speed flat plate data and models with the observed data on a transonic gas turbine rotor profile operating under realistically simulated engine operating conditions.

Experimental Approach

The tests were conducted in a transonic two-dimensional cascade in the Oxford University Isentropic Light Piston Tunnel (ILPT) as described by Schultz et al. (1977). The basic

[1]Deceased.

Contributed by the International Gas Turbine Institute and presented at the 33rd International Gas Turbine and Aeroengine Congress and Exhibition, Amsterdam, The Netherlands, June 5–9, 1988. Manuscript received by the International Gas Turbine Institute October 12, 1987. Paper No. 88-GT-232.

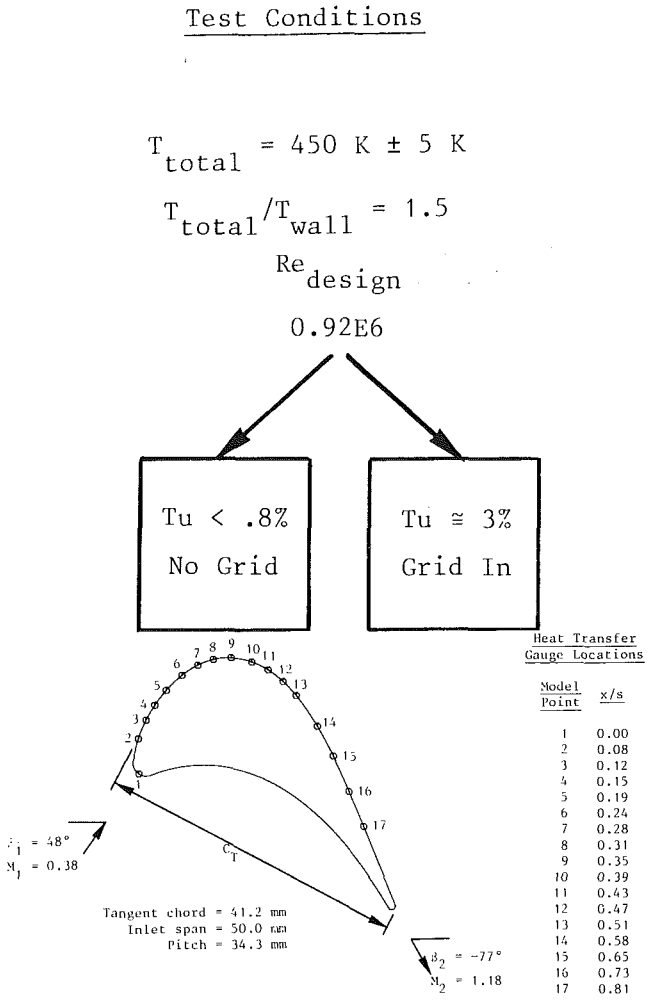

Fig. 1 Instrumental model details and test conditions

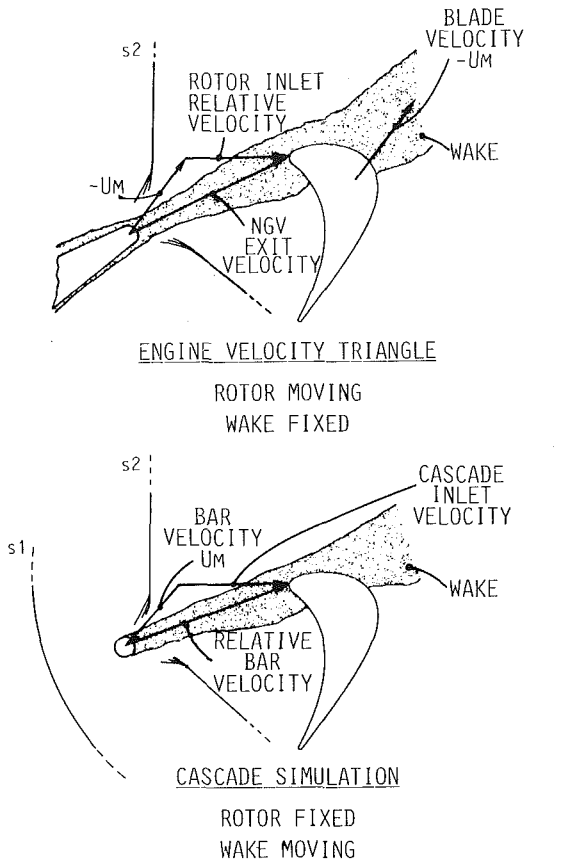

Fig. 2 Illustration of the comparative velocity triangles for the engine and cascade simulation of the NGV/rotor interaction

instrumentation technology utilized thin film heat transfer gages as described by Schultz and Jones (1973) and wide bandwidth electrical analogue circuitry as developed by Oldfield et al. (1984). The ILPT facility is capable of routinely producing test conditions appropriate to the gas turbine hot section aero/thermodynamic environment. Specifically for the current tests, stage inlet and outlet Mach numbers of 0.38 and 1.18, respectively, were produced at an effective Reynolds number of 0.92×10^6 and a gas-to-wall temperature ratio of 1.5. These conditions corresponded to the "design" condition of the particular profile tested. Free-stream turbulence levels of < 0.8 and 3 percent could also be established in the test section by an upstream grid. Grid-generated isotropic turbulence levels are believed to simulate the high-frequency components of real engine turbulence even though the overall levels in engines are higher. Standard engine definitions for aerodynamic conditions were used: Re = Reynolds number = $\rho U_2 c/\mu$, with μ derived from Sutherland's law and gas properties evaluated at inlet conditions; M = isentropic Mach number = U/a_1, where a_1 = sound speed = $\sqrt{\gamma R T_1}$.

The position of the thin film gages on the model suction surface is shown in Fig. 1. The gages, 0.5 mm wide and extending 4 mm in the spanwise direction, were closely spaced (2.5 mm) to aid in the tracking of unsteady events. The narrow span length (4 mm) enhanced the sensitivity of the gages to small-scale transient events since the thin films essentially averaged heat transfer rates along their length. The electrical analogue circuits coupled with 16 channels of simultaneous high-speed digital sampling instrumentation (500 kHz) allowed for the precise tracking of unsteady events at an effective bandwidth of nearly 100 kHz. In all, 3500 points of high-speed

Nomenclature

a = sound speed
c = tangential chord
f_t, f_ℓ = spot fractional propagation rates for trailing and leading edge
$g(x)$ = turbulent spot source rate function with mean (μ) and variance (s)
k = thermal conductivity
M = Mach number
N_s = spot production rate
q = measured heat transfer rate
R = gas constant
Re = Reynolds number
s = suction surface length
T = temperature
U = velocity
x = surface length from leading edge
α = spot spreading angle
γ = ratio of specific heats; intermittency
μ = kinematic viscosity
ρ = density

Subscripts

0 = total
1 = at inlet
2 = at exit
∞ = free stream
ℓ = laminar value
rel = relative to rotating bar
t = turbulent value
w = at wall

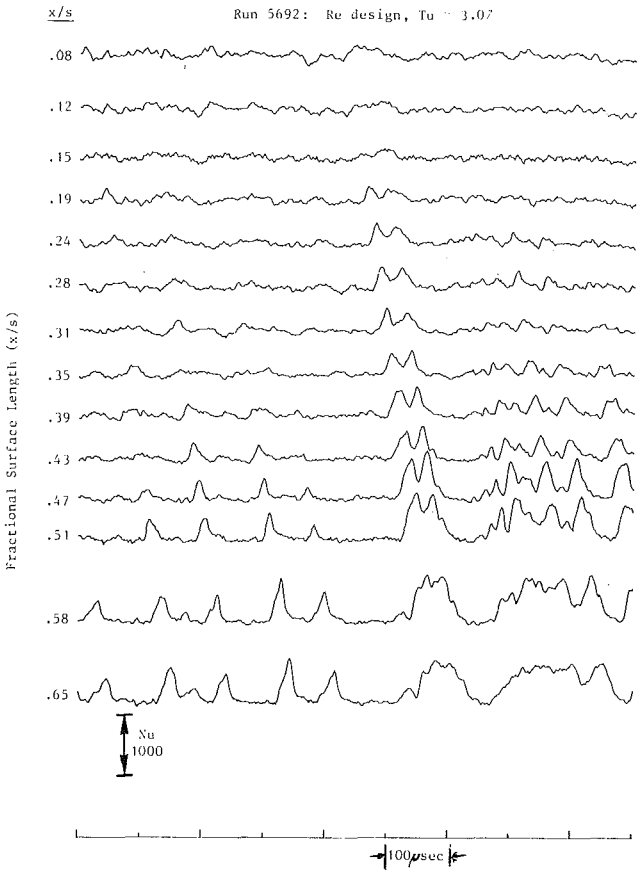

Fig. 3 Natural transition heat transfer progression along the model surface

heat transfer data were recorded in each channel giving over 7 ms of data points at intervals of 2 μs. A detailed description of the instrumentation has been reported elsewhere by Doorly and Oldfield (1985a) and Ashworth et al. (1985).

The unsteady NGV/rotor wake interaction events expected in a real engine or rotating experiment were simulated by passing the wakes from 2 mm diameter bars attached to a disk rotating upstream of the cascade. This method of simulation, developed and described by Doorly and Oldfield (1985b), is illustrated in Fig. 2. The effective wake passing frequency was reduced for this experiment to 435 Hz (well below realistic engine conditions) to allow time for detailed observations of the boundary layer condition between wake events but still fast enough to capture over three bar passing cycles. This allowed ensemble averaging and permitted repeatability evaluations to be made. The bar rotation speed was maintained at levels that allowed the correct inlet velocity triangle conditions to be assured. The tests reported herein were run with subsonic bar relative Mach number, however, to eliminate the effects of shock wave interactions that would be present in the real engine rotating environment. No attempt was made to allow for the fact that the NGV wake fluid is cooled both by heat extraction to the vanes and by the injection of cooling air in the upstream row.

Experimental Results—Natural Transition

The mean (steady-state) aerodynamic and heat transfer conditions of the blade profile tested in the present experiment have been measured and reported elsewhere by Ashworth et al. (1987). The results indicated that the flow undergoes a fairly constant acceleration through transonic conditions to a point well back on the suction surface ($x/s > 0.6$) where the acceleration parameter then becomes mildly adverse. The heat transfer records indicated that for the low-turbulence free-stream case (no turbulence grid) the boundary layer remained laminar over the entire instrumented section. The high free-stream turbulence case, however, clearly indicated a transitional boundary layer extending over much of the blade surface region where the closely spaced heat transfer gages were located.

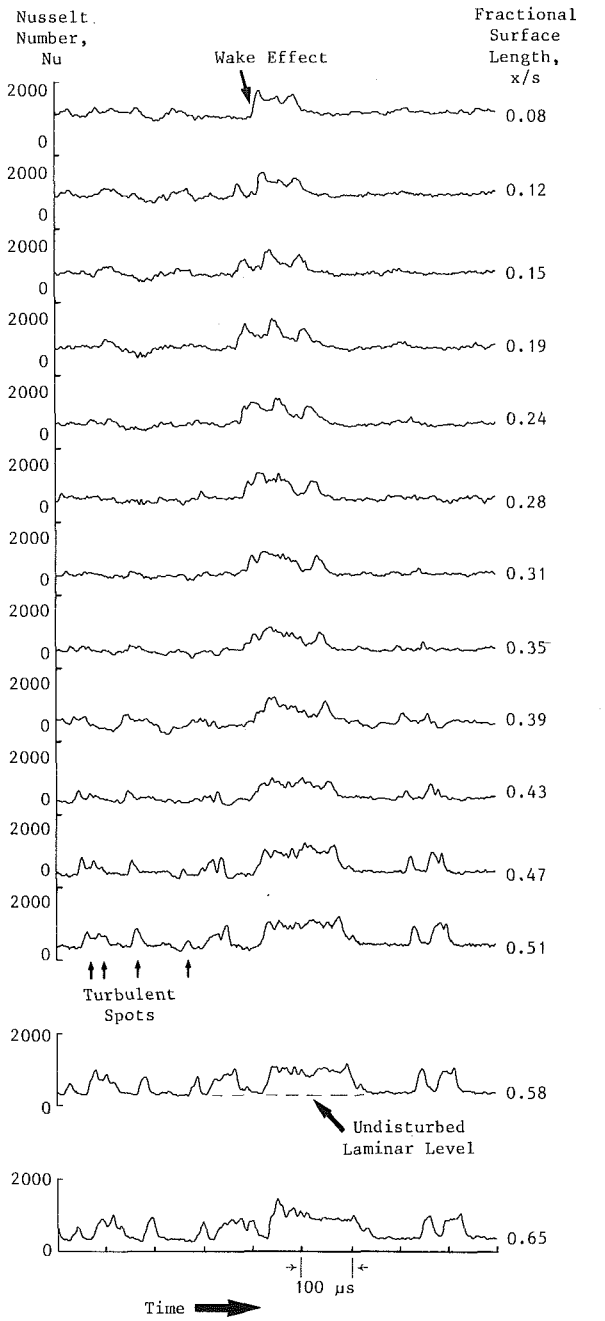

Fig. 4 Wake disturbed heat transfer rate progression along the model surface

Although the transitional nature of the boundary layer in the high free-stream turbulence case was clearly indicated by the gradually rising mean heat transfer levels along the surface, the wide-bandwidth fast sampled data gave a clearer picture of the physical processes involved (Fig. 3). In several of the figures presented by Ashworth et al. (1987), discrete, rapidly changing excursions in the heat transfer signals were seen to rise above the laminar levels, grow in extent, and eventually merge into a continuous higher level signal. This behavior is

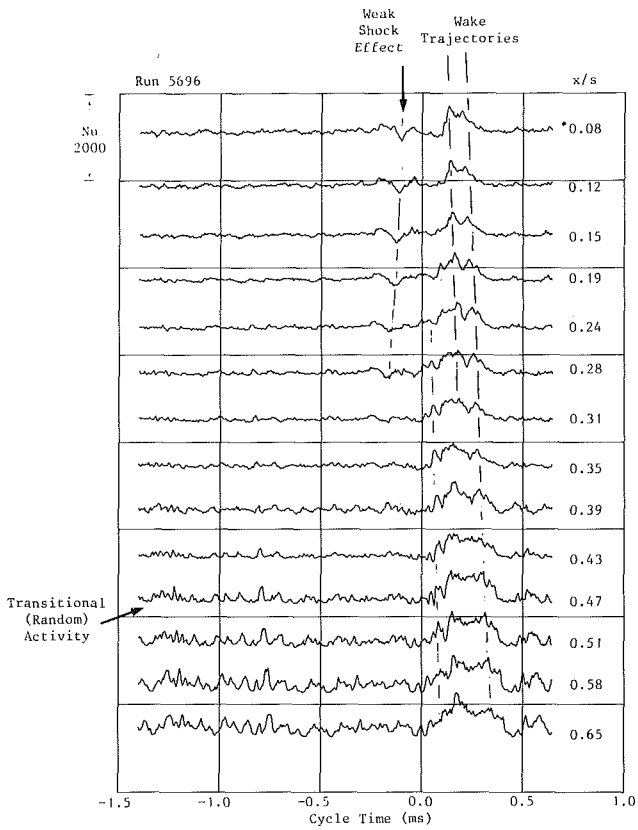

Fig. 5 Ensemble-averaged heat transfer rate progression along the model surface (three cycles)

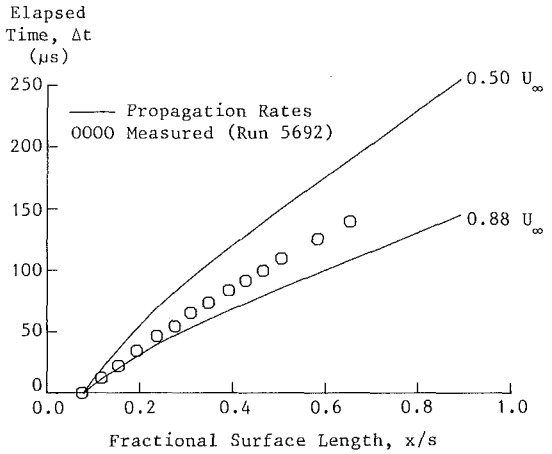

Fig. 6 Comparison of measured convection rate for turbulent spots with "standard" velocity fractions of free stream

clearly consistent with the often observed turbulent spot growth model of the final (three-dimensional) stages of boundary layer transition as reported, e.g., by Schubauer and Klebanoff (1956). The ability of the instrumentation to respond to turbulent spot development permitted quantification of the process to be made. Specifically, this analysis included assigning an intermittency value to the process by selecting a threshold value above the laminar signal and counting the fraction of time the signal was above this (see Ashworth et al., 1987). By cross-correlation analysis of adjacent channels, the same authors were also able to estimate mean convection rates of the disturbances from gage to gage. The existence of data in this form permitted detailed comparisons to be made with the numerical models of transition discussed below.

Experimental Results—Transition With Wake Passing

The second part of the experimental program repeated the undisturbed tests discussed above with wake disturbances superimposed on the flow using the rotating bar arrangement described earlier. Figure 4 shows a series of wide-bandwidth signals from consecutive channels showing clearly a single wake-passing event and an extent of undisturbed boundary layer heat transfer rate signals. On the same figure some laminar heat transfer signals from the low free-stream turbulence results are included. Heat transfer rates are given in dimensionless form using the Nusselt number (Nu), defined as

$$\mathrm{Nu} = \frac{\dot{q}}{T_o - T_w}\frac{c}{k}$$

Again clear evidence of transitional turbulent spot activity is seen in the regions of the output removed from the wake region. Although for clarity, only one wake is shown in Fig. 4, several wake events were captured by the fast data scan and ensemble averaging was therefore possible. Figure 5 is an example of one such averaging process. The ensemble-averaging process highlights additional structure not evident in the single unaveraged signals, e.g., the double peaked nature of the wake signal in the earlier channels of the blade passage. This is consistent with the existence of coherent structure remaining from the vortex shedding pattern from the rotating bars. It can also be observed from the unaveraged data in Fig. 3 that the transition process in the region between the wakes appears to develop in much the same way as the process in the naturally transitional boundary layer reported earlier.

Although the data did not permit the accurate estimation of leading edge and trailing edge propagation rates, it was possible to estimate mean spot convection rates by cross-correlation analysis of adjacent channels. The results are shown in Fig. 6 along with the trajectories predicted using the commonly observed values of leading edge and trailing edge propagation rates from low-speed turbulent spot data (e.g., Schubauer and Klebanoff, 1956). The data generally fall between the two outer limits, as might be expected with mean data.

Numerical Model—Wake Passing

The first part of the numerical modeling effort concentrated on predicting the path the rotating bar wake was expected to take as it encountered the blade row and progressed through the passage. The next section below discussed a proposed model for the random generation, growth, and convection of turbulent spots. The two models are then combined to give a prediction that can be compared with the data reported herein.

The wake itself is nearly two-dimensional in form, expected to vary only slightly in height along the bar span due to the slightly varying Reynolds number as the bar relative velocity changes (with radius). A two-dimensional model is assumed using conditions at bar midpoint. The procedure follows that described by Doorly (1983) known as a "striped air" calculation, which has now been automated. This also allows for a spreading wake width being proportional to the square root of the distance from the bar along the line of U_{rel} (see Fig. 2) with the constant of proportionality derived from a data base of wake measurements. The wake is then convected through the blade row passage using an inviscid time marching flow field calculation based on a method developed by Denton (1983). U_{rel} is assumed constant and the centerline of the undistorted wake is calculated from a specified bar position and the width added as described above. The wake is shifted back in time so that the bar will return to its correct position following the marching process of the prediction. From this initial position, elements of the wake are convected by small time

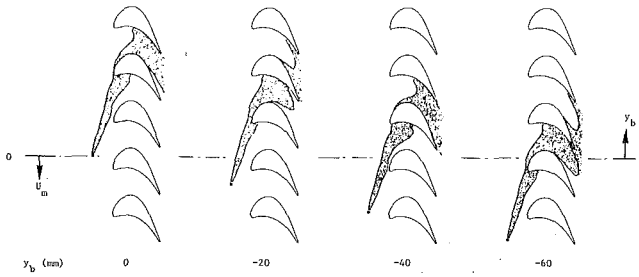

Fig. 7 Striped-air calculation for four positions of the bar

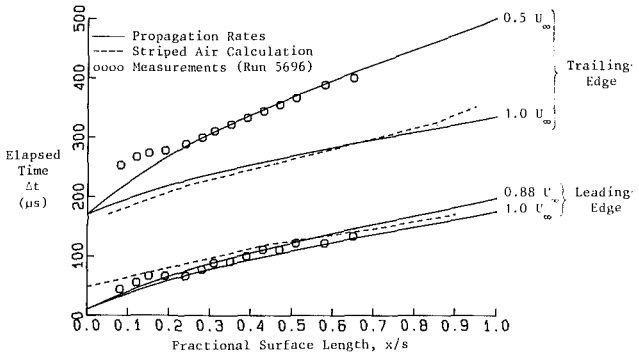

Fig. 8 Comparison of measured leading and trailing edges of a wake-induced turbulent patch with prediction

steps using the local velocity interpolated from the predictions until the bar reaches the specified location. The differential velocities in the flow field cause distortions of the wake along its length and across its width as it is accelerated through the passage. The results of such a calculation are shown in Fig. 7. The positions of the wake calculated by this method agree well with the positions shown at the same time on schlieren photographs presented by Schultz et al. (1986).

It was then possible to compare the wake passage prediction from the time marching (striped air calculation) scheme with the observed suction surface heat transfer record. It should be emphasized again that the prediction for the wake passage is based on an inviscid flow field calculation, whereas the observed heat transfer effects are measured on the blade surface, at the base of the blade viscous boundary layer. The results are shown in Fig. 8 giving predicted and observed wake path for the leading and trailing edge as a trajectory in an x–t diagram. The figure shows excellent agreement for the leading edge prediction with an expected difference in trailing edge prediction. Figure 8 also shows predicted propagation trajectories for the leading and trailing edge of the wakes based simply on a range of assumed fractions of actual local free-stream velocities. The values of $0.88U_\infty$ and $0.5U_\infty$ were selected from values commonly accepted for turbulent spot leading and trailing edge propagation rates, e.g., Schubauer and Klebanoff (1956). The time-marching prediction, of course, closely follows the 1.0 U_∞ value with small differences due to the wake spreading included in the striped-air model. The leading edge data closely follow predicted trajectories ($0.88U_\infty$–$1.0U_\infty$) whereas the trailing edge data seem to follow closely a $0.5U_\infty$ trajectory, i.e., the wake-generated patch of turbulence in the boundary layer propagates at rates closely following many observations of naturally occurring (and artificially generated) turbulent spots in low-speed flows.

Numerical Model—Natural Transition

A generalized model time-marching scheme was developed

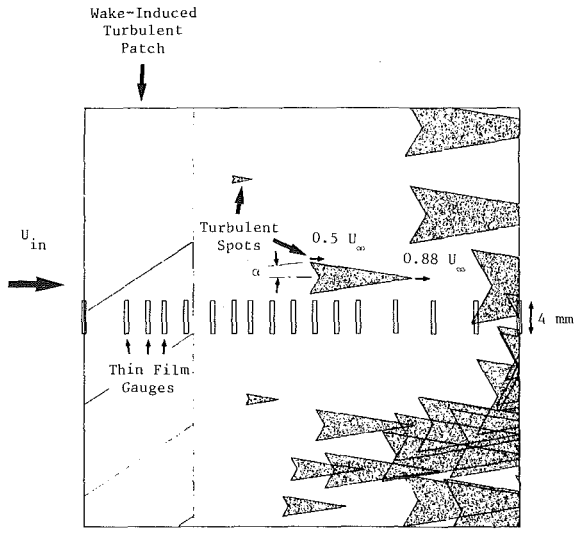

Fig. 9 Plan view of the simulation of transition on the suction surface

(see Ashworth, 1987) for the prediction of transitional intermittency using the turbulent spot model proposed by Emmons (1951) and extended later by Narisimha (1957) and Chen and Thyson (1971). This model allowed for turbulent spots to be generated randomly at any point on the blade surface and subsequently propagated downstream at an arbitrary growth angle and leading edge and trailing edge propagation rate (as a fraction of free-stream velocity). The self-similar spot growth characteristics were then combined with the blade geometry information and thin film sensor locations to predict the fraction of time the spots contact the films (or part thereof). This would then give predictions of intermittency consistent with what would be measured with the sensing elements in these experiments. The model requires input data for:

(*i*) velocity at the given streamwise location $U_\infty(x)$;

(*ii*) the scaling parameter (N_3), mean (μ), and variance (S) of the random source rate function $g(x)$

$$g(x) = -\frac{N_3}{\sqrt{2\pi s}} \exp\left(-\frac{(x-\mu)^2}{2s}\right)$$

(*iii*) spot propagation parameters

$$\sigma = \tan\alpha\,(f_t^{-1} - f_\ell^{-1})$$

where α is spot spreading angle and f_t and f_ℓ are the trailing edge and leading edge spot propagation velocities (as a fraction of free-stream velocity);

(*iv*) surface geometry and gage length and location.

A typical plan view of the model surface (with sensing elements in place) showing the coverage of turbulent spots generated by the above procedure is shown in Fig. 9 for a frozen instant of time. Also shown on the surface is the assumed footprint of a wake passing over the surface. In this way an effective intermittency can be estimated by summing the portion of the gage covered by turbulence (either from a wake or a spot). Intermittency values can then be easily converted to Nusselt number values by summing the contributions of laminar Nusselt number and turbulent Nusselt number for each gage

$$\mathrm{Nu} = (1-\gamma)\mathrm{Nu}_\ell + \gamma\mathrm{Nu}_t$$

where Nu_ℓ and Nu_t are laminar and turbulent Nusselt numbers, respectively, predicted (in this case) by an integral method. This results in heat transfer predictions such as shown in Figs. 10 and 11 for some selected sensor locations. This clearly shows the similarity between the data presented with the prediction method.

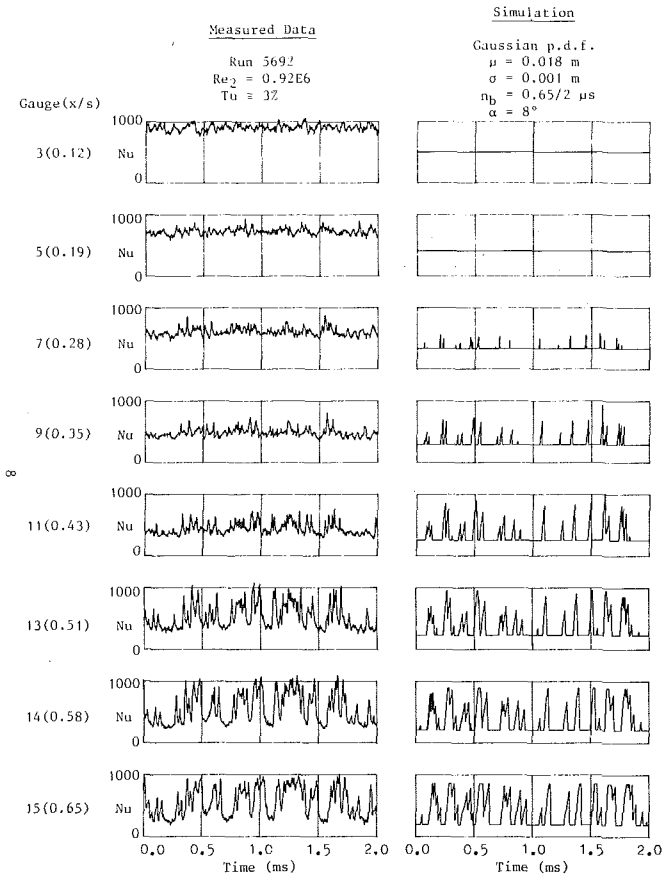

Fig. 10 Comparison of measured and simulated instantaneous heat transfer on the model surface undergoing natural transition

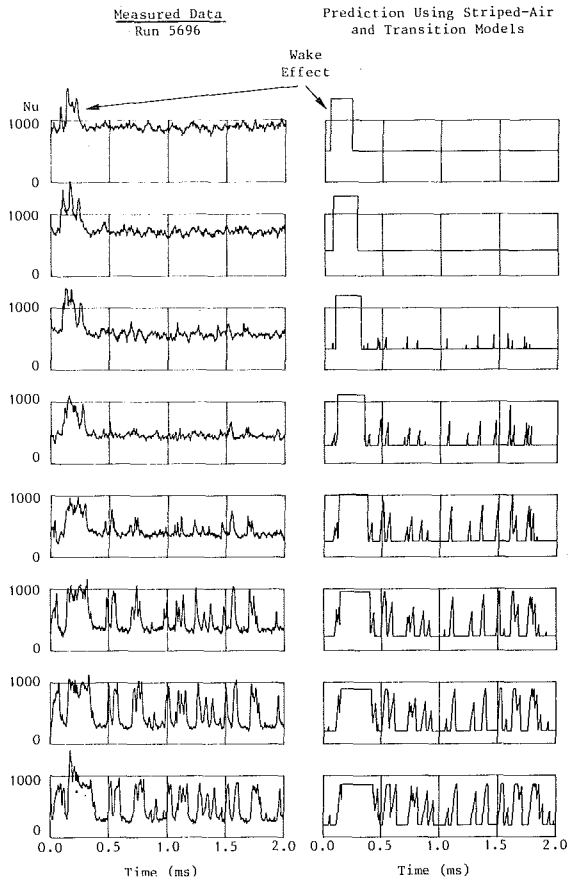

Fig. 11 Comparison of the measured and simulated instantaneous heat transfer on the model surface with wake-passing and transition

Conclusions

It was shown that wide-bandwidth heat transfer instrumentation was able to track trajectories of both unsteady wake passing events and transitional turbulent spots on a turbine airfoil under a simulated gas turbine environment. The observed behavior was accurately modeled by a time-marching simulation of both the inviscid wake passing interaction and the random generation and growth of turbulent spots based on the well-established low-speed theory and observations of the final three-dimensional stages of boundary layer transition.

Acknowledgments

The authors wish to acknowledge the invaluable contributions to this paper made by M. L. G. Oldfield during many discussions throughout the course of the work. We would also like to thank M. J. Rigby and A. B. Johnson for their help in collecting portions of the data. Professor LaGraff would also like to acknowledge the financial support of the U.S. Air Force Office of Scientific Research under grant number 85-0295, Dr. James Wilson, Program Manager, and the Division of International Programs of the National Science Foundation for providing a travel grant (INT-8509407) to facilitate the collaborative research program.

References

Ashworth, D. A., 1987, "Unsteady Aerodynamics and Heat Transfer in a Transonic Turbine Stage," D. Phil. Thesis, Oxford University, United Kingdom.

Ashworth, D. A., LaGraff, J. E., Schultz, D. L., and Grindrod, K. J., 1985, "Unsteady Aerodynamics and Heat Transfer Processes in a Transonic Turbine Stage," ASME *Journal of Engineering for Gas Turbines and Power*, Vol. 107, pp. 1022–1030.

Ashworth, D. A., LaGraff, J. E., and Shultz, D. L., 1987, "Unsteady Interaction Effects on a Transitional Turbine Blade Boundary Layer," *Proceedings of the 1987 ASME/JSME Thermal Engineering Joint Conference*, Honolulu, HI.

Chen, K. K., and Thyson, N. A., 1971, "Extension of Emmons' Spot Theory to Flows on Blunt Bodies," *AIAA Journal*, Vol. 9, No. 5, pp. 821–825.

Denton, D. J., 1983, "An Improved Time-Marching Method for Turbomachinery Flow Calculation," ASME *Journal of Engineering for Power*, Vol. 105, pp. 514–520.

Doorly, D. J., 1983, "A Study of the Effect of Wake Passing on Turbine Blades," D. Phil. Thesis, University of Oxford, United Kingdom.

Doorly, D. J., and Oldfield, M. L. G., 1985a, "Simulation of the Effects of Shock Wave Passing on a Turbine Rotor Blade," ASME *Journal of Engineering for Gas Turbines and Power*, Vol. 107, No. 4, pp. 998–1006.

Doorly, D. J., and Oldfield, M. L. G., 1985b, "Simulation of Wake Passing in a Stationary Turbine Rotor Cascade," *J. Propulsion and Power*, Vol. 1, No. 4, pp. 316–318.

Dunn, M. G., 1985, "Turbine Heat Flux Measurements: Influence of Slot Injection on Vane Trailing Edge Heat Transfer and Influence of Rotor on Vane Heat Transfer," ASME *Journal of Engineering for Gas Turbines and Power*, Vol. 107, No. 1, pp. 76–83.

Emmons, H. W., 1951, "The Laminar-Turbulent Transition in a Boundary Layer—Part I," *J. Aero. Sciences*, Vol. 18, No. 7, pp. 490–498.

Narasimha, R., 1957, "On the Distribution of Intermittency in the Transition Region of a Boundary Layer," *J. Aero. Sciences*, Vol. 24, No. 9, pp. 711–712.

Oldfield, M. L. G., Burd, H. J., and Doe, H. G., 1984, "Design of Wide Bandwidth Analogue Circuits for Heat Transfer Instrumentation in Transient Tunnels," *Papers From the 16th ICHMT Symposium on Heat and Mass Transfer*, Dubrovnik, pp. 233–258.

Pfeil, H., Herbst, R., and Schroder, T., 1983, "Investigation of the Laminar-Turbulent Transition of Boundary Layers Disturbed by Wakes," ASME *Journal of Engineering for Power*, Vol. 105, pp. 130–137.

Schubauer, G. B., and Klebanoff, P. S., 1956, "Contributions on the Mechanics of Boundary Layer Transition," NACA Report 1289.

Schultz, D. L., and Jones, T. V., 1973, "Heat Transfer Measurements in Short Duration Hypersonic Facilities," Agardograph No. 165.

Schultz, D. L., Jones, T. V., Oldfield, M. L. G., and Daniels, L. C., 1977, "A New Transient Cascade Facility for the Measurement of Heat Transfer Rates," AGARD Conference Proceedings, *High Temperature Problems in Gas Turbine Engines*, CP-229, Paper No. 31.

Schultz, D. L., Ashworth, D. A., LaGraff, J. E., Johnson, A. B., and Rigby, M. J., 1986, "Wake and Shock Interactions in a Transonic Turbine Stage," AGARD 68th(B) Specialists' Meeting, *Transonic and Supersonic Phenomena in Turbomachines*, Paper No. 3, Neubiberg, Federal Republic of Germany.

DISCUSSION

H. P. Hodson,[1] J. S. Addison,[2] and G. J. Walker[2]

The authors are to be congratulated for the fine work presented in this paper, particularly for their attempt at producing a model of boundary layer transition that takes into consideration both natural and wake-induced transition. However, concern must be expressed regarding the simplicity of the model, particularly with respect to wake-induced transition.

Figures 8, 9, and 11 and the proposed model clearly indicate the authors' belief that transition to turbulent flow takes place immediately after an upstream wake impinges on the boundary layer and that it is only between the wakes or in their absence that conventional transition can occur. However, these figures do not entirely support the hypothesis. It is the purpose of this discussion to question the authors' interpretation of the experimental data and to examine the resulting implications for the model.

Figure 8 shows that over the leading part of the suction surface ($x/s < 0.24$), the propagation rates of both the leading and trailing portions of the turbulent patch are much closer to the predicted convection rates of the wake than they are to the values commonly accepted for turbulent spots. Attention is particularly drawn to the trailing edge convection rate. While it is accepted that the prediction of the wake passage is based on an inviscid flow field, whereas the observed heat transfer effects are measured on the blade surface, the evidence strongly suggests that up to 24 percent of surface length, the "turbulent patch" convects with the wake and is not a self-sustaining turbulent flow in the blade boundary layer.

Figure 12 is an analysis of data originally obtained by Hodson (1984) at Reynolds numbers lower than those encountered by the present authors. It is a distance–time diagram, which depicts the evolution of phase-locked averaged random unsteadiness on the suction surface of an axial turbine. For the case presented in Fig. 12, the boundary layer is effectively laminar at 68 percent of surface distance and does not become turbulent until just before the trailing edge. Therefore, the ensembled random unsteadiness of Fig. 12, which convects with the wake at approximately the undisturbed free-stream velocity, cannot signify a self-sustaining turbulent patch if such a description implies that the production and dissipation rates of the turbulence are approximately equal within the patch. Hodson and Addison (1989) have also observed that for a range of conditions, the disturbances created by wakes within the suction and pressure surface boundary layers of the same axial turbine convect with the wake at about the velocity of the undisturbed free stream, providing that transition has not begun.

The differences in Reynolds number between the low-speed axial turbine tests cited above ($1.8 \times 10^5 < Re < 3.3 \times 10^5$) and those of the Oxford cascade (9.2×10^5) mean that transition, whether it is natural or wake-induced, commences much earlier in the cascade. Nevertheless, this does not mean that it will occur immediately in the presence of a wake. The data of Pfeil et al. (1982) are most clear in this respect. Similar conclusions may be drawn from Walker's (1974) observations of the suction surface boundary layer on a compressor stator at $Re = 5 \times 10^4$. The present data also suggest that this might be the case. Figure 11, for example, shows that actual change in heat transfer between supposedly laminar and turbulent levels is less than that predicted over the leading part of the surface. If the heat transfer levels between the wakes represent the laminar state, this implies that the turbulent levels are not

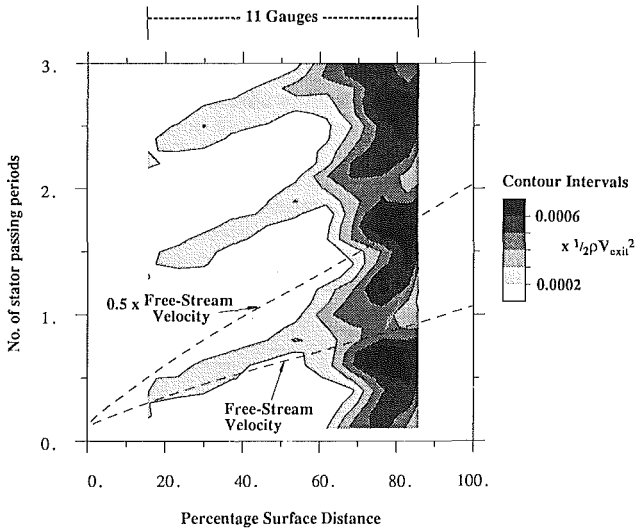

Fig. 12 Surface-mounted hot-film results: distance–time plot of phase-locked average of random unsteadiness (rms) within suction surface boundary layer of axial flow turbine rotor

reached and that near the surface at least, the dissipation of turbulence is initially greater than the combined effects of production and diffusion from the outer layers.

In conclusion, the hypothesis that a wake instantaneously induces transition in an otherwise laminar boundary layer is not supported by the experimental evidence. Transition is preceded by a region in which the dissipation of turbulence dominates the production and diffusion from the free stream. The length of this region must be determined by the stability or viscous dissipation properties of the boundary layers and therefore by Reynolds number. It is because the length of this region is short at high Reynolds numbers that the model presented appears to be successful in the particular situation described in this paper. To ensure its general validity, the model should be extended to incorporate an upstream limit at which self-sustaining turbulent spots can be initiated by passing wakes. The value of such a limit is indicated by the measurements of Hodson and Addison (1989).

References

Hodson, H. P., 1984, "Boundary Layer and Loss Measurements on the Rotor of an Axial-Flow Turbine," ASME *Journal of Engineering for Gas Turbines and Power*, Vol. 106, pp. 391–399.

Hodson, H. P., and Addison, J. S., 1989, "Wake-Boundary Layer Interactions in an Axial Flow Turbine Rotor at Off-Design Conditions," ASME JOURNAL OF TURBOMACHINERY, Vol. 111, pp. 181–192.

Pfeil, H., Herbst, R., and Schroder, T., 1983, "Investigation of the Laminar-Turbulent Transition of Boundary Layers Disturbed by Wakes," ASME *Journal of Engineering for Power*, Vol. 105, pp. 130–137.

Walker, G. J., 1974, "The Unsteady Nature of Boundary Layer Transition on an Axial Compressor Blade," ASME Paper No. 74-GT-135.

Authors' Closure

The authors appreciate the interest shown by Hodson et al. in the data and predictions shown in this paper. Many of the suggested interpretations of the data may well turn out to be valid. The authors were hesitant, however, to read too much into a limited amount of data taken at such exacting operating conditions. The characteristics of the boundary layer with high unit Reynolds numbers and transonic Mach number lead to short pretransitional lengths and rapid transit times for wake and transitional disturbances.

In spite of these reservations, it would appear that there is

[1]Whittle Laboratory, Cambridge University, United Kingdom.
[2]University of Tasmania, Australia.

a similarity between the trailing-edge convection rate characteristics presented by the authors and that shown in the above discussion. In support of this, M. L. G. Oldfield has also noted that the high velocity of the trailing edge of the wake-induced heat transfer enhancement could possibly be seen in the early suction surface in Fig. 11 of Doorly and Oldfield (1985b), although it was not interpreted as such at the time. These comments illustrate another interesting parallel between the authors' transonic results and low-speed observations. A threshold criterion for self-sustaining wake-induced turbulent patches could easily be incorporated into the existing model.

The simplified prediction models presented in the paper were primarily intended as guides for interpretation of the data, so that detailed quantitative comparison with the experimental results is inappropriate. The fact that the level of the wake-induced signal early on is not as high as the "fully turbulent" prediction does not necessarily imply that there isn't a turbulent boundary layer beneath the wake. Dissipation within the boundary layer will reduce the mixing and hence the heat transport to the surface. Perhaps the term "non-self-sustaining turbulent boundary layer" is needed here.

The authors intend to make detailed measurements of convection rates and lateral coverage of both natural and artificial disturbances in the near future.

ERRATA

Errata for "Numerical Simulation of Inviscid Transonic Flow Through Nozzles With Fluctuating Back Pressure" by A. Bölcs, T. H. Fransson, and M. F. Platzer, published in the April 1989 issue of the ASME JOURNAL OF TURBOMACHINERY, Vol. 111, pp. 169–180:

Please note the corrected form of the following equations:

Error

$$\begin{aligned} \mathbf{W}' &= D^{-1}\mathbf{W} \\ \mathbf{F}' &= D^{-1}\{\xi_t\mathbf{W}+\xi_x\mathbf{F}+\xi_y\mathbf{G}\} \\ \mathbf{G}' &= D^{-1}\{\eta_t\mathbf{W}+\eta_x\mathbf{F}+\eta y\mathbf{G}\} \\ D &= \xi_x\eta_y-\xi_y\eta_x=1/\{x_\xi y_\eta - x_\eta y_\xi\} \end{aligned} \tag{6}$$

$$\mathbf{F}' = D^{-1}\begin{pmatrix} \xi_x\rho u+\xi_y\rho v \\ \xi_x\{\rho u^2+p\}+\xi_y\rho uv \\ \xi_x\rho uv+\xi_y\{\rho v^2+p\} \\ \xi_x\rho u\{e_c+p/\rho\}+\xi_y\rho v\{e_c+p/\rho\} \end{pmatrix}$$

$$= \begin{pmatrix} y_\eta\rho u+x_\eta\rho v \\ y_\eta\{\rho u^2+p\}-x_\eta\rho uv \\ y_\eta\rho uv-x_\eta\{\rho v^2+p\} \\ y_\eta\rho u\{e_c+p/\rho\}+x_\eta\rho v\{e_c+p/\rho\} \end{pmatrix} \tag{8b}$$

$$\begin{aligned} c_1^\xi &= \frac{\xi_x}{\sqrt{\xi_x^2+\xi_y^2}}=\frac{y_\eta}{\sqrt{y_\eta^2+x_\eta^2}} \\ c_2^\xi &= \frac{\xi_y}{\sqrt{\xi_x^2+\xi_y^2}}=-\frac{x_\eta}{\sqrt{y_\eta^2+x_\eta^2}} \\ c_1^\eta &= \frac{\eta_y}{\sqrt{\eta_x^2+\eta_y^2}}=\frac{x_\xi}{\sqrt{x_\xi^2+y_\xi^2}} \\ c_1^\eta &= \frac{\eta_x}{\sqrt{\eta_x^2+\eta_y^2}}=-\frac{y_\xi}{\sqrt{x_\xi^2+y_\xi^2}} \end{aligned} \tag{22}$$

$$R^+ = f(\text{upstream infinity}) = \text{imposed} = \frac{2}{\gamma-1}a_{-\infty}+q_{-\infty} \tag{29}$$

$$\begin{aligned} u_{\text{inlet}} &= \frac{R^+-R^-}{2} \\ a_{\text{inlet}} &= \left\{\frac{R^+-R^-}{2}\right\}\cdot\left\{\frac{\gamma-1}{2}\right\} \end{aligned} \tag{30}$$

Correction

$$\begin{aligned} \mathbf{W}' &= D^{-1}\mathbf{W} \\ \mathbf{F}' &= D^{-1}\{\xi_t\mathbf{W}+\xi_x\mathbf{F}+\xi_y\mathbf{G}\} \\ \mathbf{G}' &= D^{-1}\{\eta_t\mathbf{W}+\eta_x\mathbf{F}+\eta_y\mathbf{G}\} \\ D &= \xi_x\eta_y-\xi_y\eta_x=1/\{x_\xi y_\eta - x_\eta y_\xi\} \end{aligned} \tag{6}$$

$$\mathbf{F}' = D^{-1}\begin{pmatrix} \xi_x\rho u+\xi_y\rho v \\ \xi_x\{\rho u^2+p\}+\xi_y\rho uv \\ \xi_x\rho uv+\xi_y\{\rho v^2+p\} \\ \xi_x\rho u\{e_c+p/\rho\}+\xi_y\rho v\{e_c+p/\rho\} \end{pmatrix}$$

$$= \begin{pmatrix} y_\eta\rho u+x_\eta\rho v \\ y_\eta\{\rho u^2+p\}-x_\eta\rho uv \\ y_\eta\rho uv-x_\eta\{\rho v^2+p\} \\ y_\eta\rho u\{e_c+p/\rho\}-x_\eta\rho v\{e_c+p/\rho\} \end{pmatrix} \tag{8b}$$

$$\begin{aligned} c_1^\xi &= \frac{\xi_x}{\sqrt{\xi_x^2+\xi_y^2}}=\frac{y_\eta}{\sqrt{y_\eta^2+x_\eta^2}} \\ c_2^\xi &= \frac{\xi_y}{\sqrt{\xi_x^2+\xi_y^2}}=-\frac{x_\eta}{\sqrt{y_\eta^2+x_\eta^2}} \\ c_1^\eta &= \frac{\eta_y}{\sqrt{\eta_x^2+\eta_y^2}}=\frac{x_\xi}{\sqrt{x_\xi^2+y_\xi^2}} \\ c_2^\eta &= \frac{\eta_x}{\sqrt{\eta_x^2+\eta_y^2}}=-\frac{y_\xi}{\sqrt{x_\xi^2+x_\xi^2}} \end{aligned} \tag{22}$$

$$R^+ = f(\text{upstream infinity}) = \text{imposed} = \frac{2}{\gamma-1}a_{-\infty}+q_{-\infty} \tag{29}$$

$$\begin{aligned} u_{\text{inlet}} &= \frac{R^+-R^-}{2} \\ a_{\text{inlet}} &= \left\{\frac{R^++R^-}{2}\right\}\cdot\left\{\frac{\gamma-1}{2}\right\} \end{aligned} \tag{30}$$

An Approximate Solution for the Flow Between a Rotating and a Stationary Disk

J. M. Owen
School of Engineering and Applied Sciences,
University of Sussex,
Falmer, Brighton, BN1 9QT,
United Kingdom

The linear Ekman-layer equations are solved for the case of a rotor–stator system with a superimposed radial outflow of fluid. For laminar flow, the predicted rotational speed of the core between the boundary layers on the rotor and stator agrees well with existing experimental measurements when the superimposed flow rate is zero, but the theoretical solutions underestimate the core rotation when the flow rate is nonzero. For turbulent flow, the linear theory underestimates the core rotation under all conditions. Solutions of the turbulent momentum-integral equations for the rotor are used to provide an approximation for the core rotation that agrees reasonably well with the measured values over a range of flow rates and rotational speeds. Despite the fact that the equations take no account of the presence of the peripheral shroud, the approximate solutions for the moment coefficients are in reasonable agreement with the available experimental data. It is shown that the core rotation is suppressed and the moment coefficient equals that of a free disk when the superimposed flow rate equals the free-disk entrainment rate.

1 Introduction

El-Oun and Owen (1988) have provided a theoretical model to predict the effect of frictional heating on the preswirl cooling air in a rotor–stator system. In order to calculate how the disk-cooling air affects the preswirl flow, it is necessary to be able to estimate the core rotation between the boundary layers in the rotor and stator and to calculate the frictional moment of the rotating disk. It is the object of this paper to provide approximate solutions to enable such calculations to be made.

The momentum-integral equations have been used by many authors to provide solutions of the flow between a rotating and stationary disk in which there is a zero superimposed flow (see Dorfman, 1963). The solutions available for the case of a superimposed flow are fewer, and most authors have concentrated on the case where the coolant flow rate is large (see Kapinos, 1965, and Owen et al. 1974) whereas, in modern gas turbines, the coolant flow rate is usually significantly less than the free-disk entrainment rate.

Recently Owen et al. (1985) obtained solutions of the momentum-integral equations for a rotating cavity with a superimposed flow of fluid, and their predicted velocity distributions were in good agreement with measured values. They showed that, for a large range of flow rates and rotational speeds, the linear Ekman-layer equations (in which the nonlinear inertia terms are negligibly small compared with the Coriolis terms) provide a good description of the flow. It is therefore interesting to see whether these Ekman-layer equations can be used to provide approximations for the rotor–stator problem.

Contributed by the International Gas Turbine Institute and presented at the 33rd International Gas Turbine and Aeroengine Congress and Exhibition, Amsterdam, The Netherlands, June 5–9, 1988. Manuscript received by the International Gas Turbine Institute September 15, 1987. Paper No. 88-GT-293.

In Sections 2 and 3, the linear Ekman-layer equations are solved for laminar and turbulent flow, respectively, in a rotor–stator system with a radial outflow of fluid. In Section 4, solutions of the nonlinear momentum-integral equations for the rotor are used to provide an improved approximation for the turbulent-flow case. Using these approximate solutions, the moment coefficient is calculated in Section 5.

2 Linear Equations for Laminar Flow

2.1 Flow Near a Rotating Disk. Figure 1 shows a simplified diagram of the flow between a rotating and a stationary disk where, at sufficiently large rotational speeds, separate boundary layers are formed on the rotor and stator. Between the boundary layers the fluid core rotates with a tangential component of velocity $\bar{V}_\phi$ relative to a stationary frame.

The case of the flow between two corotating disks has been studied by Owen et al. (1985) for linear and nonlinear, laminar and turbulent flow. The linear case is more readily understood by the use of coordinates referred to a rotating system. The radial and tangential components of velocity in the rotating system, u and v, respectively, are related to the components in the stationary system, V_r and V_ϕ, by

$$u = V_r, \quad v = V_\phi - \Omega r, \text{ and } \bar{v} = \bar{V}_\phi - \Omega r \tag{2.1}$$

For small values of $|v|/\Omega r$, the nonlinear inertia forces can be neglected in comparison with the Coriolis forces, and the resulting "Ekman-layer equations" are

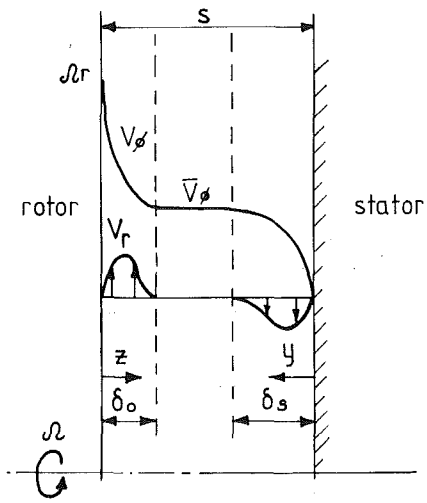

Fig. 1 Simplified diagram of the boundary-layer flow in a rotor-stator system

$$\left.\begin{aligned} -2\Omega(v-\bar{v}) &= \nu\frac{\partial^2 u}{\partial z^2} \\ 2\Omega u &= \nu\frac{\partial^2 v}{\partial z^2} \end{aligned}\right\} \quad \text{and} \quad (2.2)$$

where $u = v = 0$ when $z = 0$ (on the rotor), and $u = 0$, $v = \bar{v}$ as $z \to \infty$ (in the fluid core). The solutions of equations (2.2) are

$$\left.\begin{aligned} u &= -\bar{v}e^{-z/D}\sin(z/D) \\ v &= \bar{v}(1-e^{-z/D}\cos(z/D)) \end{aligned}\right\} \quad (2.3)$$

where $D = (\nu/\Omega)^{1/2}$.

The volumetric flow rate in the Ekman layer on the rotor, Q_0, is given by

$$Q_0 = \int_0^\infty 2\pi r u dz = -\pi r\bar{v}\left(\frac{\nu}{\Omega}\right)^{1/2} \quad (2.4)$$

If Q_o is known, equation (2.4) can be used to find $\bar{v}$; if $\bar{v}$ is known, Q_0 can be obtained.

Despite the fact that it was assumed that $|v|/\Omega r \ll 1$, the "linear solutions" were shown to provide a good approximation to the flow in a rotating cavity over a large range of core rotational speeds.

2.2 Flow Near a Stationary Disk. It is interesting (although there is little justification!) to see what happens when the linear equations are applied to the stator. If the angular speed of the core is ω, where $\bar{V}_\phi = \omega r$, then the linear Ekman-layer equations can be written as

$$\left.\begin{aligned} -2\omega(V_\phi - \bar{V}_\phi) &= \nu\frac{\partial^2 V_r}{\partial y^2} \\ 2\omega V_r &= \nu\frac{\partial^2 V_\phi}{\partial y^2} \end{aligned}\right\} \quad (2.5)$$

where $V_r = V_\phi = 0$ when $y = 0$ (on the stator), and $V_r = 0$, $V_\phi = \bar{V}_\phi$ as $y \to \infty$ (in the core). The solutions of equations (2.5) are

$$\left.\begin{aligned} V_r &= -\bar{V}_\phi e^{-y/D_s}\sin(y/D_s) \\ V_\phi &= \bar{V}_\phi(1-e^{-y/D_s}\cos(y/D_s)) \end{aligned}\right\} \quad \text{and} \quad (2.6)$$

where

$$D_s = (\nu/\omega)^{1/2}$$

The volumetric flow rate in the Ekman-layer on the stator, Q_s, is given by

$$Q_s = \int_0^\infty 2\pi r V_r dy = -\pi r\bar{V}_\phi\left(\frac{\nu}{\omega}\right)^{1/2} \quad (2.7)$$

It should be noted that as $\bar{V}_\phi > 0$ then $Q_s < 0$, whereas, as $\bar{v} < 0$ in equation (2.4), $Q_0 > 0$. That is, the flow is radially outward on the rotor and inward on the stator.

In Fig. 2, equations (2.6) are compared with Bödewadt's (1940) solutions of the Navier-Stokes equations for a rotating fluid near a stationary plate. While, not surprisingly, there are quantitative differences between the two solutions, both

Nomenclature

b = disk radius
C_m = $M/\frac{1}{2}\rho\Omega^2 b^5$ moment coefficient
C_m^* = value of C_m for $C_w = 0$
C_w = $Q/\nu b$ flow rate coefficient
D = $(\nu/\Omega)^{1/2}$ Ekman-layer thickness for rotor
D_s = $(\nu/\omega)^{1/2}$ Ekman-layer thickness for stator
G = s/b gap ratio
M = frictional moment on one side of the rotor
Q = volumetric flow rate
Re_ϕ = $\Omega b^2/\nu$ rotational Reynolds number
s = axial space between rotor and stator
u, v = radial and tangential components of velocity in a rotating coordinate system
$\bar{v}$ = value of v in the core
V_r, V_ϕ, V_z = radial, tangential, and axial components of velocity in a stationary coordinate system
$\bar{V}_\phi$ = value of V_ϕ in the core
x = r/b nondimensional radial coordinate
y = axial distance from stator
z = axial distance from rotor
α = ratio of shear stresses
β = $\bar{V}_\phi/\Omega r$ relative rotational speed of core
γ = variable in boundary-layer thickness
δ = boundary-layer thickness
η = nondimensional boundary-layer thickness
λ_L = $C_w\mathrm{Re}_\phi^{-1/2}$ laminar parameter
λ_T = $C_w\mathrm{Re}_\phi^{-4/5}$ turbulent parameter
ν = kinematic viscosity
ρ = density
τ_r, τ_ϕ = radial and tangential components of shear stress
ϕ = $\lambda_T x^{-13/5}$ turbulent parameter
ω = angular speed of core
Ω = angular speed of rotor

Subscripts

fd = free-disk value
o = refers to rotor
s = refers to stator
wj = wall-jet value
$*$ = value for $C_w = 0$

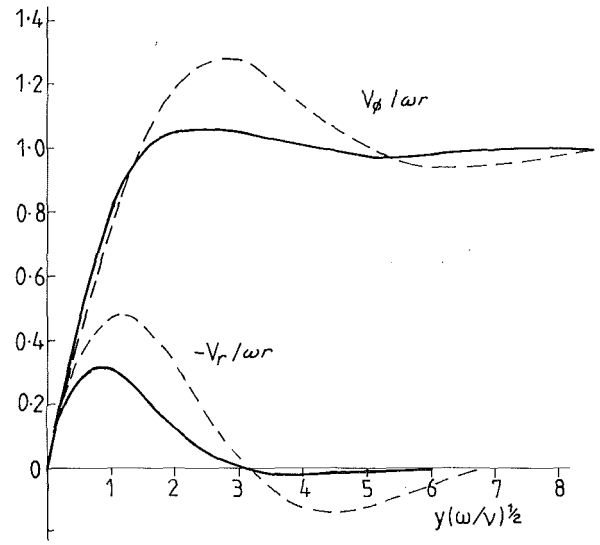

Fig. 2 The variation of the radial and tangential components of velocity in the laminar boundary layer formed by a rotating fluid and a stationary disk: —— equations (2.6), ---- Bödewadt's (1940) solution

display a similar oscillatory behavior. However, the value of Q_s obtained from the exact solution is 35 percent greater than that given in equation (2.7) for the "linear solutions." The agreement is sufficiently encouraging to investigate the use of linear solutions for the rotor–stator problem.

2.3 Flow Between a Rotating and a Stationary Disk. Consider the case where there is a superimposed radial outflow Q between the rotor and stator. Using equations (2.4) and (2.7), it follows that

$$Q = Q_o + Q_s = -\pi r\left(\bar{v}\left(\frac{\nu}{\Omega}\right)^{1/2} + \bar{V}_\phi\left(\frac{\nu}{\omega}\right)^{1/2}\right) \tag{2.8}$$

or

$$1 - \beta - \beta^{1/2} = \lambda_L/\pi x^2 \tag{2.9}$$

where

$$\beta = \bar{V}_\phi/\Omega r = \omega/\Omega$$

$$\lambda_L = C_w \mathrm{Re}_\phi^{-1/2}$$

and

$$x = r/b$$

where b is the outer radius of the rotor. Equation (2.9) can be solved to give

$$\beta = \frac{1}{2}[(3 - 2\lambda_L/\pi x^2 - (5 - 4\lambda_L/\pi x^2)^{1/2}] \tag{2.10}$$

For zero flow rate ($\lambda_L = 0$), $\beta = \beta^* = 0.382$.

It can be seen from equation (2.10) that $\beta = 0$ when $\lambda_L = \pi x^2$, that is when

$$C_w = \pi \mathrm{Re}_\phi^{1/2} x^2 \tag{2.11}$$

This value of C_w is approximately 16 percent greater than the laminar free-disk entrainment rate obtained from solutions of the Navier-Stokes equations (see Owen and Rogers, 1989). It would appear, therefore, that a superimposed flow rate approximately equal to the free-disk entrainment rate is sufficient to suppress the core rotation. For larger flow rates, it is presumed that the core velocity is zero and that there is no flow down the stator.

Figure 3 shows a comparison between the velocity distributions obtained from the linear solutions (equations (2.3) and (2.6) with $\bar{V}_\phi/\Omega r = 0.382$) and the measurements of Daily et al.

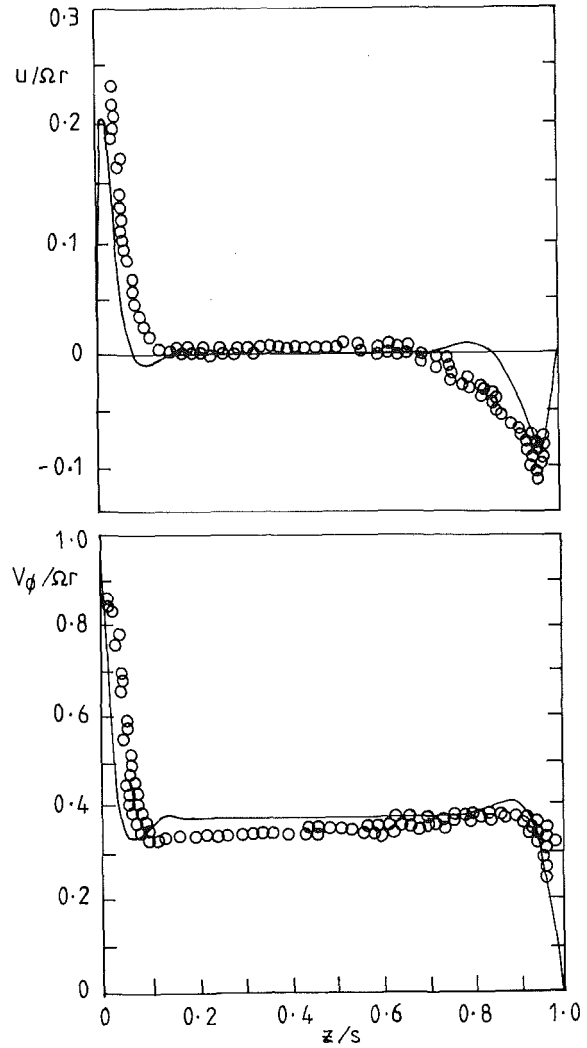

Fig. 3 The axial distribution of the radial and tangential components of velocity for laminar flow: $G = 0.069$, $C_w = 0$, and $\mathrm{Re}_\phi = 2.95 \times 10^5$: —— linear theory; o experimental data of Daily et al. (1964)

(1964). The measurements were made in an air-filled rotor–stator system and, for the results presented in the figure, $G = 0.069$, $\mathrm{Re}_\phi = 2.95 \times 10^5$, and $C_w = 0$. Although the authors used different symbols for measurements made at $x = 0.469$, 0.648, and 0.828, there was so little difference between the three sets of data that only one symbol is used in Fig. 3. Considering the assumptions made in obtaining the linear solutions, the agreement between theory and experiment is surprisingly good.

Figure 4 shows the comparison between the linear theory ($\bar{V}_\phi/\Omega b = 0.382x$) and the data of Dijkstra and van Heijst (1983). In their experiments, they used a water-filled glass rotor–stator system with a cylindrical shroud that could be either stationary or rotating. The velocity measurements were made by stereo-photography in the midaxial plane for $G = 0.07$, $C_w = 0$, and $\mathrm{Re}_\phi = 2 \times 10^5$, and the agreement between the measured data and the linear theory is reasonable. For the case where the shroud is rotating, the authors' numerical predictions of $\bar{V}_\phi/\Omega b$ are, for $x > 0.7$, greater than the values obtained from the linear theory. It should be noted that it is only at the larger radii that the presence of the shroud is significant, and the linear theory can take no account of this.

Figure 5 shows the variation of β/β^* with $\lambda_L/\pi x^2$ according to equation (2.10) with $\beta^* = 0.382$. Also shown are the computations of Vaughan (1986) and the measurements of El-Oun

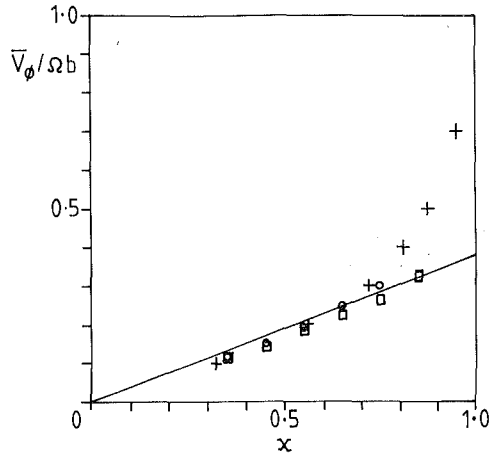

Fig. 4 The variation of $\bar{v}_\phi/\Omega b$ with x for laminar flow for $G=0.07$, $C_W=0$, and $Re_\phi=2\times10^5$ —— linear theory; (Dijkstra and Van Heijst, 1983): □ experimental data, stationary shroud; ○ experimental data, rotating shroud; + numerical data, rotating shroud

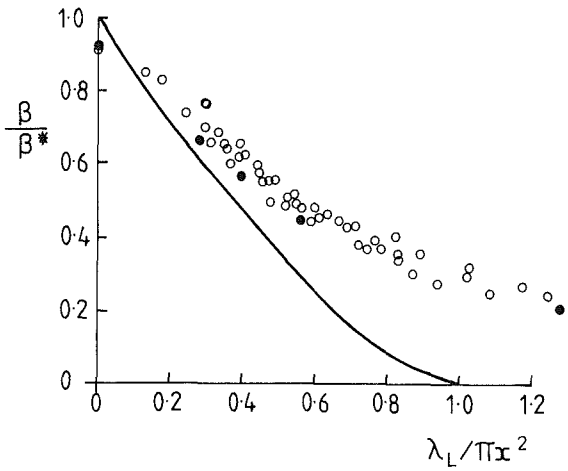

Fig. 5 The variation of the relative core rotation for laminar flow —— equation (2.10); (Vaughan, 1986): ○ experimental data; ● numerical results

and Pincombe, which are presented in Vaughan's thesis. The experimental measurements were made at a radius ratio of $r/b=0.5$ using laser-Doppler anemometry in an air-filled rotor–stator rig for a wide range of flow rates and rotational speeds. The computations were conducted using a modified TEACH program with a variable-geometry finite-difference grid with 70×90 nodes. Agreement between the computed and the measured velocities is good, but the theoretical curve tends to underestimate the data. For example, at $\lambda_L/\pi x^2=1$, equation (2.10) implies that $\beta=0$, whereas the experimental measurements suggested that $\beta\simeq0.1$.

3 Linear Equations for Turbulent Flow

3.1 Flow Near a Rotating Disk. The turbulent version of the Ekman-layer equations (2.2) can be written as

$$\left.\begin{aligned} -2\Omega(v-\bar{v}) &= \frac{1}{\rho}\frac{\partial\tau_r}{\partial z} \\ \text{and}\qquad 2\Omega u &= \frac{1}{\rho}\frac{\partial\tau_\phi}{\partial z} \end{aligned}\right\} \tag{3.1}$$

For the case of a rotating cavity, Owen et al. (1985) solved the integral version of these equations using 1/7th power law profiles. By analogy with von Karman's (1921) solution for turbulent flow over a free disk, it was assumed that

$$\left.\begin{aligned} u &= u_0\eta_0^{1/7}(1-\eta_0), \quad \eta_0\le1 \\ u &= 0, \quad \eta_0>1 \\ v &= \bar{v}\eta_0^{1/7}, \quad \eta_0\le1 \\ v &= \bar{v}, \quad \eta_0>1 \end{aligned}\right\} \tag{3.2}$$

where $\eta_0=z/\delta_0$, δ_0 being the thickness of the boundary layer on the rotating disk. The radial and tangential components of shear stress at the disk surface were taken to be

$$\tau_{r,o}=-\alpha_o\tau_{\phi,o}=0.0225\rho\left(\frac{\nu}{\delta_o}\right)^{1/4}u_o(u_o^2+\bar{v}^2)^{3/8} \tag{3.3}$$

where $\alpha_o=-u_o/\bar{v}$.

Using equations (3.2), equations (3.1) can be integrated from $z=0$ to $z=\delta_o$ to give

$$\left.\begin{aligned} -\frac{1}{4}\Omega\bar{v}\delta_o &= \frac{\tau_{r,o}}{\rho} \\ \text{and}\qquad -\frac{49}{60}\Omega u_o\delta_o &= \frac{\tau_{\phi,o}}{\rho} \end{aligned}\right\} \tag{3.4}$$

Hence, using equation (3.3),

$$\left.\begin{aligned} \alpha_o &= 0.553 \\ \text{and}\qquad \frac{\delta_o}{b} &= 0.0983\mathrm{Re}_\phi^{-1/5}\left(\frac{|\bar{v}|}{\Omega r}\right)^{3/5}x^{3/5} \end{aligned}\right\} \tag{3.5}$$

As

$$Q_o=\int_0^{\delta_o}2\pi rudz=\frac{49}{60}\pi ru_o\delta_o \tag{3.6}$$

it follows from equation (3.5) that

$$\frac{Q_o}{\nu b}=\mathrm{sgn}(\bar{v})0.140\ \mathrm{Re}_\phi^{4/5}\left(\frac{|\bar{v}|}{\Omega r}\right)^{8/5}x^{13/5} \tag{3.7}$$

Thus equation (3.7) relates the volumetric flow rate in the Ekman layer on the rotor to the rotational speed of the interior core. While the Ekman-layer equations are only strictly valid for $|v|/\Omega r<<1$, Owen et al. (1985) showed that, for a rotating cavity with a radial outflow of fluid, the linear solutions were in good agreement with both the nonlinear solutions and the experimental data for $|\bar{v}|/\Omega r<0.3$.

3.2 Flow Near a Stationary Disk. As for the laminar case, it is assumed that the turbulent Ekman-layer equations can be used to approximate the flow over the stator. If the angular speed of the core is ωr, where $\bar{V}_\phi=\omega r$, the Ekman-layer equations can be written as

$$\left.\begin{aligned} 2\omega(V_\phi-\bar{V}_\phi) &= \frac{1}{\rho}\frac{\partial\tau_r}{\partial y} \\ 2\omega V_r &= -\frac{1}{\rho}\frac{\partial\tau_\phi}{\partial y} \end{aligned}\right\} \tag{3.8}$$

The 1/7th power-law is used such that

$$\left.\begin{aligned} V_r &= u_s\eta_s^{1/7}(1-\eta_s), \quad \eta_s \le 1 \\ V_r &= 0, \quad \eta_s > 1 \\ V_\phi &= \bar{V}_\phi \eta_s^{1/7}, \quad \eta_s \le 1 \\ V_\phi &= \bar{V}_\phi, \quad \eta_s > 1 \end{aligned}\right\} \tag{3.9}$$

where $\eta_s = y/\delta_s$, and

$$\tau_{r,s} = \alpha_s \tau_{\phi,s} = -0.0225\rho\left(\frac{\nu}{\delta_s}\right)^{1/4} u_s(u_s^2 + \bar{V}_\phi^2)^{3/8} \tag{3.10}$$

where

$$\alpha_s = u_s/\bar{V}_\phi$$

(This ensures that $\tau_{\phi,s}$ and $\tau_{r,s}$ are of opposite sign, which is consistent with the fact that u_s and $\bar{V}_\phi$ are of opposite sign and that if $\bar{V}_\phi > 0$ then $\partial V_\phi/\partial z = -\partial V_\phi/\partial y < 0$.)

Using equations (3.9), equations (3.8) can be integrated from $y = 0$ to $y = \delta_s$ to give

$$\left.\begin{aligned} -\frac{1}{4}\omega\bar{V}_\phi\delta_s &= -\frac{\tau_{r,s}}{\rho} \\ \text{and} \qquad \frac{49}{60}\omega u_s\delta_s &= \frac{\tau_{\phi s}}{\rho} \end{aligned}\right\} \tag{3.11}$$

Hence, using equation (3.10)

$$\left.\begin{aligned} \alpha_s &= -0.553 \\ \text{and} \qquad \frac{\delta_s}{b} &= 0.0983\left(\frac{\nu}{\omega b^2}\right)^{1/5} x^{3/5} \end{aligned}\right\} \tag{3.12}$$

As

$$Q_s = \int_o^{\delta_s} 2\pi r V_r dy = \frac{49}{60}\pi r u_s \delta_s \tag{3.13}$$

it follows from equation (3.12) that

$$\frac{Q_s}{\nu b} = -0.140\left(\frac{\omega b^2}{\nu}\right)^{4/5} x^{13/5} \tag{3.14}$$

Having established the relationship between flow rate and core rotation, it is possible to link the flow on the rotor to that on the stator by means of the continuity equation.

3.3 Flow Between a Rotating and a Stationary Disk. For a superimposed radial outflow Q between the rotor and stator, and using equations (3.7) and (3.14), it follows that

$$C_w = \frac{Q_o}{\nu b} + \frac{Q_s}{\nu b}$$

$$= \mathrm{sgn}(1-\beta)0.140\mathrm{Re}_\phi^{4/5} x^{13/5}(1 - \beta^{8/5} - \beta^{4/5}) \tag{3.15}$$

where

$$\beta = \bar{V}_\phi/\Omega r = \omega/\Omega$$

Alternatively, equation (3.15) can be expressed as

$$(1-\beta)^{8/5} - \beta^{4/5} = \mathrm{sgn}(1-\beta)7.14\lambda_T x^{-13/5} \tag{3.16}$$

where

$$\lambda_T = C_w \mathrm{Re}_\phi^{-4/5}$$

and for $C_w = 0$, $\beta = \beta^* = 0.382$ (which is identical to the laminar result given in Section 2). The variation of β/β^* with $\lambda_T x^{-13/5}$ according to equation (3.16) is shown in Fig. 6. Also

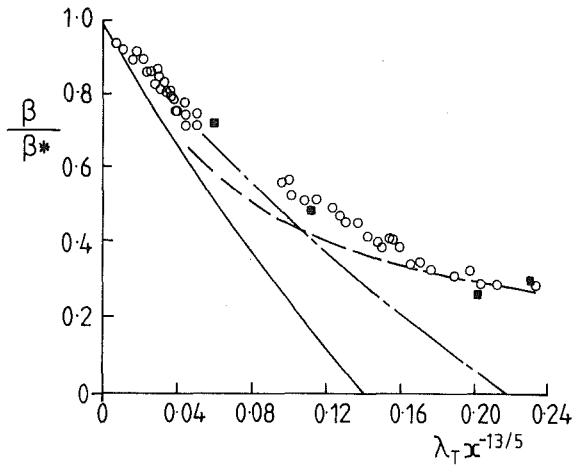

Fig. 6 The variation of the relative core rotation for turbulent flow: —— equation (3.16); ---- equation (3.17); — - —equation (4.13); Vaughan (1986): ○ experimental data; ■ numerical results

shown is an empirical correlation proposed by Daily et al. (1964) where

$$\beta/\beta^* = (12.7\lambda_T x^{-13/5} + 1)^{-1} \tag{3.17}$$

The authors based their correlation on velocity measurements conducted at $G = 0.055$ and 0.069 for $\mathrm{Re}_\phi = 6.9 \times 10^5$ and $x = 0.469$, 0.648, and 0.828, and chose an "ideal" value of $\beta^* = 0.5$. In fact, the measured values for β^* depended on the gap ratio, and the authors gave values of $\beta^* = 0.475$, 0.45, and 0.42 for $G = 0.0276$, 0.069, and 0.124, respectively.

The experimental measurements of El-Oun and Pincombe and the numerical predictions of Vaughan (1986), referred to in Section 2.3, are also shown in Fig. 6. For the turbulent-flow computations, Vaughan used a mixing-length model, and his results are in good agreement with the experimental data. The correlation of Daily et al. tends to underestimate the data, and equation (3.16) provides an even lower estimate.

An improved approximation for the turbulent radial-outflow case is discussed below.

4 An Approximate Solution for Turbulent Flow

4.1 Momentum-Integral Equations for the Rotor. The momentum-integral equations for the rotor can be written (see Appendix) as

$$\frac{d}{dx}(x\delta_o\int_0^1 V_r^2 d\eta_o) - \delta_o\int_0^1 (V_\phi^2 - \bar{V}_\phi^2)d\eta_o = -\frac{xb}{\rho}\tau_{r,o} \tag{4.1a}$$

and

$$\frac{d}{dx}(x^2\delta_o\int_0^1 V_r(V_\phi - \bar{V}_\phi)d\eta_o) + \frac{Q_o}{2\pi b}\frac{d}{dx}(x\bar{V}_\phi) = -\frac{x^2 b}{\rho}\tau_{\phi,o} \tag{4.1b}$$

where

$$Q_o = \int_0^{\delta_o} 2\pi r V_r dz$$

The velocity profiles will be assumed to be the same as those used for the linear solution in Section 3. It is convenient to write them as

$$\left.\begin{aligned} V_r &= \alpha_o\Omega r(1-\beta)\eta_o^{1/7}(1-\eta_o) \\ \text{and} \qquad V_\phi &= \Omega r(1 - \eta_o^{1/7}(1-\beta)) \end{aligned}\right\} \tag{4.2}$$

The shear stresses are given by

$$\frac{\tau_{r,o}}{\rho\Omega^2 b^2} = -\alpha_o \frac{\tau_{\phi,o}}{\rho\Omega^2 b^2} = 0.0225 \mathrm{Re}_\phi^{-1/4} \left(\frac{\delta_o}{b}\right)^{-1/4}$$

$$\times \alpha_o (1+\alpha_o^2)^{3/8} (1-\beta)^{7/4} x^{7/4} \tag{4.3}$$

In Section 3, the solution of the linear equations gave

$$\left.\begin{aligned} \alpha_o &= 0.553 \\ \frac{\delta_o}{b} &= 0.0983 \mathrm{Re}_\phi^{-1/5} (1-\beta)^{3/5} x^{3/5} \end{aligned}\right\} \tag{4.4}$$

However, these solutions are strictly valid as $\beta \to 1$, and as $\beta \to 0$ the flow must tend to the free-disk case. For the latter, von Karman's (1921) solutions are

and

$$\left.\begin{aligned} \alpha_o &= 0.162 \\ \frac{\delta_o}{b} &= 0.525 \mathrm{Re}_\phi^{-1/5} x^{3/5} \end{aligned}\right\} \tag{4.5}$$

Both solutions can be represented by

and

$$\left.\begin{aligned} \alpha_o &= \alpha_o(\beta) \\ \frac{\delta_o}{b} &= \gamma_o(\beta) \mathrm{Re}_\phi^{-1/5} (1-\beta)^{3/5} x^{3/5} \end{aligned}\right\} \tag{4.6}$$

where $\alpha_o(0) = 0.162$, $\alpha_o(1) = 0.553$, $\gamma_o(0) = 0.525$, and $\gamma_o(1) = 0.0983$.

If equations (4.2), (4.3), and (4.6) are substituted into equations (4.1), the result is

$$\left.\begin{aligned} &0.2071 \frac{d}{dx} (\alpha_o^2 \gamma_o (1-\beta)^{13/5} x^{18/5}) - \\ &- 0.02778 \gamma_o (1-\beta)^{8/5} (1+8\beta) x^{13/5} \\ &= -0.0225 \alpha_o (1+\alpha_o^2)^{3/8} \gamma_o^{-1/4} (1-\beta)^{8/5} x^{13/5} \\ &0.06806 \frac{d}{dx} (\alpha_o \gamma_o (1-\beta)^{13/5} x^{23/5}) \\ &+ 0.4083 \alpha_o \gamma_o (1-\beta)^{8/5} x^{13/5} \frac{d}{dx} (\beta^2 x) \\ &= 0.0225 (1+\alpha_o^2)^{3/8} \gamma_o^{-1/4} (1-\beta)^{8/5} x^{18/5} \end{aligned}\right\} \tag{4.7}$$

For the case where β is constant, equations (4.7) simplify to

and

$$\left.\begin{aligned} &0.7456 \alpha_o^2 \gamma_o (1-\beta) - 0.02778 \gamma_o (1+8\beta) \\ &= -0.0225 \alpha_o (1+\alpha_o^2)^{3/8} \gamma_o^{-1/4} \\ &0.3131 \alpha_o \gamma_o (1-\beta) + 0.8167 \alpha_o \gamma_o \beta \\ &= 0.0225 (1+\alpha_o^2)^{3/8} \gamma_o^{-1/4} \end{aligned}\right\} \tag{4.8}$$

Hence

and

$$\left.\begin{aligned} \alpha_o &= 0.162 (1+8\beta)^{1/2} (1-0.229\beta)^{-1/2} \\ \gamma_o &= 0.526 (1-0.019\beta)^{0.3} (1-0.229\beta)^{0.1} \\ &\times (1+8\beta)^{0.4} (1+1.608\beta)^{-0.8} \end{aligned}\right\} \tag{4.9}$$

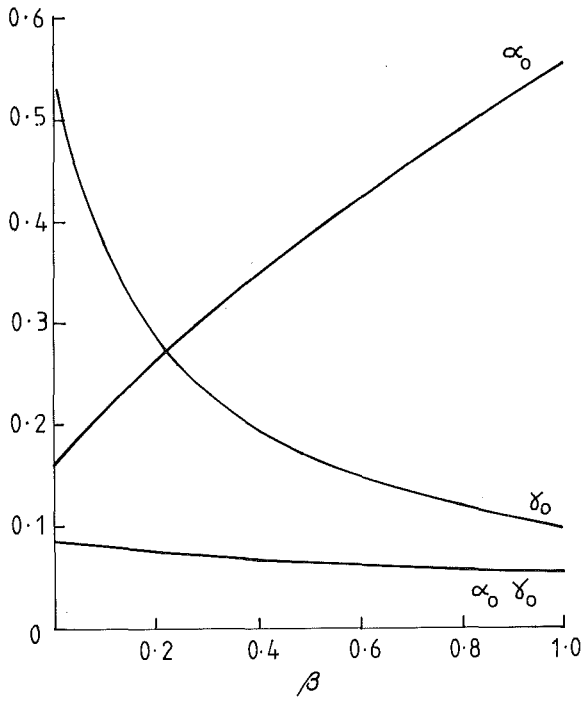

Fig. 7 The variation of α_o, γ_o, and $\alpha_o\ \gamma_o$ with β according to equations (4.9)

For the two cases where $\beta = 0$ and $\beta = 1$, these results reduce (within rounding errors) to the free-disk and linear cases, respectively.

The volumetric flow rate in the boundary layer can be determined by integrating V_r in equation (4.2) to give

$$\frac{Q_o}{\nu b} = \frac{49\pi}{60} \mathrm{Re}_\phi^{4/5} \alpha_o \gamma_o (1-\beta)^{8/5} x^{13/5} \tag{4.10}$$

The variation of α_o, γ_o, and $\alpha_o \gamma_o$ with β is shown in Fig. 7.

4.2 An Approximate Solution for the Rotor-Stator Problem. The complete solution of the momentum-integral equations for the rotor and stator requires the solution of four coupled first-order differential equations together with the continuity equation. However, it is possible to use the results obtained in Section 4.1 to obtain an improvement on the linear solutions presented in Section 3.

It is assumed that equations (4.6) together with equations (4.9) are sufficiently accurate even if β is not constant. As there is no simple solution of the momentum-integral equations for the stator, the results derived in Section 3.2 are used. Hence, for the case of a superimposed outflow, equations (3.14) and (4.10) can be used to give

$$C_w = \frac{Q_o}{\nu b} + \frac{Q_s}{\nu b}$$

$$= \frac{49\pi}{60} \mathrm{Re}_\phi^{4/5} x^{13/5} [\alpha_o \gamma_o (1+\beta)^{8/5} + \alpha_s \gamma_s \beta^{4/5}] \tag{4.11}$$

where $\alpha_s = -0.553$, $\gamma_s = 0.0983$, and α_o and γ_o are given by equations (4.9). However, for $0 < \beta < 0.5$ (the range of interest for radial outflow), $\alpha_o \gamma_o$ can be approximated with acceptable accuracy by

$$\alpha_o \gamma_o = 0.0852 (1 - 0.51\beta) \tag{4.12}$$

and so equation (4.11) can be written as

$$(1-\beta)^{8/5} (1 - 0.51\beta) - 0.638 \beta^{4/5} = 4.57 \lambda_T x^{-13/5} \tag{4.13}$$

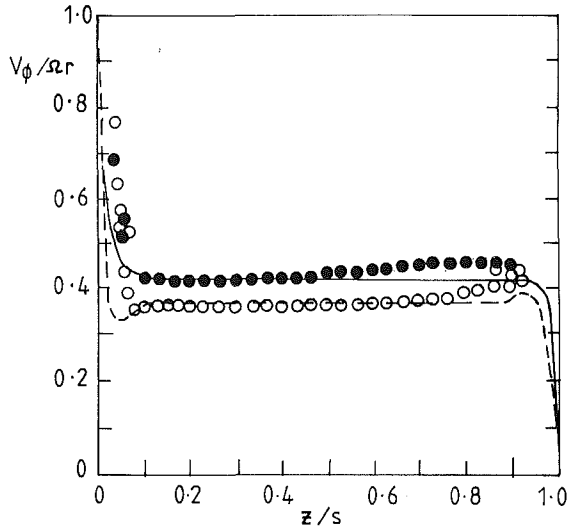

Fig. 8 The axial distribution of the tangential component of velocity: $G=0.069$, $C_w=0$, and $Re_\phi = 6.9\times10^5$: ---- laminar linear theory; —— turbulent approximation; experimental data of Daily et al. (1964): ○ $x=0.469$; ● $x=0.829$

For $\lambda_T=0$, $\beta=\beta^*=0.426$, which lies in the range $0.42<\beta^*<0.475$ given by Daily et al. (1964). Figure 8 shows a comparison between the tangential components of velocity derived from the turbulent approximation and those measured by the above authors for $G=0.069$, $C_w=0$, and $Re_\phi=6.9\times10^5$. The turbulent curve is in good agreement for $x=0.828$, and the laminar curve (based on the results in Section 2) is in good agreement for $x=0.469$. As the local rotational Reynolds number at $x=0.469$ is 1.5×10^5, it is not surprising that laminar flow occurs at this radius.

The variation of β/β^* with $\lambda_T x^{-13/5}$, according to equation (4.13), is shown in Fig. 6. For $\lambda_T x^{-13/5} \lesssim 0.1$, the approximate solution is in good agreement with the experimental data of El-Oun and Pincombe and the computations of Vaughan; for larger values, the approximate solution underestimates the data. It should be pointed out that the approximate solution, and the experimental and numerical data, were based on a value of $\beta^*=0.426$.

Equation (4.13) gives $\beta=0$ at $\lambda_T x^{-13/5}=0.219$, that is $\beta=0$ when

$$C_w = 0.219 Re_\phi^{4/5} x^{13/5} \tag{4.14}$$

which is the same as the entrainment rate predicted by von Karman for the turbulent free disk. So, as was approximately the case for laminar flow, the turbulent approximation implies that the core rotation is suppressed when the superimposed flow rate is equal to the free-disk entrainment rate. For larger flow rates, it is again presumed that the core rotation is zero and that there is no flow down the stator. However, the experimental data suggest that for $\lambda_T x^{-13/5}=0.219$, $\beta\simeq0.13$, which implies that the turbulent approximation underestimates the flow rate necessary to suppress the core rotation.

As the turbulent approximation appears to provide a reasonable estimate of the tangential component of velocity over a range of conditions of practical importance, its application to the calculation of the moment coefficient is discussed below.

5 Calculation of Moment Coefficient

5.1 Introduction. The frictional moment M on one side of the rotor is given by

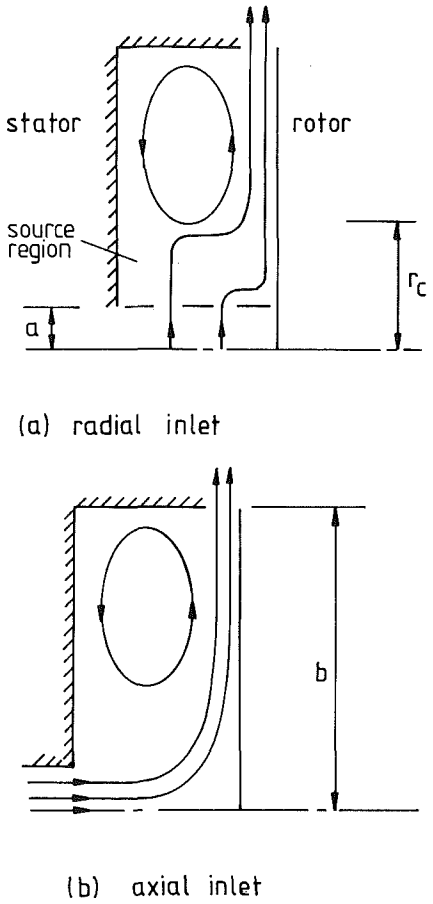

Fig. 9 Simplified flow structure in a rotor-stator system with a superimposed outflow of fluid

$$M = -\int_0^b 2\pi r^2 \tau_{\phi,o}\, dr \tag{5.1}$$

The moment coefficient C_m is defined as

$$C_m = \frac{M}{\frac{1}{2}\rho\Omega^2 b^5} = -4\pi\int_0^1 x^2 \frac{\tau_{\phi,o}}{\rho\Omega^2 b^2} dx \tag{5.2}$$

and $\tau_{\phi,o}/\rho\Omega^2 b^2$ can be determined from equation (4.3) if δ_o/b, α_o, and β are known. It is convenient to consider the flow in two regions: $x\le x_c$, where $\beta=0$; $x\ge x_c$, where $\beta\le0$. From equation (4.13), $\beta=0$ (that is, $x=x_c$) when

$$x_c = 1.79\lambda_T^{5/13} \tag{5.3}$$

The physical significance of x_c is that it marks the point at which the "source region" ends and core rotation begins. A description of the source region for flow inside a rotating cavity is given by Owen et al. (1985), and its effect on the moment coefficient on the rotating disk is discussed below.

5.2 Source Region. Figure 9 shows a simplified diagram of the assumed flow structure where $r_c=x_c b$ is the radius of the source region. In the radial-inlet case, flow enters uniformly without swirl at $r=a$ and is gradually entrained into the boundary layer on the rotor; in the axial-inlet case, the flow impinges on the rotor and moves radially outward as a wall jet. For $r>r_c$, both flows are the same: There is core rotation and a radially inward flow on the stator. Such flows have been observed, in the source region of a rotating cavity, by Owen et al., and it is assumed here that they occur in rotor-stator systems for $r<r_c$. It should be pointed out, however, that, at sufficiently low flow rates, it is possible for the axial-inlet case to behave in a similar manner to that of the radial-inlet such

that no wall jet is formed and the flow is progressively entrained into the boundary layer.

For $x \le x_c$, where $\bar{V}_\phi = 0$, equation (4.1b) can be written as

$$\frac{d}{dx}\left(x^2\delta_o \int_0^1 V_r V_\phi d\eta_o\right) = -\frac{x^2 b}{\rho}\tau_{\phi,o} \tag{5.4}$$

Using equations (4.2) and (4.3) with $\beta = 0$, equation (5.4) becomes

$$3.025\frac{d}{dx}\left(\alpha_o x^4\left(\frac{\delta_o}{b}\right)\right)$$

$$= \mathrm{Re}_\phi^{-1/4}\left(\frac{\delta_o}{b}\right)^{-1/4}(1+\alpha_o^2)^{3/8}x^{15/4} \tag{5.5}$$

Let

$$\alpha_o x^4\left(\frac{\delta_o}{b}\right) = cx^n \tag{5.6}$$

where c and n are constants; then equation (5.5) becomes

$$\alpha_o^{1/4}(1+\alpha_o^2)^{3/8} = 3.025c^{5/4}n\mathrm{Re}_\phi^{1/4}x^{(5n-23)/4} \tag{5.7}$$

For the radial-inlet case (assuming a rotating disk entraining fluid from a quiescent environment) von Karman's (1921) solutions (equations (4.5)) give $c = 0.08505\ \mathrm{Re}_\phi^{-1/5}$ and $n = 23/5$, which, not surprisingly, satisfy equation (5.7). For the axial-inlet case, it is assumed that the volumetric flow rate in the wall jet is constant and is equal to the superimposed flow rate Q. Integrating V_r in equation (4.2) gives, for $\beta = 0$,

$$\alpha_o = 0.3898C_w\mathrm{Re}_\phi^{-1}\left(\frac{\delta_o}{b}\right)^{-1}x^{-2} \tag{5.8}$$

Hence, from equation (5.6), $c = 0.3898\ C_w\mathrm{Re}_\phi^{-1}$ and $n = 2$, and equation (5.7) becomes

$$\alpha_o^{1/4}(1+\alpha_o^2)^{3/8} = 1.863\phi^{5/4} \tag{5.9}$$

where

$$\phi = C_W\mathrm{Re}_\phi^{-4/5}x^{-13/5} = \lambda_T x^{-13/5} \tag{5.10}$$

At $x = x_c$, $\phi = 0.219$, and equation (5.9) gives $\alpha_o = 0.00605$, compared with a value of 0.162 for the free-disk case. Also, from equations (4.5) and (5.8), it follows that the thickness of the boundary layer for the wall jet, for $\phi = 0.219$, is 27 times that of the free disk.

From equation (4.3) it follows that

$$-\left(\frac{\tau_{\phi,o}}{\rho\Omega^2 b^2}\right)_{fd} = 0.0267\mathrm{Re}_\phi^{-1/5}x^{8/5} \tag{5.11a}$$

and

$$-\left(\frac{\tau_{\phi,o}}{\rho\Omega^2 b^2}\right)_{wj} = 0.0530C_w\mathrm{Re}_\phi x^{-1} \tag{5.11b}$$

where the subscripts fd and wj refer to the free disk and wall jet, respectively. It is convenient to define a moment coefficient C_{m1} for the source region such that

$$C_{m1} = -4\pi\int_0^{x_c} x^2\frac{\tau_{\phi,o}}{\rho\Omega^2 b^2}\,dx \tag{5.12}$$

It follows using equations (5.11) that, for $x_c \le 1$,

$$C_{m1,fd} = C_{m1,wj} = C_{m1} = 0.0729\mathrm{Re}_\phi^{-1/5}x_c^{23/5} \tag{5.13}$$

Thus, despite the fact that the shear stress distributions for the free disk and wall jet are different, the two moment coefficients are identical! The explanation of this paradox can be found by considering equation (5.4), from which it follows that

$$C_{m1} = \frac{4\pi}{\Omega^2 b^2}\left(x^2\frac{\delta_o}{b}\int_0^x V_r V_\phi d\eta_o\right)_{x=x_c} \tag{5.14}$$

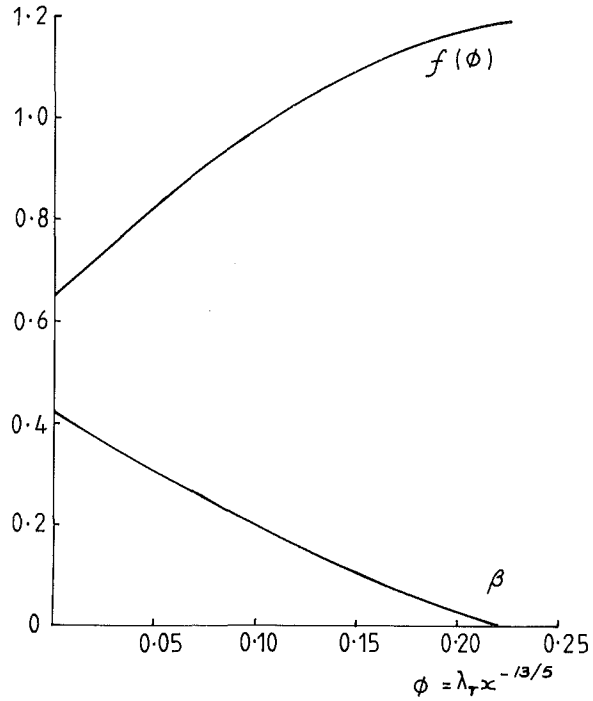

Fig. 10 Variation of β and $f(\phi)$ with ϕ

and the angular-moment term $\delta_b/b\int_0^x V_r V_\phi d\eta_o$ is the same for both the free-disk and the wall jet at $x = x_c$.

If $x_c > 1$ (that is, according to equation (5.3), $\lambda_T > 0.219$), then the free-disk solution is inapplicable. Under these conditions, equation (5.13) becomes

$$C_{m1,wj} = 0.333C_w\mathrm{Re}_\phi^{-1} \tag{5.15}$$

5.3 Moment Coefficient for the Entire Disk. Using equations (4.3) and (4.6), it follows that, for $x \ge x_c$ (that is, $\phi \le 0.219$),

$$-\left(\frac{\tau_{\phi,o}}{\rho\Omega^2 b^2}\right) = 0.0225f(\phi)\mathrm{Re}_\phi^{-1/5}x^{8/5} \tag{5.16}$$

where

$$f(\phi) = (1+\alpha_o^2)^{3/8}\gamma_o^{-1/4}(1-\beta)^{8/5}$$

The variation of $f(\phi)$ and β with ϕ, according to the results derived in Section 4, is shown in Fig. 10, and, for $0 \le \phi \le 0.219$, $f(\phi)$ can be approximated by the quadratic $f_2(\phi)$ where

$$f_2(\phi) = A + B\phi + C\phi^2 \tag{5.17}$$

with $A = 0.648$, $B = 4.13$, and $C = -7.64$.

Figure 11 shows the radial variation of $\tau_\phi/\tau_{\phi,\max}$, according to equations (5.11) and (5.16), where $\tau_{\phi,\max}$ is the value of τ_ϕ at $x = 1$. Also shown are the values of shear stress computed by Vaughan (1986) using the numerical procedure mentioned above. It can be seen that the free-disk model, equation (5.11a), provides a closer fit to the numerical results in the source region than does the wall-jet model, equation (5.11b).

It is convenient to define a moment coefficient C_{m2} for $x \ge x_c$ by

$$C_{m2} = -4\pi\int_{x_c}^1 x^2\frac{\tau_{\phi,o}}{\rho\Omega^2 b^2}dx \tag{5.18}$$

Hence, using equations (5.16) and (5.17)

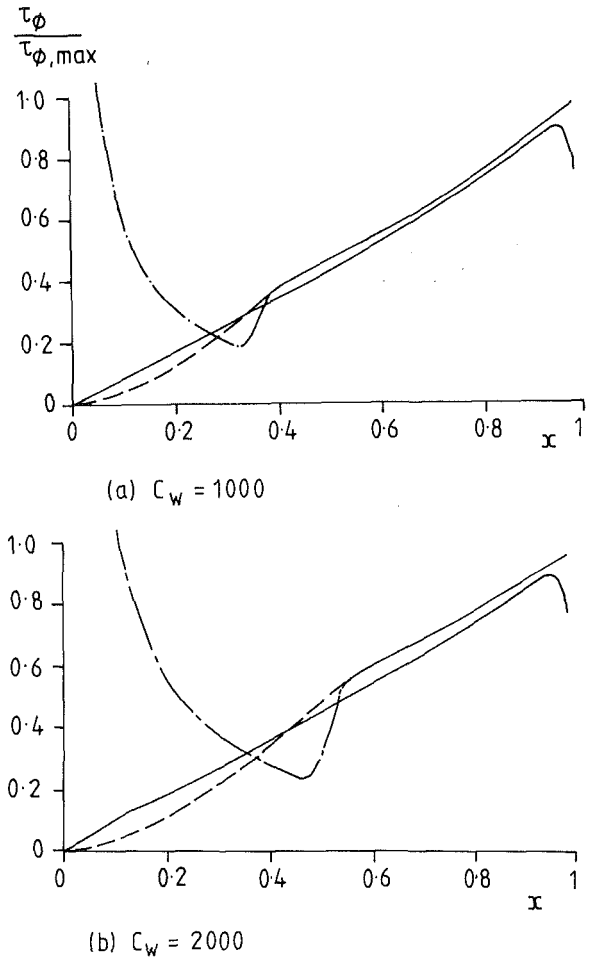

Fig. 11 Radial variation of shear stress for $Re_\phi = 8 \times 10^5$: - - - - equations (5.11a) and (5.16); —·— equations (5.11b) and (5.16); —— Vaughan (1986)

$$C_{m,2}Re_\phi^{1/5} = 4\pi\int_{x_c}^{1} 0.0285 f_2(\phi)x^{18/5}dx$$

$$= 0.0398((1-x_c^{23/5}) + 14.7\lambda_T(1-x_c^2) + 90.4\lambda_T^2(1-x_c^{-3/5})) \quad (5.19)$$

The complete moment coefficient defined by equation (5.2) can be found from

$$C_m = C_{m1} + C_{m2} \quad (5.20)$$

where, for $x_c \le 1$ (that is, $\lambda_T \le 0.219$), C_{m1} and C_{m2} are given by equations (5.13) and (5.19). for $\lambda_T > 0.219$, the wall-jet solution given by equation (5.15) can be written as

$$C_m Re_\phi^{1/5} = 0.333\lambda_T \quad (5.21)$$

The variation of $C_m Re_\phi^{1/5}$ with λ_T is shown in Fig. 12. For $\lambda_T = 0$ (that is $x_c = 0$), $C_m = C_{m*}$ where

$$C_{m*} Re_\phi^{1/5} = 0.0398 \quad (5.22)$$

For $\lambda_T = 0.219$ (that is $x_c = 1$) $C_m = C_{m,fd}$ where

$$C_{m,fd} Re_\phi^{1/5} = 0.0729 \quad (5.23)$$

Thus C_{m*}, the moment coefficient for the rotor-stator system without a superimposed flow, is approximately 50 percent of von Karman's free-disk value. Also, regardless of whether the flow enters the system through a radial or an axial inlet, $C_m = C_{m,fd}$ when the superimposed flow rate equals the free-disk entrainment rate (that is, $\lambda_T = 0.219$). At $\lambda_T = 0.219$, there is a discontinuity in the slope of the $C_m Re_\phi^{1/5}$ versus λ_T curve as the wall-jet solution departs from that of the free-disk.

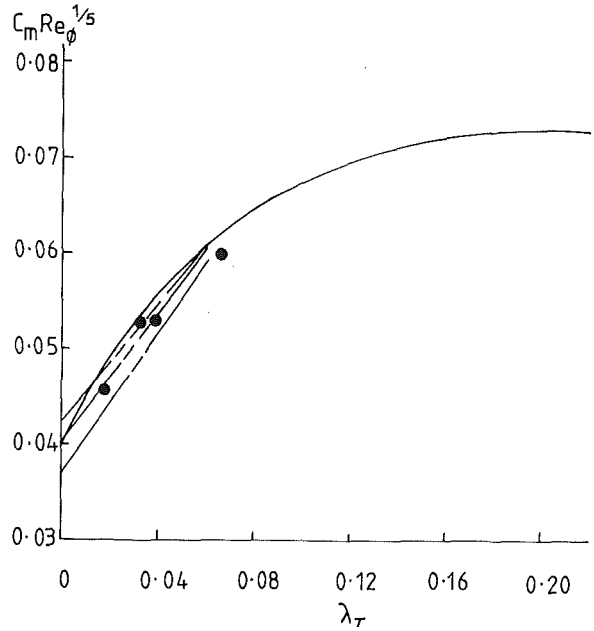

Fig. 12 The variation of $C_m Re_\phi^{1/5}$ with λ_T: —— equation (5.20); equation (5.24): — - - $G = 0.0276$; — - - - $G = 0.069$; — - - - - $G = 0.124$; ● $G = 0.1$ (Vaughan, 1986)

Table 5.1 Values of G, β^*, and $C_{m*}Re_\phi^{1/5}$ according to Daily et al. (1964)

G	0.0276	0.069	0.124
β^*	0.475	0.45	0.42
$C_{m*}Re_\phi^{1/5}$	0.0367	0.0397	0.0420

Also shown in Fig. 12 is the correlation of Daily et al. (1964) for their shrouded rotor-stator system. For $G = 0.0276$, 0.069, and 0.124, $2 \times 10^6 < Re_\phi < 10^7$ and $0 < \lambda_T < 0.06$, their measured moment coefficients for a water-filled system were correlated to within ±5 percent by

$$C_m = C_{m*}(1 + 13.9\beta^*\lambda_T G^{-1/9}) \quad (5.24)$$

where C_{m*} and β^*, for the case of a sealed system with $\lambda_T = 0$, are given in Table 5.1. Despite the fact that the approximate solution given by equation (5.20) takes no account of gap ratio, it is in reasonable agreement with the correlations for the larger two gap ratios. Included in Fig. 12 are Vaughan's computations for $G = 0.1$, which are within 5 percent of the approximate solution.

6 Conclusions

The linear Ekman-layer equations can be used to calculate the flow rate in the boundary layers, and the rotation of the fluid core between them, for the case of a rotor-stator system with a radial outflow of fluid. For laminar flow, the predicted values of the core rotation (equation (2.9)) agree with experimental measurements when the superimposed flow rate is zero, but underestimate the core rotation when the superimposed flow is nonzero. For turbulent flow, the linear theory (equation (3.16)) underestimates the core rotation under all conditions.

A solution of the turbulent momentum-integral equations for the rotor has been found (equation (4.9)) that tends to the linear solution as the rotation of the core approaches that of the rotor and produces the free-disk solution when the core rotation is zero. Matching this solution for the rotor to the

linear solution for the stator produces an approximation for the core rotation (equation (4.13)) that is in reasonable agreement with measured values over a range of flow rates and rotational speeds. Despite the fact that the approximate solution takes no account of a peripheral shroud, the predicted moment coefficients (equation (5.20)) are in reasonable agreement with measured and computed values. The approximate solution predicts that the core rotation tends to zero and the moment coefficient tends to the free-disk level when the superimposed flow rate is equal to the free-disk entrainment rate.

Acknowledgments

I should like to thank Dr. R. H. Rogers for her comments and for the useful discussions that helped to formulate the ideas in this paper.

References

Bödewadt, U. T., 1940, "Die Drehströmung über festem Grunde," *Z. Angew. Math. Mech.*, Vol. 20, p. 241.

Daily, J. W., Ernst, W. D., and Asbedian, V. V., 1964, "Enclosed Rotating Discs With Superimposed Throughflow," Report No. 64, Department of Civil Engineering, Hydrodynamics Laboratories, Massachusetts Institute of Technology, Cambridge, MA.

Dijkstra, D., and Van Heijst, G. J. F., 1983, "The Flow Between Two Finite Rotating Disks Enclosed by a Cylinder," *J. Fluid Mech.*, Vol. 128, p. 123.

Dorfman, L. A., 1963, *Hydrodynamic Resistance and Heat Loss of Rotating Solids*, Oliver & Boyd, Edinburgh.

El-Oun, Z., and Owen, J. M., 1988, "The Effect of Superimposed Flows on the Temperatures in an Adiabatic Rotor-Stator System," ASME Paper No. 88-GT-276; ASME JOURNAL OF TURBOMACHINERY, in press.

Kapinos, V. M., 1965, "Heat Transfer From a Disk Rotating in a Housing With a Radial Flow of Coolant," *J. Engng. Phys.*, Vol. 8, p. 35.

Karman, Th.von., 1921, "Uber laminaire und turbulente Reibung," *Z. Angew. Math. Mech.*, Vol. 1, p. 233.

Owen, J. M., Haynes, C. M., and Bayley, F. J., 1974, "Heat Transfer From an Air-Cooled Rotating Disk," *Proc. R. Soc. Lond.*, Vol. A336, p. 453.

Owen, J. M., Pincombe, J. R., and Rogers, R. H., 1985, "Source-Sink Flow Inside a Rotating Cylindrical Cavity," *J. Fluid Mech.*, Vol. 155, p. 233.

Owen, J. M., and Rogers, R. H., 1989, *Flow and Heat Transfer in Rotating-Disc Systems. Vol. I: Rotor-Stator Systems*, Research Studies Press, Taunton, United Kingdom.

Vaughan, C., 1986, "A Numerical Investigation Into the Effect of an External Flow Field on the Sealing of a Rotor-Stator Cavity," D. Phil thesis, University of Sussex, United Kingdom.

APPENDIX

Derivation of the Momentum-Integral Equations

For steady, incompressible, axisymmetric flow in a stationary, cylindrical-polar coordinate system, the boundary-layer equations can be written (see Dorfman, 1963) as

$$\left.\begin{aligned} &\frac{\partial}{\partial r}(rV_r)+\frac{\partial}{\partial z}(rV_z)=0 \\ &V_r\frac{\partial V_r}{\partial r}+V_z\frac{\partial V_r}{\partial z}-\frac{V_\phi^2}{r}=-\frac{1}{\rho}\frac{dp}{dr}+\frac{1}{\rho}\frac{\partial \tau_r}{\partial z} \\ &V_r\frac{\partial V_\phi}{\partial r}+V_z\frac{\partial V_\phi}{\partial z}+\frac{V_\phi V_r}{r}=\frac{1}{\rho}\frac{\partial \tau_\phi}{\partial z} \end{aligned}\right\} \quad \text{(A1)}$$

Referring to Fig. 1, if the fluid in the core outside the boundary layer is rotating with a tangential component of velocity $\bar{V}_\phi$ and the radial component of velocity is zero, then

$$\frac{1}{\rho}\frac{dp}{dr}=\frac{\bar{V}_\phi^2}{r} \quad \text{(A2)}$$

The momentum-integral equations can be obtained by integrating equations (A1) from $z=0$ to $z=\delta_o$. For the case of a rotor-stator system, most authors appear to ignore the terms containing V_z (see Dorfman), which results in the integral equations

$$\left.\begin{aligned} &r\int_0^{\delta_o} V_r\frac{\partial V_r}{\partial r}dz-\int_0^{\delta_o} V_\phi^2 dz \\ &\quad=-\int_0^{\delta_o}\frac{r}{\rho}\frac{dp}{dr}dz-\frac{r}{\rho}\tau_{r,o} \\ &r\int_0^{\delta_o} V_r\frac{\partial V_\phi}{\partial r}dz+\int_0^{\delta_o} V_\phi V_r dz=-\frac{r}{\rho}\tau_{\phi,o} \end{aligned}\right\} \quad \text{(A3)}$$

However, if the V_z terms are included, equations (A1) can be rewritten as

$$\frac{\partial}{\partial r}(rV_r^2)+\frac{\partial}{\partial z}(r^2V_rV_z)-V_\phi^2=-\frac{r}{\rho}\frac{dp}{dr}+\frac{r}{\rho}\frac{\partial \tau_r}{\partial z} \quad \text{(A4)}$$

and

$$\frac{\partial}{\partial r}(r^2V_rV_\phi)+\frac{\partial}{\partial z}(r^2V_zV_\phi)=\frac{r^2}{\rho}\frac{\partial \tau_\phi}{\partial z}$$

Integrating between $z=0$ and δ_o gives

$$\left.\begin{aligned} &\frac{d}{dr}\left(r\int_0^{\delta_o} V_r^2dz\right)-\int_0^{\delta_o} V_\phi^2dz=-\int_0^{\delta_o}\frac{r}{\rho}\frac{dp}{dr}dz \\ &-\frac{r}{\rho}\tau_{r,o}=-\int_0^{\delta_o}\frac{r}{\rho}\frac{dp}{dr}dz-\frac{r}{\rho}\tau_{r,o} \end{aligned}\right\} \quad \text{(A5)}$$

and

$$\left.\begin{aligned} &\frac{d}{dr}\left(r^2\int_0^{\delta_o} V_rV_\phi dz\right)-r\bar{V}_\phi\frac{d}{dr}\left(\int_0^{\delta_o} rV_r dz\right) \\ &\quad=-\frac{r^2}{\rho}\tau_{\phi,o} \end{aligned}\right\}$$

Equations (A5) and (A3) are only equal if

$$\frac{\partial}{\partial z}(rV_z)=\frac{\partial}{\partial r}(rV_r)=0$$

which is not usually the case for a rotor-stator system.

Using equation (A2), equations (A5) can be rewritten as

$$\left.\begin{aligned} &\frac{d}{dr}\left(r\int_0^{\delta_o} V_r^2dz\right)-\int_0^{\delta_o}(V_\phi^2-\bar{V}_\phi^2)dz=-\frac{r}{\rho}\tau_{r,o} \\ &\text{and} \\ &\frac{d}{dr}\left(r^2\int_0^{\delta_o} V_r(V_\phi-\bar{V}_\phi)dz\right)+\frac{d}{dr}(r\bar{V}_\phi)\int_0^{\delta_o} V_r dz \\ &\quad=-\frac{r^2}{\rho}\tau_{\phi,o} \end{aligned}\right\} \quad \text{(A6)}$$

which is equivalent to equation (4.1) in Section 4.

Turbulent Flow Velocity Between Rotating Co-axial Disks of Finite Radius

J. F. Louis
Professor.

A. Salhi
Graduate Student.

Department of Aeronautics and Astronautics,
Massachusetts Institute of Technology,
Cambridge, MA 02139

The turbulent flow between two rotating co-axial disks is driven by frictional forces. The prediction of the velocity field can be expected to be very sensitive to the turbulence model used to describe the viscosity close to the walls. Numerical solutions of the Navier–Stokes equations, using a k–ϵ turbulence model derived from Lam and Bremhorst, are presented and compared with experimental results obtained in two different configurations: a rotating cavity and the outflow between a rotating and stationary disk. The comparison shows good overall agreement with the experimental data and substantial improvements over the results of other analyses using the k–ϵ models. Based on this validation, the model is applied to the flow between counterrotating disks and it gives the dependence of the radial variation of the tangential wall shear stress on Rossby number.

1 Introduction

The velocity field and heat transfer distribution between co-axial rotating disks is of great importance in the design of disk components and other cavities of gas turbine engines, as it is for other applications using co-axial rotating geometries. The design difficulty resides in the special fact that the turbulent flow of a fluid between co-axial disks is driven by the wall frictional forces and influenced by spatially varying centrifugal and Coriolis accelerations. The fundamental aspects of the rotating flows, such as the formation of Ekman layers, are well understood as described in Greenspan (1969). The difficulty arises, for example, in predicting the radial extent of the Ekman layers in a rotating cavity with throughflow as the radial extent of these layers will influence both torque and heat transfer. The validity of such detailed flow prediction is therefore singularly sensitive to the type of turbulence model used, and particularly important will be the use of a valid description of the viscosity in the vicinity of the disks.

A first step in the development of such a predictive capability is the validation of solutions for flows under isothermal conditions for which compressibility and buoyancy effects are negligible and for which detailed velocity measurement have been made by Pincombe (1981) and Owen (1969). This paper describes such an investigation and also compares its results with two other numerical predictions of turbulent flow in rotating cavities by Chew (1984) and Morse (1987).

The main parameters influencing the velocity field are the rotational Reynolds number and the disk rotating ratios, which can vary from $+1$ for a rotating cavity to -1 for a counterrotating disk, moving with equal angular velocities. The rotational Reynolds number controls the thickness of the Ekman layers over the rotating disks. The magnitude of the throughflow, often expressed by the Rossby number and the end conditions at the inner and outer radii, strongly influences the complex flow and temperature fields between the disks. The flow field can be divided in several regions, the Ekman layers over the disks, the two end regions at the inner and outer radii, and the interior core bounded by the Ekman layers and end regions. The resolution of the full flow field with its three regions requires the solution of the Navier–Stokes equation using a detailed turbulent transport model.

The most recent turbulent flow analysis of this class of flows was performed by Chew (1984) and Morse (1987) in an attempt to produce a reliable method for the prediction of the fluid flow in rotating disk systems using a modified teach code. Both investigators use two k–ϵ models. The first is a high-turbulence model using a logarithmic law in the vicinity of the wall identical to the expression used by Gosman et al. (1976). The second is a variation of the low-turbulence model used successfully by Launder and Sharma (1974) to describe the flow above a rotating free disk. This modified k–ϵ model includes the direct effect of molecular viscosity and pressure strain on the shear stress near the wall and provides dissipation rates in the buffer layer. Both investigators find that the high-turbulence model was inaccurate in the prediction of experimental data. This seems reasonable since the use of wall functions best describes situations in which the Reynolds number is sufficiently high for viscous effects to be small and wall functions cannot be expected to be accurate for flows that are driven by turbulent viscous effects. The agreement between the low-turbulence model and experimental data was better, particularly in the investigation of Morse (1987). The prediction for the inflow rotating cavity was good, but it was less satisfactory on outflow rotating cavities, particularly at low flow rates and low rotational speeds.

Contributed by the International Gas Turbine Institute and presented at the 33rd International Gas Turbine and Aeroengine Congress and Exhibition, Amsterdam, The Netherlands, June 5–9, 1988. Manuscript received by the International Gas Turbine Institute July 28, 1987. Paper No. 88-GT-47.

The present investigation was initiated after the publication of the paper by Chew and was essentially complete when the investigation of Morse became available. The present work was guided by the comparison made by Patel et al. (1985) of k–ϵ turbulence models. It showed that the model proposed by Lam and Bremhorst (1981) generally agreed with experimental data throughout the fully turbulent, sublaminar, and laminar regions of the flow. The Lam and Bremhorst model includes additional functions to modify the constants in the standard k–ϵ model, and to describe better the effect of molecular viscosity and pressure strain on the shear stress. It includes dissipation rates in the buffer layer. The numerical solution of the Navier–Stokes equations using the the Lam–Bremhorst turbulence model is applied to three types of flows between rotating disks:

1 a rotating cavity, $s = +1$;
2 a rotating and stationary disk, $s = 0$;
3 counterrotating disks with $s = -1$.

In the first two cases, the predictions compare favorably with experimental data of Pincombe and Owen and may be considered as a validation of the model for these type flows. After this validation, the flow between counterrotating disks is explored and the radial variation of the tangential shear stress on the Rossby number is determined.

2 Turbulent Flow Models

The degree of success in the prediction of the flow distribution is closely related to the choice of an appropriate turbulent transport model. In recent years, considerable attention has been paid to turbulent models. The turbulence k–ϵ model proposed by Launder and Spaulding (1972) was implemented by most of the investigators with different degrees of success. Patankar et al. (1978) used elliptic finite difference procedure and wall functions to solve the k–ϵ turbulence model for the velocity and temperature in shrouded rotating disks with either inflow or outflow. The comparison with experimental work of Sparrow and Goldstein (1976) showed satisfactory agreements.

The k–ϵ turbulence model was also applied by Gosman et al. (1976) and Yu et al. (1973) to rotating disk systems. Comparison with the experimental data of Haynes and Owen (1975) and Yu et al. for the flow and heat transfer distributions showed good agreement for high Reynolds number, whereas the Nusselt number deviated by up to 30 percent at low Reynolds number.

In their investigation, both Chew (1984) and Morse (1987) used the same k–ϵ model as Gosman (1976) and found that this model could not accurately predict the experimental data of Pincombe and Owen over the flow domain even of higher Reynolds number. This prediction failure can be associated with the use of wall functions that relate surface boundary conditions to points in the fluid close to the wall above the laminar sublayer, thus avoiding an accurate description of the direct influence of viscosity close to the wall. The validity of the application of wall functions can be expected to be limited to flows with Reynolds number sufficiently high so that viscous effects are small; this is certainly not the case for flows driven by viscous forces.

Recently, many modified forms of k–ϵ that avoid the use of wall functions were proposed, namely those of Chien (1982), Dutaya and Michard (1981), Hassaid and Poreh (1978), Hofman (1975), Lam and Bremhorst (1981), Launder and Sharma (1974), and Reynolds (1976). These are variants of the k–ϵ model in which the Reynolds stress is related to the local velocity gradient by eddy viscosity ν_t, which is computed from modeled transport equations for k and ϵ.

Relevant equations of these models for two-dimensional layers are:

$$-\overline{\rho uv} = \rho \nu_t \frac{\partial U}{\partial y}$$

$$\nu_t = C_\mu f_\mu (k^2/\tilde{\epsilon})$$

$$\epsilon = \tilde{\epsilon} + D$$

$$U\frac{\partial k}{\partial x} + V\frac{\partial k}{\partial y} = \frac{\partial}{\partial y}\left(\left(\nu + \frac{\nu_t}{\sigma_k}\right)\frac{\partial k}{\partial y}\right) + \nu_t\left(\frac{\partial U}{\partial y}\right)^2 - \epsilon$$

$$U\frac{\partial \tilde{\epsilon}}{\partial x} + V\frac{\partial \tilde{\epsilon}}{\partial y} = \frac{\partial}{\partial y}\left(\left(\nu + \frac{\nu_t}{\sigma_\epsilon}\right)\frac{\partial \tilde{\epsilon}}{\partial y}\right) + C_{\epsilon 1} f_1 \frac{\tilde{\epsilon}}{k}\nu_t\left(\frac{\partial U}{\partial y}\right)^2 - C_{\epsilon 2} f_2 \frac{\tilde{\epsilon}^2}{k} + E$$

$$R_t = k^2/\nu\tilde{\epsilon}$$

$$R_y = \frac{\sqrt{k}y}{\nu} \qquad y^+ = \frac{yu_\tau}{\nu}$$

The models in the k–ϵ group differ from their basic version by the inclusion of the viscous diffusion terms and of functions f to modify the empirical constants C. Moreover, extra

Nomenclature

a = inlet radius
b = outer radius of cavity
C_f = moment coefficient
C_w = flow rate parameter $= Q/\nu b$
C_μ, C_1, C_2, C_3 = constants used in the turbulence model
D = Ekman layer scale $= (\nu/\Omega)^{1/2}$
f_μ, f_1, f_2 = additional functions used in the turbulence model
G_e = term in k and ϵ conservation equations
H = distance between disks
k = turbulence kinetic energy
M = frictional torque
p = static pressure
Pr = Prandtl number
Q = volumetric flow rate
r = radial radius
Re_r = radial Reynolds number
$\mathrm{Re}_t, \mathrm{Re}_z$ = turbulent Reynolds numbers
Re_θ = rotational Reynolds number $= \Omega b^2/\nu$
S_ϕ = source term in the conservation equation
u, v, w = time-averaged radial, tangential, and axial velocities
y = distance of "near-wall" grid points to wall
z = axial distance
Γ_ϕ = exchange coefficient
ϵ = energy dissipation rate
ϵ_r = Rossby number $= Q/(4\pi r^2 \Omega D)$
δ = boundary layer thickness
ν = kinematic viscosity
ν_t = turbulence kinematic viscosity
ν_{eff} = effective kinematic viscosity
ρ = density
σ_ϕ = effective Prandtl/Schmidt number
τ_θ = tangential shear stress on the disk
ϕ = represents the main variables in the general form of the conservation equation
Ω = angular velocity

terms, denoted by D and E, are added in some cases to represent better the near-wall behavior. Patel et al. (1985) reviewed these different models in detail and the expressions for the different functions and constants.

In very recent investigations, Chew (1984) and Morse (1987) also used low-Reynolds-number k–ϵ models, derived from Launder and Sharma (1974), to predict radial inflow and outflow in a rotating cavity for a wide range of flow conditions. Although the predictions of Morse for the former are in good agreement with experimental data, the model performs less well for radial outflow, particularly at low flow rates and rotational speeds. This shortcoming is consistent with the results of Chew, and Morse (1987) remarks that "the most salient conclusion that can be drawn is that although it provides an adequate description of near-wall flow for fully turbulent conditions beyond the viscous sublayer, it does not portray with desirable accuracy the onset and persistence of turbulent flow in the Ekman layers for radial outflow."

Patel et al. applied the different (k–ϵ) models to the boundary layer on a flat plate, equilibrium adverse pressure gradient boundary layers, relaminarizing boundary layers, and sink flow boundary layers. Agreement with published experimental data was very good with Lam and Bremhorst for the different cases except for the adverse pressure gradient flow.

In the flow between rotating disks, the Ekman layers have a tendency to relaminarize, as pointed out by Hide (1968); the flow in the end regions can have the character of sink flow boundary layers and the centripetal acceleration dominates over the pressure gradient. Therefore, the Lam and Bremhorst (1981) model seems to be well suited for this application and is selected for this study based on the evaluation of Patel et al. (1985).

3 Governing Equations and Mathematical Model

In a cylindrical coordinate system (r, θ, z), with the assumption of axisymmetry, the governing equations for steady, incompressible, and viscous flow may be written in the form:

Momentum equations

$$\frac{1}{r}\frac{\partial}{\partial r}(ru\phi)+\frac{\partial}{\partial z}(w\phi)=\frac{1}{r}\frac{\partial}{\partial r}\left(\Gamma_\phi r\frac{\partial\phi}{\partial r}\right)+\frac{\partial}{\partial z}\left(\Gamma_\phi\frac{\partial\phi}{\partial z}\right)+S_\phi$$

Continuity equation

$$\frac{1}{r}\frac{\partial}{\partial r}(ru)+\frac{\partial}{\partial z}(w)=0$$

Here, the variable ϕ represents any of the main mean variables u, v, w, k. The exchange coefficient Γ_ϕ is given by

$$\Gamma_\phi=\frac{\nu_{\text{eff}}}{\sigma_\phi}$$

where σ_ϕ is an effective Prandtl or Schmidt number for turbulence energy ($\sigma_\kappa=1.0$) and energy dissipation rate ($\sigma_\epsilon=1.3$), and the effective viscosity is defined by $\nu_{\text{eff}}=\nu+\nu_t$.

The turbulent eddy viscosity is found from the relation

$$\nu_t=C_\mu f_\mu\frac{k^2}{\epsilon}$$

which in addition to the empirical constant C_μ incorporates the Lam–Bremhorst function f_μ given by

$$f_\mu=(1-\exp(-0.0165\ \text{Re}_z))^2\left(1+\frac{20.5}{\text{Re}_t}\right)$$

The function f_μ multiplies the eddy viscosity relation and it is introduced to simulate the direct effect of molecular viscosity on the shear stress. Launder (1975) noted that the shear stress near the wall is also reduced by the action of the fluctuating pressure field via the pressure strain correlation. This process is, to a first approximation, independent of viscosity and therefore, cannot be correlated by Reynolds numbers Re_t, Re_z, or y^+. However, it is difficult to separate the two effects as both occur in the vicinity of a wall. The function f_μ attempts to model both the viscous and pressure strain effects, although they are correlated only to the former.

The turbulence Reynolds numbers Re_z and Re_t are based on axial distance z from each disk surface and energy dissipation rate, respectively, i.e.

$$\text{Re}_z=\frac{\sqrt{k}z}{\nu}$$

$$\text{Re}_t=\frac{k^2}{\nu\epsilon}$$

The empirical constant $C_\mu=0.09$ is then modified by f_μ. It can be noted that for large distances from the wall and high turbulence levels the function f_μ tends toward unity.

The source term S_ϕ in equation (1) is different in each case and is given by

$$S_u=-\frac{\partial}{\partial r}\left(\frac{p}{\rho}+\frac{2}{3}k\right)+\frac{1}{r}\frac{\partial}{\partial r}\left(\nu_{\text{eff}}r\frac{\partial u}{\partial r}\right)+\frac{\partial}{\partial z}\left(\nu_{\text{eff}}\frac{\partial w}{\partial z}\right)-2\nu_{\text{eff}}\frac{u}{r^2}+\frac{v^2}{r}$$

$$S_v=-\nu_{\text{eff}}\frac{v}{r^2}-\frac{v}{r}\frac{\partial\nu_t}{\partial r}-\frac{uv}{r}$$

$$S_w=-\frac{\partial}{\partial z}\left(\frac{p}{\rho}+\frac{2}{3}k\right)+\frac{1}{r}\frac{\partial}{\partial r}\left(\nu_{\text{eff}}r\frac{\partial u}{\partial r}\right)+\frac{\partial}{\partial z}\left(\nu_{\text{eff}}\frac{\partial w}{\partial z}\right)$$

$$S_k=G_e-\epsilon$$

$$S_\epsilon=\frac{\epsilon}{k}C_1f_1G_e-\frac{\epsilon^2}{k}C_2f_2$$

where

$$G_e=\nu_t\left(2\left(\left(\frac{\partial w}{\partial z}\right)^2+\left(\frac{\partial u}{\partial r}\right)^2+\left(\frac{u}{r}\right)^2\right)+\left(\frac{\partial w}{\partial z}+\frac{\partial u}{\partial z}\right)^2+\left(\frac{\partial v}{\partial z}\right)^2+\left(r\frac{\partial(w/r)}{\partial r}\right)^2\right)$$

C_1 and C_2 are empirical constants equal to 1.44 and 1.92, respectively. The function f_1 is given by

$$f_1=1+\left(\frac{0.05}{f_\mu}\right)^3$$

Far from each disk surface the function f_1 is approximately unity. However, in the near-wall region, the function f_1 assumes larger values in order to increase the predicted dissipation rate.

The function f_2 is introduced primarily to incorporate low-Reynolds-number effects in the destruction term of the ϵ equation. The physical basis for this is provided by experiments in the final period of the decay of isotropic turbulence, which show that the exponent in the decay law $k\propto r^{-n}$ changes from 1.25 at high Reynolds number to 2.5 in the final stage. The Lam–Bremhorst model excludes the prediction of the final state of isotropic turbulence. The fact that all formulae reach their asymptotic value of unity at Reynolds number Re_t smaller than 15 leads to the conclusion that their effect is limited to the viscous sublayer.

The Lam–Bremhorst function f_2 is given by

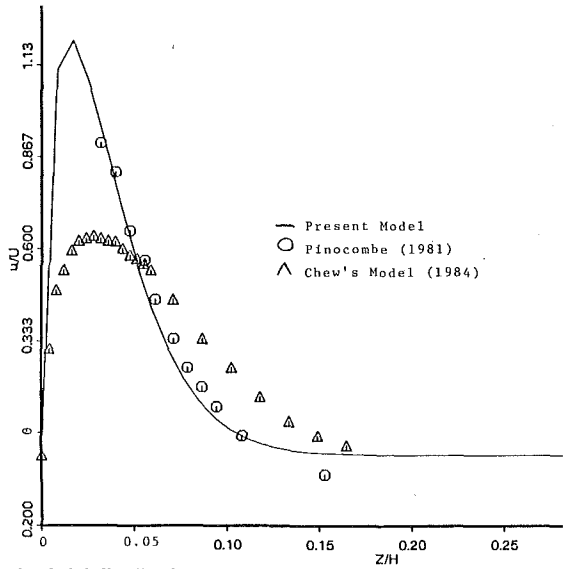

Fig. 1 Axial distribution of the radial velocity at $r/b = 0.833$; $C_w = 1092$, $Re_o = 1.e+5$

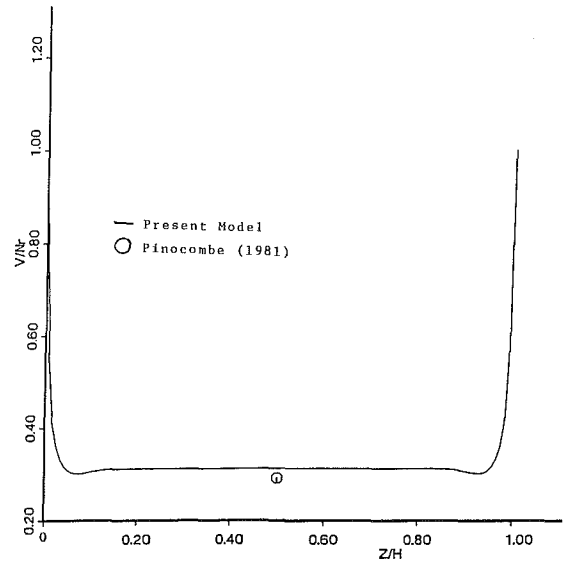

Fig. 2 Axial distribution of the tangential velocity at $r/b = 0.833$; $C_w = 1092$, $Re_o = 1.e+5$

$$f_2 = 1 - \exp(-\mathrm{Re}_t^2)$$

As noted by Lam and Bremhorst (1981), since ϵ and its derivatives ϵ/x_j and ϵ/x_j^2 are infinite at either wall, f_2 must tend toward zero as Re_t goes to zero. Many k-ϵ turbulence models overlook this requirement.

The necessary wall boundary condition for ϵ was resolved by Lam and Bremhorst, employing the k equation and assuming ν constant to yield

$$\epsilon_w = \nu \frac{\partial^2 k}{\partial z^2}$$

As noted by Patel et al. (1985), this is not a very convenient boundary condition to implement numerically since it involves parts of the solution of coupled partial differential equations. A more useful form is simply

$$\left.\frac{\partial \epsilon}{\partial z}\right|_w = 0$$

The wall value ϵ_ω is thus a direct result of the numerical computation.

The set of partial differential equations governing the flow

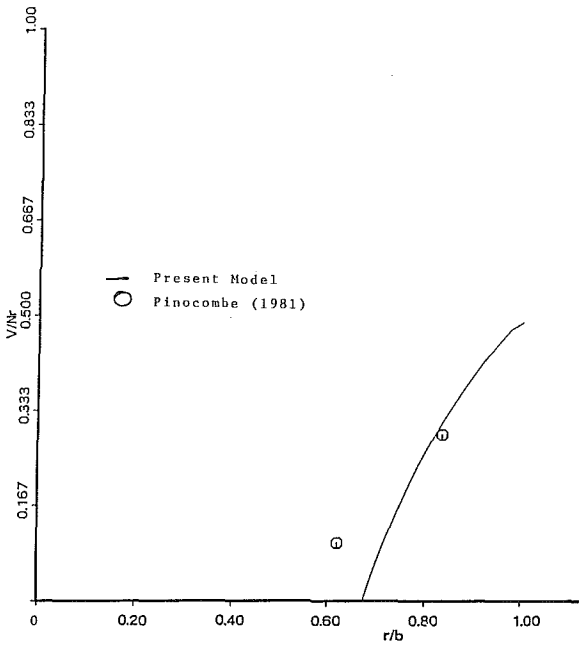

Fig. 3 Radial distribution of the tangential velocity at $z/H = 0.5$; $C_w = 1092$, $Re_o = 1.e+5$

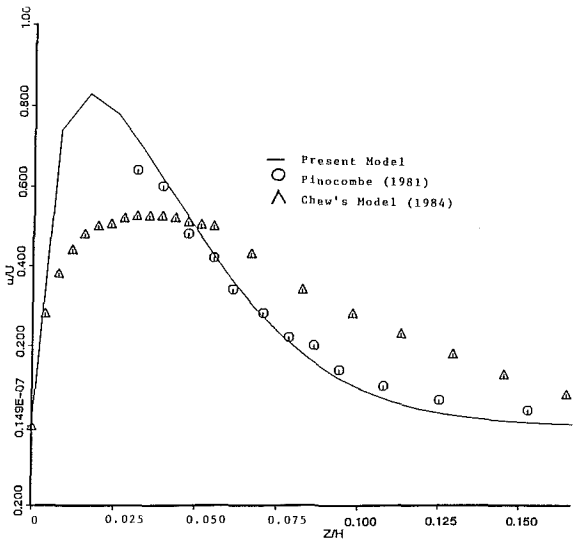

Fig. 4 Axial distribution of the radial velocity at $r/b = 0.833$, $C_w = 1544$, $Re_o = 1.e+5$

field was solved numerically based on the integral momentum equations (Spalding, 1983). This approach has been employed frequently in computational fluid dynamics. The solution was then obtained by the iterative method. The procedure is presented in detail by Salhi (1987). Because of the complexity of the problem, the degree of success depends upon the complete specification of the flow and boundary conditions. In addition, since the mathematical model contains nonlinear and coupled equations, it might have multiple solutions besides the physical one and it is found that the selection of the right initial flow field is very important in obtaining convergence.

4 Validation of the Turbulence Model and Application

The validation of the modified k-ϵ turbulence model was performed numerically by comparing results with the experimental work of Pincombe and Owen, and the numerical investigation of Chew (1984).

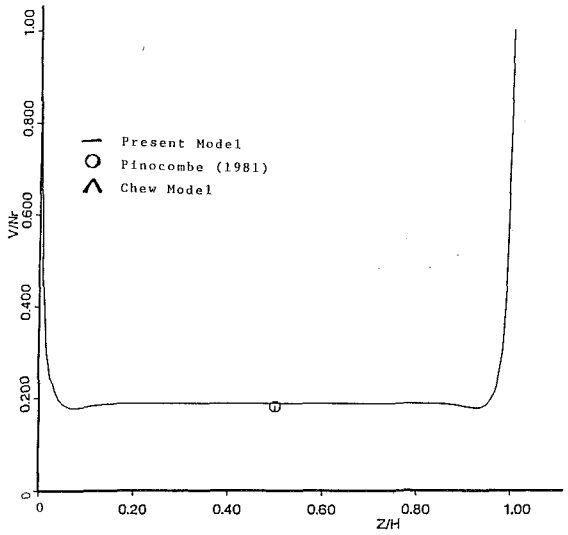

Fig. 5 Axial distribution of the tangential velocity at $r/b = 0.833$; $C_w = 1544$, $Re_o = 1.e+5$

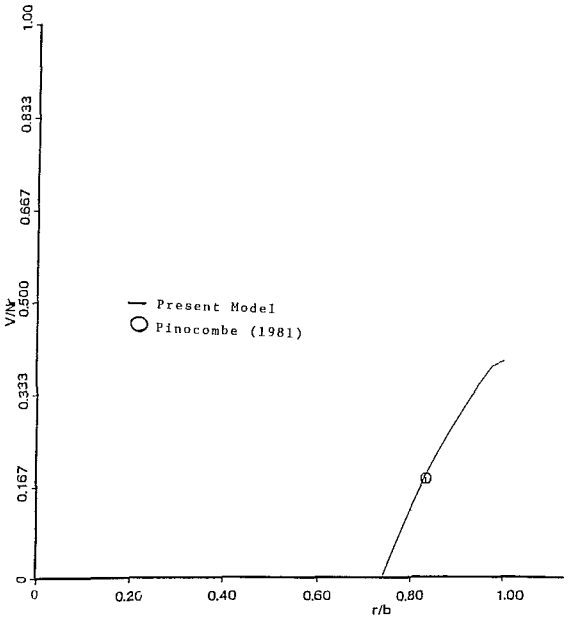

Fig. 6 Radial distribution of the tangential velocity at $r/b = 0.833$; $C_w = 1544$, $Re_o = 1.e+5$

Rotating Cavity With Radial Outflow. The experiment conducted by Pincombe (1981) consisted of a rotating cavity where the two open-ended disks rotate with the same angular speed and in the same direction ($s = +1$). The disks had an inner radius $a = 44.25$ mm, an outer radius $b = 442.5$ mm, and a gap $H = 59$ mm.

In the experiment the air entered the cavity through a central axial inlet, while in the present study, a uniform radial inlet ($r = a$) is assumed. This should only affect the results within the "source region" of the flow and allow the flow to be symmetric about the midaxial plane ($z = H/2$).

Boundary Conditions. The boundary conditions were specified as follows: on both disks, the requirement of no-slip conditions leads to

$$u = w = 0, \quad v = \Omega r$$

$$\frac{\partial k}{\partial z} = \frac{\partial \epsilon}{\partial z} = \frac{\partial p}{\partial z} = 0 \qquad \text{at } z = 0, H$$

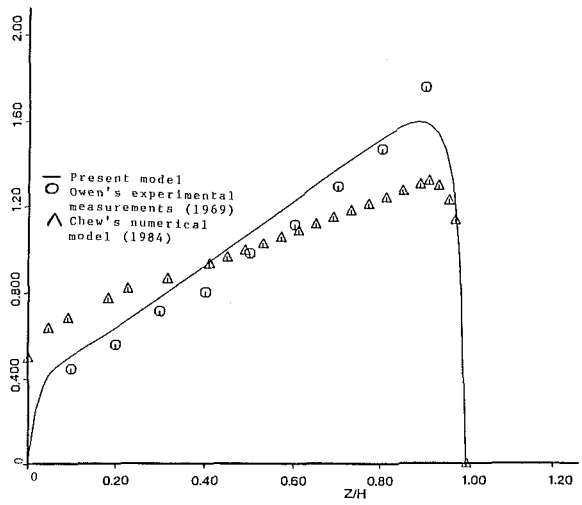

Fig. 7 Turbulent flow between a rotating and stationary disk; axial distribution of the radial velocity at $r/b = 1$, $Re_o = 3.4e+6$, $C_w = 5.4e+4$

at the inlet and outlet, a uniform radial flow was assumed

$$u = \frac{Q}{2\pi a H}, \quad v = w = 0 \qquad \text{at } r = a$$

$$u = \frac{Q}{2\pi b H}, \quad \frac{\partial (v/r)}{\partial r} = w = 0 \qquad \text{at } r = b$$

The turbulence kinetic energy at the inlet was taken as 0.25 percent of the square of the inlet velocity according to Chew (1984). The values of k and ϵ at the outlet and ϵ at the inlet were calculated as for a solid surface.

Interpretation of the Results. The numerical solution was given for two different values of the flow parameter C_w (1092 and 1544) and a rotational Reynolds number $Re_\theta = 10^5$. In both cases, the axial distribution of the radial and tangential components of the velocity and the radial distribution of the tangential component of the velocity are presented.

As shown in Figs. 1 and 4, the radial velocity is successfully predicted. However, the minute reverse flow that was observed experimentally was not obtained numerically. This discrepancy needs to be resolved. Both the predicted axial (Figs. 2 and 5) and radial (Figs. 3 and 6) distributions of the tangential velocity are given and they agree with the few experimental data available. The overall agreement based on radial and tangential velocity is quite satisfactory.

Radial Outflow Between a Rotating and Stationary Disk. The experiment performed by Owen (1969) consisted of a rotating disk ($s = 0$), with an outer radius $b = 380$ mm and a gap $H = 11.4$ mm. Air entered the cavity through a central inlet, radius $a = 51$ mm, in the stationary disk. Chew (1984) considered one set of results ($C_w = 5.4 \times 10^4$, $Re_\theta = 3.4 \times 10^6$).

Boundary Conditions. The boundary conditions were chosen, according to Chew, as follows:

$$u = v = w = 0 \qquad \text{at } z = 0, \ a < r < b$$

$$u = v = 0, \quad w = \frac{Q}{\pi a^2} \qquad \text{at } z = 0, \ 0 < r < a$$

$$\frac{\partial (ru)}{\partial r} = \frac{\partial (rv)}{\partial r} = w = \frac{\partial p}{\partial r} = \frac{\partial k}{\partial r} = \frac{\partial \epsilon}{\partial r} = 0$$

$$\text{at } r = 0$$

As for the rotating cavity, the value of k at the inlet was taken

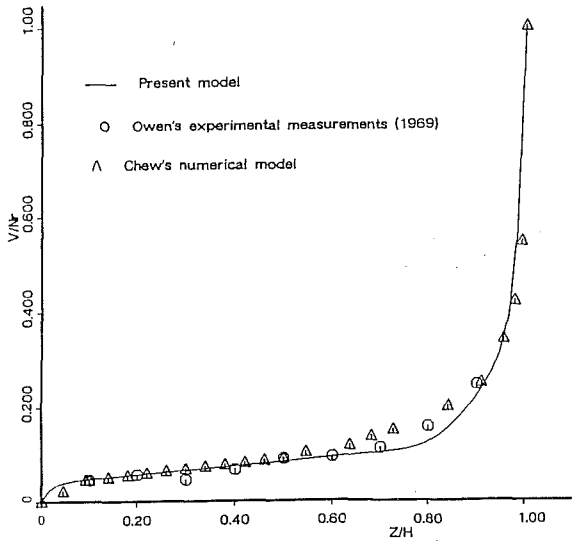

Fig. 8 Turbulent flow between a rotating and stationary disk; $Re_o = 3.4e+6$, $C_w = 5.4e+4$

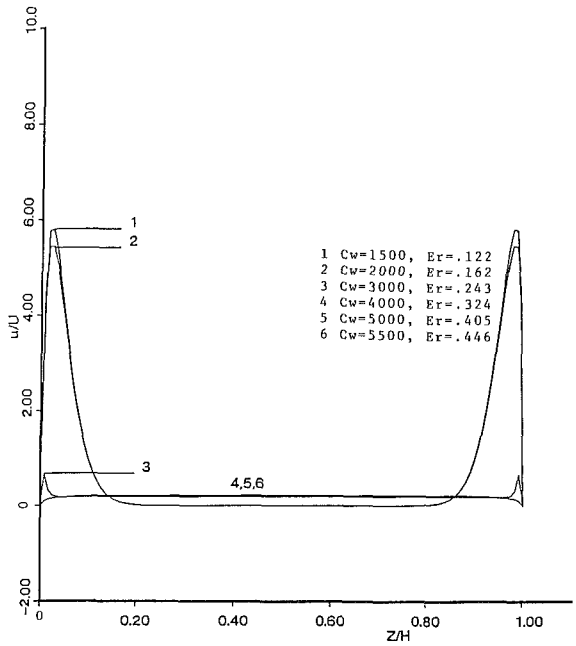

Fig. 9 Axial distribution of the radial velocity at $r/b = 0.6$; $Re_o = 2.e+6$, $s = -1$

as 0.25 percent of the square of the inlet velocity and ϵ was calculated as for a solid surface.

Interpretation of the Results. Comparisons between predicted and measured radial velocities and tangential velocities are given in Figs. 6 and 7, respectively. As shown in Fig. 6, the radial velocity predicted by the modified k–ϵ turbulence model is slightly higher than that obtained experimentally for most of the flow except for one data point that may be inaccurate according to Owen (private communication). On the other hand, Fig. 8 shows excellent agreement of the tangential velocity with the experimental data.

Counterrotating Disks With Radial Outflow. Based on the substantial agreement of the present numerical results with the experimental data, the modified k–ϵ turbulence model is applied to shrouded counterrotating disks ($s = -1$). The geometry assumed here corresponds to that considered for the rotating cavity with a slit in the shroud equal to one tenth of the gap between the disks.

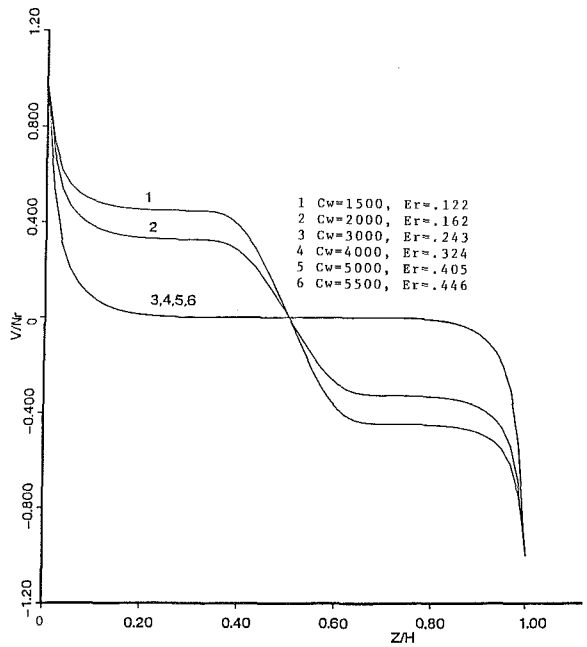

Fig. 10 Axial distribution of the tangential velocity at $r/b = 0.6$; $Re_o = 2.e+6$, $s = -1$

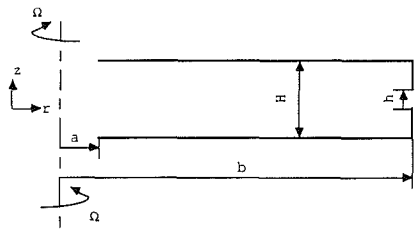

Boundary Conditions. On both disks

$$u = w = 0, \quad v = s\Omega r \quad (s = \pm 1)$$

$$\frac{\partial k}{\partial z} = \frac{\partial \epsilon}{\partial z} = \frac{\partial p}{\partial z} = 0$$

At the inflow boundary ($r = a$)

$$u = \frac{Q}{2\pi aH}, \quad v = w = 0$$

At the outflow boundary (slit)

$$u = \frac{Q}{2\pi bH}, \quad w = \frac{\partial (v/r)}{\partial r} = 0$$

For the turbulence kinetic energy and the energy dissipation rate the same considerations as for the rotating cavity were assumed. The rotational Reynolds number was chosen $Re_\theta = 2 \times 10^6$ based on gas turbine application and the flow rate parameter to vary between $C_w = 1500$ and 5500.

Interpretation of Results. As shown in Figs. 9 and 12 the axial distribution of the radial velocity is similar to that obtained in the rotating cavity, in which the development of Ekman layers occurs on both disks at the lowest Rossby numbers. For the specified flow conditions, the inner end region reaches the location $r/b = 0.6$ for a Rossby number 0.243, while it reaches the location $r/b = 0.833$ for a Rossby number equal to 0.446. These observations are consistent with the predictions of Hide (1962) and Owen and Pincombe (1980) and clearly indicate the influence of Rossby number on the radial coverage of the Ekman layers.

Figures 10 and 13 show that the core near each disk rotates

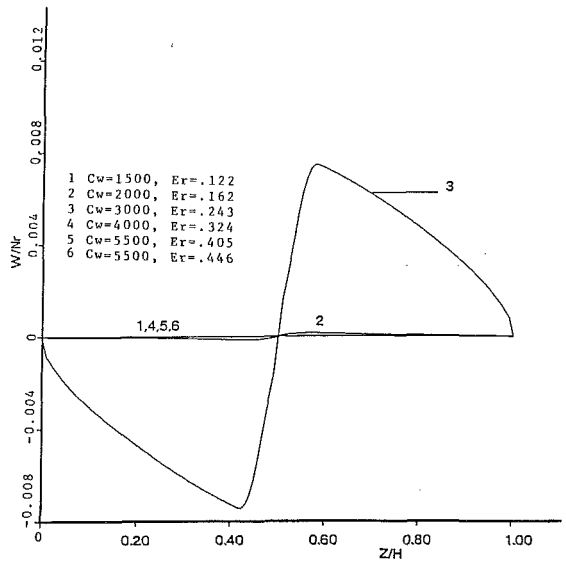

Fig. 11 Axial distribution of the axial velocity at $r/b = 0.6$; $Re_o = 2.e+6$, $s = -1$

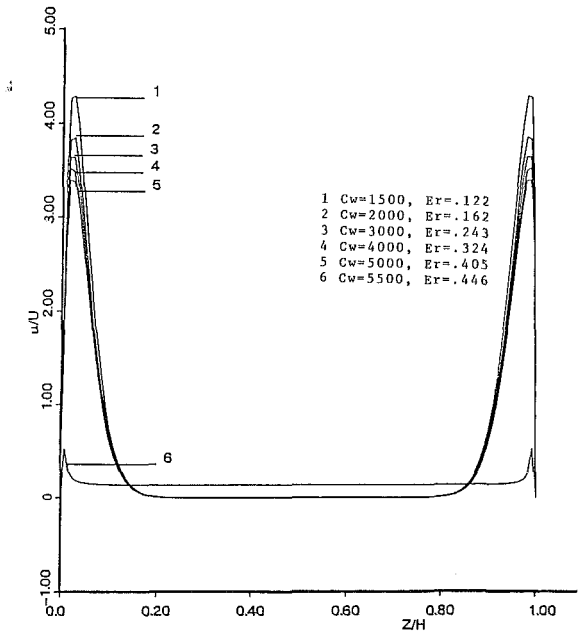

Fig. 12 Axial distribution of the radial velocity at $r/b = 0.833$; $Re_o = 2.e+6$, $s = -1$

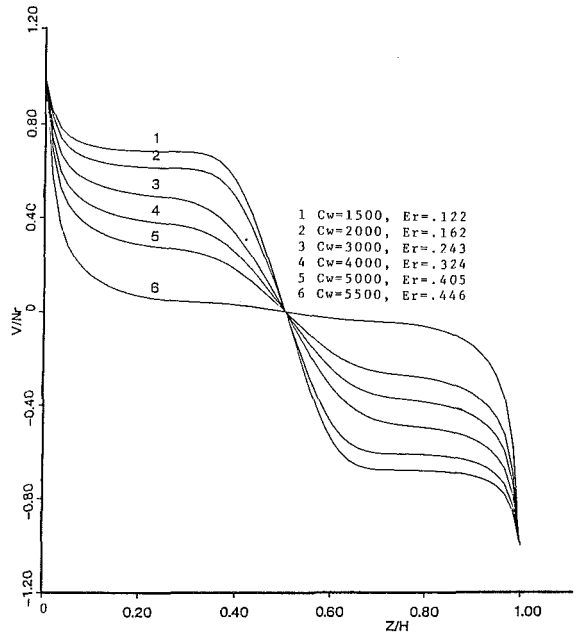

Fig. 13 Axial distribution of the tangential velocity at $r/b = 0.833$; $Re_o = 2.e+6$, $s = -1$

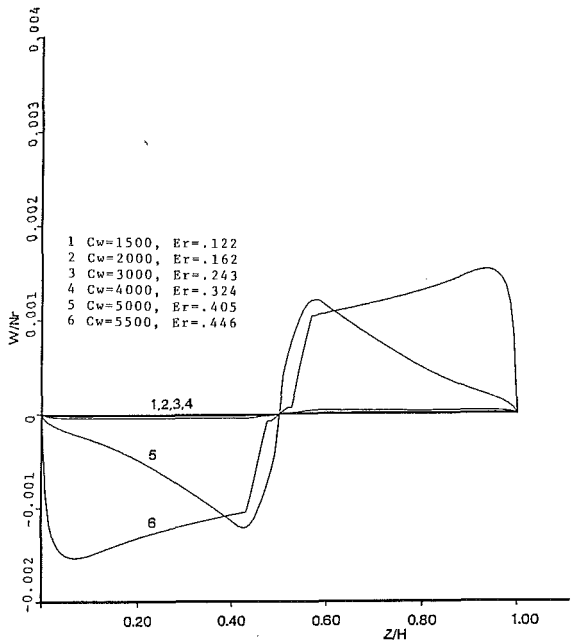

Fig. 14 Axial distribution of the axial velocity at $r/b = 0.833$; $Re_o = 2.e+6$, $s = -1$

with a uniform speed where the Ekman layer is developed, and there is a middle transition layer that allows the angular velocity to change sign. Furthermore the axial distribution of the axial component of the velocity (Figs. 11 and 14) is consistent with the predictions of Hide and Pincombe, who showed that, for a fully developed Ekman layer regime, the axial velocity is negligible.

The variation of the tangential shear stress, presented in Fig. 15, indicates that the radial decrease of the shear stress coincides with the development of Ekman layers. This figure clearly indicates the variation of radial tangential wall shear stress with Rossby number and suggests a strong dependence of the torque on Rossby number.

5 Conclusions

The turbulent flow velocity field between disks of finite radius is driven by the wall frictional forces and therefore their prediction depends usually on the correct detailed estimation of turbulent transport.

The use of the k–ϵ model as first proposed by Launder and Spalding, with logarithmic wall functions, does not seem appropriate for this problem since it relates surface boundary conditions to points above the sublayer, thus avoiding the task of modeling the detailed influence of viscosity near the wall. Indeed the investigations of Chew and Morse indicate that the predictions obtained by this model do not agree with the experiments.

Many modified forms of k–ϵ models have been proposed that eliminate the use of wall function. Chew and Morse used slightly different modifications of the low turbulence model of Launder and Sharma. The first investigation found a rough agreement while the second achieved relatively good agreement for radial inflow but with relatively poor agreement for

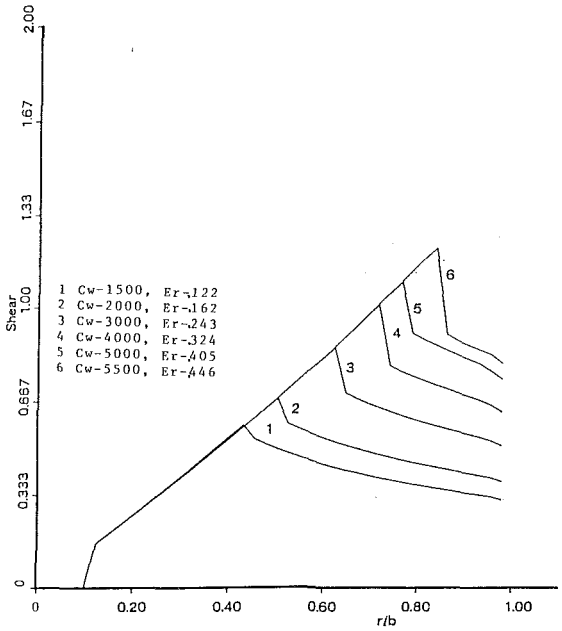

Fig. 15 Variation of the tangential shear stress with radius; $Re_0 = 2.e+6$, $s = -1$

radial outflow. The model proposed by Lam and Bremhorst is used in this study and the predictions compare very favorably with the experimental results of Pincombe for an outflowing cavity and of Owen for the flow between rotating and stationary disks. Based on this validation of the model, the flow between counterrotating disks is predicted as is the variation of the radial tangential wall shear stress with Rossby number. The model does not include any effect of possible turbulence anisotropy due to rotational effects and it would be of interest to map the flow regimes for which the Lam–Bremhorst model can be used.

References

Chew, J. W. 1985, "Prediction of Flow in Rotating Disc System Using k-ϵ Turbulence Model," *International Journal of Turbo and Jet Engines*, Vol. 2, pp. 253–261.

Chien, K. Y., 1982, "Predictions of Channel and Boundary-Layer Flow With a Low Reynolds Number Turbulence Model," *AIAA Journal*, Vol. 20, pp. 33–38.

Dubya, D., and Michard, P., 1981, "A Program for Calculating Boundary Layers Along Compressor and Turbine Blades," *Numerical Methods in Heat Transfer*, R. W. Lewis, K. Morgan, and D. C. Zienkiewicz, eds., Wiley, New York.

Gosman, A. D., Koosinlin, M. L., Lockwood, F. C., and Spaulding, D. B., 1976, "Transfer of Heat in Rotating System," ASME Paper No. 76-GT-25.

Greenspan, M. G., 1969, *The Theory of Rotating Fluids*, Cambridge University Press, United Kingdom.

Hassid, S., and Poreh, M., 1978, "A Turbulent Energy Dissipation Model for Flows With Drag Reduction," ASME *Journal of Fluids Engineering*, Vol. 100, pp. 107–112.

Haynes, C. M., and Owen, J. M., 1975, "Heat Transfer From Shrouded Disk System With Radial Outflow of Coolant," ASME *Journal of Engineering for Power*, Vol. 97, p. 28.

Hide, R., 1968, "On Source-Sink Flows in a Rotating Fluid," *Journal of Fluid Mechanics*, Vol. 32, p. 737.

Hoffman, G. H., 1975, "Improved Form of the Low Reynolds Number k-ϵ Turbulence Model," *Physics of Fluids*, Vol. 18, pp. 309–312.

Lam, C. K. G., and Bremhorst, K., 1981, "A Modified Form of k-ϵ Model for Predicting Wall Turbulence," ASME *Journal of Fluids Engineering*, Vol. 103, pp. 456–460.

Launder, B. E., and Sharma, B. I., 1974, "Application to Energy Dissipation Model of Turbulence to the Calculation of Flow Near a Spinning Disc," *Letters in Heat and Mass Transfer*, Vol. 1, pp. 131–138.

Morse, A. P., 1987, "Numerical Prediction of Turbulent Flow in Rotating Cavities," Trans. ASME.

Owen, J. M., 1969, "Flow Between a Rotating and a Stationary Disc," Ph.D. Thesis, School of Engineering and Applied Sciences, University of Sussex, United Kingdom.

Owen, J. M., and Pincombe, J. R., 1980, "Velocity Measurements Inside a Rotating Cylindrical Cavity With a Radial Outflow of Fluid," *Journal of Fluid Mechanics*, Vol. 99, Part 1, pp. 111–127.

Patankar, S. V., Sparrow, E. M., and Ivanovic, M., 1978, "Thermal Interactions Among the Confining Walls of a Turbulent Recirculating Flow," *International Journal of Heat and Mass Transfer*, Vol. 21, pp. 269–274.

Patel, V. C., Rodi, W., and Scheuerer, G., 1985, "Turbulence Models for Near-Wall and Low Reynolds Number Flows: A Review," *AIAA Journal*, Vol. 23, No. 9, p. 1308.

Pincombe, J. R., 1981, "Velocity Measurements in the MK II Rotating Cavity Rig With a Radial Outflow," School of Engineering and Applied Sciences, University of Sussex, United Kingdom.

Reynolds, W. C., 1976, "Computation of Turbulent Flows," *Annual Review of Fluid Mechanics*, Vol. 8, pp. 183–208.

Salhi, A., 1987, "Analysis of the Flow Field Between Co-axial Rotating Disks Using a Modified k-ϵ Turbulence Model," M.Sc. Thesis, MIT, Cambridge, MA.

Sparrow, E. M., Buszkiewicz, T. C., and Eckert, E. R. G., 1975, "Heat Transfer and Temperature Field Experiments in a Cavity With Rotation, Recirculation and Coolant Throughflow," ASME *Journal of Heat Transfer*, Vol. 97, p. 22.

Sparrow, E. M., and Goldstein, L., 1976, "Effect of Rotation and Coolant Throughflow on the Heat Transfer and Temperature Field in an Enclosure," ASME *Journal of Heat Transfer*, Vol. 98, p. 387.

Yu, J. P., Sparrow, E. M., and Eckert, E. R. G., 1973, "Experiment on a Shrouded Parallel Disk System With Rotating and Coolant Throughflow," *International Journal of Heat and Mass Transfer*, Vol. 16, p. 311.

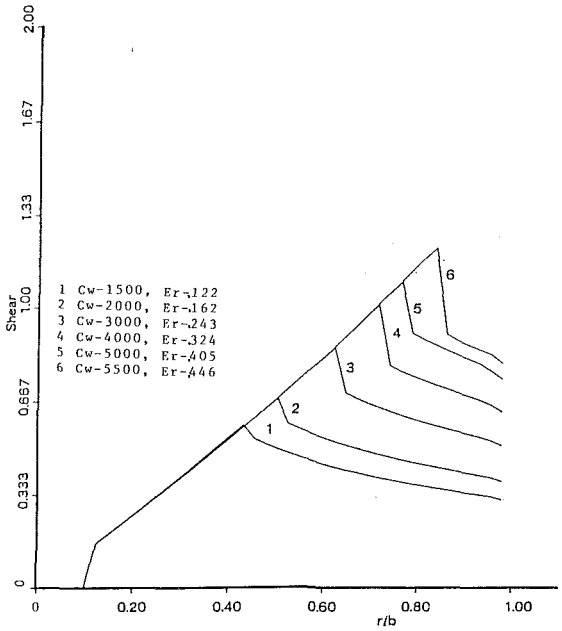

Fig. 15 Variation of the tangential shear stress with radius; $Re_0 = 2.e+6$, $s = -1$

radial outflow. The model proposed by Lam and Bremhorst is used in this study and the predictions compare very favorably with the experimental results of Pincombe for an outflowing cavity and of Owen for the flow between rotating and stationary disks. Based on this validation of the model, the flow between counterrotating disks is predicted as is the variation of the radial tangential wall shear stress with Rossby number. The model does not include any effect of possible turbulence anisotropy due to rotational effects and it would be of interest to map the flow regimes for which the Lam-Bremhorst model can be used.

References

Chew, J. W. 1985, "Prediction of Flow in Rotating Disc System Using k-ϵ Turbulence Model," *International Journal of Turbo and Jet Engines*, Vol. 2, pp. 253-261.

Chien, K. Y., 1982, "Predictions of Channel and Boundary-Layer Flow With a Low Reynolds Number Turbulence Model," *AIAA Journal*, Vol. 20, pp. 33-38.

Dubya, D., and Michard, P., 1981, "A Program for Calculating Boundary Layers Along Compressor and Turbine Blades," *Numerical Methods in Heat Transfer*, R. W. Lewis, K. Morgan, and D. C. Zienkiewicz, eds., Wiley, New York.

Gosman, A. D., Koosinlin, M. L., Lockwood, F. C., and Spaulding, D. B., 1976, "Transfer of Heat in Rotating System," ASME Paper No. 76-GT-25.

Greenspan, M. G., 1969, *The Theory of Rotating Fluids*, Cambridge University Press, United Kingdom.

Hassid, S., and Poreh, M., 1978, "A Turbulent Energy Dissipation Model for Flows With Drag Reduction," ASME *Journal of Fluids Engineering*, Vol. 100, pp. 107-112.

Haynes, C. M., and Owen, J. M., 1975, "Heat Transfer From Shrouded Disk System With Radial Outflow of Coolant," ASME *Journal of Engineering for Power*, Vol. 97, p. 28.

Hide, R., 1968, "On Source-Sink Flows in a Rotating Fluid," *Journal of Fluid Mechanics*, Vol. 32, p. 737.

Hoffman, G. H., 1975, "Improved Form of the Low Reynolds Number k-ϵ Turbulence Model," *Physics of Fluids*, Vol. 18, pp. 309-312.

Lam, C. K. G., and Bremhorst, K., 1981, "A Modified Form of k-ϵ Model for Predicting Wall Turbulence," ASME *Journal of Fluids Engineering*, Vol. 103, pp. 456-460.

Launder, B. E., and Sharma, B. I., 1974, "Application to Energy Dissipation Model of Turbulence to the Calculation of Flow Near a Spinning Disc," *Letters in Heat and Mass Transfer*, Vol. 1, pp. 131-138.

Morse, A. P., 1987, "Numerical Prediction of Turbulent Flow in Rotating Cavities," Trans. ASME.

Owen, J. M., 1969, "Flow Between a Rotating and a Stationary Disc," Ph.D. Thesis, School of Engineering and Applied Sciences, University of Sussex, United Kingdom.

Owen, J. M., and Pincombe, J. R., 1980, "Velocity Measurements Inside a Rotating Cylindrical Cavity With a Radial Outflow of Fluid," *Journal of Fluid Mechanics*, Vol. 99, Part 1, pp. 111-127.

Patankar, S. V., Sparrow, E. M., and Ivanovic, M., 1978, "Thermal Interactions Among the Confining Walls of a Turbulent Recirculating Flow," *International Journal of Heat and Mass Transfer*, Vol. 21, pp. 269-274.

Patel, V. C., Rodi, W., and Scheuerer, G., 1985, "Turbulence Models for Near-Wall and Low Reynolds Number Flows: A Review," *AIAA Journal*, Vol. 23, No. 9, p. 1308.

Pincombe, J. R., 1981, "Velocity Measurements in the MK II Rotating Cavity Rig With a Radial Outflow," School of Engineering and Applied Sciences, University of Sussex, United Kingdom.

Reynolds, W. C., 1976, "Computation of Turbulent Flows," *Annual Review of Fluid Mechanics*, Vol. 8, pp. 183-208.

Salhi, A., 1987, "Analysis of the Flow Field Between Co-axial Rotating Disks Using a Modified k-ϵ Turbulence Model," M.Sc. Thesis, MIT, Cambridge, MA.

Sparrow, E. M., Buszkiewicz, T. C., and Eckert, E. R. G., 1975, "Heat Transfer and Temperature Field Experiments in a Cavity With Rotation, Recirculation and Coolant Throughflow," ASME *Journal of Heat Transfer*, Vol. 97, p. 22.

Sparrow, E. M., and Goldstein, L., 1976, "Effect of Rotation and Coolant Throughflow on the Heat Transfer and Temperature Field in an Enclosure," ASME *Journal of Heat Transfer*, Vol. 98, p. 387.

Yu, J. P., Sparrow, E. M., and Eckert, E. R. G., 1973, "Experiment on a Shrouded Parallel Disk System With Rotating and Coolant Throughflow," *International Journal of Heat and Mass Transfer*, Vol. 16, p. 311.

DISCUSSION

J. W. Chew[1]

The performance of different turbulent models in rotating disk flows is certainly of interest and I agree with the authors' statement that it would be of interest to map out the flow regimes for which the Lam-Bremhorst model can be used.

The present results for the rotating cavity show similar agreement with experiment to those of Morse (1987), who used a different version of the k-ϵ model. Morse presented a more thorough evaluation against experimental data, giving results at higher rotational Reynolds numbers and for both radial outflow and inflow of fluid. It is a pity that the present results are restricted to $Re_\theta = 10^5$ when data are available for Re_θ up to 10^6. Can the authors give any indication of the performance of the Lam-Bremhorst model at higher values of Re_θ?

As noted by the authors there is some discrepancy between prediction and measurements near the rotor in Fig. 1, which gives the radial velocity profile for flow between a rotating and stationary disk. As a further guide to the accuracy of the model in this important near-wall region, it would be useful to compare the predicted and measured disk moment coefficients.

The predictions for the flow between counterrotating disks in Figs. 9 to 15 show surprising features. For example, from Figs. 9, 11, and 12 it appears that the formation of the Ekman-type layers occurs abruptly when a critical radius is reached. This contrasts with the progressive entrainment of flow into the disk boundary layers identified by Chew et al. (1984). As numerical solution of the governing equations for these flows is known to present some difficulties the question of the accuracy of the present solutions naturally arises. Did the authors encounter any difficulties in obtaining convergence of the iterative solution and to what degree are the results affected by truncation error?

[1]Rolls-Royce plc, Derby, United Kingdom.

References

Chew, J. W., Owen, J. M., and Pincombe, J. R., 1984, "Numerical Predictions for Laminar Source-Sink Flow in a Rotating Cylindrical Cavity," *Journal of Fluid Mechanics*, Vol. 143, pp. 451-466.

Boundary-Layer Flows in Rotating Cavities

C. L. Ong

J. M. Owen

School of Engineering and Applied Sciences,
University of Sussex,
Falmer, Brighton, BN1 9QT, United Kingdom

A rotating cylindrical cavity with a radial outflow of fluid provides a simple model of the flow between two corotating air-cooled gas-turbine disks. The flow structure comprises a source region near the axis of rotation, boundary layers on each disk, a sink layer on the peripheral shroud, and an interior core of rotating inviscid fluid between the boundary layers. In the source region, the boundary layers entrain fluid; outside this region, nonentraining Ekman-type layers are formed on the disks. In this paper, the differential boundary-layer equations are solved to predict the velocity distribution inside the entraining and nonentraining boundary layers and in the inviscid core. The equations are discretized using the Keller-box scheme, and the Cebeci–Smith eddy-viscosity model is used for the turbulent-flow case. Special problems associated with reverse flow in the nonentraining Ekman-type layers are successfully overcome. Solutions are obtained, for both laminar and turbulent flow, for the "linear equations" (where nonlinear inertial terms are neglected) and for the full nonlinear equations. These solutions are compared with earlier LDA measurements of the radial and tangential components of velocity made inside a rotating cavity with a radial outflow of air. Good agreement between the computations and the experimental data is achieved for a wide range of flow rates and rotational speeds.

Introduction

The heat transfer and fluid flow between air-cooled corotating gas turbine disks can be modeled by a rotating cavity with a radial outflow of fluid, as illustrated in Fig. 1. In Fig. 1(*a*), the flow enters as a uniform source at $r = a$ and leaves via a series of holes or a circular slot in the shroud at $r = b$. The source region distributes the flow into the boundary layers on the disks, and in the sink layer the fluid is transported to the holes in the shroud. Between the boundary layers is an interior core of inviscid rotating fluid. In Fig. 1(*b*), the flow enters axially through the center of one disk (the "upstream disk") and forms a wall jet on the downstream disk, but outside the source region the flow is the same as that described above for the radial-inlet case. It is useful to note that the source region ends when all the flow entering at $r = a$ has been entrained into the boundary layers. The nonentraining boundary layers outside the source region are usually referred to as Ekman-type layers.

Owen et al. (1985) obtained solutions of the momentum-integral equations for source-sink flow in a rotating cavity. For turbulent flow they used 1/7th power laws for the velocity profiles and the Blasius relationships for the shear-stresses. Chew and Rogers (1988) extended the method to include solution of the energy-integral equation and were able to predict Nusselt numbers that agreed closely with the measurements of Northrop and Owen (1988).

Numerical solutions of the Navier–Stokes equations for source-sink flow were obtained by Chew et al. (1984), and Chew (1984, 1985) obtained solutions of the turbulent elliptic equations using both the k–ϵ and the mixing-length turbulence models. Recently Morse (1988) has solved the elliptic equations using a low-Reynolds-number k–ϵ model, and his predicted values were in good agreement with the experimental data of Pincombe (1983).

Although the elliptic equations can provide a comprehensive description of the complete flow, grid-independent solutions can be expensive in terms of computer storage and computational time. By contrast, the boundary-layer equations can be solved more efficiently, and they can provide good solutions for the aspects of the problem that are important for design purposes, such as pressure distributions, moment coefficients, and Nusselt numbers. The differential boundary-layer equations provide a compromise between the elliptic equations and the momentum-integral equations.

Shirazi and Truman (1988) solved the turbulent differential boundary-layer equations for the case of a superimposed radial outflow between corotating disks, and their solutions were in good agreement with experimental data. However, they only solved the equations for the case where the axial clearance between the disks was small enough for the two boundary layers to merge: there was no intermediate core of inviscid fluid.

In most gas turbines, the disk spacing is wide enough for the occurrence of the source-sink flow discussed above. Under these conditions, there is often a reversal of the radial component of velocity near the "edge" of the boundary layer

Contributed by the International Gas Turbine Institute and presented at the 33rd International Gas Turbine and Aeroengine Congress and Exhibition, Amsterdam, The Netherlands, June 5–9, 1988. Manuscript received by the International Gas Turbine Institute September 15, 1987. Paper No. 88-GT-292.

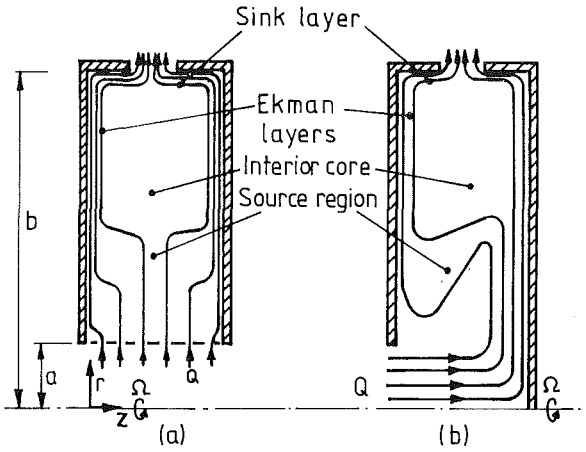

Fig. 1 Schematic diagram of the flow structure inside a rotating cavity with a radial outflow of coolant: (*a*) radial inlet; (*b*) axial inlet

adjacent to the inviscid core. This flow reversal creates serious problems when a numerical "marching" procedure is used to solve the boundary-layer equations. How this problem can be overcome and how the boundary-layer equations can be solved under these conditions are the main subjects of this paper.

In Section 2, the differential boundary-layer equations are presented for both stationary and rotating coordinate systems. The latter allows simplifications to be made enabling the linear Ekman-layer equations to be derived. Solution procedures for both the linear and nonlinear equations are discussed in Section 3, and in Section 4 these solutions are compared with available experimental data.

2 Boundary-Layer Equations

2.1 Nonlinear Equations. For incompressible axisymmetric flow, the continuity equation and the radial and tangential momentum equations can be expressed in stationary coordinates as

$$\frac{1}{r}\frac{\partial}{\partial r}(ru)+\frac{\partial w}{\partial z}=0 \tag{2.1}$$

$$u\frac{\partial u}{\partial r}+w\frac{\partial u}{\partial z}-\frac{v_\phi^2}{r}=-\frac{1}{\rho}\frac{dp}{dr}+\frac{1}{\rho}\frac{\partial \tau_r}{\partial z} \tag{2.2}$$

and

$$u\frac{\partial v_\phi}{\partial r}+w\frac{\partial v_\phi}{\partial z}+\frac{uv_\phi}{r}=\frac{1}{\rho}\frac{\partial \tau_\phi}{\partial z} \tag{2.3}$$

where

$$\tau_r=\mu\frac{\partial u}{\partial z}-\rho\overline{u'w'} \tag{2.4}$$

and

$$\tau_\phi=\mu\frac{\partial v_\phi}{\partial z}-\rho\overline{v_\phi' w'}$$

Expressed in a coordinate system rotating with the same angular speed as the cavity, equations (2.2) and (2.3) become

$$u\frac{\partial u}{\partial r}+w\frac{\partial u}{\partial z}-\frac{v^2}{r}-2\Omega v=-\frac{1}{\rho}\frac{dp_1}{dr}+\frac{1}{\rho}\frac{\partial \tau_r}{\partial z} \tag{2.5}$$

$$u\frac{\partial v}{\partial r}+w\frac{\partial v}{\partial z}+\frac{uv}{r}+2\Omega u=\frac{1}{\rho}\frac{\partial \tau_\phi}{\partial z} \tag{2.6}$$

where

$$v=v_\phi-\Omega r \tag{2.7}$$

and

$$p_1=p-1/2\rho\Omega^2 r^2 \tag{2.8}$$

2.2 Linear Equations. Equations (2.5) and (2.6) can be simplified by considering the flow in the core outside the boundary layer, where values are denoted by an overbar on the symbols. In the limit as $z \to \infty$, where axial gradients of u and v are zero, equations (2.5) and (2.6) become

$$\overline{u}\frac{d\overline{u}}{dr}-\frac{\overline{v}^2}{r}-2\Omega\overline{v}=-\frac{1}{\rho}\frac{dp_1}{dr} \tag{2.9}$$

$$\overline{u}\left(\frac{d\overline{v}}{dr}+\frac{\overline{v}}{r}+2\Omega\right)=0 \tag{2.10}$$

Equation (2.10) implies that either $\overline{u}=0$ or

$$\overline{v}+\Omega r=\overline{v}_\phi=\frac{c}{r} \tag{2.11}$$

where c is an arbitrary constant. Equation (2.11) represents free-vortex flow in the core, and unless this special case exists it follows that $\overline{u}=0$ and, from equation (2.1), $\partial\overline{w}/\partial z=0$. If symmetry exists about the midaxial plane of the cavity (which

Nomenclature

a = inner radius of cavity
A^+ = empirical constant in turbulence model, equation (2.18)
b = outer radius of cavity
c = swirl fraction
C_w = mass flow parameter $\equiv Q/\nu b$
f = nondimensional stream function $\equiv \psi/r^2\,(\nu\Omega)^{1/2}$
g' = nondimensional tangential component of velocity $\equiv v_\phi/\Omega r$
l = mixing length
n = exponent in equation (2.18)
p = static pressure
p_1 = reduced pressure in equation (2.8)
p^* = nondimensional static pressure $\equiv p/(1/2\rho\Omega^2 r^2)$
Q = volumetric flow rate
Q_l = local volumetric flow rate
r = radial distance
Re_r = radial Reynolds number, $\equiv Q/2\pi\nu r$
Re_ϕ = rotational Reynolds number $\equiv \Omega b^2/\nu$
Ro = radial Rossby number $\equiv C_w/4\pi x^2\mathrm{Re}_\phi^{1/2}$
(u, v_ϕ, w) = time-averaged velocity components relative to stationary (r, ϕ, z) coordinate system
(u, v, w) = time-averaged velocity components relative to rotating (r, ϕ, z) coordinate system
(u', v_ϕ', w') = fluctuating velocity components
$-\overline{u'w'}$, $-\overline{v_\phi' w'}$ = Reynolds stresses

is the case for an isothermal cavity with uniform source-sink flow), $\partial\bar{w}/\partial z = 0$ implies that $\bar{w} = 0$; the boundary layers are nonentraining.

Equations (2.5) and (2.6) can now be rewritten as

$$\left\{u\frac{\partial u}{\partial r} + w\frac{\partial u}{\partial z} - \frac{v^2-\bar{v}^2}{r}\right\} - 2\Omega(v-\bar{v}) = \frac{1}{\rho}\frac{\partial \tau_r}{\partial z} \quad (2.12)$$

$$\left\{u\frac{\partial v}{\partial r} + w\frac{\partial v}{\partial z} + \frac{uv}{r}\right\} + 2\Omega u = \frac{1}{\rho}\frac{\partial \tau_\phi}{\partial z} \quad (2.13)$$

If $|\bar{v}|/\Omega r << 1$, the nonlinear terms in the curly brackets can be neglected to give the so-called linear Ekman-layer equations

$$-2\Omega(v-\bar{v}) = \frac{1}{\rho}\frac{\partial \tau_r}{\partial z} \quad (2.14)$$

$$2\Omega u = \frac{1}{\rho}\frac{\partial \tau_\phi}{\partial z} \quad (2.15)$$

2.3 Turbulence Model. An isotropic eddy-viscosity model is assumed where

$$\left.\begin{aligned}\frac{1}{\rho}\tau_r &= \nu_{eff}\frac{\partial u}{\partial z}\\ \text{and}\qquad \frac{1}{\rho}\tau_\phi &= \nu_{eff}\frac{\partial v_\phi}{\partial z}\end{aligned}\right\} \quad (2.16)$$

The model used below is a modification of that proposed by Cebeci and Smith (1974) in which the boundary layer is assumed to comprise an inner and an outer region, denoted by the subscripts i and o, respectively. The effective viscosity ν_{eff} is made up from the laminar component, $\nu = \mu/\rho$, and a turbulent component ν_t.

For the inner region, close to the disk surface, the eddy viscosity ν_t is based on Prandtl's mixing-length hypothesis. Using the resultant mean-velocity gradient, $(\nu_t)_i$ for the swirling boundary layer on the disk is given by

$$(\nu_t)_i = l^2\left[\left(\frac{\partial u}{\partial z}\right)^2 + \left(\frac{\partial v_\phi}{\partial z}\right)^2\right]^{1/2} \qquad 0 \le z \le z_c \quad (2.17)$$

where z_c is the axial location at which $(\nu_t)_i = (\nu_t)_o$ and l is the mixing length defined by

$$l = \kappa z[1 - \exp(-z^+(\tau^+)^n/A^+)] \quad (2.18)$$

In the above expression, z^+ and τ^+ are respectively the nondimensional axial distance and local shear stress defined by

$$z^+ = z(\tau_w\rho)^{1/2}/\mu \text{ and } \tau^+ = \tau/\tau_w$$

with τ_w being the resultant wall shear stress. By convention, the empirical constants κ and A^+ are assigned the values of 0.4 and 26.0, respectively.

Different values of the exponent n in the damping function have been examined and assessment made of their effectiveness for the cases where $n = 0$, 0.5, and 1.5. For $n = 0$, the formulation for l is identical to that proposed by Cebeci and Smith. This has been found appropriate for fully turbulent conditions occurring at high values of Re_ϕ. The reduction in shear stress with increasing n is relatively greater for low values of Re_ϕ giving improved overall predictions. However, with $n = 1.5$, numerical instabilities arise due to the strong nonlinearity of τ^+, but these were overcome by using values of τ^+ formed from upstream values. The penalties for using nonzero values of n are that an increased number of iterations are required for convergence of the solution. For a wide range of Re_ϕ, the use of $n = 0.5$ appears to be satisfactory, requiring no upstream values and offering reasonable rates of convergence, and this value was used for the results presented in Section 4.

For the outer region of the boundary layer, the eddy viscosity, $(\nu_t)_o$, is based on Clauser's (1956) velocity defect approach. The expression for $(\nu_t)_o$ is given by

$$(\nu_t)_o = \alpha(\Omega r - \bar{v}_\phi)\delta^* \qquad z_c \le z \le \delta \quad (2.19)$$

where δ^*, the displacement thickness, is defined as

$$\delta^* = \frac{1}{|\Omega r - \bar{v}_\phi|} \times \left|\int_o^\infty \{(\Omega r - \bar{v}_\phi) - [u^2 + (\Omega r - \bar{v}_\phi)^2]^{1/2}\}dz\right| \quad (2.20)$$

The parameter α in expression (2.19) is generally assumed to be a universal constant equal to 0.0168 for fully turbulent flow.

Continuity between the inner and outer regions is maintained by choosing

$$\nu_t = \min\{(\nu_t)_i, \quad (\nu_t)_o\}.$$

Nomenclature (cont.)

U, V = nondimensional radial and tangential velocity components $\equiv u/\Omega r$, $v/\Omega r$, respectively
x = nondimensional radius $\equiv r/b$
z = axial distance
z^+ = nondimensional axial distance $\equiv z(\tau_w\rho)^{1/2}/\mu$
α = empirical constant in turbulence model, equation (2.19)
δ = boundary-layer thickness
η = nondimensional axial distance $\equiv (\Omega/\nu)^{1/2}z$
κ = empirical constant in turbulence model, equation (2.18)
μ = dynamic viscosity
ν = kinematic viscosity $\equiv \mu/\rho$
ν_t^+ = nondimensional eddy viscosity, $\equiv \nu_t/\nu$
ρ = density
τ = resultant shear stress
τ_r, τ_ϕ = radial and tangential shear stress components
τ^+ = nondimensional shear stress $\equiv \tau/\tau_w$
ψ = stream function
Ω = angular velocity of cavity

Subscripts

eff = effective
i = inner
o = outer
t = turbulent
w = wall

3 Numerical Solutions

3.1 Ekman-Layer Equations

3.1.1 Laminar Flow. For laminar flow, equations (2.14) and (2.15) become

$$-2\Omega(v-\bar{v})=\nu\frac{\partial^2 u}{\partial z^2} \tag{3.1}$$

$$2\Omega u=\nu\frac{\partial^2 v}{\partial z^2} \tag{3.2}$$

with the boundary conditions

$$\left.\begin{aligned} &u=v=0 \text{ at } z=0\\ &u=0,\quad v=\bar{v} \text{ as } z\to\infty \end{aligned}\right\} \tag{3.3}$$

The solutions are

$$\left.\begin{aligned} u&=-\bar{v}\,e^{-\eta}\sin\eta\\ v&=\bar{v}(1-e^{-\eta}\cos\eta) \end{aligned}\right\} \tag{3.4}$$

where

$$\eta=(\Omega/\nu)^{1/2}z \tag{3.5}$$

The local volumetric flow rate Q_l can be calculated from

$$Q_l=\int_o^\infty 2\pi r u dz \tag{3.6}$$

and, using equation (3.4),

$$\frac{Q_l}{\nu b}=-\pi\,\mathrm{Re}_\phi^{1/2}\frac{\bar{v}}{\Omega r}x^2 \tag{3.7}$$

where $x = r/b$. Since the Ekman layers are nonentraining, $Q_l = 1/2\ Q$, and so

$$\frac{\bar{v}}{\Omega r}=-\frac{1}{2\pi}C_w\,\mathrm{Re}_\phi^{-1/2}x^{-2} \tag{3.8}$$

3.1.2 Turbulent Flow. It is convenient to rewrite equations (2.14) and (2.15) as

$$-2(V-\bar{V})=\frac{\partial}{\partial\eta}\left[(1+\nu_t^+)\frac{\partial U}{\partial\eta}\right] \tag{3.9}$$

$$2U=\frac{\partial}{\partial\eta}\left[(1+\nu_t^+)\frac{\partial V}{\partial\eta}\right] \tag{3.10}$$

where

$$\left.\begin{aligned} V&=v/\Omega r\\ U&=u/\Omega r\\ \nu_t^+&=\nu_t/\nu \end{aligned}\right\} \tag{3.11}$$

and η is given by equation (3.5).

Two different finite-difference methods were used to solve equations (3.9) and (3.10). In method A, an artificial transient term was introduced into the equations to ensure diagonal-dominance of the resulting coefficient matrix. The equations were then solved using Gauss–Seidel fixed-point iteration, and the transient term was damped out as the solution converged to its steady-state value. In method B, the equations were reformulated as a system of first-order equations (as described below for the nonlinear equations).

The main advantages of method A were its simplicity and its modest storage requirements. However, method B, which required much larger storage and far more computer coding, was much faster. For example, with 300 axial gridpoints method A would require over a minute of CPU time on a VAX 8500 for each radial location, compared with about two seconds for method B.

3.1.3 Relationship Between Shear Stress and Flow Rate. Referring to equation (3.10)

$$2\int_o^\infty U d\eta=-\left[(1+\nu_t^+)\frac{\partial V}{\partial\eta}\right]_{\eta=0} \tag{3.12}$$

but $\nu_t^+ = 0$ at $\eta = 0$, hence

$$-\left(\frac{\partial V}{\partial\eta}\right)_{\eta=0}=2\int_o^\infty U d\eta=\frac{1}{2\pi}C_w\,\mathrm{Re}_\phi^{-1/2}x^{-2} \tag{3.13}$$

Equation (3.13) therefore gives a relationship between the tangential component of velocity (hence, the shear stress) at the surface of the disk and the flow rate. It provides a useful convergence criterion for the numerical solutions of the Ekman-layer equations.

The term on the right-hand side of equation (3.13) is equal to twice the Rossby number, Ro, defined in the Nomenclature. The significance of this parameter in laminar flow has long been recognized: The size of the source region depends on Ro, and the linear equations are only valid if Ro $\ll$ 1. However, it would appear that Ro is also an important parameter for turbulent flow, and it is shown in Section 4 that the difference between the linear and nonlinear turbulent solutions increases with increasing Ro.

3.2 Nonlinear Equations

3.2.1 Transformation of the Boundary-Layer Equations. It is convenient to define a stream function ψ where

$$ur=\frac{\partial\psi}{\partial z}\text{ and }wr=-\frac{\partial\psi}{\partial r} \tag{3.14}$$

and a nondimensional stream function $f(r, \eta)$ as

$$f=\psi/r^2(\nu\Omega)^{1/2} \tag{3.15}$$

where η is defined in equation (3.5).

In addition

$$g'(r,\eta)=v_\phi/\Omega r \tag{3.16}$$

and

$$p^*(r)=p/\rho\Omega^2r^2 \tag{3.17}$$

Equations (2.2) and (2.3) can then be expressed as

$$((1+\nu_t^+)f'')'+2ff''-(f')^2+(g')^2=r\left(f'\frac{\partial f'}{\partial r}-f''\frac{\partial f}{\partial r}+\frac{\partial p^*}{\partial r}\right)+2p^* \tag{3.18}$$

$$((1+\nu_t^+)g'')'+2fg''-2f'g'=r\left(f'\frac{\partial g'}{\partial r}-g''\frac{\partial f}{\partial r}\right) \tag{3.19}$$

where the primes indicate differentiation with respect to η. The appropriate boundary conditions are

$$\left.\begin{aligned} &\eta=0: f(r,0)=f'(r,0)=g(r,0)=0,\\ &\qquad g'(r,0)=1\\ &\eta\to\infty: f'(r,\infty)=g''(r,\infty)=0 \end{aligned}\right\} \tag{3.20}$$

The pressure gradient can be calculated using the fact that as $\eta \to \infty$ equation (3.18) reduces to

$$2p^*+r\frac{dp^*}{dr}=(g'(r,\infty))^2 \tag{3.21}$$

In the source region, free-vortex flow is assumed to occur such that

$$g'(r,\infty)=cx^{-2} \tag{3.22}$$

where c is related to the initial swirl of the fluid entering the cavity. Hence, p^* can be readily calculated.

Outside the source region, where the boundary layers are nonentraining, the volumetric flow Q is given by

$$Q=4\pi\int_o^\infty r u dz \tag{3.23}$$

and, from equation (3.15),

$$ru = \Omega r^2 f'(r, \eta) \tag{3.24}$$

Hence

$$f(r, \infty) = \frac{1}{4\pi} C_w \, \mathrm{Re}_\phi^{1/2} x^{-2} \tag{3.25}$$

and this provides an additional equation from which the pressure gradient can be determined.

3.2.2 Solution of the Equations. Equations (3.18) and (3.19) were converted to a system of first-order differential equations and were solved by the Keller–Box (1972) method.

For laminar flow, the exact solutions of the Ekman-layer equations (see equations 3.4) are oscillatory in η. There are alternating regions of positive and negative flow in the Ekman layers; this can also occur in the nonlinear turbulent-flow solutions. The reverse-flow regions (where $u < 0$) present serious problems in the numerical solution of the equations and special treatment is necessary.

The simplest solution is to ignore the reverse flow region by setting any negative radial component of velocity to zero. The resulting solutions, while being inaccurate near the edge of the boundary layer, yield reasonable approximations near the disk. In particular, "wall fluxes" (shear stress, heat flux) may be calculated accurately enough for design purposes.

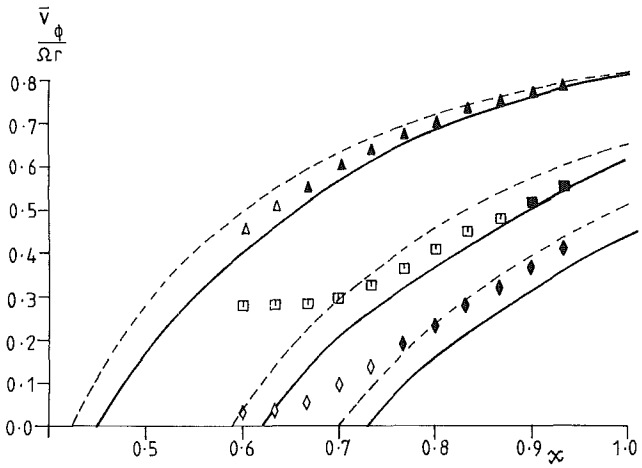

Fig. 2 Effect of C_w on the radial variation of the tangential component of velocity for laminar flow ($\mathrm{Re}_r < 180$) and $\mathrm{Re}_\phi = 5 \times 10^4$: ——— nonlinear solution; ···· linear solution; experimental data (Pincombe, 1983): ▲ $C_w = 253$; ■ $C_w = 487$; ◆ $C_w = 689$

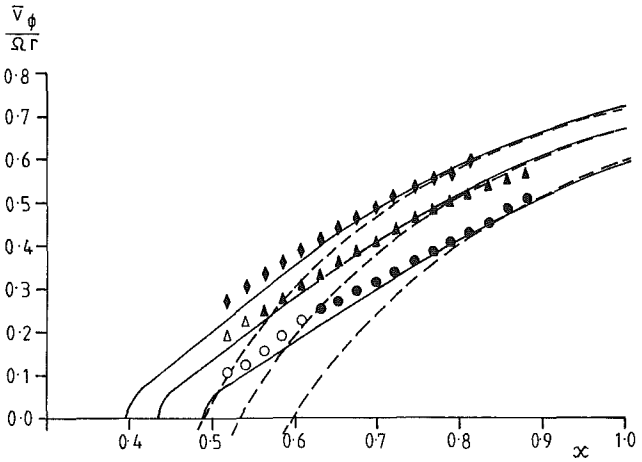

Fig. 3 Effect of Re_ϕ on the radial variation of the tangential component of velocity for turbulent flow ($\mathrm{Re}_r > 180$) and $C_w = 2500$: ———nonlinear solution; ···· linear solution; experimental data (Pincombe, 1983): • $\mathrm{Re}_\phi = 5.47 \times 10^5$; ▲ $\mathrm{Re}_\phi = 8.17 \times 10^5$; ◆ $\mathrm{Re}_\phi = 1.1 \times 10^6$

Another solution is to divide the boundary layer into two regions: (I) $\eta \le \eta_{II}$ where $u \ge 0$; (II)$\eta_{II} < \eta \le \eta_\infty$ where $u < 0$. Problems can occur in region II where the radial convection terms in equations (3.18) and (3.19)

$$\left(rf' \frac{\partial f'}{\partial r} + (f')^2, \qquad rf' \frac{\partial g'}{\partial r} + f'g' \right)$$

are associated with convection in the *local* downstream direction. If the direction of integration is radially outward (which is the downstream direction in region I) then integration proceeds in an upstream direction in II. The equations can become unstable unless these convection terms are reduced or removed.

One way of avoiding these instabilities is by use of the FLARE procedure, proposed by Reyhner and Flugge-Lotz (1968), where the radial convection terms are set to zero as soon as reverse flow is detected. This technique, which was used for the nonlinear turbulent computations discussed below, was found to be stable and yielded results of acceptable accuracy.

The procedure can be extended using multiple sweeps alternating between the radially outward and radially inward directions. However, the small improvements of accuracy achieved are more than offset by the computing time and

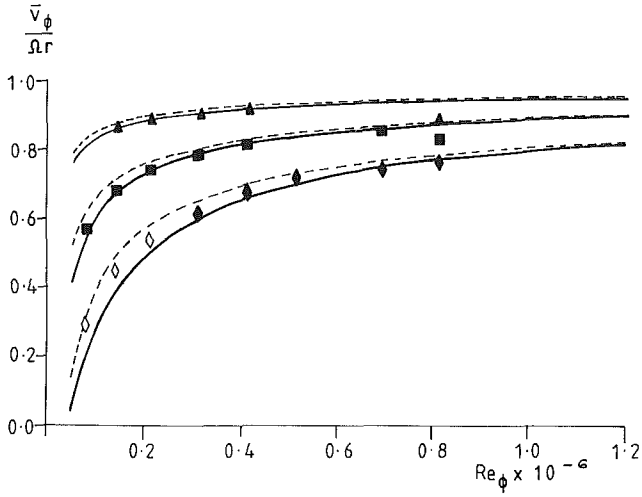

Fig. 4 Effect of C_w on the variation of the tangential component of velocity with Re_ϕ for laminar flow ($\mathrm{Re}_r < 180$) at $x = 0.767$: ——— nonlinear solution; ···· linear solution; experimental data (Pincombe, 1983): ▲ $C_w = 170$; ■ $C_w = 396$; ◆ $C_w = 710$

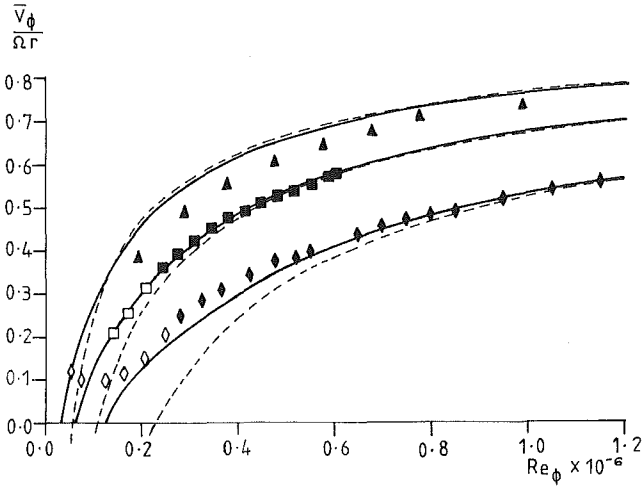

Fig. 5 Effect of C_w on the variation of the tangential component of velocity with Re_ϕ for turbulent flow ($\mathrm{Re}_r > 180$) at $x = 0.767$: ——— nonlinear solution; ···· linear solution; experimental data (Pincombe, 1983): ▲ $C_w = 940$; ■ $C_w = 1414$; ◆ $C_w = 2500$

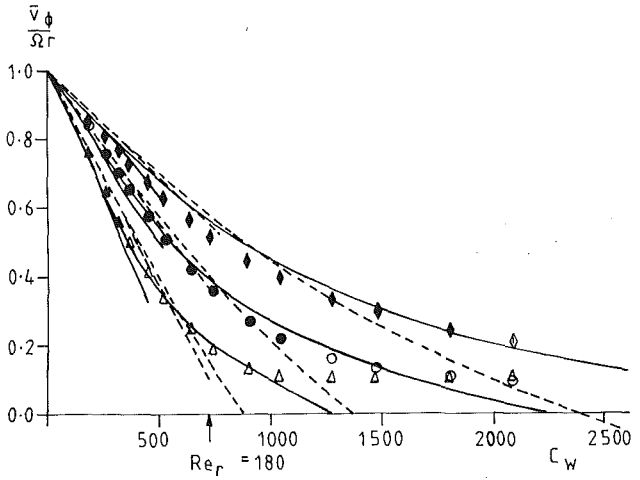

Fig. 6 Effect of Re_ϕ on the variation of the tangential component of velocity with C_w at $x = 0.633$: ———nonlinear solution; ···· linear solution; experimental data (Pincombe, 1983): ▲ $Re_\phi = 10^5$; • $Re_\phi = 2 \times 10^5$; ◆ $Re_\phi = 4 \times 10^5$

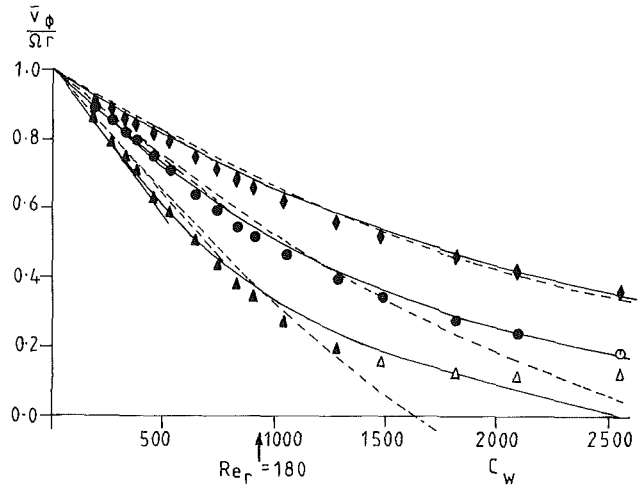

Fig. 7 Effect of Re_ϕ on the variation of the tangential component of velocity with C_w at $x = 0.833$: ———nonlinear solution; ···· linear solution; experimental data (Pincombe, 1983): ▲ $Re_\phi = 10^5$; • $Re_\phi = 2 \times 10^5$; ◆ $Re_\phi = 4 \times 10^5$

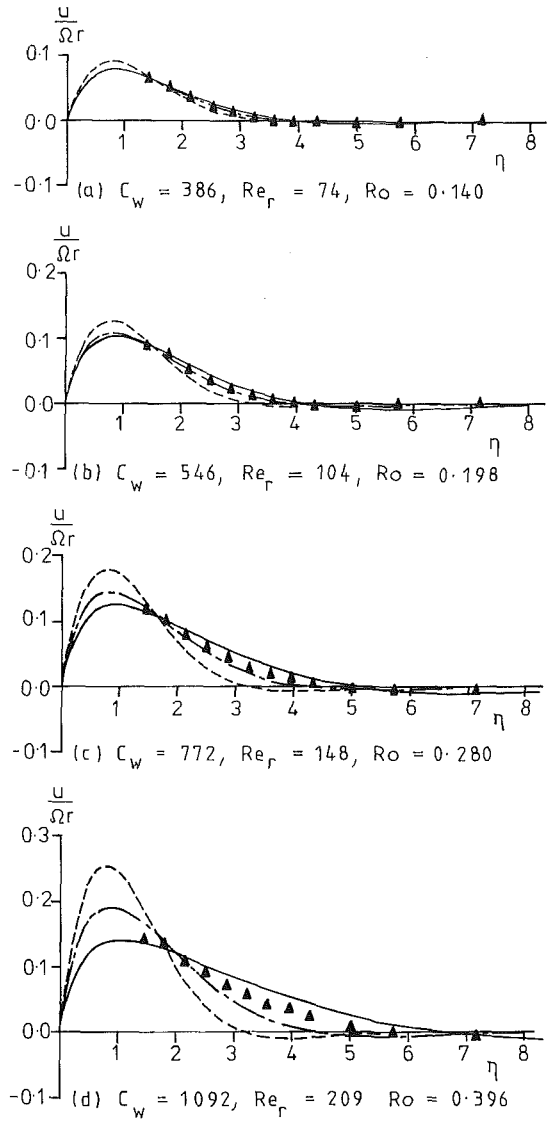

Fig. 8 Axial distribution of the radial component of velocity in the boundary layer for $Re_\phi = 10^5$ at $x = 0.833$: ——turbulent nonlinear solution; ——·—— turbulent "linear" solution; ···· laminar linear solution; ▲ Pincombe (1983)

storage requirements. For the results presented below, multiple sweeps were only used for the nonlinear laminar equations.

In the computations, a geometrically increasing nonuniform grid, with typically 300 axial points, was found to be satisfactory in controlling instabilities due to truncation errors. In the radial direction, a distribution of approximately 110 grids was used. With this grid resolution, typical run times were less than 15 min when the FLARE approximation was used on a VAX 8500. With the full multiple-sweep treatment, a run time of 2½ times that required for the FLARE approximation was necessary.

4 Comparison Between Theory and Experiment

The experimental data were obtained by Pincombe (1983) using laser-Doppler anemometry in air-filled rotating cavities. Several rigs and a variety of optical instrumentation were used, and the interested reader is directed to the above reference or to the related work of Owen et al. (1985) for further details.

4.1 Tangential Component of Velocity. Figure 2 shows the effect of C_w on the radial variation of $\bar{v}_\phi/\Omega r$ for laminar flow. Measurements that were made in the source region are denoted here and elsewhere by hollow symbols. For $C_w = 253$ and 487, the flow entered the cavity axially; for $C_w = 689$, it entered radially. The linear theory tends to overpredict, and the nonlinear theory underpredicts, the measured velocities.

In Fig. 3, the agreement between the measured and computed radial variation of $\bar{v}_\phi/\Omega r$ for turbulent flow is, in the main, good. The measurements were all made with an axial inlet of the flow into the cavity. It should be noted, however, that the source region was smaller than for the laminar flow cases, and as a consequence most of the measurements were made in the interior core between the boundary layers.

The effect of C_w on the variation of $\bar{v}_\phi/\Omega r$ with Re_ϕ is shown in Figs. 4 and 5 for laminar and turbulent flow, respectively. Apart from the results for $C_w = 940$, the agreement between the measured values and the nonlinear curves is generally very good. The linear curves tend to overpredict the results for laminar flow and to underpredict most of the results for turbulent flow.

Owen et al., (1985) suggested that laminar to turbulent transition should occur inside an Ekman layer when $Re_r \simeq 180$. In Fig. 5 for $C_w = 940$ and $x = 0.767$ (where $Re_r = 195$), it

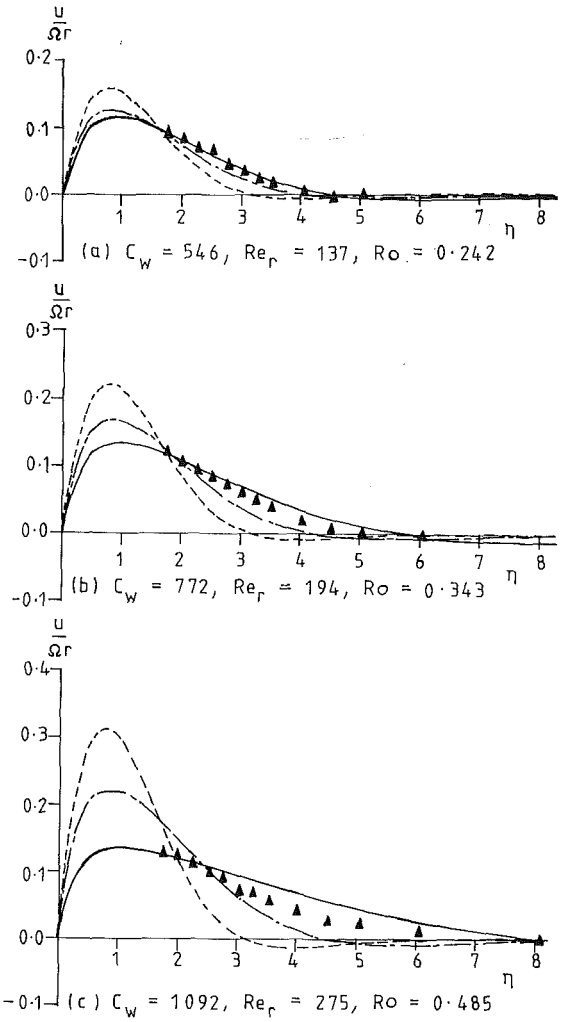

Fig. 9 Axial distribution of the radial component of velocity in the boundary layer for $Re_\phi = 2 \times 10^5$ at $x \simeq 0.633$: ——— turbulent nonlinear solution; ——·—— turbulent "linear" solution; ···· laminar linear solution; ▲ Pincombe (1983)

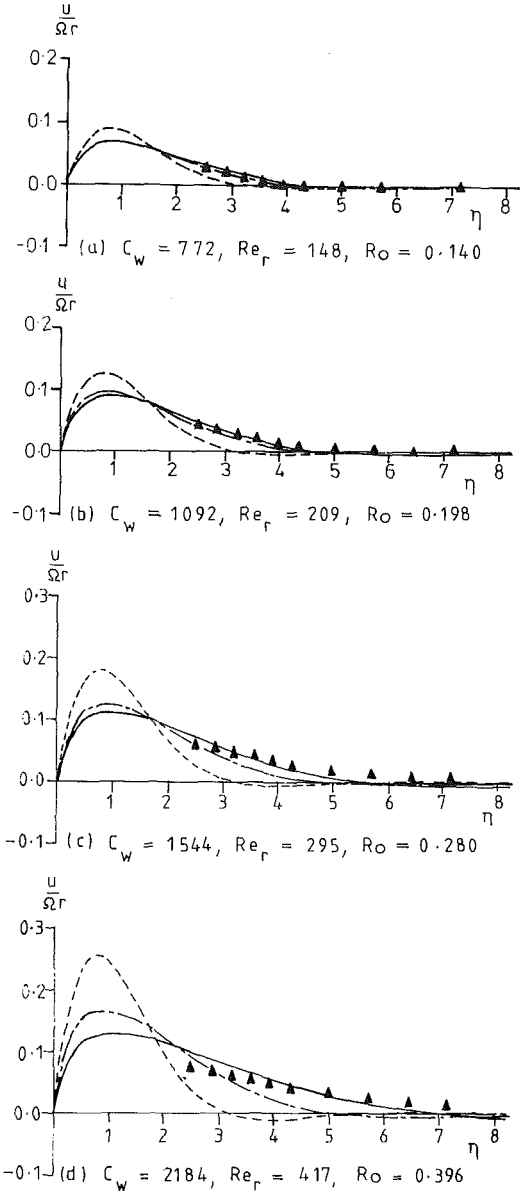

Fig. 10 Axial distribution of the radial component of velocity in the boundary layer for $Re_\phi = 4 \times 10^5$ at $x = 0.833$: ——— turbulent nonlinear solution; ——·—— turbulent "linear" solution; ···· laminar linear solution; ▲ Pincombe (1983)

can be seen that there is a comparatively large discrepancy between the turbulent solutions and the experimental data; the solutions of the turbulent momentum-integral equations by Owen et al. also showed a similar discrepancy. Although (to avoid confusion) the laminar curves are not shown in Fig. 5, for $C_w = 940$ the data were in fact bounded by the laminar and turbulent nonlinear curves. It would appear therefore that, for this condition, the flow is not fully turbulent.

The effect of Re_ϕ on the variation of $\bar{v}_\phi/\Omega r$ with C_w is shown in Figs. 6 and 7 for $x = 0.633$ and 0.833, respectively. In both cases, the agreement between the measured values and the nonlinear curves is mainly good, even in the source region. The linear curves tend to overestimate the laminar results and to underestimate the turbulent ones.

4.2 Radial Component of Velocity. Figures 8, 9, and 10 show the axial variation of the radial component of velocity for various values of C_w, Re_ϕ, and x. The turbulent curves fit the data better than do the laminar curves even when $Re_r < 180$!

For $Ro \leq 0.25$ (where $Ro = C_w/4\pi x^2 Re_\phi^{1/2}$), both the linear and nonlinear turbulent curves are in good agreement with the data. For the larger values of Ro, however, the nonlinear curves tend to overpredict; but they are in better agreement with the data than are the linear curves, which tend to underpredict both the magnitude of u and the thickness of the boundary layer.

5 Conclusions

The boundary-layer equations have been solved for a rotating cavity with a radial outflow of fluid. By neglecting the nonlinear inertial terms, the so-called linear Ekman-layer equations provide a simple description of the flow. For laminar flow, exact solutions of the Ekman-layer equations exist; for turbulent flow, the linear equations are easier to solve than are the full nonlinear boundary-layer equations. The latter were solved using a Cebeci–Smith effective-viscosity model and a Keller–Box numerical scheme. The problem of integrating the equations over regions of reverse flow has been successfully overcome.

For laminar flow ($Re_r < 180$), the nonlinear solutions tended to underpredict slightly the measured values of the tangential component of velocity, while the linear solutions tended to overpredict. For turbulent flow ($Re_r > 180$), the agreement

between the nonlinear solutions and the experimental data was, in the main, good; the turbulent linear theory tended to underpredict most of the measured values of the tangential components of velocity.

The radial components of velocity tended to be underpredicted by the laminar linear theory whereas the turbulent nonlinear theory provided a good fit to most of the data (even when $Re_r < 180$). The linear turbulent theory had a tendency to underpredict the measured radial components, particularly at the larger values of Rossby number ($Ro > 0.25$).

Acknowledgments

We wish to thank the Science and Engineering Research Council, Rolls-Royce plc, and Ruston Gas Turbines plc for supporting the work described in this paper. We are also grateful for the help received from our colleagues, particularly Drs. J. W. Chew, J. R. Pincombe, and R. H. Rogers.

References

Cebeci, T., and Smith, A. M. O., 1974, *Analysis of Turbulent Boundary Layers*, Academic Press, New York.

Chew, J. W., 1984, "Prediction of Flow in Rotating Disc Systems Using the k–ϵ Turbulence Model," ASME Paper no. 84-GT-229.

Chew, J. W., 1985, "Prediction of Flow in a Rotating Cavity With Radial Outflow Using a Mixing Length Turbulence Model," *Proc. 4th Int. Conf. on Num. Meth. in Laminar and Turbulent Flow*, Pineridge Press, United Kingdom, p. 318.

Chew, J. W., Owen, J. M., and Pincombe, J. R., 1984, "Numerical Predictions for Laminar Source-Sink Flow in a Rotating Cylindrical Cavity," *J. Fluid Mech.*, Vol. 143, p. 451.

Chew, J. W., and Rogers, R. H., 1988, "An Integral Method for the Calculation of Turbulent Forced Convection in a Rotating Cavity With Radial Outflow," *Int. J. Heat and Fluid Flow*, Vol. 9, p. 37.

Clauser, F. H., 1956, "The Turbulent Boundary Layer," *Advances in Applied Mechanics*, Vol. 4, p. 1.

Keller, H. B., and Cebeci,T., 1972, "Accurate Numerical Methods for Boundary-Layer Flows II: Two-Dimensional Turbulent Flows," *AIAA J.*, Vol. 10, p. 1193.

Morse, A. P., 1988, "Numerical Prediction of Turbulent Flow in Rotating Cavities," ASME JOURNAL OF TURBOMACHINERY, Vol. 110, pp. 202–212.

Northrop, A., and Owen, J. M., 1988, "Heat Transfer Measurements in Rotating-Disc Systems. Part II: The Rotating Cavity With a Radial Outflow of Cooling Air," *Int. J. Heat and Fluid Flow*, Vol. 9, p. 27.

Owen, J. M., Pincombe, J. R., and Rogers, R. H., 1985, "Source-Sink Flow Inside a Rotating Cylindrical Cavity," *J. Fluid Mech.*, Vol. 155, p. 233.

Pincombe, J. R., 1983, "Optical Measurements of the Flow in a Rotating Cylinder," D. Phil. Thesis, University of Sussex, United Kingdom.

Reyhner, T. A., and Flugge-Lotz, I., 1968, "The Interaction of a Shock Wave With a Laminar Boundary Layer," *Int. J. Non-linear Mech.*, Vol. 3, p. 173.

Shirazi, S. A., and Truman, C. R., 1988, "Prediction of Turbulent Source Flow Between Corotating Disks With an Anisotropic Two-Equation Turbulence Model," ASME JOURNAL OF TURBOMACHINERY, Vol. 110, pp. 187–194.

J. W. Chew
Rolls-Royce plc,
Derby, United Kingdom

P. R. Farthing

J. M. Owen

Thermo-Fluid Mechanics Research Center,
School of Engineering and
Applied Sciences,
University of Sussex,
Brighton, United Kingdom

B. Stratford
Rolls-Royce plc,
Derby, United Kingdom

The Use of Fins to Reduce the Pressure Drop in a Rotating Cavity With a Radial Inflow

A combined theoretical and experimental study of radial inflow through a rotating cavity is reported. It is shown that radial fins attached to one of the disks are effective in reducing the pressure drop across the cavity. The mathematical model is an extension of earlier plane-disk momentum-integral methods; the fins are treated as rectangular rib elements and a rough-disk model is derived. Numerical solutions of the integral equations are given. An approximate linear solution is also derived. Experiments were conducted when both disks were plane and when one of the disks was fitted with 60 radial fins. Flow visualization revealed the flow structure in the cavity and confirmed some of the assumptions used in the theoretical model. Measurements and predictions of the pressure drop across the cavity were in reasonable agreement.

Introduction

In a gas turbine engine, a small percentage of the mainstream air is bled off for cooling purposes. If this cooling air is extracted radially inward between a pair of corotating compressor disks, the resulting pressure drop can approach that of a free vortex. Various known design techniques may be used to reduce the pressure drop, but they do not necessarily suit every situation. In the present study, radial fins on one of the disks, as illustrated in Figs. 1 and 2, are used to prevent the formation of a free vortex. A theoretical model is developed to predict the pressure drop, and comparisons are made with measurements from a rotating-cavity rig.

A complete review of previous work will not be attempted here, but it is useful to indicate some of the most relevant contributions. Previous studies of radial inflow between corotating disks have concentrated on a rotating cylindrical cavity comprising two plane disks and a peripheral shroud through which the air entered the system. Typically, values of the ratios of inner to outer radii and of axial spacing to outer radius of order 0.1 have been studied. In this case the general flow structure is reasonably well established from flow visualization (Firouzian et al., 1985) and from numerical studies (Chew 1982, 1987; Morse 1988). As shown in Fig. 3, the flow comprises a source region near the shroud, separate Ekman-type layers on the disks, a sink layer near the outlet at the center of the cavity, and an interior core of rotating fluid. This flow structure occurs in both laminar and turbulent flow.

The extent of the different regions depends on the rotational speed, throughflow rate, and swirl of the fluid at inlet. At relatively high flow rates and low rotational speeds the source region will fill most of the cavity and the free vortex condition is approached. At low flow rates and high rotational speeds the moment on the disks reduces the angular velocity of the fluid as it moves radially inward and a forced vortex condition is approached. It should be noted that the recirculation, shown in the source region in Fig. 3, does not occur when the fluid enters the cavity with the same angular speed as that of the shroud.

The development of momentum-integral solutions for this

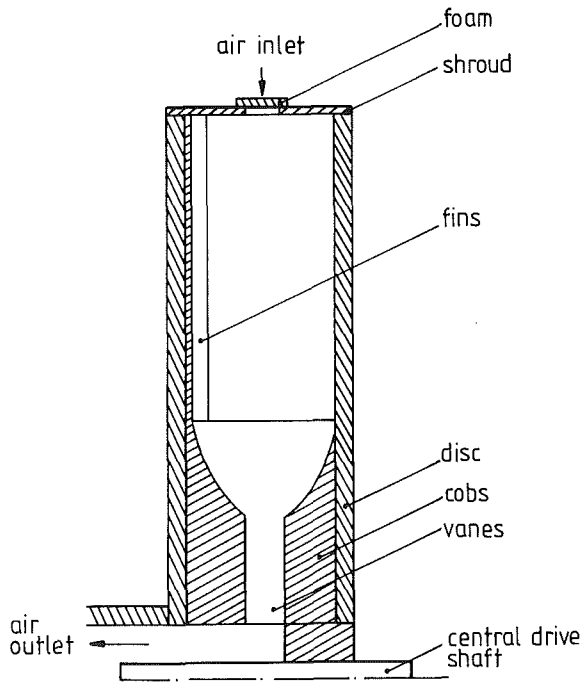

Fig. 1 Simplified diagram of the rotating-cavity rig

Contributed by the International Gas Turbine Institute and presented at the 33rd International Gas Turbine and Aeroengine Congress and Exhibition, Amsterdam, The Netherlands, June 5-9, 1988. Manuscript received by the International Gas Turbine Institute October 13, 1987. Paper No. 88-GT-58.

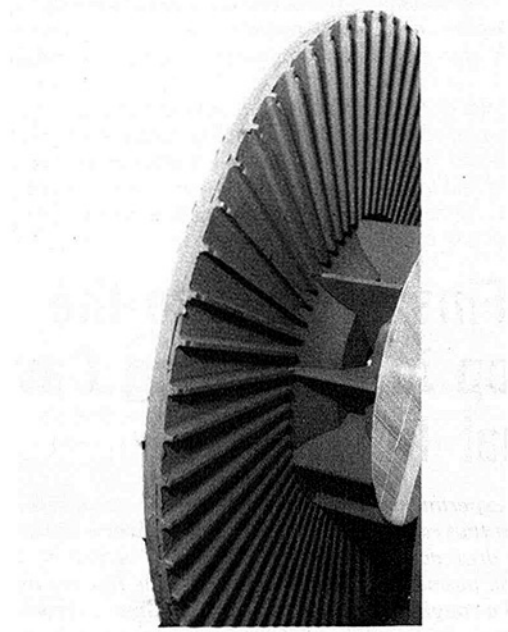

Fig. 2 The left-hand disk showing the fins and central vanes

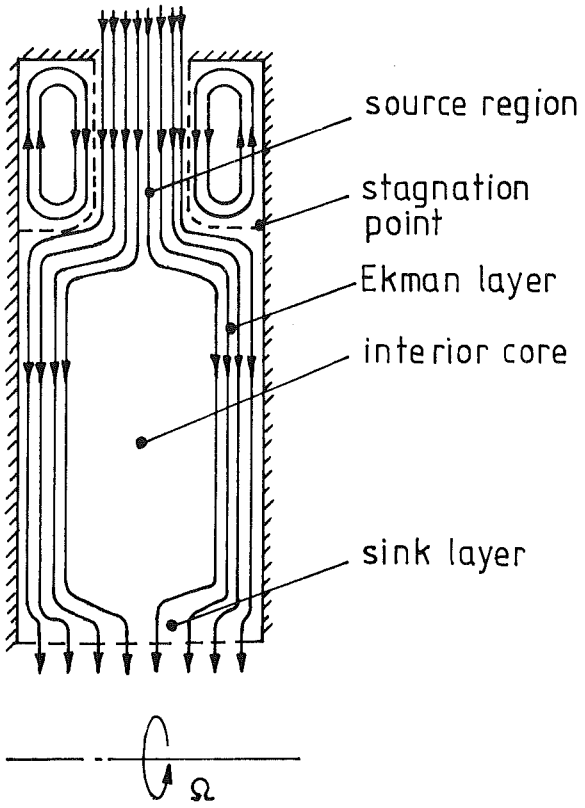

Fig. 3 Schematic diagram of a rotating cavity with radial inflow

class of flow in turbulent conditions is of particular relevance to the present contribution. Owen et al. (1985) have applied von Karman's (1921) integral method to the Ekman-type layers that develop on the disks in a rotating cavity. They derived analytically a linear Ekman-layer solution, which assumes the flow to be a small perturbation from solid body rotation, and also obtained numerical solutions of the full nonlinear integral equations. Predictions for the rotational velocity in the core region were found to be in good agreement with measurements for both radial outflow and inflow. The linear solution was shown to have a surprisingly wide range of validity, and the nonlinear solutions were found to be relatively insensitive to the choice of starting conditions.

Further experimental verification of the integral method was provided by Firouzian et al. (1986), who showed good agreement of core-velocity measurements with the nonlinear theory and reasonable agreement of pressure measurements with a simple model based on the linear solution. In a recent paper Chew and Rogers (1987) have extended the integral method to include treatment of the entraining bounday layer

Nomenclature

a = inner radius of disk
A = face area of fin
b = outer radius of disk
c = swirl fraction at inlet $= (v_\phi/\Omega r)_{r=b}$
C_p = pressure drop coefficient $= (p_b - p_a)/\frac{1}{2}\rho\Omega^2 b^2$
C_w = mass flow coefficient $= \dot{m}/\mu b$
F = friction factor
h = fin height
I = coefficient in momentum-integral equations
K = empirical constant in equation (2.13)
$\dot{m}$ = inlet mass flow rate
n = number of fins
p = static pressure
Q = volumetric flow rate
q = velocity distribution for flow over a flat plate
r = radial coordinate
Re_ϕ = rotational Reynolds number $= \Omega b^2/\nu$
s = axial spacing between disks
u = radial component of velocity
u_o = function of r in equation (2.1)
v = tangential component of velocity relative to disk
$\bar{v}$ = tangential component of velocity relative to disk outside the boundary layer
v_ϕ = tangential component of velocity in a stationary frame
x_e = nondimensional radius of source region $= r_e/b$
δ = boundary-layer thickness
ΔD = increase in drag caused by fin
ΔP_c = radial pressure drop across cavity
λ_L = laminar parameter $= C_w \mathrm{Re}_\phi^{-1/2}$
λ_T = turbulent parameter $= C_w\ \mathrm{Re}_\phi^{-4/5}$
μ = dynamic viscosity
ν = kinematic viscosity $= \mu/\rho$
ρ = density
$\tau_{\phi,o}$, $\tau_{r,o}$ = tangential and radial shear stress components on disk
ϕ = angular coordinate
Φ = nondimensional parameter $= (4bC_w/knh\mathrm{Re}_\phi)^{1/2}$
Ω = angular velocity of disk

Subscripts

a = inner radius of cavity
b = outer radius of cavity
c = outer edge of cobs
e = inner edge of source region
l = local value
L = leakage

in the source region, allowance for fluid property variations, and solution of an energy equation. This gives a more satisfactory starting condition for the nonlinear Ekman-type layer solution than was previously available and allows use of the method at engine conditions. Chew and Snell (1988) have applied this method to the prediction of radial inflow between corotating disks and present predictions of the pressure drop through the cavity in graphic form for the case where fluid enters the cavity with the same tangential velocity as the disk. Extension of the method to conditions where the inlet swirl is less than disk speed is possible but need not be discussed here as the experiments were designed to give equal fluid and disk tangential velocities at inlet.

2 Theory

2.1 General Considerations. With a finned-disk system, such as that shown in Fig. 2, the flow will obviously be three-dimensional and complex. Nevertheless, it is possible to make certain deductions about the flow from quite simple considerations. If the fins are sufficiently high compared with the plane-disk boundary-layer thickness, then viscous effects will be small. In rotationally dominated inviscid flow the radial pressure gradient is determined by the centripetal force term. Simple calculations also indicate that the tangential force exerted on the fluid by the fins will be much greater than that by the opposing plane disk. Thus, if fluid enters the cavity at disk speed, we would expect it to travel radially inward between the fins where the opposing centrifugal force is reduced. Ideally it might be supposed that the spaces between the fins would act rather like tubes and the resulting pressure distribution would be close to that of a forced vortex.

In practice, however, some interchange of fluid between the main part of the cavity and the inter-fin spaces will occur. This interchange will serve to equalize the radial pressure gradient in the interfin spaces with that in the main part of the cavity. A rotating core is expected to form next to the fins, similar in principle to that formed in plane disk flows but with a rotational speed closer to that of the rotor.

Despite the three-dimensional effects, the broad situation described above can be simulated by averaging the effect of the fins over the disk area and treating the problem as axisymmetric. In the model developed below the tangential force exerted on the fluid by the fins will be assumed to be principally a function of the velocity of the rotating core relative to the disk. This is considered to give a conservative estimate of the effects of the fins as it disregards the possibility of the tube-like behavior mentioned above. With these assumptions the integral method for plane disk flow can be quite naturally modified to the present situation. Treatment of the fins is similar to that of a rough disk, but with special consideration given to the tangential shear stress. The plane-disk theory will be summarized first.

2.2 The Integral Method for Plane Disks. The momentum-integral equations for plane-disk flow may be derived by integrating the full equations of motion across the disk boundary layer, or by considering mass and momentum balances on a control volume of vanishing radial thickness extending across the width of the boundary layer. Full details are given in the references mentioned above but the method is outlined here for completeness. The von Karman 1/7th power law assumptions for the velocity profiles are

$$u = u_0(1 - z/\delta)(z/\delta)^{1/7}, \quad v = \bar{v}(z/\delta)^{1/7} \tag{2.1}$$

where u and v are the radial and tangential velocity components in a cylindrical coordinate system (r, ϕ, z) rotating with the disk at $z = 0$. δ denotes the boundary-layer thickness, u_0 is a function of r only, and $\bar{v}$ is the tangential velocity at the boundary-layer edge $z = \delta$. Using the above profiles the radial and tangential momentum-integral equations may be written

$$\frac{I_2}{r}\frac{d}{dr}(r\rho u_0^2\delta) + \frac{\rho}{r}\delta\bar{v}^2 I_5 + 2\rho\delta\bar{v}\Omega I_4 = -\tau_{r,0} \tag{2.2}$$

$$\frac{I_3}{r^2}\frac{d}{dr}(r^2\rho u_0\bar{v}\delta) - \frac{I_1\bar{v}}{r}\frac{d}{dr}(r\rho u_0\delta) + 2I_1\rho u_0\Omega\delta = -\tau_{\phi,0} \tag{2.3}$$

Here Ω is the angular velocity of the disk, $\tau_{r,0}$ and $\tau_{\phi,0}$ are the radial and tangential shear stresses on the disk, and ρ denotes fluid density. The coefficients I are given by

$$I_1 = \frac{49}{120}, \quad I_2 = \frac{343}{1656}, \quad I_3 = \frac{49}{144}, \quad I_4 = \frac{1}{8}, \quad I_5 = \frac{2}{9} \tag{2.4}$$

Equations (2.2) and (2.3) are derived assuming u_0, δ, $\bar{v}$, and ρ are unknown functions of r, and ρ is obtained from the equations of state. A further equation is needed to close the problem; this is provided by either $\bar{v}$ being known as in the source region (where $r(\bar{v} + \Omega r)$ is constant as in a free vortex) or the mass flow in the boundary-layer being known as in the Ekman-type layers.

For plane disks the following formulae, based on Blasius' expression, have been used for the wall shear stress:

$$\tau_{\phi,0} = 0.0225\rho\left(\frac{\nu}{\delta}\right)^{1/4}\bar{v}[u_0^2 + \bar{v}^2]^{3/8} \tag{2.5}$$

$$\tau_{r,0} = 0.0225\rho\left(\frac{\nu}{\delta}\right)^{1/4}u_0[u_0^2 + \bar{v}^2]^{3/8} \tag{2.6}$$

where ν is the kinematic viscosity of the fluid. Substituting from these expressions into equations (2.2) and (2.3) and nondimensionalizing, it may be shown that for radial inflow with fluid entering the cavity at disk speed, the solution of the integral equations for uniform-property flow will depend on just two nondimensional variables. These are the inner-to-outer radius ratio a/b, and the group $\dot{m}/\rho\nu^{0.2}\Omega^{0.8}b^{2.6}$, where $\dot{m}$ is the net mass flow rate. The latter group is denoted by λ_T and may be written $C_w/\mathrm{Re}_\phi^{4/5}$ where $C_w = \dot{m}/\mu b$ is a mass flow parameter and $\mathrm{Re}_\phi = \Omega b^2/\nu$ is a rotational Reynolds number.

2.3 Extension of the Model to Finned Disks. In modeling the finned disk, equations (2.2) and (2.3) are assumed to hold but $\tau_{\phi,0}$ is taken to represent the tangential force per unit area exerted by the fins rather than the disk shear stress. The use of equation (2.1) for the velocity profiles is clearly questionable but, if $\tau_{\phi,0}$ is estimated correctly, this model can be expected to give a reasonable guide to the likely effect of the fins.

In the course of the present investigation several methods of estimating $\tau_{\phi,0}$ were tried. Initially, to obtain a quick result, a constant multiplying factor was introduced into equation (2.5). Considering the drag of each fin to be similar to that of a flat plate in a free stream, values of order 100 were estimated for this factor. After further consideration the treatment of the tangential shear stress was modified; first the finned disk was treated as a rough surface and secondly a method based on Wieghardt's (1953) measurements on single roughness elements on a flat plate (as reported by Schlichting, 1979) was used to estimate the disk friction factor. All the methods gave broadly similar results and so only the final formulation will be described here.

By analogy with treatment of flow in pipes and over flat plates (e.g., Schlichting)

$$\tau_{\phi,0} = F\frac{1}{2}\rho\bar{v}^2 \tag{2.7}$$

For smooth surfaces F is a function of local Reynolds number, but for a uniformly very rough surface F will be constant. In

the present model $\tau_{\phi,0}$ represents the tangential force on the fins averaged over the disk area, with frictional effects being neglected. The drag on the fins is estimated from Wieghardt's results for single rectangular rib elements. For a thin element Wieghardt's results are represented by

$$\frac{\Delta D}{A} \simeq 1.3 \frac{\rho}{2} \frac{1}{h} \int_0^h q^2 dz \tag{2.8}$$

where ΔD, A, h, z, and q are the drag, the frontal area of the element, height of the element, distance normal to the wall, and the velocity distribution for a smooth wall. Applying this result to each fin, summing the drag over all the fins, and equating this drag to a tangential shear stress on an "equivalent" rough disk gives

$$F = \frac{1.3nh}{2\pi r} \int_0^h \left(\frac{v}{\bar{v}}\right)^2 \frac{dh}{h} \tag{2.9}$$

In deriving this equation, the smooth-wall velocity distribution in equation (2.8) has been replaced by the tangential velocity distribution for the equivalent rough disk. Note that if the boundary-layer thickness δ is small compared to the fin height h, this result is equivalent to estimating the drag on each fin as for a flat plate in the free stream with a drag coefficient of 1.3; such a value of the drag coefficient is reasonable (e.g., Massey, 1979). In fact even when $\delta = h$ the presence of the integral in equation (2.9) reduces F by just 22 percent (assuming a 1/7th power-law velocity profile).

It is informative to consider the dimensional analysis of the integral equation for the finned disk. It is reasonable to assume that the radial shear stress given by equation (2.6) will be small compared with $\tau_{\phi,0}$ given by equation (2.7). It may then be deduced that, provided δ/h is small, instead of the parameter λ_T that occurs for plane disks, the pressure coefficient will depend on the ratio of a representative fluid radial velocity to disk tangential velocity, without reference to viscosity or Reynolds number; nevertheless, it is convenient to retain the ratio C_w/Re_ϕ. Although viscosity is present in the definitions of C_w and Re_ϕ, it cancels when the ratio is taken, so that C_w/Re_ϕ is proportional to a velocity ratio multiplied by the nondimensional fin height h/b. A further nondimensional group nh/b is also introduced through equation (2.9). When the inlet swirl is close to disk speed, the size of the source region can be expected to be small and then the dependence on C_w/Re_ϕ and nh/b will be through the group $bC_w/nh\ \mathrm{Re}_\phi$ only.

2.4 Numerical Solution of the Equations. Numerical solutions of the integral equations (2.2) and (2.3) are presented below. These were obtained using a standard ordinary-differential-equation solver as described in earlier studies. Starting values for the dependent variables are specified to give a very small boundary-layer mass flow and thickness as has been done previously for radial outflow between corotating disks. It was further assumed that the tangential force from the fins was much greater than the tangential shear stress of the facing plane disk, or, equivalently, the radial inflow on the plane disk was neglected. This assumption, which was subsequently verified by flow visualization as described below, allowed the existing plane-disk computer program to be easily adapted to solve the finned disk problem.

To compare predictions with the measurements it was also necessary to estimate the pressure field on the flow downstream of the fins in the innermost part of the cavity. For the experiments without the central vanes fited (see Fig. 1) the pressure drop across this region was estimated from an integral solution for flow between plane disks using a "mixed-out" mean value of the tangential component of velocity immediately downstream of the finned part of the disk to give inlet conditions. Some uncertainty regarding the flow in this region must be recognized. For the experiments with central vanes the pressure drop across this region was assumed to be that of a forced vortex. Thus the central region has less effect on the overall pressure drop, and the corresponding experiments were considered to be a better test of the finned-disk model.

2.5 Linear Solution. In this section an approximate analytical solution, analogous to Owen et al.'s (1985) linear Ekman-layer solution in plane-disk flow, is derived. Treating the flow as a small perturbation from solid-body rotation, equation (2.3) approximates to

$$2I_1 \rho U_0 \Omega \delta = -F \frac{1}{2} \rho \bar{v}^2 \tag{2.10}$$

where $\tau_{\phi,0}$ has been evaluated using equation (2.7). In terms of the local volumetric flow rate entrained by the finned disk equation (2.10) may be written as

$$\frac{\Omega Q_l}{\pi r} = -\frac{F}{2} \bar{v}^2 \tag{2.11}$$

where Q_l is negative for radial inflow.

For the particular case of interest, flow enters the cavity at $r = b$ with a tangental velocity equal to disk speed, and in the source region $\bar{v}$ is given by the free-vortex relation. In this region equation (2.11) then gives

$$Q_l = -\frac{\pi F}{2} \left[\left(\frac{b}{r}\right)^2 - 1\right]^2 \Omega r^3 \tag{2.12}$$

Assuming the tangential force on each fin to be proportional to $\bar{v}^2$, the following formula for F may be deduced:

$$F = Knh/2\pi r \tag{2.13}$$

where K is a constant of order unity. Substituting equation (2.13) into (2.12) gives

$$Q_l = -\frac{Kn}{4} \left[\left(\frac{b}{r}\right)^2 - 1\right]^2 \Omega h r^2 \tag{2.14}$$

The source region ends at $r = r_e$ where all the available fluid has been entrained into the passages of the finned disk. As in the previous section, the flow in the boundary layer on the plane disk is neglected, and it follows that

$$r_e/b = \frac{1}{2} [(\Phi^2 + 4)^{1/2} - \Phi] \tag{2.15}$$

where

$$\Phi = \left(\frac{4b}{Knh} \frac{C_w}{\mathrm{Re}_\phi}\right)^{1/2} \tag{2.16}$$

For $r < r_e$, downstream of the source region, equation (2.11) with $Q_l = Q$ is used to calculate $\bar{v}$. Using equation (2.13) for F gives

$$\frac{v}{\Omega b} = \Phi \tag{2.17}$$

The radial pressure gradient is calculated from the radial momentum equation in the core, which is

$$\frac{1}{\rho} \frac{dp}{dr} = \frac{(\bar{v} + \Omega r)^2}{r} \tag{2.18}$$

For the tests in which central vanes were fitted a forced vortex is assumed for $a \le r \le r_c$, where r_c is the outer radius of the vanes. The pressure drop in the region $r_c \le r \le r_e$ is obtained from equations (2.17) and (2.18), and the free-vortex relationship is used in the source region, $r_e \le r \le b$. The resulting expression for the pressure drop coefficient across the cavity is

$$C_p = \left[\left(\frac{b}{r_e}\right)^2 - 1\right] + \left[\left(\frac{r_e}{b}\right)^2 - \left(\frac{a}{b}\right)^2\right] + 4\Phi \left[\frac{r_e}{b} - \frac{r_c}{b}\right] + 2\Phi^2 \ln\left(\frac{r_e}{r_c}\right) \tag{2.19}$$

where r_e and Φ are calculated from equations (2.15) and (2.16).

3 Experimental Apparatus

3.1 Rotating-Cavity Rig. A simplified section through the finned-disk rotating cavity is shown in Fig. 1.

The cavity was formed from two steel disks 762 mm in diameter and a peripheral shroud 1.5 mm thick made from Paxolin. The shroud contained 30 holes 28.6 mm in diameter, located in the midaxial plane, covered with porous foam to ensure that the air entered the cavity with a swirl fraction of unity (that is, the tangential speed of the air was equal to that of the shroud). There was a drive shaft 25 mm in diameter at the center of the cavity, and the air left the system through an annular hole, with inner and outer diameters of 25 and 76 mm, in the left-hand disk.

"Cobs" (that is, bulbous hubs) made from Rohacell, a lightweight high-strength foam material, were attached to the center of each disk: These were identical to those used by Farthing and Owen (1988) for heat transfer tests with radial outflow. The minimum axial spacing between the cobs was 28 mm, and the parallel section, which extended to a radius of 107 mm, was blended into the plane disk at a radius of 168 mm.

Sixty radial fins were attached to the plane section of the left-hand disk, extending from $r = 168$ to $r = 381$ mm. The fins, which were made from 5-mm-thick Rohacell, were of rectangular section with an axial height of 10 mm. The axial clearance between the end of the fins and the right-hand disk was 87 mm. In addition, ten radial vanes made from 5-mm-thick Rohacell extended axially across the space between the two cobs from $r = 38$ to $r = 168$ mm. The finned disk and central vanes are shown in Fig. 2.

The air flow was supplied from a centrifugal compressor capable of producing one kg/s at a pressure ratio of 1.4:1. PTFE seals were fitted between the rotating tube attached to the left-hand disk and the stationary piping attached to the compressor inlet. However, as discussed below, some air leaked into the system (which was at subatmospheric pressure) through the seals.

The cavity assembly could be rotated at speeds up to 2000 rev/min by a variable-speed electric motor and toothed-belt drive.

3.2 Instrumentation. The radial pressure drop across the cavity was measured using a static-pressure tap attached to the stationary piping immediately downstream of the left-hand disc. As discussed in Section 5, this measurement included not only the pressure drop across the cavity itself but also the "inlet and exit losses." The resulting overall pressure drop was measured by means of either a water-filled micromanometer with a resolution of ± 0.1 mm or, for the higher pressures, a mercury-filled manometer with a resolution of ± 1 mm.

The flow rate of the air was measured using Annubar differential-pressure devices in the stationary piping between the cavity and the compressor inlet. Although the overall flow rate could be measured to an accuracy of approximately ± 3 percent, the leakage through the seals, referred to above, reduced the effective accuracy. From a series of calibrations, it was found that this leakage flow rate, Q_L, was proportional to $\Delta P_c^{1/2}$, where ΔP_c was the pressure difference indicated by the pressure tap downstream of the cavity. Q_L was found to be independent of rotational speed, and the measured flow rate was corrected to allow for the leakage. For the tests with the fins and central vanes the maximum leakage was 15 percent of the measured flow rate, but for some tests with only the fins fitted the leakage was greater than this.

The rotational speed of the cavity was measured to an accuracy of ± 1 rev/min by a magnetic transducer and a timer-counter.

For flow visualization, a 4 W argon-ion laser and cylindrical lens were used to produce a flat sheet of light, which illuminated the r–z plane of the cavity (corresponding to that shown in Fig. 1). A smoke generator produced clouds of micron-sized oil particles, which, when released into the air in the laboratory, were drawn into the cavity by the compressor referred to above. Photographs and video recordings were taken and used to study the flow structure, as described below. It should be noted that the holes in the transparent polycarbonate shroud used for the flow visualization were 11 mm in diameter. The larger hole foam-covered shroud restricted the optical access into the cavity.

4 Flow Visualization

4.1 Flow Structure. Figures 4 to 6 show photographs taken using the flow-visualization apparatus referred to in Section 3. Interpretation of the flow structure is aided by reference to Fig. 3: The bottom of each photograph corresponds to the center-line of the cavity, and the top to the shroud. The fins, on the left-hand side, and the cobs, near the center, stand out as black regions in constrast to the white smoke-filled areas. A number of photographs was taken as soon as the smoke entered the cavity, and the notation (*i*), (*ii*), and (*iii*) refers to the photographs taken at different times but at the same flow conditions.

Figure 4 shows photographs taken for $C_w = 100$ and $\mathrm{Re}_\phi = 3 \times 10^4$ (laminar flow) with the opaque foam removed from the shroud. (While the foam was fitted during the pressure tests, its removal facilitated interpretation of the photographs.) In frame (*i*), the white source region near the shroud is clearly visible, and smoke is beginning to fill the boundary layers and sink region. The flow rates in the boundary layers on the two disks are clearly unequal; most of the smoke reaches the sink from the finned disk rather than from the plane disk. In frames (*ii*) and (*iii*), as smoke continues to fill the cavity, a compound structure becomes evident; there appears to be an inner and an outer source-sink flow with the sink region for the outer part of the cavity acting as a source region for the flow between the cobs. An inviscid core (appearing as a black region) is present between the

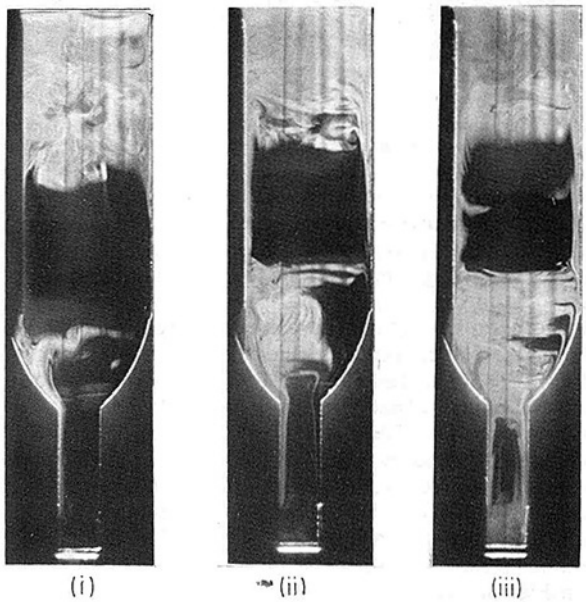

Fig. 4 Laminar flow in the finned-disk cavity for $C_w = 100$, $\mathrm{Re}_\phi = 3 \times 10^4$ (no foam rubber on shroud)

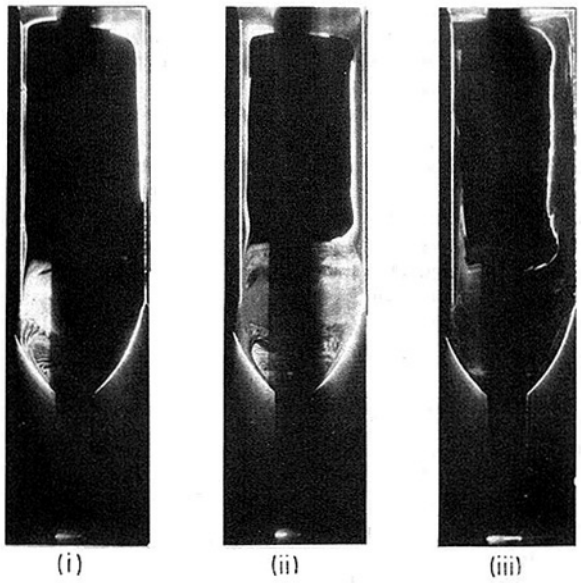

Fig. 5 Laminar flow in the finned-disk cavity for $C_w = 100$, $Re_\phi = 3 \times 10^4$ (foam rubber on shroud)

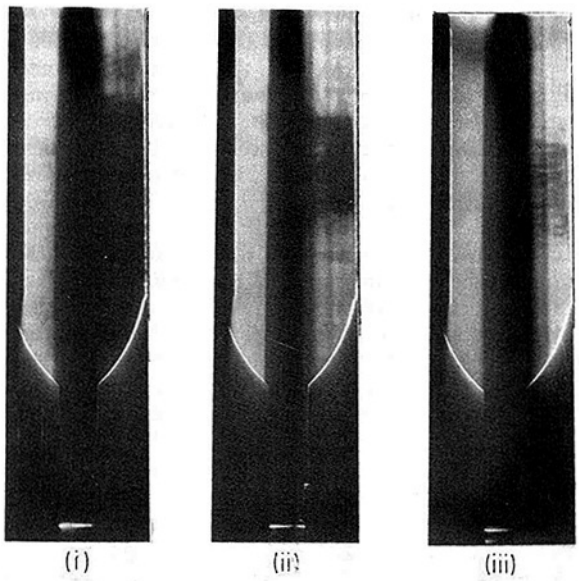

Fig. 6 Turbulent flow in the finned-disk cavity for $C_w = 2700$, $Re_\phi = 2 \times 10^5$ (foam rubber on shroud)

boundary layers on the disks, and another core can be seen between the boundary layers on the cobs.

Figure 5 shows photographs taken at the same values of C_w and Re_ϕ as for Fig. 4 but with the foam in place on the shroud. As a consequence, a black band appears through the middle of the photographs, and the flow between the cobs can no longer be seen. As the foam creates solid-body rotation at inlet to the cavity, the source region (which is visible near the shroud on either side of the black band) is significantly smaller than for the previous case. There is still evidence of an inviscid core between the boundary layers on the two disks, and frame (*i*) shows that smoke reaches the sink region more rapidly from the finned disk. Referring to frame (*iii*), the apparent thickening of the boundary layer on the plane disk is attributed to a weak axial flow toward the finned disk.

In Fig. 6, where $C_w = 2700$ and $Re_\phi = 2 \times 10^5$, the flow is turbulent throughout the cavity. At this relatively high flow rate, smoke penetrates very quickly and so it is more difficult

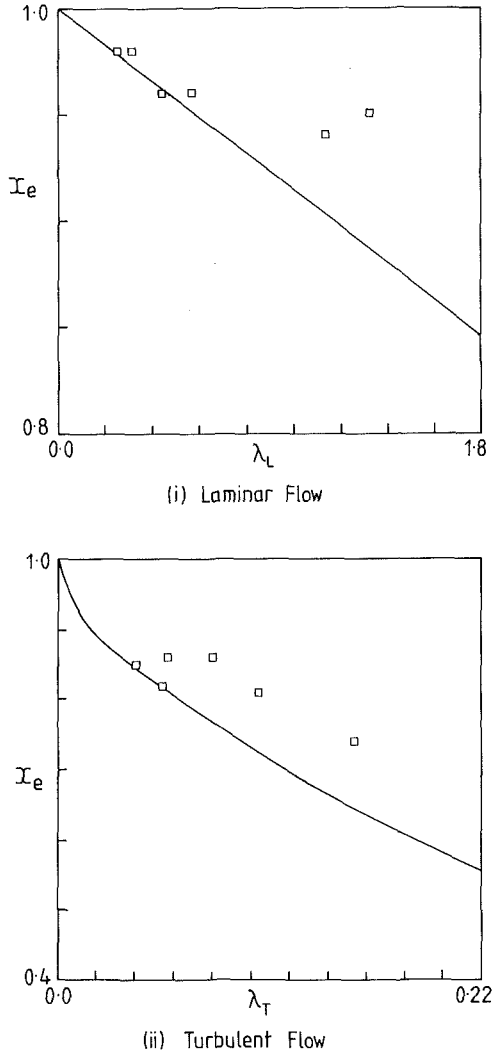

Fig. 7 Size of source region for the finned-disk cavity: □ measured values; _____ equation (4.1) with $c = 1$

to determine the flow structure. However, to the right of the black band created by the foam, there is evidence of source and sink regions, with boundary-layer flow on the plane disk and an adjacent inviscid core. It is also apparent that, as for laminar flow, the flow rate is much larger on the finned disk.

4.2 Size of the Source Region. Firouzian et al. (1985) measured the radial extent, r_e, of the source region for radial inflow in a rotating cavity with plane disks. The measurements correlated closely with their theoretical model, which assumed that the source region ends when all the fluid has been entrained into the boundary layers on the disks. Using linear Ekman-layer theory for the boundary layers, and assuming free-vortex flow in the source region, the nondimensional radius x_e, which marks the edge of the source region, is given by

$$x_e = \left(c - \frac{1}{2\pi}|\lambda_L|\right)^{1/2} \tag{4.1a}$$

for laminar flow, and

$$x_e = (c - 2.22\,|\lambda_T|^{5/8} x_e^{3/8})^{1/2} \tag{4.1b}$$

for turbulent flow, where $\lambda_L = C_w Re_\phi^{-1/2}$, $\lambda_T = C_w Re_\phi^{-4/5}$, and c is the swirl fraction.

Figure 7 shows a comparison between the values of x_e obtained from flow visualization with the foam-covered shroud and equation (4.1) with $c = 1$ (corresponding to solid-body

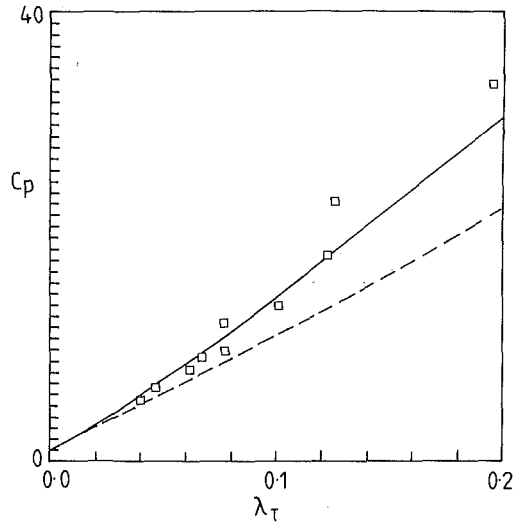

Fig. 8 The variation of C_p with λ_T for the plane-disk cavity: — — — linear theory; ——— nonlinear theory; □ experimental results

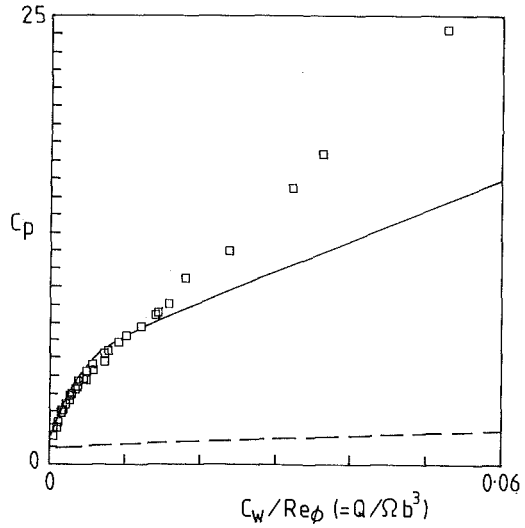

Fig. 9 The variation of C_p with $C_w Re_\phi^{-1}$ for the finned-disk cavity without central vanes: □ measurements; ——— nonlinear theory; — — — component of C_p from finned part of cavity (theory)

rotation at the inlet). For both laminar and turbulent flow, the measured values of x_e tend to be larger (that is, the radial thickness of the source region is smaller) than the theoretical values for plane disks. This is consistent with the fact that the entrainment rate of the finned disk is greater than that of the plane disk. As the size of the source region varied from one side of the cavity to the other, an average value was used.

5 Pressure Measurements

5.1 Tests With the Plane-Disk Cavity. As mentioned in Section 3.2, the measured pressure difference included the radial pressure drop across the cavity together with the "inlet and exit losses." The losses represented the pressure drops across the shroud and those through the outlet of the cavity from the rotating to the stationary pipes upstream of the static-pressure tap. Firouzian et al. (1985), using basically the same rig as that employed in the current tests, estimated the inlet and exit losses by measuring the overall pressure drop with the cavity stationary. Assuming that the losses were not significantly affected by rotation, they subtracted their correlated pressure losses from the overall pressure drop measured when the cavity was rotating. As these "corrected" pressure drops across the rotating cavity were in mainly good agreement with theoretical values, obtained from solutions of the linear Ekman-layer equations, it was concluded that the "corrections" were reasonable.

Since, with the present rig, it was not possible to estimate the inlet and exit losses when the cavity was rotating, the technique described above was used. The pressure losses were found to be proportional to C_w^2, and it was easy to obtain correlations with which to correct the pressure measurements obtained for the rotating cavity. These correlations were obtained for the plane-disk and for the finned-disk cavities, and for both cases the holes in the shroud were covered with porous foam.

Figure 8 shows the variation of the pressure coefficient C_p (based on the corrected pressure measurements) with λ_T for the plane disk cavity. According to the integral theory for turbulent flow, C_p is a function of λ_T for these conditions. Firouzian et al.'s linear integral solution and Chew and Snell's (1988) numerical solution of the full nonlinear integral equations are shown in this figure. It can be seen that, in the main, the nonlinear curve is in good agreement with the measured data, whereas the linear curve tends to underpredict. These

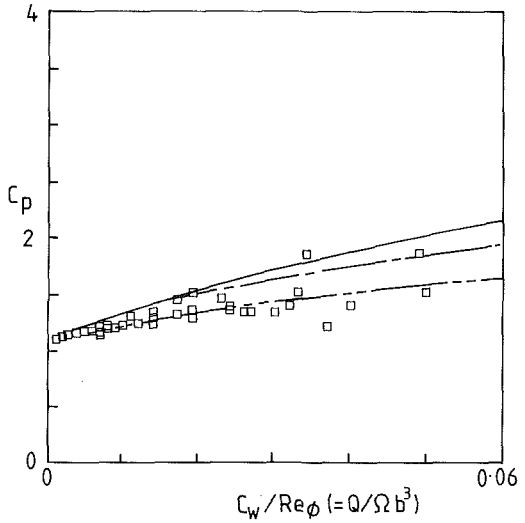

Fig. 10 The variation of C_p with $C_w Re_\phi^{-1}$ for the finned-disk cavity with central vanes: □ measurements; ——— nonlinear theory; — — — — linear theory $k = 1.0$; — — — — linear theory $k = 2.0$

results provide some reassurance that the corrections referred to above are reasonable.

It can be seen from Fig. 8 that C_p increases significantly as λ_T increases. If the fluid in the cavity were in solid-body rotation then $C_p \simeq 1$. Thus, with no fins in the cavity, values of C_p more than thirty times that associated with solid-body rotation have been predicted and measured!

5.2 Tests With the Finned-Disk Cavity. Tests were conducted for $0.15 < C_w/10^4 < 1$ and $0.1 < Re_\phi/10^6 < 2$ with the 60 fins fitted and for $0.1 < Re_\phi/10^6 < 1$ with the fins and central vanes. Corrected pressure coefficients were determined for both cases, and the results are plotted in Figs. 9 and 10.

Results without the central vanes fitted are shown in Fig. 9, together with the theoretical predictions. As expected, the integral solution was found to depend only on C_w/Re_ϕ for these conditions. The measurements confirm this result but show quantitative disagreement with the theory at the higher values of C_w/Re_ϕ. The theoretical results show that the bulk of the

pressure drop occurs in the inner part of the cavity, downstream of the fins, where a free vortex forms.

The component of C_p representing the relatively small pressure drop across the finned part of the cavity is shown in Fig. 9. It should be noted that use of the fins has reduced the pressure drop across the cavity so that the inlet and exit correction is a much greater proportion of the total pressure drop than for the plane-disk cavity. For example, for the result at $C_w/\mathrm{Re}_\phi \simeq 0.05$, the correction is of similar magnitude to the difference between theory and measurement. Also, the high tangential velocity of the fluid at the exit, which is not accounted for in this correction, may well affect the exit losses.

The above considerations led to the series of tests with the central vanes, for which the results are shown in Fig. 10. Clearly the central vanes are effective in eliminating the free vortex at the inner radii, and the measured values of C_p are much less than in the earlier tests. These results are considered to be a more reliable test of the theoretical treatment of the finned disk than those in Fig. 9. Some scatter of the measurements is apparent but generally, considering the simplifications in the theory and the experimental difficulties, the agreement between the nonlinear theory and the measurements is reasonable. As stated in section 2.1, this theory was intended to give a conservative estimate of the effect of the vanes.

Also shown in Fig. 10 are the values of C_p obtained from the linear theory described in section 2.5. The curves are based on equation (2.19) using values of $K=1$ and 2 in equation (2.16), and it can be seen that a value of $K=2$ provides the better fit to the experimental data. Obviously some uncertainty remains regarding the expression used to estimate the tangential force on the fins, but the above theory has been reasonably successful in predicting the overall pressure drop.

6 Conclusions

It has been shown both theoretically and experimentally that radial fins attached to one of the disks in a rotating cavity are effective in reducing the pressure drop associated with radial inflow.

A mathematical model has been developed using the momentum-integral equations for the boundary layers on the disks. For plane disks, 1/7th power-law velocity profiles were used in conjunction with the Blasius skin-friction relationships for turbulent flow. For the finned disks, the radial fins were treated as "rib-roughness" elements. The full integral equations have been solved numerically, and an approximate linear solution has been derived that gives a simple expression for the pressure coefficient.

Flow visualization and pressure measurements have been carried out in a rotating cavity with a radial inflow of air. The cavity tested comprised two disks, with inner and outer diameters of 76 and 762 mm, and a peripheral porous shroud. Cobs were attached to the center of each disk, and 60 radial fins extending from the outer edge of the cob to the shroud could be fitted to one of the disks. In addition, ten radial vanes could be fitted between the two cobs at the center of the cavity. Tests were conducted for a range of flow rates and rotational speeds: $0.1 < C_w/10^4 < 1$ and $0.1 < \mathrm{Re}_\phi/10^6 < 2$.

Flow visualization revealed that the basic flow structure for the finned-disk cavity was similar to that observed in earlier tests for the plane-disk case; there was a source region near the shroud, boundary layers on the two disks, a sink region near the center of the cavity, and an interior core of inviscid fluid. However, unlike the earlier plane-disk case, for the finned-disk cavity the flow was not equally divided between the two boundary layers: Most of the radial inflow occurred on the finned disk. The source region was smaller and the flow in the sink region was more complex.

The measured radial pressure drop across the cavity was empirically corrected for "inlet and exit losses." For the plane-disk case, the pressure coefficient increased as $C_w\mathrm{Re}_\phi^{-4/5}$ increased; the corrected pressures were in good agreement with the nonlinear theory, and pressure drops over 30 times those associated with solid-body rotation were predicted and measured. With the fins and vanes fitted, the maximum pressure coefficient was only about twice that associated with solid-body rotation.

Considering the approximations made in the theory and the uncertainties in the experiments, agreement between the theory and the measurements is remarkably good. It is also worth pointing out that the nonlinear theory was developed in advance of the experiments, and the flow visualization and pressure measurements have confirmed many of the assumptions made. This gives some confidence in our understanding of the flow and enables us to extrapolate to engine conditions.

Acknowledgments

The authors wish to thank the Science and Engineering Research Council, Rolls Royce plc, and Ruston Gas Turbines plc for sponsoring the research described in this paper.

References

Chew, J. W., 1982, "Computation of Flow and Heat Transfer in Rotating Cavities," D. Phil. thesis, University of Sussex, United Kingdom.

Chew, J. W., 1987, "Computation of Flow and Heat Transfer in Rotating Disk Systems," *Proc. of the 2nd ASME-JSME Thermal Engineering Joint Conf.*, Vol. 3, pp. 361–367.

Chew, J. W., and Rogers, R. H., 1987, "An Integral Method for the Calculation of Turbulent Forced Convection in a Rotating Cavity With Radial Outflow," *Int. J. Heat and Fluid Flow*, Vol. 9, pp. 37–48.

Chew, J. W., and Snell, R. J., 1988, "Prediction of the Pressure Distribution for Radial Inflow Between Co-rotating Discs," ASME Paper No. 88-GT-61.

Farthing, P. R., and Owen, J. M., 1988, "The Effect of Disk Geometry on Heat Transfer in a Rotating Cavity With a Radial Outflow of Fluid," ASME *Journal of Engineering for Gas Turbines and Power*, Vol. 10, pp. 70–77.

Firouzian, M., Owen, J. M., Pincombe, J. R., and Rogers, R. H., 1985, "Flow and Heat Transfer in a Rotating Cavity With a Radial Inflow of Fluid. Part 1: The Flow Structure," *Int. J. Heat and Fluid Flow*, Vol. 6, pp. 228–234.

Firouzian, M., Owen, J. M., Pincombe, J. R., and Rogers, R. H., 1986, "Flow and Heat Transfer in a Rotating Cavity With a Radial Inflow of Fluid. Part 2: Velocity, Pressure and Heat Transfer Measurements," *Int. J. Heat and Fluid Flow*, Vol. 7, pp. 21–27.

Karman, T. von, 1921, "Uber laminare und turbulente Reibung," *Z. angew. Math. Mech.*, Vol. 1, pp. 233–252.

Massey, B. S., 1979, *Mechanics of Fluids*, 4th ed., van Nostrand Reinhold Company, New York, p. 310.

Morse, A. P., 1988, "Numerical Prediction of Turbulent Flow in Rotating Cavities," ASME JOURNAL OF TURBOMACHINERY, Vol. 110, pp. 202–212.

Owen, J. M., Pincombe, J. R., and Rogers, R. H., 1985, "Source-Sink Flow Inside a Rotating Cylindrical Cavity," *J. Fluid Mech.*, Vol. 155, pp. 233–265.

Schlichting, H., 1979, *Boundary Layer Theory*, 7th ed., McGraw-Hill, New York, p. 655.

Wieghardt, K., 1953, "Erhohung des Turbulenten reibungswiderstandes durch oberflachen storungen," *Forschungshefte für Schiffstechnik*, Vol. 1, pp. 65–81.